Interpreting Wave Propagation in a Homogeneous, Isotropic, Steel Cylinder

By

Darryl Keith Stoyko, B.Sc. (ME), EIT

A Thesis submitted to the Faculty of Graduate Studies in partial fulfilment of the requirements for the degree of

Master of Science

Department of Mechanical and Manufacturing Engineering
University of Manitoba
Winnipeg, Manitoba, Canada

Abstract

The majority of commercially available ultrasonic transducers used to excite and measure wave propagation in structures can be coupled only to a free surface. While convenient, this method is likely to excite multiple structural modes, making data interpretation difficult. Furthermore, the many modes excited make predicting the structure's response a computationally intensive task. Here the dynamic radial displacement induced by a transient radial point load is calculated at more than 230,000 points on the outer surface of a virgin steel pipe to simulate a typical experiment. The radial component of the displacement field is calculated by convolving the Green's functions of the pipe with the transient load. These functions are calculated on personal computers (in a distributed arrangement) by employing modal summation. The mode shapes are obtained from a Semi-Analytical Finite Element formulation used in conjunction with a separation of variables. The results are presented in a four dimensional animation, providing easier interpretations and insight into how to best select observation points for the detection of defects. The accuracy of the calculated displacements is verified experimentally. Agreement is good when magnitude and phase corrections are incorporated from the frequency response curves of the transducers used.

Acknowledgements

I wish to thank my examining committee, Dr. N. Popplewell, Dr. A. Shah and Dr. S. Balakrishnan, for their guidance, encouragement and support. The suggestions, assistance and encouragement provided by my colleagues Dr. H. Bai, Mr. A. Mahmoud and Mr. A. Rattan were invaluable. The assistance of Mr. V. Stoyko, Mr. K. Tarte and Mr. I. Penner helped to make the experimental apparatus a success. The support of my family was essential. I wish to further thank Dr. N. Popplewell for providing the financial support from his National Science and Engineering Research Council of Canada (NSERC) research grant. Moreover, I would like to thank the Department of Mechanical and Manufacturing Engineering for providing the financial support and experience that came in the form of a teaching assistantship. This research was also supported in part by The University of Manitoba, together with the Canada Manitoba Economic Development Partnership Agreement (Western Economic Diversification Canada and the Government of Manitoba) and Sun Microsystems of Canada, through the use of the University of Manitoba's High Performance Computing Facilities (http://www.umanitoba.ca/campus/acn/hpc/).

Darryl K. Stoyko
December 2004

Table of Contents

List of Figures

List of Tables

List of Nomenclature

Roman Letters:

0: Null matrix

a: Constant used in forcing function, s^{-2}

A: Amplitude of forcing function, V for experiments, non-dimensional force for computer predictions

$\boldsymbol{A}(n,\omega)$: Coefficient matrix resulting from linearizing quadratic eigenvalue problem

b: Constant used in temporal exponential window, s^{-1}

b_x: Body force in the direction indicated by the subscript, in this case x, lb_f/in^3 (N/m^3)

$\boldsymbol{B}(n)$: Coefficient matrix resulting from linearizing quadratic eigenvalue problem

$\boldsymbol{B}_i$: The i-th strain transformation matrix, in^{-1} (m^{-1}) for i=1, 2, dimensionless for i=3

c: Phase speed, in/s (m/s)

c_2: Torsional wave speed, in/s (m/s)

$\boldsymbol{D}$: Symmetric matrix of the isotropic elastic moduli, psi (Pa)

$\boldsymbol{D}_i$: The i-th stress matrix, lb_f/in^3 (N/m^3) for i=1, 2, psi (Pa) for i=3

D_{ij}: Elastic constant appearing in the i-th row and j-th column of the symmetric matrix of the isotropic elastic moduli, psi (Pa)

D: Cylinder's diameter, in (m)

e: Temporal exponential window

$\boldsymbol{e}_F$: Unit vector that points in the direction of the vector indicated in the subscript, in this case $\boldsymbol{F}$

E: Young's modulus, psi (Pa)

$\boldsymbol{f}$: Applied force vector, lb_f/in^3 (N/m^3)

f: Frequency, Hz

f: Forcing function, V for experiments, non-dimensional force for computer predictions

f_c: "Centre" frequency of forcing function, Hz

$\boldsymbol{F}$: Unit magnitude force vector, lb_f/in (N/m)

$\boldsymbol{F}$: Consistent load vector, lb_f/in (N/m)

$\boldsymbol{F}_0$: Radial distribution describing force vector, lb_f/in (N/m)

$F(n,m)$: Flexural mode (n and m integers)

g: Arbitrary function

G: Shear modulus, psi (Pa)

$\boldsymbol{G}_n$: A vector determined by summing over m axial wavenumbers, see equation (2.66)

$\boldsymbol{H}$: "Refined" convolved FRF

$\boldsymbol{H}'$: Corrected "refined" convolved FRF

H: Thickness of cylinder, thickness of a layer when subscripted, in (m)

$\underline{\boldsymbol{I}}$: Identity matrix

I: Discrete Fourier transform of OEM supplied input to a transducer, V

j: Fundamental complex number, $j=\sqrt{-1}$

k_n: Fourier transform parameter that transforms the discretized equations of motion from the spatial domain to the wave number domain

k_{nm}: Axial wave number, in^{-1} (m^{-1})

$\boldsymbol{K_i}$: The i-th stiffness matrix of system, lb_f/in^2 (N/m^2) for i=1, 2, 4, lb_f/in (N/m) for i=3, 5, and lb_f (N) for i=6

$\boldsymbol{L_x}$: Differential operator that operates on the displacement vector. It performs the required operations in the coordinate indicated by the subscript, in this case x, to transform the displacement vector into the strain vector, in^{-1} (m^{-1})

$L(0,m)$: Longitudinal mode (m an integer)

m: A positive integer indicating the m-th axial mode

$\boldsymbol{M}$: Mass matrix of system, slug/in (kg/m)

$\boldsymbol{n}$: Vector of interpolation (shape) functions

n: Circumferential wave number (an integer)

n_x: Interpolation (shape) function associated with the nodal surface indicated by the subscript, in this case x

$\boldsymbol{N}$: Assembled interpolation functions over the entire cylinder

N: Number of layers/elements used in radial discretization of cylinder or number of measurements

$\bar{O}$: Discrete Fourier transform of OEM supplied output from a transducer, V

$\boldsymbol{P}$: Consistent load vector, lb_f/in^3 (N/m^3)

$\boldsymbol{P_n}$: Known vector of linearized eigenvalue problem

q_0: Concentration of a narrow spatial pulse, lb_f/in (N/m)

$\boldsymbol{Q_n}$: Solution vector of linearized eigenvalue problem

r: Radial coordinate in cylindrical coordinate system, in (m)

r_0: Radial coordinate at which a point load is applied, in (m)

R: Mean radius of cylinder, in (m)

s: Arbitrary field variable or value of field variable at indicated nodal surface when subscripted

s: Scaling factor used in forcing function

$\underline{T}$: Kinetic energy, $in\text{-}lb_f$ (J) or period, s

$\underline{\bar{T}}$: Normalized transfer function

$\bar{T}^*$: Maximum magnitude of $\bar{O}/\bar{I}$ over forcing bandwidth

$T(0,m)$: Torsional mode (m an integer)

t: Time, s

$\boldsymbol{u}$: Displacement vector, in (m)

u: Radial component of displacement, in (m)

$\boldsymbol{U}$: Array of nodal displacements, in (m)

U: Nodal displacements in radial direction, in (m)

v: Circumferential component of displacement, in (m)

vol: Indicates the entire volume of the cylinder

V: Nodal displacements in circumferential direction, in (m)

V: Total potential energy or potential energy due to external forces when subscripted with e, $in\text{-}lb_f$ (J)

w: Axial component of displacement, in (m)

W: Nodal displacements in axial direction, in (m)

x: Coordinate axis in Cartesian coordinate system, in (m)

x: Measured radial displacement, V

y: Coordinate axis in Cartesian coordinate system, in (m)
z: Axial coordinate in Cartesian and cylindrical coordinate systems, in (m)

Greek Letters:
α_{Fx}: Direction cosine of the vector indicated by the first subscript, in this case, $\boldsymbol{F}$, in the direction indicated by the second subscript
γ_{xy}: Engineering shear strain in the direction indicated by the subscripts, in this case xy, in/in (m/m)
$\underline{\delta}$: Dirac delta function
$\bar{\delta}$: First variation of a functional
δ_{mp}: Kronecker delta, $\delta_{mp}=1$ if $m=p$, 0 otherwise
ϵ: Engineering strain vector, in/in (m/m)
ϵ_{xx}: Normal strain in the direction indicated by the subscripts, in this case xx, in/in (m/m)
ζ: Dimensionless radial coordinate in the local, isoparametric, element's coordinate system
θ: Circumferential coordinate in cylindrical coordinate system, Degrees (radians)
λ: A Lame constant, psi (Pa)
λ: Dummy variable of integration
μ: A Lame constant, psi (Pa)
ν: Poisson's ratio
σ: Stress vector, psi (Pa)
σ: Dummy variable of integration
σ_{xy}: Stress in the direction indicated by the subscripts, in this case xy, psi (Pa)
τ: Constant used in forcing function, s
ρ: Mass density, slug/in^3 (kg/m^3)
ϕ: Eigenvalue of linearized eigenvalue problem
ω: Angular frequency, rad/s
ω_0: Constant used in forcing function, rad/s

Roman Subscripts:
0: Denotes a quantity related to a point load
b: Denotes the back (inner) nodal surface
e: Denotes a quantity due to the presence of external forces
f: Denotes the front (outer) nodal surface
k: The k-th layer of the finite element mesh in the radial direction
l: Lower half of a partitioned vector
m: Denotes the middle nodal surface or the m-th axial wave number
n: Denotes a term in a Fourier series expansion of a quantity in the circumferential coordinate or circumferential wave number
o: Denotes outer (e.g. an outer diameter)
p: A dummy index
r: Indicates the radial direction in a cylindrical coordinate system
rec: Indicates receiver

ref: A reference quantity for a non-dimensional form
RMS: Denotes a root mean square average
$trans$: Indicates transmitter
u: Upper half of a partitioned vector
z: Indicates the axial direction in a Cartesian or cylindrical coordinate system

Roman Superscripts:
L, R: Denote a left and right eigenvector, respectively

Greek Subscripts:
θ: Indicates the circumferential direction in a cylindrical coordinate system

Notation:
x^*: Denotes a non-dimensional or normalized quantity. Two asterisks indicate a non-dimensional quantity that has also been normalized
$\boldsymbol{X}$: Boldface, vector or matrix, in this case $\boldsymbol{X}$ is a vector or matrix
$X_{,x}$: Comma followed by a spatial variable indicates partial differentiation of the variable appearing before the comma with respect to the spatial variable that follows, in this case $\boldsymbol{X}$ is partially differentiated with respect to x
$\mathscr{F}$: Fourier transform operator
$\bar{\underline{x}}$: Fourier transform of the variable that the overbar appears over, in this case x
$\bar{X}$: Average of the variable that the overbar appears over. The subscript indicates the type of average, no subscript is used in the case of arithmetic average
$\dot{x}$: Overdot, differentiation with respect to time, once for each overdot. In this case x is differentiated with respect to time once
$\tilde{x}$: Overtilde denotes the complex conjugate, in this case the complex conjugate of x
$\Re$: Indicates the real part
$\boldsymbol{X}^T$: Superscript T, matrix transpose of the matrix, in this case $\boldsymbol{X}$

List of Abbreviations and Acronyms

A/D:	Analog to Digital
AI:	Artificial Intelligence
ANSI®:	American National Standards Institute
ASCII:	American Standard Code for Information Interchange
ASTM:	American Society for Testing and Materials
AVI:	Audio Video Interleave
CPU:	Central Processing Unit
CSV:	Comma Separated Value
DWC:	Digital Wave Corporation
DN:	Diameter Nominal
EUB:	(Alberta) Energy and Utilities Board
FRF:	Frequency Response Function
GB:	Gigabyte
GE:	General Electric (Panametrics)
GPIB:	General Purpose Interface Bus
IEEE:	Institute of Electrical and Electronics Engineers
IMSL™:	International Mathematical and Statistical Library
MB	Megabyte
NDE:	Non-Destructive Evaluation
NDT:	Non-Destructive Testing
NPS:	Nominal Pipe Size
NSERC:	National Science and Engineering Research Council of Canada
OEM:	Original Equipment Manufacturer
PC:	Personal Computer
RAM:	Random Access Memory
RMS:	Root Mean Square
SAFE:	Semi-Analytical Finite Element
SNR:	Signal to Noise Ratio
UI:	Ultrasonic Inspection

Chapter 1 - Introduction

1.1 Introduction

This dissertation is devoted to the visualization and interpretation of (elastic guided) wave propagation in a homogeneous, isotropic, steel cylinder having a (right) circular cross section. The primary objective is to develop insight into how to best select the number and location of observation points to detect defects in homogeneous, isotropic cylinders using Ultrasonic Inspection (UI), which is a form of Non-Destructive Evaluation (NDE). More specifically, the following two questions are addressed.

1. How precisely and consistently does an ultrasonic measurement need to be for reliable interpretation?

and

2. How well do computational models (see, for instance, Zhuang [1;2]) predict the behaviour of a homogeneous, isotropic cylinder to a given force?

The second question relates to a "forward" problem in the sense that the input and a system's properties are prescribed and the response of the system is sought to an externally applied stimulus. In contrast, the "inverse" problem describes the case in which the identification of the system itself is desired, that is the input and response of the system are known but the system's properties are required. The current study is part of a broader research program that seeks to develop a method that can intelligently and reliably detect and characterize defects in an industrial setting using ultrasonic wave scattering. This is an inverse problem. The results presented later may be used to provide "baseline" information for a defect free cylinder that can be used to train a suitable form of Artificial Intelligence (AI) to recognize various types of defects that occur most frequently in cylinders. The use of AI could reduce,

in principle, the "considerable" experience [3] required for the meaningful interpretation of UI measurements and allow them to be automated. The motivation to consider cylinders is twofold; (1) cylindrical geometries are ubiquitous in industrial applications, and (2) a numerical model is readily available for checking the experimental data.

1.2 Overview

The objectives and techniques of NDE are discussed in Chapter 1 in general terms but with a focus on UI. Furthermore, a literature review is presented that outlines the development of the use of elastic guided waves in cylinders as a NDE technique. Chapter 2 presents a theoretical overview of the numerical procedures developed by Zhuang [1;2] to calculate the three dimensional, steady state Green's functions of an infinitely long cylinder. Using Green's functions, the (displacement) time history created by an arbitrarily located, external point load is recovered at another point of the cylinder by treating a Green's function as a Frequency Response Function (FRF) and convolving it with this load. An illustrative example is presented for a cylinder having both historical and practical significance. (See the literature review presented later in this chapter.) Chapter 3 details the experimental apparatus used to measure the (radial) displacement time history on a cylinder's outer surface. Selected experimental data are presented for the same cylinder considered in Chapter 2. Chapter 4 provides comparisons between the numerically and experimentally determined, radial displacement at several cross sections of the cylinder's outer surface. In addition, the temporal evolution of the radial displacement field is given over a "significant" portion of the cylinder's outer surface. Conclusions are drawn in Chapter 5 and recommendations for future work are given.

1.3 Non-Destructive Evaluation

Non-Destructive Evaluation (NDE) and Non-Destructive Testing (NDT) are two terms that are often used interchangeably to describe a family of inspection methods that provide information about a material without destroying it [3]. There are seven core NDE techniques [3], viz:

1. visual inspection
2. acoustic emission inspection
3. liquid penetration inspection
4. magnetic particle inspection
5. radiographic inspection
6. eddy current inspection
7. ultrasonic inspection.

NDE is used typically to [3]:

1. prevent accidents
2. reduce costs
3. improve product reliability
4. determine acceptability for a given requirement, and
5. give information on repair criteria.

Each of the core methods has its own advantages and disadvantages that define an individual method's range of applicability. The focus here, however, is the field of Ultrasonic Inspection (UI) which uses the properties of ultrasonic wave propagation to infer the condition of a material.

1.4 Ultrasonic Inspection

UI uses sound energy, usually above the audible frequency range, to interrogate a material [4]. Ultrasonic waves are generated in UI by temporarily introducing a "small" stress in the material. The resulting stress induced waves are measured, normally at a "point[+]" on the surface of the material, in the form of an amplitude-time history by using a suitable transducer. A typical UI apparatus has five subsystems, viz the part to be tested, a signal generator (possibly equipped with a power-amplifier), a "transmitting" ultrasonic transducer, a "receiving" ultrasonic transducer (usually with a pre-amplifier), and a data collection system (typically an analog to digital converter and a personal computer). The signal generator is used to "drive" the transmitting transducer, an electromechanical device that converts the electrical potential introduced across the faces of its piezoelectric crystal into a displacement or force. The resulting displacement or force is imparted to the material's surface and produces a mechanical stress wave that propagates through it. The wave is scattered by defects. Scattering describes the process that occurs when an incident wave impinges on a defect and part of the wave's energy is transmitted around the defect, with the remainder being reflected back. The receiving transducer, another electromechanical device, is used to recover information about the stress waves as they propagate. The receiving transducer will typically produce an electrical potential that is proportional to the component of displacement normal to the surface at the measurement "point." This signal is amplified and it may be stored, for later analysis, by using a suitable data collection system. It should be noted that different configurations of the transmitting

---

[+] The "point" is strictly a small area.

and receiving transducers are possible, which leads to different measurement procedures (such as pitch-catch, through testing, pulse-echo, etc.) as well as different ways of presenting the data (e.g., A-scan, B-scan, C-scan, etc.). A comparison of the commonly used procedures may be found in references [5] and [6]. A schematic of a typical ultrasonic pitch-catch NDE apparatus, which is used in this study, is shown in Figure 1.1.

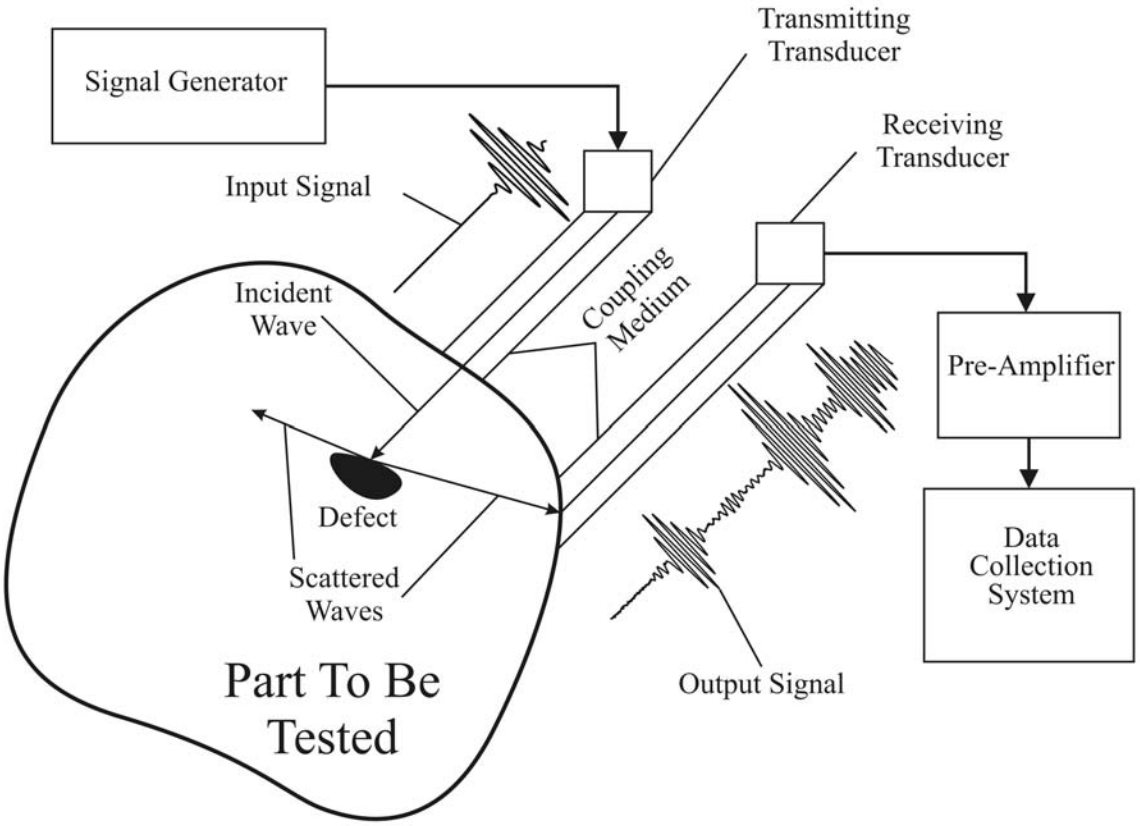

Figure 1.1. Schematic Diagram of a Typical UI Apparatus

Alternatives to (contact) piezoelectric transducers exist to excite ultrasonic waves and measure surface displacements. They include non-contact air coupling, water coupling, laser/optical coupling, thermal coupling, and magnetic coupling. Each technique has its own advantages and disadvantages. However, a complete discussion of each alternative is

beyond the scope of this work. In general, each alternative suffers from one or more of the following limitations that makes it unsuitable for a typical industrial application:

1. capital expense
2. poor signal to noise ratio
3. poor depth of penetration
4. inconvenient or requires extensive surface preparation.

The claimed advantages of UI [4] are given below.

1. It is sensitive to both surface and subsurface discontinuities.
2. The depth of penetration for flaw detection is superior to other NDE methods.
3. Only single-sided access to the material is needed when the pulse-echo technique is used.
4. It is highly accurate in determining a reflector's (i.e. a defect) position and it is also capable of estimating the defect's size and shape.
5. Minimal part preparation is required.
6. Electronic equipment provides instant data.
7. Detailed images can be produced with automated systems.
8. It has other uses, in addition to flaw detection, such as thickness measurement or characterization of a material's properties.

The disadvantages of UI [4] are presented next.

1. The material's surface must be accessible to transmit ultrasound.
2. Additional skill and training is required to meaningfully interpret UI measurements.
3. A coupling medium is normally required to transfer sound energy into the test specimen.

4. Materials that are rough, irregular in shape, very small, exceptionally thin or inhomogeneous are difficult to inspect.

5. Cast iron and other coarse grained materials are difficult to inspect due to low sound transmission and, hence, low signal to noise ratios.

6. Linear defects, which are oriented parallel to the sound beam, may go undetected.

7. Reference standards are required for both equipment calibration and the characterization of flaws.

1.5 Literature Review

It was stated previously that cylindrical geometries are ubiquitous in industrial applications. The Alberta Energy and Utilities Board (EUB) [7], for example, reports that there is approximately 165 000 miles (266 000 km) of energy-related pipelines under its jurisdiction as of the end of 1997. (See [7] for the criteria for a pipeline to be under EUB jurisdiction.) Of this pipeline, 94 percent is steel. The 3 inch Nominal Pipe Size (NPS) (80 mm Diameter Nominal [DN]) steel cylinder considered here constitutes about 26 percent of the steel pipeline in Alberta under EUB jurisdiction. This is the greatest percentage of any given size. Moreover, 94 percent of the steel pipeline is not protected from internal corrosion. During the 1980-1997 period, 12,137 pipeline failures were recorded, an average of 674 failures per year. Corrosion is the major cause of failure. Internal corrosion, which is not visible, is citied as causing approximately 50 per cent of all pipeline failures. External corrosion accounts for another 13 per cent. Clearly a better method is required to rapidly, reliably and nondestructively inspect steel pipeline, both internally and externally.

Current UI techniques that are based on guided waves are superior to the earlier techniques involving body waves for the following reasons.

1. Their multi-modal and dispersive behaviour can quickly provide information over a range of frequencies [8].

2. The propagation speed of guided waves is very sensitive to material properties [8].

3. They are capable of rapidly interrogating entire structures including inaccessible regions [9] because guided waves can propagate long distances (say tens of metres [10]) .

4. Compared to body waves, guided waves have a low rate of attenuation with propagation distance [10].

The use of guided waves also potentially allows inspection of buried parts of a pipeline, as demonstrated in [11], because a guided wave can potentially propagate along a pipe over long distances without adverse effects from a coating [11]. Moreover, it is stated in [11] that clamps have no influence on the propagation of the (selected) guided waves. There seems to be some contention, however, over the validity of these statements. For example, [12] suggests that elastic coatings introduce new dispersive modes and they also change, considerably, the modes that exist in bare steel. It is stated further in [12] that the damping from a coating layer has a significant effect on the mode shapes. It is demonstrated in [13] that high wave attenuation associated with coated or buried pipelines significantly reduces the inspection range and defect detection capability of guided wave techniques. Moreover, it is contrary to the author's experience (see Chapter 3 for more details) that clamps would not influence the propagation of guided waves. The shoe transducers used in [11] would likely excite flexural modes, in addition to the desired longitudinal modes, that would be sensitive to clamps according to [14].

The very advantages of guided waves that make their use attractive introduce their own challenges. For example it is difficult, in practice, to generate a single pure mode so

that a signal generally contains more than one mode [10]. Mode conversions by defects and geometrical discontinuities, which are commonly found in pipeline at welds, flanges, etc., complicate matters further [10]. Moreover, the modes are generally dispersive so that the shape of a propagating wave changes as it travels to "interrogate" even an unflawed pipe. These factors combine to make the interpretation of guided wave signals difficult.

The preferred approach to make data interpretation more tractable is to limit the number of propagating modes by using an excitation, that is constrained to a limited frequency range. The axisymmetric (torsional and longitudinal) modes are employed most often. For example pulse-echo techniques, combined with the use of special transducers, are used to selectively excite longitudinal and torsional modes in order to detect circumferential and axial defects, respectively, in "small thin-walled" tubes [15]. The reflection of the second longitudinal mode, excited by a ring of dry-coupled piezoelectric transducers [10], is used in [16;17] to detect circumferential notches in pipes. Comb and wedge type transducers have also been utilized to selectively excite modes in cylinders [11;18-21]. Furthermore, time-delay, periodic ring arrays have been employed [22-24]. The use of multiple transducers to "focus" ultrasonic energy onto a target so that a more discernible reflection occurs, if a defect exists at the target location, has been explored by several research groups [25;26].

The perfect excitation of a single (or selectively few) mode(s) in a cylinder, even with the employment of specially designed transducers, is generally difficult to achieve in practice because of asymmetries which often occur in a cylinder [10]. For instance, the objective in [10] is to excite and receive only the second longitudinal mode, but the first

longitudinal mode as well as several flexural modes are also excited noticeably. Moreover, the use of single (or selectively few) mode(s) can be disadvantageously time consuming when the nature and orientation of the defect(s) is not known a priori. Defects that are claimed to be detected successfully in [16;17] are excessively large to be of practical interest for most pressure vessels. Indeed, defects are not likely to occur in the form studied in [16;17], because pitting is a more common problem than a notch so that the use of longitudinal modes may be limited. Focussing techniques can aid the characterization of a defect if the defect's location is known a priori. This situation is unusual in practice. For these reasons, an excitation that simultaneously excites many modes may be preferable. However, guided wave signals can be interpreted meaningfully only with a thorough understanding of the wave fields involved. Therefore a brief history of the development of the theory of elastic wave propagation and scattering in cylinders is presented next.

The first published dispersion relation for elastic wave propagation in an infinite, homogeneous, isotropic (solid) cylinder, known as the Pochhammer-Chree equation, appears to be the solutions given independently in [27] and [28]. Due to the complexity of the Pochhammer-Chree equation, very few analytical solutions exist. Consequently several approximate methods have evolved which are summarized in [29]. The first reported numerical solution to the Pochhammer-Chree equation considers purely longitudinal waves [30]. A more thorough study [31] gives phase and group velocities over a wide range of frequencies.

The theory of elasticity has been applied to the study of wave propagation in hollow, infinitely long, homogeneous, isotropic cylinders. Several three-dimensional solutions have

been developed [32;33], based on linear elasticity and a normal mode expansion, to find the guided wave fields in an infinitely long, homogenous, isotropic (hollow) cylinder. At the present time there is no published (analytical) solution for guided waves in cylindrical shells having the most general form of constitutive relations [34] (i.e. a composite cylinder exhibiting general anisotropy). Solutions are available, however, for special cases of laminated and/or composite cylinders. For example, an analytical solution exists to describe the propagation of longitudinal [35] and torsional [36] waves in infinitely long, solid, composite rods when the rod consists of a solid, internal, homogeneous and isotropic rod that is perfectly bonded to a surrounding coaxial, external, hollow cylinder having a different homogeneous, isotropic material. An exact yet cumbersome solution also exists [37] for an infinitely long, composite cylinder composed of any number of perfectly bonded, concentric, transversely isotropic cylinders. A still analytical, yet more numerically efficient method based on three dimensional elasticity is developed in [38] to solve the dispersion relation for an infinitely long, composite cylinder composed of any number of perfectly bonded, concentric, isotropic (as opposed to transversely isotropic) cylinders.

To solve the dispersion relations more generally, i.e. for more complicated composite cylinders exhibiting anisotropy, several approximate theories have been developed. One-dimensional, stiffness based, finite element methods are used to solve the dispersion relation in circular cylinders composed of an arbitrary number of perfectly bonded elastic, cylindrically orthotropic cylinders [39] and a cylinder with cylindrical anisotropy [40]. Similar methods are employed [1;2;41] to solve the dispersion relations for laminated composite cylinders.

Having the dispersion and wave fields in an unflawed cylinder provides a "baseline" to gauge UI measurements. To solve the inverse problem of flaw detection, knowledge is required of wave scattering by different defects. The simplest case of wave scattering, reflection from a free end, is well documented [42-44]. Only recently, however, have (numerical) solutions to wave scattering by cracks in cylinders become available because faster computing resources are more readily accessible. For example, [45] and [46] respectively use a hybrid wave function expansion - finite element technique to examine axisymmetric guided waves scattered by joints in laminated cylinders as well as cracks and welds in steel pipes. Wave scattering in isotropic and laminated composite cylinders is considered by using symmetric and anti-symmetric arguments for partial circumferential cracks in conjunction with the boundary element method for arbitrarily oriented cracks [34;47;48].

A fair number of experimental and analytical techniques have been developed using guided waves for UI in cylinders. There is, however, no universal agreement of the "best" approach. The need for an appropriate selection of modes to interrogate a cylinder, which is likely controlled by the types of defects that may be present, exists because the behaviour of guided waves in cylinders is not visualized easily. Insight can come from analytical models. However, a complete description, in a form suitable for direct comparison to experimental data, of the wave fields even in an unflawed cylinder is lacking presently. This situation exists because the computational effort required to evaluate the wave fields over a large portion of a cylinder is tremendous. Consequently, results are presented and compared in this dissertation to experimental data over a large portion of a commonly used

cylinder. The data is presented in a way that makes visualization of the wave field possible. It may also be useful for several other purposes, including forming the baseline training for a form of AI or forming the input to the analysis of circumferential cracks using the methods presented in [34;47]. The more comprehensive data presented here may also form a basis for the study of wave focussing in cylinders, which is similar in nature to that appearing in [26].

Chapter 2 - Theoretical Basis, Implementation Details, and Illustrative Example

2.1 Introduction

The theoretical basis is presented in this chapter of the numerical procedures developed by Zhuang [1;2] to calculate the three dimensional, steady state Green's functions of an infinitely long cylinder. A Semi-Analytical Finite Element (SAFE) formulation is used in conjunction with a separation of variables due to the complexities associated with an analytical solution. The axial and circumferential variations, as well as all time dependencies of the wave field, are treated analytically. The radial dependence is modelled by using one-dimensional, quadratic finite elements. The governing differential equations are discretized such that a quadratic, algebraic eigenvalue problem is produced. A Fourier series representation of the circumferential dependence of the wave field allows the latter to be written as a summation. For a given circumferential wave number, the solution of the resulting, three parameter, quadratic eigenvalue problem provides the dispersion relation for the cylinder. The response of the cylinder to a harmonic load can be described, for a given circumferential wave number, by a modal summation over the axial modes. A summation over the circumferential wave numbers gives the steady state Green's functions. Then the (output) time response to a transient (input) point load is determined by treating the Green's functions as a Frequency Response Function (FRF) and convolving it with the transient point load. Finally an illustrative example is presented that demonstrates the modelling technique for a typical experimental setup.

2.2 Description of the Cylinder

Figure 2.1 shows half of an infinitely long cylinder having a mean radius, R, and total

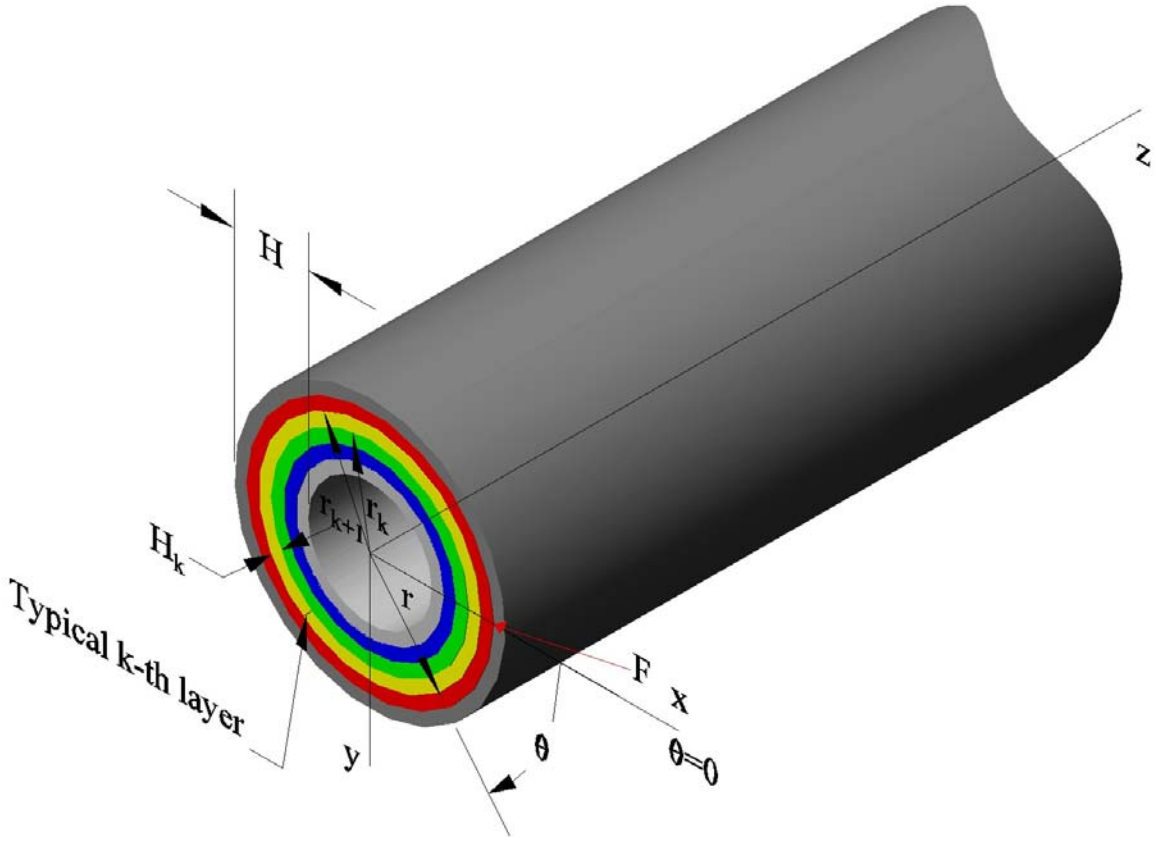

Figure 2.1. Geometry and Coordinate System of a Discretized Cylinder Subject to a Point Load, ***F***

thickness *H*. The cylinder is assumed to be uniform, homogenous, and isotopic. It is straightforward, however, to remove this last restriction. (See, for example, Zhuang [1].) The cylinder is subjected to a point load, ***F***, which is shown as a red leader in the Figure 2.1. The inner and outer surfaces of the cylinder are assumed to be traction free. A right hand, cylindrical coordinate system in the coordinates (r, θ, z) is also shown in the figure. It is superimposed over a right hand, Cartesian coordinate system having coordinates (x, y, z). The common origin of the two coordinate systems is located at the geometric centre of a generic cross-section of the cylinder with the z axis pointing along the longitudinal (axial) axis of the cylinder. The point load is applied at y=0 in the plane z=0. In the cylindrical

coordinate system, $\theta=0$ corresponds to the point of application of the point load. The cylinder is divided into N layers through the thickness. (Note that a particular colour in Figure 2.1 denotes a given layer so that six layers are shown in this illustration.) Each layer corresponds to a quadratic, one dimensional finite element in the cylinder's radial direction. The thickness of, say, the k-th layer is H_k and it extends radially from r_k to r_{k+1}, as shown in the figure.

2.3 Governing Equations of Motion

The wave fields of interest are the displacement, $\boldsymbol{u}$, engineering strain, ϵ, and stress, σ. For a given layer in the cylindrical coordinate system shown in Figure 2.1, the time dependent quantities can be represented by the following column vectors:

$$\boldsymbol{u}(r,\theta,z,t)=[u,v,w]^T \tag{2.1}$$

$$\epsilon(r,\theta,z,t)=[\epsilon_{rr},\epsilon_{\theta\theta},\epsilon_{zz},\gamma_{\theta z},\gamma_{rz},\gamma_{r\theta},]^T \tag{2.2}$$

and

$$\sigma(r,\theta,z,t)=[\sigma_{rr},\sigma_{\theta\theta},\sigma_{zz},\sigma_{\theta z},\sigma_{rz},\sigma_{r\theta}]^T. \tag{2.3}$$

Time is represented by t, u is the radial displacement, v is the circumferential displacement, w is the axial displacement, ϵ (γ) indicates an engineering normal (shear) strain, and σ indicates a stress. Subscripts r, θ, and z correspond to the radial, circumferential, and axial directions, respectively. Superscript T indicates the transpose of a matrix.

The strain and displacement vectors are related by the standard differential equation:

$$\epsilon=[\boldsymbol{L}_r+\boldsymbol{L}_\theta+\boldsymbol{L}_z]\boldsymbol{u}. \tag{2.4}$$

The differential operators $\boldsymbol{L}_r$, $\boldsymbol{L}_\theta$, and $\boldsymbol{L}_z$ in the above equation are given by:

$$\boldsymbol{L}_r=\begin{bmatrix} \frac{\partial}{\partial r} & 0 & 0 \\ \frac{1}{r} & 0 & 0 \\ 0 & 0 & 0 \\ 0 & 0 & 0 \\ 0 & 0 & \frac{\partial}{\partial r} \\ 0 & \frac{\partial}{\partial r}-\frac{1}{r} & 0 \end{bmatrix};\ \boldsymbol{L}_\theta=\begin{bmatrix} 0 & 0 & 0 \\ 0 & \frac{1}{r}\frac{\partial}{\partial\theta} & 0 \\ 0 & 0 & 0 \\ 0 & 0 & \frac{1}{r}\frac{\partial}{\partial\theta} \\ 0 & 0 & 0 \\ \frac{1}{r}\frac{\partial}{\partial\theta} & 0 & 0 \end{bmatrix};\ \boldsymbol{L}_z=\begin{bmatrix} 0 & 0 & 0 \\ 0 & 0 & 0 \\ 0 & 0 & \frac{\partial}{\partial z} \\ 0 & \frac{\partial}{\partial z} & 0 \\ \frac{\partial}{\partial z} & 0 & 0 \\ 0 & 0 & 0 \end{bmatrix}. \tag{2.5}$$

The constitutive relationship between the stress and strain vectors is:

$$\boldsymbol{\sigma}=\boldsymbol{D}\boldsymbol{\epsilon} \tag{2.6}$$

where $\boldsymbol{D}$ is a symmetric matrix of isotropic elastic moduli given by:

$$\boldsymbol{D}=\begin{bmatrix} D_{11} & D_{12} & D_{13} & 0 & 0 & 0 \\ D_{12} & D_{22} & D_{23} & 0 & 0 & 0 \\ D_{13} & D_{23} & D_{33} & 0 & 0 & 0 \\ 0 & 0 & 0 & D_{44} & 0 & 0 \\ 0 & 0 & 0 & 0 & D_{55} & 0 \\ 0 & 0 & 0 & 0 & 0 & D_{66} \end{bmatrix}. \tag{2.7}$$

The (differential) equations of wave motion, expressed in the cylindrical coordinate system, are given by:

$$\begin{aligned} \sigma_{rr,r}+\frac{1}{r}\sigma_{r\theta,\theta}+\sigma_{rz,z}+\frac{1}{r}\left(\sigma_{rr}-\sigma_{\theta\theta}\right)+b_r&=\rho\ddot{u} \\ \sigma_{\theta r,r}+\frac{1}{r}\sigma_{\theta\theta,\theta}+\sigma_{\theta z,z}+\frac{2}{r}\sigma_{\theta r}+b_\theta&=\rho\ddot{v} \end{aligned} \tag{2.8}$$

and

$$\sigma_{zr,r}+\frac{1}{r}\sigma_{z\theta,\theta}+\sigma_{zz,z}+\frac{1}{r}\sigma_{zr}+b_z=\rho\ddot{w}$$

where b is a body force and ρ is the cylinder's mass density. A comma in equation (2.8)

denotes differentiation with respect to the spatial variable that follows and an overdot indicates differentiation with respect to time.

2.4 Discretization of the Governing Equations of Motion

The formulation presented in the previous section is given in terms of differential equations. Here, a Semi-Analytical Finite Element (SAFE) formulation, which is based on the continuity of the displacement field $\boldsymbol{u}$, is used to develop approximate governing equations that are more suitable for numerical solution. The wall of the cylinder is divided, as before, into N concentric cylindrical layers, each layer corresponding to a quadratic finite element. Associated with each layer are three, equally spaced nodal surfaces. The nodal surfaces of a given layer, from the innermost radial coordinate to the outermost, are termed the back (inner), middle, and front (outer) nodal surfaces, respectively. They are denoted by subscript b, m, and f, respectively. Applying the finite element methodology to the discretized cylinder requires the use of interpolation (shape) functions that characterize the kinematic behaviour in a given layer. The interpolation functions, $\boldsymbol{n}$, used here in a typical, say the k-th layer, are:

$$\boldsymbol{n}(\zeta)=[n_b(\zeta),n_m(\zeta),n_f(\zeta)]=\left[\frac{1}{2}\zeta(\zeta-1),(1-\zeta^2),\frac{1}{2}\zeta(\zeta+1)\right]. \tag{2.9}$$

Here, n_b, n_m, and n_f are the shape functions associated with the back (inner), middle, and front (outer) nodal surfaces, respectively. Also, ζ is a dimensionless radial coordinate in the local, isoparametric element coordinate system that is given by:

$$\zeta=\frac{2(r-r_{km})}{H_k},-1\le\zeta\le 1. \tag{2.10}$$

Moreover r is the radial coordinate of a representative point in the k-th layer having thickness H_k and r_{km} is the radial coordinate of this layer's middle surface. By using the interpolation functions, any field variable, say s, can be written (approximately) as:

$$s = n_b(\zeta)s_b + n_m(\zeta)s_m + n_f(\zeta)s_f \tag{2.11}$$

over the entire layer where s_b, s_m, and s_f are the values of the field variable at the back (inner), middle, and front (outer) nodal surfaces, respectively.

Vector, $\boldsymbol{u}$, which describes the displacement over the entire cylinder can be written as:

$$\boldsymbol{u}(r,\theta,z,t) = \begin{bmatrix} u(r,\theta,z,t) \\ v(r,\theta,z,t) \\ w(r,\theta,z,t) \end{bmatrix} = \begin{bmatrix} N(r) & 0 & 0 \\ 0 & N(r) & 0 \\ 0 & 0 & N(r) \end{bmatrix} \begin{bmatrix} U(\theta,z,t) \\ V(\theta,z,t) \\ W(\theta,z,t) \end{bmatrix} \tag{2.12}$$

or, more conveniently,

$$\boldsymbol{u}(r,\theta,z,t) = \boldsymbol{N}(r)\boldsymbol{U}(\theta,z,t). \tag{2.13}$$

The $\boldsymbol{N}(r)$ in equations (2.12) and (2.13) are the assembled interpolation functions over the entire cylinder and $\boldsymbol{U}(\theta,z,t)$ is the corresponding array of nodal displacements. For a cylinder that has been discretized by using N layers, $\boldsymbol{U}(\theta,z,t)$ is a vector having $3\times(2N+1)$ elements. Substituting equation (2.13) and its derivatives into (2.4) gives the strain vector as:

$$\boldsymbol{\epsilon} = \boldsymbol{B_1}\boldsymbol{U} + \boldsymbol{B_2}\boldsymbol{U}_{,\theta} + \boldsymbol{B_3}\boldsymbol{U}_{,z} \tag{2.14}$$

where a comma again denotes differentiation with respect to the spatial variable that follows. The strain transformation matrices, $\boldsymbol{B_i}$, $i=1, 2, 3,$ are given by:

$$\boldsymbol{B_1}=\begin{bmatrix} \boldsymbol{N_{,r}} & 0 & 0 \\ \boldsymbol{N/r} & 0 & 0 \\ 0 & 0 & 0 \\ 0 & 0 & 0 \\ 0 & 0 & \boldsymbol{N_{,r}} \\ 0 & \boldsymbol{N_{,r}-N/r} & 0 \end{bmatrix};\ \boldsymbol{B_2}=\begin{bmatrix} 0 & 0 & 0 \\ 0 & \boldsymbol{N/r} & 0 \\ 0 & 0 & 0 \\ 0 & 0 & \boldsymbol{N/r} \\ 0 & 0 & 0 \\ \boldsymbol{N/r} & 0 & 0 \end{bmatrix};\ \boldsymbol{B_3}=\begin{bmatrix} 0 & 0 & 0 \\ 0 & 0 & 0 \\ 0 & 0 & \boldsymbol{N} \\ 0 & \boldsymbol{N} & 0 \\ \boldsymbol{N} & 0 & 0 \\ 0 & 0 & 0 \end{bmatrix}. \tag{2.15}$$

Moreover, the stress vector, $\boldsymbol{\sigma}$, can be found by substituting equation (2.14) into the constitutive relation (2.6), so that:

$$\boldsymbol{\sigma}=\boldsymbol{D_1U}+\boldsymbol{D_2U_{,\theta}}+\boldsymbol{D_3U_{,z}} \tag{2.16}$$

where the matrices, $\boldsymbol{D_i}$ $i=1,\ 2,\ 3,$ are given by:

$$\boldsymbol{D_1}=\boldsymbol{DB_1};\ \boldsymbol{D_2}=\boldsymbol{DB_2};\ \boldsymbol{D_3}=\boldsymbol{DB_3}. \tag{2.17}$$

$\boldsymbol{D}$ is a symmetric matrix composed of the isotropic elastic moduli.

The equations of motion are obtained by using Hamilton's principle expressed in the form:

$$\bar{\delta}\int_{t_1}^{t_2}(T-V)dt=0 \tag{2.18}$$

where $\bar{\delta}$ indicates the first variation, t is time and T, V are the kinetic and total potential energies, respectively. The latter are given by:

$$T=\frac{1}{2}\int_{vol}\rho\,\dot{\boldsymbol{u}}^{\boldsymbol{T}}\dot{\boldsymbol{u}}\,d(vol)\ \text{ and }\ V=\frac{1}{2}\int_{vol}\boldsymbol{\epsilon}^{\boldsymbol{T}}\boldsymbol{D}\boldsymbol{\epsilon}\,d(vol)+V_e \tag{2.19}$$

where *vol* indicates that the integrals are to be evaluated over the entire volume of the cylinder. In the last equation, ρ is the cylinder's mass density, $\dot{\boldsymbol{u}}$ is the time derivative of the displacement, $\boldsymbol{u}$, $\boldsymbol{\epsilon}$ is the strain, $\boldsymbol{D}$ is a symmetric matrix of isotropic elastic moduli, and

V_e is the potential energy due to the external forces. Now,

$$V_e = -\boldsymbol{U}^T\boldsymbol{P} \tag{2.20}$$

where $\boldsymbol{P}$ represents the consistent load vector, the specific form of which involves the product of the applied surface tractions and their corresponding displacement interpolations, $\boldsymbol{U}$.

The integrand of equation (2.18) can be expressed, with the help of the time differentiation of equation (2.13), in terms of the displacement interpolations by substituting equations (2.14) and (2.19) into equation (2.18). The variation of the resulting expression gives the following discrete system of equations:

$$\boldsymbol{K}_1\boldsymbol{U}+\boldsymbol{K}_2\boldsymbol{U}_{,\theta}+\boldsymbol{K}_3\boldsymbol{U}_{,z}-\boldsymbol{K}_4\boldsymbol{U}_{,\theta\theta}-\boldsymbol{K}_5\boldsymbol{U}_{,\theta z}-\boldsymbol{K}_6\boldsymbol{U}_{,zz}+\boldsymbol{M}\ddot{\boldsymbol{U}}=\boldsymbol{F}. \tag{2.21}$$

The stiffness matrices, $\boldsymbol{K}_i$, $i=1, 2, 3, 4, 5, 6,$ as well as the mass matrix, $\boldsymbol{M}$, and consistent load vector, $\boldsymbol{F}$, are given by:

$$\begin{aligned} &\boldsymbol{K}_1=2\pi\int \boldsymbol{B}_1{}^T\boldsymbol{D}\boldsymbol{B}_1 r dr\,;\ \boldsymbol{K}_2=2\pi\int\left(\boldsymbol{B}_1{}^T\boldsymbol{D}\boldsymbol{B}_2-\boldsymbol{B}_2{}^T\boldsymbol{D}\boldsymbol{B}_1\right)r dr \\ &\boldsymbol{K}_3=2\pi\int\left(\boldsymbol{B}_1{}^T\boldsymbol{D}\boldsymbol{B}_3-\boldsymbol{B}_3{}^T\boldsymbol{D}\boldsymbol{B}_1\right)r dr\,;\ \boldsymbol{K}_4=2\pi\int \boldsymbol{B}_2{}^T\boldsymbol{D}\boldsymbol{B}_2 r dr \\ &\boldsymbol{K}_5=2\pi\int\left(\boldsymbol{B}_2{}^T\boldsymbol{D}\boldsymbol{B}_3+\boldsymbol{B}_3{}^T\boldsymbol{D}\boldsymbol{B}_2\right)r dr\,;\ \boldsymbol{K}_6=2\pi\int \boldsymbol{B}_3{}^T\boldsymbol{D}\boldsymbol{B}_3 r dr \end{aligned} \tag{2.22}$$

$$\boldsymbol{M}=2\pi\int \rho\boldsymbol{N}^T\boldsymbol{N} r dr \tag{2.23}$$

and

$$\boldsymbol{F}=2\pi\int \boldsymbol{N}^T\boldsymbol{P} r dr \tag{2.24}$$

using the previously defined notation. Note that $\boldsymbol{K}_1$, $\boldsymbol{K}_4$, $\boldsymbol{K}_5$, $\boldsymbol{K}_6$, and $\boldsymbol{M}$ are symmetric but $\boldsymbol{K}_2$ and $\boldsymbol{K}_3$ are antisymmetric matrices.

2.5 Steady State Loading and the Algebraic Eigenvalue Problem

Assume that the applied loads give a consistent load vector, $\boldsymbol{F}$, which is time harmonic (with angular frequency ω) and periodic in the circumferential coordinate. Such loads can be expressed in a Fourier series as:

$$\boldsymbol{F}(\theta,z,t)=e^{-j\omega t}\boldsymbol{F}(\theta,z)=e^{-j\omega t}\sum_{n=-\infty}^{n=\infty} e^{jn\theta}\boldsymbol{F}_n(z)\,. \tag{2.25}$$

It is assumed conventionally that the resulting displacement interpolation functions, $\boldsymbol{U}$, are also: (1) time harmonic with angular frequency ω, and (2) periodic in the circumferential coordinate. They can be expressed as:

$$\boldsymbol{U}(\theta,z,t)=e^{-j\omega t}\boldsymbol{U}(\theta,z)=e^{-j\omega t}\sum_{n=-\infty}^{n=\infty} e^{jn\theta}\boldsymbol{U}_n(z)\,. \tag{2.26}$$

In equations (2.25) and (2.26), $j=\sqrt{-1}$, n is the circumferential wave number and θ is the circumferential coordinate. The $\boldsymbol{F}_n$ and $\boldsymbol{U}_n$ in these equations are coefficients of the Fourier series of the consistent load vector, $\boldsymbol{F}$, and the displacement interpolation, $\boldsymbol{U}$, respectively. Examination of equation (2.16) shows that, if the displacement interpolation functions can be expanded into a Fourier series in the circumferential coordinate, the nodal stresses can also be expressed in a Fourier series as:

$$\boldsymbol{\sigma}(\theta,z,t)=e^{-j\omega t}\boldsymbol{\sigma}(\theta,z)=e^{-j\omega t}\sum_{n=-\infty}^{n=\infty} e^{jn\theta}\boldsymbol{\sigma}_n(z) \tag{2.27}$$

where $\boldsymbol{\sigma}_n$ are the coefficients of the Fourier series of the nodal stress vector.

Substituting equations (2.25) and (2.26) into equation (2.21) yields a system of ordinary differential equations for the Fourier coefficients, $\boldsymbol{U}_n$, in terms of z. The n-th term

has the form:

$$\left(\boldsymbol{K}_1 + jn\boldsymbol{K}_2 + n^2\boldsymbol{K}_4 - \omega^2\boldsymbol{M}\right)\boldsymbol{U}_n + \left(\boldsymbol{K}_3 - jn\boldsymbol{K}_5\right)\boldsymbol{U}_{n,z} - \boldsymbol{K}_6\boldsymbol{U}_{n,zz} = \boldsymbol{F}_n. \tag{2.28}$$

Applying the Fourier integral transform (defined by the following transform pair:

$$\bar{g}(k_n) = \int_{-\infty}^{\infty} g(z) e^{-jk_n z} dz \; ; \; g(z) = \frac{1}{2\pi}\int_{-\infty}^{\infty} \bar{g}(k_n) e^{jk_n z} dk_n \, , \tag{2.29}$$

where, in general, g is an arbitrary function and an overbar indicates the Fourier transform to equation (2.28)), transforms the discretized governing equations from the spatial (z) domain to the (axial) wave number (k_n) domain. The n-th term of the discretized governing equations can be expressed in the wave number domain as:

$$\left(\boldsymbol{K}_1 + jn\boldsymbol{K}_2 + n^2\boldsymbol{K}_4 - \omega^2\boldsymbol{M}\right)\bar{\boldsymbol{U}}_n + jk_n\left(\boldsymbol{K}_3 - jn\boldsymbol{K}_5\right)\bar{\boldsymbol{U}}_n + k_n^2\boldsymbol{K}_6\bar{\boldsymbol{U}}_n = \bar{\boldsymbol{F}}_n. \tag{2.30}$$

Equation (2.30) governs the motion of the n-th circumferential harmonic in the (axial) wave number domain. Also note that equation (2.30) has the form of a three parameter, algebraic eigensystem if the transformed form of the consistent load vector is the null matrix. Any one of the variables ω, n, or k_n can be used as the eigenvalue parameter. Specific values are assigned here to both ω and n because k_n is used as the eigenvalue parameter. [Note that n must be an integer.] Clearly the eigensystem in equation (2.30) is quadratic in k_n.

Equation (2.30) can be rewritten in a first order form as:

$$\left[\boldsymbol{A}(n,\omega) - k_n\boldsymbol{B}(n)\right]\bar{\boldsymbol{Q}}_n = \bar{\boldsymbol{P}}_n \tag{2.31}$$

where:

$$\boldsymbol{A}(n,\omega)=\begin{bmatrix} \mathbf{0} & \boldsymbol{I} \\ (\boldsymbol{K}_1+jn\boldsymbol{K}_2+n^2\boldsymbol{K}_4-\omega^2\boldsymbol{M}) & j(\boldsymbol{K}_3-jn\boldsymbol{K}_5) \end{bmatrix};$$

and

$$\boldsymbol{B}_n=\begin{bmatrix} \boldsymbol{I} & \mathbf{0} \\ \mathbf{0} & -\boldsymbol{K}_6 \end{bmatrix};\ \bar{\boldsymbol{Q}}_n=\begin{bmatrix} \bar{\boldsymbol{U}}_n \\ k_n\bar{\boldsymbol{U}}_n \end{bmatrix};\ \bar{\boldsymbol{P}}_n=\begin{bmatrix} \mathbf{0} \\ \bar{\boldsymbol{F}}_n \end{bmatrix}. \tag{2.32}$$

Here, $\mathbf{0}$ is the null matrix and $\boldsymbol{I}$ is the identity matrix. The response to the n-th circumferential mode in the Fourier series expansion of the applied load can written by using a modal summation of the normal vectors of the homogeneous form of the system described by equation (2.31).

2.6 Recovery of the Response of the n-th Circumferential Mode Using Modal Summation

The linearization of equation (2.30) that produces equation (2.31) doubles the size of the unknown vector; if the size of the displacement vector $\bar{\boldsymbol{U}}_n$ is M, then $\bar{\boldsymbol{Q}}_n$ has size $2M$. A non-trivial solution of equation (2.31) requires that the determinant of the coefficient matrix of $\bar{\boldsymbol{Q}}_n$ vanish. The resulting polynomial equation in k_n is used as the (approximate) dispersion relation for the cylinder. The solution of the dispersion relation yields $2M$ roots; each root, k_{nm}, is an eigenvalue of equation (2.31) and it represents an axial wave number for the assigned frequency, ω, and circumferential wave number, n. A real axial wave number corresponds to a propagating wave travelling along an infinitely long cylinder. An imaginary (complex) axial wave number, on the other hand, represents a spatially decaying, non-propagating (or evanescent) mode in a semi-infinitely long cylinder that decays monotonically (sinusoidally) as the axial (z) coordinate increases [49]. The $2M$ roots of the dispersion relation have the property that if $\boldsymbol{k}_{nm}$ is an axial wave number, then $-\tilde{\boldsymbol{k}}_{nm}$ is also

an axial wave number, where an overtilde denotes the complex conjugate. Physically, half the 2*M* axial wave numbers correspond to wave modes that travel from the origin and decay in the positive axial direction; the other half travel from the origin and decay in the negative axial direction. Associated with each eigenvalue, k_{nm}, of equation (2.31) is a right and left eigenvector, ϕ_{nm}^{R}, and ϕ_{nm}^{L}, respectively. These eigenvectors are used to represent the nodal displacement distributions over the cylinder's thickness in the following way.

The right and left eigenvectors satisfy the relations [1]:

$$\left[A(n,\omega)-k_{nm}B(n)\right]\phi_{nm}^{R}=0;\ \left[A^{T}(n,\omega)-k_{nm}B^{T}(n)\right]\phi_{nm}^{L}=0 \tag{2.33}$$

and

$$\phi_{nm}^{L\ T}B(n)\,\phi_{np}^{R}=B_{nm}\delta_{mp};\ \phi_{nm}^{L\ T}A(n,\omega)\,\phi_{np}^{R}=k_{nm}B_{nm}\delta_{mp} \tag{2.34}$$

where δ_{mp} is the Kronecker delta defined as:

$$\delta_{mp}=\begin{cases}1, & m=p\\ 0, & m\neq p\end{cases}. \tag{2.35}$$

Equation (2.33) results from back substituting the eigenvalues into the homogeneous form of equation (2.31). Equation (2.34), on the other hand, are the bi-orthogonality relations of an eigensystem. Based on the definition of $\bar{Q}_n$, and noting that the upper half of $\bar{Q}_n$ is $\bar{U}_n$ and the lower half is the product of $\bar{U}_n$ and k_n, the right and left eigenvectors can be partitioned into the following upper and lower halves:

$$\phi_{nm}^{R}=\begin{bmatrix}\phi_{nmu}^{R}\\ \phi_{nml}^{R}\end{bmatrix};\ \phi_{nm}^{L}=\begin{bmatrix}\phi_{nmu}^{L}\\ \phi_{nml}^{L}\end{bmatrix}. \tag{2.36}$$

Subscripts *u* and *l* denote the upper and lower halves, respectively. The bi-orthogonality relations given in equation (2.34) can be expressed in terms of the upper and lower halves

of the right and left eigenvectors as [1]:

$$\left.\begin{aligned} &\boldsymbol{\phi}_{nmu}^{L\ T}\boldsymbol{\phi}_{npu}^{R}-\boldsymbol{\phi}_{npl}^{L\ T}\boldsymbol{K}_6\boldsymbol{\phi}_{nml}^{R}=\delta_{mp}B_{np} \\ &\text{and} \\ &\boldsymbol{\phi}_{nml}^{L\ T}\boldsymbol{\phi}_{npu}^{R}+\boldsymbol{\phi}_{nml}^{L\ T}(\boldsymbol{K}_1+jn\boldsymbol{K}_2+n^2\boldsymbol{K}_4-\omega^2\boldsymbol{M})\boldsymbol{\phi}_{npu}^{R}+j\boldsymbol{\phi}_{nml}^{L\ T}(\boldsymbol{K}_3-jn\boldsymbol{K}_5)\boldsymbol{\phi}_{npu}^{R}=\delta_{mp}k_{np}B_{np}\,. \end{aligned}\right\} \quad \textbf{(2.37)}$$

The solution vector, $\bar{\boldsymbol{Q}}_n$, in the transformed domain of the linear eigenvalue problem can be represented by summing the $2M$ right eigenvectors as:

$$\bar{\boldsymbol{Q}}_n=\sum_{m=1}^{2M} Q_{nm}\boldsymbol{\phi}_{nm}^{R}\,. \quad \textbf{(2.38)}$$

The coefficients, Q_{nm}, in the last equation can be found by substituting equation (2.38) into the linear eigenvalue problem, equation (2.31), and using the bi-orthogonality relations (2.34) to give:

$$Q_{nm}=\frac{\boldsymbol{\phi}_{mn}^{L\ T}\bar{\boldsymbol{P}}_n}{(k_{nm}-k_n)B_{nm}}\,. \quad \textbf{(2.39)}$$

Thus, the explicit form of $\bar{\boldsymbol{Q}}_n$ is given by:

$$\bar{\boldsymbol{Q}}_n=\sum_{m=1}^{2M}\frac{\boldsymbol{\phi}_{mn}^{L\ T}\bar{\boldsymbol{P}}_n}{(k_{nm}-k_n)B_{nm}}\boldsymbol{\phi}_{nm}^{R}\,. \quad \textbf{(2.40)}$$

The solution vector, $\bar{\boldsymbol{U}}_n$, that occupies the upper half of $\bar{\boldsymbol{Q}}_n$ can be written as:

$$\bar{\boldsymbol{U}}_n=\sum_{m=1}^{2M}\frac{\boldsymbol{\phi}_{mnl}^{L\ T}\bar{\boldsymbol{F}}_n}{(k_{nm}-k_n)B_{nm}}\boldsymbol{\phi}_{nmu}^{R} \quad \textbf{(2.41)}$$

by using equations (2.32), (2.36) and (2.40).

The inverse Fourier transform, equation (2.29), when applied to equation (2.41) gives the response of the cylinder to the n-th circumferential harmonic in the spatial domain, $\boldsymbol{U}_n(z)$

as:

$$\boldsymbol{U}_n(z)=\frac{1}{2\pi}\sum_{m=1}^{2M}\int_{-\infty}^{\infty}\frac{\boldsymbol{\Phi}_{mnl}^{L\,T}\bar{\boldsymbol{F}}_n}{(k_{nm}-k_n)B_{nm}}\boldsymbol{\Phi}_{nmu}^{R}e^{jk_nz}dk_n. \tag{2.42}$$

It is quite often the case that $\bar{\boldsymbol{F}}_n$, $\boldsymbol{\Phi}_{mnl}^{L}$, $\boldsymbol{\Phi}_{mnu}^{R}$, and B_{nm} are independent of the axial wave number, k_n. Then Cauchy's residue theorem gives the modal response, $\boldsymbol{U}_n(z)$, straightforwardly.

2.7 N-th Circumferential Harmonic Component of the Load

The form that one harmonic component of the Fourier series expansion of the source load given in equation (2.25) takes in the spatial and wave number domains is described next. The harmonic of the Fourier series expansion is considered to have unit magnitude and to be applied at the radial coordinate, r_0. It is assumed further that r_0 coincides with a nodal surface of a finite element. Then the n-th harmonic of the source load, $\boldsymbol{F}$, has the form:

$$\boldsymbol{F}(\theta,z)=e^{jn\theta}\delta(z)\boldsymbol{F}_0 \tag{2.43}$$

in the spatial domain, where δ is the Dirac delta function such that:

$$f(z_0)=\int_{-\infty}^{\infty}f(z)\delta(z_0)\,dz. \tag{2.44}$$

$\boldsymbol{F}_0$ describes the radial distribution of the force vector. For a point load, the radial distribution of the force vector has zero entries everywhere except for those that correspond to the nodal surface $r=r_0$. Suppose that the non-zero components of $\boldsymbol{F}_0$ for the special case of the unit point load correspond to the direction cosines α_{Fr}, $\alpha_{F\theta}$, and α_{Fz} in the r, θ, and z directions, respectively. Then:

$$\boldsymbol{F}_0^{\,T}=\left[\boldsymbol{F}_{0r}^{T};\,\boldsymbol{F}_{0\theta}^{T};\,\boldsymbol{F}_{0z}^{T}\right]=\left[0,0,...,\alpha_{Fr},...,0;\;0,0,...,\alpha_{F\theta},...,0;\;0,0,...,\alpha_{Fz},...,0\right]. \tag{2.45}$$

Moreover, let $\boldsymbol{e}_F$ be the unit vector that defines the line of action of the load vector. Then $\boldsymbol{e}_F$ can be expressed as:

$$\boldsymbol{e}_F=\alpha_{Fr}\boldsymbol{e}_r+\alpha_{F\theta}\boldsymbol{e}_\theta+\alpha_{Fz}\boldsymbol{e}_z \tag{2.46}$$

where $\boldsymbol{e}_r$, $\boldsymbol{e}_\theta$, and $\boldsymbol{e}_z$ are the base vectors of the cylindrical coordinate system illustrated in Figure 2.1. Also, a comparison of equations (2.25) and (2.43) shows that:

$$\boldsymbol{F}_n(z)=\delta(z)\boldsymbol{F}_0\,. \tag{2.47}$$

The Fourier transform of equation (2.47) gives the n-th harmonic component of $\boldsymbol{F}$, $\bar{\boldsymbol{F}}_n(k_n)$, as:

$$\bar{\boldsymbol{F}}_n(k_n)=\boldsymbol{F}_0 \tag{2.48}$$

in the wave number domain by using equations (2.29) and (2.44).

The displacement of the cylinder due to $\bar{\boldsymbol{F}}_n(k_n)$ can be obtained in the spatial domain by substituting equation (2.48) into equation (2.42) and using the Cauchy residue theorem. It can be written as the superposition of two summations. Each summation occurs over a range, *M*, which corresponds to the number of modes that propagate in both the positive and negative axial directions, that is,

$$\boldsymbol{U}_n(z)=-j\sum_{m=1}^{M}\frac{\boldsymbol{\Phi}_{mnl}^{L\,T}\boldsymbol{F}_0}{B_{nm}}\boldsymbol{\Phi}_{nmu}^{R}e^{jk_{nm}z}-j\sum_{m=M+1}^{2M}\frac{\boldsymbol{\Phi}_{mnl}^{L\,T}\boldsymbol{F}_0}{B_{nm}}\boldsymbol{\Phi}_{nmu}^{R}e^{-jk_{nm}z}. \tag{2.49}$$

The analogous stresses can be derived by using equations (2.16) and (2.29) in conjunction with equation (2.49) to be:

$$\sigma_n(z)=\begin{cases} -j\sum_{m=1}^{M}(\boldsymbol{D}_1+jn\boldsymbol{D}_2+jk_{nm}\boldsymbol{D}_3)\dfrac{\boldsymbol{\phi}_{mnl}^{L\,T}\boldsymbol{F}_0}{B_{nm}}\boldsymbol{\phi}_{nmu}^{R}e^{jk_{nm}z} \\ -j\sum_{m=M+1}^{2M}(\boldsymbol{D}_1+jn\boldsymbol{D}_2-jk_{nm}\boldsymbol{D}_3)\dfrac{\boldsymbol{\phi}_{mnl}^{L\,T}\boldsymbol{F}_0}{B_{nm}}\boldsymbol{\phi}_{nmu}^{R}e^{-jk_{nm}z}. \end{cases} \quad \textbf{(2.50)}$$

2.8 Approximation of a Point Load

The Green's functions describe the (displacement) response of an elastic body caused by the application of a unit force at a point of the body. A point load applied at $r=r_0,\ z=0,\ \theta=0$ can be represented in the spatial domain as:

$$\boldsymbol{F}(\theta,z)=\delta(\theta)\,\delta(z)\,\boldsymbol{F}_0 \quad \textbf{(2.51)}$$

where $\boldsymbol{F}_0$ again describes the radial distribution of the force vector. The previous formulation of the displacement and stress fields indicates that the force vector can be expanded into a Fourier series in the circumferential direction. The Fourier series of the Dirac delta function, however, does not converge. Consequently the Dirac delta function is approximated circumferentially in the manner of [1] by using a "narrow" pulse of uniform intensity, q_0, that extends over a circumferential distance $2r_0\theta_0$. For this pulse to be "equivalent" to the Dirac delta function, it must have unit amplitude, that is,

$$\left.\begin{aligned} &\int_{-\theta_0}^{\theta_0} q_0 r_0 d\theta = 1 \\ \text{or} \quad &\\ &q_0=\frac{1}{2r_0\theta_0}. \end{aligned}\right\} \quad \textbf{(2.52)}$$

Then a point load applied at $r=r_0,\ z=0,\ \theta=0^\circ$ can be approximated in the spatial domain as:

$$F(\theta,z)=\begin{cases}\dfrac{1}{2r_0\theta_0}\delta(z)F_0\,, & -\theta_0\le\theta\le\theta_0\\ 0\,, \text{ otherwise}\,.\end{cases} \tag{2.53}$$

A Fourier series expansion of equation (2.53), may be written as:

$$F(\theta,z)=\sum_{n=-\infty}^{n=\infty} e^{jn\theta}F_n(z)=\sum_{n=-\infty}^{n=\infty} e^{jn\theta}\frac{\text{sinc}(n\theta_0)}{2r_0\pi}F_0\delta(z) \tag{2.54}$$ [+]

in the circumferential direction, where:

$$F_n(z)=\frac{\text{sinc}(n\theta_0)}{2r_0\pi}F_0\delta(z)\,. \tag{2.55}$$

Applying the Fourier transform pairs, equation (2.29), to equation (2.55) transforms the n-th term of the pulse's approximation from the spatial domain to the wave number domain. The n-th term of this transformation is expressed as:

$$\bar{F}_n(k_n)=\frac{\text{sinc}(n\theta_0)}{2r_0\pi}F_0 \tag{2.56}$$

where equation (2.44) has been used again.

2.9 N-th Circumferential Harmonic of the Green's Functions

Substituting equation (2.56) into equation (2.42) gives the n-th circumferential harmonic of the Green's functions in the spatial domain as:

[+] The sinc function is defined as:

$$\text{sinc}(x)=\begin{cases}\dfrac{\sin(x)}{x}, & x\neq 0\\ 1, \text{ otherwise.}\end{cases}$$

$$\boldsymbol{U_n}(z)=\frac{\operatorname{sinc}(n\theta_0)}{4\pi^2 r_0}\sum_{m=1}^{2M}\int_{-\infty}^{\infty}\frac{\boldsymbol{\phi}_{mnl}^{L\ T}\boldsymbol{F_0}}{(k_{nm}-k_n)B_{nm}}\boldsymbol{\phi}_{nmu}^{R}e^{jk_n z}dk_n. \tag{2.57}$$

Applying Cauchy's residue theorem gives the n-th circumferential mode of the Green's function as:

$$\boldsymbol{U_n}(z)=\frac{-j\operatorname{sinc}(n\theta_0)}{2\pi r_0}\sum_{m=1}^{M}\frac{\boldsymbol{\phi}_{mnl}^{L\ T}\boldsymbol{F_0}}{B_{nm}}\boldsymbol{\phi}_{nmu}^{R}e^{jk_{nm}z}. \tag{2.58}$$

Note that (axial) cross sections having a positive z are only considered in equation (2.58). (The displacements at an axial cross section having a negative z may be obtained by replacing the lower and upper limits of the summation in equation (2.58) with M+1 and 2M, respectively and changing the sign of the exponential.) Substituting equation (2.58) into equation (2.16) gives the corresponding stress field as:

$$\boldsymbol{\sigma_n}(z)=\frac{-j\operatorname{sinc}(n\theta_0)}{2\pi r_0}\sum_{m=1}^{M}(\boldsymbol{D_1}+jn\boldsymbol{D_2}+jk_{nm}\boldsymbol{D_3})\frac{\boldsymbol{\phi}_{mnl}^{L\ T}\boldsymbol{F_0}}{B_{nm}}\boldsymbol{\phi}_{nmu}^{R}e^{jk_{nm}z}. \tag{2.59}$$

2.10 Green's Functions

Substituting equation (2.58) into equation (2.26) gives the Green's functions as:

$$\boldsymbol{U}(\theta,z,t)=e^{-j\omega t}\frac{-j}{2\pi r_0}\sum_{n=-\infty}^{n=\infty}\operatorname{sinc}(n\theta_0)\left[\sum_{m=1}^{M}\frac{\boldsymbol{\phi}_{mnl}^{L\ T}\boldsymbol{F_0}}{B_{nm}}\boldsymbol{\phi}_{nmu}^{R}e^{jk_{nm}z}\right]e^{jn\theta} \tag{2.60}$$

for positive z cross sections of the cylinder. Similarly, substituting equation (2.59) into equation (2.27) gives the corresponding stress field as:

$$\boldsymbol{\sigma}(\theta,z,t)=e^{-j\omega t}\frac{-j}{2\pi r_0}\sum_{n=-\infty}^{n=\infty}\operatorname{sinc}(n\theta_0)\left[\sum_{m=1}^{M}(\boldsymbol{D_1}+jn\boldsymbol{D_2}+jk_{nm}\boldsymbol{D_3})\frac{\boldsymbol{\phi}_{mnl}^{L\ T}\boldsymbol{F_0}}{B_{nm}}\boldsymbol{\phi}_{nmu}^{R}e^{jk_{nm}z}\right]e^{jn\theta}. \tag{2.61}$$

2.11 Response for Multi-Frequency Input Forces

It has been assumed previously that the applied loads give a consistent load vector that is time harmonic with a (single) angular frequency, ω, for which the Green's functions and stress field have been recovered. As the differential equations are linear, the response to a multi-frequency input force can be found by merely superimposing the responses caused by each individual frequency component. The input force of interest here has a continuous frequency distribution so that the corresponding Fourier transform may be used to determine its frequency content. The Fourier transform pair that relates the time (t) domain to the frequency (ω) domain is:

$$\bar{g}(\omega)=\int_{-\infty}^{\infty} g(t)e^{j\omega t}dt\,;\; g(t)=\frac{1}{2\pi}\int_{-\infty}^{\infty}\bar{g}(\omega)e^{-j\omega t}d\omega \tag{2.62}$$

where g is an arbitrary function and an overbar indicates the Fourier transform. Note that the signs of the exponentials in equation (2.62) are different from those of equation (2.29). The former are chosen so that waves with (real) positive wave numbers propagate in the positive z direction as time increases. The displacement and stress fields (at positive z) which arise from a unit magnitude, input force that is harmonic are given, in the frequency domain, by:

$$\bar{\boldsymbol{U}}(\theta,z,\omega)=\frac{-j}{2\pi r_0}\sum_{n=-\infty}^{n=\infty}\operatorname{sinc}(n\theta_0)\left[\sum_{m=1}^{M}\frac{\boldsymbol{\phi}^{L}_{mnl}{}^{T}(\omega)\boldsymbol{F_0}}{B_{nm}(\omega)}\boldsymbol{\phi}^{R}_{nmu}(\omega)\,e^{jk_{nm}(\omega)z}\right]e^{jn\theta} \tag{2.63}$$

and

$$\bar{\sigma}(\theta,z,\omega)=\left\{\begin{array}{c}\dfrac{-j}{2\pi r_0}\sum_{n=-\infty}^{n=\infty}\operatorname{sinc}(n\theta_0)\times \\ \left[\sum_{m=1}^{M}(\boldsymbol{D_1}+jn\boldsymbol{D_2}+jk_{nm}(\omega)\boldsymbol{D_3})\dfrac{\boldsymbol{\phi}_{mnl}(\omega)^{\boldsymbol{L}\,\boldsymbol{T}}(\omega)\boldsymbol{F_0}}{B_{nm}(\omega)}\boldsymbol{\phi}^{\boldsymbol{R}}_{\boldsymbol{nmu}}(\omega)\,e^{jk_{nm}(\omega)z}\right]e^{jn\theta}.\end{array}\right. \tag{2.64}$$

The displacement field of the cylinder may be found by using equation (2.63) and summing the contribution of each frequency component contained in the input force. Consequently:

$$\begin{aligned}\boldsymbol{U}(\theta,z,t)&=\frac{-j}{4\pi^2 r_0}\int_{-\infty}^{\infty}\bar{f}(\omega)e^{-j\omega t}\sum_{n=-\infty}^{n=\infty}\operatorname{sinc}(n\theta_0)\left[\sum_{m=1}^{M}\frac{\boldsymbol{\phi}^{\boldsymbol{L}}_{\boldsymbol{mnl}}{}^{\boldsymbol{T}}(\omega)\boldsymbol{F_0}}{B_{nm}(\omega)}\boldsymbol{\phi}^{\boldsymbol{R}}_{\boldsymbol{nmu}}(\omega)\,e^{jk_{nm}(\omega)z}\right]e^{jn\theta}\,d\omega \\ &=\frac{-j}{4\pi^2 r_0}\int_{-\infty}^{\infty}\bar{f}(\omega)e^{-j\omega t}\sum_{n=-\infty}^{n=\infty}\operatorname{sinc}(n\theta_0)\boldsymbol{G_n}(\omega,z)\,e^{jn\theta}\,d\omega\end{aligned} \tag{2.65}$$

in the time domain where:

$$\boldsymbol{G_n}(\omega,z)=\left[\sum_{m=1}^{M}\frac{\boldsymbol{\phi}^{\boldsymbol{L}}_{\boldsymbol{mnl}}{}^{\boldsymbol{T}}(\omega)\boldsymbol{F_0}}{B_{nm}(\omega)}\boldsymbol{\phi}_{\boldsymbol{nmu}}{}^{\boldsymbol{R}}(\omega)\,e^{jk_{nm}(\omega)z}\right] \tag{2.66}$$

and $\bar{f}(\omega)$ is the Fourier transform of the input force. The corresponding stress field is given by:

$$\sigma(\theta,z,t)=\left\{\begin{array}{c}\dfrac{-j}{4\pi^2 r_0}\left\{\int_{-\infty}^{\infty}\bar{f}(\omega)e^{-j\omega t}\sum_{n=-\infty}^{n=\infty}\operatorname{sinc}(n\theta_0)\times\right. \\ \left.\left[\sum_{m=1}^{M}(\boldsymbol{D_1}+jn\boldsymbol{D_2}+jk_{nm}(\omega)\boldsymbol{D_3})\dfrac{\boldsymbol{\phi}^{\boldsymbol{L}}_{\boldsymbol{mnl}}{}^{\boldsymbol{T}}(\omega)\boldsymbol{F_0}}{B_{nm}(\omega)}\boldsymbol{\phi}^{\boldsymbol{R}}_{\boldsymbol{nmu}}(\omega)\,e^{jk_{nm}(\omega)z}\right]e^{jn\theta}\,d\omega\right\}.\end{array}\right. \tag{2.67}$$

Note that $\bar{f}(\omega)$ in equations (2.65) and (2.67) serves to (amplitude) scale and phase shift the Green's and stress functions for each frequency component contained in the input force.

2.12 Illustrative Example

2.12.1 Overview

Computer programs have been developed to implement the previously outlined mathematical model. (These programs are contained on the accompanying electronic media where copyright permits it. See also Appendix B). However, it is useful to describe the available computing facilities before presenting the mechanical properties of the particular homogenous isotropic cylinder considered. Then conventional dispersion curves are given for this cylinder. Green's functions and stress fields are determined at the cylinder's outer surface for the special case of a time harmonic point load that is applied radially[+] at the cylinder's outer surface. Typical Frequency Response Functions (FRF) are evaluated at the cylinder's outer surface. By using the FRF, the radial displacement induced by the point load (whose functional form is presented in Appendix A) is calculated at the outer surface of the cylinder. Details are given for each step of the analysis to illustrate the implementation and approximate computer times taken on a reference Intel® Pentium® 4 based, Personal Computer (PC). Figure 2.2 shows a flow chart of the procedure followed. Note that the calculated Green's functions, stress functions, frequency responses, displacement and stress components, unlike their experimental counterparts, could be presented over the cylinder's thickness. They are omitted not only for brevity but also

---

[+] A radial load is considered because it is the easiest to implement experimentally. For a radial load, equation (2.45) takes the form:

$$\boldsymbol{F}_{\mathbf{0}}{}^{\boldsymbol{T}}=\left[\boldsymbol{F}_{\mathbf{0}r}{}^{\boldsymbol{T}};\ \boldsymbol{F}_{\mathbf{0}\theta}{}^{\boldsymbol{T}};\ \boldsymbol{F}_{\mathbf{0}z}{}^{\boldsymbol{T}}\right]=[0,0,\ldots,1,\ldots,0;\ 0,0,\ldots,0,\ldots,0;\ 0,0,\ldots,0,\ldots,0].$$

(Loads having an arbitrary line of action may be found by using either equation (2.45) directly or by considering separate loads that act in the radial, circumferential, and axial directions and using the principle of superposition.)

because a radial displacement-like quantity is measured most easily on the cylinder's outer surface for later comparisons. (See Chapter 3 for further details.)

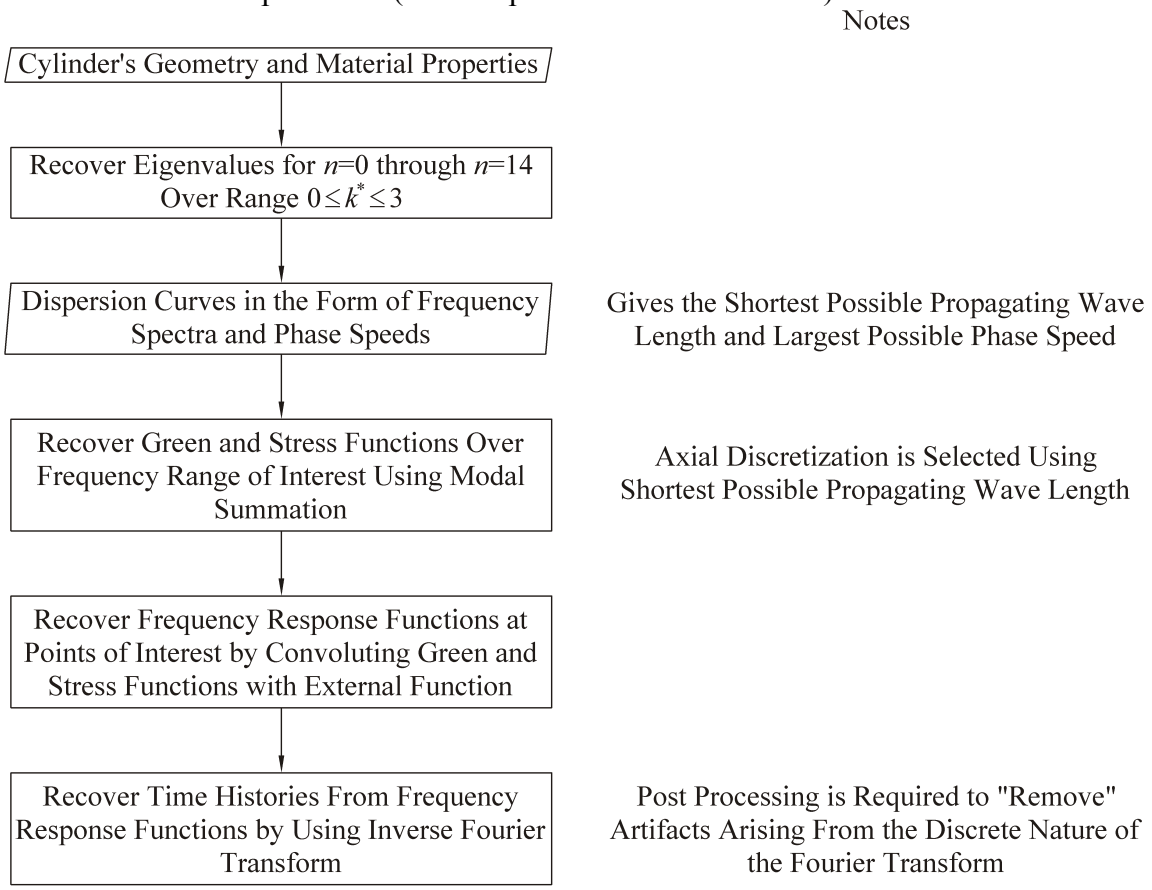

Figure 2.2. Procedure to Recover Radial Displacement History

2.12.2 Available Computer Facilities

Table 2.1 lists pertinent specifications of the available computer facilities. The approximate relative speed is the ratio between the number of locations at which radial displacement histories are recovered with a given Central Processing Unit (CPU) to the number for the reference CPU using the identical program in the same period. In the case of a parallel/multiple processor computer, the total number of locations is divided first by the total number of processors used so that the performance of a single processor can be assessed.

Table 2.1. Specifications of the Computer Facilities

Machine Designation[+]	Central Processing Unit (CPU)	Motherboard	Random Access Memory (RAM)	Operating System	Approximate Relative Speed
Rm414[++]	2.4 GHz Intel® Pentium® 4 (400 MHz Front Side Bus)	ASUS™ P4B533-E (Rev. 1.02)	1x1 GB (ECC) PC2100 SDRAM	Microsoft® Windows® XP Professional (Service Pack 1)	1.0
Hal	AMD™ Athlon™ XP 1800+, multiplier "unlocked" to 2300+ (333 MHz Front Side Bus)[+++]	ASUS™ A7V8X-X (Rev. 1.01)	2x512 MB PC2700 SDRAM	Microsoft® Windows® XP Professional (Service Pack 1)	1.4
Hal2k	950 MHz AMD™ Athlon™ (Thunderbird) operating at 1GHz (133 MHz Front Side Bus)[++++]	ASUS™ A7V133 (Rev. 1.04)	2x512 MB PC133 SDRAM	Microsoft® Windows® XP Professional (Service Pack 1)	0.8
Darkmenace	400 MHz Intel® Pentium® II (100 MHz Front Side Bus)	ASUS™ P2B (Rev. 1.02.)	1x256 MB PC133 SDRAM 1x128 MB PC100 SDRAM 1x32 MB PC100 SDRAM	Microsoft® Windows® XP Professional (Service Pack 1)	0.2
Polaris[+++++]	24 1050 MHz Sun® Microsystems UltraSPARC® III (150 MHz Front Side Bus)	6 Sun® Microsystems "Uniboard" (CPU/Memory boards)	192x256 MB 7ns ECC SDRAM	Sun Microsystems™ Solaris™ 8 (SunOS™ 5.8)	0.3

[+] This is the computer's network name.

[++] The reference computer.

[+++] A stock Athlon™ XP 1800+ has an internal clock speed of 1530 MHz Speed (11.5x133 MHz). This CPU is run as an Athlon™ XP 2300+ at 1866 MHz (14x133 MHz).

[++++] An Athlon™ 950 has an internal clock speed of 950 MHz (9.5x100 MHz). This CPU is run at 1000 MHz (7.5x133 MHz).

[+++++] This is a parallel computer which runs in a time shared environment. Consequently direct comparisons with PCs are difficult. The relative speed is based on a single CPU even though three CPUs are used simultaneously. The poor performance of this computer, relative to that of the PCs, is likely due the "overhead" of running a serial program on a parallel computer.

2.12.3 Mechanical Properties of the Cylinder

The illustrative cylinder corresponds to a 3 inch Nominal Pipe Size (NPS) (80 mm Diameter Nominal [DN]), Schedule 40, seamless, carbon steel pipe. This particular cylinder is selected because it is commercially important and has been studied extensively. See, for example, [7;16;17;22;34;47;50]. The symmetric matrix of the elastic moduli, $\boldsymbol{D}$, can be expressed for an isotropic material as:

$$\boldsymbol{D}=\begin{bmatrix} D_{11} & D_{12} & D_{13} & 0 & 0 & 0 \\ D_{12} & D_{22} & D_{23} & 0 & 0 & 0 \\ D_{13} & D_{23} & D_{33} & 0 & 0 & 0 \\ 0 & 0 & 0 & D_{44} & 0 & 0 \\ 0 & 0 & 0 & 0 & D_{55} & 0 \\ 0 & 0 & 0 & 0 & 0 & D_{66} \end{bmatrix} = \begin{bmatrix} \lambda+2\mu & \lambda & \lambda & 0 & 0 & 0 \\ \lambda & \lambda+2\mu & \lambda & 0 & 0 & 0 \\ \lambda & \lambda & \lambda+2\mu & 0 & 0 & 0 \\ 0 & 0 & 0 & \mu & 0 & 0 \\ 0 & 0 & 0 & 0 & \mu & 0 \\ 0 & 0 & 0 & 0 & 0 & \mu \end{bmatrix} \tag{2.68}$$

where λ and μ are Lame's constants. Note that Lame's constants can be related to the more familiar Young's modulus, E, and Poisson's ratio, ν, through:

$$\lambda=\frac{E\nu}{(1+\nu)(1-2\nu)} \tag{2.69}$$

and

$$\mu=\frac{E}{2+2\nu} \tag{2.70}$$

where μ is identical to the shear modulus, G. All the material properties are taken to coincide with the values used in [16;34;47;50;51]. Consequently:

$$\lambda=16\ 410\ ksi\ (113.2\ GPa) \tag{2.71}$$

and

$$\mu = 12\ 230\ ksi\ (84.3\ GPa) \tag{2.72}$$

which correspond to a Young's modulus and Poisson's ratio of:

$$E = 31\ 460\ ksi\ (216.9\ GPa) \tag{2.73}$$

and

$$\nu = 0.2865. \tag{2.74}$$

The mass density of the cylinder, ρ, is:

$$\rho = 8.906 \times 10^{-3}\ slug/in^3\ (7932\ kg/m^3). \tag{2.75}$$

Its outer diameter, D_o, and total thickness are:

$$D_o = 3.4960\ in\ (88.8\ mm) \tag{2.76}$$

and

$$H = 0.220\ in\ (5.59\ mm). \tag{2.77}$$

Then the mean radius of the cylinder, R, is related to D_o and H by:

$$R = \left(\frac{D_o - H}{2} \right) \tag{2.78}$$

so that, by using equations (2.76) through (2.78),

$$R = 1.638\ in\ (41.6\ mm) \tag{2.79}$$

and

$$H/R = 0.134. \tag{2.80}$$

2.12.4 Dispersion Curves and Phase Speeds

A frequency spectrum shows the relation between the frequency and (axial) wave number (i.e. the dispersion relationship) for modes that can propagate for a given circumferential wave number. By convention, the wave number and frequency are plotted

on the abscissa and ordinate, respectively. The results are presented usually in non-dimensional form. Then the non-dimensional wave number, k^*, is given by:

$$k^* = \frac{k}{k_{ref}} \tag{2.81}$$

where k is the axial wave number and k_{ref} is:

$$k_{ref} = \frac{1}{H}. \tag{2.82}$$

Similarly, the non-dimensional frequency, ω^*, is given by:

$$\omega^* = \frac{\omega}{\omega_{ref}} \tag{2.83}$$

where:

$$\omega_{ref} = \frac{1}{H}\sqrt{\frac{\mu}{\rho}} = \frac{c_2}{H} \tag{2.84}$$

and

$$c_2 = \sqrt{\frac{\mu}{\rho}} \tag{2.85}$$

is the torsional wave speed. For the cylinder under consideration:

$$k_{ref} = 4.542 \ in^{-1} \ (0.179 \ mm^{-1}) \tag{2.86}$$

$$\omega_{ref} = 5.829 \times 10^5 \ rad/s \tag{2.87}$$

and

$$c_2 = 10 \ 696 \ ft/s \ \ (3 \ 260 \ m/s). \tag{2.88}$$

The (non-dimensional) phase speed, c^*, is given by:

$$c^* = \frac{c}{c_2} = \frac{\lambda f}{c_2} = \frac{\omega}{k c_2} = \frac{\omega^*}{k^*} \tag{2.89}$$

where c is the dimensional phase speed and λ (f) is the wavelength (frequency) of a propagating mode. Note that:

$$\lambda = \frac{2\pi}{k} \tag{2.90}$$

and the frequency, f, is:

$$f = \frac{\omega}{2\pi}. \tag{2.91}$$

Wave numbers are found by solving the eigenvalues of equation (2.31) using a FORTRAN implementation of an eigensolver from the International Mathematical and Statistical Library (IMSL™). The stiffness matrices, $\boldsymbol{K_i}$, i=1, 2, 3, 4, 5, 6, as well as the mass matrix, $\boldsymbol{M}$, appearing in equations (2.31) and (2.32) are calculated by using Gauss integration with three control points. Eighty (quadratic) elements are employed in the discretization of the cylinder's thickness. Eighty is deemed sufficient because only the first (lowest) three eigenvalues are of interest here. The lowest eigenvalues are usually found most accurately and eighty elements gives sufficient accuracy to estimate the shortest wavelength of the propagating modes. The wave number/frequency pairs are written to a plain (American Standard Code for Information Interchange [ASCII]) text file. This computer program is not included on the accompanying electronic media due to copyright. For each circumferential wave number considered (14 in total), approximately 1 hour is required to calculate the eigenvalues over the frequency range of interest using 120 discrete

frequency points and the finite element discretization described before. Note from Figure A.1 of Appendix A that the magnitude of the Fourier transform of the transient point load is essentially zero outside about 35 kHz to 107 kHz, or ω^* from 0.377 to 1.153.

Figures 2.3 through 2.5 show the frequency spectra for circumferential wave numbers in the range from n=0 through n=14 and k^*=0 to k^*=3 inclusive. The frequency region of interest, that is the frequencies which the transient point load is likely to excite, is shaded in Figures 2.3 through 2.5 for clarity. It can be seen from these figures that, in this frequency range, there are three propagating modes for each circumferential wave number, n, equal to zero through five inclusive. Two propagating modes occur for circumferential wave numbers corresponding to n of six through eight, and one propagating mode exists for circumferential wave numbers when n ranges between nine to thirteen. There are no propagating modes (in the frequency range of interest) for circumferential wave numbers larger than thirteen. Thus the total number of potentially propagating modes is 29. These modes are labelled following the convention used in [14]. For n=0, modes are designated as either torsional or longitudinal. The torsional [longitudinal] modes are indicated by T(0,m) [L(0,m)] where m is a positive integer giving the eigenvalue to which the mode corresponds. On the other hand, modes are designated as flexural for n greater than zero. A flexural mode is denoted by F(n,m) where n is the circumferential wave number and m is again a positive integer indicating the eigenvalue to which the mode corresponds. Note that, from equation (2.90), the shortest wavelength of a propagating mode is related to the largest (real) wave number. The shortest wavelength determines, in part, the axial spacing that is used later to find the radial displacement field. A careful examination of Figures 2.3 through

2.5 shows that the largest wave number in the frequency range of interest is approximately 1.84. It corresponds to the longitudinal mode n=0 and m=1 or L(0,1). This point is marked by using a circle in Figure 2.3 (a). Defining the non-dimensional wavelength, λ^*, as:

$$\lambda^* = \frac{\lambda}{H} = \frac{2\pi}{k^*}, \tag{2.92}$$

the shortest non-dimensional wavelength that can propagate in the frequency range of interest is approximately 3.41.

Experience suggests that it is desirable to have at least four spatial points to uniformly cover the distance corresponding to the shortest wavelength in order to reasonably compute the cylinder's displacement field. This restriction corresponds to a non-dimensional axial separation of about $z^* \approx 3.41/4 \approx 0.85$ where z^* is defined as:

$$z^* = \frac{z}{H}. \tag{2.93}$$

The z is the axial coordinate described in the coordinate system shown in Figure 2.1. Figures 2.6 through 2.8 present the phase speeds for circumferential wave numbers corresponding to n=0 through n=14 over the range ω^*=0 to ω^*=2 inclusive. The figures are generated by using equation (2.89) and the same wave number/frequency pairs that are utilized for the wave spectra plots. A shaded area represents the same frequency range given in Figures 2.3 through 2.5. Phase speeds for the modes having a cutoff frequency below the lowest noticeable frequency component of the transient point load are essentially independent of frequency in the range of interest. Consequently these modes are essentially non-dispersive. On the other hand, the phase speeds of the modes which have a cutoff frequency within this

range are very dispersive, particularly around the cut-off frequency.

Figures 2.3 through 2.8 are used, in conjunction with the FRF, to determine different waves' times of flight in order to identify the propagating modes excited by the transient point load. They suggest that the wave numbers and phase speeds are similar for many modes at a given frequency. Consequently, identifying individual modes from the Green's functions, stress functions, and computed radial displacement field time histories may be difficult.

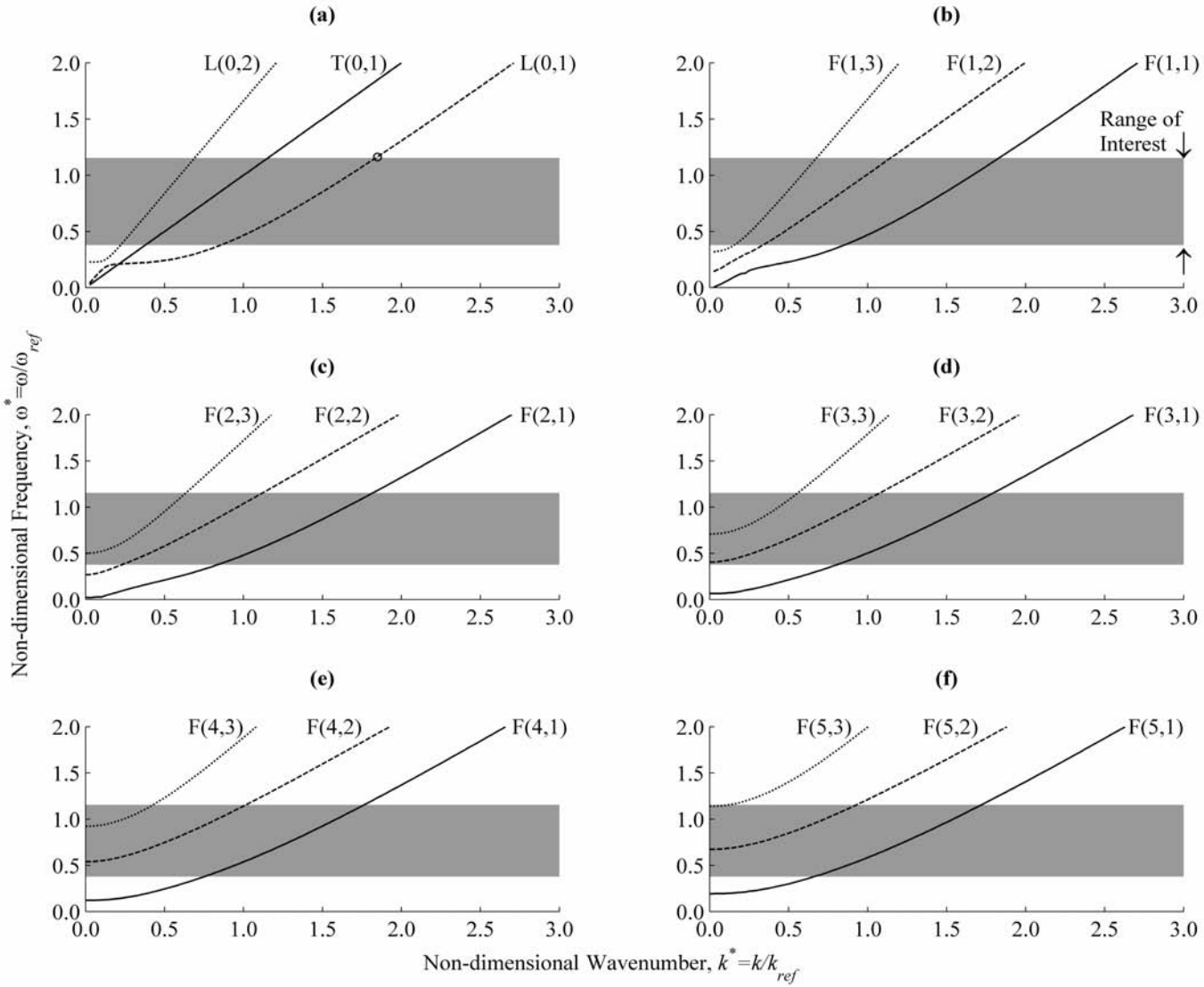

Figure 2.3. Frequency Spectra for n=0 through n=5

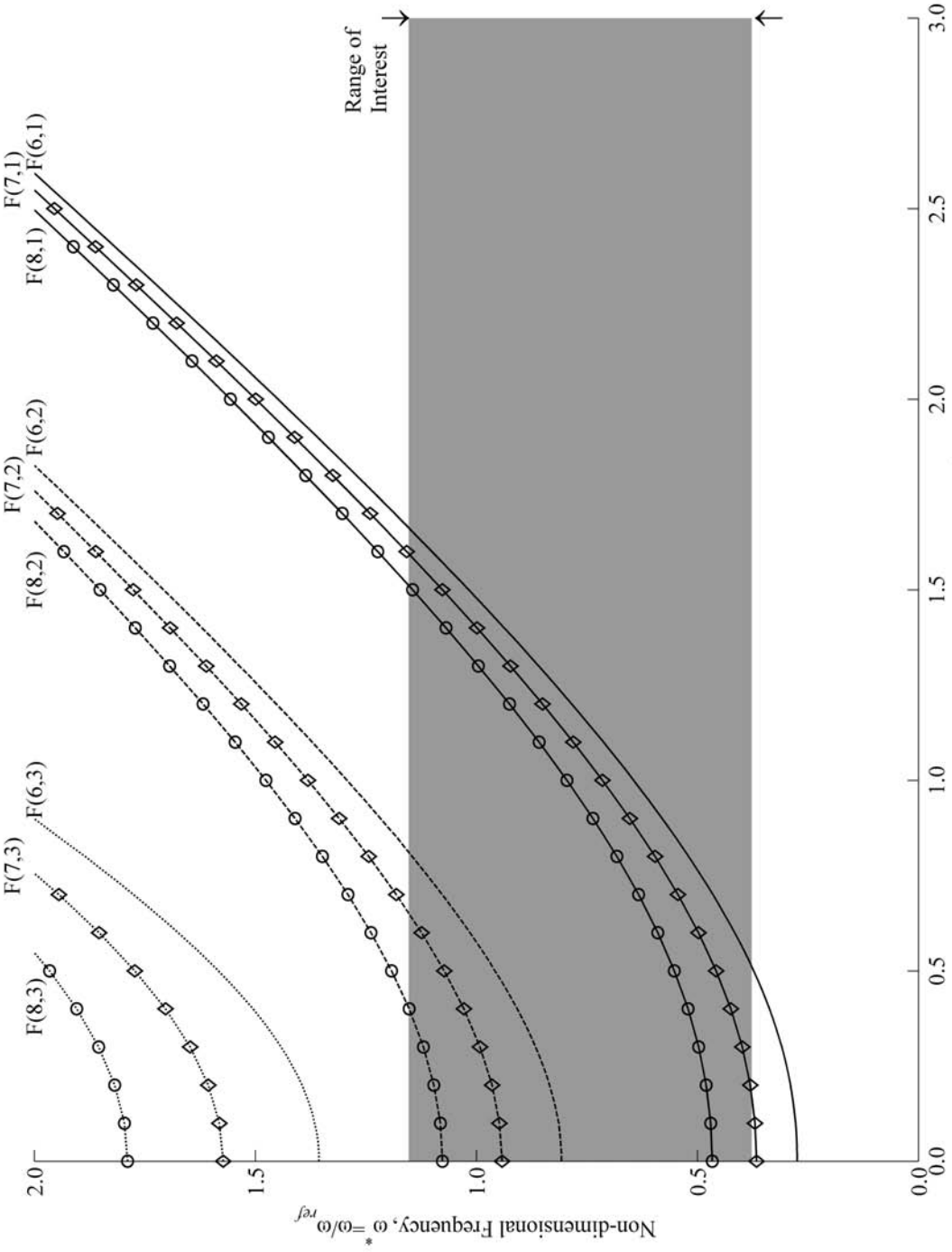

Figure 2.4. Frequency Spectra for n=6 through n=8

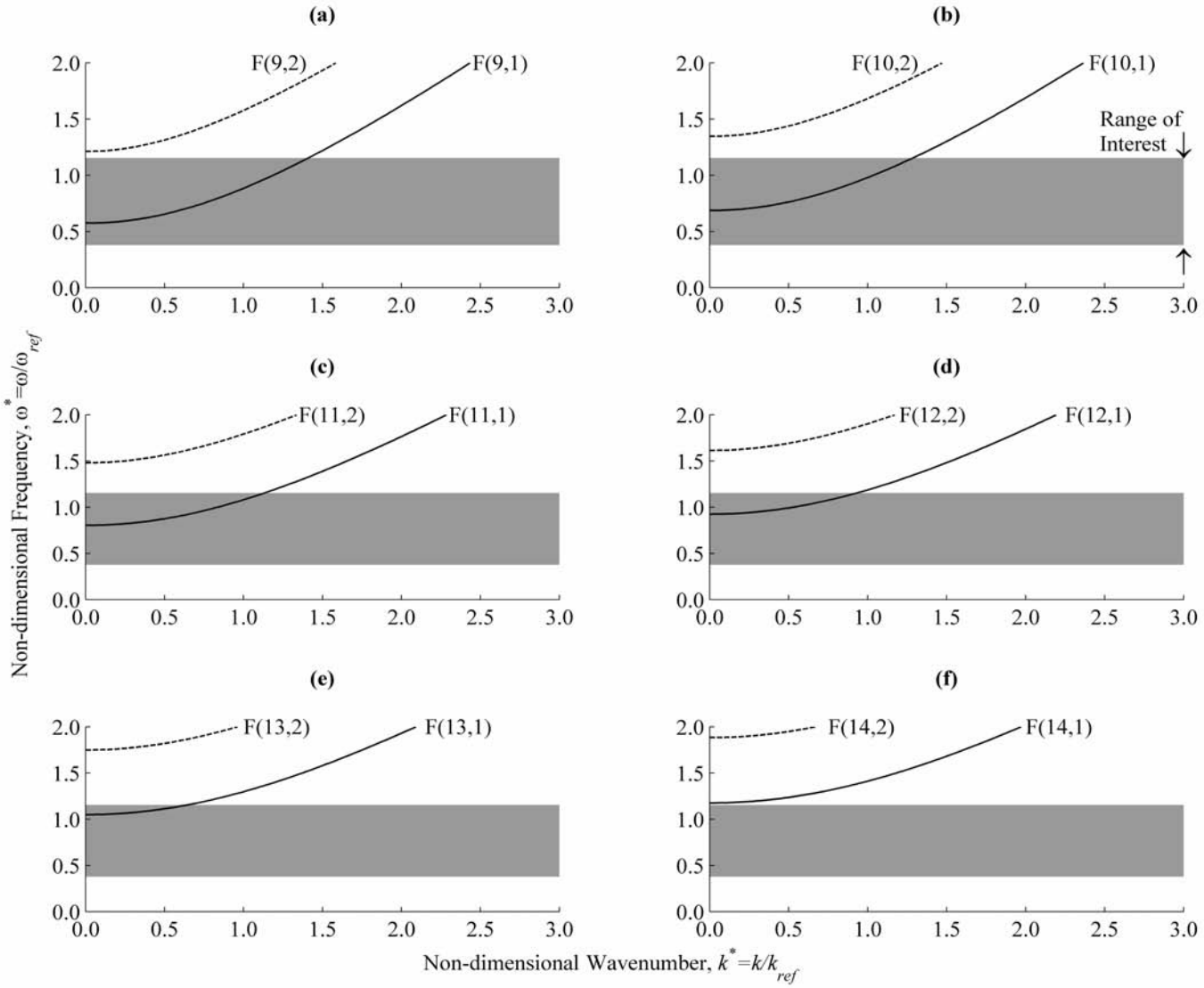

Figure 2.5. Frequency Spectra for n=9 through n=14

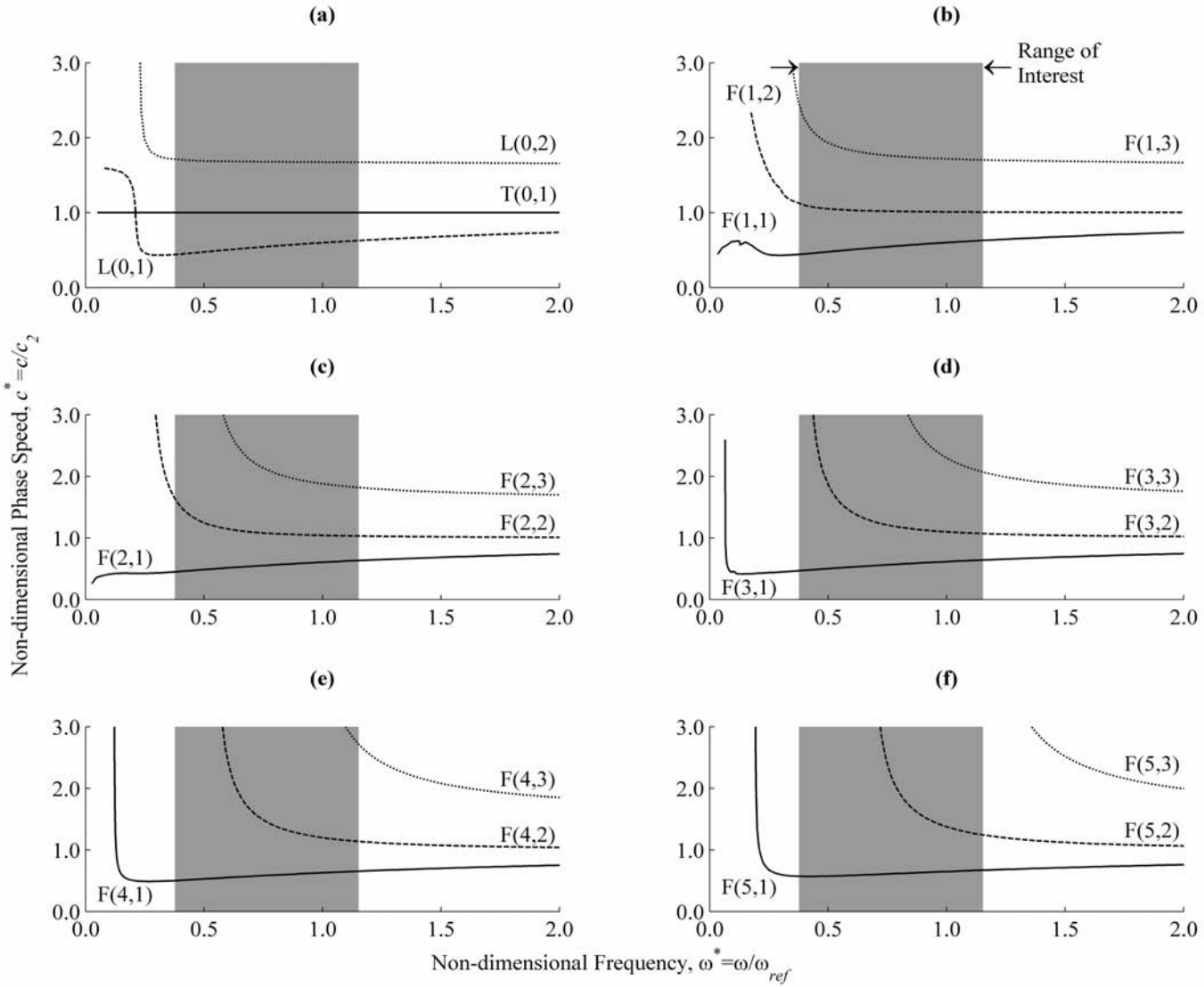

Figure 2.6. Phase Speeds for n=0 through n=5

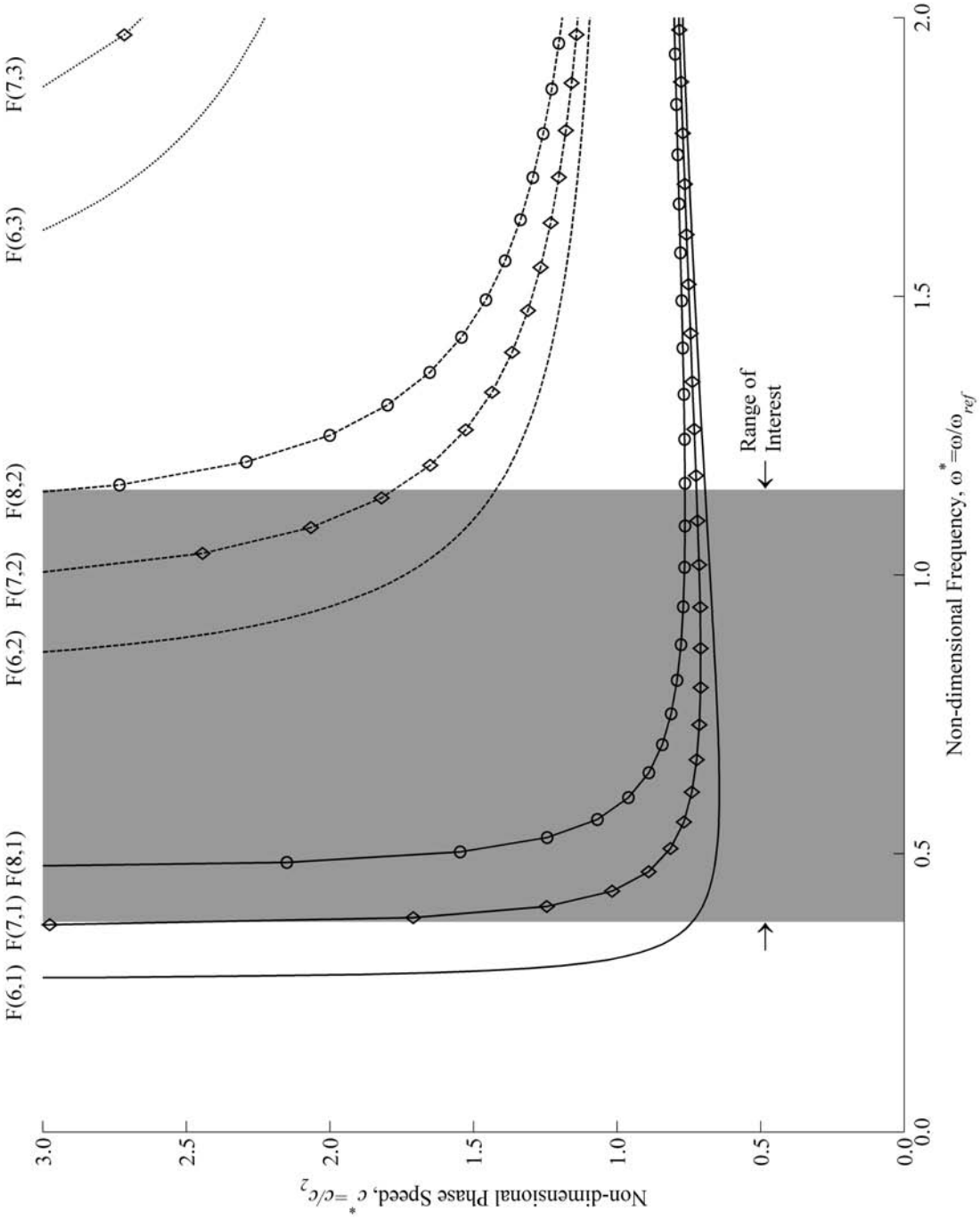

Figure 2.7. Phase Speeds for n=6 through n=8

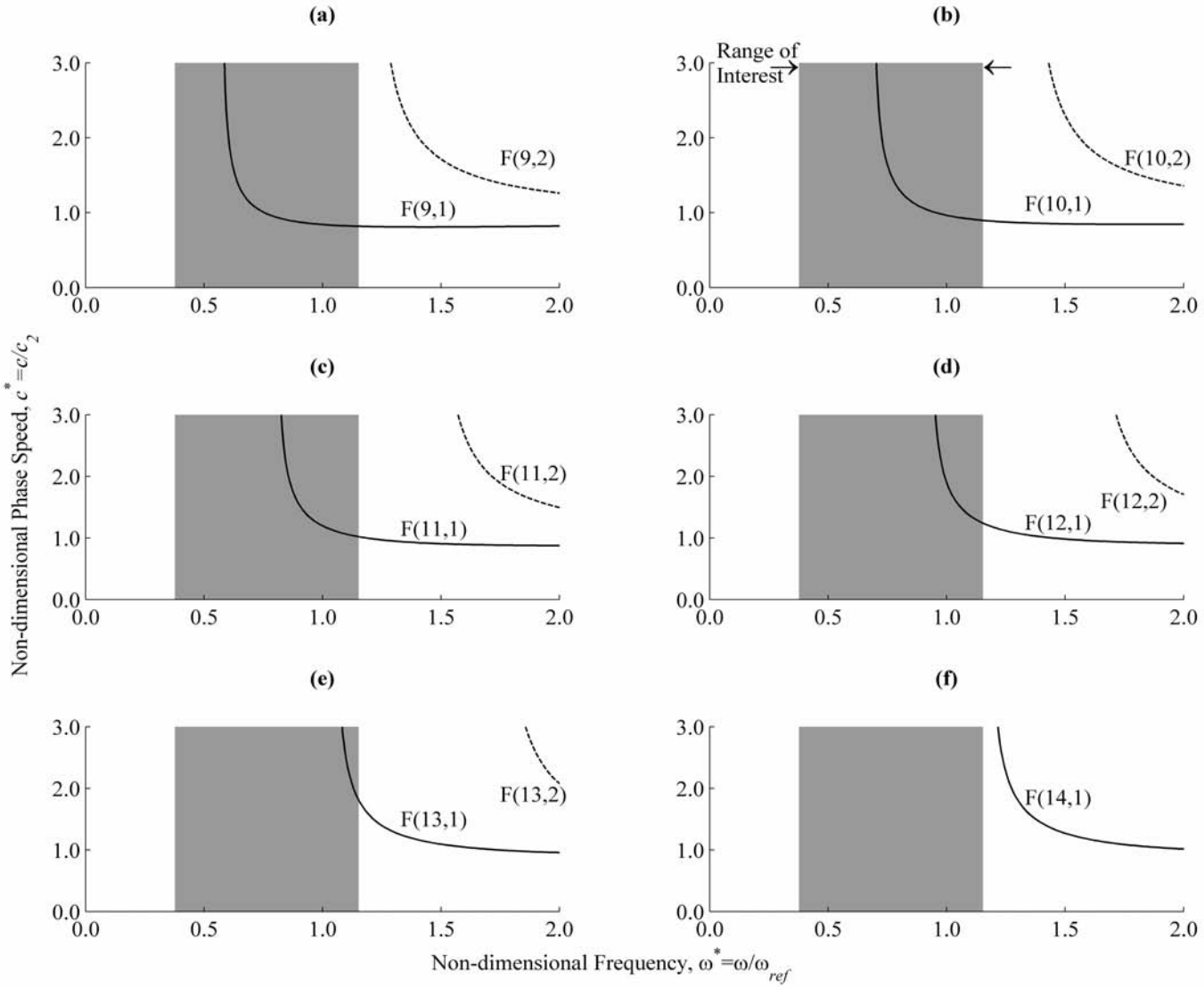

Figure 2.8. Phase Speeds for n=9 through n=14

2.12.3 Green's functions and Stresses

Consider a time harmonic point load that is applied radially at the outer surface of the cylinder and has a non-dimensional magnitude of unity [see equation (2.94)]. The Green's functions and stresses are calculated by using a modal summation. They are computed for 145 equally spaced frequency points at each of 330 equally spaced, positive z cross sections and 181 equally spaced circumferential locations. Half the symmetrical cylinder's circumference is represented at each axial cross section. Non-dimensional frequencies between about 0.377 to 1.153 are considered so that, once again, the significant frequencies of the transient point load are accommodated. (In dimensional terms, the frequency points correspond to 35 kHz through 107 kHz in 0.5 kHz increments.) The cross sections are located from z^*=0 to z^*=279.65 in steps of 0.85, that is from z=0 ft (0 m) to approximately z=5.1 ft (1.6 m) with a 0.19 in (0.47 cm) step size. Circumferential locations are recovered from θ=0° to θ=180° at each cross section in 1° steps. Symmetry arguments are employed to determine the Green's functions and stresses for the other half of the cylinder as well as for the negative z cross sections.

The circumferential angle, $2\theta_0$, over which the spatial pulse approximates the Dirac delta function [see equation (2.53)] is taken to be 0.002 radians. Furthermore, 601 circumferential terms (corresponding to n=-300 through n=300) are employed. These values have been shown previously [1] to adequately represent the displacement and stress fields in the "near field" ($z^* \leq 2$) where convergence of a modal summation is the slowest. For the same reason, ten (quadratic) elements are used to discretize the cylinder's thickness.

To obtain the required non-dimensional (body) force, $\boldsymbol{P}$, which has a unit magnitude,

the actual force, $\boldsymbol{f}$, is non-dimensionalized by using:

$$\boldsymbol{P}=\frac{H}{\mu}\boldsymbol{f} \tag{2.94}$$

where H is the thickness and μ is the Lame's constant (shear modulus) of the cylinder. Moreover, for the cylinder under consideration,

$$\frac{H}{\mu}\approx 1.799\times 10^{-8}\ in^3/lb_f\ (6.631\times 10^{-14}\ m^3/N) \tag{2.95}$$

so that:

$$\boldsymbol{f}\approx 55\ 591 ksi/in^3\ (15\ 081\ GN/m^3). \tag{2.96}$$

To compute the Green and stress functions by using modal summation, the contributions of each of $\boldsymbol{F}$'s circumferential harmonic components need to be determined first. To this end, the stiffness and mass matrices which appear in equations (2.31) and (2.32) are calculated for each frequency point by again using Gauss integration and three control points. The axial wave numbers and mode shapes are found for each circumferential harmonic by solving the eigenvalues and the (left and right) eigenvectors of equation (2.31) using the previously described eigensolver. After solving the eigenvalue problem, the sums over m that appear in the square brackets of equations (2.60) and (2.61) are calculated for each value of n and every selected z. Note that this sum is independent of θ. The sums are written, for each circumferential wave number and axial cross section, to two separate ASCII text files. One file stores the displacement components and the other stores the stress components. Note, however, that the eigenvalues, eigenvectors and mode shapes are not stored due to hard disk storage limitations. Again this program is left off the accompanying electronic

media due to copyright.

Solving the eigenvalue problem once (for each frequency and circumferential harmonic component) and storing the sums over the axial wave number for every selected z minimizes the number of times that the eigenvalue problem needs to be evaluated. This saving happens because the eigenvalues and eigenvectors are not a function of either z or θ. Once the eigenvalue problem is solved for a given frequency and circumferential harmonic component, the contribution to the Green's functions and stress functions can be determined, for this harmonic component, at all the cross sections of interest by evaluating the summations over n appearing in equations (2.60) and (2.61).

Each file, which contains the results of the summations over m in equations (2.60) and (2.61), is approximately 876 MegaBytes (MB) in size for the 330 cross sections and 601 circumferential harmonics considered at each frequency point. Therefore approximately 1.7 GigaBytes (GB) of hard disk storage is required. This information is archived so that the loading due to a radial harmonic point force acting on a cross section having a circumferential defect can be found easily. However, defects are not considered in this thesis. Due to storage limitations, files are compressed by using a commercial package, WinZip® Command Line Support Add-On Version 1.0 from WinZip Computing, Inc. A compression ratio of approximately 90 percent (i.e., each file is compressed to approximately 10 percent of its original size) is possible. Had mode shapes also been stored, storage requirements would multiply by a factor of 63. (Note, however, that this factor depends directly upon the number of elements used to discretized the cylinder's thickness.)

To reduce the waiting time of the computer user, different frequency points are run

simultaneously on four available PCs in a distributed fashion. The PCs process the problem independently but they are networked to share hard disk resources. The solution of the eigenvalue problem at all the selected axial cross sections takes approximately 90 minutes for each frequency point. About 4 percent of this 90 minutes is required to compress the files.

The summations (over the axial wave numbers) at each circumferential harmonic that are required to compute the displacements and stresses at all the selected cross sections are stored in two "interlaced" files for efficiency. However, these files are difficult to manipulate due to their large sizes. (Around 1 GB of Random Access Memory [RAM] is required to load the complete file into memory and many programs "crash" when opening files of this size.) This difficulty is overcome by employing a Matlab® (The MathWorks, Inc.) script file to extract the compressed files (using the WinZip® Command Line Support Add-On) and sort the data for each axial cross section. Both files are split effectively into 330 ASCII files that are easier to manipulate. To reduce storage requirements (as the same total data is spread among many smaller files), the files created for each frequency are compressed into one WinZip® archive. Consequently the total data is compressed by approximately 92 percent but the procedure takes about 20 additional minutes for each frequency point.

Another Matlab® script file extracts, for each frequency considered, the sorted displacement and stress files and performs the sums over n that appear in equations (2.60) and (2.61), for each circumferential location at each cross section. (The previously calculated sum over the axial wave numbers is independent of θ.) This procedure gives the

Green's functions and stress functions. The summations for each θ location are evaluated at a given cross section and frequency but only at the cylinder's outer surface to save time and storage. The resulting data is written to MathWorks "mat" files which have a binary file format that is much more efficient to store than an ASCII file. Once again, there is one file for each of the displacements and the stresses. As before, the summed data for each frequency is archived by using WinZip® Command Line Support Add-On to compress the data by approximately 60 percent. These manipulations take approximately 60 minutes per frequency. As for the eigenvalue problem, different frequencies are run simultaneously on four PCs.

The resulting Figures 2.9 through 2.11 show, in perspective and plan, the magnitudes and phase angles [i.e. in the frequency domain, see, for example, equation (2.63)] of the Green's functions at the 70 kHz "centre frequency" (where ω^* is 0.755) of the input forcing signal. (Note that the "colour bars" given in Figures 2.9 through 2.11 represent the same scale as the displacement, stress or phase angle axis as appropriate. Moreover, the scale of the displacement, stress or phase angle axes of corresponding perspective and plan views are identical.) The displacement components are non-dimensionalized as:

$$u^* = \frac{u}{H};\ v^* = \frac{v}{H};\ w^* = \frac{w}{H}. \tag{2.97}$$

Figures 2.12 and 2.13, on the other hand, present the corresponding magnitudes and phases of the non-zero stress functions, $\sigma_{\theta z}$ and σ_{zz}, which are non-dimensionalized according to:

$$\sigma_{\theta z}^* = \frac{\sigma_{\theta z}}{\mu};\ \sigma_{zz}^* = \frac{\sigma_{zz}}{\mu}. \tag{2.98}$$

Again μ is Lame's constant (shear modulus). Figures 2.9 through 2.13 show that the Green's functions and stress functions are approximately periodic, both axially and circumferentially, with periods of about $8H$ and 18°, respectively. Moreover, it can be seen that u^* is about twice v^*, and about an order of magnitude larger than w^*. Although it is not clear from Figures 2.12 and 2.13 (because σ_{rz}^* is identically zero on the cylinder's outer surface), $\sigma_{r\theta}^*$ and σ_{rz}^* have similar magnitudes and σ_{zz}^* is much larger over the cylinder's thickness. Similar magnitude ratios are seen for the other frequencies. These observations are consistent with the limited data published previously. Because the radial displacement is the largest in magnitude it will be examined later in further detail.

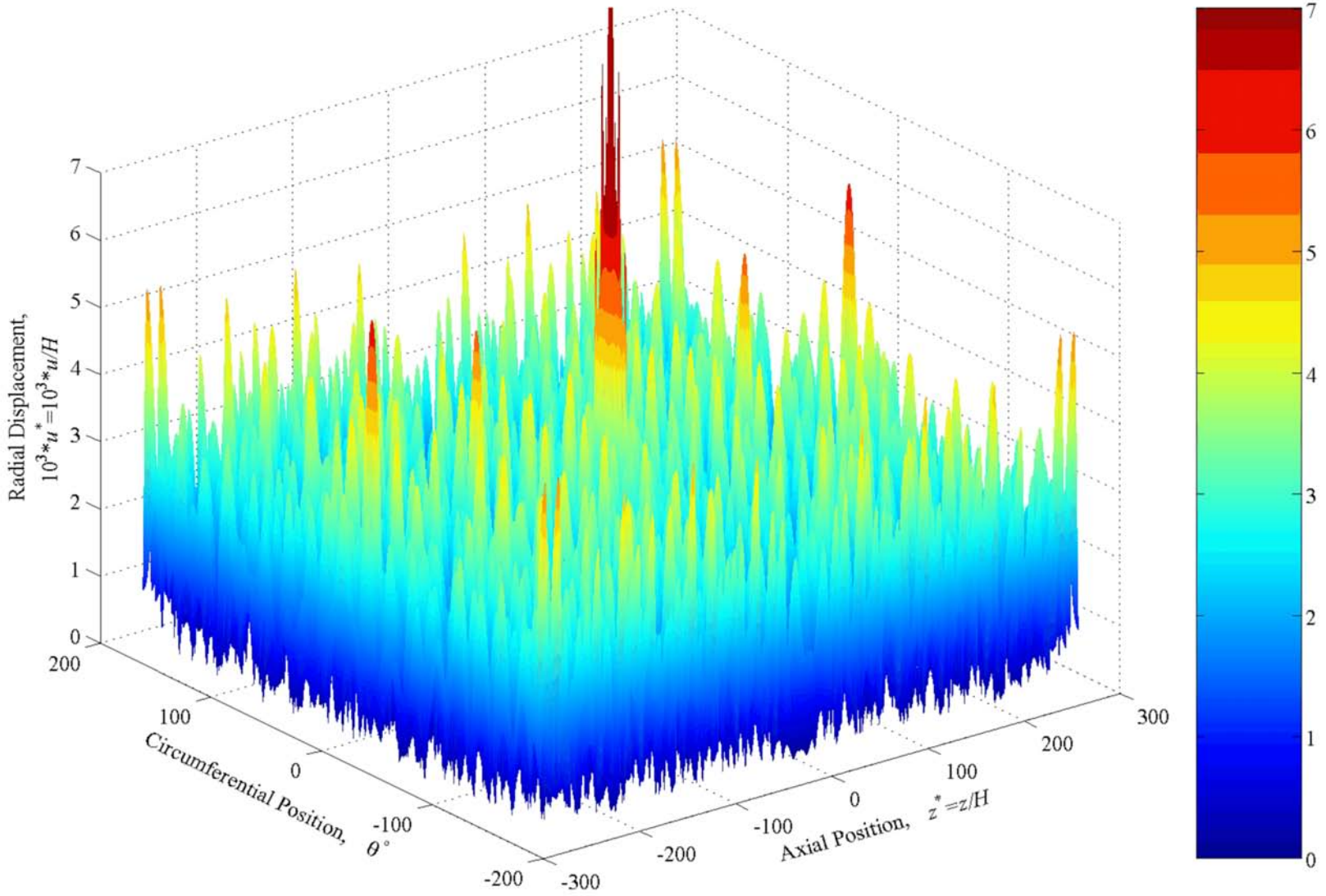

Figure 2.9 (a). Perspective View of Radial Component of Green's Function at $\omega^*=0.755$

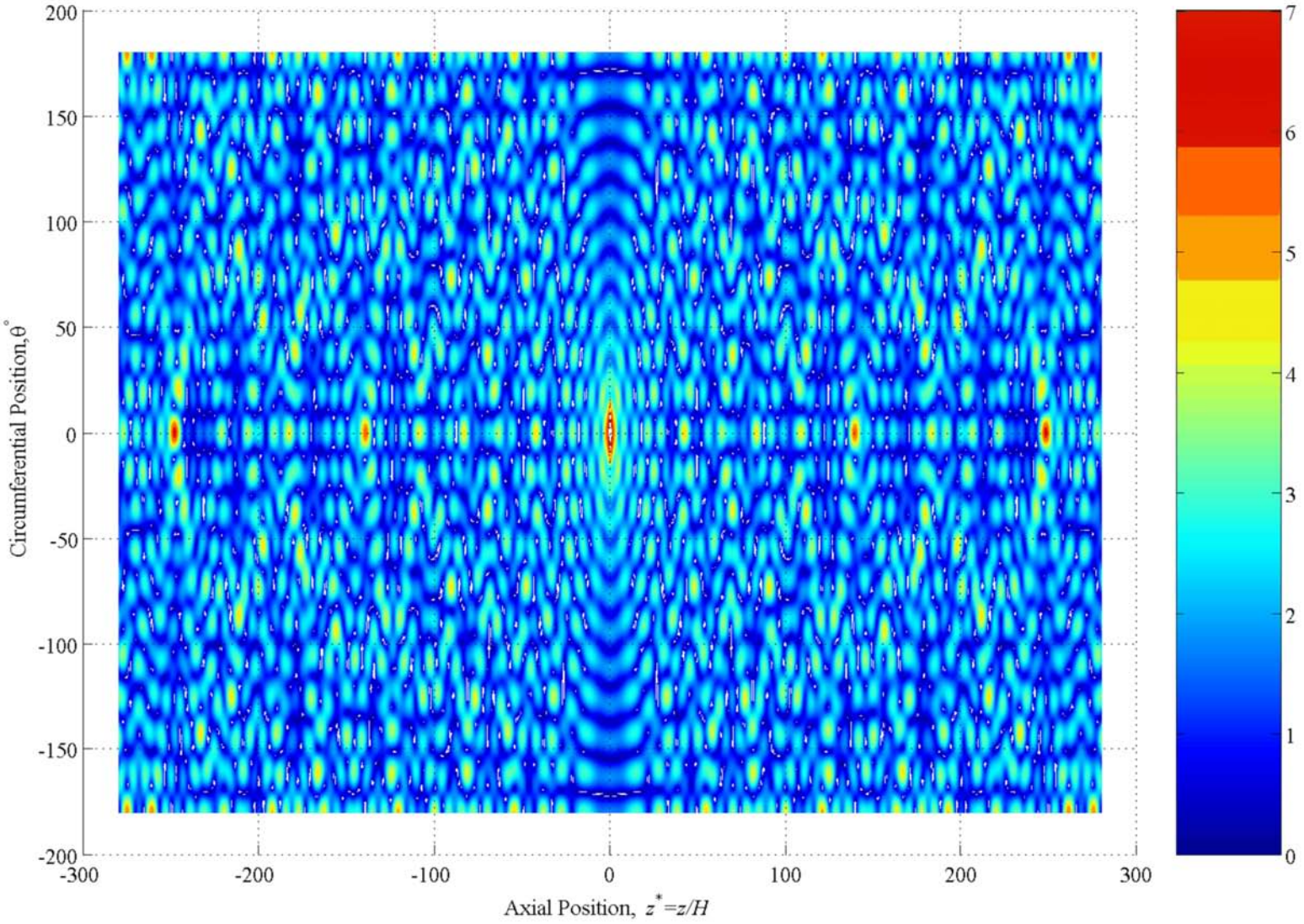

Figure 2.9 (b). Plan View of Radial Component of Green's Function at ω^*=0.755 [See also Figure 2.9 (a).]

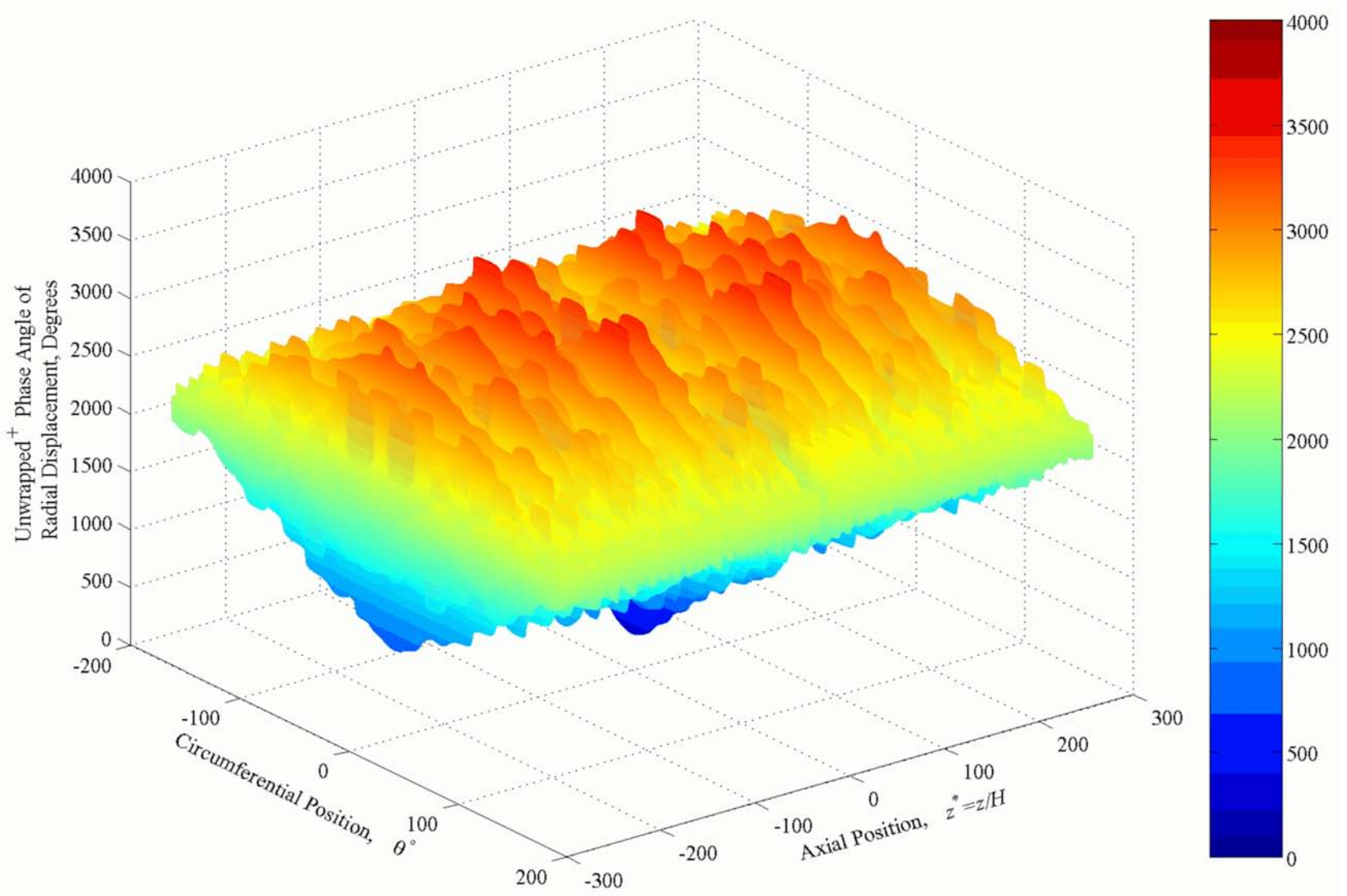

Figure 2.9 (c). Perspective View of Unwrapped Phase Angle of Radial Component of Green's Function at $\omega^*=0.755$

[+] Unless stated otherwise, all phase angles are unwrapped i.e. the phase is made continuous across 360º phase discontinuities by adding multiples of ±360˚, as needed. (See, for example, [52].) Phase angles are relative to $\Re(e^{-j\omega t})$

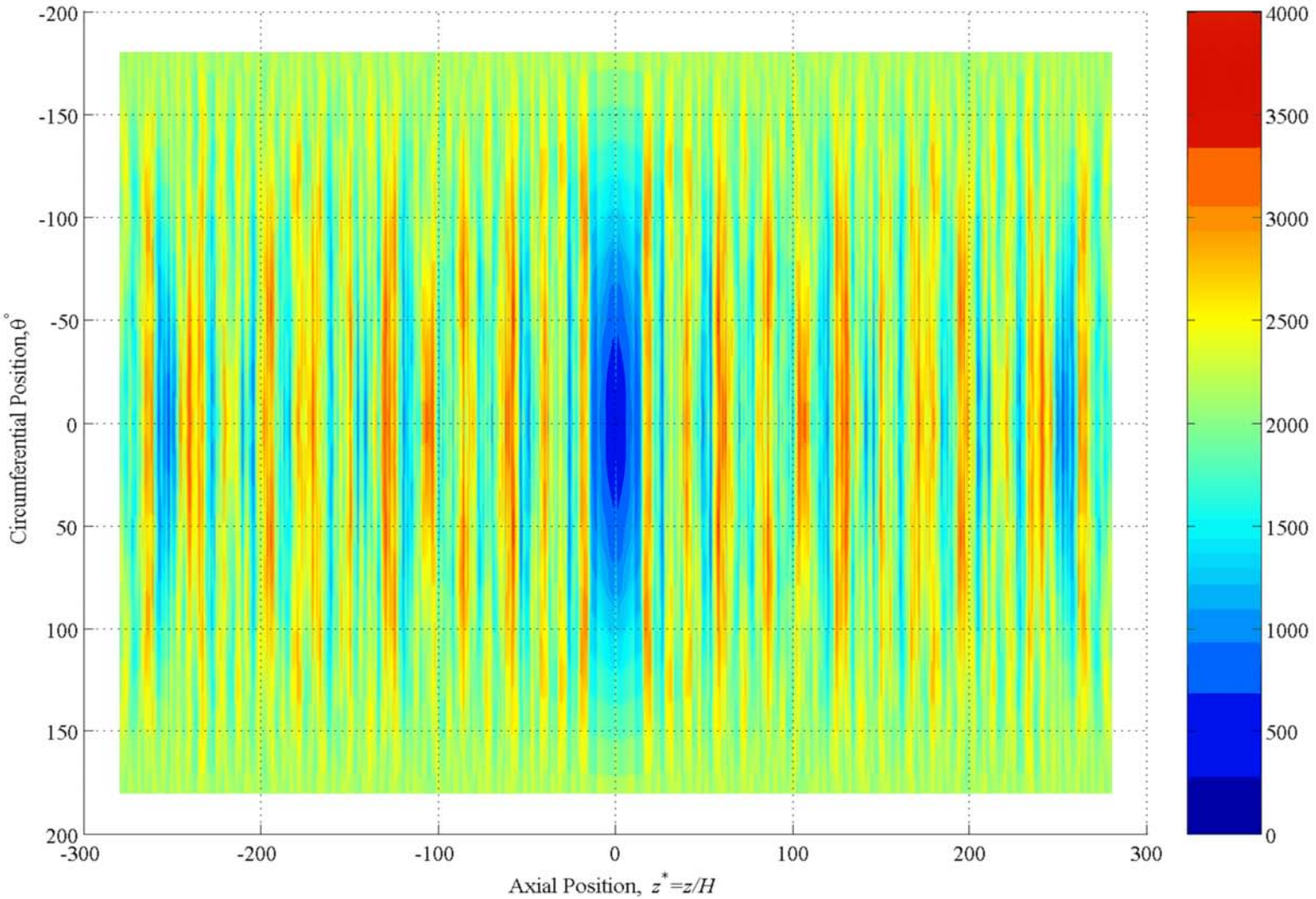

Figure 2.9 (d). Plan View of Unwrapped Phase Angle of Radial Component of Green's Function at $\omega^*=0.755$ [See also Figure 2.9 (c).]

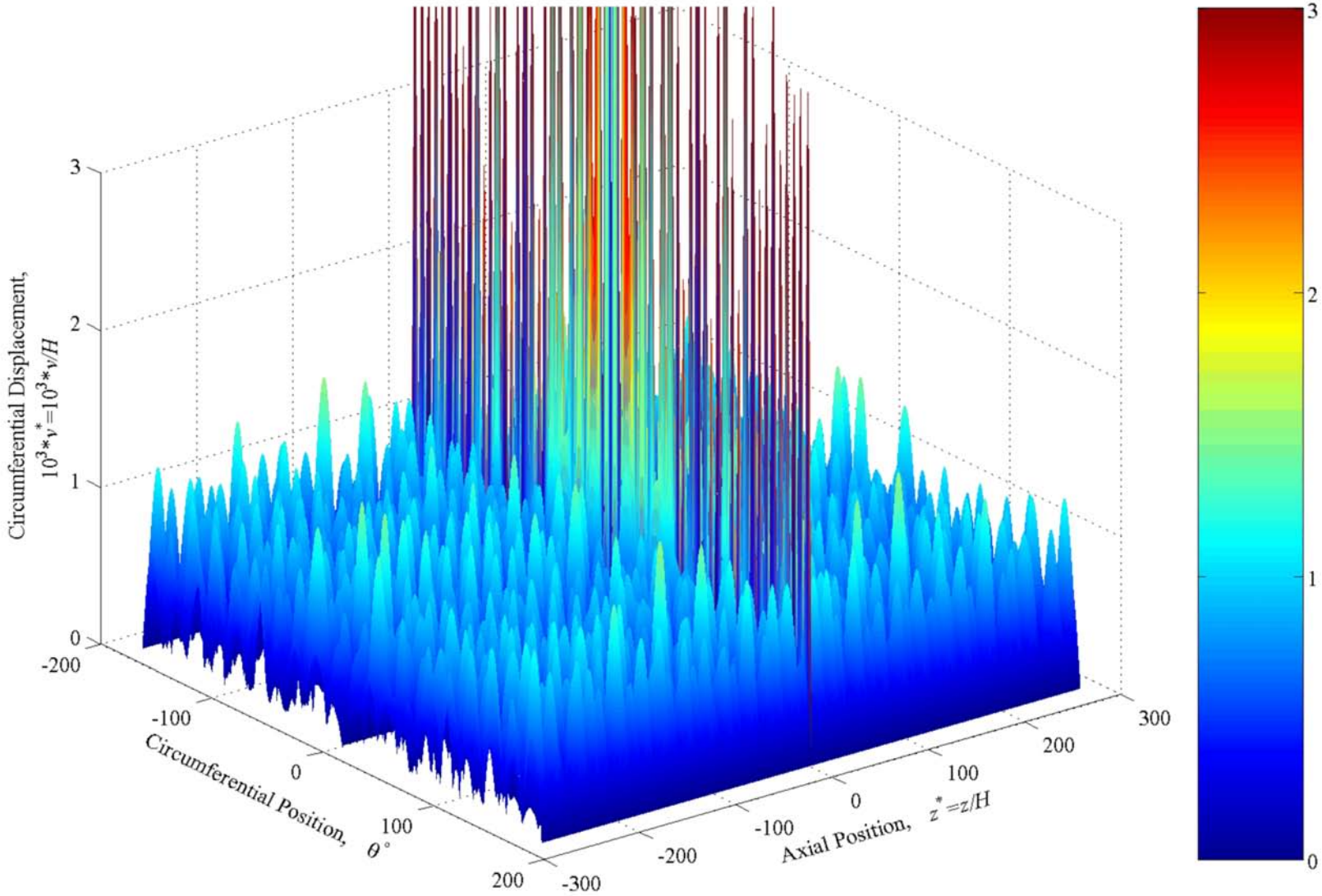

Figure 2.10 (a). Perspective View of Circumferential Component of Green's Function at ω^*=0.755

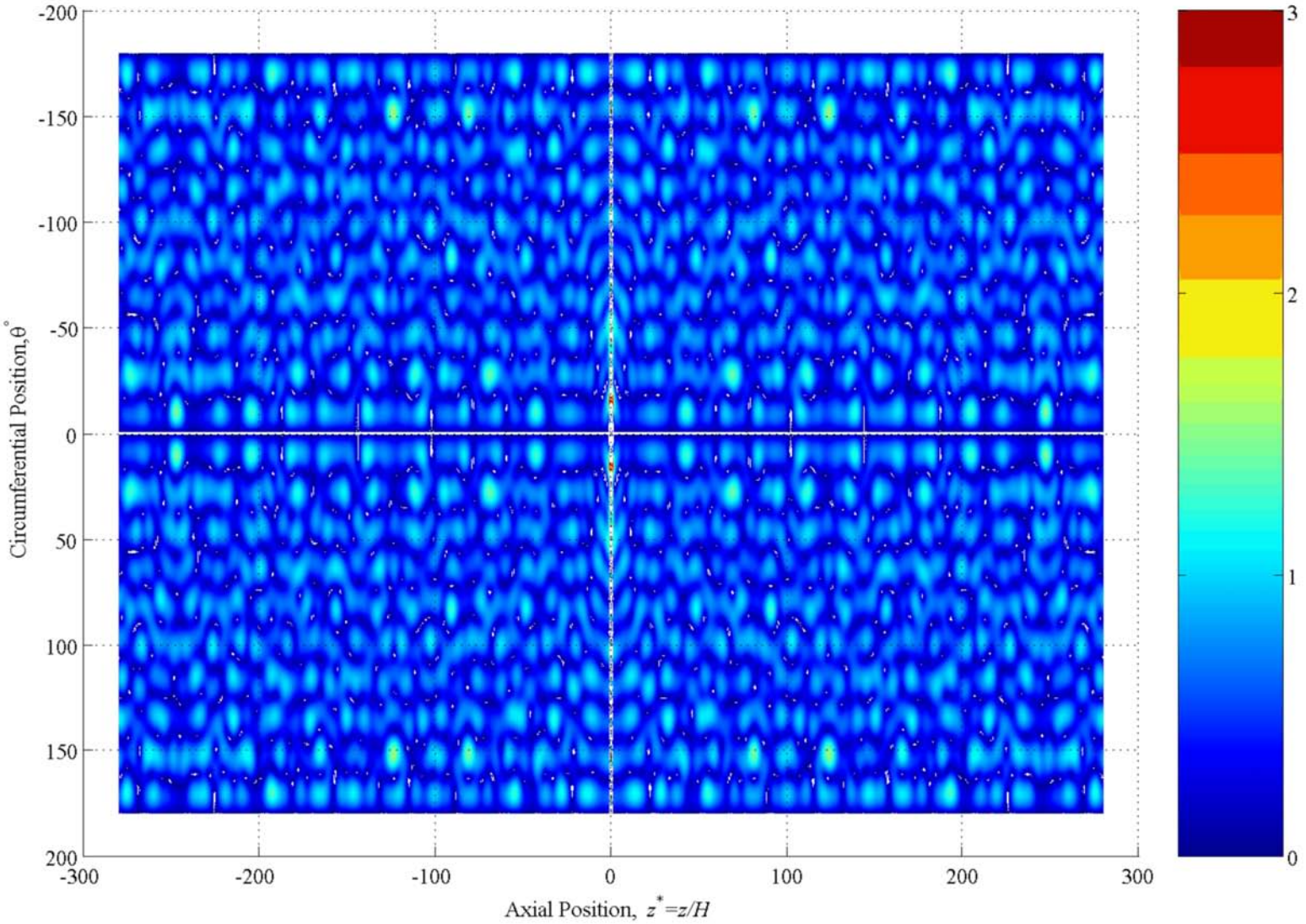

Figure 2.10 (b). Plan View of Circumferential Component of Green's Function at ω^*=0.755 [See also Figure 2.10 (a).]

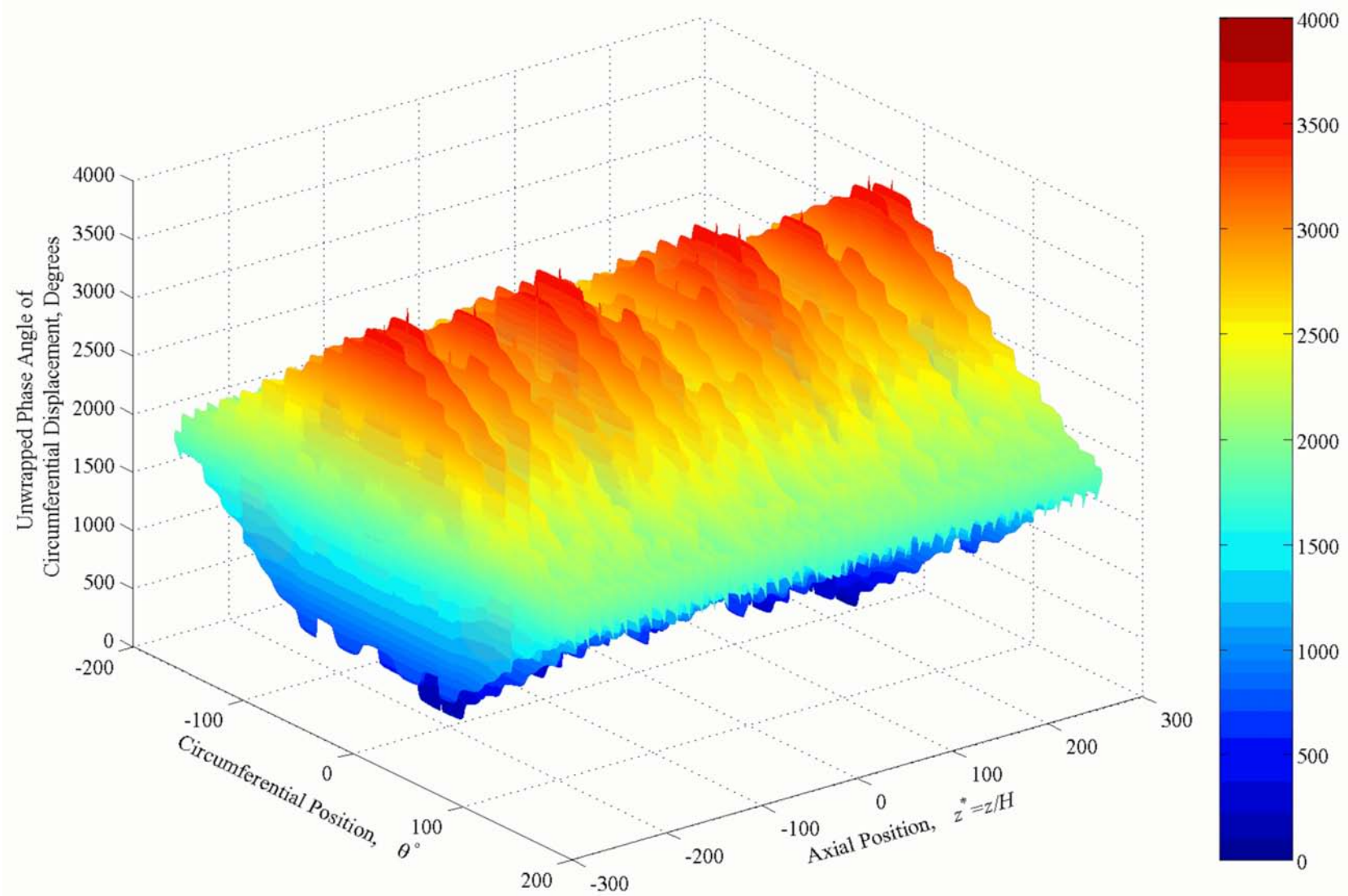

Figure 2.10 (c). Perspective View of Unwrapped Phase Angle of Circumferential Component of Green's Function at ω^*=0.755

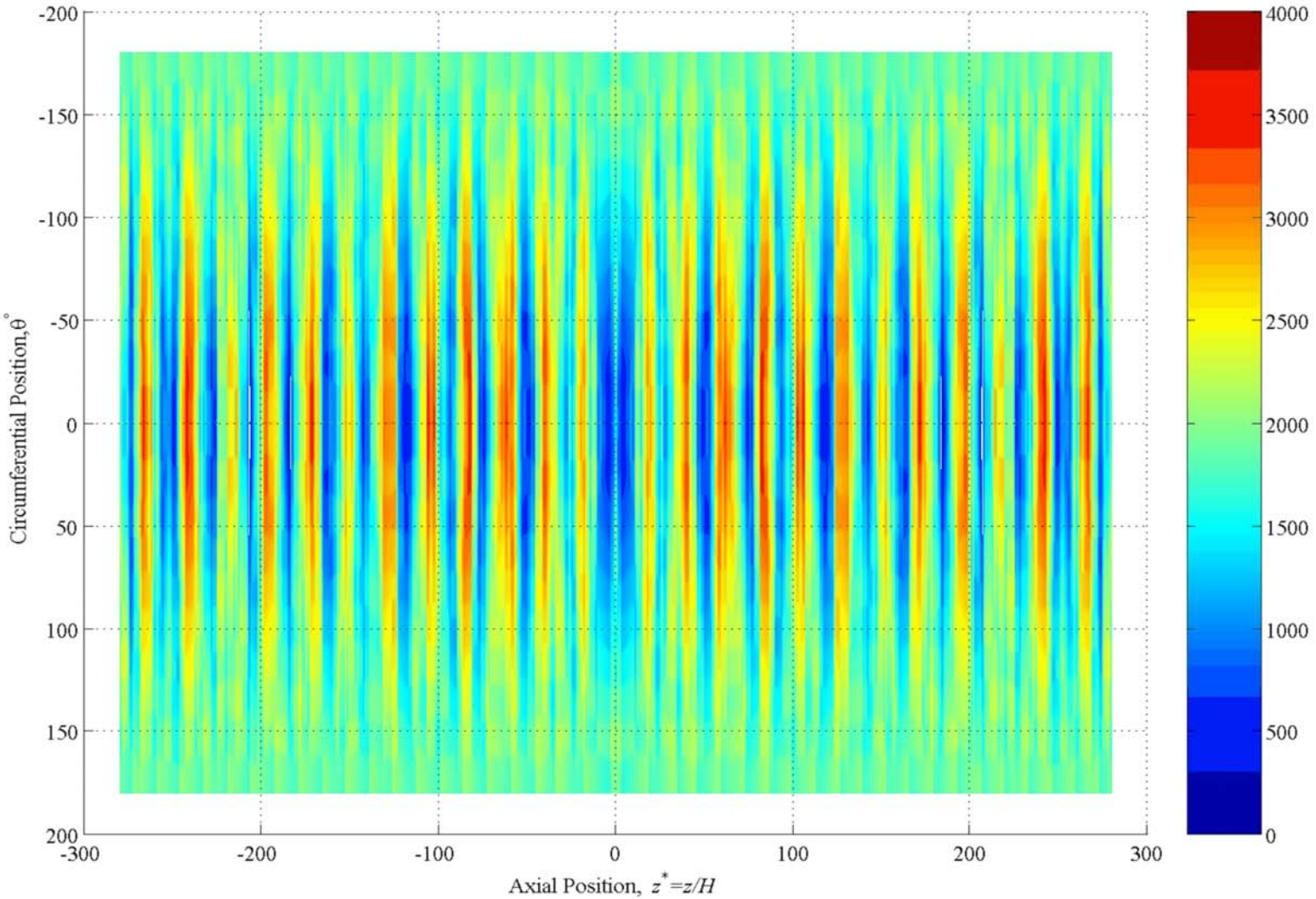

Figure 2.10 (d). Plan View of Unwrapped Phase Angle of Circumferential Component of Green's Function at $\omega^*=0.755$ [See also Figure 2.10 (c).]

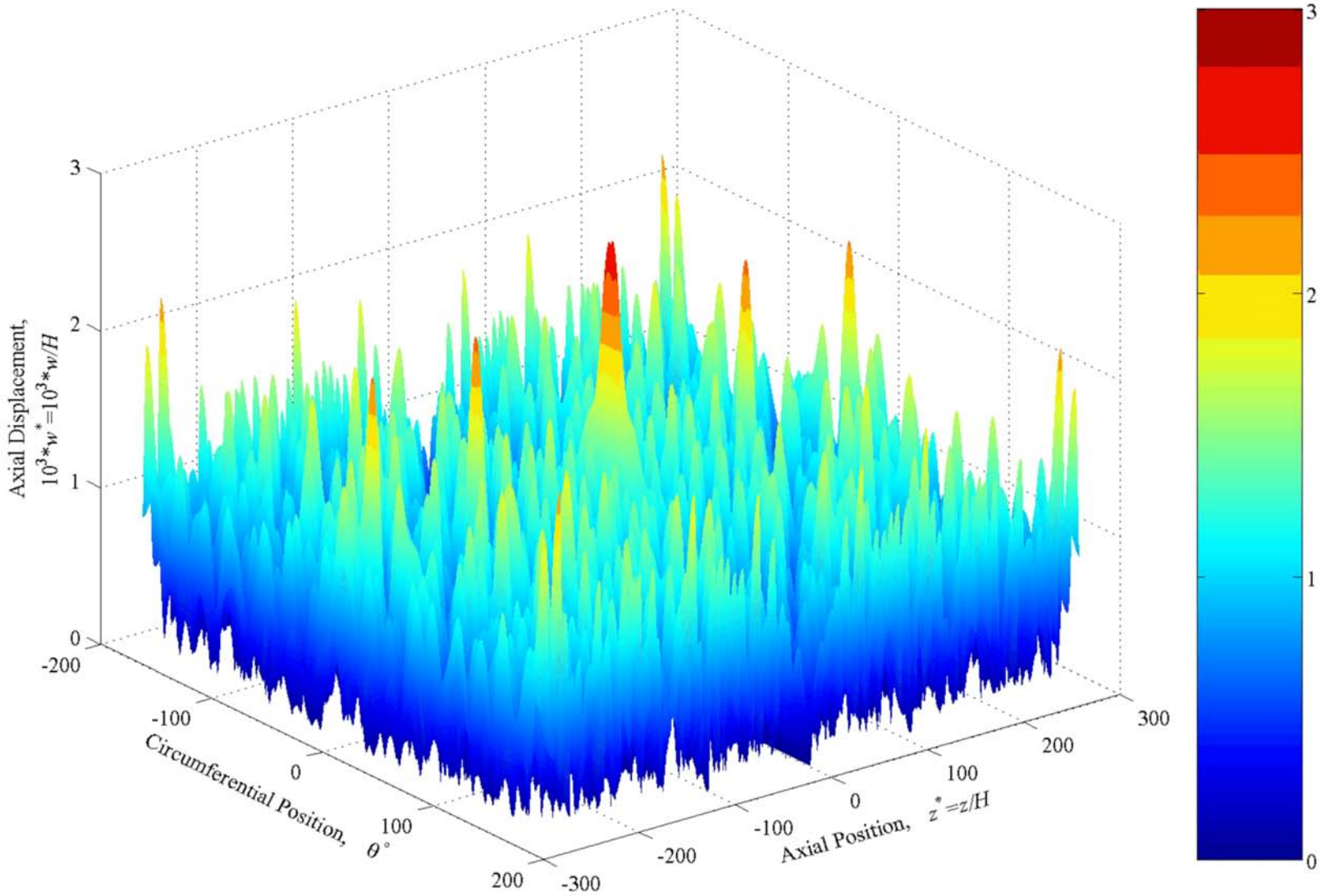

Figure 2.11 (a). Perspective View of Axial Component of Green's Function at ω^*=0.755

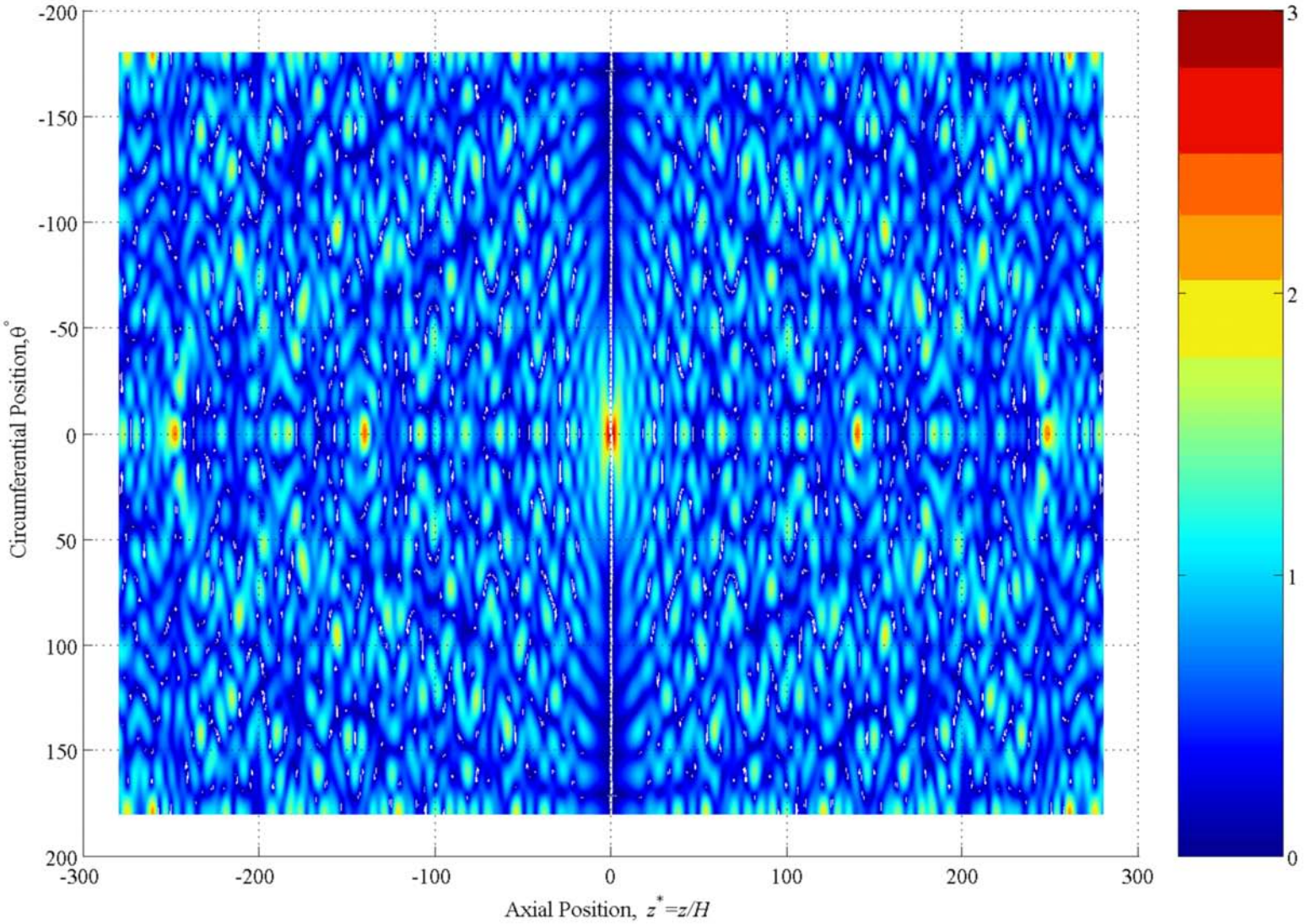

Figure 2.11 (b). Plan View of Axial Component of Green's Function at ω^*=0.755 [See also Figure 11 (a).]

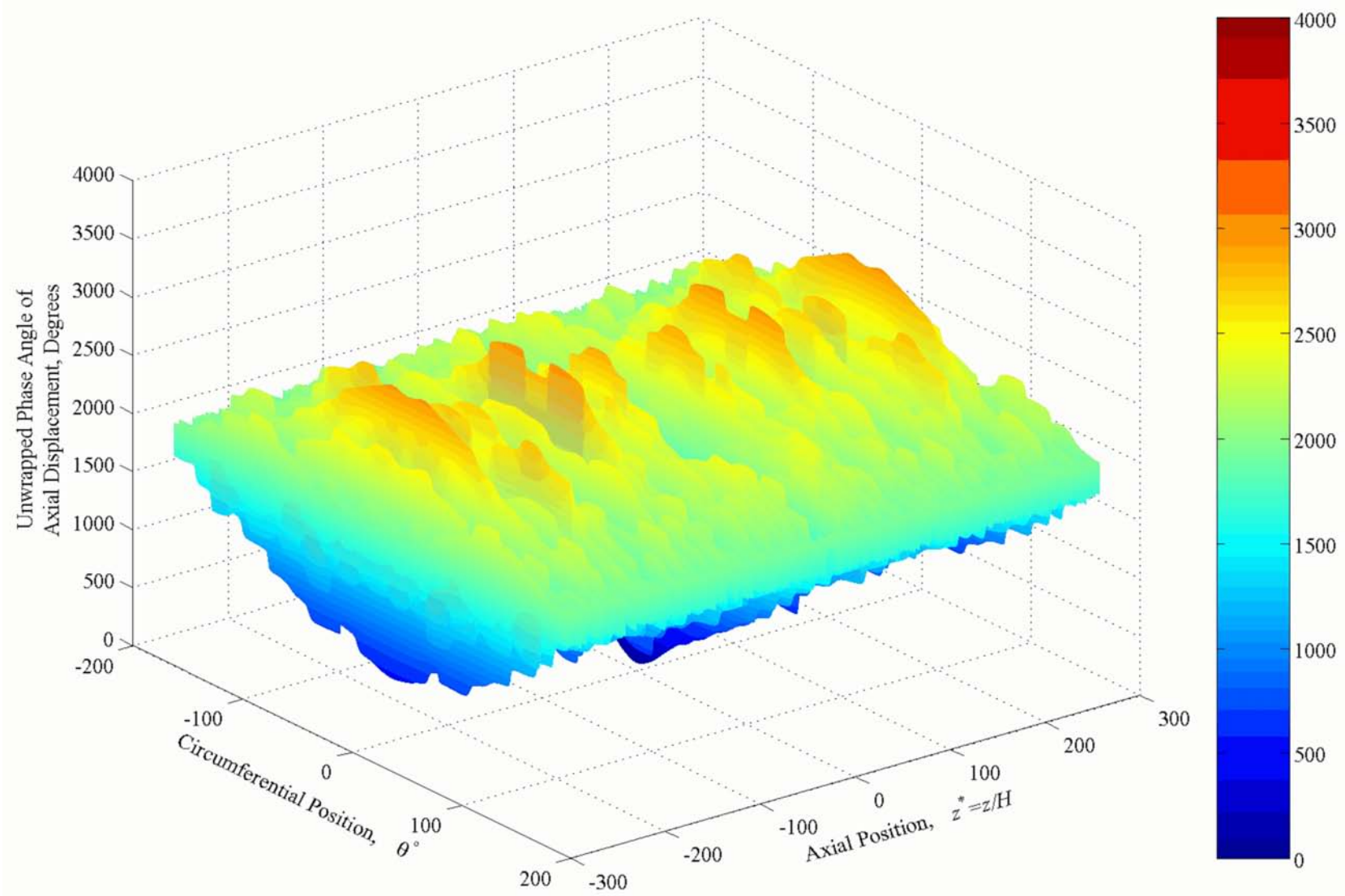

Figure 2.11 (c). Perspective View of Unwrapped Phase Angle of Axial Component of Green's Function at ω^*=0.755

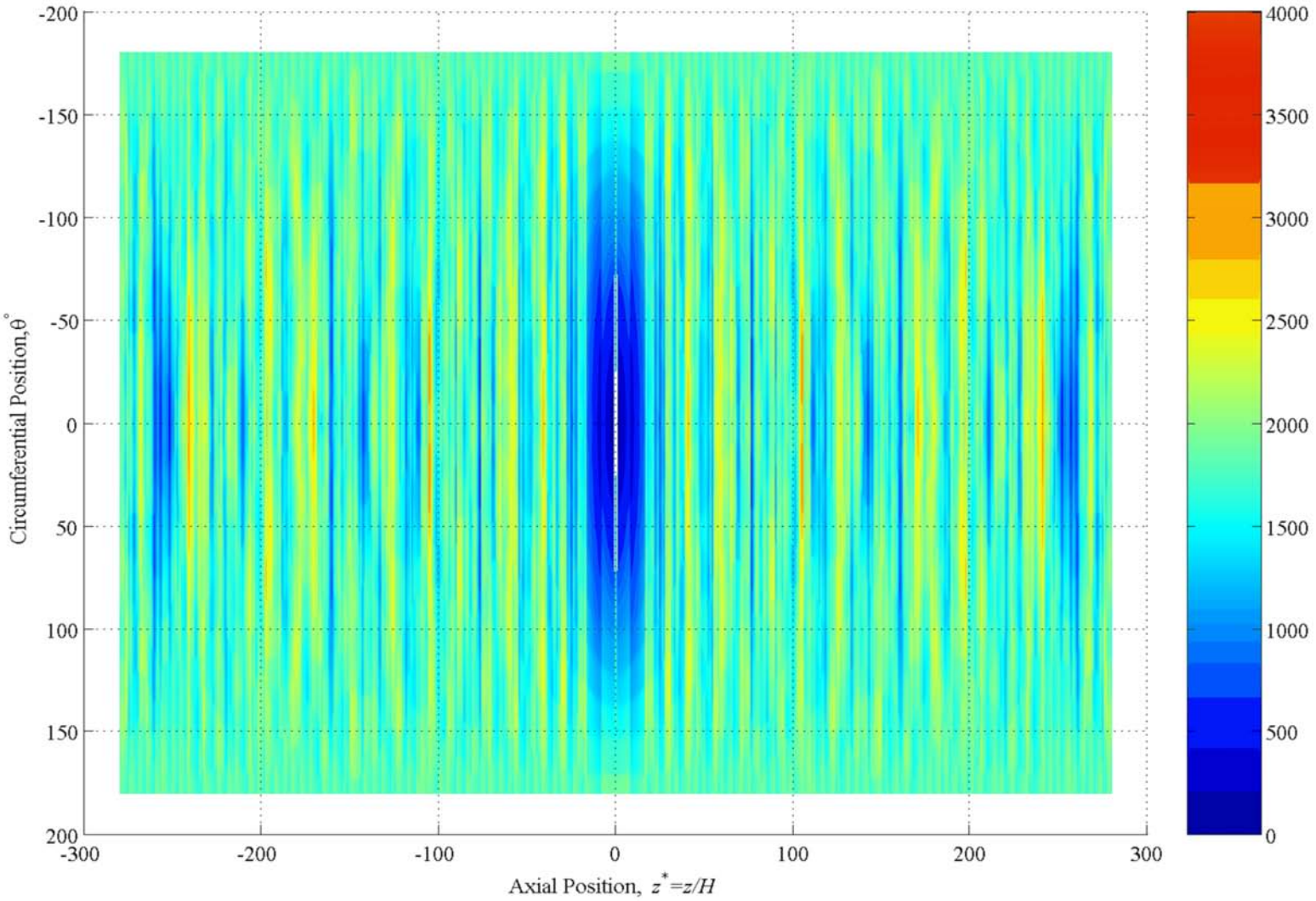

Figure 2.11 (d). Plan View of Unwrapped Phase Angle of Axial Component of Green's Function at $\omega^*=0.755$ [See also Figure 2.11 (c).]

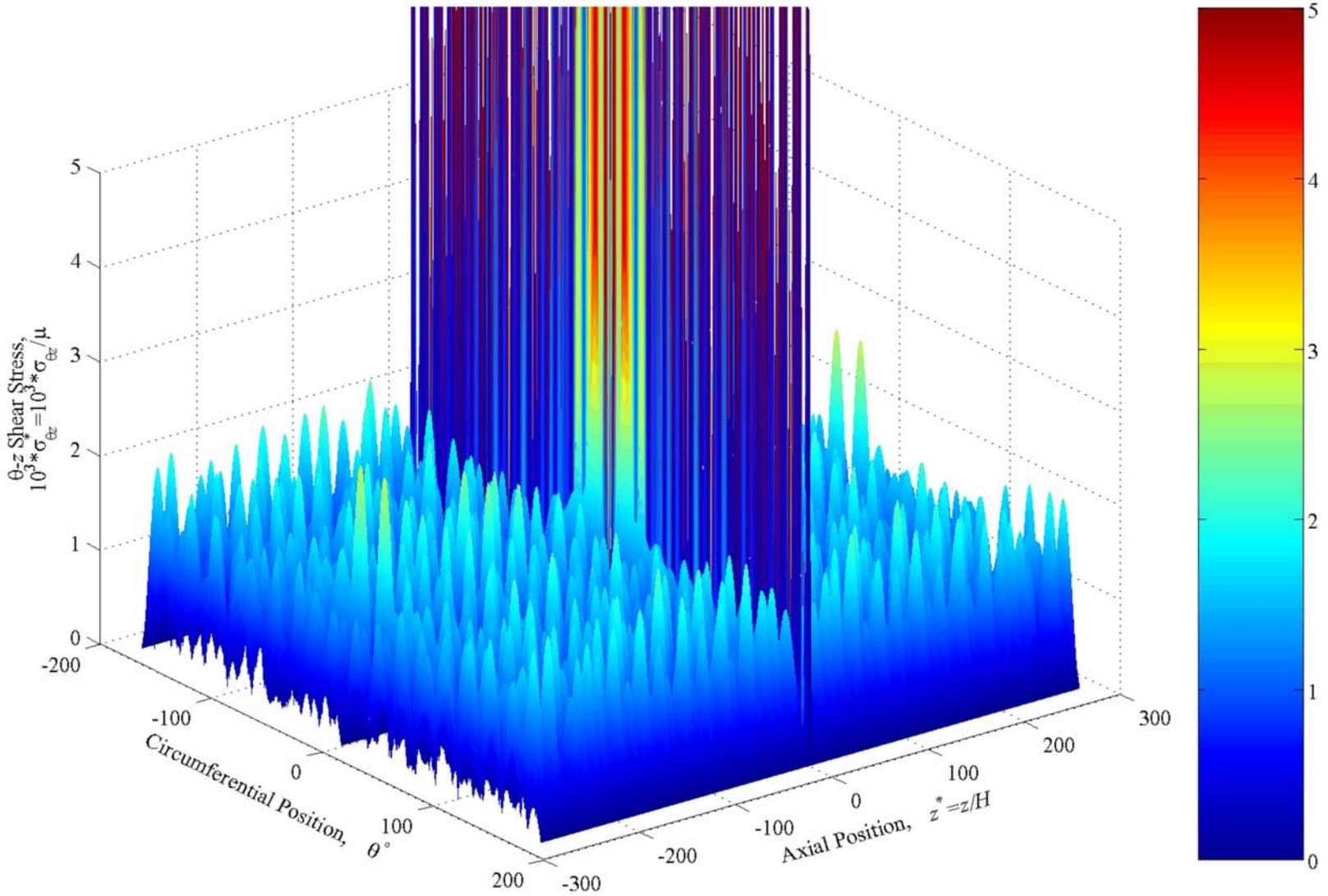

Figure 2.12 (a). Perspective View of θ-*z* Shear Stress Function at ω^*=0.755

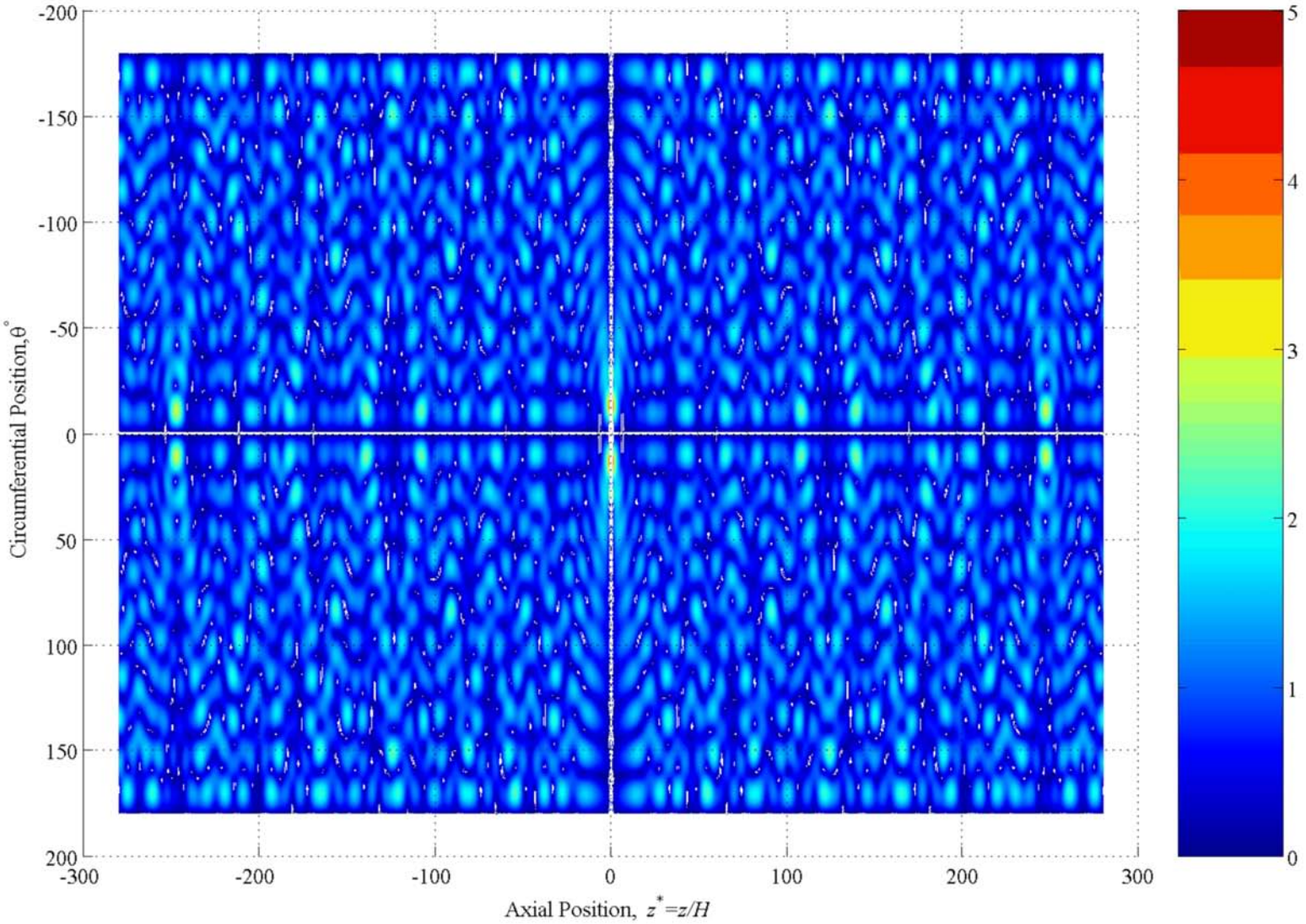

Figure 2.12 (b). Plan View of θ-*z* Shear Stress Function at ω^*=0.755 [See also Figure 2.12 (a).]

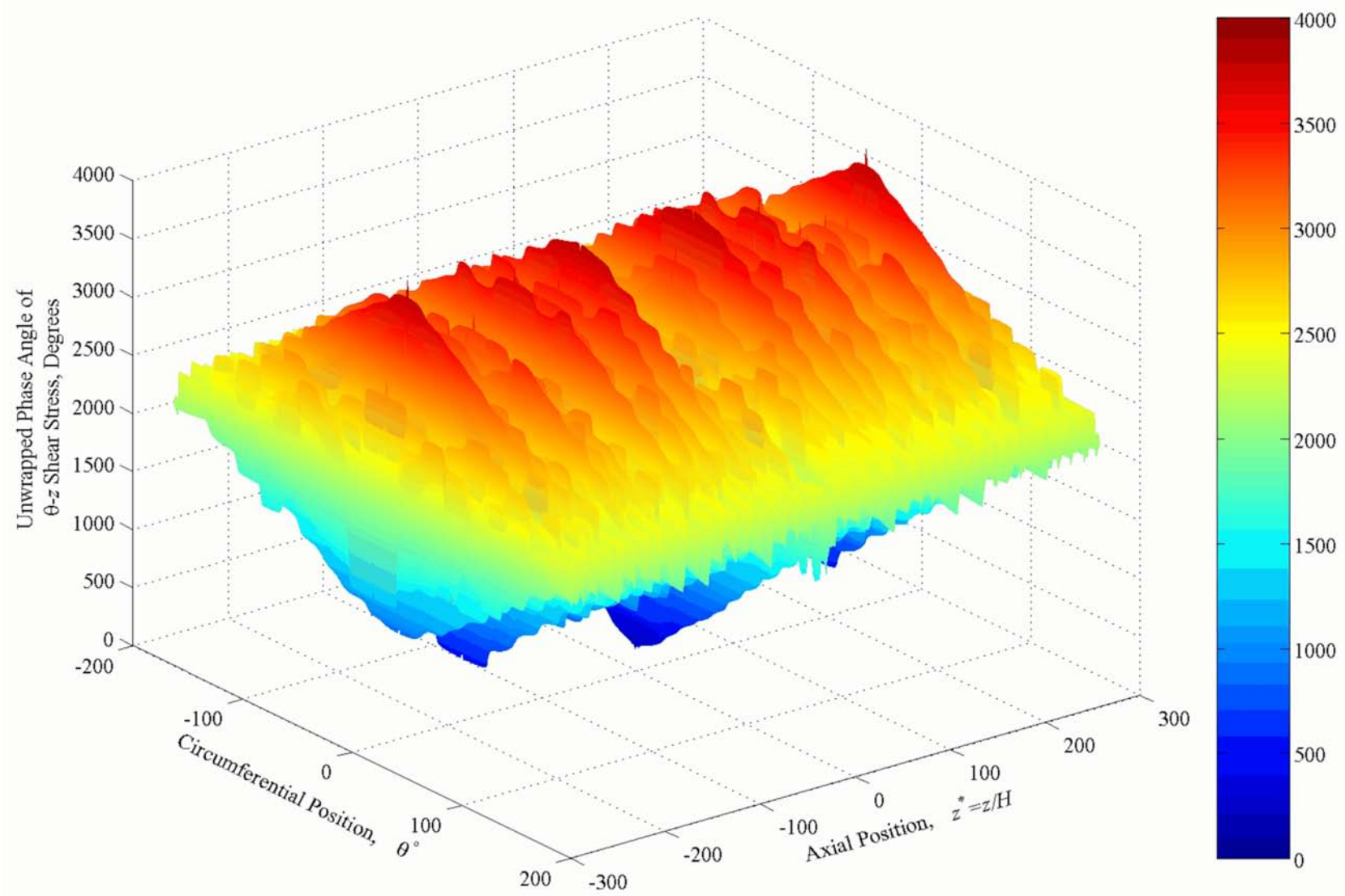

Figure 2.12 (c). Perspective View of Unwrapped Phase Angle of θ-*z* Shear Stress Function at ω^{*}=0.755

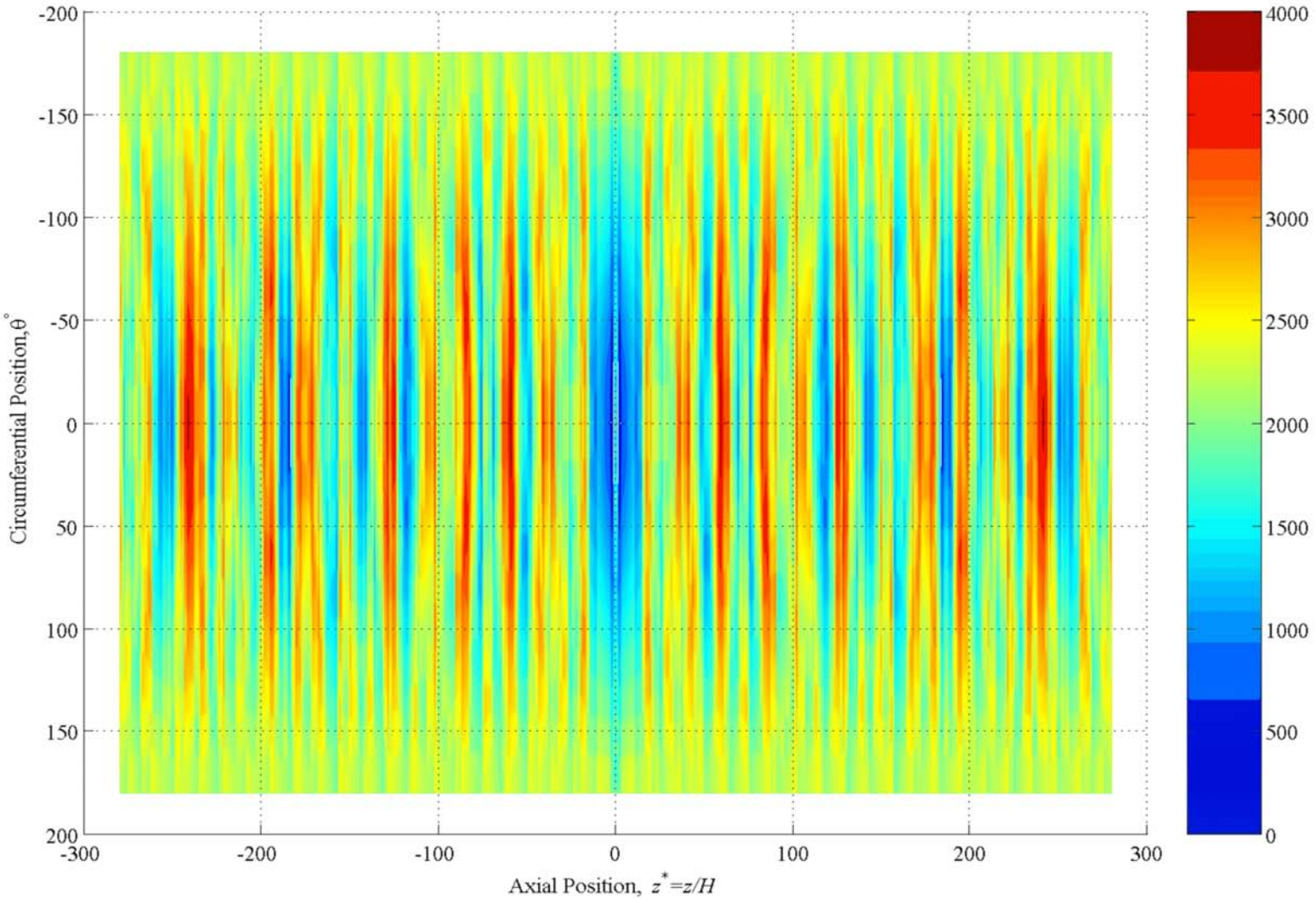

Figure 2.12 (d). Plan View of Unwrapped Phase Angle of θ-*z* Shear Stress Function at ω^*=0.755 [See also Figure 2.12 (c).]

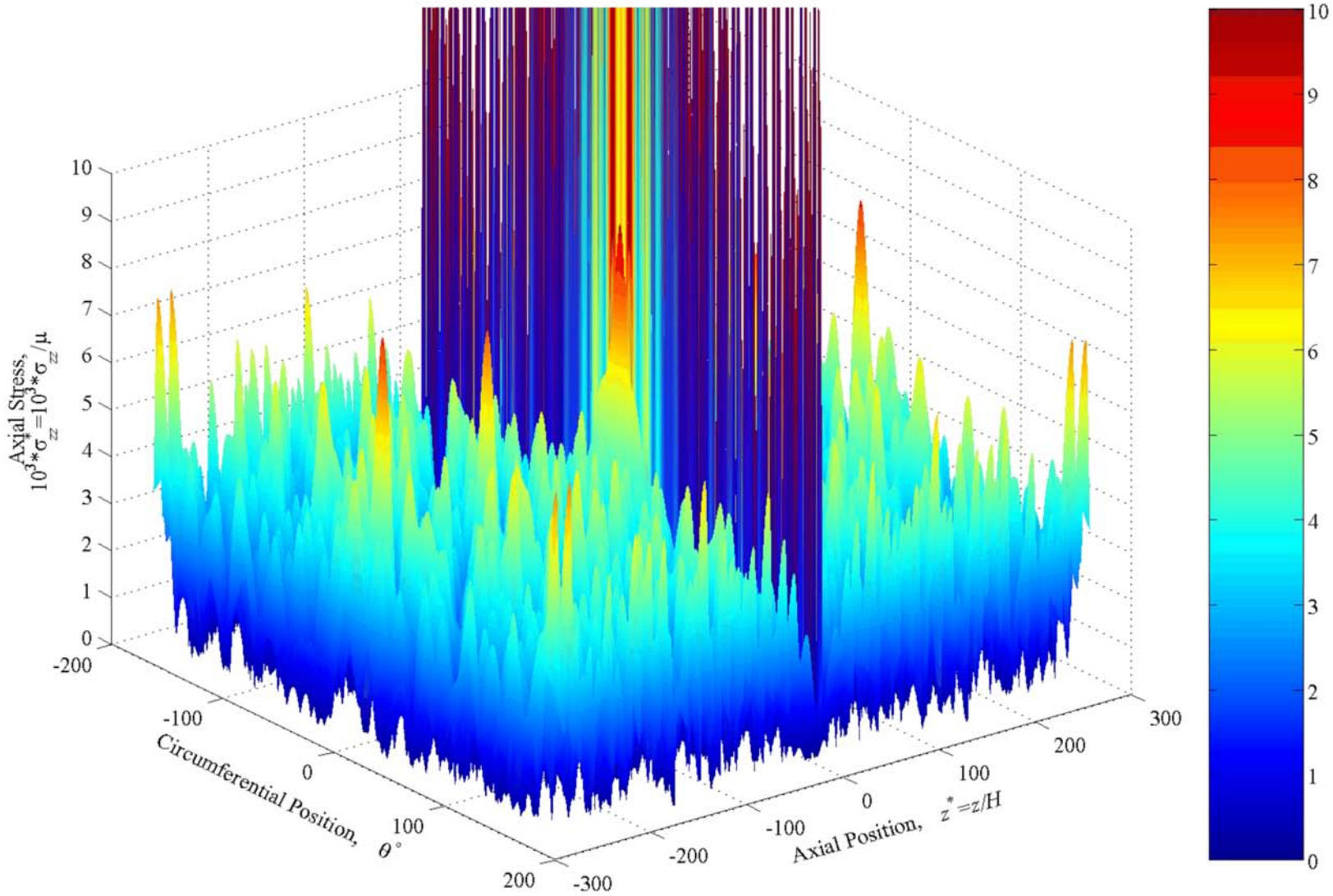

Figure 2.13 (a). Perspective View of Axial Stress Function at ω^*=0.755

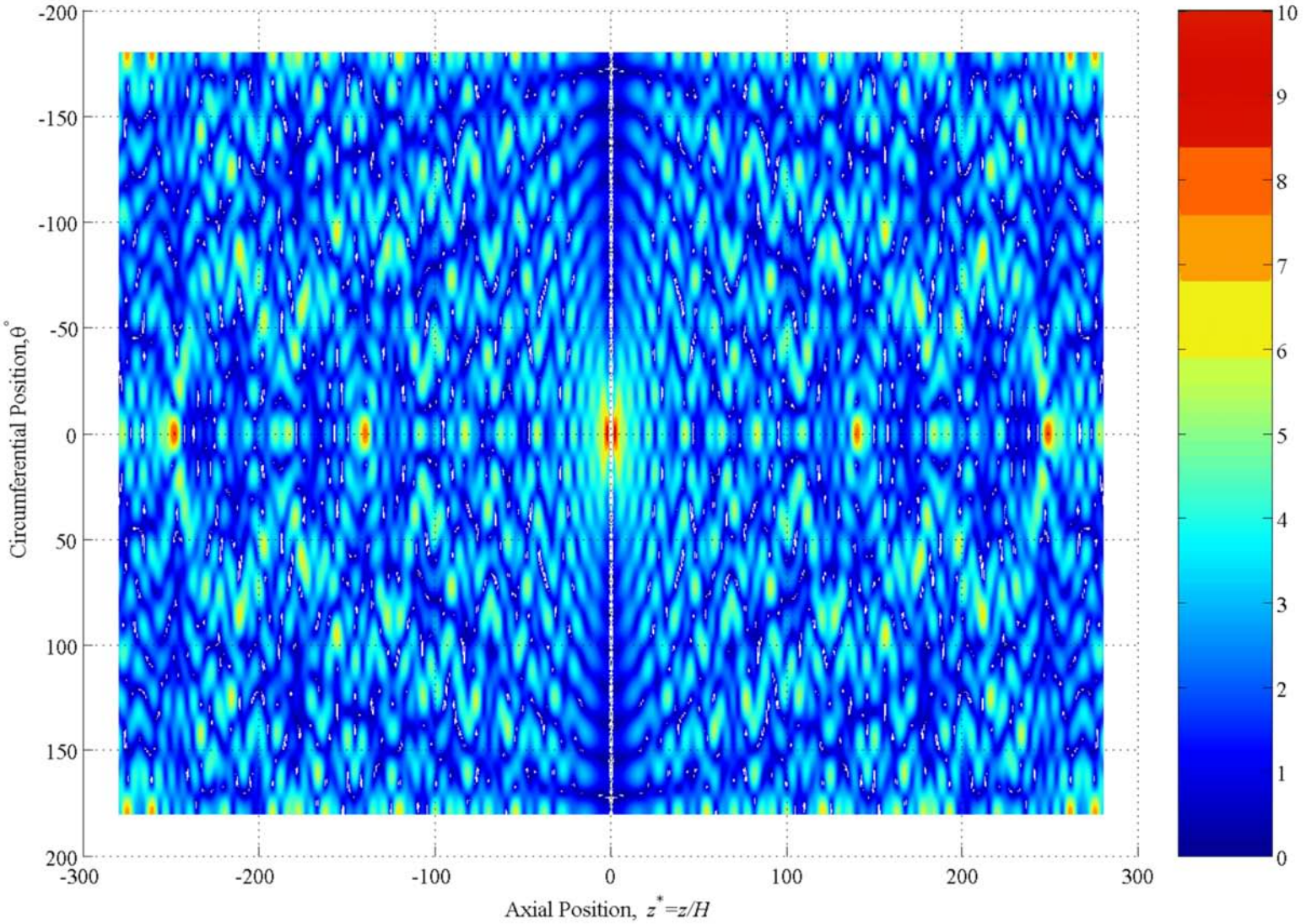

Figure 2.13 (b). Plan View of Axial Stress Function at ω^*=0.755 [See also Figure 2.13 (a).]

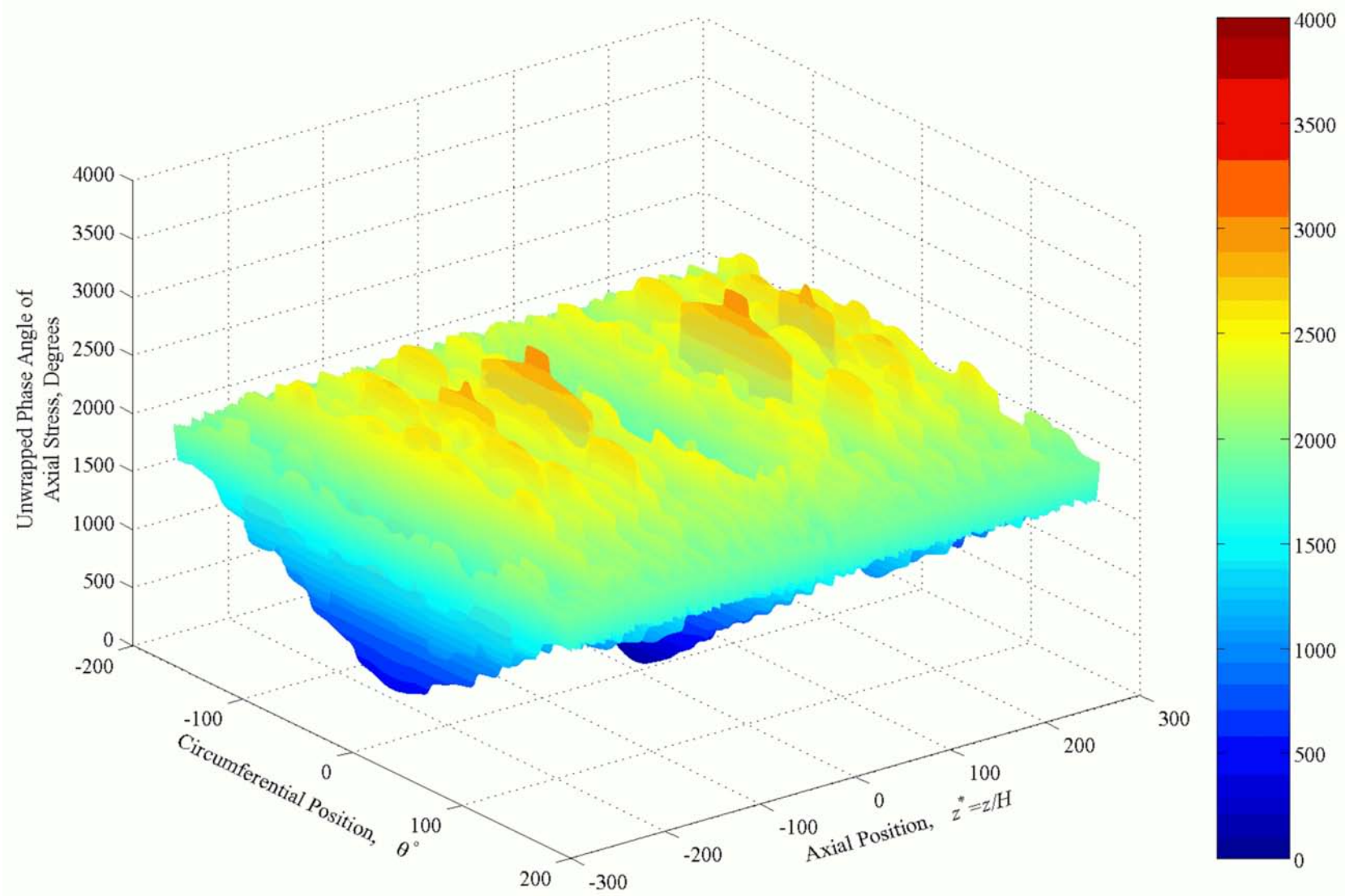

Figure 2.13 (c). Perspective View of Unwrapped Phase Angle of Axial Stress Function at ω^{*}=0.755

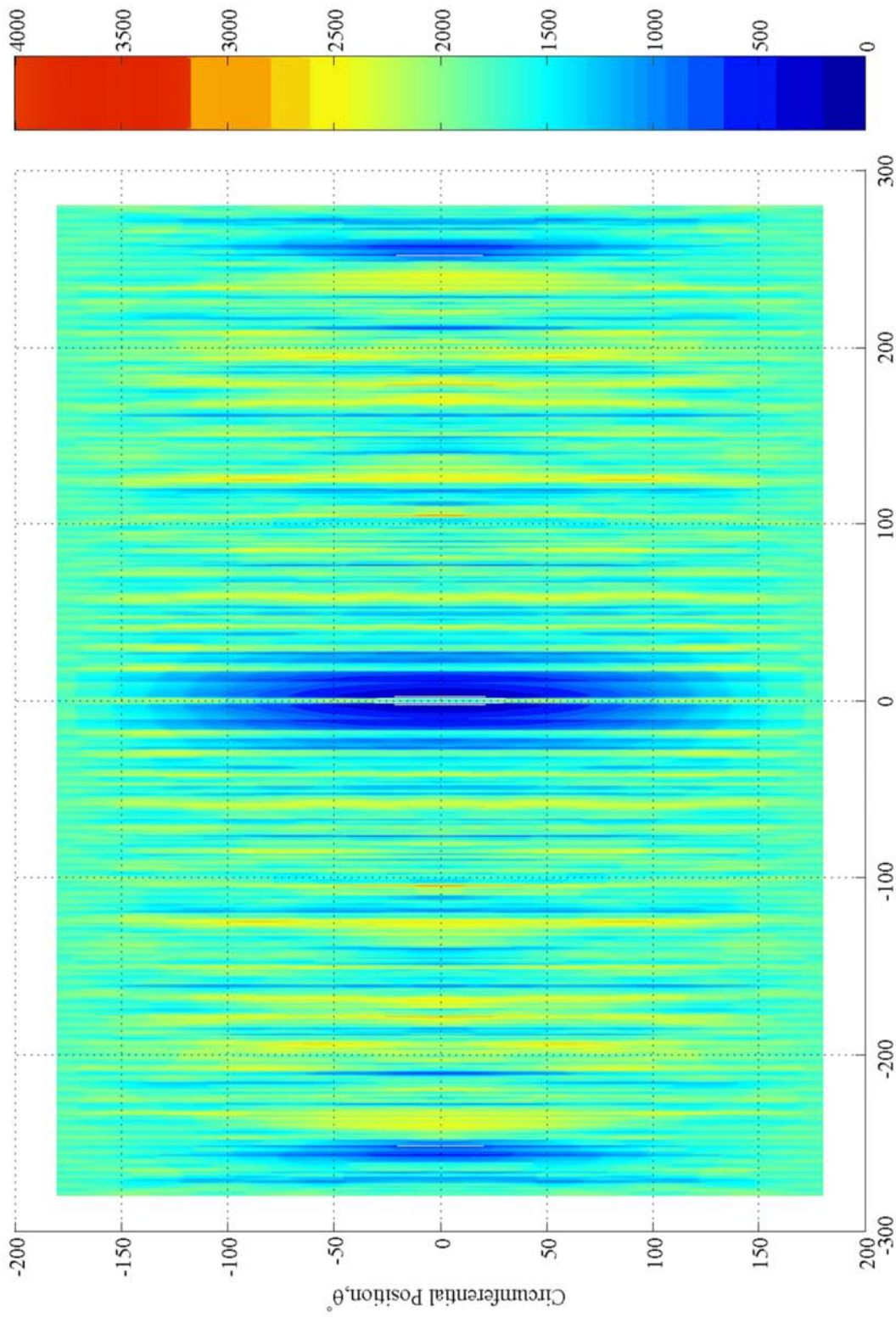

Figure 2.13 (d). Plan View of Unwrapped Phase Angle of Axial Stress Function at ω^*=0.755 [See also Figure 2.13 (c).]

2.12.4 Frequency Response Functions and Corresponding Time Histories of Radial Displacements

The radial FRF gives u^* as a function of frequency at a particular location. [See equations (2.63) and (2.97).] It is available straightforwardly if the Green's functions are known. Figure 2.14 shows the radial FRF for $\theta=0$ and $z^*=5.10$ at the cylinder's outer surface. The FRF, when convolved with the transient point load and integrated over frequency gives the dynamic radial displacement. The convolution is carried out here by multiplying the complex FRF and the Fourier transform of the transient point load at a given frequency for each of the 145 (uniformly spaced) frequency points selected. The outcome is shown in Figure 2.15 at the same location considered in Figure 2.14. Note how the convolved FRF is "smooth" compared to the FRF and tapers to virtually zero outside the frequencies of interest. This smooth and essentially band limited form of the convolved FRF is highly desirable if the dynamic radial response is going to be recovered from it. Then the convolved FRF can be approximated using a finite number of points and numerically summed over the discrete frequency data. The smoothing and band limited behaviour of the convolved FRF seen here is due to the specific form of the spectrum of the forcing function. The important properties of this spectrum are discussed further in Appendix A. Also note that the seven "peaks" of the FRF are reduced to two dominant peaks after the convolution. This simplification suggests that the convolved FRF may be represented by using fewer frequency points and a variable frequency increment. This last approach could lead to a significant saving in computational time as fewer frequency points would be needed to recover a reasonable approximation of the convolved FRF. (A fine frequency step could be

used where the convolved FRF is changing "rapidly" and a coarse frequency step could be employed for "slow"changes.) For this approach to be feasible, however, the approximate locations of the two peaks must be known a priori. The approach is not investigated further.

Using the now available convolved FRF, equation (2.65) is evaluated at each instant of interest to recover the dynamic radial displacement. The integration is performed numerically by employing a(n extended) trapezoidal integration scheme [53]. This scheme is chosen because it is straightforward to program and gives good accuracy for "smooth" curves [53], like the convolved FRF. The integration is approximated at each instant by:

$$\boldsymbol{u}^*(\theta,z,t) \approx \begin{cases} \boldsymbol{u}^*(\theta,z,t) = \dfrac{-j}{4\pi^2 r_0 H}\displaystyle\int_{-\infty}^{\infty} \bar{f}(\omega) e^{-j\omega t} \sum_{n=-\infty}^{n=\infty} \operatorname{sinc}(n\theta_0)\boldsymbol{G_n}(\omega,z)\, e^{jn\theta}\, d\omega \\ \Re\left(\dfrac{-j}{2\pi^2 r_0 H}\displaystyle\sum_{i=2}^{I-1} \bar{f}(\omega_i) e^{-j\omega_i t} \sum_{n=-\infty}^{n=\infty} \operatorname{sinc}(n\theta_0)\boldsymbol{G_n}(\omega,z)\, e^{jn\theta}\Delta\omega + \right. \\ \dfrac{-j}{4\pi^2 r_0 H}\bar{f}(\omega_1) e^{-j\omega_1 t} \displaystyle\sum_{n=-\infty}^{n=\infty} \operatorname{sinc}(n\theta_0)\boldsymbol{G_n}(\omega,z)\, e^{jn\theta}\Delta\omega + \\ \left. \dfrac{-j}{4\pi^2 r_0 H}\bar{f}(\omega_I) e^{-j\omega_I t} \displaystyle\sum_{n=-\infty}^{n=\infty} \operatorname{sinc}(n\theta_0)\boldsymbol{G_n}(\omega,z)\, e^{jn\theta}\Delta\omega \right). \end{cases} \quad \textbf{(2.99)}$$

In equation (2.99) I is the total number of discrete frequency points at which the FRF is available and $\Re$ indicates the real part. Note that only positive frequencies are considered because the convolved FRF for negative and positive frequencies are complex conjugates (i.e. the response of a real system to a real input is real).

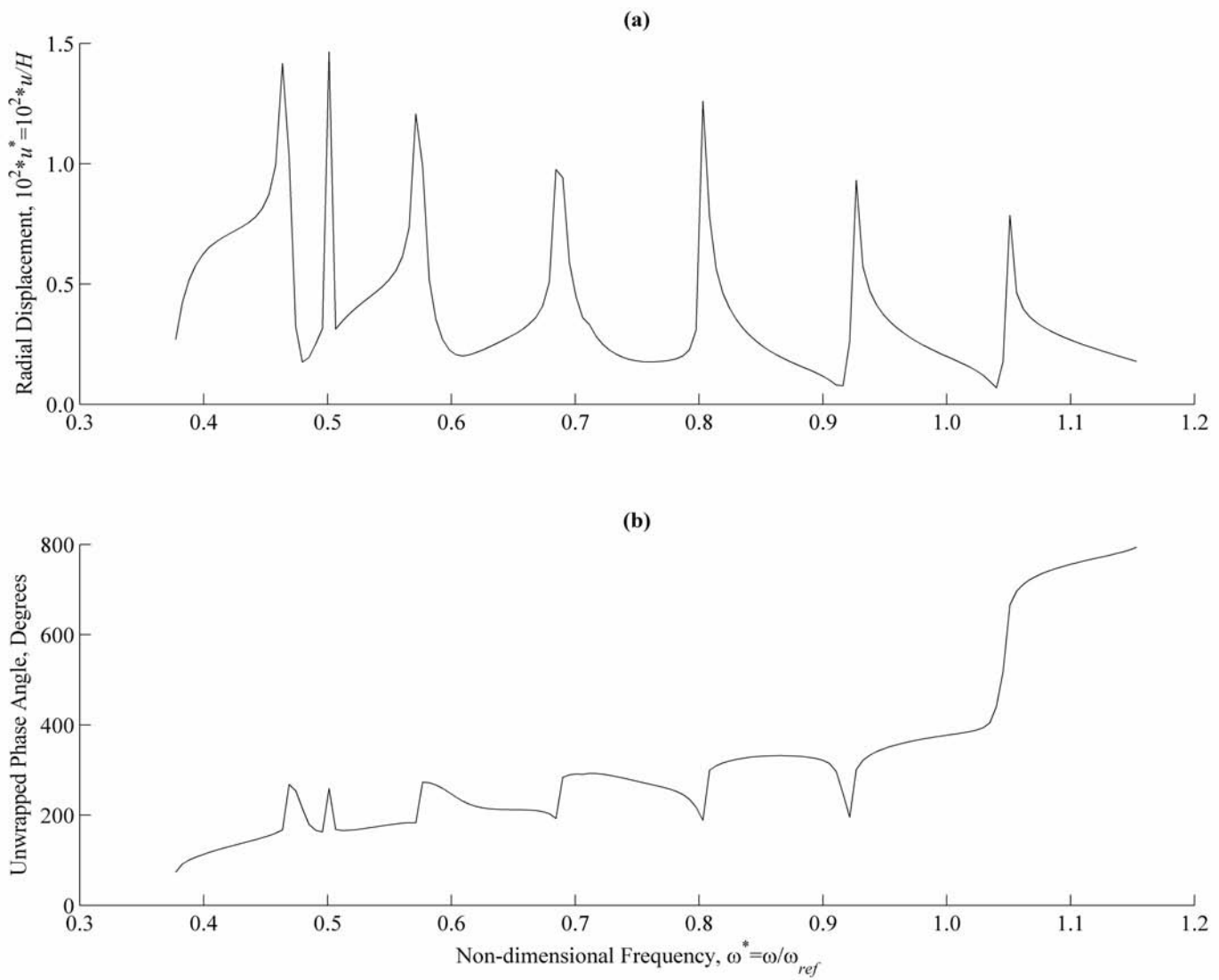

Figure 2.14. Radial FRF for θ=0 and z^*=5.10 at the Cylinder's Outer Surface

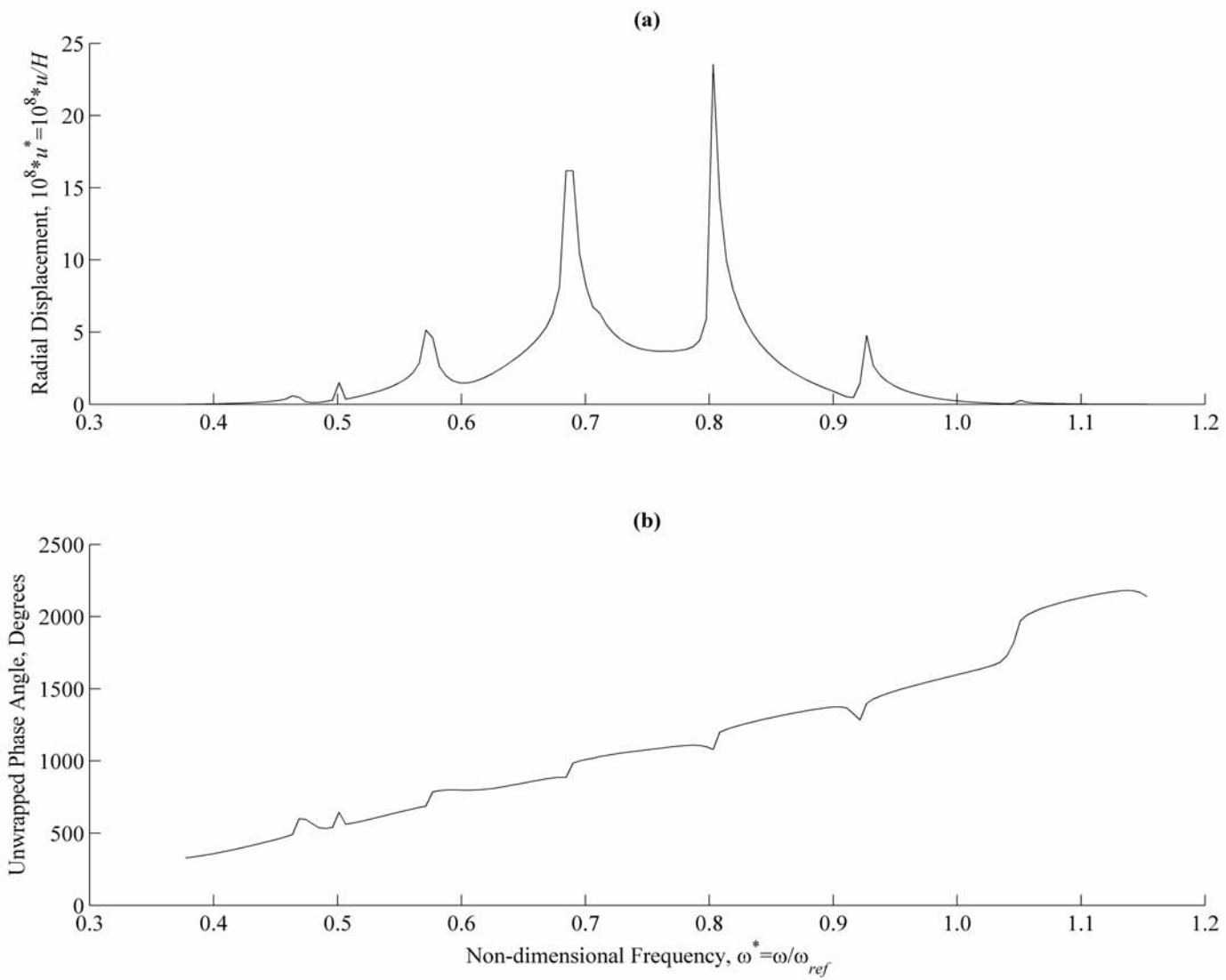

Figure 2.15. Convolved Radial FRF for θ=0 and z^*=5.10 at the Cylinder's Outer Surface

Figure 2.16 shows u^* evaluated by using equation (2.99) at the cylinder's outer surface and $\theta=0$, $z^*=5.10$. Note that time has been non-dimensionalized using:

$$t^*=t\omega_{ref} \tag{2.100}$$

where ω_{ref} is defined in equation (2.83). The temporal history shown in the figure corresponds to $-2000\ \mu s \le t \le 4000\ \mu s$ with the computations performed in $\Delta t=0.35\ \mu s$ increments. On physical grounds, the origin should be the instant when the transient point load is first applied (i.e. the system should be causal). Figure 2.16 indicates, however, that two artifacts arise in numerically evaluating equation (2.99). First, the signal repeats every:

$$T=\frac{1}{\Delta f}=\frac{1}{500\ Hz}=2000\ \mu s. \tag{2.101}$$

Second, the signal is clearly non-causal because a non-zero response can observed before the load is applied. These artifacts are alleviated, in part, by convolving equation (2.63) with a temporal exponential window, that is, by essentially introducing artificial "viscous" damping. Such a window takes the form:

$$e(t)=\begin{cases} 0, & t<0 \\ e^{(-bt)}, & t\ge 0 \end{cases} \tag{2.102}$$

where $b>0$. The Fourier transform of equation (2.102) has the simple analytical form:

$$\bar{e}(\omega)=\mathcal{F}\{e(t)\}=\frac{1}{b-j\omega}. \tag{2.103}$$

which makes the convolution's enumeration straightforward. Constant b is selected somewhat arbitrarily on a trail and error basis as 2500 s^{-1}, a value that leads to:

$$e(0.002\ s)=e^{[-b(0.002\ s)]}\le 0.01. \tag{2.104}$$

This value is selected as a compromise between the desire for the exponential window to have little effect on the recovered displacement history (i.e., it should have a slow decay rate) yet still make this history virtually zero outside the time of interest. The 0.002 s duration over which the exponential is applied corresponds to the periodicity of the time history recovered from equation (2.99).

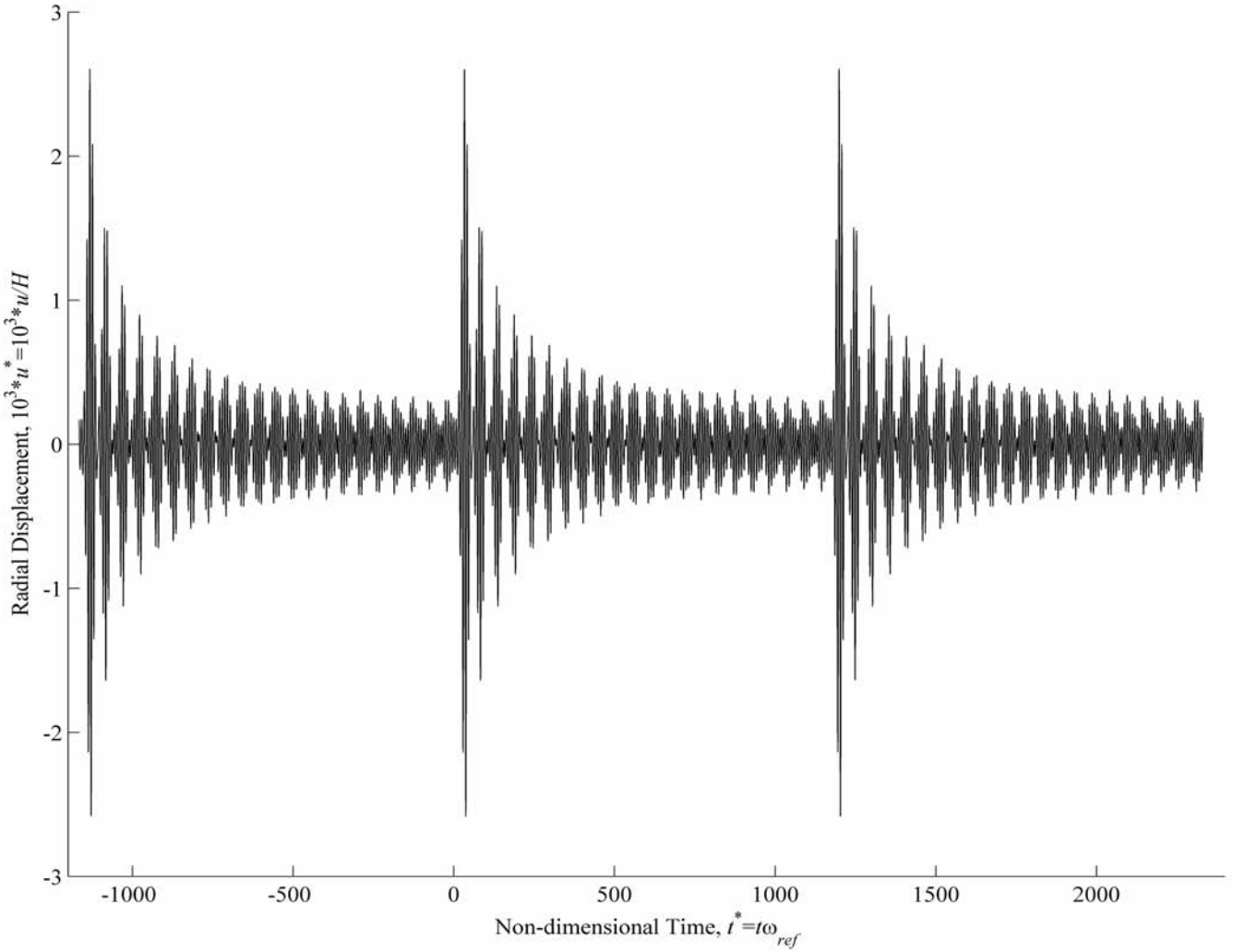

Figure 2.16. Radial Displacement Recovered Using Equation (2.99) for $\theta=0$ and $z^*=5.10$ at the Cylinder's Outer Surface

Equations (2.102) and (2.103) are plotted in Figures 2.17 and 2.18, respectively, for b equal 2500 s^{-1}. Figure 2.18 shows that the frequency content of the resulting exponential window tapers almost to zero around 307 kHz. Consequently, 307 kHz is selected as the upper bound at which the convolution integral [equation (2.105) below] is truncated. Then the convolution of equations (2.65) and (2.102) can be expressed as:

$$\left.\begin{aligned} \boldsymbol{H}(\theta,z,\omega) &= \frac{-j}{2\pi r_0 H}\int_{-\infty}^{\infty} \bar{e}(\omega-\lambda)\bar{f}(\omega)\sum_{n=-\infty}^{n=\infty} \mathrm{sinc}(n\theta_0)\boldsymbol{G_n}(\omega,z)\, e^{jn\theta}\, d\lambda \\ \text{or} \\ \boldsymbol{H}(\theta,z,\omega) &\approx \frac{-j}{2\pi r_0 H}\int_{-2\pi(307\ 000)}^{2\pi(307\ 000)} \bar{e}(\omega-\lambda)\bar{f}(\omega)\sum_{n=-\infty}^{n=\infty} \mathrm{sinc}(n\theta_0)\boldsymbol{G_n}(\omega,z)\, e^{jn\theta}\, d\lambda \end{aligned}\right\} \quad \textbf{(2.105)}$$

giving a "refined" convolved FRF. As for equation (2.99), equation (2.105) is evaluated numerically using trapezoidal integration. The "refined" convolved FRF is approximated at the discrete frequencies ω_k (the same discrete frequencies that the Fourier transform of the exponential window is calculated) by:

$$\boldsymbol{H}(\theta,z,\omega_k) \approx \left\{\begin{aligned} &\frac{-j}{2\pi r_0 H}\left[\sum_{i=2}^{I-1} \bar{e}(\omega_i-\lambda_k)\bar{f}(\omega_i)\sum_{n=-\infty}^{n=\infty} \mathrm{sinc}(n\theta_0)\boldsymbol{G_n}(\omega_i,z)\, e^{jn\theta}\Delta\lambda\right] + \\ &\frac{-j}{4\pi r_0 H}\left[\bar{e}(\omega_1-\lambda_k)\bar{f}(\omega_1)\sum_{n=-\infty}^{n=\infty} \mathrm{sinc}(n\theta_0)\boldsymbol{G_n}(\omega_1,z)\, e^{jn\theta}\Delta\lambda\right] + \\ &\frac{-j}{4\pi r_0 H}\left[\bar{e}(\omega_I-\lambda_k)\bar{f}(\omega_I)\sum_{n=-\infty}^{n=\infty} \mathrm{sinc}(n\theta_0)\boldsymbol{G_n}(\omega_I,z)\, e^{jn\theta}\Delta\lambda\right] \end{aligned}\right. \quad \textbf{(2.106)}$$

where λ is a "dummy" integration variable. Again, I is the total number of (positive) frequency points at which the original FRF is considered. Note that, by convolving the exponential window and the FRF in the above fashion, advantageous use is made of the "narrow" frequency band of the transient point load selected. Furthermore, the exponential

window's Fourier transform uses the same frequency sampling rate as the FRF itself to avoid interpolation between different frequencies. Figure 2.19 gives the result of convolution (2.106) for $\theta=0$ and $z^*=5.10$ at the cylinder's outer surface. The ensuing dynamic response is determined by again using trapezoidal integration to be:

$$\left.\begin{aligned} \boldsymbol{u}^*(\theta,z,t) &= \frac{1}{2\pi}\int_{-\infty}^{\infty} \boldsymbol{H}(\theta,z,\omega)e^{-j\omega t}\,d\omega \\ \boldsymbol{u}^*(\theta,z,t) &\approx \begin{cases} \dfrac{1}{2\pi}\displaystyle\sum_{k=2}^{K-1} \boldsymbol{H}(\theta,z,\omega)e^{-j\omega_k t}\Delta\omega + \\ \dfrac{1}{4\pi}\boldsymbol{H}(\theta,z,\omega_1)e^{-j\omega_1 t}\Delta\omega + \dfrac{1}{4\pi}\boldsymbol{H}(\theta,z,\omega_K)e^{-j\omega_K t}\Delta\omega \end{cases} \end{aligned}\right\} \quad (2.107)$$

where K is the total number of discrete frequencies at which the Fourier transform of the exponential window is calculated. Figure 2.20 presents the "refined" radial displacement corresponding to the unprocessed data of Figure 2.17. The displacement history of Figure 2.17 still repeats itself every $2000\ \mu s$ but "ringing" is reduced noticeably between consecutive cycles. The artificial effect of the postprocessing may be diminished further by dividing the radial displacement history by the exponential window of equation (2.102). The result is shown in Figure 2.21. This figure demonstrates that the "noise" around the temporal origin is reduced in comparison to the history given in Figure 2.17.

The MatLab® script used to evaluate equations (2.106) and (2.107) and remove the exponential window is included on the accompanying electronic media. This process takes approximately 5 hours for each cross section. Note that the computational effort to evaluate equation (2.107) is increased over that of equation (2.99) because the frequency range of integration is now increased to -307 kHz to +307kHz from 35 kHz to 107 kHz.

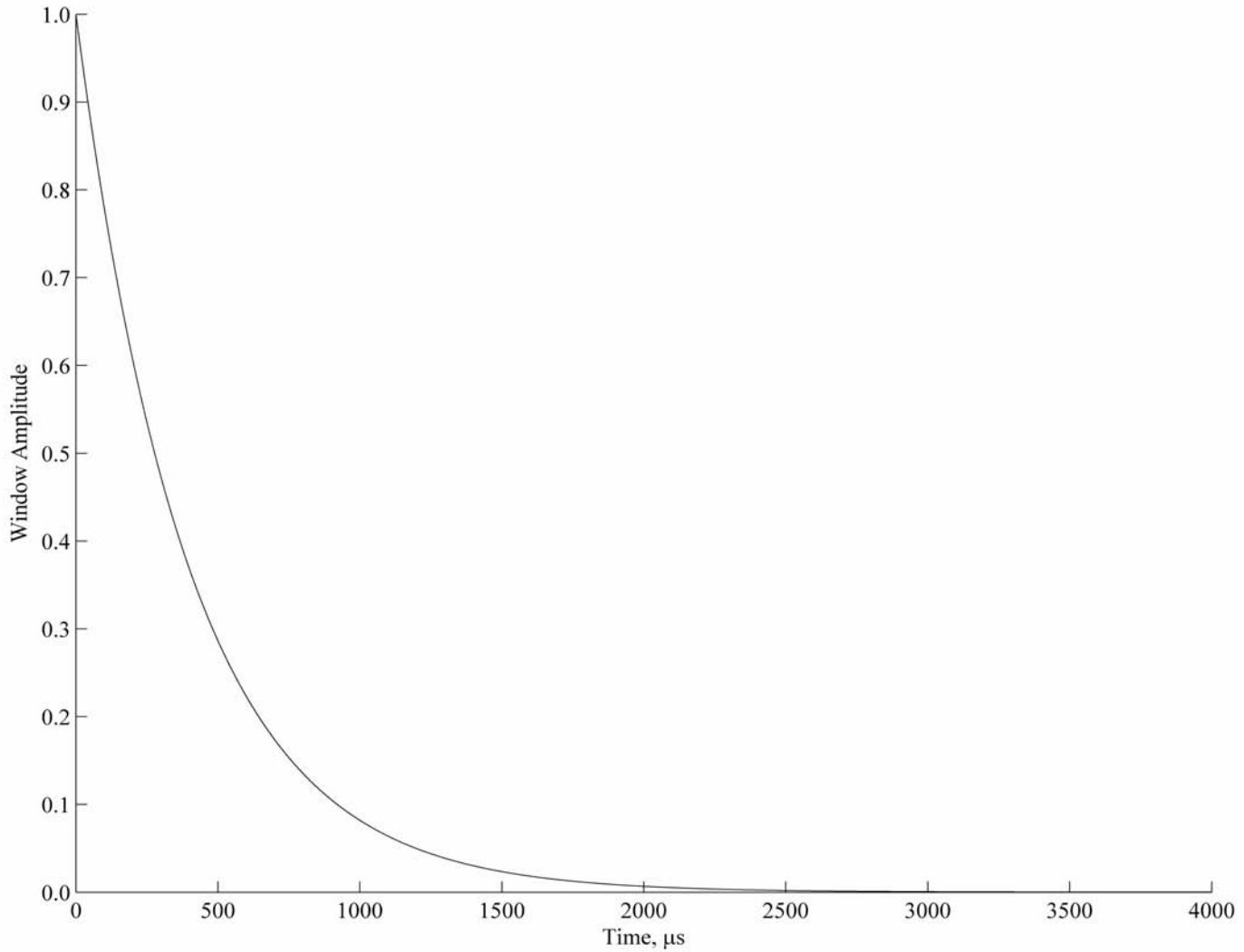

Figure 2.17. Exponential Window in the Time Domain

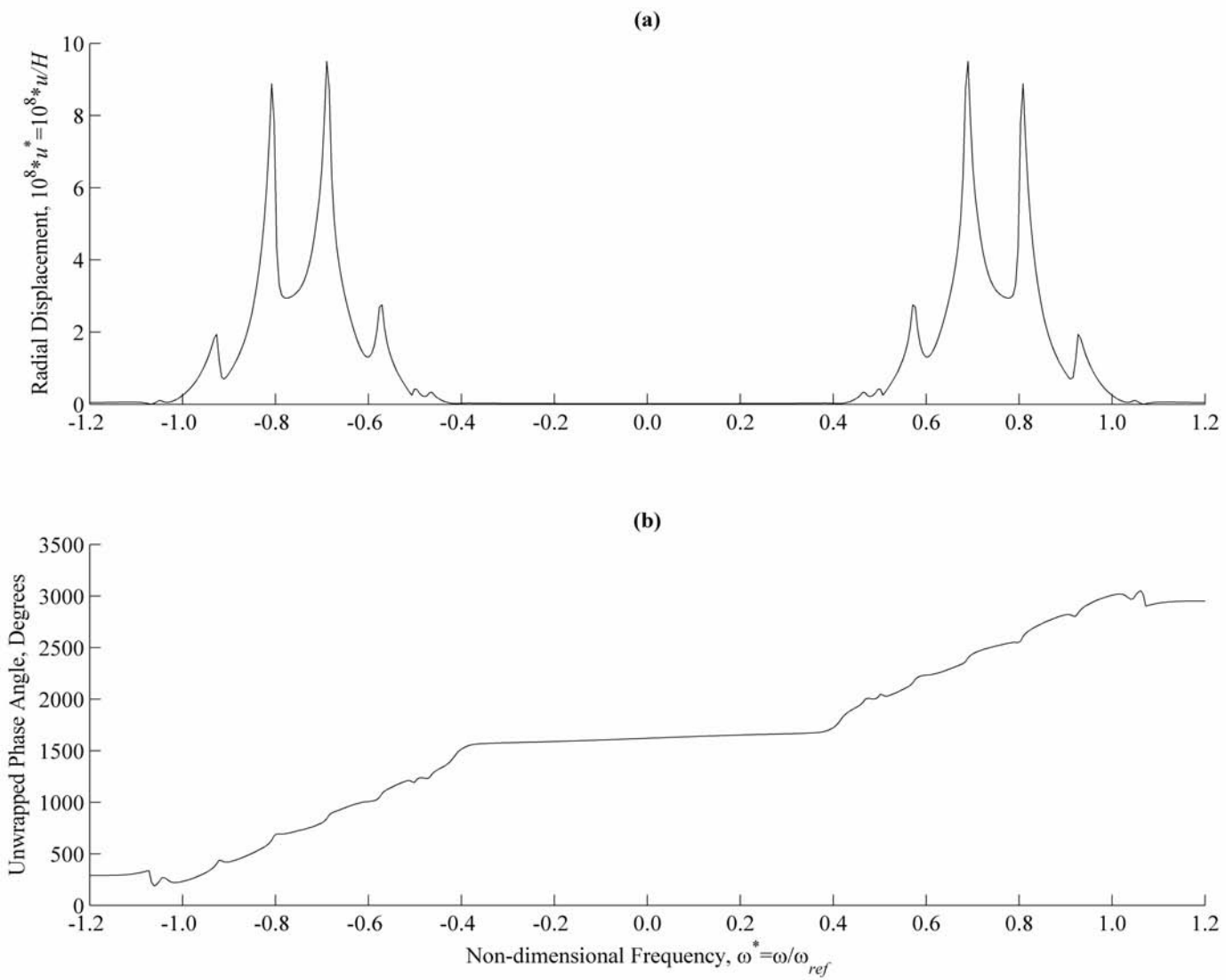

Figure 2.18. Exponential Window in the Frequency Domain

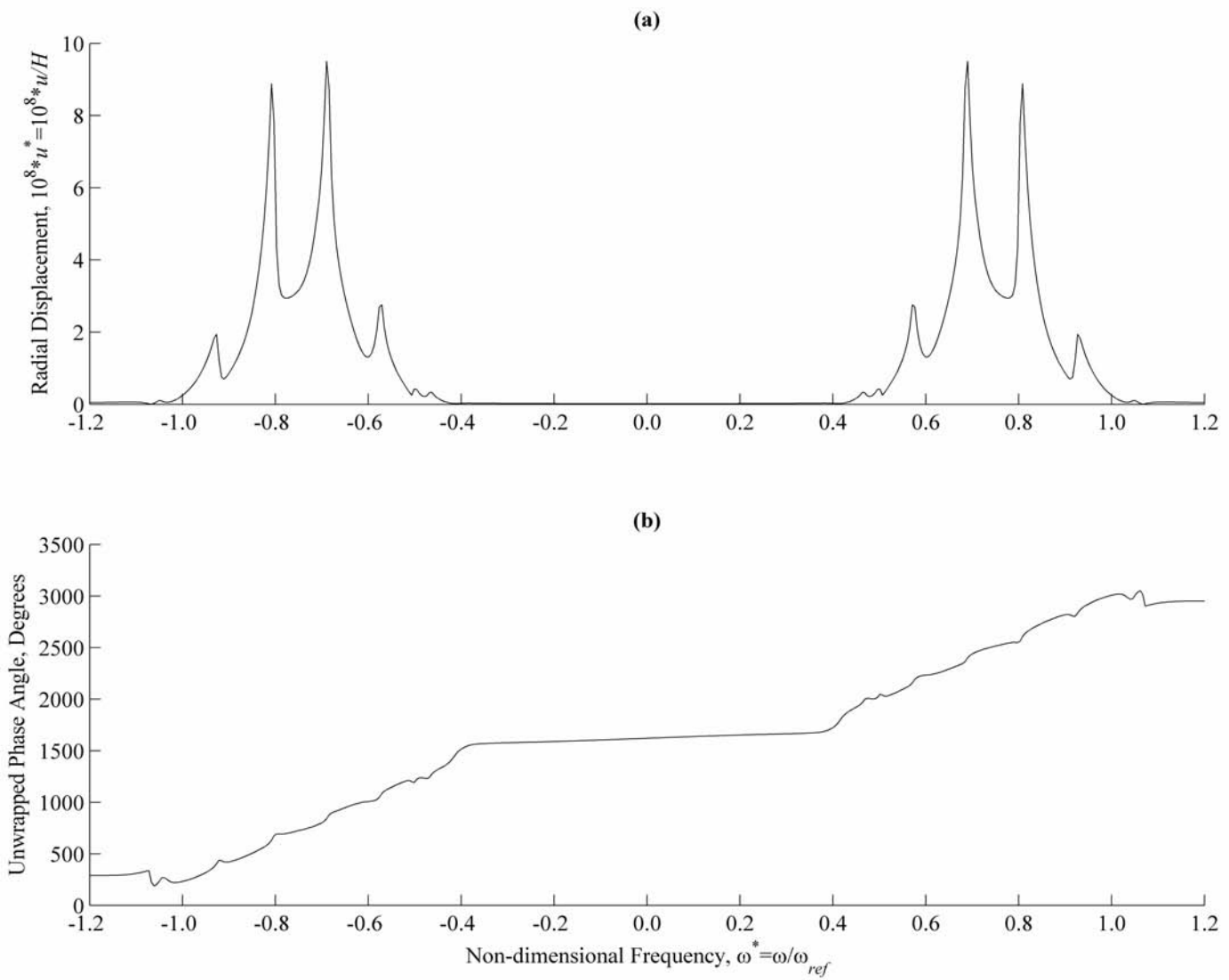

Figure 2.19. Refined Convolved FRF for θ=0 and z^*=5.10 at the Cylinder's Outer Surface

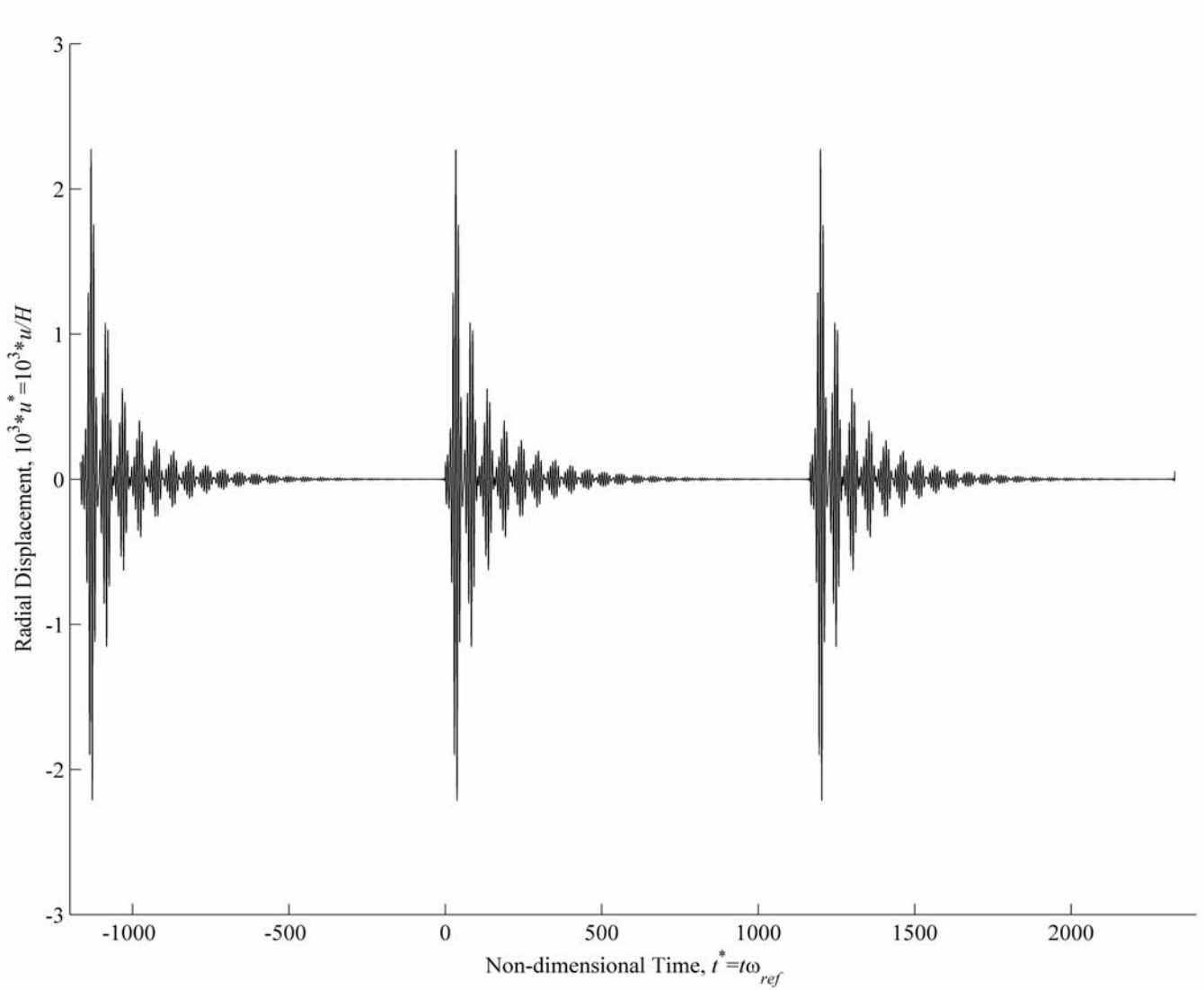

Figure 2.20. Refined Radial Displacement for θ=0 and z^*=5.10 at the Cylinder's Outer Surface

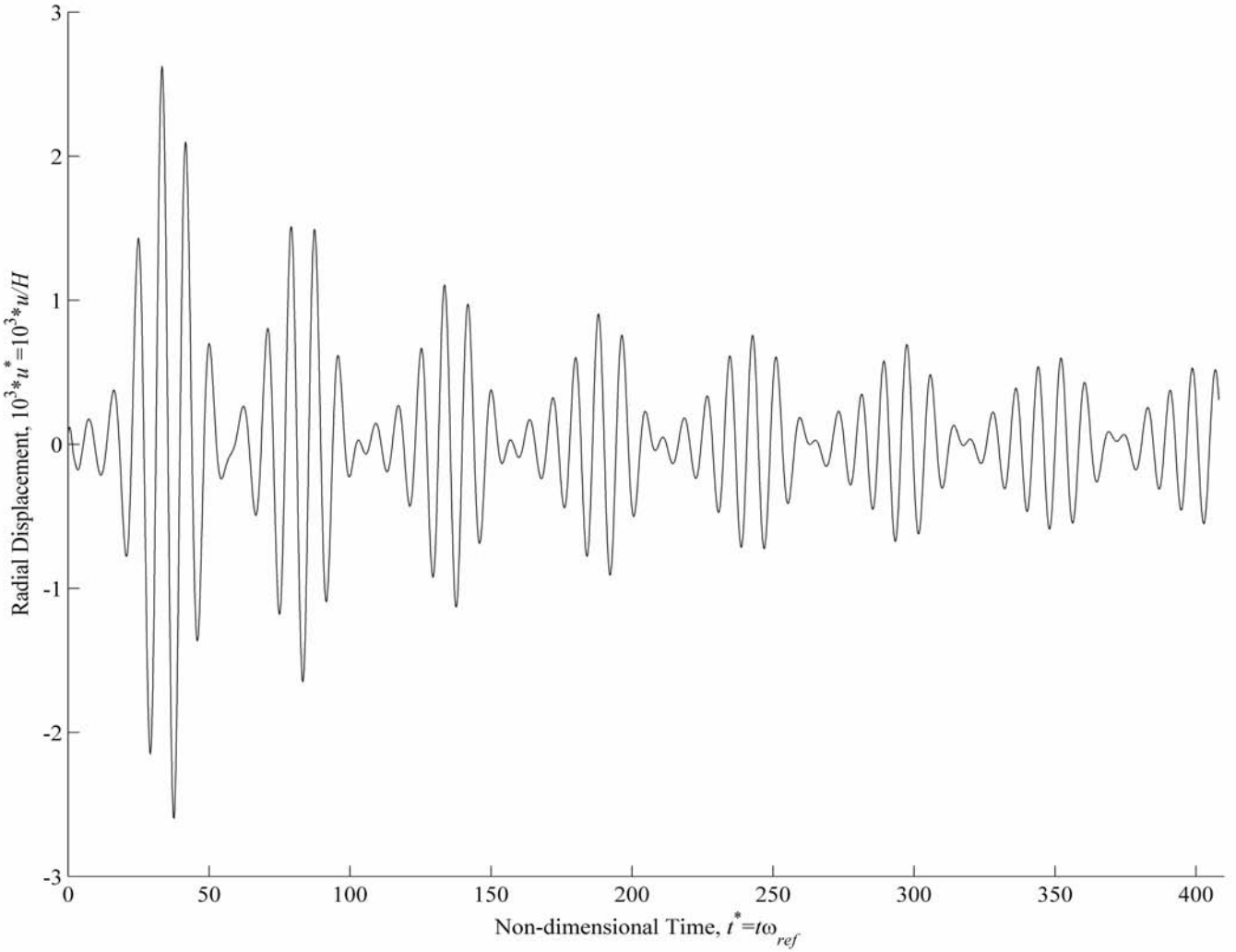

Figure 2.21. Refined Radial Displacement for θ=0 and z^*=5.10 at the Cylinder's Outer Surface After Processing's Removal

2.12.5 Closure

Due to the computational effort required, previously published descriptions of the Green's functions and stress functions tend to be very limited. Only a few spatial points are considered over a limited frequency range. Consequently, little physical insight is gained into the complicated wave propagation. An overall visualisation and interpretation of data is nearly impossible. To overcome these difficulties, the Green's functions, stress functions, and the dynamic radial displacement field are calculated here at more than 230,000 points on a cylinder's outer surface. Computations are performed on readily available PCs that otherwise would be "idle." This approach is straightforward and cost effective to implement because four suitable PCs can be acquired for approximately CDN$3000. Existing commercial software is used wherever possible and storage constraints are circumvented by employing a commercially available compression scheme.

Comprehensive data enables an animation to be developed which clearly shows the displacement's evolution over a significant portion of the cylinder's outer surface. Such an animation is contained on the accompanying electronic media. If desired, "snapshots"may be selected at certain instants for a better understanding of the wave propagation. Several of these snapshots may be found in Chapter 4.

It would have been possible to reduce the user's waiting time (for results) by "parallelizing" the FORTRAN code to run on a parallel computer. However this procedure would require specialized hardware and software that is presently relatively rare and expensive. Also, parallel systems usually appear in a time-sharing environment where a serious degradation of performance occurs with an increasing number of simultaneous users.

Furthermore there is “overhead” associated with managing parallel programs. Moreover, recovering the radial displacements requires the “same” problem to be solved many times. It does not entail the “sub-structuring” of a problem into smaller sized problems that can be solved independently which is the ideal procedure for parallel computing. For these reasons a multiple PC approach is more attractive than a “true” parallel implementation. (See, for example, the performance of a parallel computer relative to a typical PC which is given in Table 2.1.)

Chapter 3 - Experimental Details

3.1 Introduction

A series of experiments are conducted on a steel pipe to validate the computational model. The pipe and available measurement equipment are described first. Then representative experimental data[+] are presented from which the consistency of the transducers' coupling to the pipe may be examined. The transducers' sensitivity is determined by using a thin, nominally uniform aluminum sheet. Experiments are performed subsequently to verify that the pipe is symmetrical and that the principle of reciprocity is satisfied. It is then shown that the effect of the transducers' orientation can be neglected as the transducers and pipe are rotated together about the pipe's longitudinal axis. Comparisons are presented in both time and frequency between the measured and predicted radial displacements on the pipe's outer surface that arise from a radial "point" load. All the transducers are assumed to act at a "point"[++]. The comparisons suggest that a

---

[+] Unless indicated otherwise, all measured histories involve the forcing function described in Appendix A and a centre frequency of 70 kHz. The signal averaging procedure described in Appendix C is always used to improve the Signal to Noise Ratio (SNR).

[++] A transducer does not truly act a point but, rather, over a finite contact area. (See Appendix D for the nominal contact areas of each transducer.) The actual contact area depends on the test piece's curvature, roughness and stiffness. These effects are neglected because the pipe has a relatively smooth surface, the contact forces are "small" [less than 5 lb_f (22 N)], and the deformations of the pipe and transducers encountered are imperceptible (i.e. the pipe and transducers are essentially rigid). Furthermore the forces involved in coupling the transducer to the pipe are static so that they do not affect the measured dynamic behaviour. Appendix D discusses the effect of a finite contact area further. All separations between the transmitting and receiving transducers are nominal, geometric centre-to-centre unless stated otherwise. Also of note, the series representation of the Dirac delta function [equation (2.53)] does not act at a point in the circumferential direction and can be used to model the finite circumferential dimension of a transducer, if necessary.

straightforward modification should be incorporated to accommodate the frequency varying sensitivity of the experimental transducers. A more thorough discussion of the theoretical and experimental comparisons is deferred until Chapter 4.

3.2 Available Equipment

The following ultrasonic and periphery instrumentation is available.

1. One (1) Digital Wave Corporation (DWC) B1080LD broadband (50 kHz - 2 MHz) ultrasonic transducer (with integral line driver) having serial number 0697098. The presence of the integral line driver makes this transducer unsuitable for use as a transmitter.

2. Two (2) DWC B1025 broadband (50 kHz - 2 MHz) ultrasonic transducers having serial numbers 022020 and 071087.

3. Three (3) DWC B225 low frequency (1kHz - 500 kHz) ultrasonic transducers having serial numbers 022041, 092029, and 092035.

4. One (1) General Electric (GE) Panametrics X1054, narrow band (1.18 MHz - 2.96 MHz at 6 dB down points from centre frequency) ultrasonic transducer, having serial number 338769.

5. Two (2) DWC PA2040G/A broadband (5 kHz - 4 MHz) pre-amplifiers which are compatible with the DWC ultrasonic transducers. These pre-amplifiers have serial numbers 325 and 330. One is configured for use with a transducer having an integral line driver and the other for those without (325 and 330, respectively). The voltage gain is set to 40 dB unless specified otherwise.

6. One (1) Agilent Technologies 54624A, four channel, 100 MHz digital storage oscilloscope with serial number MY40001587. This oscilloscope is equipped with the optional Institute of Electrical and Electronics Engineers (IEEE) 488 General Purpose Interface Bus (GPIB) interface module whose serial number is MY40003651.

7. One (1) Agilent Technologies 33120A 15 MHz function/arbitrary waveform generator with integrated GPIB interface having serial number MY40008995.

8. One (1) Intel® Pentium® based Personal Computer (PC) equipped with an Agilent Technologies 82350A GPIB interface card (serial number A1A01143).

9. One (1) 3 inch Nominal Pipe Size (NPS) (80 mm Diameter Nominal [DN]), schedule

40 seamless carbon steel pipe that is approximately 10 ft (3m) long.

10. One (1) **0.099±0.001** in (2.52±0.02 mm) thick [10 gauge], aluminum sheet having the dimensions 24.69 in×46.19 in×24.81 in×46.06 in (62.7 cm×117.3 cm×63.0 cm×117.0 cm). [All dimensions are quoted to ± 0.06 in (± 0.2 cm).] The grade of the aluminum is unknown but it is most likely American National Standards Institute (ANSI®) 6061-T6.

Further details can be found, along with Original Equipment Manufacturer (OEM) supplied data sheets and calibration curves, in Appendix D. This equipment is always arranged in the conventional pitch-catch arrangement illustrated in Figure1.1. The storage oscilloscope (54624A) is used for the Analog to Digital (A/D) conversion of the measured signals which are downloaded and stored on the hard disk of the PC for later analysis.

3.3 Description of Pipe

The pipe conforms with the American Society for Testing and Materials (ASTM) standard ASTM A106. Therefore the allowable variations of its dimensions from the nominal specifications are described in the American National Standards Institute (ANSI®) standard ANSI® B 36.10. Its material properties are specified by ASTM A530/A530M. Copies of the OEM's material data sheets for this pipe are given in Appendix E.

A protective coating was removed and light oiling was applied to the pipe to minimize its oxidation. A photograph of the resulting pipe is shown in Figure 3.1. The clearly visible, alternating "dark" and "light" bands that "spiral" around the pipe arise from the manufacturing process. They indicate that the pipe is not perfectly uniform along its length. On the other hand, the pipe may be considered "infinite" in length because end reflections are "time gated" out of all the experimental data. Also, note that the rollers supporting the pipe (which are clearly visible in Figure 3.1) are "far" from the measurement

region so that their effects are also "time gated" from the measurements. A theodolite is used to verify that the pipe is level and "square" to the supports to within the theodolite's ±0.04 in (±1mm) resolution.

Figure 3.1. Pipe and Roller Supports

The pipe's outer diameter (wall thickness) is measured at two different cross sections (one end) by using a micrometer (dial caliper). The dimensions, as well as their (arithmetic) average values and standard deviations, are presented in Tables 3.1 and 3.2. These tables (and the experimental data presented later) indicate that the pipe's geometry has sufficient uniformity that a commercially superior specimen is unlikely to be found. Note, moreover, that the pipe's geometry and dimensions are nominally identical to those of the cylinder considered theoretically in Chapter 2.

Material properties of the cylinder were not measured. However, the values assumed

in Chapter 2 should be reasonably accurate because their agreement with published data for typical mild steels is quite good. Furthermore, the composition and heat treatment of steel does not usually have a large effect on its elastic properties. (See, for example, [54].) Only the strength and ductility may be affected but these properties do not appear in the computational model.

Table 3.1. Pipe's Outer Diameter Measured at Two Cross Sections

Cross Section	Outer Diameter, Inches (mm)
1	3.5000±0.0005 (88.90±0.01)
1	3.4950±0.0005 (88.77±0.01)
1	3.5000±0.0005 (88.90±0.01)
1	3.4965±0.0005 (88.81±0.01)
2	3.4910±0.0005 (88.67±0.01)
2	3.4930±0.0005 (88.72±0.01)
Average	3.4959±0.0005 (88.80±0.01)
Standard Deviation	0.0037±0.0005 (0.09±0.01)

Table 3.2. Pipe's Measured Wall Thickness

Wall Thickness, Inches (mm)
0.216±0.001 (5.49±0.02)
0.217±0.001 (5.51±0.02)
0.223±0.001 (5.66±0.02)
0.220±0.001 (5.59±0.02)
0.228±0.001 (5.79±0.02)
0.214±0.001 (5.44±0.02)
0.224±0.001 (5.69±0.02)
0.216±0.001 (5.49±0.02)
Average: 0.220±0.001 (5.59±0.02)
Standard Deviation: 0.0049±0.0009 (0.12±0.02)

3.4 Coupling

Contact or non-contact transducers may be used to induce and measure ultrasonic waves in elastic solids. Contact transducers (like those used here) make "contact" with the

test piece directly or through a thin coupling layer of oil, wax, etc. Non-contact transducers (e.g., laser/optical, thermal or magnetic based transducers) are generally coupled to the test piece through air or water. Contact transducers are cost effective, they produce "good" signal to noise ratios as well as depth penetrations, and they are robust compared with non-contact transducers. Furthermore, they can be used with most materials and only commercially smooth surfaces are required. Consequently a contact transducer is most likely to be chosen for industrial applications. The primary disadvantages of contact transducers are the variability that may be introduced by the coupling and the possible static deformation of the test piece caused by the transducer's weight. Although non-contact transducers do not deform the test piece and the coupling is more consistent, signal to noise ratios are typically smaller due to the extremely large (acoustic) impedance mismatch[+] between air or water and most elastic solids. Moreover the mismatch limits a signal's penetration. Exceptionally (sub-micron) smooth surfaces are often required for laser/optical techniques which limits their application. Magnetic based techniques are also limited in application as a test material must be amenable to magnetism.

A thin layer of carefully applied beeswax or a dry coupling induced by a "small" static force (e.g. by a small weight or weak spring) is used here. Beeswax is attractive because it also acts as an adhesive which can "support" a "light" transducer's weight for any orientation of the transducer. This advantage may be offset by the variability, over time, in

---

[+] The impedance mismatch causes much of the power developed by the transducer to be reflected from the test piece's surface and lost. It also reduces a signal's amplitude so that signal to noise ratio problems may occur. Contact transducers also suffer from an impedance mismatch but not as severely as non-contact transducers.

the coupling's adhesion and the time required to (re)apply the beeswax when a transducer is relocated numerously. Ensuring that a transducer is orientated normally to a curved surface is difficult due to the possibility of a non-uniform application of beeswax. These difficulties are minimized by relocating the transducers as infrequently as possible and checking the orientation of the transducers by using a machinist's square. The use of a constant force reduces these difficulties because the variability in the coupling layer is eliminated. However, a constant force is difficult to generate, in practice, for an arbitrary transducer orientation on a curved surface. Although the presented (experimental) data applies to receiving transducers, similar trends are seen for transmitting transducers.

Figure 3.2 shows the variability in the measured radial displacement at the pipe's external surface when beeswax coupling is used. The DWC B1080LD transducer acts as the receiver and the DWC B1025 transducer (serial number 022020) is used as the transmitter.[+] Ten "engagements" of the receiving transducer are shown for a permanently located transmitter. Each "engagement" involves a new application of beeswax on the receiving transducer which is subsequently placed carefully in nominally the same location. A pure axial (within $\pm 1^{\circ}$) offset of 4.00±0.03 in (10.16±0.08 cm) relative to the transmitting transducer is used. The transducers' longitudinal axes are nominally normal to the pipe's surface. Their data cables are aligned (within $\pm 2^{\circ}$) with the pipe's longitudinal axis. The transmitting transducer is "pulsed" and the ensuing radial displacement is measured.

It can be seen from Figure 3.2 that the overall shape of the radial displacement is

---

[+] The DWC B225 transducers, which are used for all the remaining experiments, were unavailable when this experiment was conducted.

essentially identical for each engagement but the amplitude changes. To further illustrate this point, Figure 3.3 shows each of these engagements with the radial displacement normalized as:

$$x_{ij}^{*} = \frac{x_{ij}}{\max\left(|x_j|\right)}. \tag{3.1}$$

The x in equation (3.1) is the measured radial displacement (in volts) of the i-th sample obtained in engagement j. Furthermore, $\max\left(|x_j|\right)$ is the largest absolute value of x in engagement j. Note that the definition of equation (3.1) requires that $-1 \le x_{ij}^{*} \le 1$. All 10 traces are presented in Figure 3.3. They are virtually identical. Hence the x_{ij}^{*}, unlike the x_{ij}, can be determined consistently.

Figure 3.4 presents the results of repeating the previous experiment but with a dry contact force of 2.2±0.1 lb_f (9.7±0.5 N) that is applied consistently through a compression spring. The 10 traces of Figure 3.4, like those of Figure 3.2, have the same shape again but now the $\max\left(|x_j|\right)$ are within about 7 percent for all 10 traces. [Note, however, that it is typical for larger (smaller) contact forces to produce larger (smaller) $\max\left(|x_j|\right)$.] While beeswax coupling is convenient, the variability of the measured amplitude does not allow the magnitude of traces to be compared meaningfully[+] and hence, only the shape of traces can be compared. Consistent dry coupling, on the other hand, is less convenient but does allow the magnitude of traces to be compared meaningfully (within experimental uncertainties).

[+] One application that requires a comparison of the trances' magnitudes is the measurement of a material's attenuation.

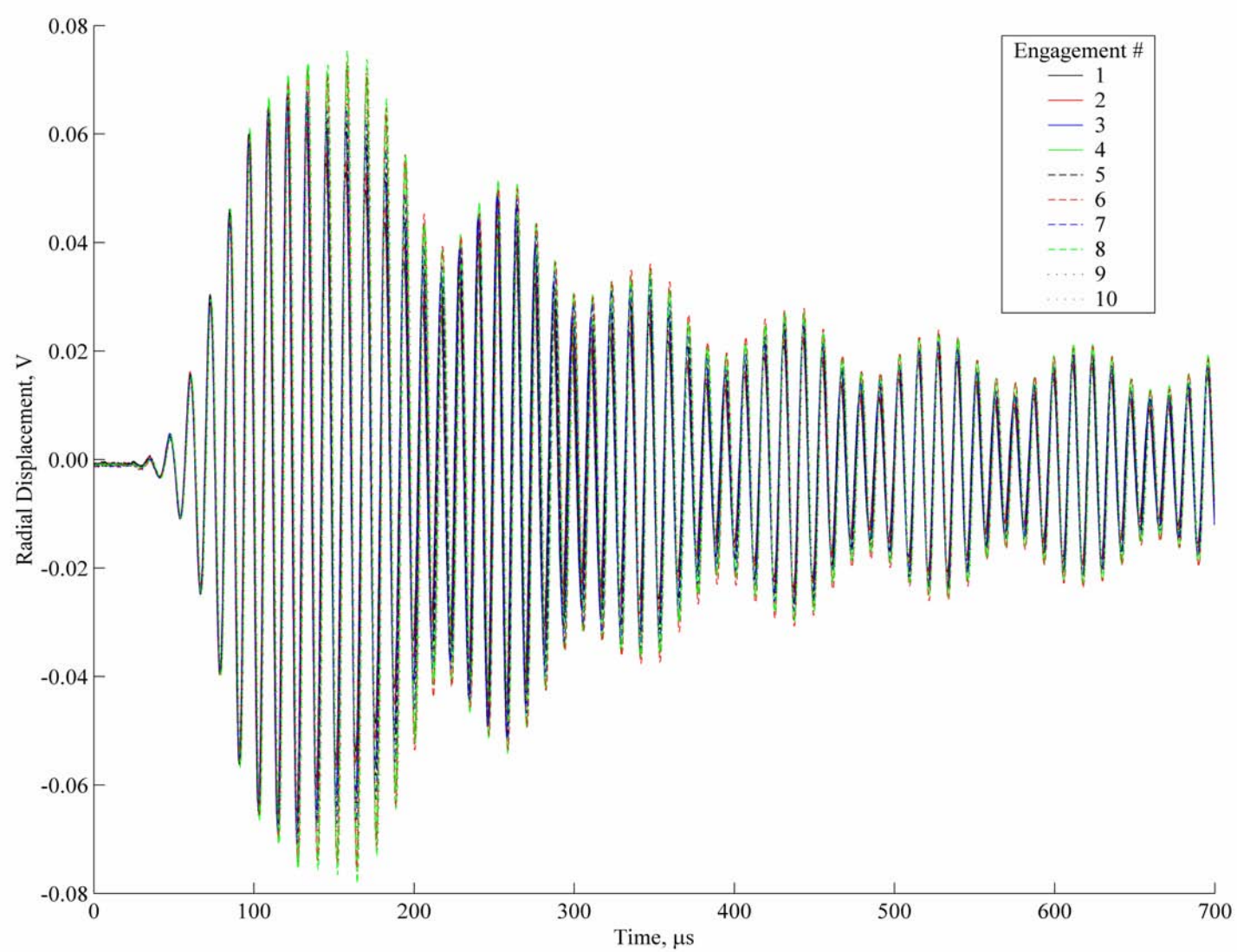

Figure 3.2. Variability in Measured Radial Displacement for Beeswax Coupling

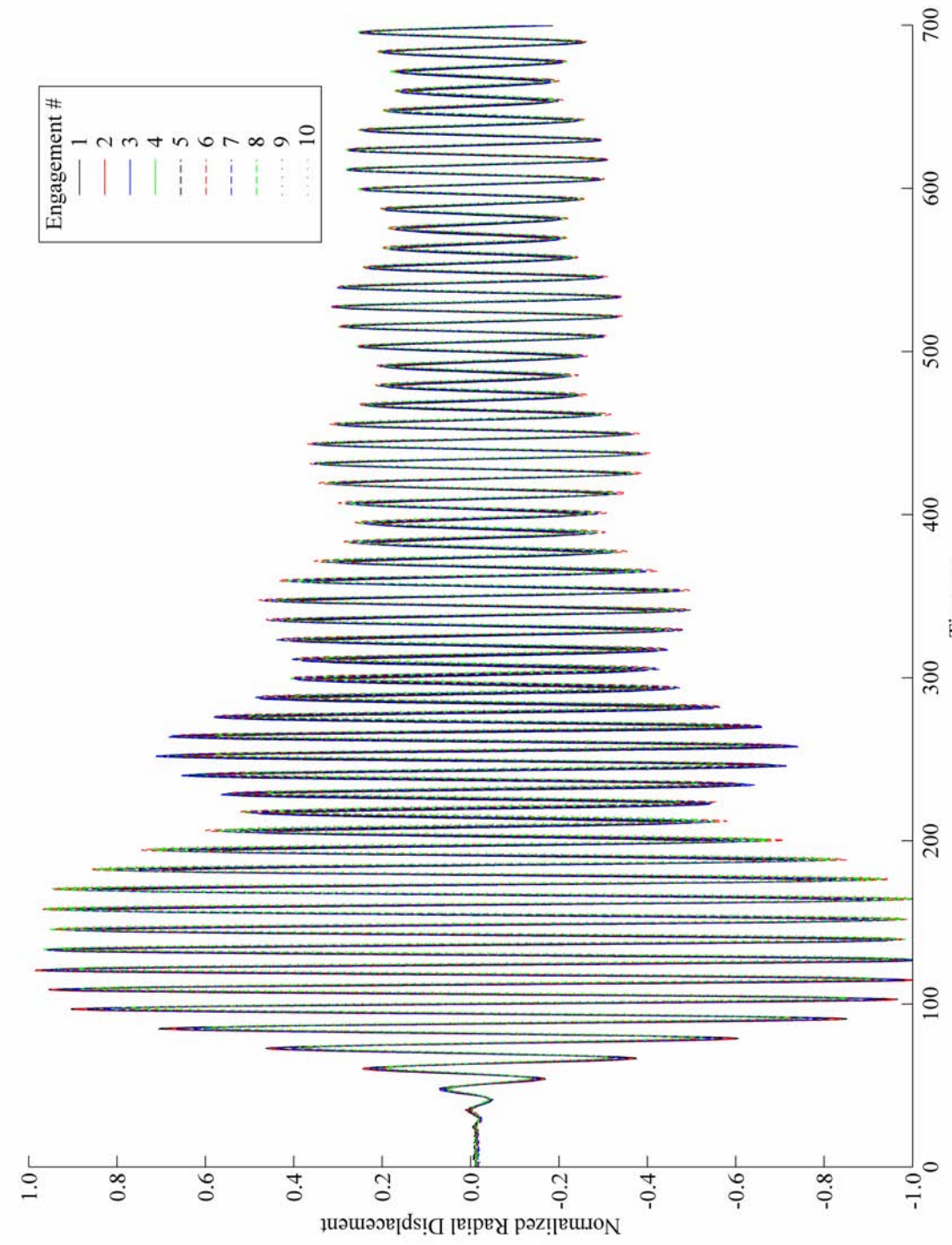

Figure 3.3. Variability of Normalized Radial Displacement for Beeswax Coupling

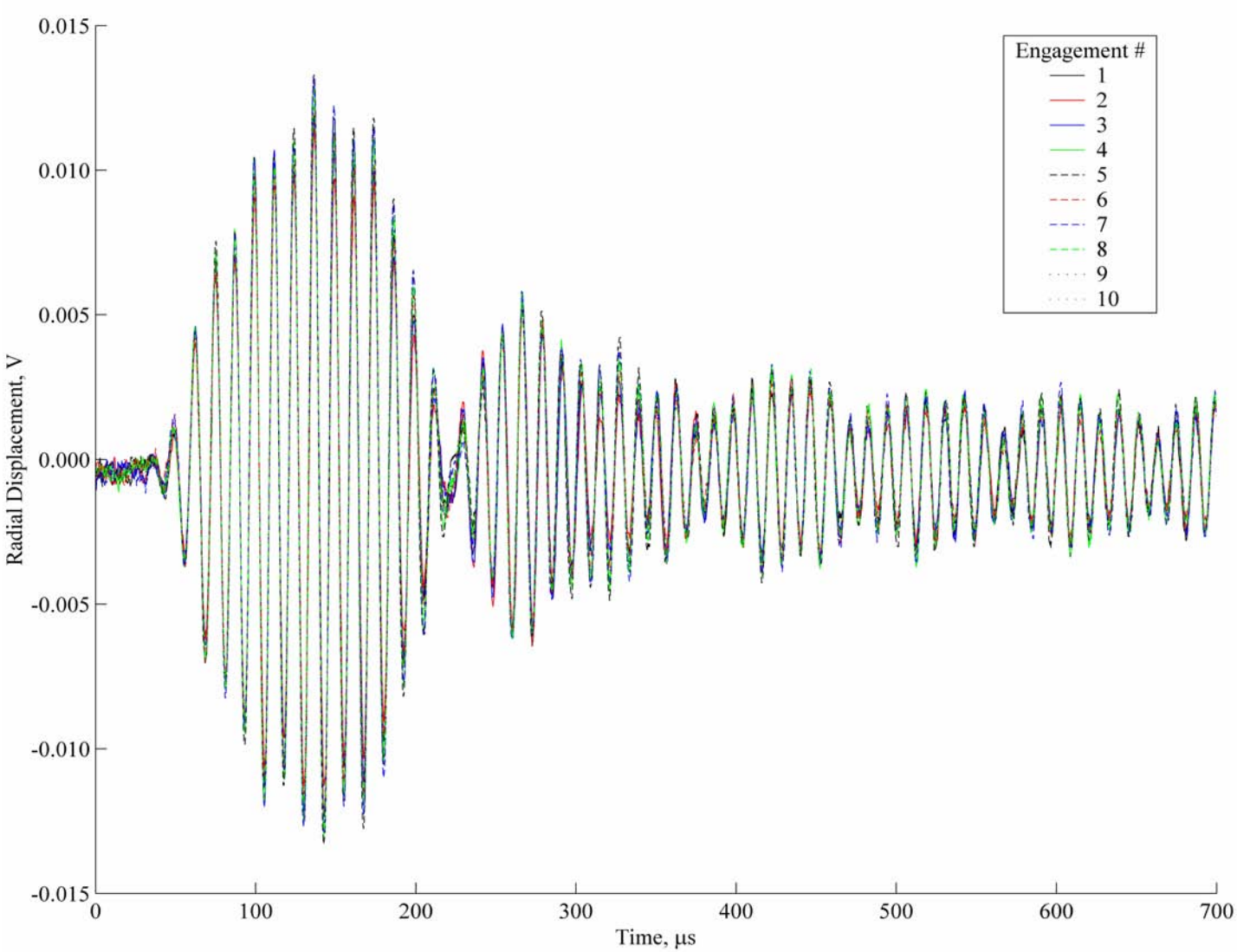

Figure 3.4. Variability in Measured Radial Displacement With Dry Coupling

Figure 3.5 illustrates the effect that a misalignment of the transducer's longitudinal axis with the normal to the pipe's surface has on the measured radial displacement. The figure compares radial displacements when measured with the receiving transducer's longitudinal axis normal to the pipe's surface and when inclined approximately 5° from the normal (in roughly the longitudinal direction). The transducers' data cables are aligned (within ±2°) with the pipe's longitudinal axis. The DWC B225 transducers (serial numbers 092029 and 092035) are used as the transmitter and receiver, respectively. Both transducers are placed on the pipe's outer (curved) surface using beeswax. The receiver always remains at the same location. The separation between the transmitter and receiver is an axial offset (to within ±1°) of 0.56±0.03 in (0.14±0.08 cm).

It can be seen from Figure 3.5 that the shapes of the two traces are similar but their amplitudes differ vastly once again. Similar results are seen for other "small"[+] perturbations of the receiving transducer from the normal of the pipe's surface. Consequently the measured displacement's shape, unlike its amplitude, is essentially independent of a 5° or smaller misalignment of the transducer's longitudinal axis with the normal to the pipe's surface.

As a brief example of how clamps can affect the measured radial displacements, consider Figure 3.6. This figure illustrates the effect of a hose clamp (effectively an axisymmetric geometrical discontinuity) immediately downstream of the receiving transducer. The transducers are arranged as in the previous experiment but the axial offset

---

[+] A "small" perturbation is a misalignment of the transducer's longitudinal axis with the normal to the pipe's surface that does not make the entire contact surface of the transducer leave the pipe's surface.

is changed to 1.87±0.03 in (4.75±0.08 cm). The figure compares radial displacements measured with and without a hose clamp present. Clearly the hose clamp has an effect on the measured radial displacement. It can be seen from Figure 3.6 that the shapes of the two traces are similar but their amplitudes differ. Again, as with the case of receiving transducer misalignment, the measured displacement's shape, unlike its amplitude, is essentially independent of the axisymmetric geometrical discontinuity.

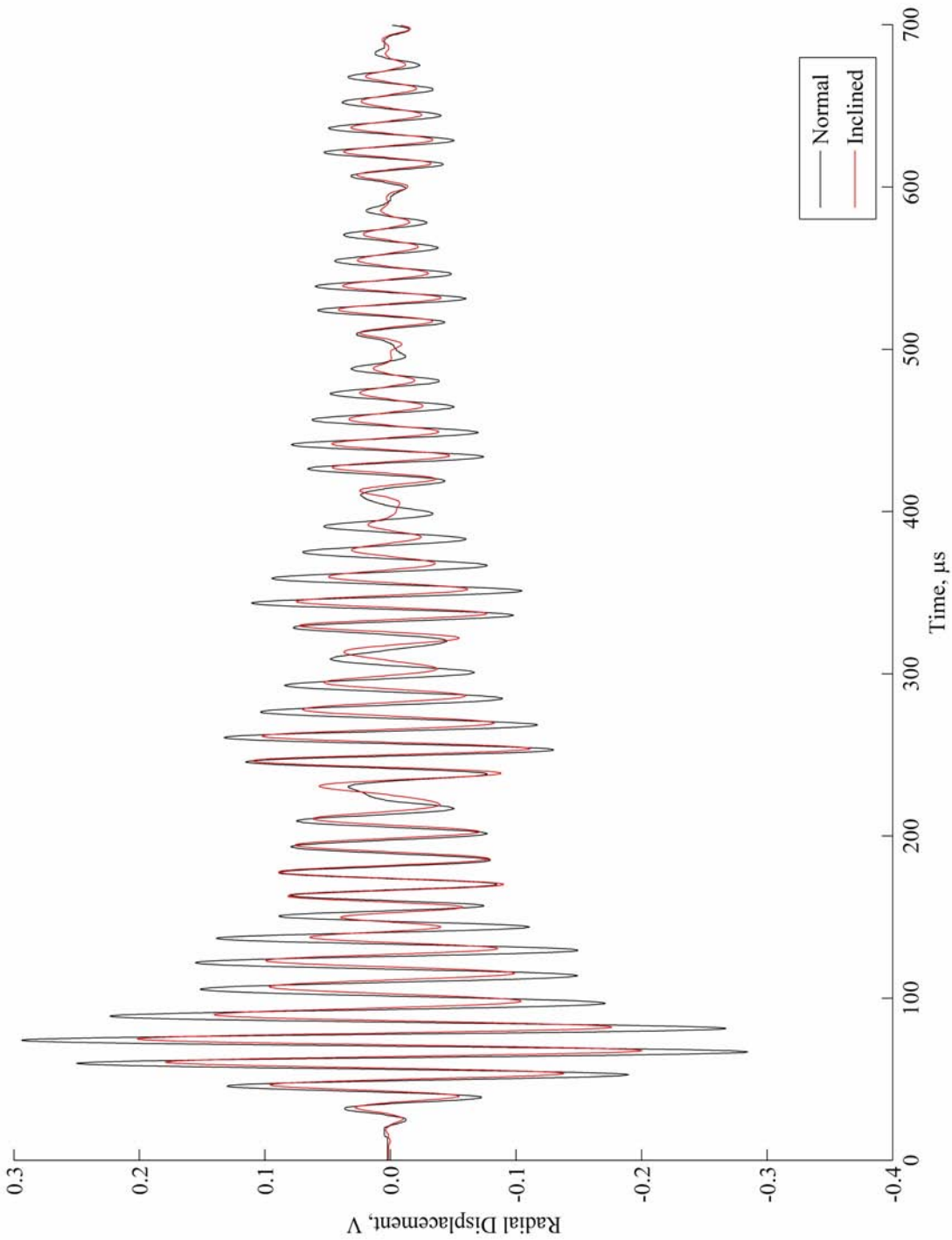

Figure 3.5. Effect of Receiving Transducer's Misalignment

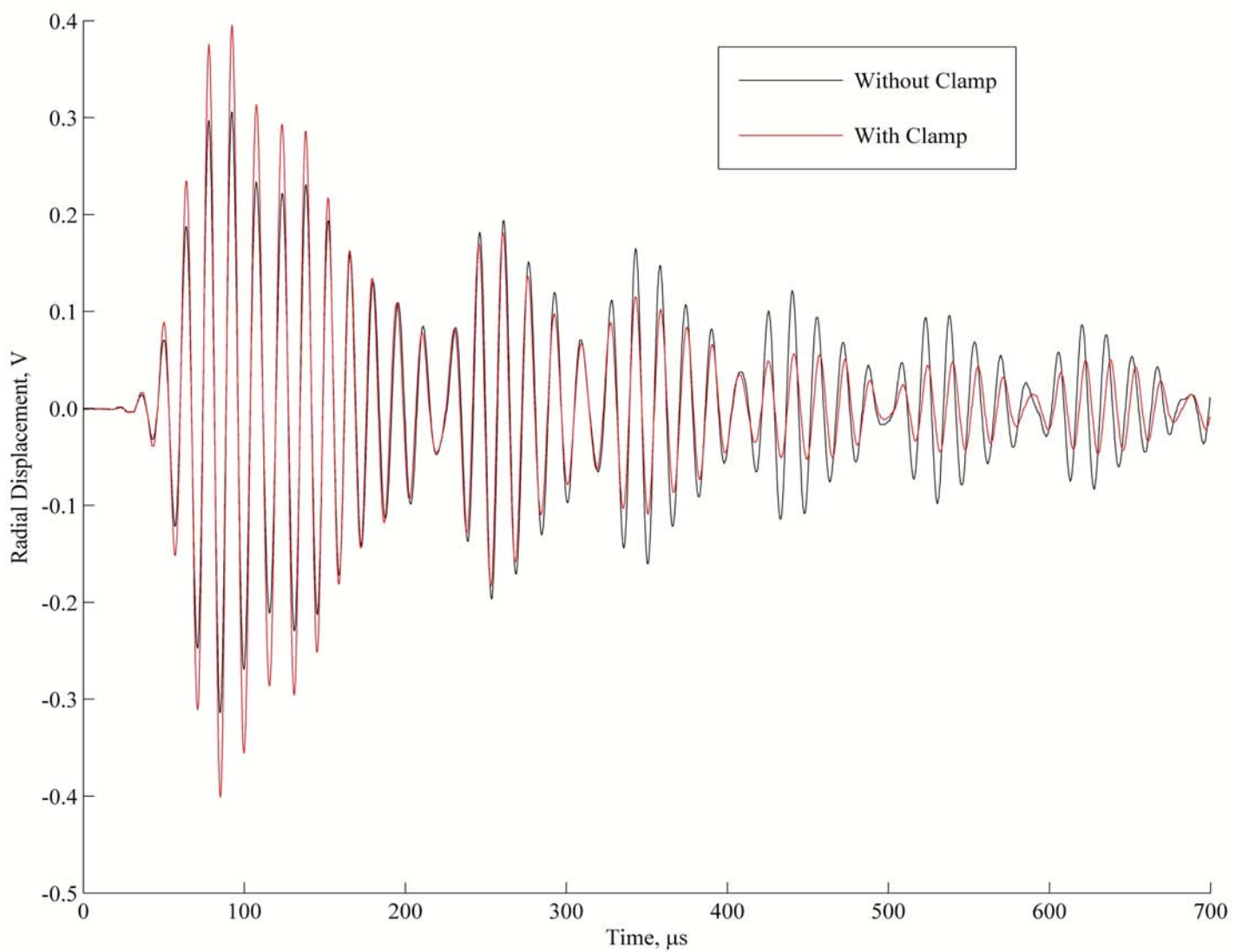

Figure 3.6. Effect of a Hose Clamp on the Measured Radial Displacement

3.5 Transducer Sensitivity, Symmetry Checks, Reciprocity and Pipe Rotation

3.5.1 Transducer Sensitivity

Ensuring that a transducer's longitudinal axis is normal to a planar sheet is more straightforward than for a cylindrical pipe. Furthermore, compensations may be made to account for any directionality of a transducer's sensitivity. These compensations are possible because a sheet has an open cross section and, if reflections from the sheet's edges are avoided, waves do not "wrap around" as in a closed section pipe. For these reasons an aluminum sheet is used to check the directionality and sensitivity of the transducers. Various combinations of transmitting and receiving transducers are tested at different orientations and centre frequencies of the forcing function. Each transducer's longitudinal axis is always carefully aligned with the sheet's normal. The transmitter (receiver) induces (measures) an out-of-plane force (displacement like quantity). Dry coupling afforded by simple weights is used throughout. Representative data is presented for the DWC B225 transducers because they are used in later experiments. Data for the remaining transducer combinations are presented more conveniently in Appendix F.

A square grid with a 1.00±0.03 in (2.54±0.08 cm) spacing is laid out from the geometric centre point of the aluminum sheet. A (right hand) Cartesian coordinate system, with its origin at the centre of the sheet, is overlaid as a means of describing a transducer's position and orientation. The grid and coordinate system can be seen in Figure 3.7. The sheet is placed on a steel backing plate, as shown in Figure 3.8, to increase its effective (bending) stiffness so that the sheet does not deflect under the weight of the transducers and the dry contact, coupling force.

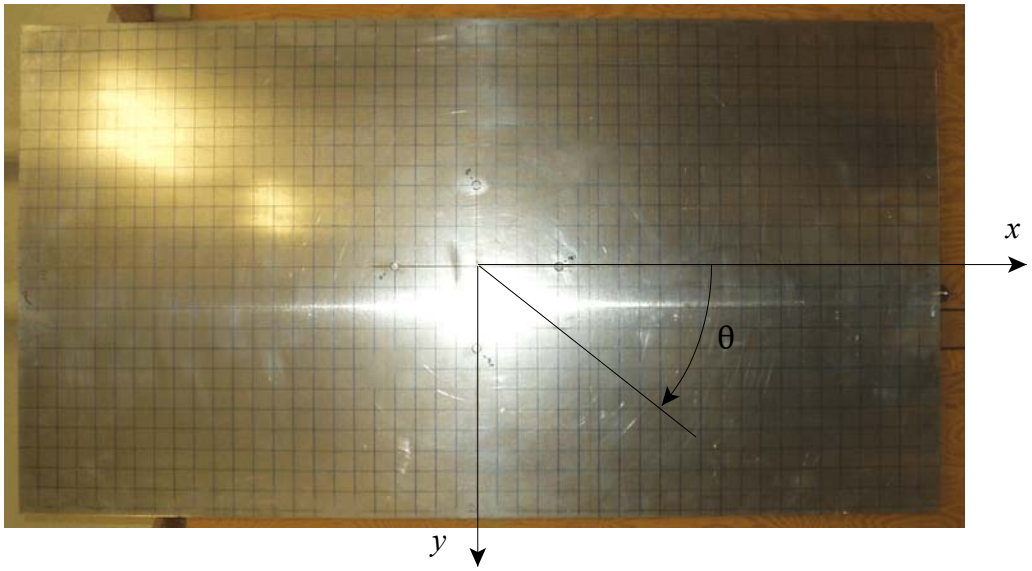

Figure 3.7. Grid and Coordinate System

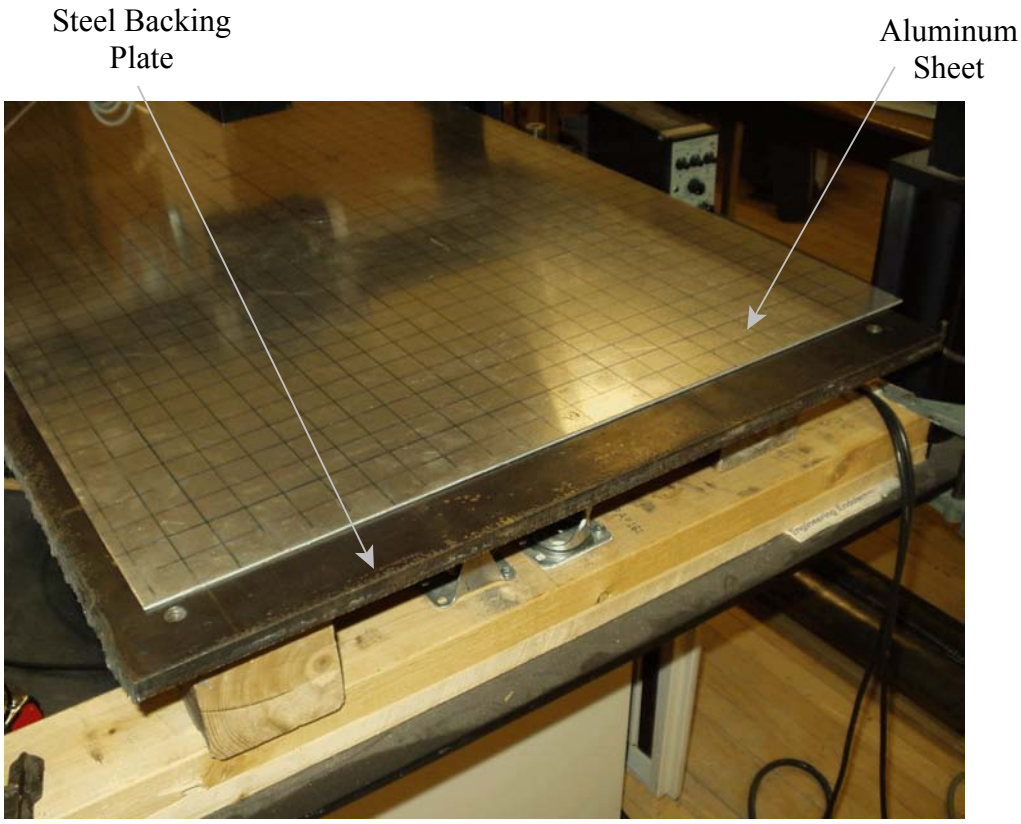

Figure 3.8. Aluminum Sheet on Steel Backing Plate

For each combination of transducers, either the transmitter or the receiver remains in the same location for the duration of an experiment. A 4.00±0.03 in (10.16±0.08 cm) separation is maintained between any two transducers. Four different orientations of the moveable transducer are examined, viz. 0±3°, 90±3°, 180±3°, and 270±3°. The orientation is specified by the angle, θ, that the cable connection of the DWC transducers and a thin line on the casing of the GE Panametrics transducer makes with the *x* axis when viewed along the transducer's longitudinal axis. (See Figure 3.7.) The positive direction corresponds to a counterclockwise rotation viewed from the positive *z* axis. The 0° orientation is tested twice for each transducer combination to assess the coupling's consistency. Table 3.3 summarizes the data for the evaluated transducer combinations. Included in this table are the orientations of the transducers, the contact forces[+], and the centre frequencies of the forcing function. Figures 3.9 through 3.12 show the out-of-plane displacement measured for the transducer combinations marked with an asterisk (*) in Table 3.3. Traces for the other transducer combinations appear more conveniently in Appendix F.

An individual trace in one of Figures 3.9 through 3.12 should be identical to the other traces given in the same figure. It can be seen from Figures 3.9 through 3.12 that this is reasonably so in all cases. Hence, the DWC B225 transducer is essentially omnidirectional over its working frequency range - regardless of whether it is operated as a transmitter or as a receiver. This observation is also found to be true for the remaining DWC B225 transducers but no other transducer tested has this desirable property.

[+] The contact force listed in Table 3.3 does not include the weight of the transducer.

Table 3.3. Transducer Combinations Tested for Orientation Dependence

Designation	Transmitting Transducer and Orientation(s)	Receiving Transducer and Orientation(s)	Transmitter's Contact Force, lb_f (N)	Receiver's Contact Force, lb_f (N)	Centre Frequency, kHz
Series 1 - 70	DWC B1025 (022020) at 0°, 90°, 180°, 270°, and 360°	DWC B1080LD (0697098) at 0°	2.6879±0.0002 (11.956±0.001)	2.2±0.1 (9.7±0.5)	70
Series 1 - 450	DWC B1025 (022020) at 0°, 90°, 180°, 270°, and 360°	DWC B1080LD (0697098) at 0°	2.6879±0.0002 (11.956±0.001)	2.2±0.1 (9.7±0.5)	450
Series 1 - 1500	DWC B1025 (022020) at 0°, 90°, 180°, 270°, and 360°	DWC B1080LD (0697098) at 0°	2.6879±0.0002 (11.956±0.001)	2.2±0.1 (9.7±0.5)	1500
Series 2 - 70*	DWC B225 (022041) at 0°, 90°, 180°, 270°, and 360°	DWC B1080LD (0697098) at 0°	2.6879±0.0002 (11.956±0.001)	2.2±0.1 (9.7±0.5)	70
Series 2 - 250*	DWC B225 (022041) at 0°, 90°, 180°, 270°, and 360°	DWC B1080LD (0697098) at 0°	2.6879±0.0002 (11.956±0.001)	2.2±0.1 (9.7±0.5)	250
Series 3 - 2000	GE Panametrics X1054 (338769) at 0°, 90°, 180°, 270°, and 360°	DWC B1080LD (0697098) at 0°	3.3486±0.0002 (14.895±0.001)	2.2±0.1 (9.7±0.5)	2000
Series 4 - 70	DWC B1025 (022020) at 0°	DWC B1080LD (0697098) at 0°, 90°, 180°, 270°, 360°	2.6879±0.0002 (11.956±0.001)	2.2±0.1 (9.7±0.5)	70
Series 4 - 450	DWC B1025 (022020) at 0°	DWC B1080LD (0697098) at 0°, 90°, 180°, 270°, 360°	2.6879±0.0002 (11.956±0.001)	2.2±0.1 (9.7±0.5)	450
Series 4 - 1500	DWC B1025 (022020) at 0°	DWC B1080LD (0697098) at 0°, 90°, 180°, 270°, 360°	2.6879±0.0002 (11.956±0.001)	2.2±0.1 (9.7±0.5)	1500
Series 5 - 70*	DWC B1025 (022020) at 0°	DWC B225 (022041) at 0°, 90°, 180°, 270°, and 360°	2.6879±0.0002 (11.956±0.001)	2.6879±0.0002 (11.956±0.001)	70

Table 3.3. Transducer Combinations Tested for Orientation Dependence (Continued)

Designation	Transmitting Transducer and Orientation(s)	Receiving Transducer and Orientation(s)	Transmitter's Contact Force, lb_f (N)	Receiver's Contact Force, lb_f (N)	Centre Frequency, kHz
Series 5 - 250*	DWC B1025 (022020) at 0°	DWC B225 (022041) at 0°, 90°, 180°, 270°, and 360°	2.6879±0.0002 (11.956±0.001)	2.6879±0.0002 (11.956±0.001)	250
Series 6 - 70	DWC B225 (092029) at 0°, 90°, 180°, 270°, and 360°	DWC B225 (092035) at 0°	2.2526±0.0002 (10.020±0.001)	2.6879±0.0002 (11.956±0.001)	70
Series 6 - 250	DWC B225 (092029) at 0°, 90°, 180°, 270°, and 360°	DWC B1025 (092035) at 0°	2.2526±0.0002 (10.020±0.001)	2.6879±0.0002 (11.956±0.001)	250
Series 7 - 70	DWC B225 (092035) at 0°, 90°, 180°, 270°, and 360°	DWC B225 (092029) at 0°	2.6879±0.0002 (11.956±0.001)	2.2526±0.0002 (10.020±0.001)	70
Series 7 - 250	DWC B225 (092035) at 0°, 90°, 180°, 270°, and 360°	DWC B1025 (092029) at 0°	2.6879±0.0002 (11.956±0.001)	2.2526±0.0002 (10.020±0.001)	250
Series 8 - 70	DWC B225 (092029) at 0°	DWC B225 (092035) at 0°, 90°, 180°, 270°, and 360°	2.2526±0.0002 (10.020±0.001)	2.6879±0.0002 (11.956±0.001)	70
Series 8 - 250	DWC B225 (092029) at 0°	DWC B225 (092035) at 0°, 90°, 180°, 270°, and 360°	2.2526±0.0002 (10.020±0.001)	2.6879±0.0002 (11.956±0.001)	250
Series 9 - 70	DWC B225 (092035) at 0°	DWC B225 (092029) at 0°, 90°, 180°, 270°, and 360°	2.6879±0.0002 (11.956±0.001)	2.2526±0.0002 (10.020±0.001)	70
Series 9 - 250	DWC B225 (092035) at 0°	DWC B225 (022029) at 0°, 90°, 180°, 270°, and 360°	2.6879±0.0002 (11.956±0.001)	2.2526±0.0002 (10.020±0.001)	250

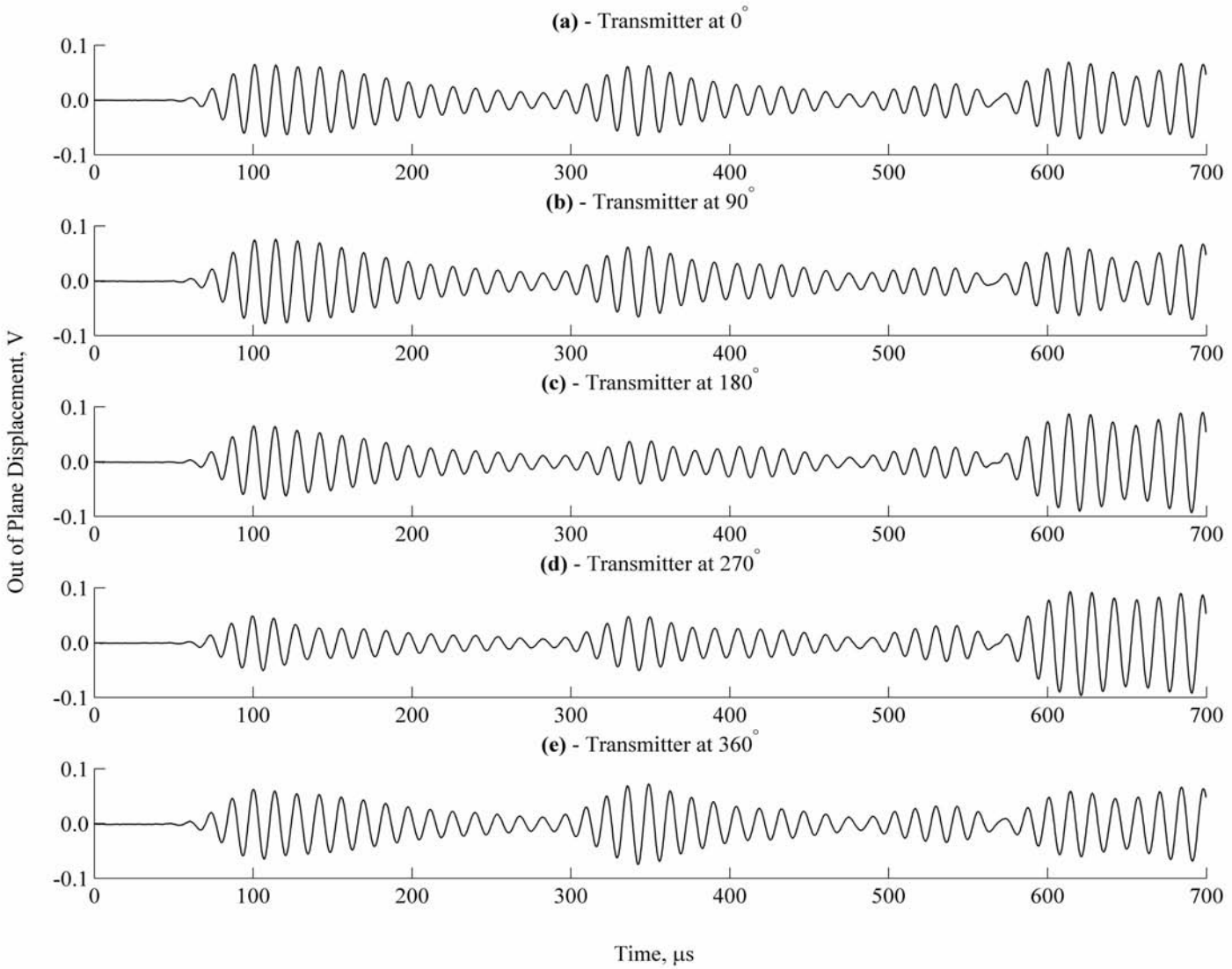

Figure 3.9. Transducer Orientation Dependance, Series 2 - 70

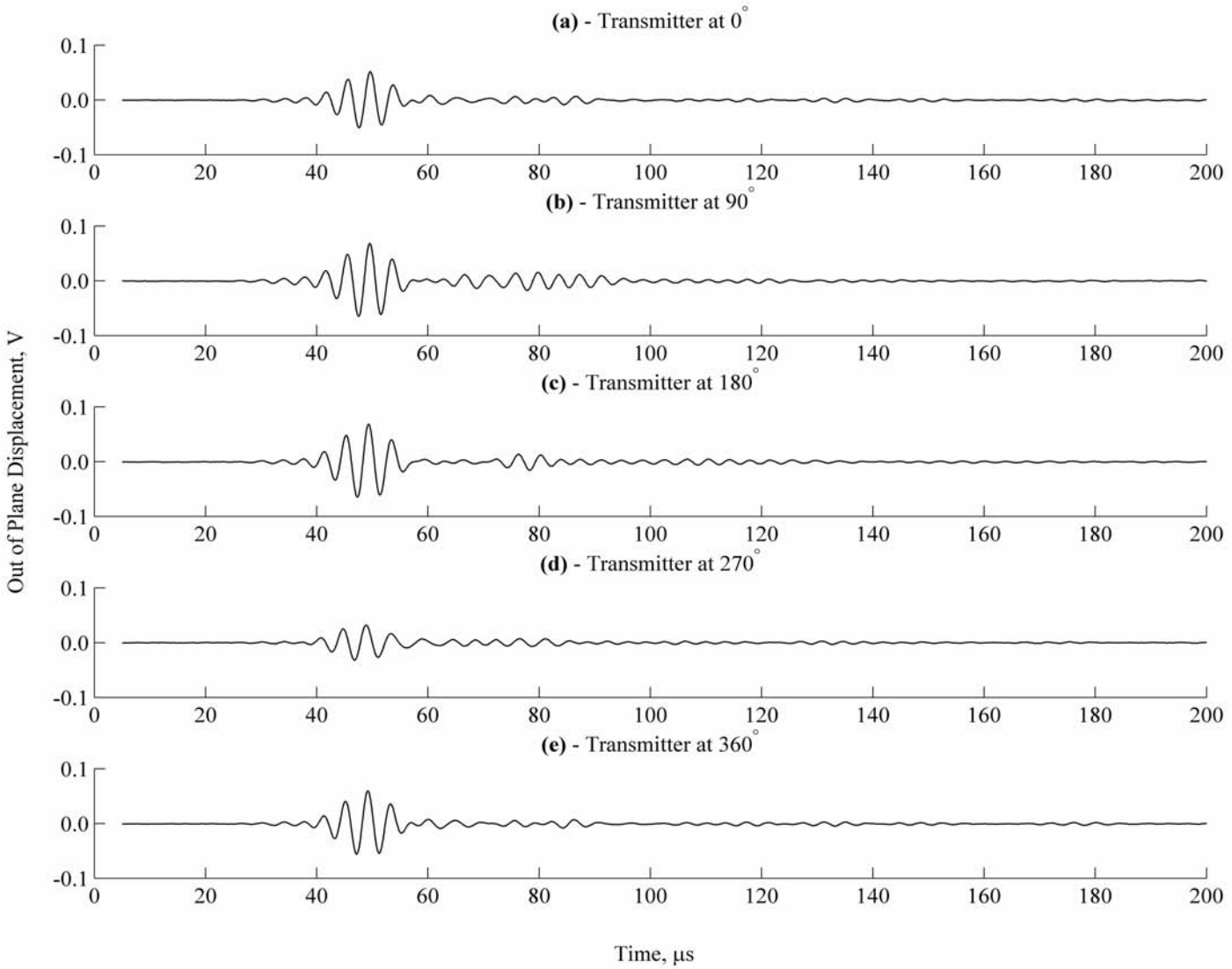

Figure 3.10. Transducer Orientation Dependance, Series 2 - 250

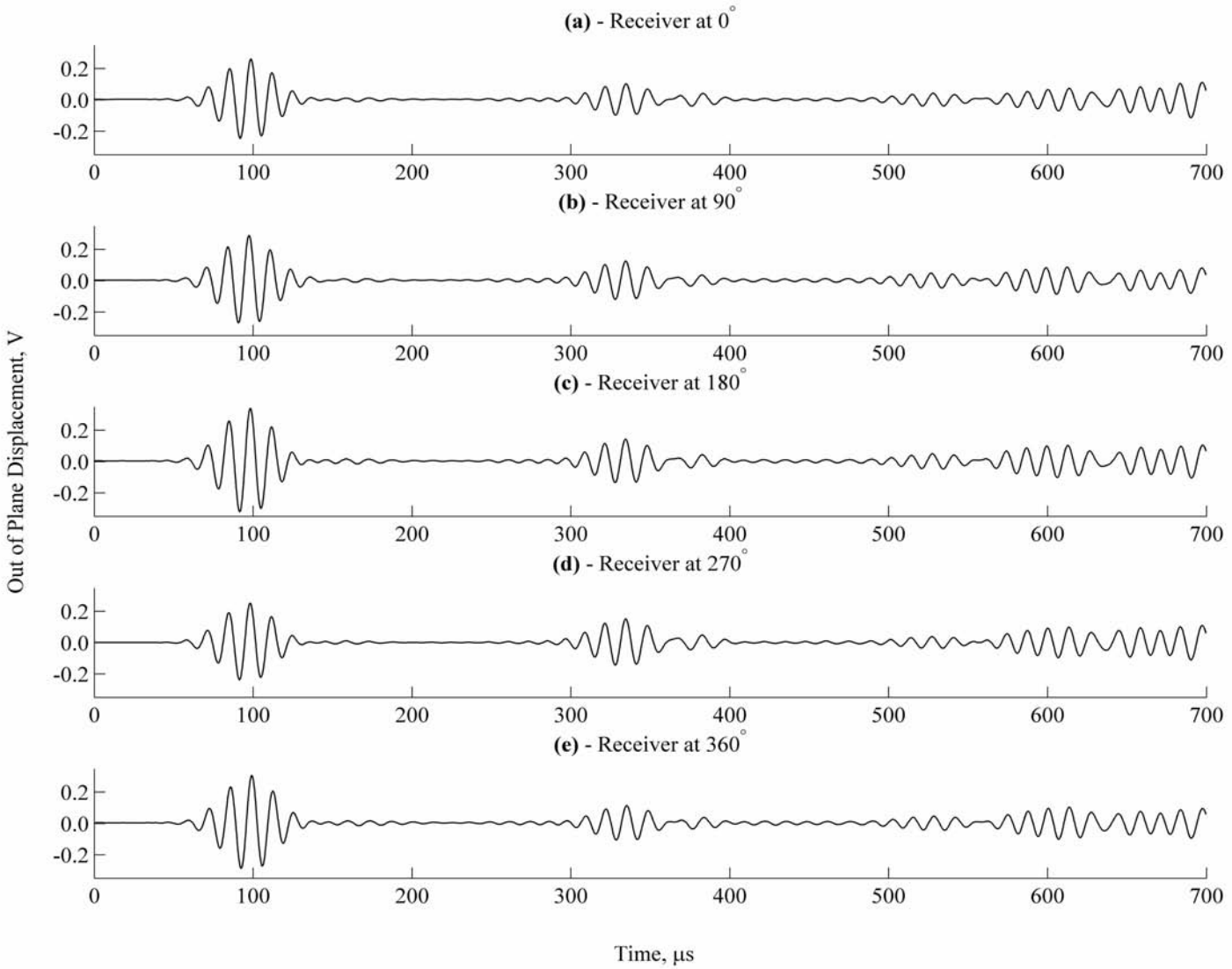

Figure 3.11. Transducer Orientation Dependance, Series 5 - 70

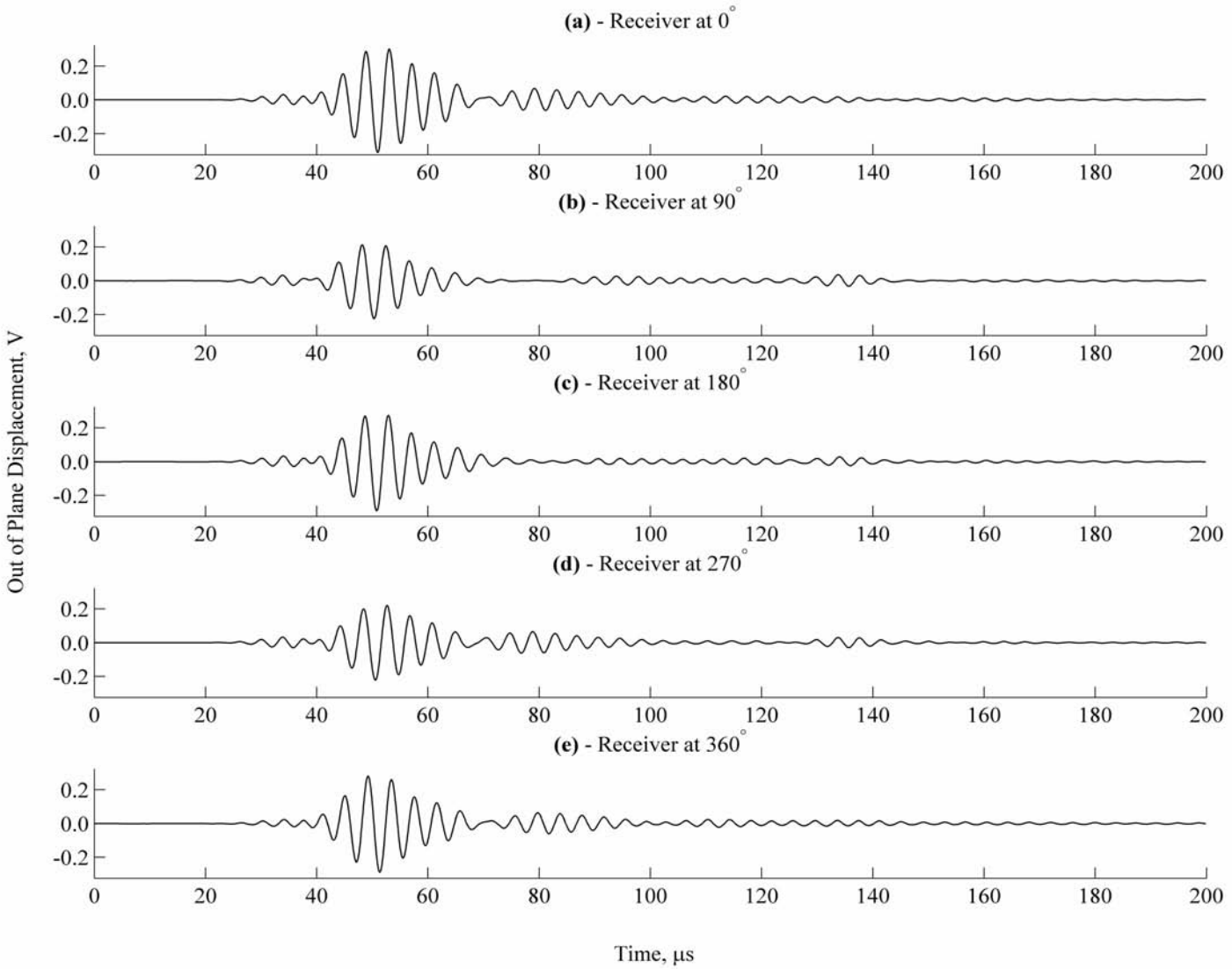

Figure 3.12. Transducer Orientation Dependance, Series 5 - 250

3.5.2 Symmetry

The symmetry of the pipe is checked by using the DWC B225 transducers. The transducer having serial number 022041 is used as the transmitter. The two other B225 transducers are the receivers. (Note that, although all three transducers are coupled simultaneously to the pipe, the radial displacement is measured at each of the two receiving transducers in two independent experiments.) All three transducers are coupled to the pipe's external surface by using beeswax. Care is taken, by using a machinist's square, to ensure that the transducers' longitudinal axes are normal to the pipe's surface. Several axial and circumferential offsets are examined by using different centre frequencies for the forcing function. The results are similar for all the centre frequencies examined so that a typical example involving a centre frequency of 70 kHz is detailed here.

Figure 3.13 shows the transducer arrangement for the symmetry experiments. The axial offset between the transmitting and receiving transducers, which is used to obtain Figures 3.14 through 3.16, is 4.000±0.001 in (10.160±0.003 cm). The corresponding circumferential offset between the transmitting transducer and the receiving transducer is either 0±1° or 45±1° as shown in Figure 3.13 and Table 3.4. The relative positions between the transmitting transducer and the receiving transducers are achieved by first locating the receiving transducers with a 45±1° circumferential offset with respect to each other. Then the transmitting transducer is (re)positioned to achieve the required axial and circumferential offsets shown in Figure 3.13 and Table 3.4. Note that transmitter locations 3 and 4 are repeated at a different cross section from those used originally.

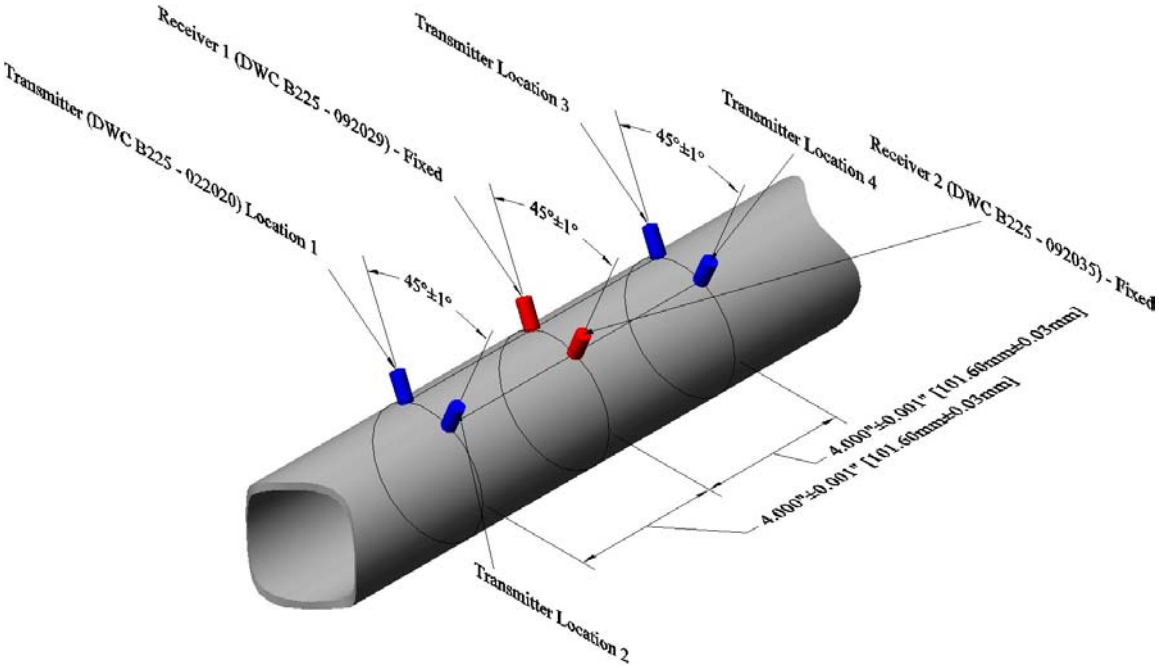

Figure 3.13. Transducer Arrangements for Symmetry Experiments

Table 3.4. Circumferential Offsets for Symmetry Experiments

Transmitter Location	Circumferential Offset for Receiver 1	Trace for Receiver 1	Circumferential Offset for Receiver 2	Trace for Receiver 2
1	0°	Figure 3.13 (a)	45°	Figure 3.13 (d)
2	45°	Figure 3.13 (b)	0°	Figure 3.13 (c)
3	0°	Figure 3.14 (a)	45°	Figure 3.14 (d)
4	45°	Figure 3.14 (b)	0°	Figure 3.14 (c)
3 (Repeated)	0°	Figure 3.15 (a)	45°	Figure 3.15 (d)
4 (Repeated)	45°	Figure 3.15 (b)	0°	Figure 3.15 (c)

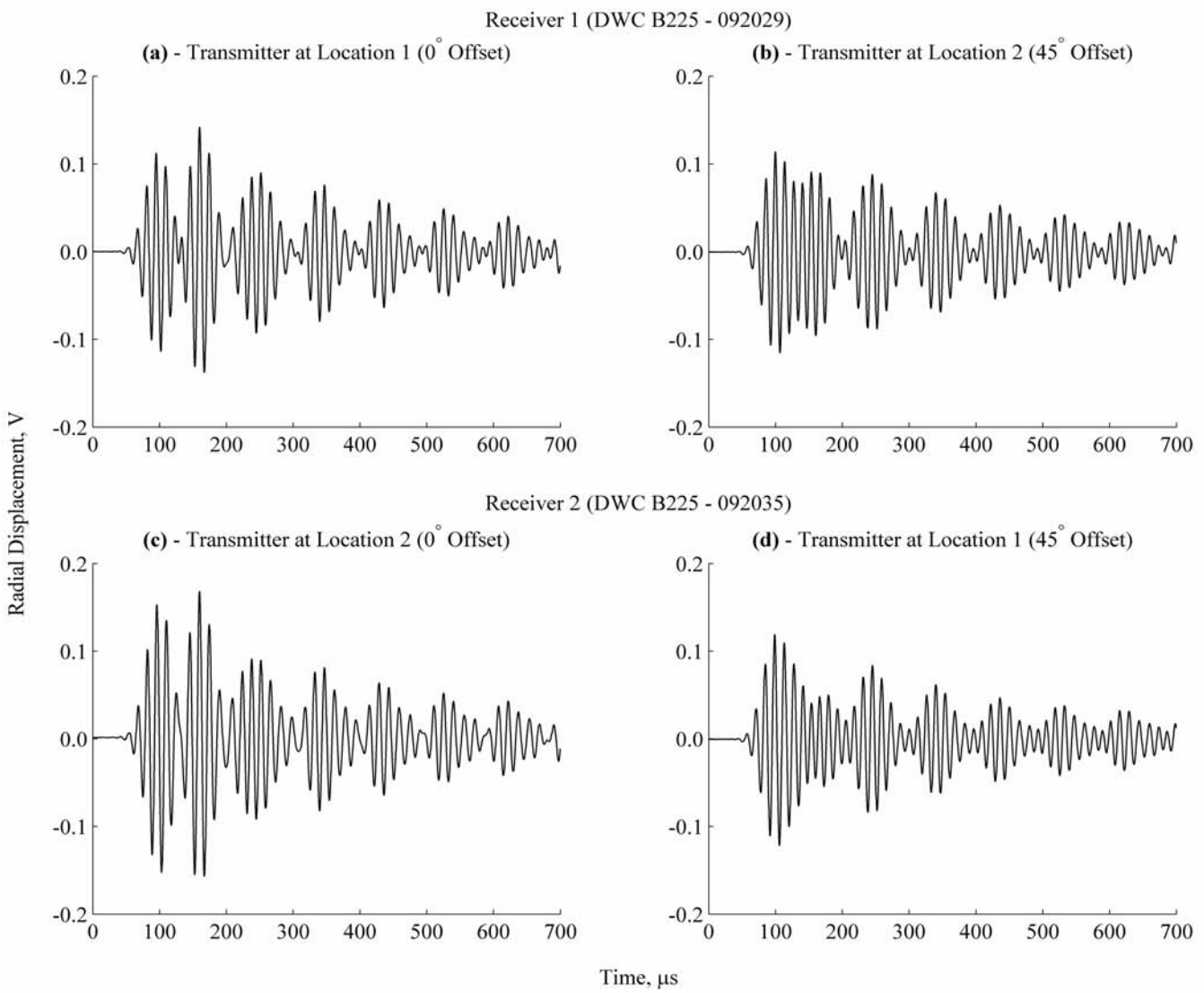

Figure 3.14. Transmitter at Locations 1 and 2

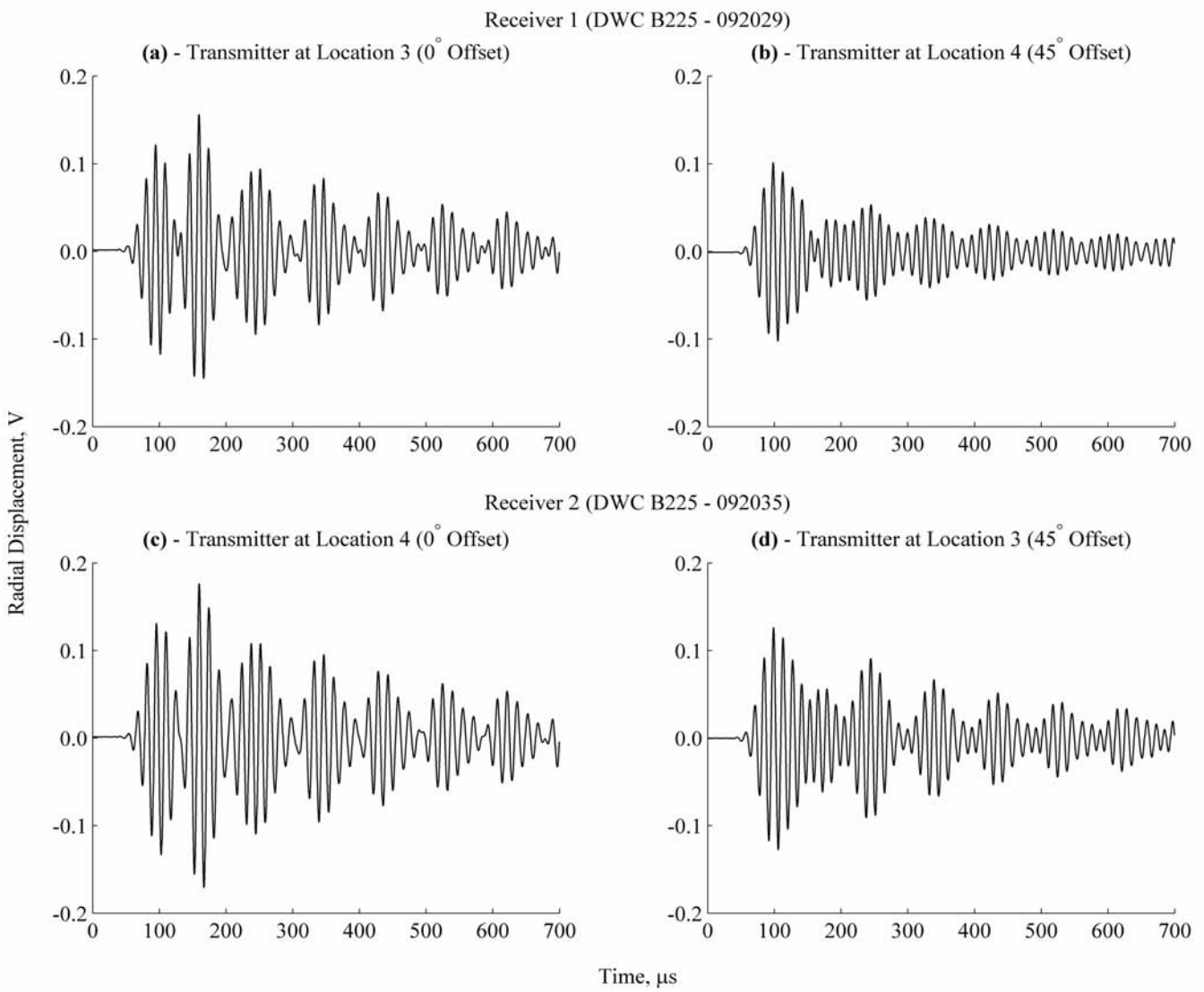

Figure 3.15. Transmitter at Locations 3 and 4

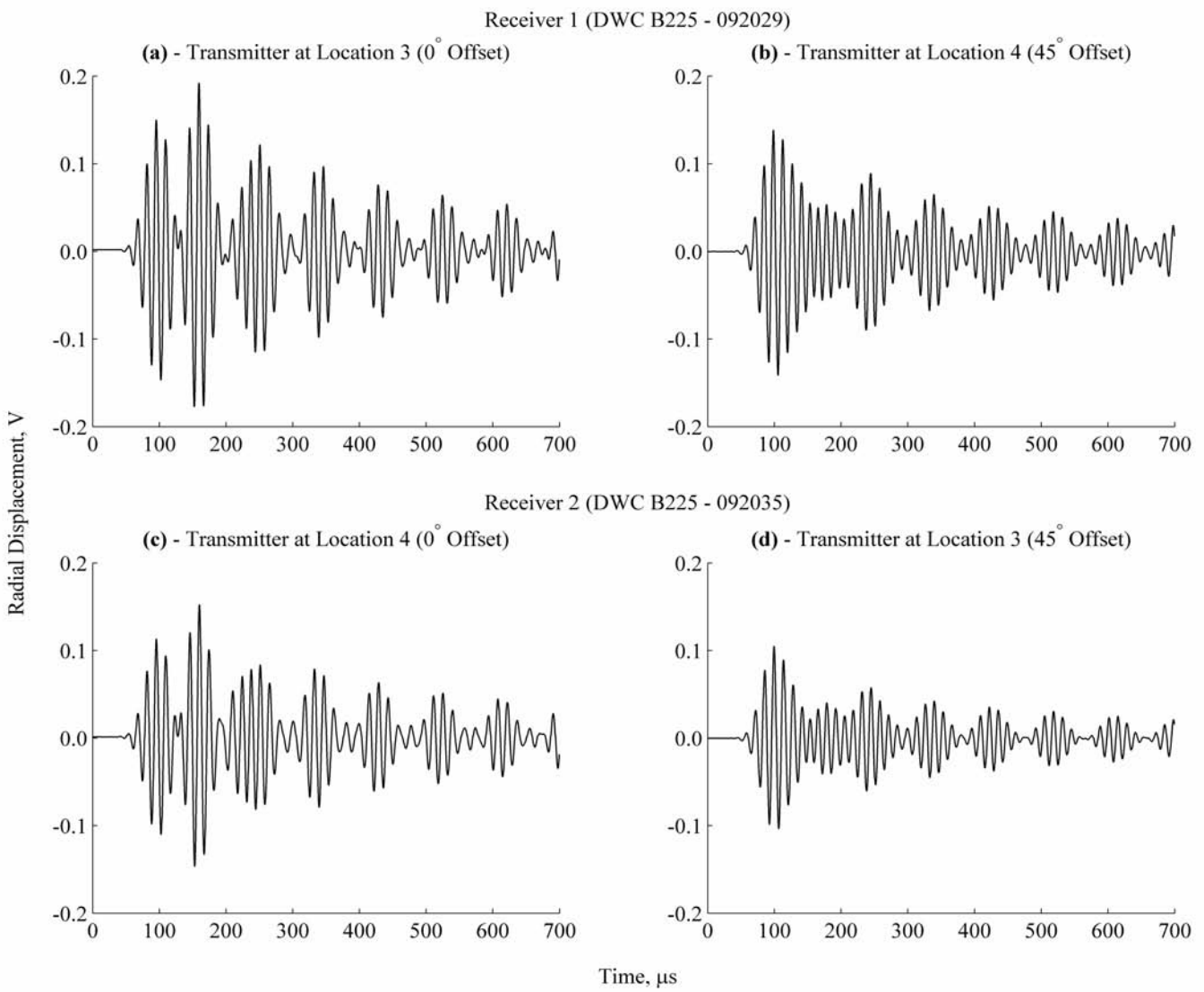

Figure 3.16. Transmitter at Locations 3 and 4 (Repeated)

Figures 3.14 through 3.16 indicate all the traces corresponding to a 45° circumferential offset have similar (but not exactly the same) shapes and amplitudes. (Note that this trend is not seen when the transducers are not omni-directional.) The same trend, with slightly better correlation, can be seen for the 0° circumferential offset. The change in amplitude may be explained by the coupling's variability when relocating the transmitting transducer, and the change in shape may be explained by the geometrical variability of the pipe. If the pipe were perfectly symmetrical and uniform, the shape of the measured radial displacement for corresponding circumferential offsets would be identical. This is not the case in Figures 3.14 through 3.16, showing that the pipe is not perfectly symmetrical and uniform, but only approximately so which is to be expected from the measurements of the pipe's wall thickness and outer diameter.

3.5.3 Reciprocity and Pipe Rotation

Reciprocity is verified by positioning the DWC B225 (serial numbers 092029 and 092035) with a 45±1° circumferential offset from each other. The longitudinal axis of each transducer is normal to the pipe's surface. One of the transducers is pulsed and the ensuing radial displacement is measured by using the other transducer. Then the transducer's leads are reversed and the process is repeated. Figures 3.17 (a) and (b) [(c) and (d)] shows the outcome when the longitudinal axis of the transmitter having serial number 092029 [092035] is aligned vertically. The four traces of Figure 3.17 are indistinguishable so that reciprocity is satisfied.

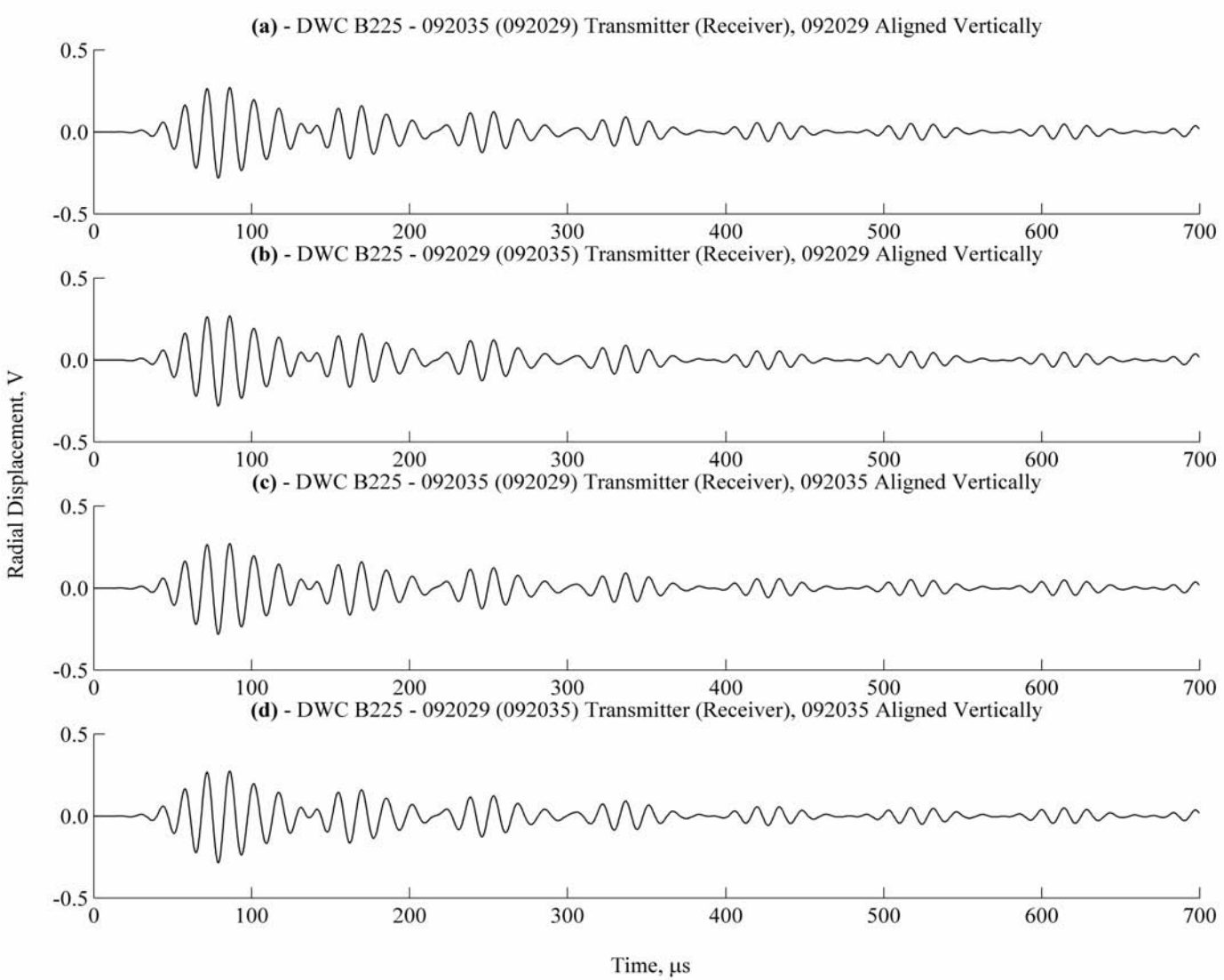

Figure 3.17. Traces Showing That Reciprocity is Satisfied

Another experiment is conducted to ensure that the orientation of a transducer's longitudinal axis with respect to the vertical has no noticeable effect on the measured radial displacement. The same transducers are placed with a $90\pm1^{\circ}$ circumferential offset from each other. The transducer having serial number 092029 (092035) is used as the transmitter (receiver). The longitudinal axis of the transmitter is initially aligned vertically with its weight "pushing" into the pipe. Then the transmitter is pulsed and the ensuing radial displacement is measured at the receiving transducer. The pipe (with the transducers remaining attached) is rotated 180° about its longitudinal axis. This rotation results in the longitudinal axis of the transmitter being aligned vertically with its weight "pulling" from the pipe. (Note that the longitudinal axis of the receiver is horizontal in both arrangements.) Then the experiment is repeated. The radial displacements measured for the two configurations are shown in Figure 3.18. They are nearly identical so that the effect of orientation of the transducers as they are rotated with the pipe is insignificant.

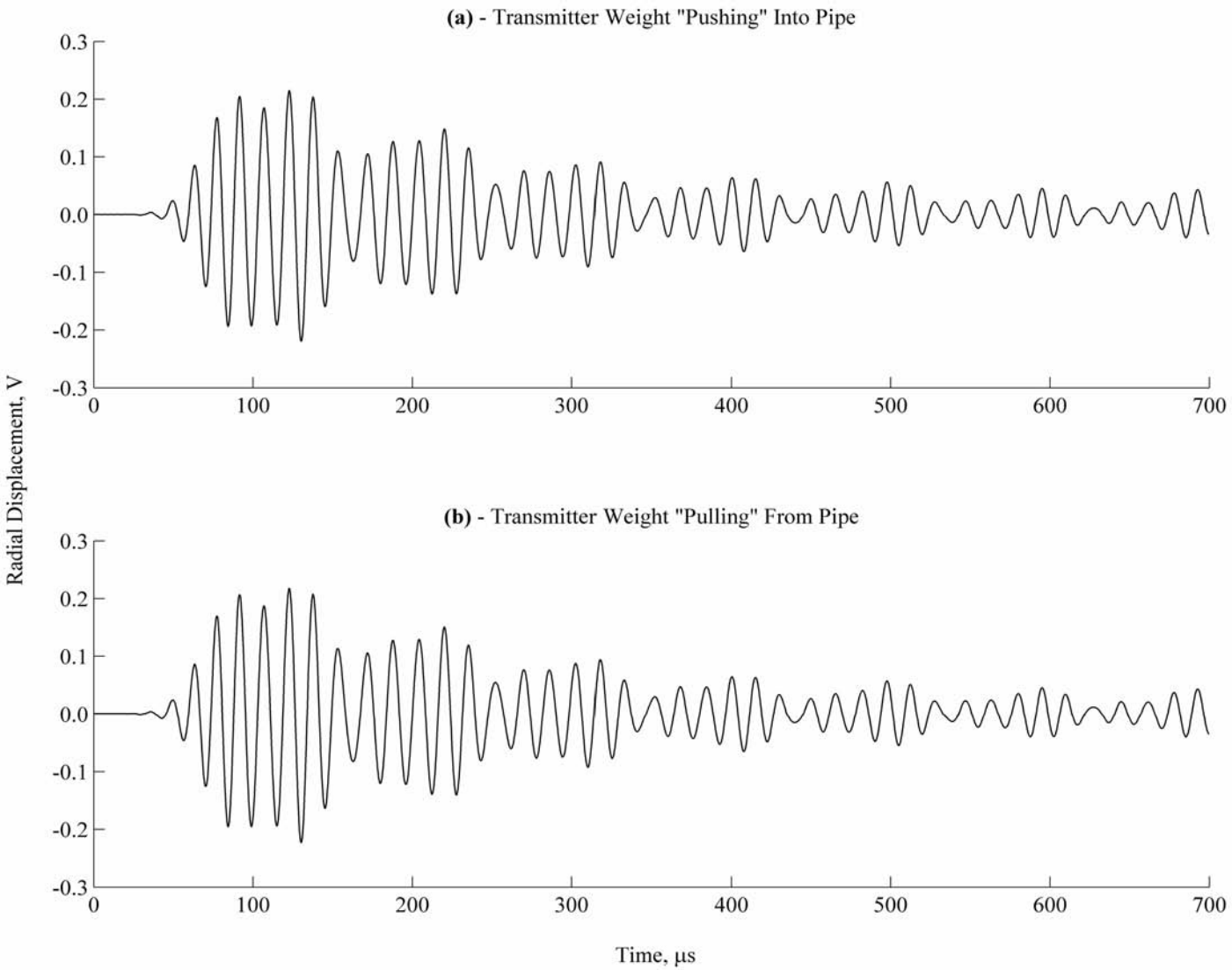

Figure 3.18. Traces Showing the Effect of Gravity

3.6 Comparison of Measured and Predicted Radial Displacements

Having established that the experimental apparatus is reliable, the radial displacement is measured at an axial offset of 1.122±0.001 in (2.850±0.003 cm)[+] from the transmitting transducer. The DWC B225 transducers having serial numbers 092029 and 092035 are used as the transmitter and receiver, respectively. The resulting history of the radial displacement measurement is shown in Figure 3.19 with the corresponding (discrete) Fourier transform and the analogous predictions. To make comparisons easier, Figure 3.19 shows plots of the measured and predicted radial displacements in time and frequency that are normalized to bring the peak absolute values of the time histories to unity. This is done because the amplitudes of the measured and predicted data are necessarily different due to normalization and variable coupling. The measured displacement history is normalized by using equation (3.1). The predicted radial displacement history, on the other hand, is normalized by using:

$$u_i^{**} = \frac{u_i^*}{\max(|u^*|)}. \tag{3.2}$$

where $-1 \le u_i^{**} \le 1$ (u_i^*) is the i-th sample of the normalized predicted non-dimensional displacement (predicted non-dimensional displacement) and $\max(|u^*|)$ is the largest absolute value of u_i^*. The frequency results shown are determined by taking the discrete Fourier transform of the normalized displacement histories. (Note that, by taking the discrete Fourier transform of the predicted time history which is recovered at the same instants as those measured, the effect of "spectral leakage" due to the "boxcar" window used

---

[+] This axial offset corresponds non-dimensionally to z^*=5.10.

are identical for both the measured and predicted radial displacement histories.) All further comparisons between measurements and predictions have been normalized in this fashion. A comparison of the time histories of the measurement and prediction, which are given in Figure 3.19, indicates that their shapes are similar for the radial displacement but agreement is far from perfect. A comparison of the frequency domain representations in Figure 3.19, on the other hand, shows that the frequency "peaks" are identical but their relative magnitudes are different. An examination of the OEM supplied frequency behaviour of the DWC B225 transducers (given in Figures 3.20 and 3.22 and Appendix D) shows that the responses of their sensitivities are not frequency independent (i.e. "flat") over the 35 kHz to 107 kHz forcing bandwidth. To account for the frequency variations, equation (2.106) is modified to:

$$\boldsymbol{H}'(\theta,z,\omega_k)\approx$$

$$\left\{\begin{array}{l}
\dfrac{-j}{2\pi r_0 H}\left[\displaystyle\sum_{i=2}^{I-1}\bar{T}_{rec}(\omega_k)\bar{e}(\omega_i-\lambda_k)\bar{T}_{trans}(\omega_k)\bar{f}(\omega_i)\sum_{n=-\infty}^{n=\infty}\operatorname{sinc}(n\theta_0)\boldsymbol{G_n}(\omega_i,z)e^{jn\theta}\Delta\lambda\right]+ \\
\dfrac{-j}{4\pi r_0 H}\left[\bar{T}_{rec}(\omega_1)\bar{e}(\omega_1-\lambda_k)\bar{T}_{trans}(\omega_1)\bar{f}(\omega_1)\displaystyle\sum_{n=-\infty}^{n=\infty}\operatorname{sinc}(n\theta_0)\boldsymbol{G_n}(\omega_1,z)e^{jn\theta}\Delta\lambda\right]+ \\
\dfrac{-j}{4\pi r_0 H}\left[\bar{T}_{rec}(\omega_I)\bar{e}(\omega_I-\lambda_k)\bar{T}_{trans}(\omega_I)\bar{f}(\omega_I)\displaystyle\sum_{n=-\infty}^{n=\infty}\operatorname{sinc}(n\theta_0)\boldsymbol{G_n}(\omega_I,z)e^{jn\theta}\Delta\lambda\right].
\end{array}\right\} \quad \textbf{(3.3)}$$

Then equation (2.107) is used to calculate the non-dimensional displacement, $\boldsymbol{u}^*$, with $\boldsymbol{H}$ replaced by $\boldsymbol{H}'$. Here, $\bar{T}_{rec}$ and $\bar{T}_{trans}$ are the "normalized transfer functions" of the receiving and transmitting transducer, respectively. They are determined by using:

$$\bar{T}(\omega)=\frac{1}{\bar{T}^*}\frac{\bar{O}(\omega)}{\bar{I}(\omega)}\neq 1 \quad \textbf{(3.4)}$$

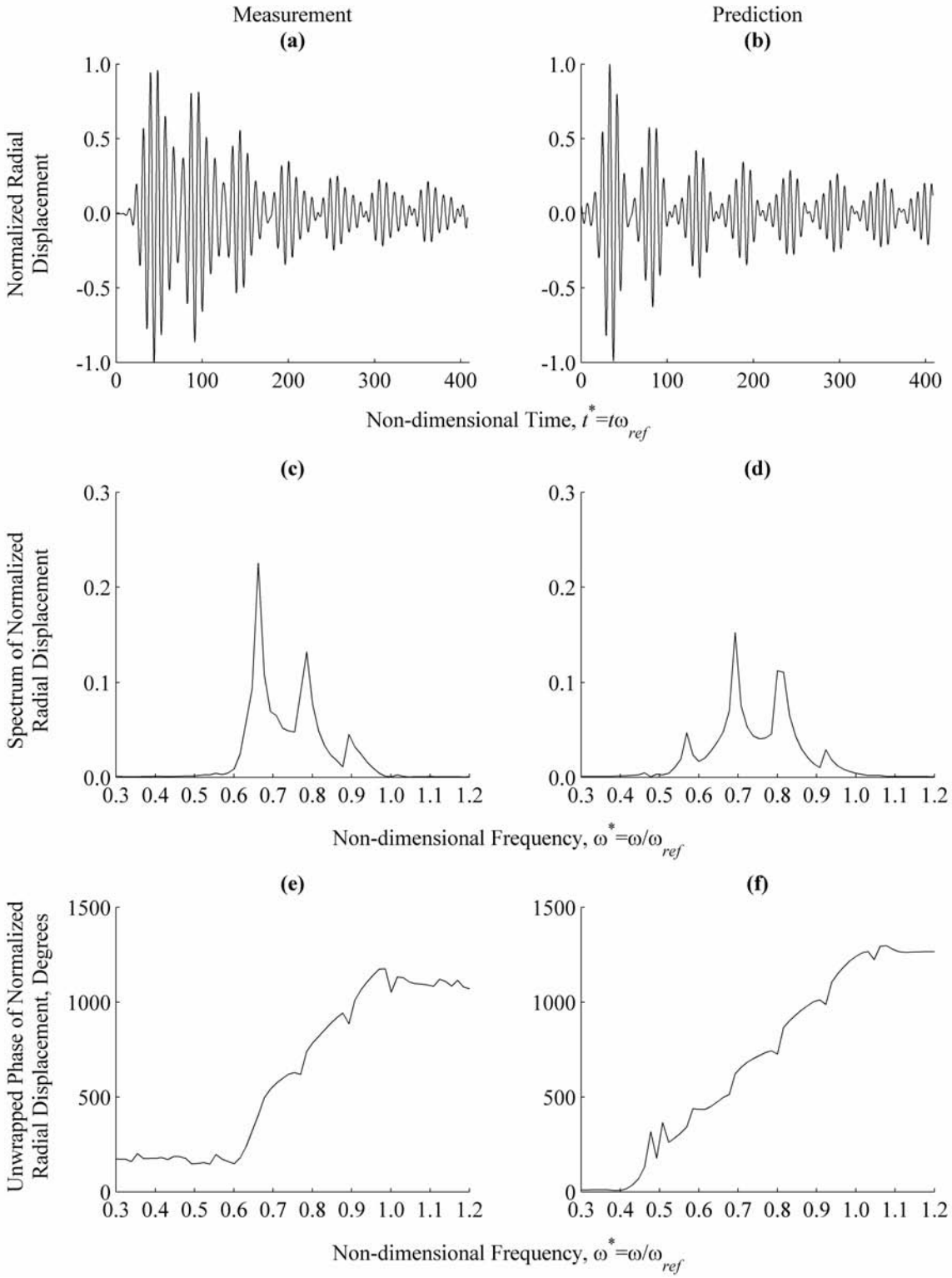

Figure 3.19. Comparison Between Measurement and Prediction at $\theta=0$, $z^*=5.10$ Before Transducer Corrections

where $\bar{O}$ $(\bar{I})$ is the discrete Fourier transform of the OEM supplied output (input) from (to) the transducer and $\bar{T}^*$ is the maximum magnitude of $\bar{O}/\bar{I}$ over the forcing bandwidth. The definition of $\bar{T}$ results in the normalized transfer function having a value of unity over the forcing bandwidth from an ideal transducer. The $\bar{T}_{rec}$ and $\bar{T}_{trans}$ in equation (3.3) serve to appropriately "scale" and "phase shift" the displacement response and forcing input, respectively, when each transducer is presumed to be linear.

It should be noted that $\bar{O}(\omega)$ and $\bar{I}(\omega)$ are determined from OEM supplied time histories that are determined in a "back to back" calibration. They are given in the calibration curves of Figures 3.20 and 3.22, which are also presented in Appendix D and electronically on the accompanying media. The input corresponds to an electrical input into a "reference" transducer whose frequency behaviour is unknown but assumed to be flat over frequency. The output is from the transducer that is being calibrated. The sampling rate and, hence, the frequency points at which $\bar{O}(\omega)$ and $\bar{I}(\omega)$ are determined is dictated by the OEM's calibration procedure. However, these frequency points differ from those used to find the FRF. Consequently linear interpolation is used for $\bar{T}_{rec}$ and $\bar{T}_{trans}$ when evaluating equation (3.3). Figures 3.21 and 3.23 show $\bar{T}_{rec}$ and $\bar{T}_{trans}$ when the DWC B225 transducers are used as the transmitter (serial number 092029) and receiver (serial number 092035). The discrete values that are used to plot these curves are tabulated in Appendix G. They are also given in the accompanying electronic media. [Note that $\bar{T}^*$ in Figures 3.21 and 3.23 as well as Appendix D is taken as the maximum magnitude of $\bar{O}/(\bar{I})$ over the bandwidth of the transducer rather the maximum magnitude of $\bar{O}/(\bar{I})$ over the forcing bandwidth because the former is independent of the forcing bandwidth. The normalized transfer function required

in equation (3.3) can be determined from Figures 3.21 and 3.23 and Appendix G by dividing the given magnitude of a normalized transfer functions given by the maximum magnitude of the normalized transfer functions over the forcing bandwidth. For the forcing function used here, the maximum magnitude of the normalized transfer functions over the forcing bandwidth is taken to occur at a frequency of about 111.4 kHz. Also note that the unwrapped phase angles of the normalized transfer functions are given relative to $\Re(e^{+j\omega t})$ in Figures 3.21 and 3.23, Appendix G, and on the electronic media.]

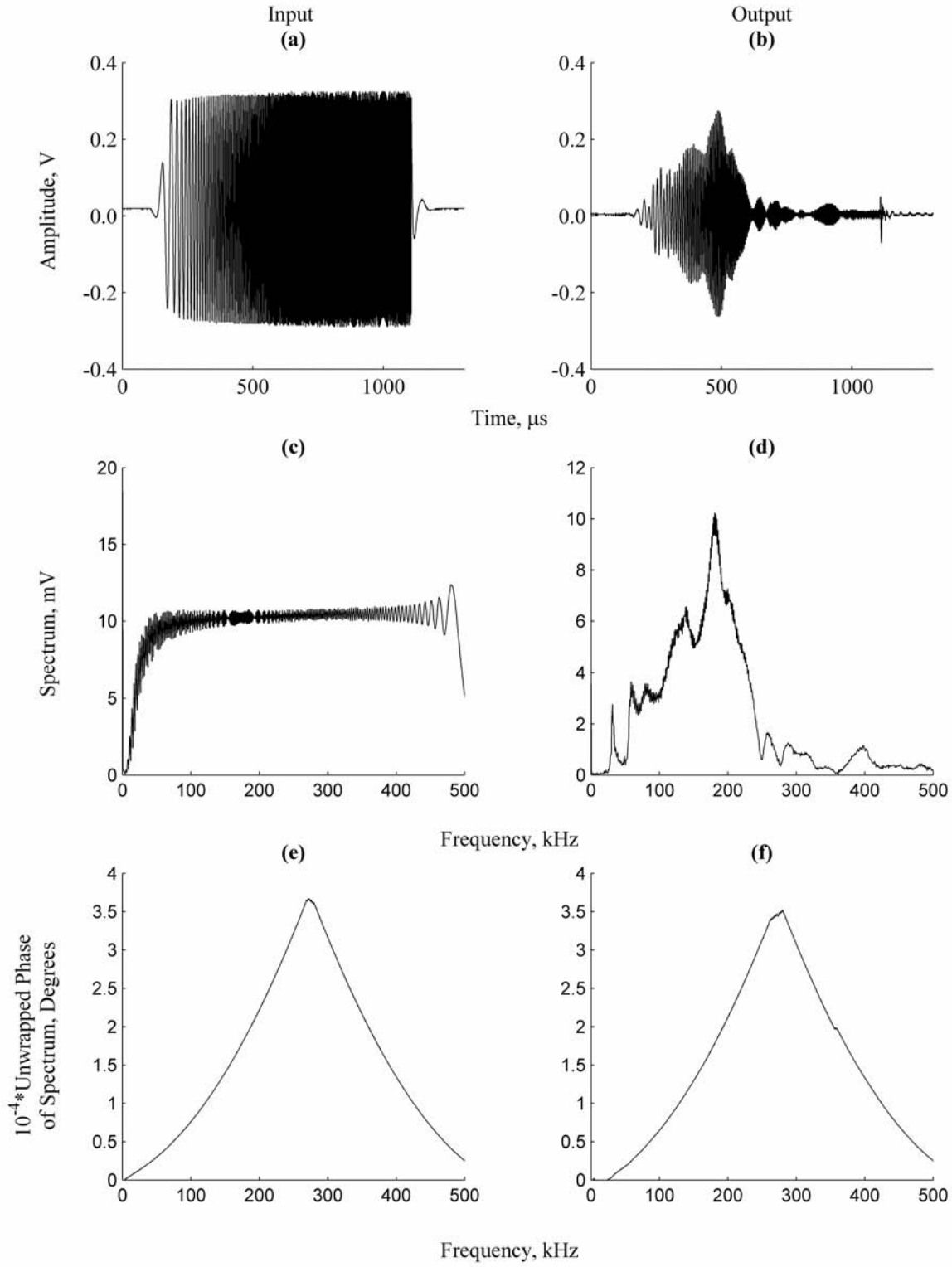

Figure 3.20. OEM Supplied, Input and Output Calibration Curves for B225 (With Serial Number 092029)

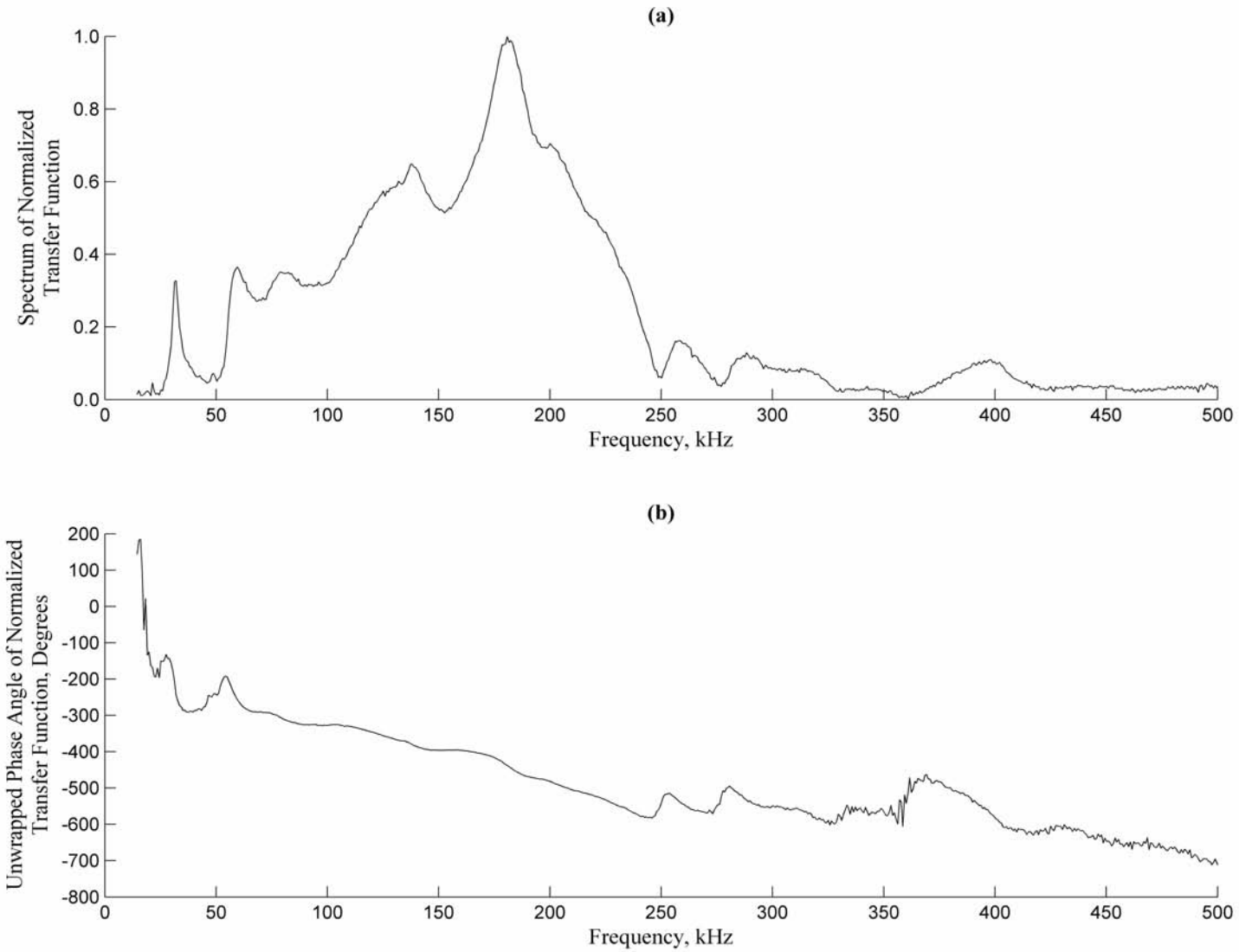

Figure 3.21. Normalized Transfer Function for B225 (With Serial Number 092029)

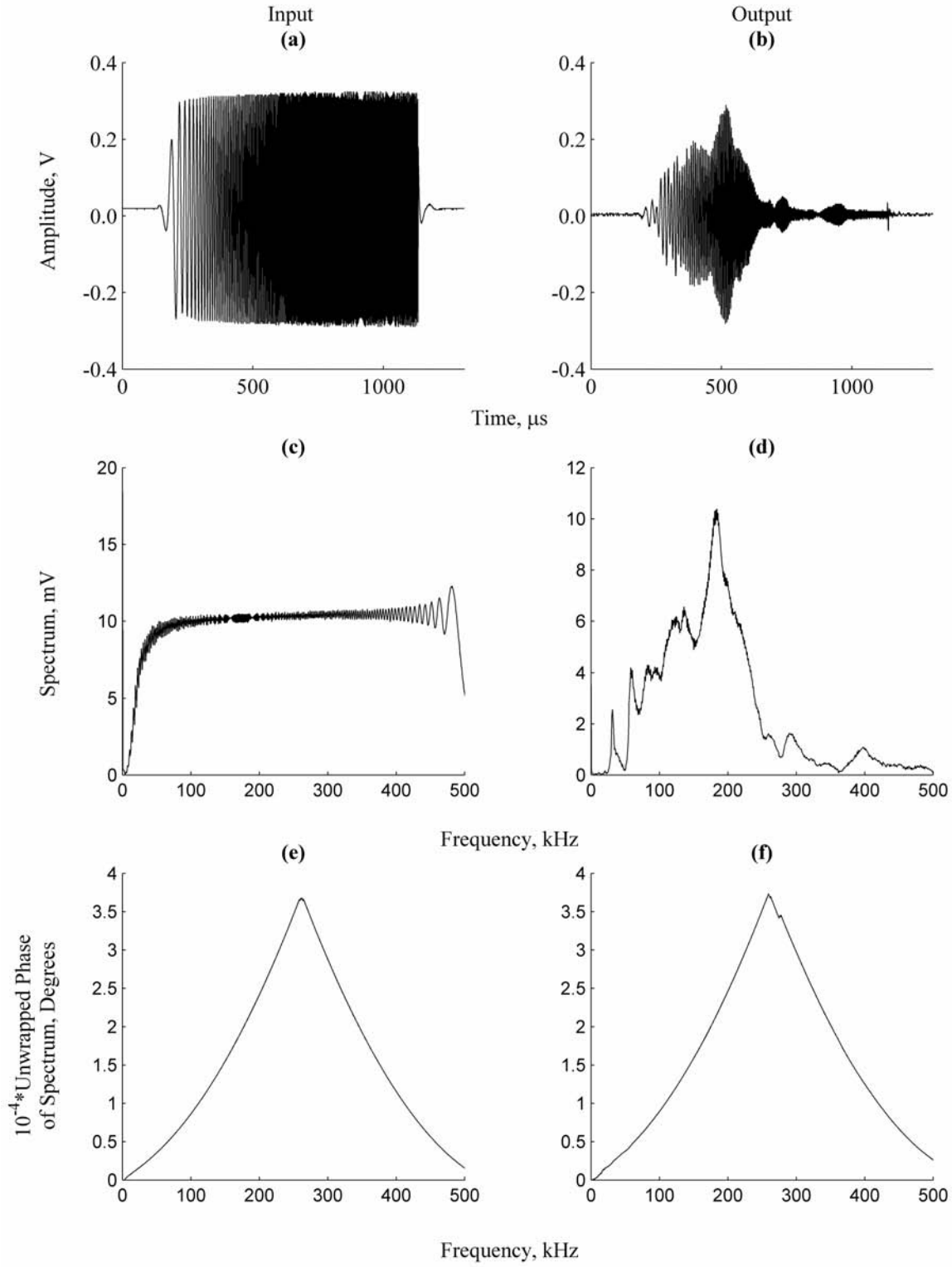

Figure 3.22. OEM Supplied, Input and Output Calibration Curves for B225 (With Serial Number 092035)

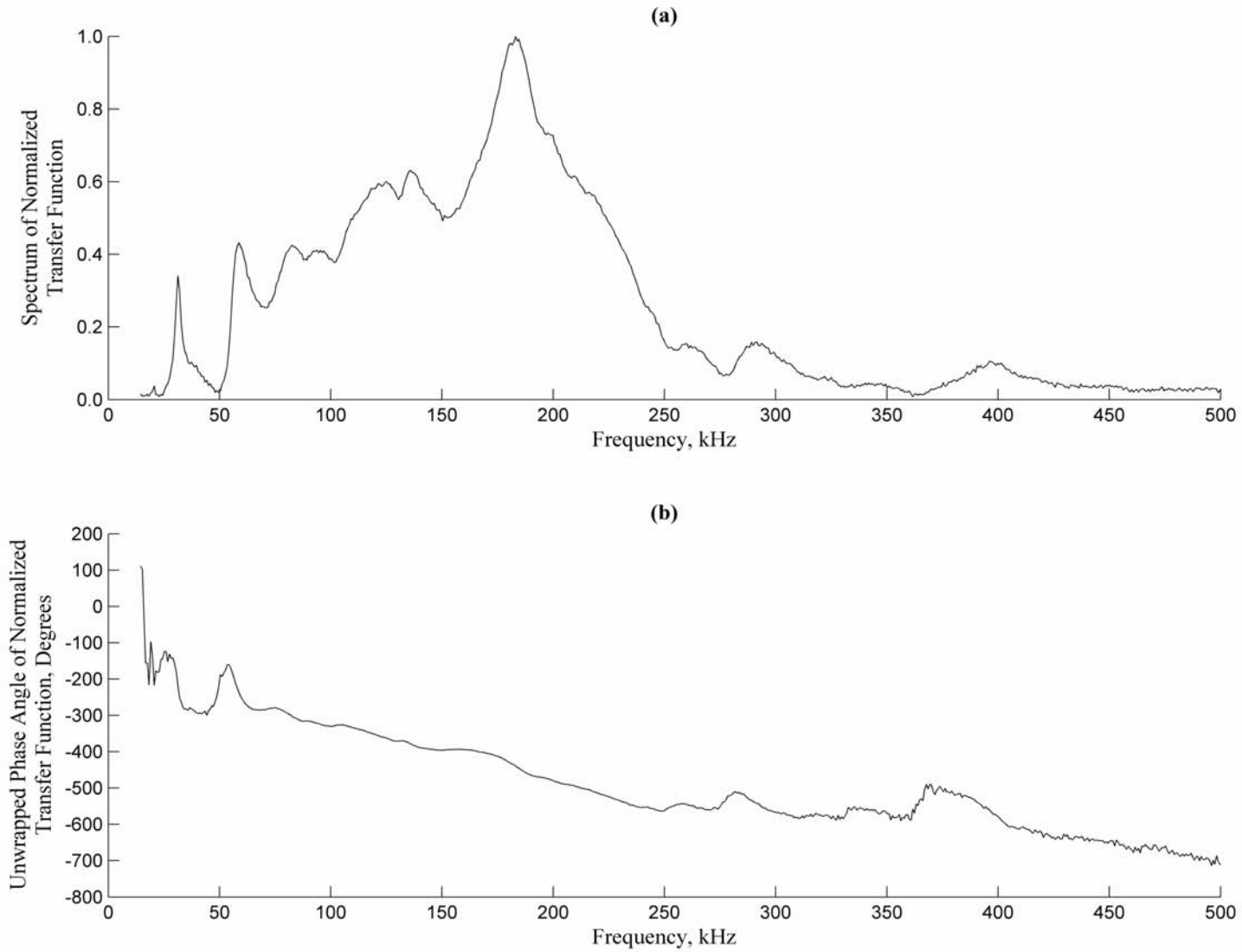

Figure 3.23. Normalized Transfer Function for B225 (With Serial Number 092035)

Figure 3.24 shows the measured and predicted radial displacement (in non-dimensional form) after accommodating the frequency sensitivity variations of the transducers. A comparison of Figures 3.19 and 3.24 indicates that the agreement in the shapes of the time histories and the relative magnitudes of the spectra of the measured and predicted radial displacement is much better with the corrections. It can be seen from Figure 3.24 that the agreement between the measured and predicted radial displacements is extremely good at the location considered. Chapter 4 provides many more such comparisons, at several points at several cross sections rather than at sparsely located, individual locations. Also, a more thorough description is presented in "snapshots" and an animation of the time evolution of the radial displacement field on the pipe's outer surface.

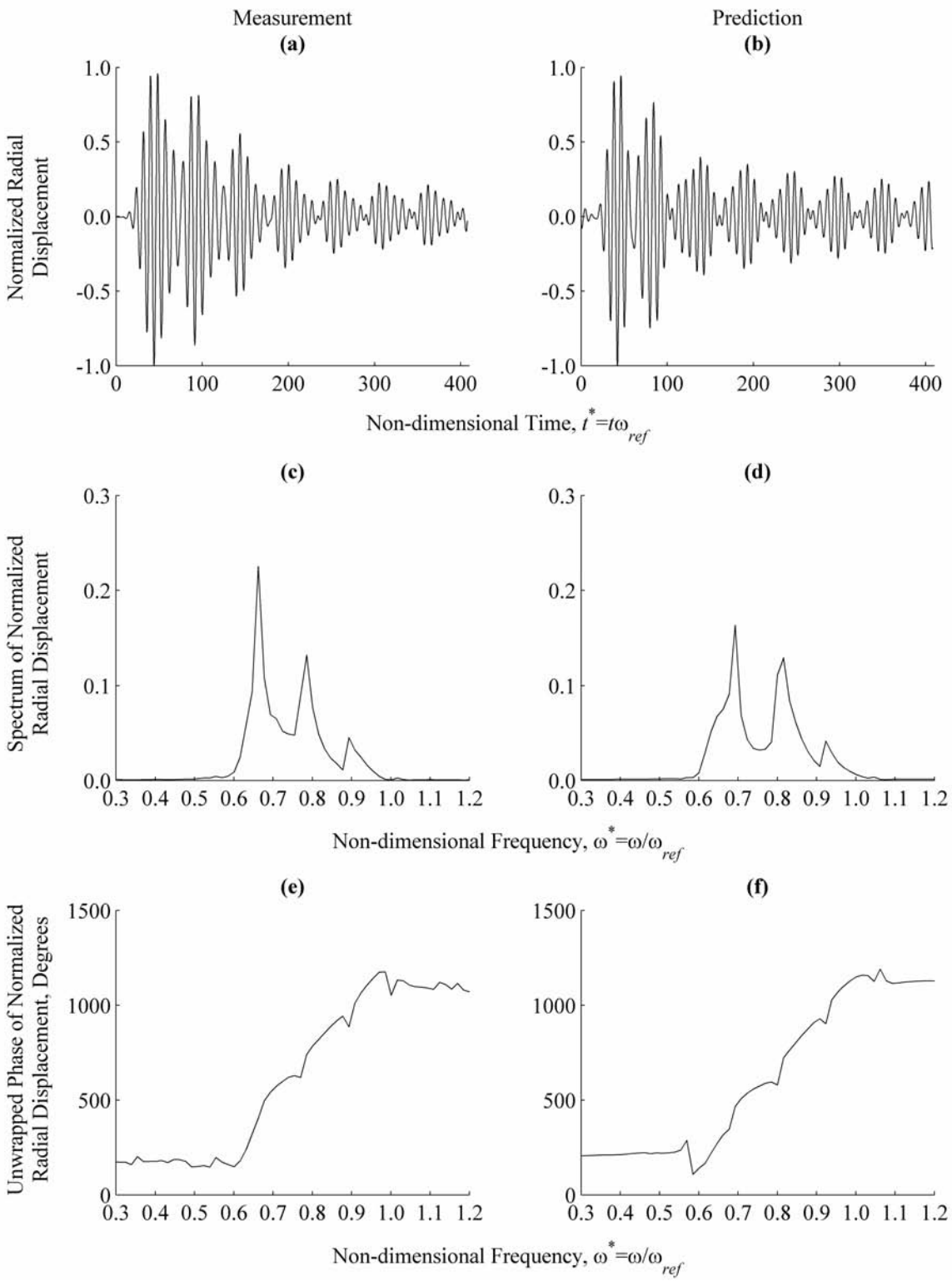

Figure 3.24. Comparison Between Measurement and Prediction at θ=0, z^*=5.10 After Transducer Corrections

Chapter 4 - Comparisons, "Snapshots" and Animations

4.1 Introduction

Chapter 2 introduced the steady state Green and stress functions for a uniform, homogenous, isotopic cylinder from which the FRF and, ultimately, the time response of the radial displacement was recovered. Chapter 3 provided a comparison between the measured and predicted radial displacements at a single pipe location. Agreement was extremely good after incorporating the frequency varying behaviour of the transducers. To provide further experimental validation of the computer model, the radial displacement is measured at several points on five different axial cross sections that can be classified as being in the "near," "intermediate," and "far" fields of the point force. The measurements are compared to the analogous predicted radial displacements in the manner presented in Chapter 3. Insight into the dynamic behaviour of the cylinder is provided by several instantaneous "snapshots" of the radial component of the Green's functions at the cylinder's outer surface instants over a period, T, corresponding to the centre frequency of the external forcing. Similar snapshots are also given to illustrate the temporal evolution of the complete radial displacement field on the cylinder's outer surface.

4.2 Further Comparisons

Table 4.1 summarizes the locations where the radial displacement is measured, relative to the transmitting transducer. The measured displacements and their discrete Fourier transforms, as well as the analogous predicted data (with accommodations made for the frequency varying behaviour of the transducers), are given more conveniently in Appendix H. (Note that the normalization introduced in Chapter 3 is used in Appendix H

to make the peak absolute values of the time histories unity.)

Table 4.1. Locations for Radial Displacement Measurements

Axial Offset, in (cm) [Non-dimensional Value]	**Circumferential Offset**
0.000±0.001 (0.000±.003) [z^*=0.00]	20°, 30°, 40°, 50°, 60°, 70°, 80°, 90°, 100°, 110°, 120°, 130°, 140°, 150°, 160°, 170°, 180°
0.560±0.001 (1.423±.003) [z^*=2.55]	0°, 10°, 20°, 30°, 40°, 50°, 60°, 70°, 80°, 90°, 100°, 110°, 120°, 130°, 140°, 150°, 160°, 170°, 180°
1.121±0.001 (2.847±.003) [z^*=5.10]	0°, 10°, 20°, 30°, 40°, 50°, 60°, 70°, 80°, 90°, 100°, 110°, 120°, 130°, 140°, 150°, 160°, 170°, 180°, 190°, 200°, 210°, 220°, 230°, 240°, 250°, 260°, 270°, 280°, 290°, 300°, 310°, 320°, 330°, 340°, 350°
2.241±0.001 (5.693±.003) [z^*=10.20]	0°, 10°, 20°, 30°, 40°, 50°, 60°, 70°, 80°, 90°, 100°, 110°, 120°, 130°, 140°, 150°, 160°, 170°, 180°
5.604±0.001 (14.233±.003) [z^*=25.50]	0°, 10°, 20°, 30°, 40°, 50°, 60°, 70°, 80°, 90°, 100°, 110°, 120°, 130°, 140°, 150°, 160°, 170°, 180°

In most of the cases examined, the (normalized) measured displacements agree well with the (normalized) predicted displacements. There is a slight degradation of the agreement, however, in the extreme "near" and "far" fields. Regardless, the agreement is generally best around 0° and 180° angular orientations with respect to the point force. Agreement begins to deteriorate with an increasing circumferential offset from around 60° but improves beyond 130°. The main discrepancy in the time histories is around the arrival of the second "wave packet." (See Figure H.1 for an illustration of this region.) The main discrepancy in the frequency domain appears around $\omega^* \approx 0.65$ as the measurement has a larger relative peak at this frequency than the prediction. This relative peak corresponds

approximately to the 60 kHz peak in the normalized transfer functions of both the transmitter and receiver. For the most part, the unwrapped phase angle of the predicted radial displacement is in good agreement with that of the measurement.

Possible explanations for the discrepancies include material properties differing from those assumed, geometric and material inhomogeneity/anisotropy, transducer transfer functions differing from those assumed due to coupling, the transducers not acting at a point, and the applied load being a surface traction rather than a body load. Of the possible explanations, the most likely one is likely different material properties. Further work is underway to explore this possibility.

4.3 "Snapshots" of the Radial Green's Function and Radial Displacement

Figures 4.1 through 4.7 show snapshots, in perspective and plan, of the radial component of the Green's functions over the cylinder's outer surface at seven uniformly incremented instants over one period, T, of the external forcing's vibration 70 kHz centre frequency. See, for example, equation (2.60). (Note that the "colour bars" given in Figures 4.1 through 4.7 represent the same scale as the displacement axis. Moreover, the scales of the displacement axes of corresponding perspective and plan views are identical.) The figures are presented in non-dimensional form. They represent the steady state time displacement of the cylinder to a radially applied, point, harmonic load having unit magnitude. An animation showing the evolution of the corresponding radial component of the steady state Green's function is contained on the accompanying electronic media. Snapshots of the remaining displacement components and the non-zero stress functions are similar to the given radial component. They are omitted for brevity.

Figures 4.8 through 4.14 give snapshots at seven uniformly incremented instants. They illustrate the evolution of the radial displacement field for the external forcing described in Appendix A. (Again note that the "colour bars" given in Figures 4.8 through 4.14 represent the same scale as the displacement axis and that the scale of the displacement axes of corresponding perspective and plan views is identical.) These figures are presented again in non-dimensional form and they also incorporate corrections for the frequency varying behaviour of the transducers. Note that the initial wavefront is defined clearly at each instant but small numerical "noise" can be seen ahead of the wavefront. The corresponding animation is included on the accompanying electronic media. The snapshots and animations can be used to provide a "baseline" for comparisons with analogous data from a defective cylinder. Furthermore, the presented evolution of the radial displacement appears intuitively to be plausible.

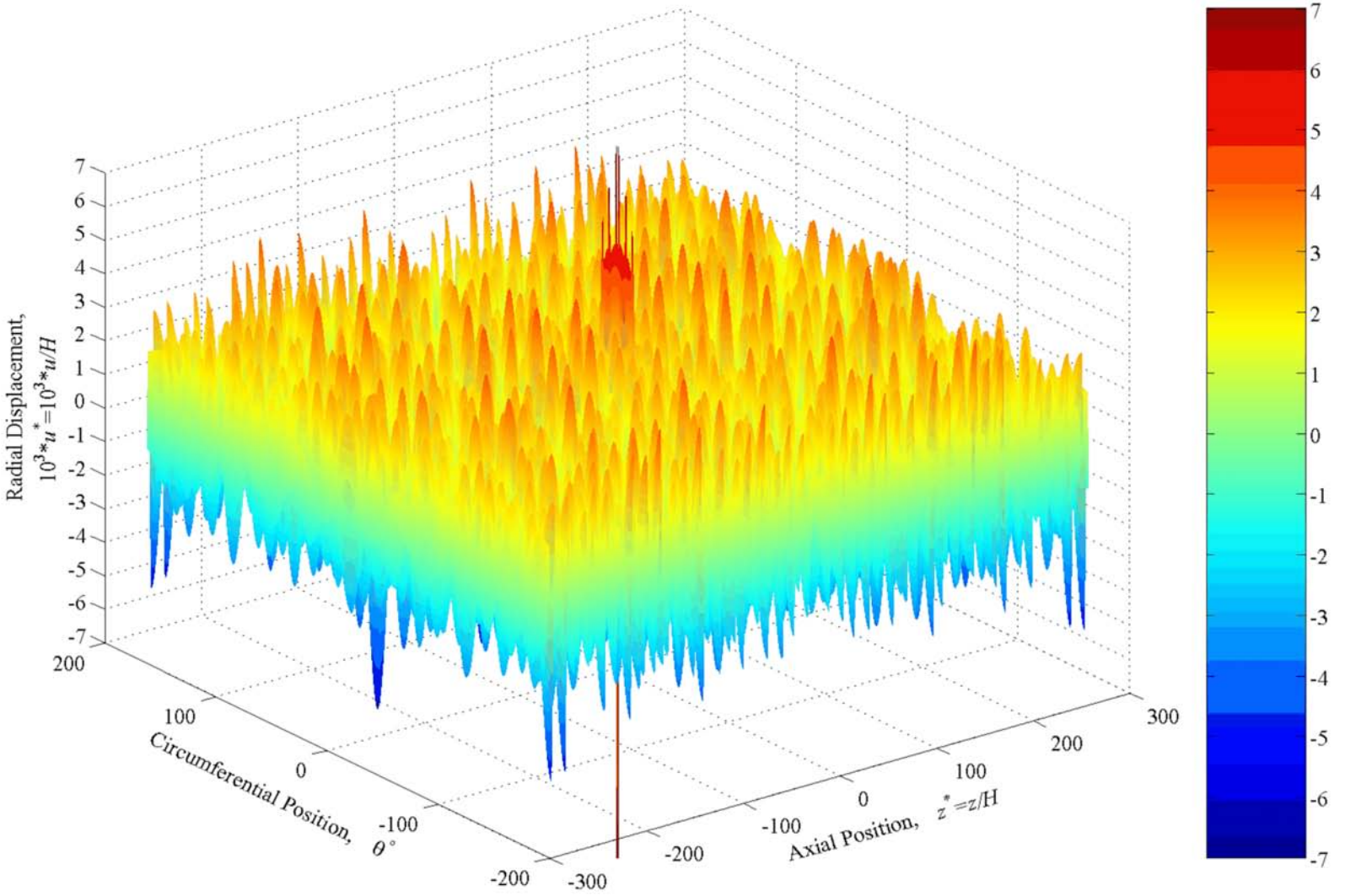

Figure 4.1 (a). Perspective View of Radial Component of Green's Function at Beginning of Period, *T*

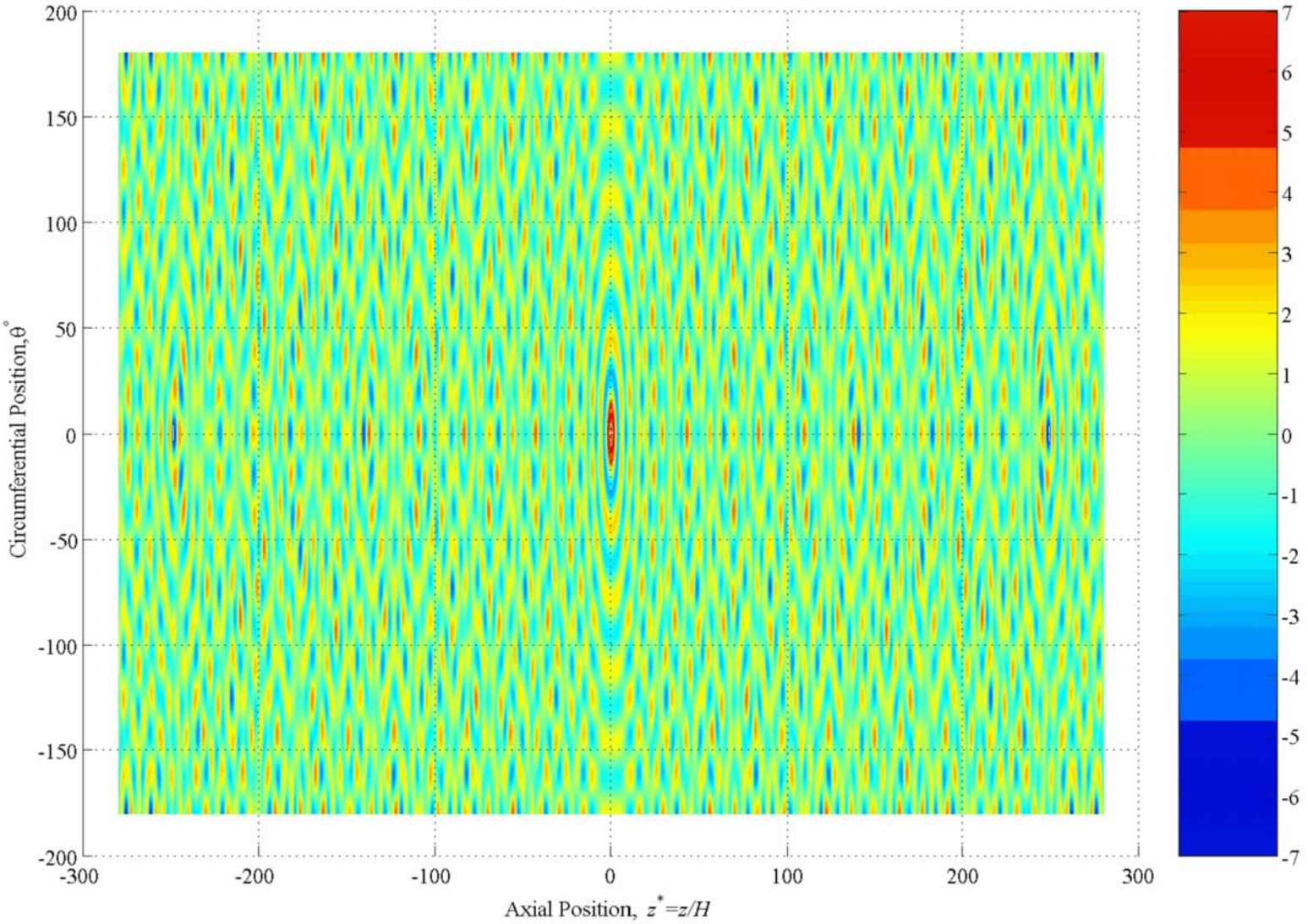

Figure 4.1 (b). Plan View of Radial Component of Green's Function at Beginning of Period, *T*

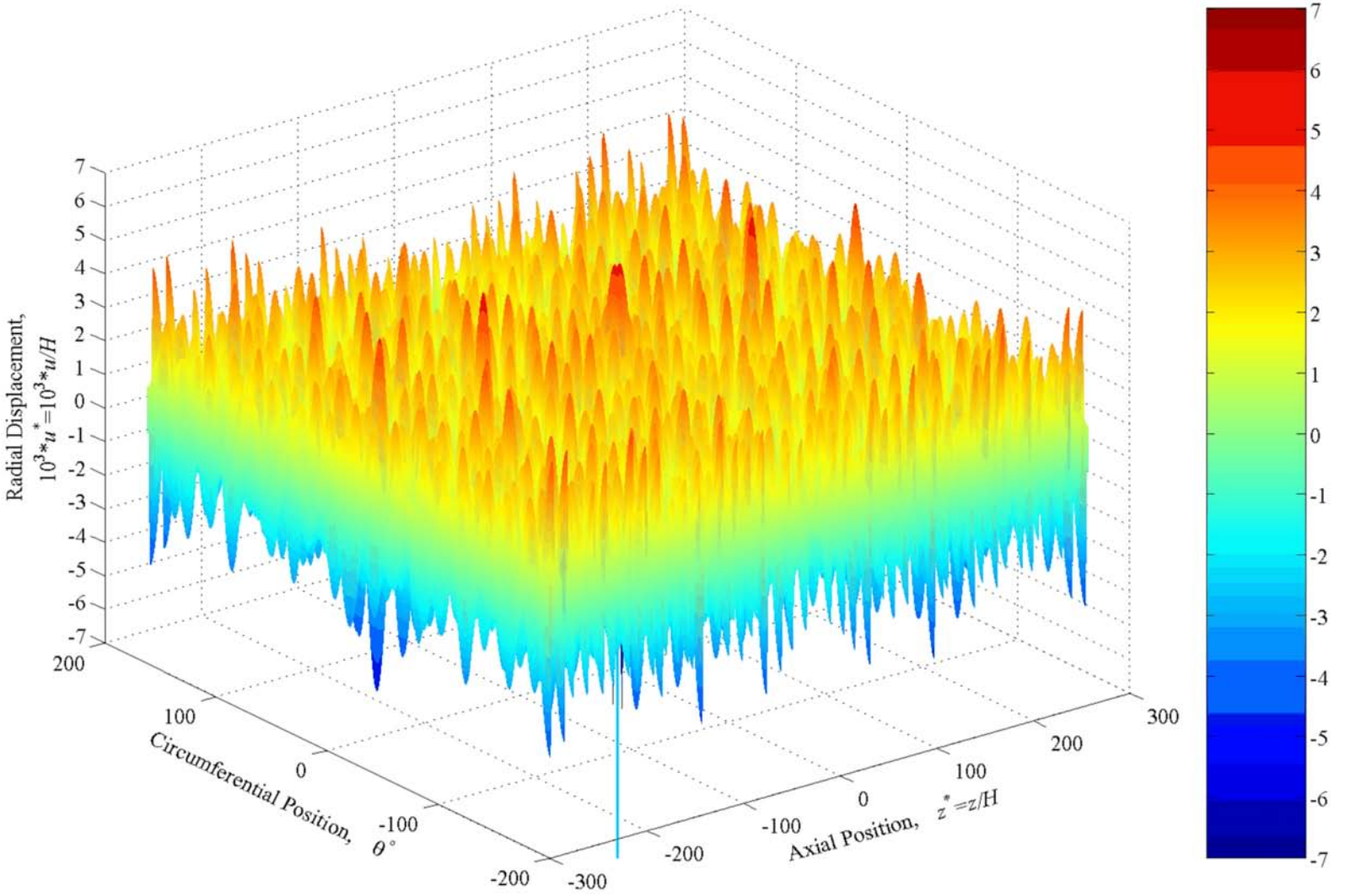

Figure 4.2 (a). Perspective View of Radial Component of Green's Function at Instant1/6 of Period, *T*

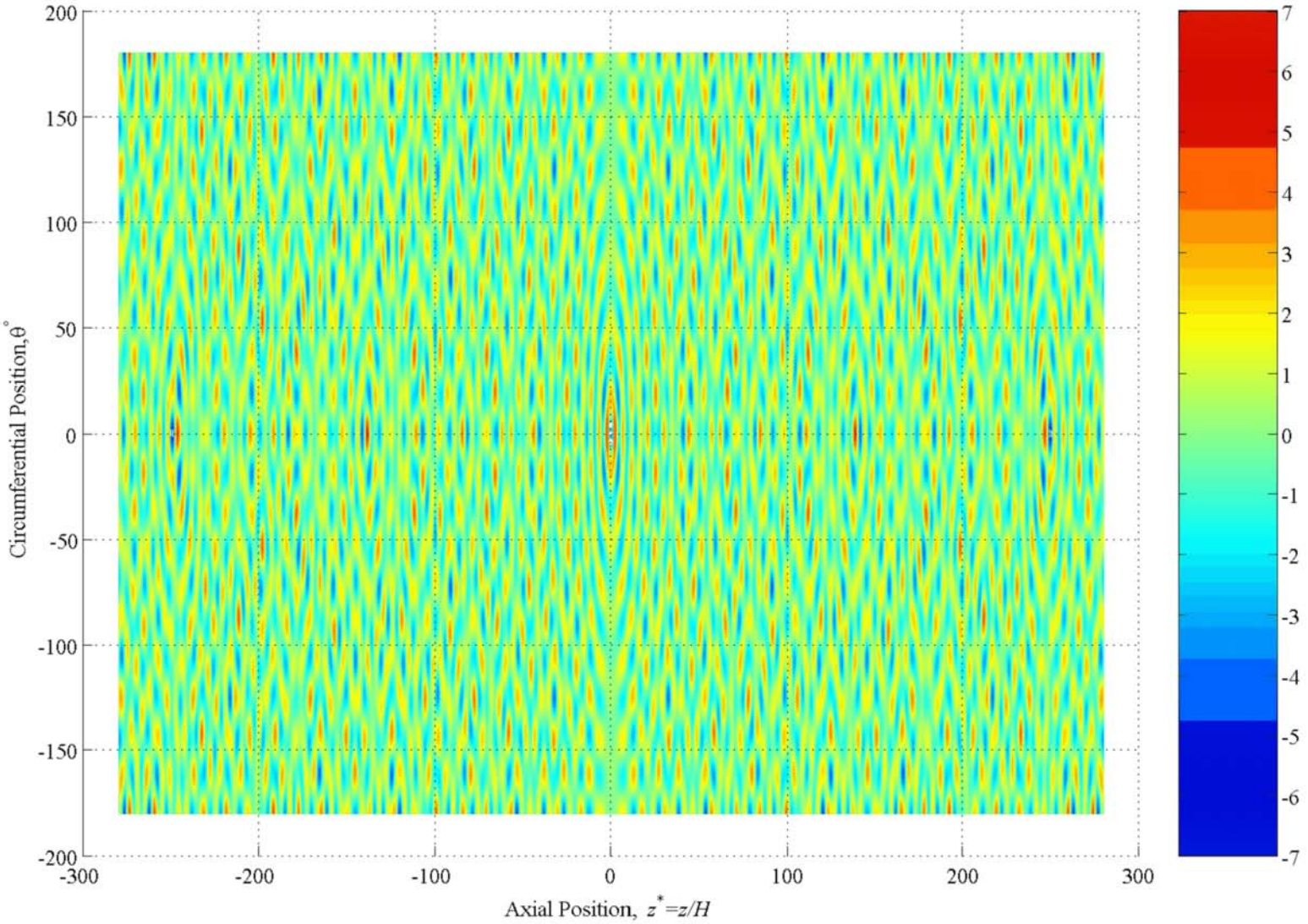

Figure 4.2 (b). Plan View of Radial Component of Green's Function at Instant 1/6 of Period, *T*

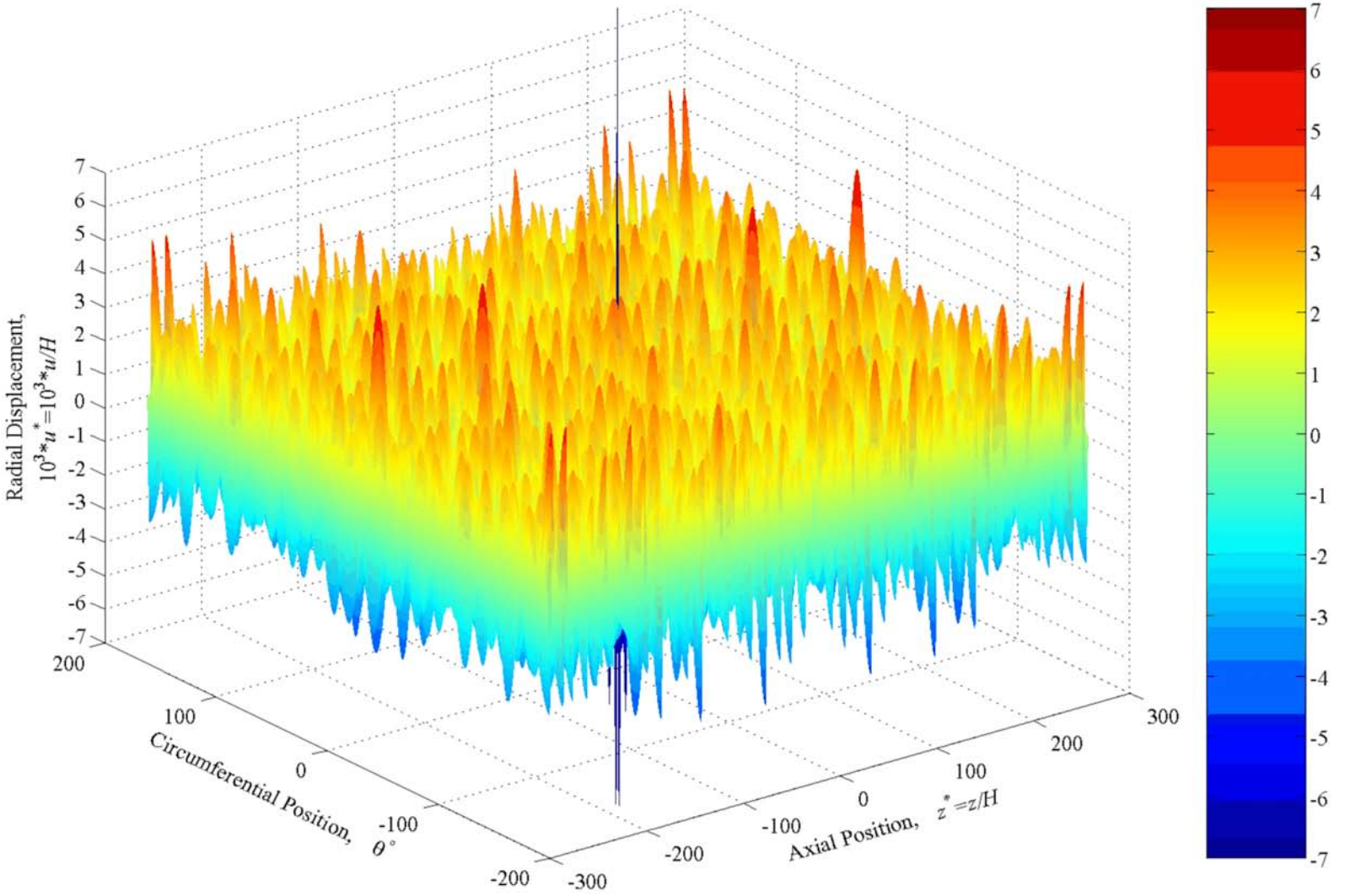

Figure 4.3 (a). Perspective View of Radial Component of Green's Function at Instant 1/3 of Period, *T*

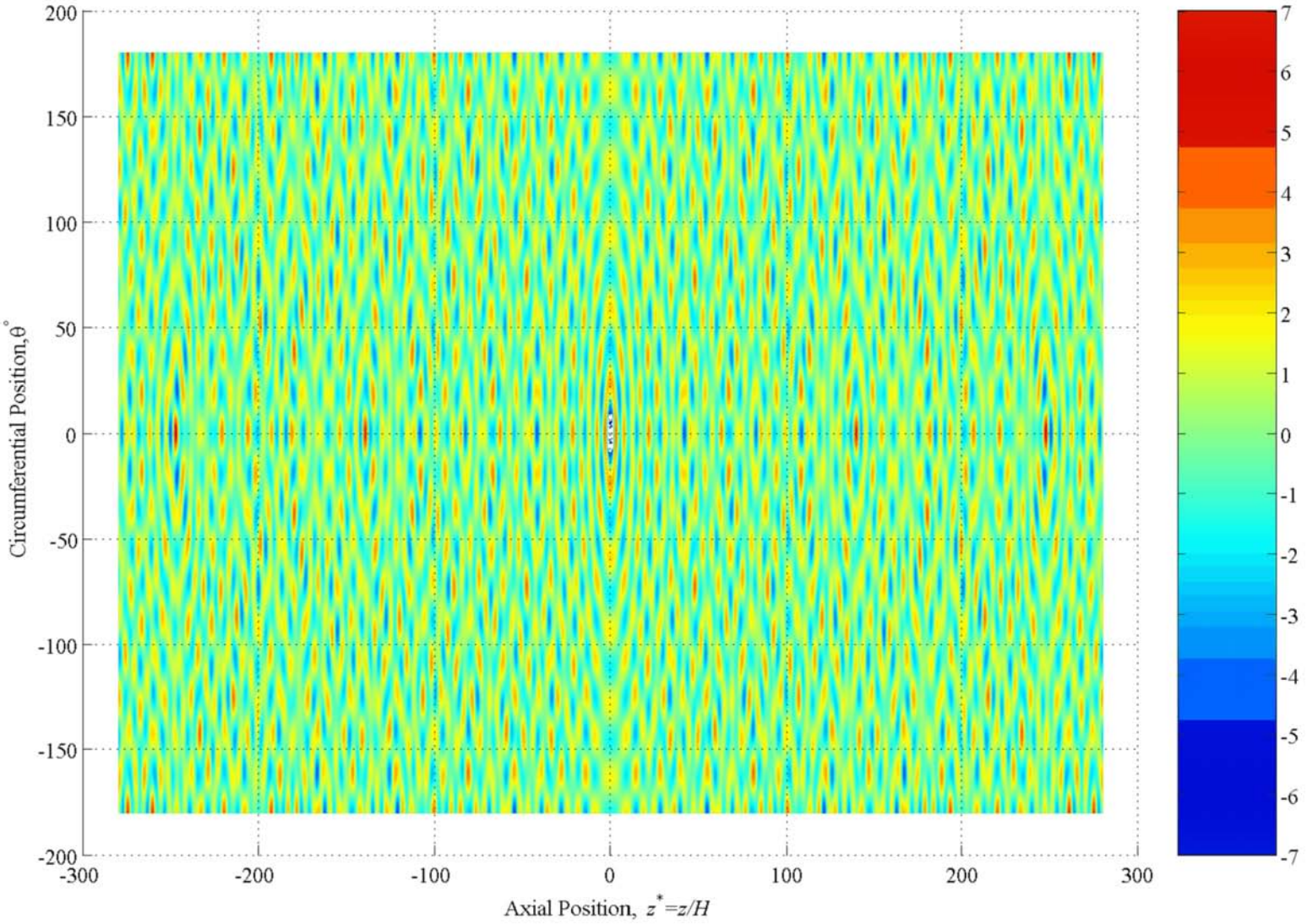

Figure 4.3 (b). Plan View of Radial Component of Green's Function at Instant 1/3 of Period, *T*

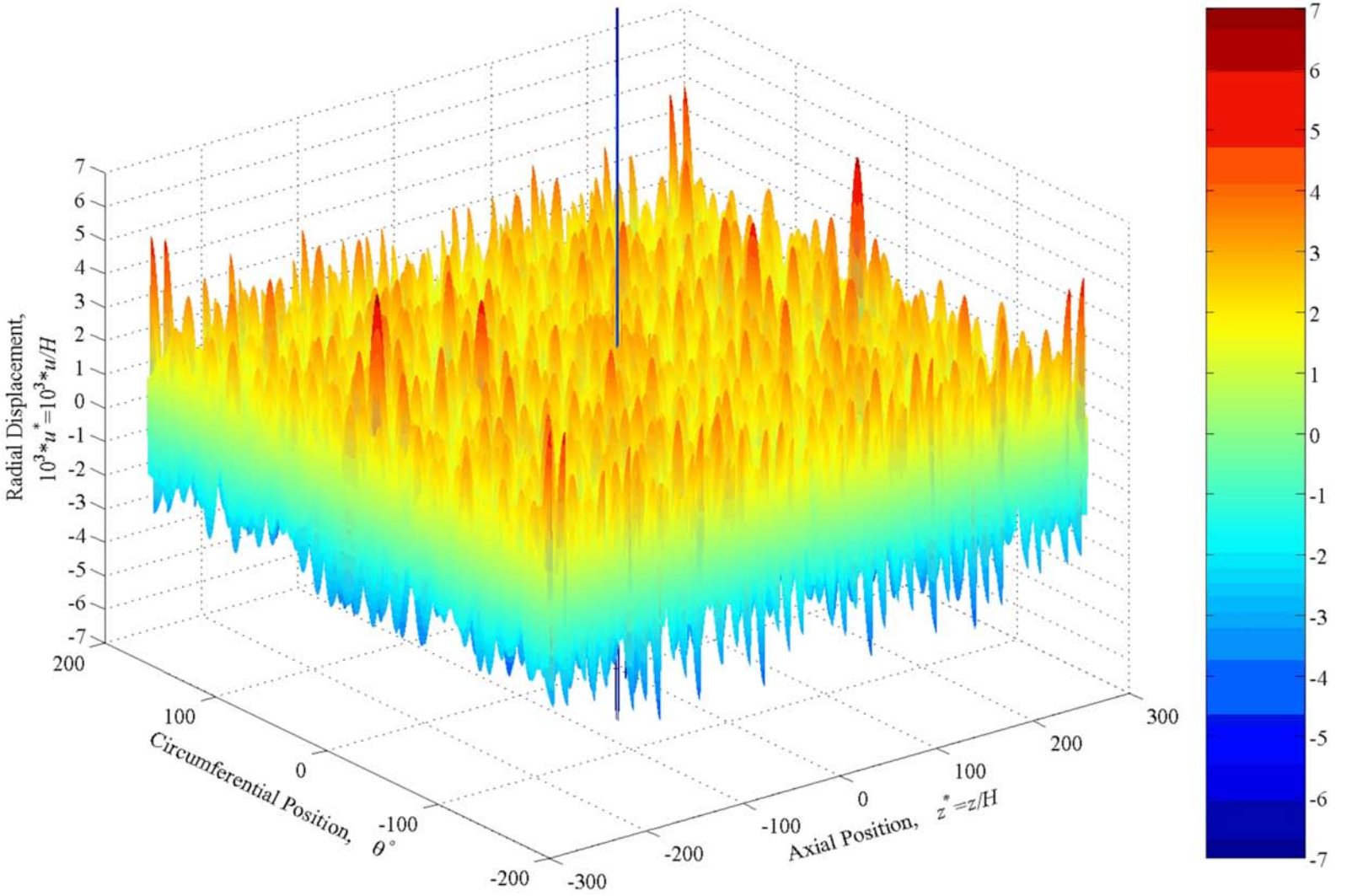

Figure 4.4 (a). Perspective View of Radial Component of Green's Function at Instant 1/2 of Period, *T*

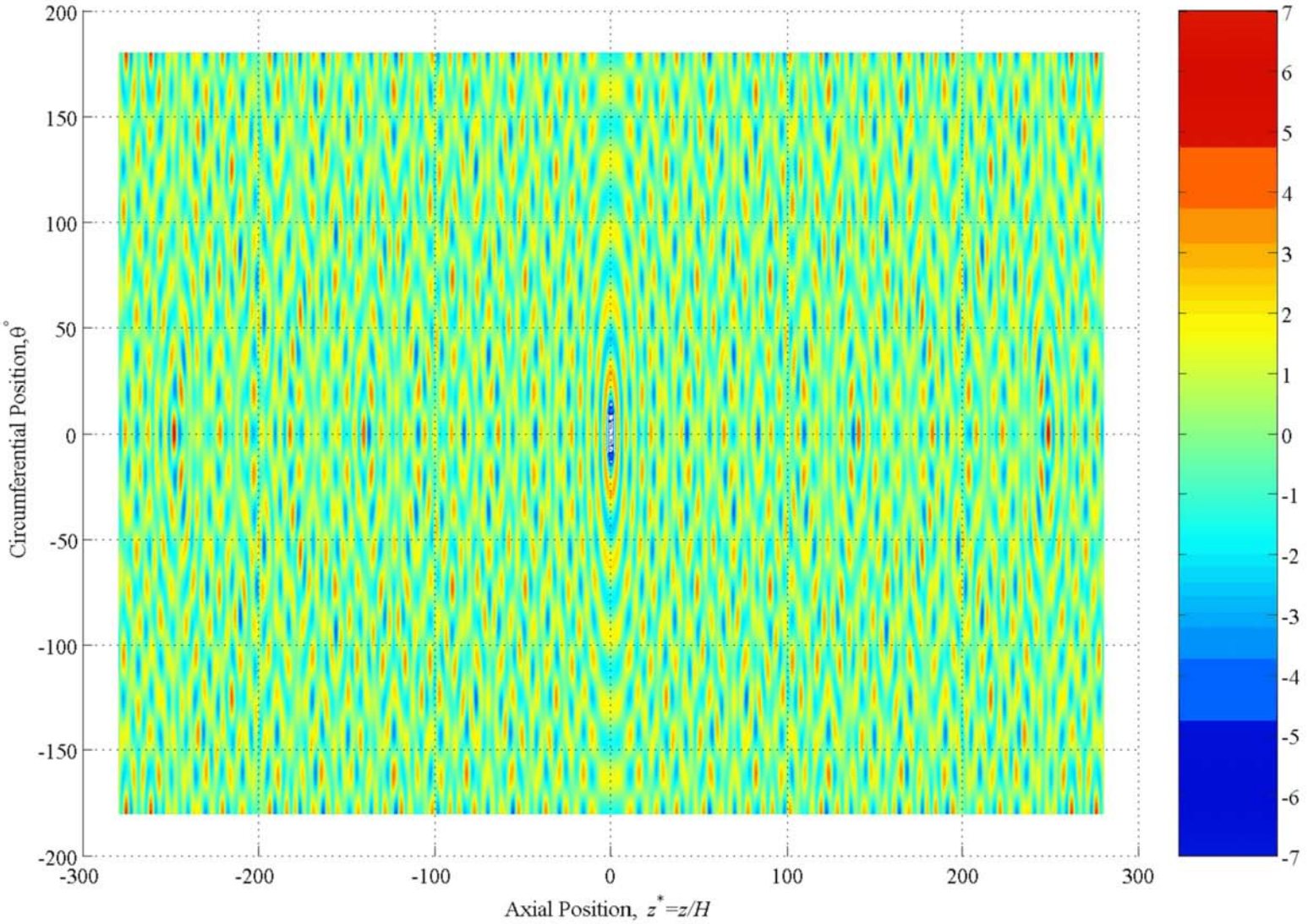

Figure 4.4 (b). Plan View of Radial Component of Green's Function at Instant 1/2 of Period, *T*

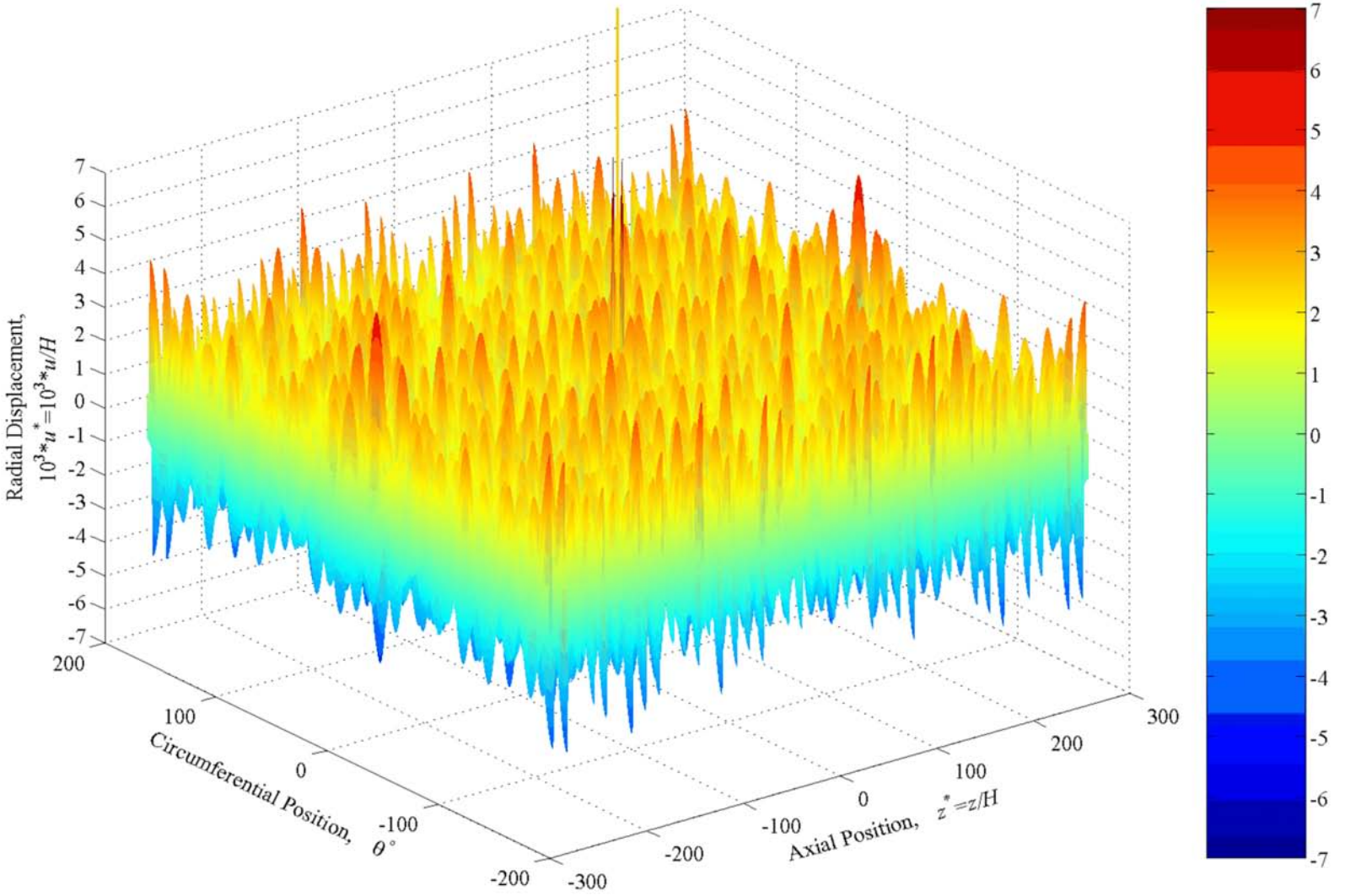

Figure 4.5 (a). Perspective View of Radial Component of Green's Function at Instant 2/3 of Period, *T*

Figure 4.5 (b). Plan View of Radial Component of Green's Function at Instant 2/3 of Period, T

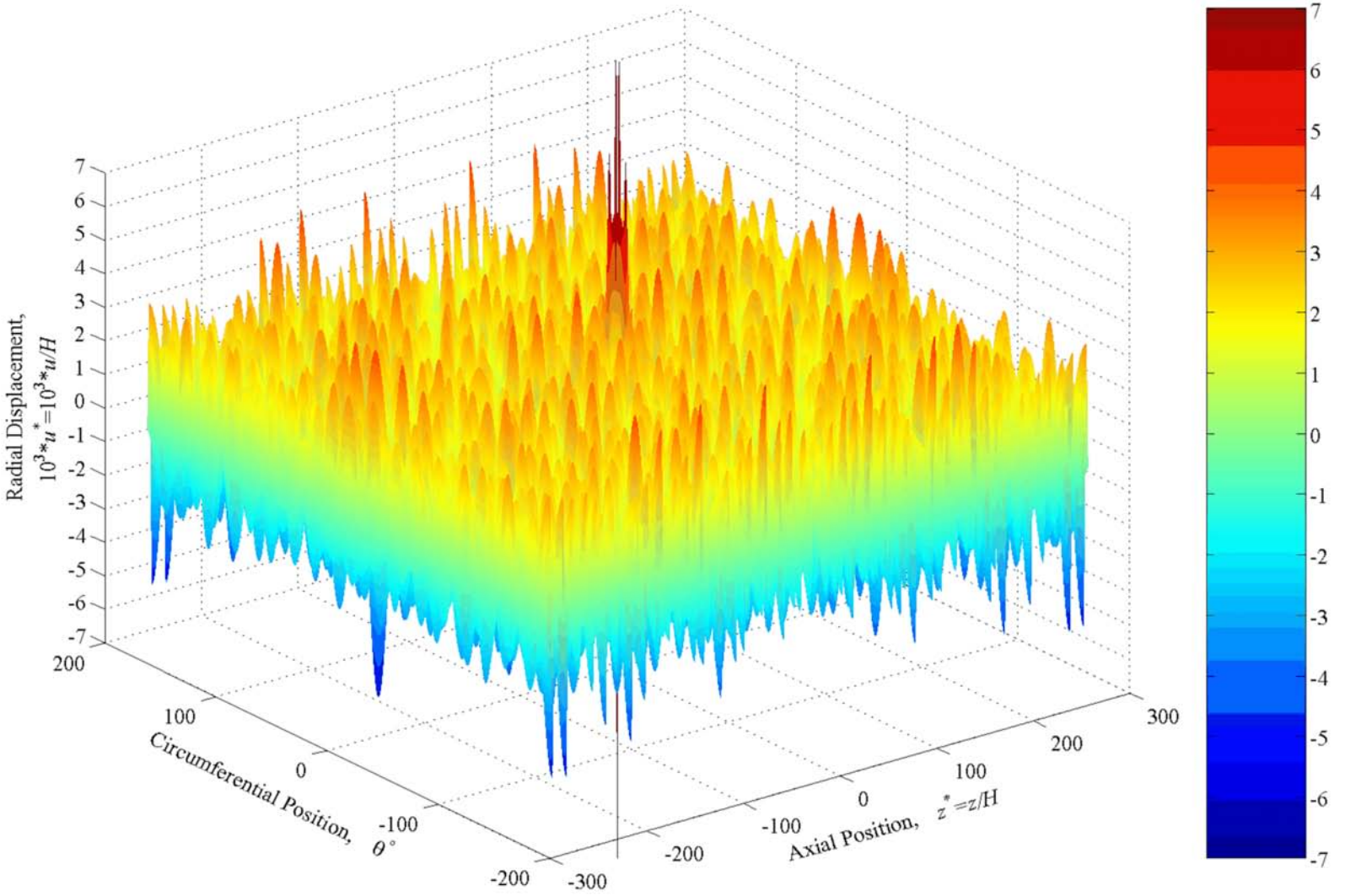

Figure 4.6 (a). Perspective View of Radial Component of Green's Function at Instant 5/6 of Period, *T*

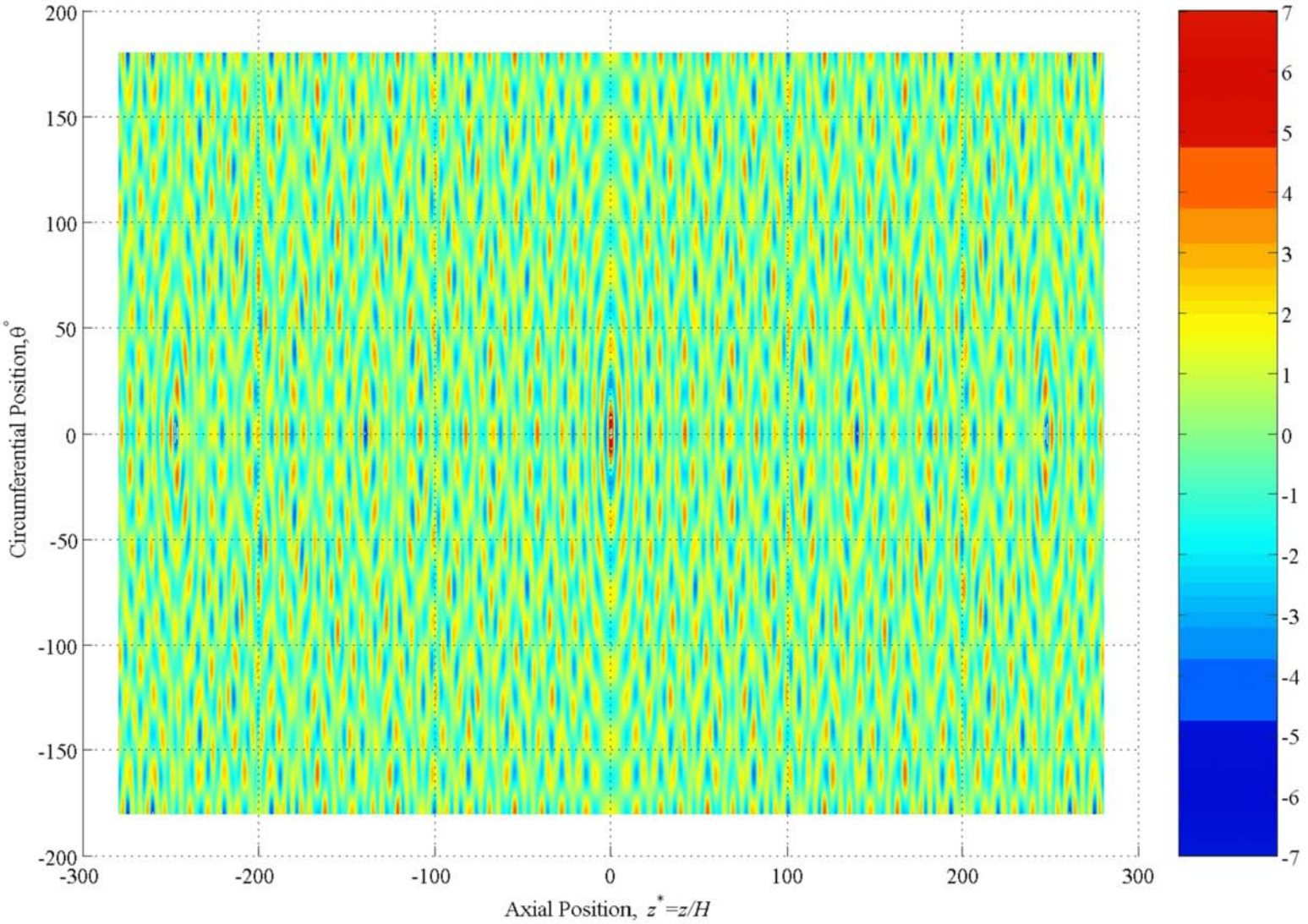

Figure 4.6 (b). Plan View of Radial Component of Green's Function at Instant 5/6 of Period, *T*

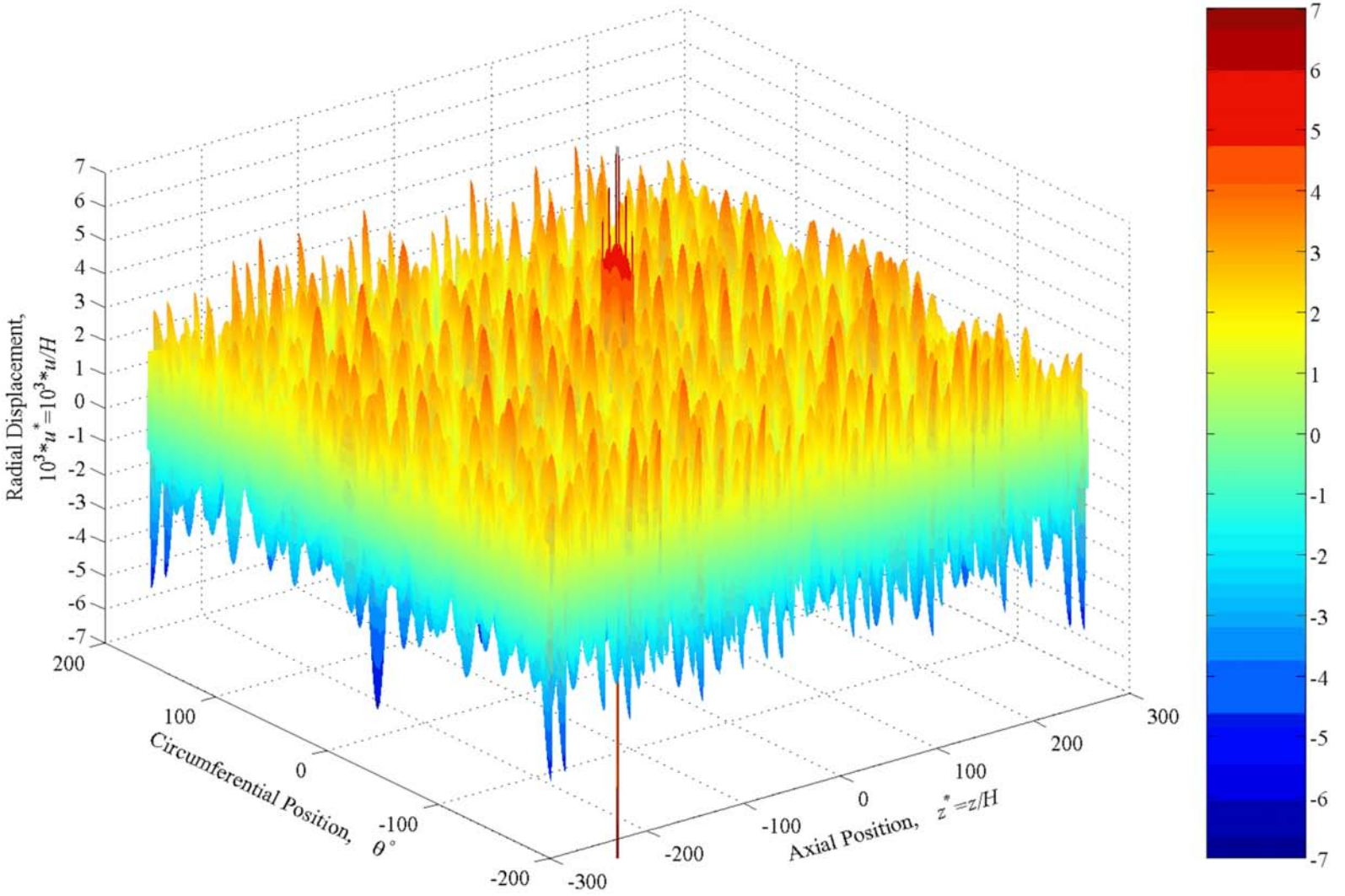

Figure 4.7 (a). Perspective View of Radial Component of Green's Function at End of Period, *T*

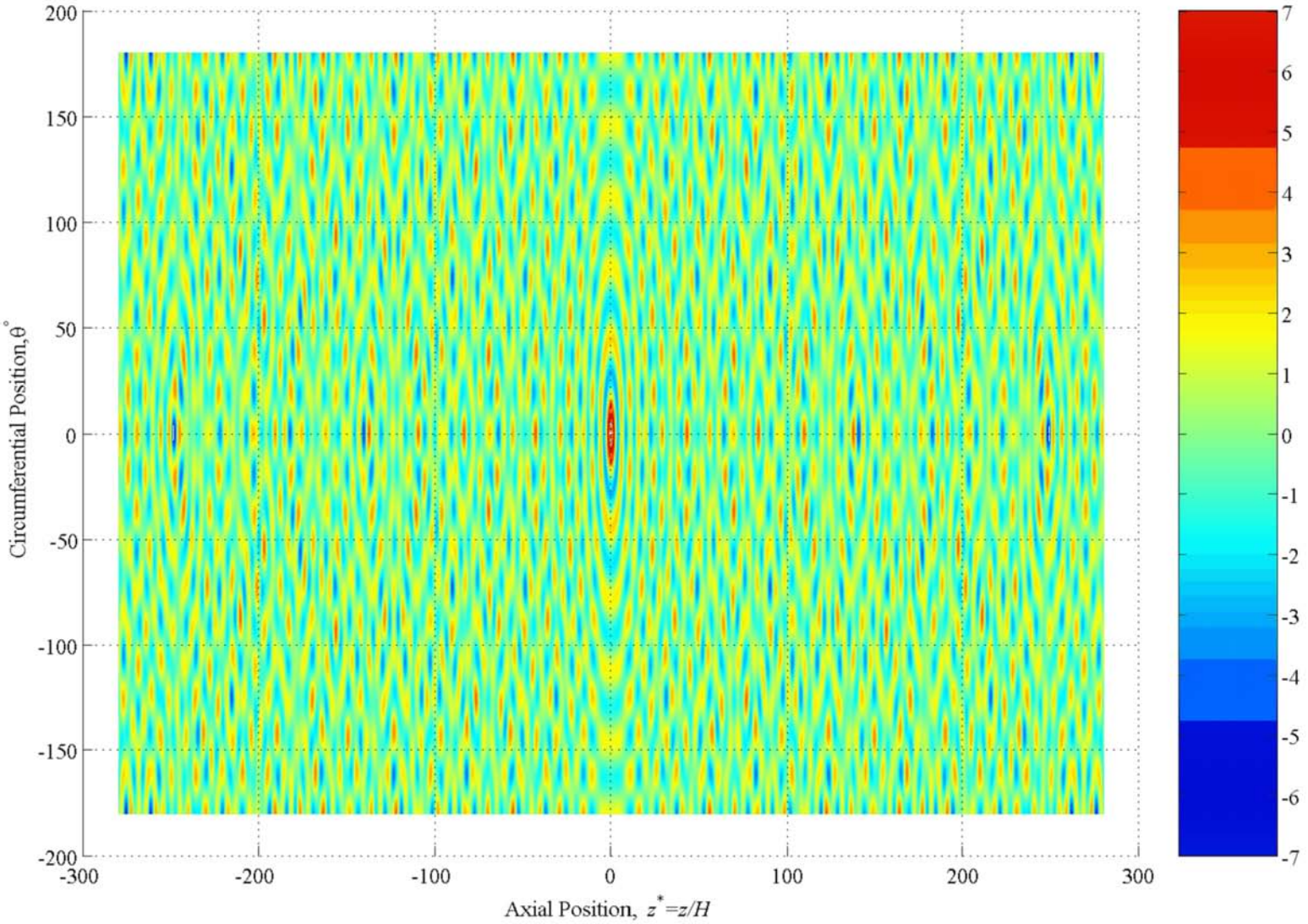

Figure 4.7 (b). Plan View of Radial Component of Green's Function at End of Period, T

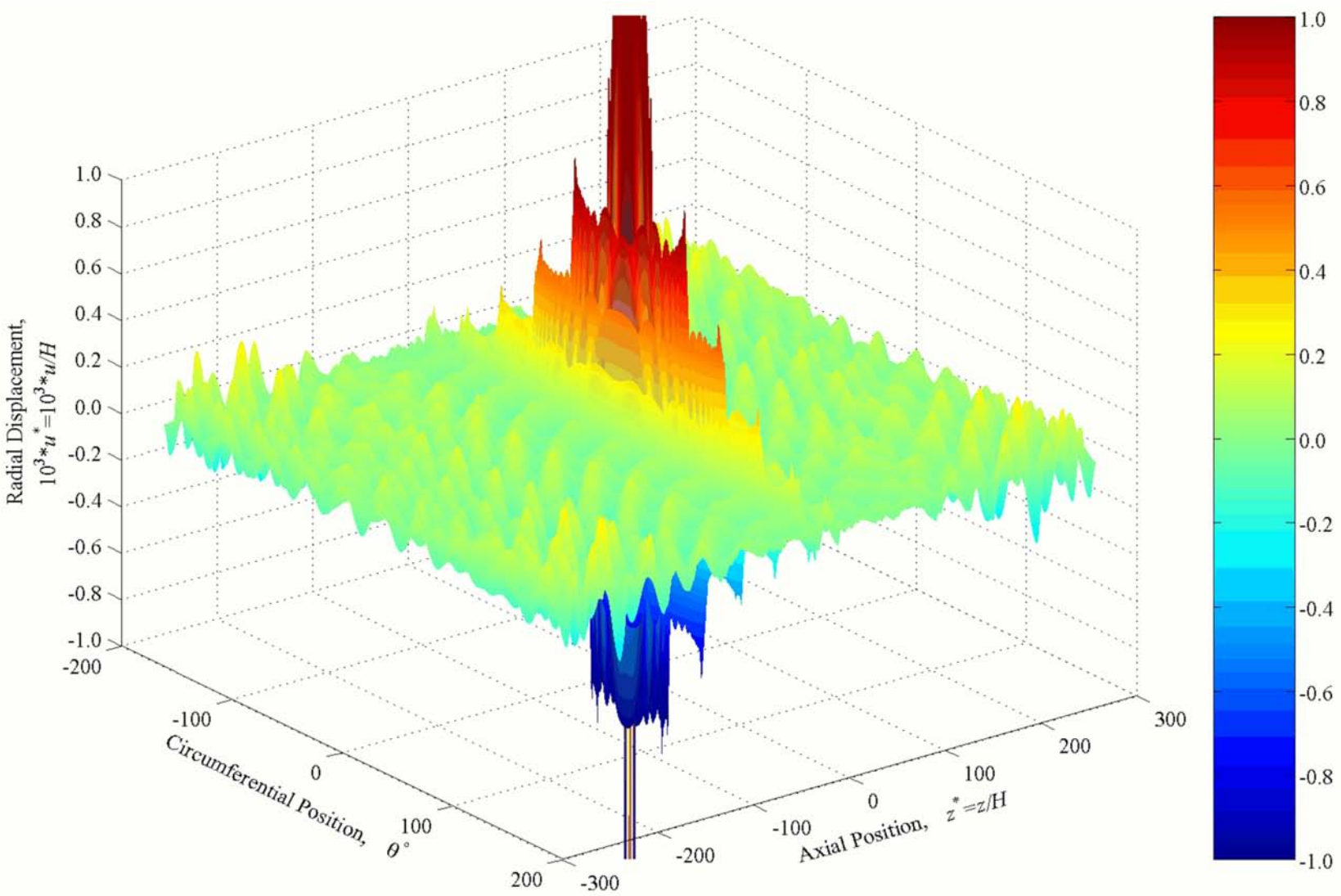

Figure 4.8 (a). Perspective View of Radial Displacement at t^*=40.6

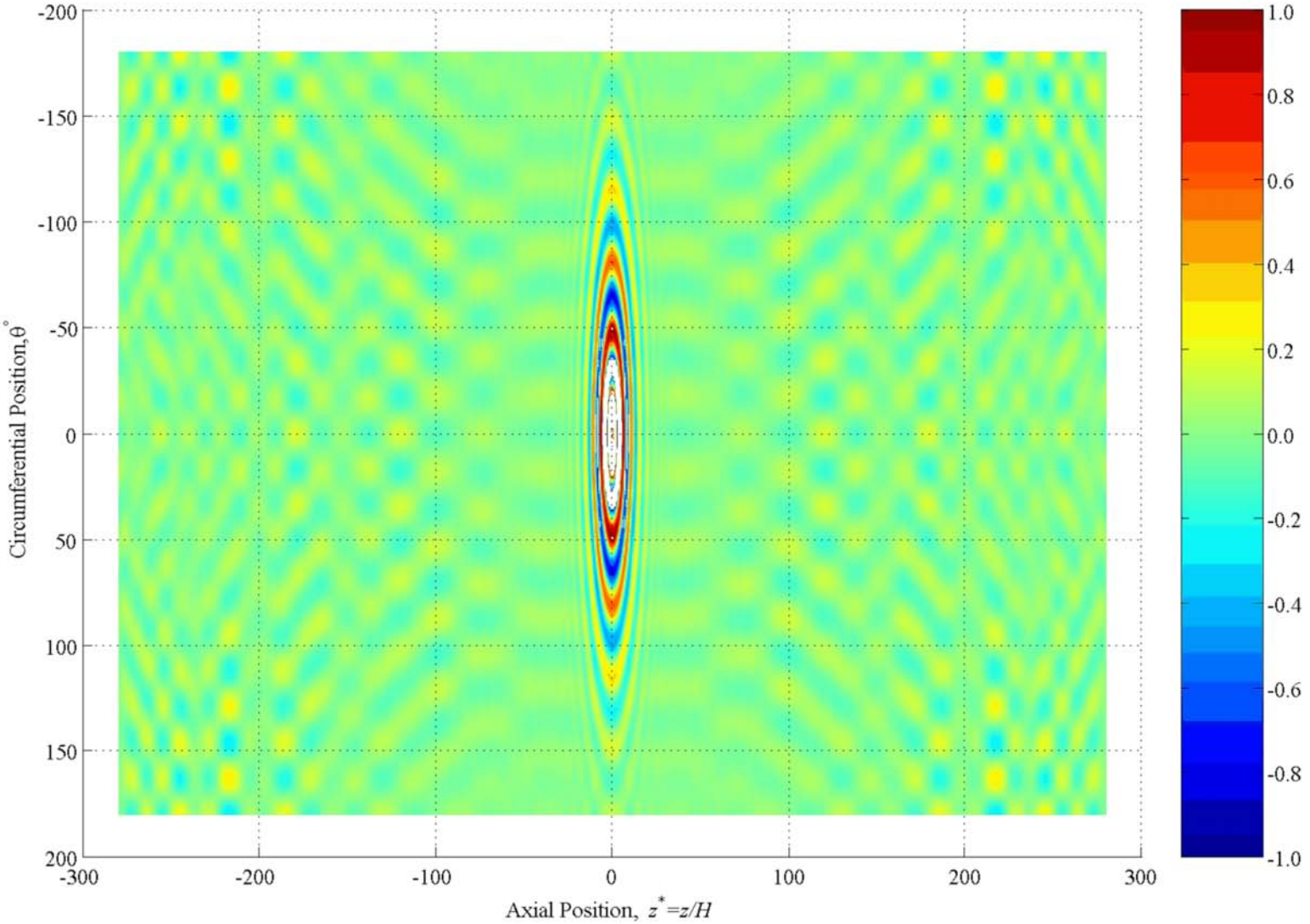

Figure 4.8 (b). Plan View of Radial Displacement at t^*=40.6

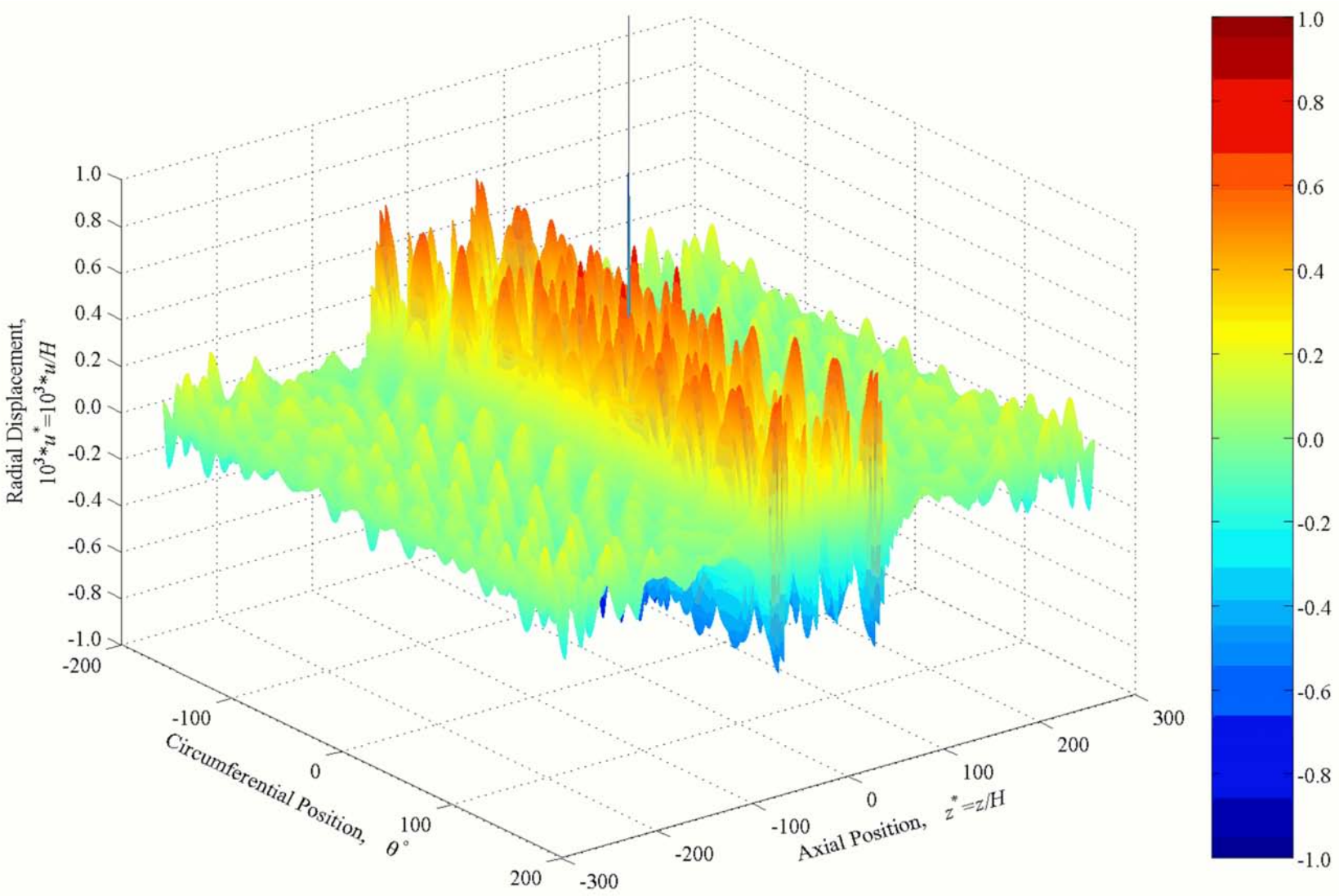

Figure 4.9 (a). Perspective View of Radial Displacement at t^*=101.8

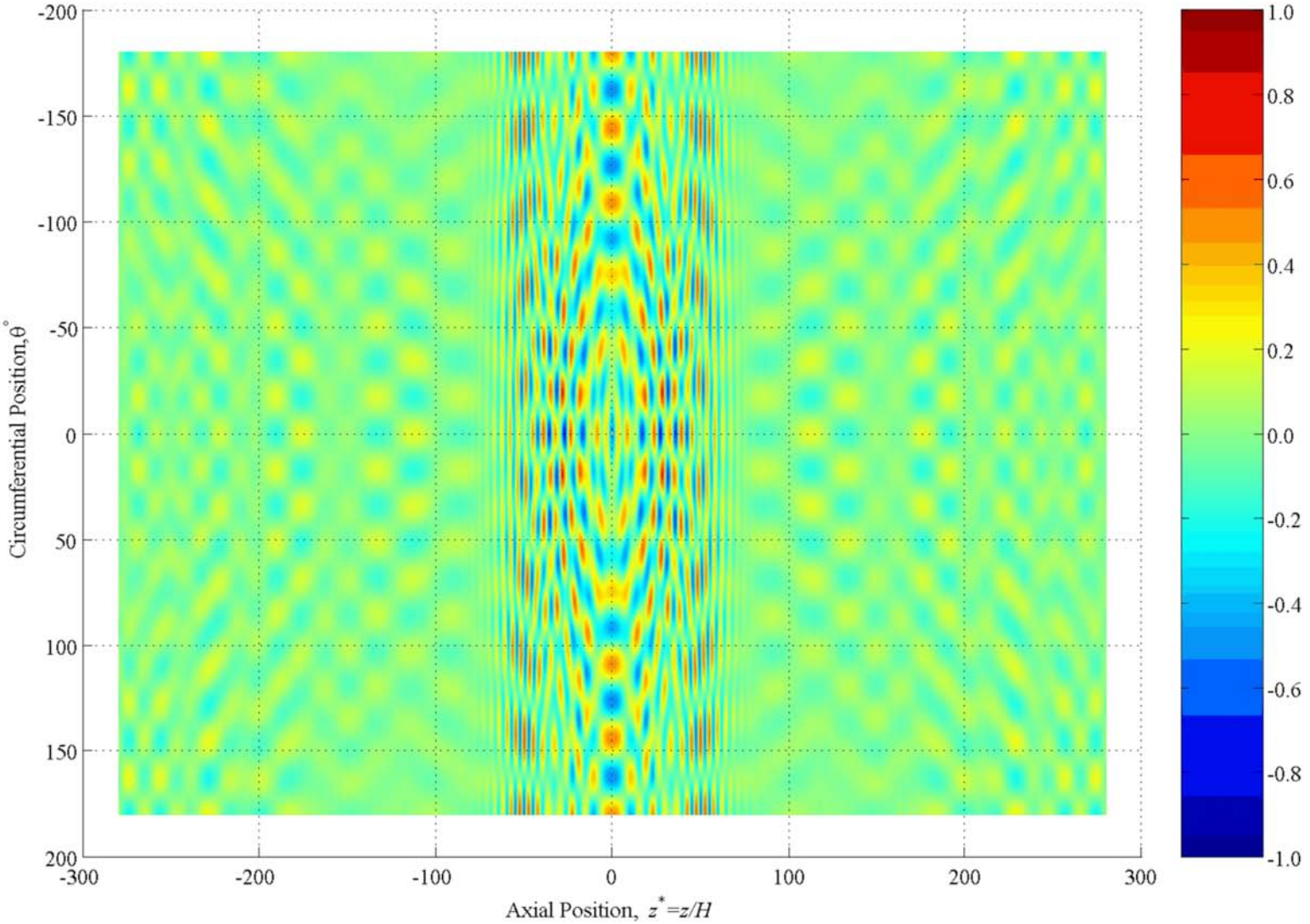

Figure 4.9 (b). Plan View of Radial Displacement at t^*=101.8

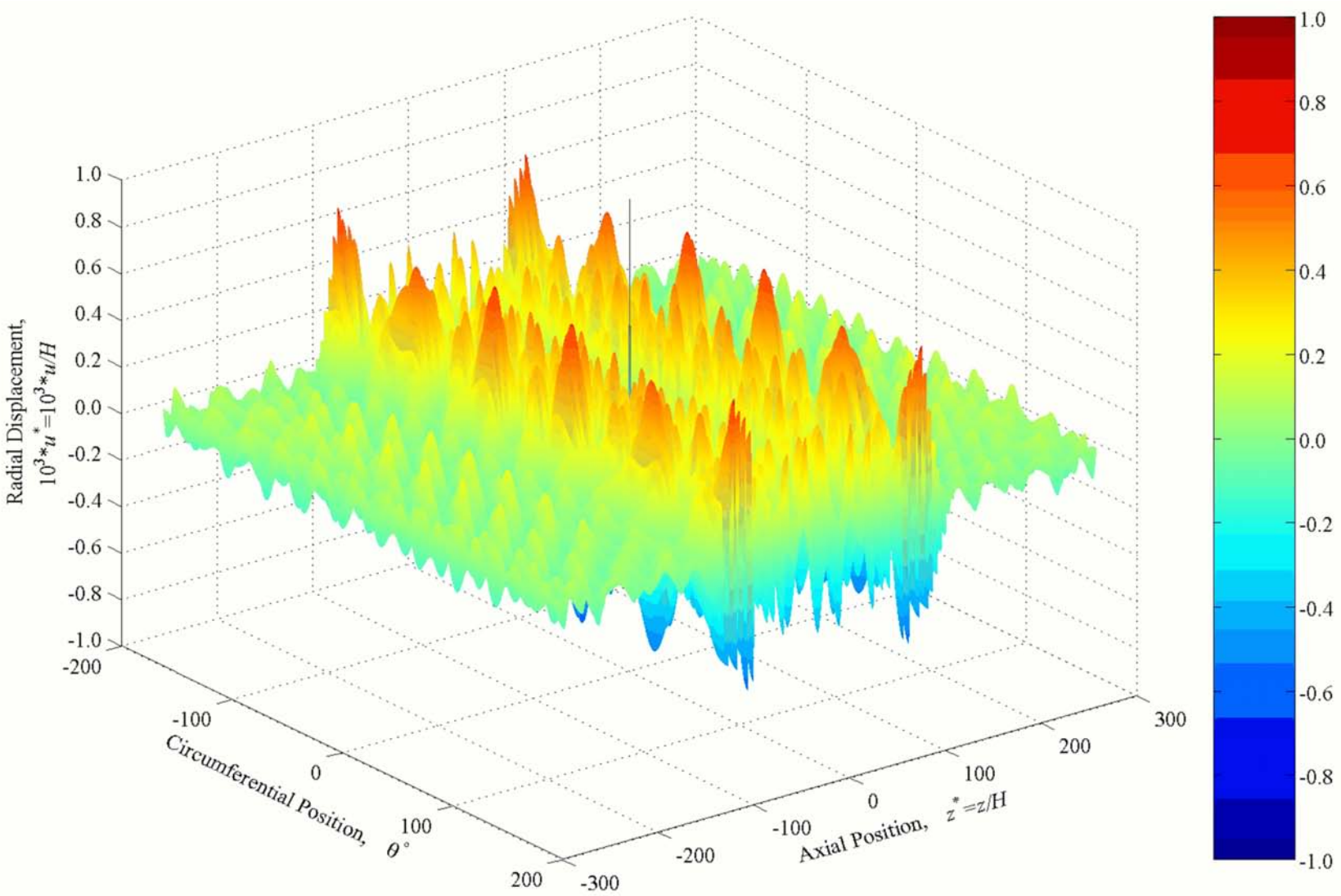

Figure 4.10 (a). Perspective View of Radial Displacement at t^*=163.0

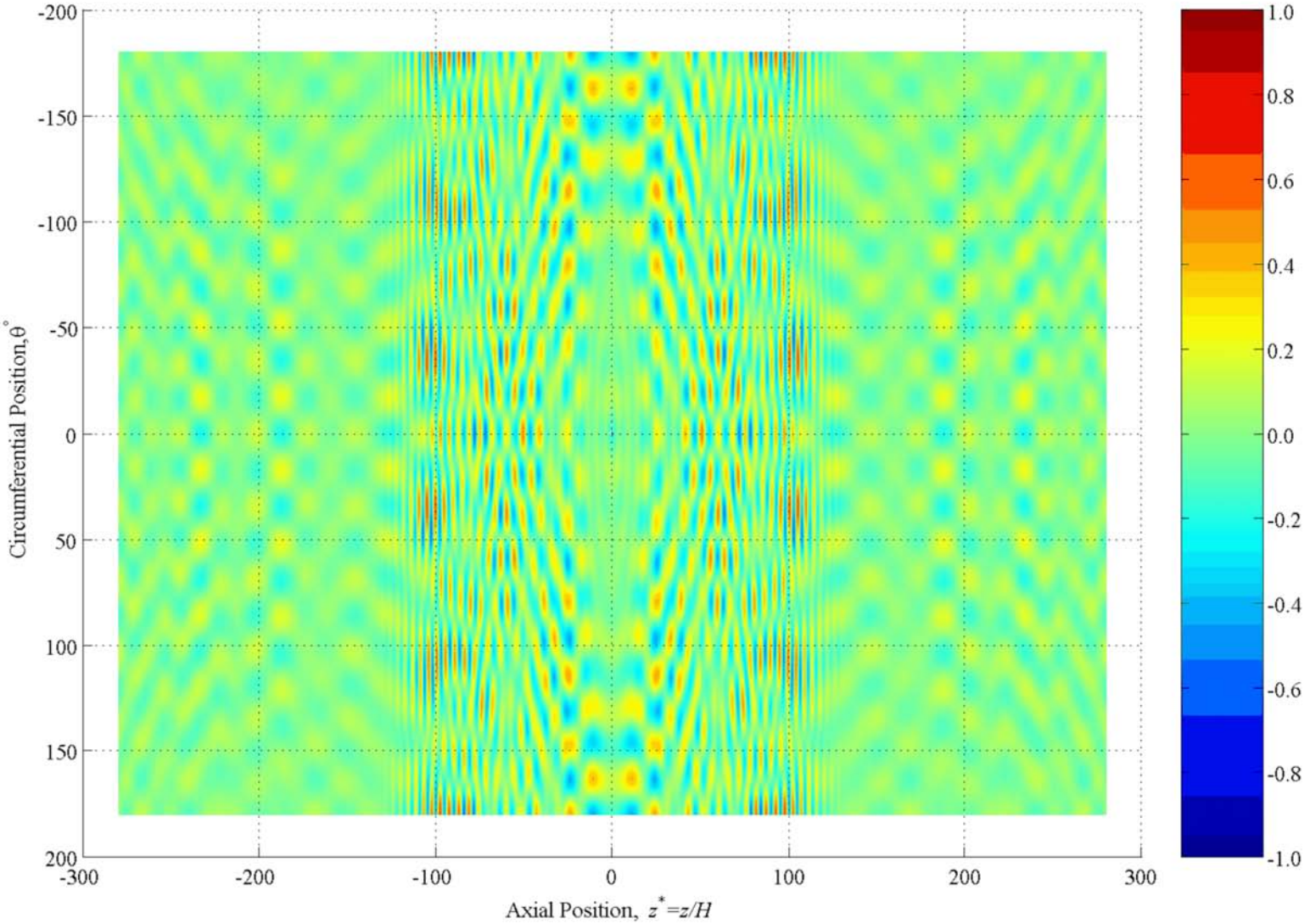

Figure 4.10 (b). Plan View of Radial Displacement at t^*=163.0

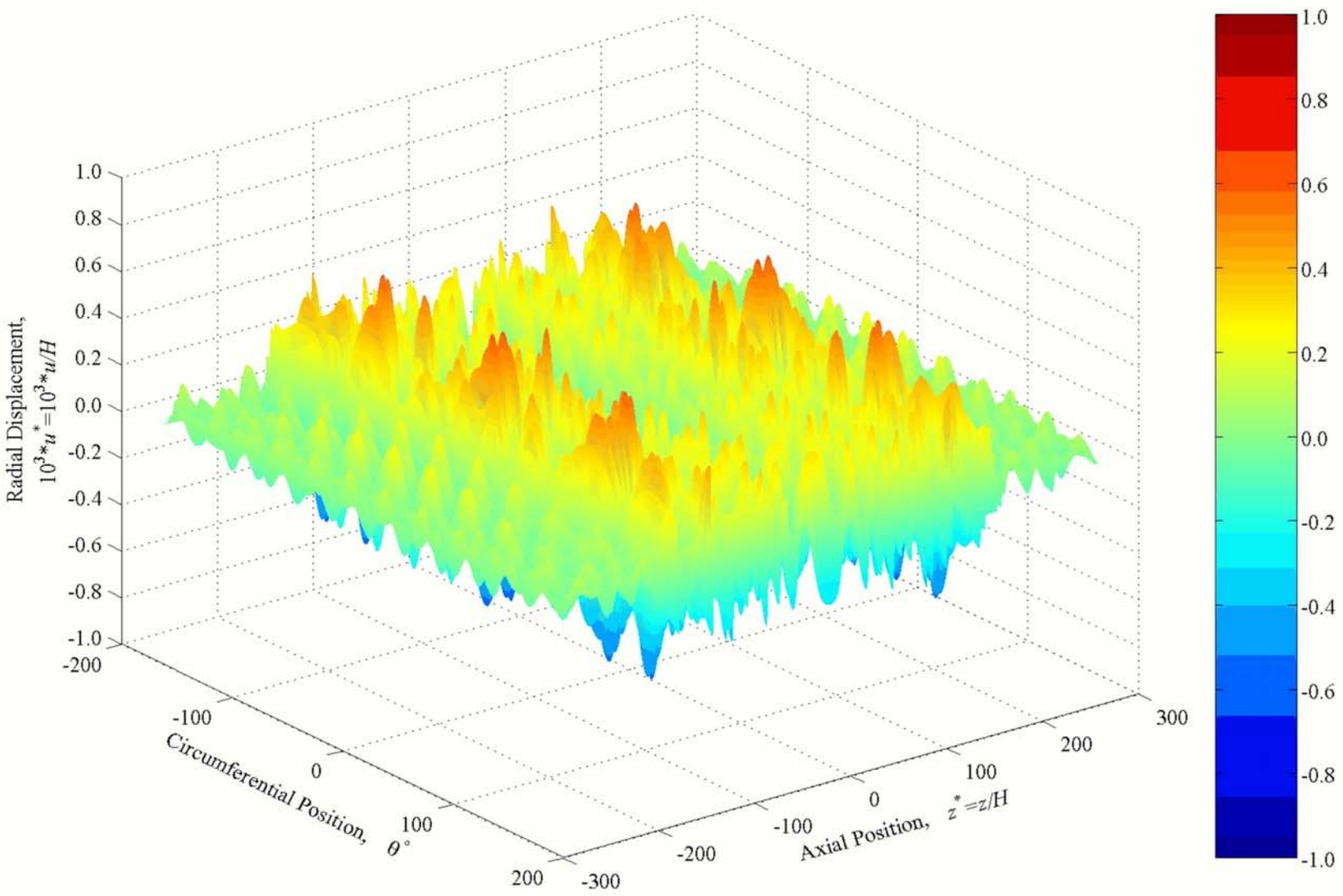

Figure 4.11 (a). Perspective View of Radial Displacement at t^*=224.2

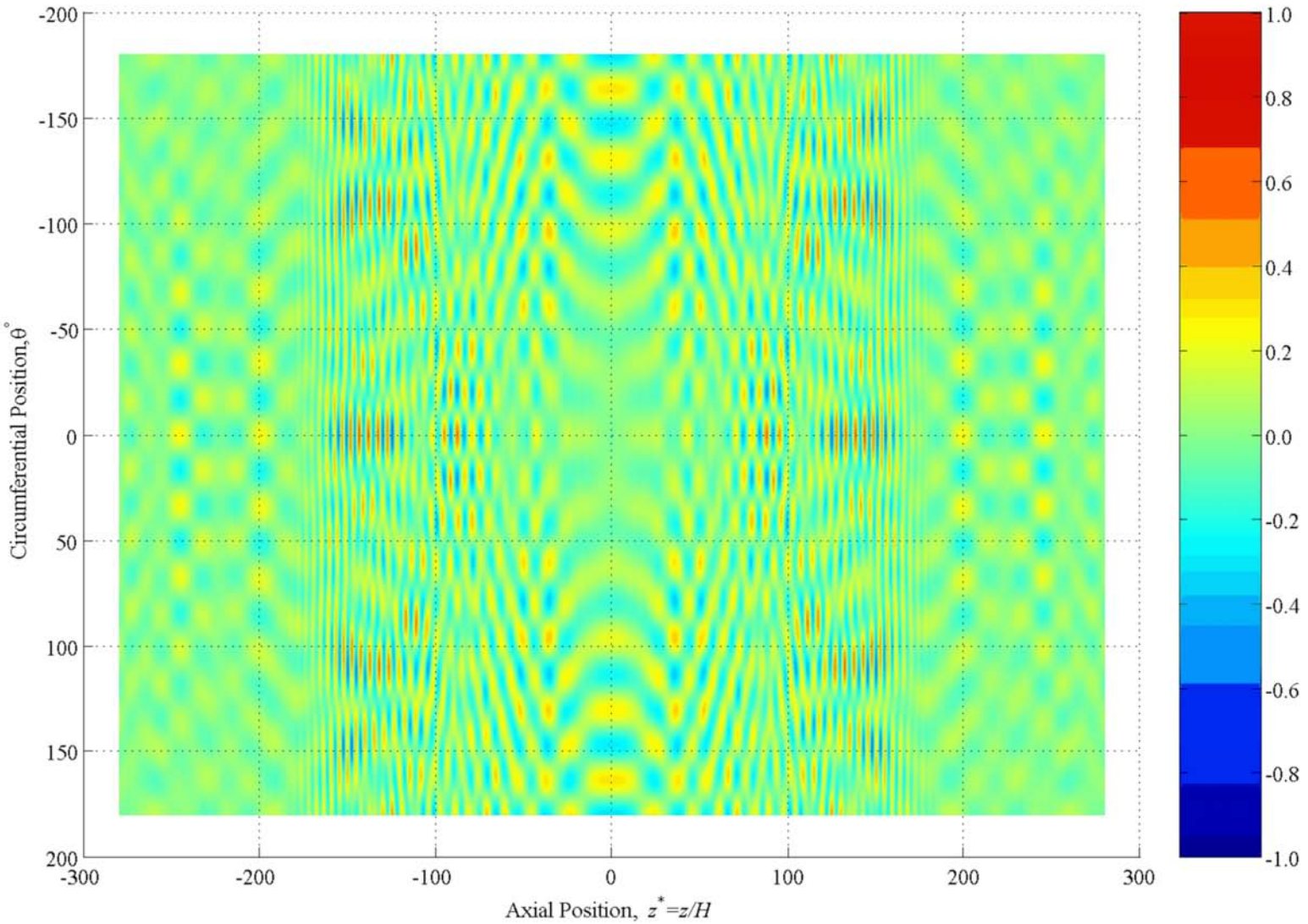

Figure 4.11 (b). Plan View of Radial Displacement at t^*=224.2

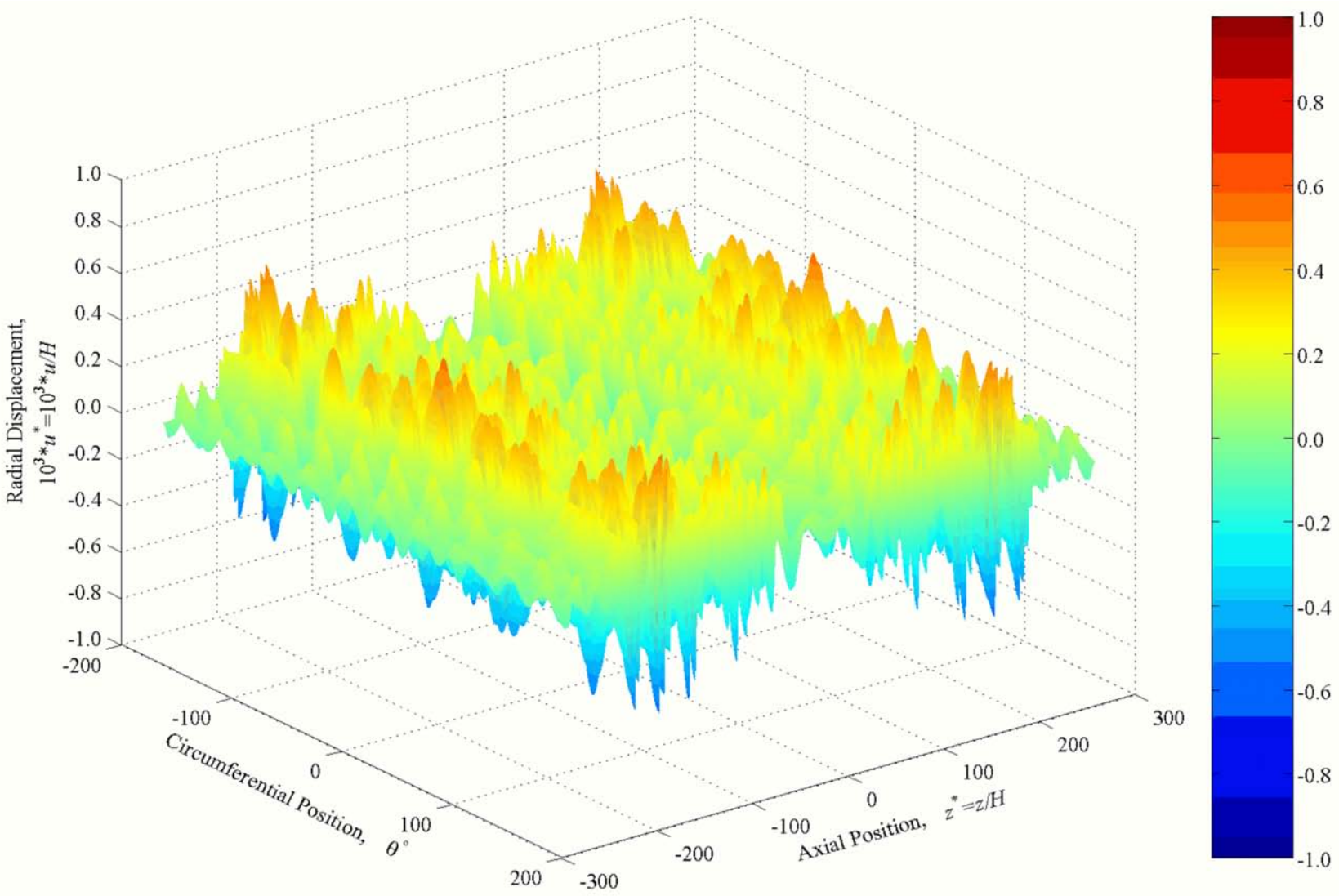

Figure 4.12 (a). Perspective View of Radial Displacement at t^*=285.4

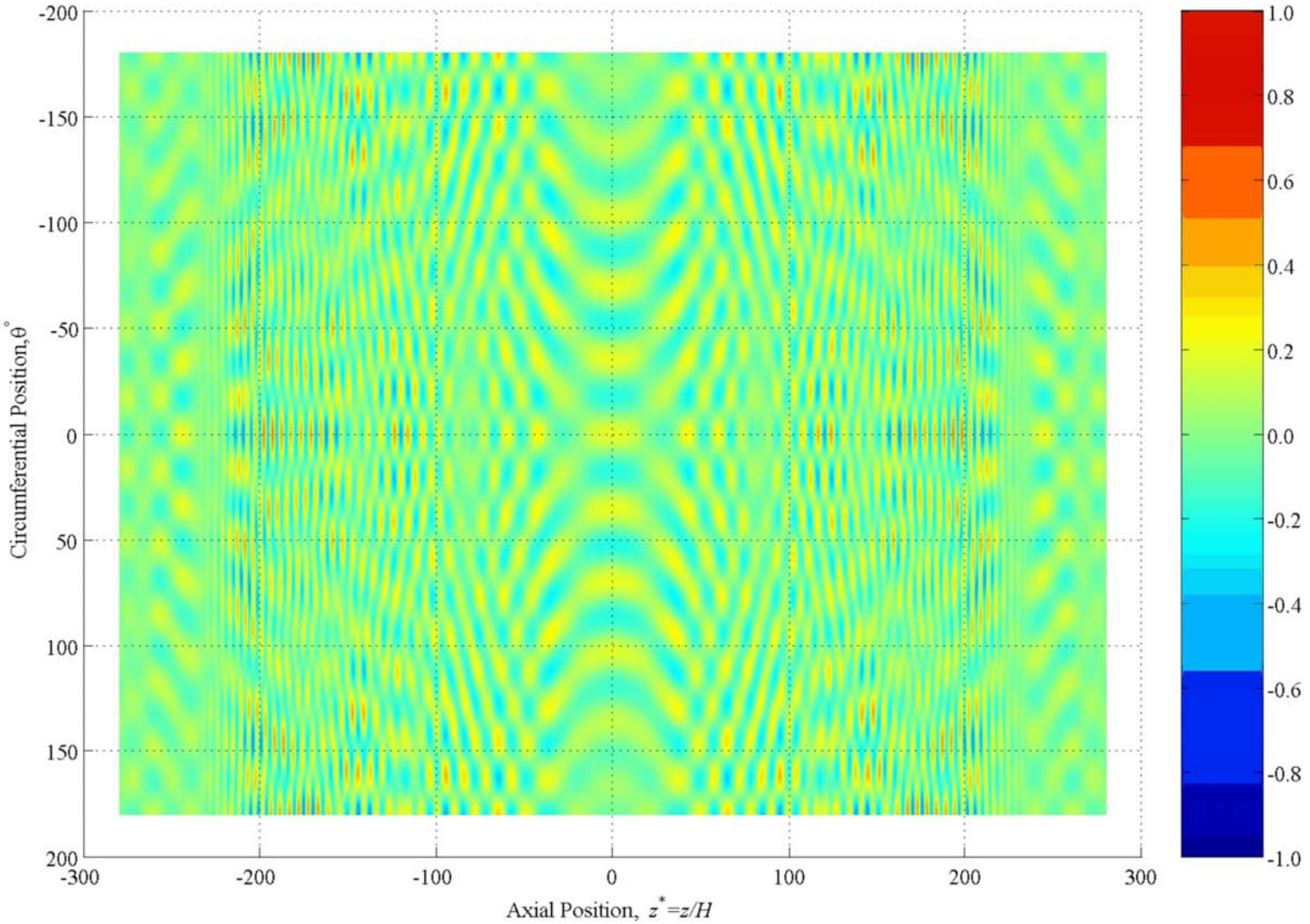

Figure 4.12 (b). Plan View of Radial Displacement at t^*=285.4

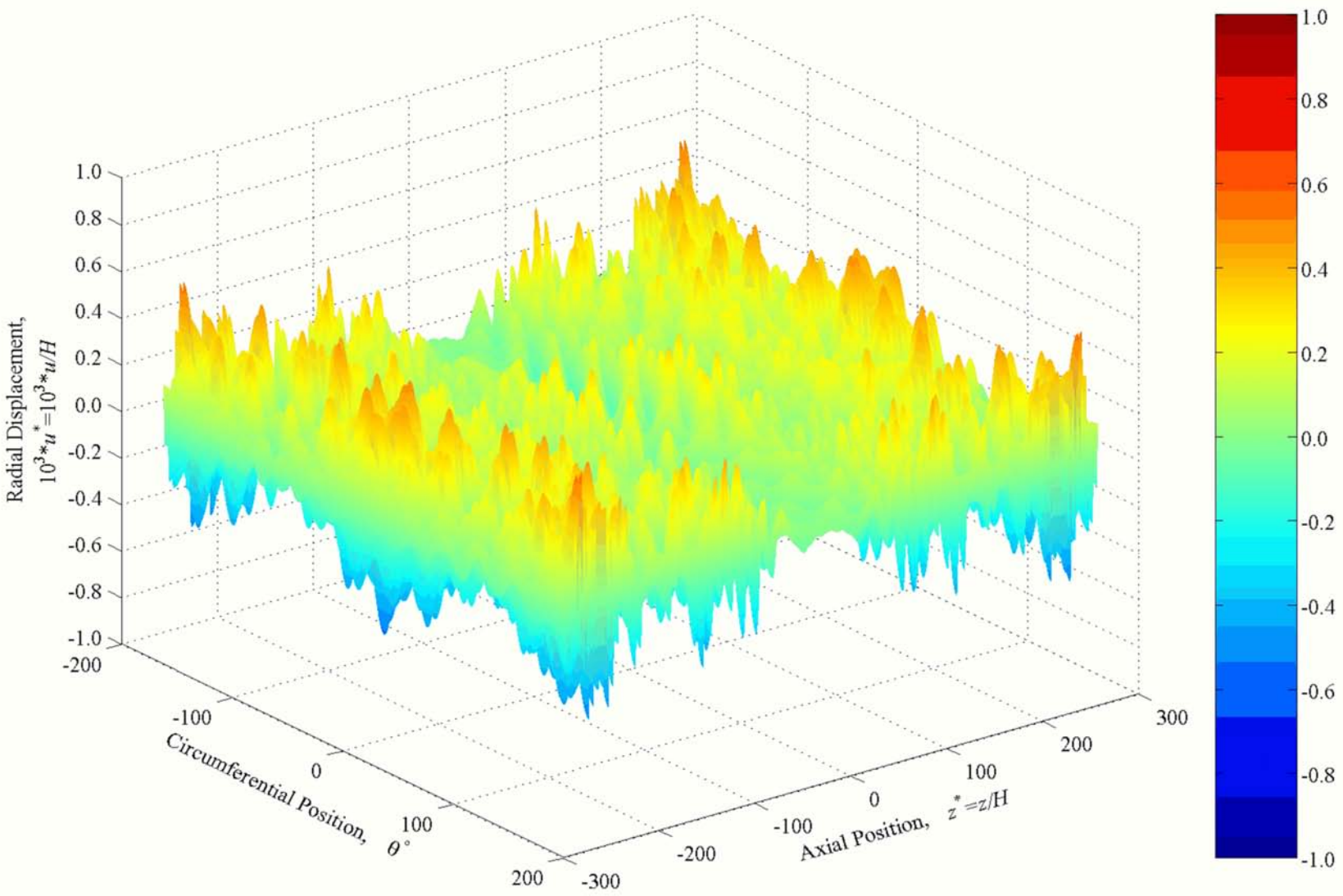

Figure 4.13 (a). Perspective View of Radial Displacement at t^*=346.6

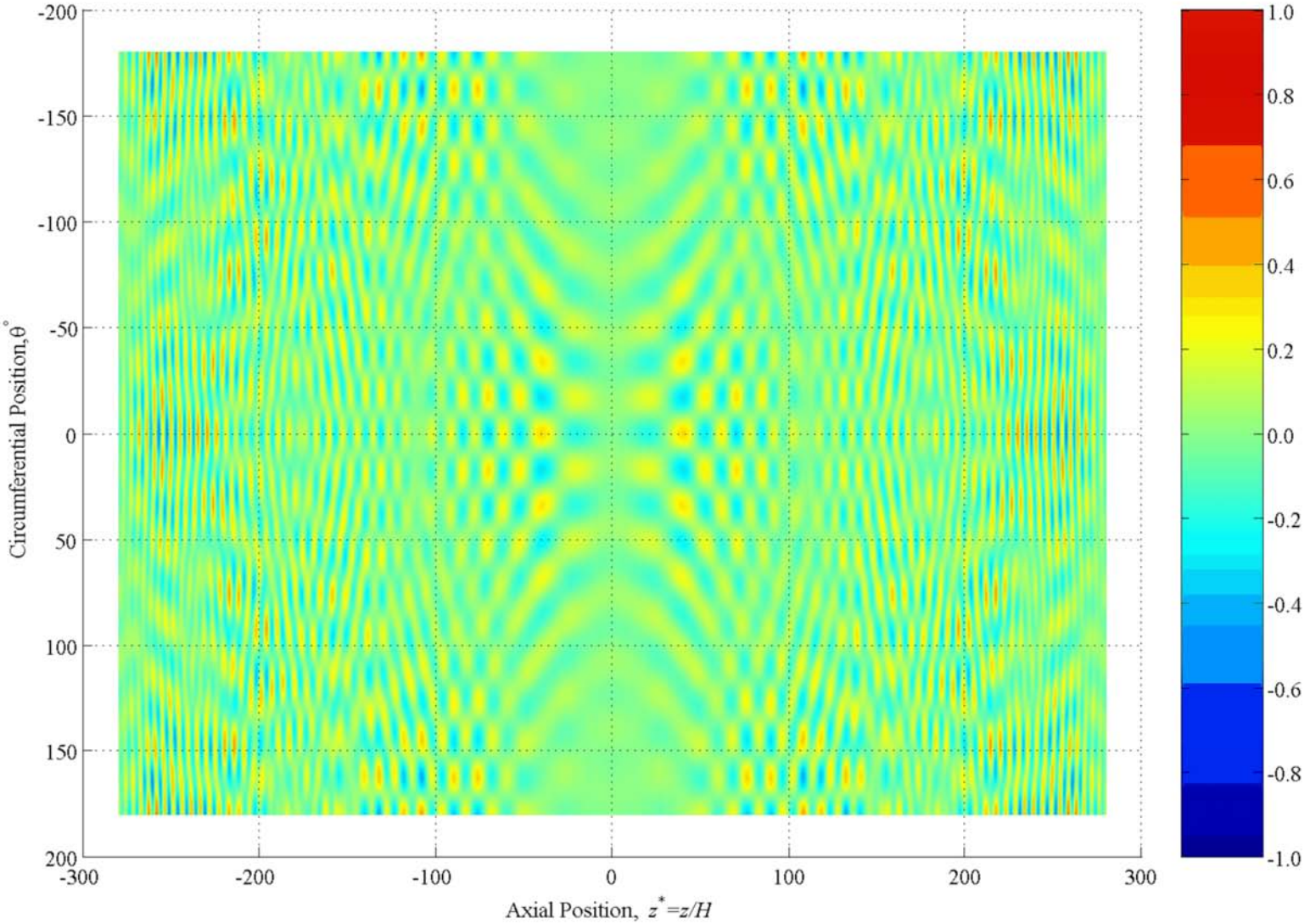

Figure 4.13 (b). Plan View of Radial Displacement at t^*=346.6

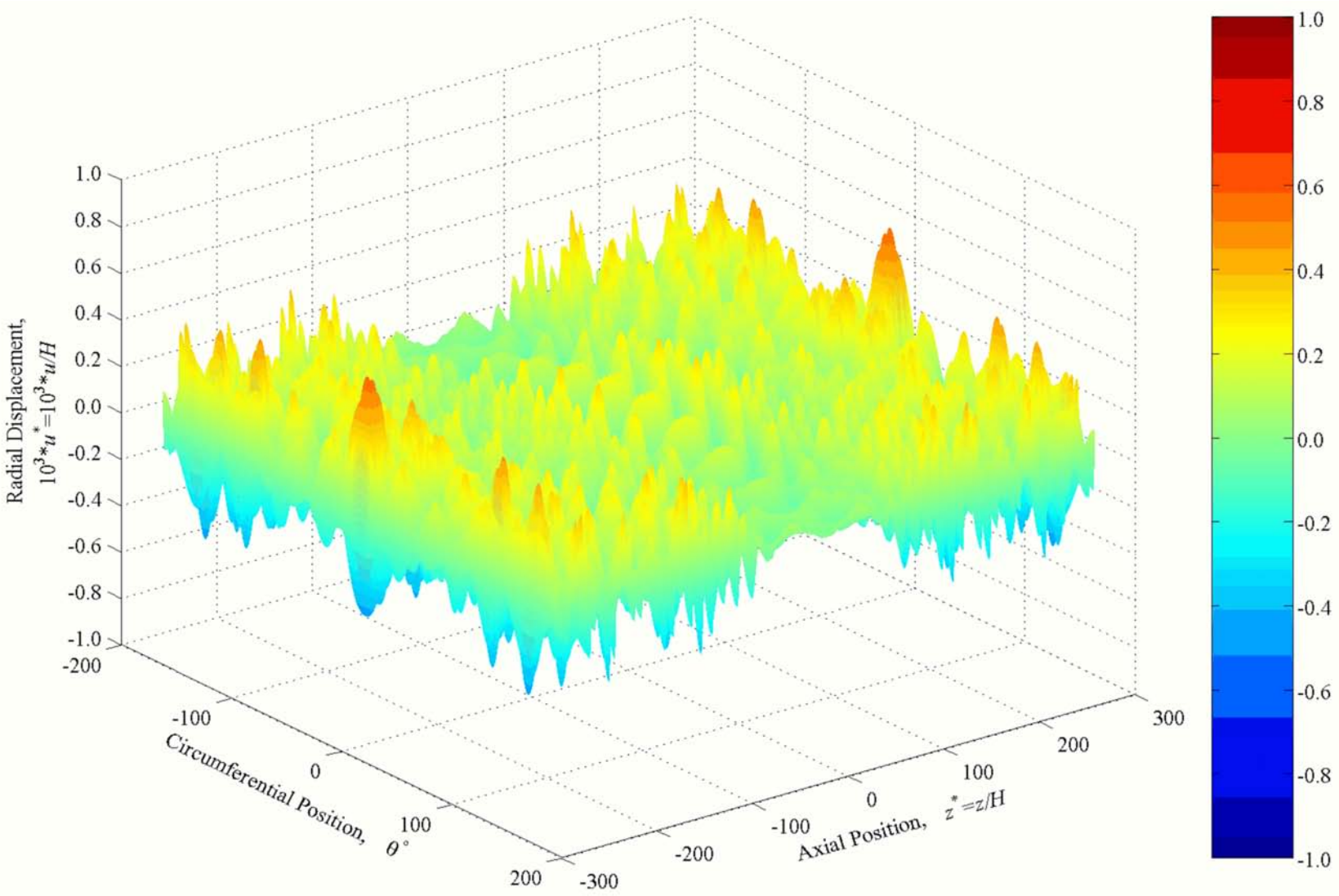

Figure 4.14 (a). Perspective View of Radial Displacement at t^*=407.8

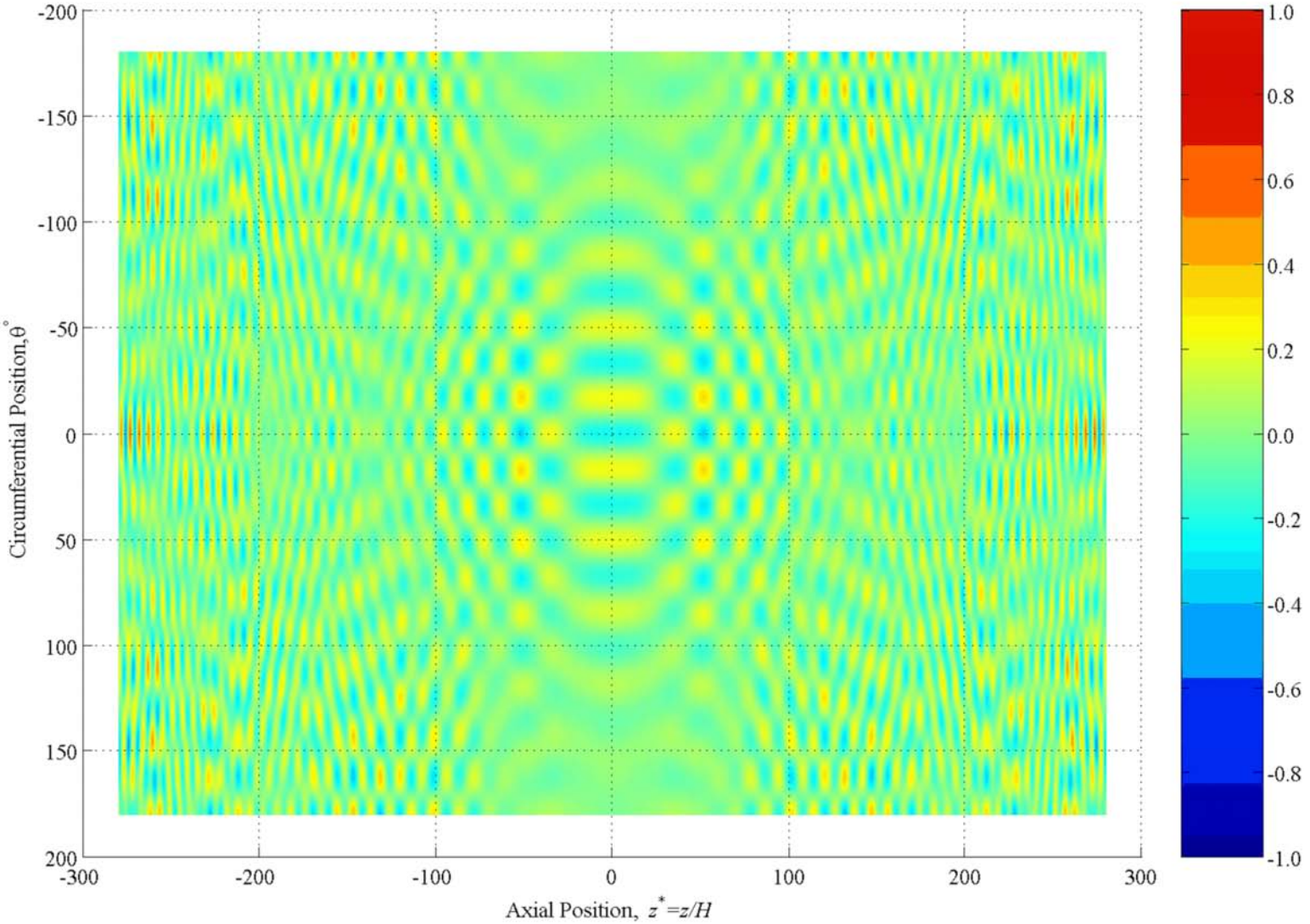

Figure 4.14 (b). Plan View of Radial Displacement at t^*=407.8

Chapter 5 - Conclusions and Recommendations

5.1 Conclusions

By convolving the Green's functions of a virgin steel pipe with a transient, normal point load, the resulting dynamic radial displacement is calculated at more than 230,000 points on the pipe's outer surface to simulate a typical experiment. The functions are calculated on personal computers (in a distributed arrangement) by employing modal summation. The mode shapes are obtained from a Semi-Analytical Finite Element formulation used in conjunction with a separation of variables. Data are presented in a four dimensional animation, providing easier interpretations and insight into how to best select observation points for the detection of defects, say. The accuracy of the calculated displacements is verified experimentally. Agreement, although imperfect, is good when magnitude and phase corrections are incorporated from the frequency response curves of the experimental transducers. The evolution of the radial displacement field can be used with confidence to provide a "baseline" for comparisons with a degraded pipe.

5.2 Recommendations

The following issues remain.

1. The pipe's material properties should be determined experimentally and compared to the standard textbook values assumed.
2. A perturbation study should be undertaken to assess the sensitivity of a pipe's response to "small"[+] changes in its material properties and geometry.

[+] In this context "small" refers to changes that are the same order as the uncertainty of a typical measurement the of material properties and the pipe's geometry.

3. Only normalized comparisons between measured and predicted radial displacements have been presented because an absolute displacement reference is not available. A cost feasibility study should be conducted to assess the potential of using an optical (laser) based displacement measurement technique to overcome this problem.

4. The current technique of locating transducers by "hand" is extremely tedious, time consuming, somewhat variable, and potentially error prone. A feasibility study should be conducted to assess the potential of automation to reduce the measurement time as well as to improve the consistency and precision of the measurements.

5. The method used to improve the lack of causality and reduce the ringing (caused by the approximation of the inverse Fourier transform) is not computationally effective. Alternative signal processing techniques should be examined.

6. Due to the extraordinary computational expense associated with recovering the radial displacement field over such a large portion of the pipe, the numerical processes used should be examined to determine if they could be made more efficient.

7. An analogous study to that presented should be conducted on a pipe having a vertical, surface breaking, circumferential crack to provide insight into how to best select methods to ultrasonically detect and characterize defects in pipes.

8. The effect of the experimental transducer's finite contact area should be examined in more detail, both numerically and experimentally.

Bibliography

[1] W. Zhuang, "Numerical Modeling for Elastodynamic Problems in Laminated Composite Cylinders." Ph.D. Thesis, University of Manitoba, 1999.

[2] W. Zhuang, A. H. Shah, and S. B. Dong, "Elastodynamic Green's Function for Laminated Anisotropic Circular Cylinders," *Journal of Applied Mechanics, Transactions of the ASME*, vol. 66, no. 3, pp. 665-674, 1999.

[3] Non Destructive Testing Association, "http://www.winzurf.co.nz/ndta," 1996.

[4] NDT Resource Center, "http://www.ndt-ed.org/EducationResources/CommunityCollege/Ultrasonics/cc_ut_index.htm," Iowa State University, 2001.

[5] Southwest Research Institute, *Nondestructive Testing: A Survey*. Washington: Technology Utilization Office, National Aeronautics and Space Administration, 1973.

[6] National Aeronautics and Space Administration, "Preferred Reliability Practices: Ultrasonic Testing of Aerospace Materials, Practice No. PT-TE-1422,"1999.

[7] Alberta Energy and Utilities Board, "Pipeline Performance in Alberta 1980-1997," Alberta Energy and Utilities Board, Calgary, Alberta, Canada,1998.

[8] N. Rattanawangcharoen, "Propagation and Scattering of Elastic Waves in Laminated Circular Cylinders." Ph.D. Thesis, University of Manitoba, 1993.

[9] M. Kley, C. Valle, L. J. Jacobs, J. Qu, and J. Jarzynski, "Development of Dispersion Curves for Two-layered Cylinders Using Laser Ultrasonics," *Journal of the Acoustical Society of America*, vol. 106, no. 2, pp. 582-588, 1999.

[10] D. N. Alleyne and P. Cawley, "Excitation of Lamb Waves in Pipes Using Dry-coupled Piezoelectric Transducers," *Journal of Nondestructive Evaluation*, vol. 15, no. 1, pp. 11-20, 1996.

[11] J. L. Rose and M. J. Quarry, "Feasibility of Ultrasonic Guided Waves for Non-Destructive Evaluation of Gas Pipelines," Gas Research Institute, Chicago, Illinois,1999.

[12] E. Pan, J. Rogers, S. K. Datta, and A. H. Shah, "Mode Selection of Guided Waves for Ultrasonic Inspection of Gas Pipelines with Thick Coating," *Mechanics of Materials*, vol. 31, no. 3, pp. 165-174, 1999.

[13] H. Kwun, S. Y. Kim, M. S. Choi, and S. M. Walker, "Torsional Guided-wave Attenuation in Coal-Tar-Enamel-Coated, Buried Piping," *NDT and E International*, vol. 37, no. 8, pp. 663-665, 2004.

[14] M. G. Silk and K. F. Bainton, "Propagation in Metal Tubing of Ultrasonic Wave Modes Equivalent to Lamb Waves," *Ultrasonics*, vol. 17, no. 1, pp. 11-19, 1979.

[15] W. Mohr and P. Hoeller, "On Inspection of Thin-walled Tubes for Transverse and Longitudinal Flaws by Guided Ultrasonic Waves," *IEEE Transactions on Sonics and Ultrasonics*, vol. SU-23, no. 5, pp. 369-374, 1976.

[16] D. N. Alleyne, M. J. S. Lowe, and P. Cawley, "Reflection of Guided Waves from Circumferential Notches in Pipes," *Journal of Applied Mechanics, Transactions of the ASME*, vol. 65, no. 3, pp. 635-641, 1998.

[17] M. J. S. Lowe, D. N. Alleyne, and P. Cawley, "Mode Conversion of a Guided Wave by a Part-Circumferential Notch in a Pipe," *Journal of Applied Mechanics, Transactions of the ASME*, vol. 65, no. 3, pp. 649-656, 1998.

[18] J. L. Rose, S. P. Pelts, and M. J. Quarry, "Comb Transducer for Mode Control in Guided Wave NDE," in *Proceedings of the IEEE Ultrasonics Symposium,* 2nd ed Toronto, Canada: IEEE, Piscataway, NJ, USA, 1997, pp. 1033-1036.

[19] J. L. Rose, S. P. Pelts, and M. J. Quarry, "Comb Transducer Model for Guided Wave NDE," *Ultrasonics*, vol. 36, no. 1-5, pp. 163-169, 1998.

[20] S. P. Pelts, D. Jiao, and J. L. Rose, "Comb Transducer for Guided Wave Generation and Mode Selection," in *Proceedings of the IEEE Ultrasonics Symposium,* 2 nd ed San Antonio, TX, USA: IEEE, Piscataway, NJ, USA, 1996, pp. 857-860.

[21] J. J. Ditri, J. L. Rose, and A. Pilarski, "Generation of Guided Waves in Hollow Cylinders by Wedge and Comb Type Transducers," in *Review of Progress in Quantitative Nondestructive Evaluation,* 12 ed. D. O. Thompson and D. E. Chimenti, Eds. New York: Plenum Press, 1993, pp. 211-218.

[22] W. Zhu, "An FEM Simulation for Guided Elastic Wave Generation and Reflection in Hollow Cylinders with Corrosion Defects," *Journal of Pressure Vessel Technology, Transactions of the ASME*, vol. 124, no. 1, pp. 108-117, 2002.

[23] W. Zhu, "A Finite Element Analysis of the Time-delay Periodic Ring Arrays for Guided Wave Generation and Reception in Hollow Cylinders," *IEEE Transactions on Ultrasonics, Ferroelectrics, and Frequency Control*, vol. 48, no. 5, pp. 1462-1470, 2001.

[24] W. Zhu and J. L. Rose, "Lamb Wave Generation and Reception with Time-delay Periodic Linear Arrays: a BEM Simulation and Experimental Study," *IEEE Transactions on Ultrasonics, Ferroelectrics, and Frequency Control*, vol. 46, no. 3, pp. 654-664, 1999.

[25] J. Li and J. L. Rose, "Excitation and Propagation of Non-axisymmetric Guided Waves in a Hollow Cylinder," *Journal of the Acoustical Society of America*, vol. 109, no. 2, pp. 457-464, 2001.

[26] T. Hayashi, K. Kawashima, Z. Sun, and J. L. Rose, "Analysis of Flexural Mode Focusing by a Semianalytical Finite Element Method," *Journal of the Acoustical Society of America*, vol. 113, no. 3, pp. 1241-1248, 2003.

[27] L. Pochhammer, "Uber Die Fortpflanzungsgeschwindigkeiten Kleiner Schwingungen in Einem Unbegrenzten Isotropen Kreiszylinder," *Journal fur die Reine und Angewandte Mathematik*, vol. 81, pp. 324-336, 1876.

[28] C. Chree, "The Equations of an Isotropic Elastic Solid in Polar and Cylindrical Coordinates, Their Solutions and Applications," *Transactions of the Cambridge Philosophical Society*, vol. 14, pp. 250-269, 1889.

[29] W. A. Green, "Dispersion Relations for Elastic Waves in Bars," in *Progress in Solid Mechanics*. I. N. Sneddon and R. Hill, Eds. Amsterdam: North-Holland Publishing Company, 1960, pp. 225-261.

[30] D. Bancroft, "The Velocity of Longitudinal Waves in Cylindrical Bars," *Physical Review*, vol. 59, pp. 588-593, 1941.

[31] M. Onoe, H. D. McNiven, and R. D. Mindlin, "Dispersion of Axially Symmetric Waves in Elastic Rods," *Journal of Applied Mechanics, Transactions of the ASME*, vol. 29, pp. 729-734, 1962.

[32] D. C. Gazis, "Three-Dimensional Investigation of Propagation of Waves in Hollow Circular Cylinders," *Journal of the Acoustical Society of America*, vol. 31, no. 5, pp. 568-578, 1959.

[33] A. E. Armenakas, D. C. Gazis, and G. Herrmann, *Free Vibrations of Circular Cylindrical Shells*, 1st ed. Oxford: Pergamon Press, 1969.

[34] H. Bai, "Elastic Wave Scattering in Cracked Cylinders." Ph.D. Thesis, University of Manitoba, 2002.

[35] H. D. McNiven, J. L. Sackman, and A. H. Shah, "Dispersion of Axially Symmetric Waves in Composite, Elastic Rods," *Journal of the Acoustical Society of America*, vol. 35, no. 10, pp. 1602-1609, 1963.

[36] A. E. Armenakas, "Torsional Waves in Composite Rods," *Journal of the Acoustical Society of America*, vol. 38, no. 3, pp. 439-446, 1965.

[37] H. E. Keck and A. E. Armenakas, "Wave Propagation in Transversely Isotropic, Layered Cylinders," *Journal of Engineering Mechanics*, vol. 97, pp. 541-558, 1971.

[38] N. Rattanawangcharoen and A. H. Shah, "Guided Waves in Laminated Isotropic Circular Cylinders," *Computational Mechanics*, vol. 10, no. 2, pp. 97-105, 1992.

[39] R. B. Nelson, S. B. Dong, and R. D. Karla, "Vibrations and Waves in Laminated Orthotropic Circular Cylinders," *Journal of Sound and Vibration*, vol. 18, no. 3, pp. 429-444, 1971.

[40] K. H. Huang and S. B. Dong, "Propagating Waves and Edge Vibrations in Anisotropic Composite Cylinders," *Journal of Sound and Vibration*, vol. 96, no. 3, pp. 363-379, 1984.

[41] N. Rattanawangcharoen, A. H. Shah, and S. K. Datta, "Wave Propagation in Laminated Composite Circular Cylinders," *International Journal of Solids and Structures*, vol. 29, no. 6, pp. 767-781, 1992.

[42] H. D. McNiven, "Extensional Waves in Semi-Infinite Elastic Rods," *Journal of the Acoustical Society of America*, vol. 33, no. 1, pp. 23-27, 1961.

[43] H. D. McNiven and A. H. Shah, "The Influence of End Mode on the Resonant Frequencies of Finite, Hollow, Elastic Rods," *Journal of Sound and Vibration*, vol. 6, pp. 8-19, 1967.

[44] J. Zemanek, "An Experimental and Theoretical Investigation of Elastic Wave Propagation in a Cylinder," *Journal of the Acoustical Society of America*, vol. 51, no. 1, pp. 265-283, 1972.

[45] N. Rattanawangcharoen, W. Zhuang, A. H. Shah, and S. K. Datta, "Axisymmetric Guided Waves in Jointed Laminated Cylinders," *Journal of Engineering Mechanics*, vol. 123, no. 10, pp. 1020-1026, 1997.

[46] W. Zhuang, A. H. Shah, and S. K. Datta, "Axisymmetric Guided Wave Scattering by Cracks in Welded Steel Pipes," *Journal of Pressure Vessel Technology, Transactions of the ASME*, vol. 119, no. 4, pp. 401-406, 1997.

[47] H. Bai, A. H. Shah, N. Popplewell, and S. K. Datta, "Scattering of Guided Waves by Circumferential Cracks in Steel Pipes," *Journal of Applied Mechanics, Transactions of the ASME*, vol. 68, no. 4, pp. 619-631, 2001.

[48] H. Bai, A. H. Shah, N. Popplewell, and S. K. Datta, "Scattering of Guided Waves by Circumferential Cracks in Composite Cylinders," *International Journal of Solids and Structures*, vol. 39, no. 17, pp. 4583-4603, 2002.

[49] K. F. Graff, *Wave Motion in Elastic Solids*. Oxford: Clarendon Press, 1975.

[50] A. Mahmoud, A. H. Shah, and N. Popplewell, "Parallel Hybrid Algorithm for Three-Dimensional Elastic Wave Scattering in Steel Pipes," *Journal of Pressure Vessel Technology*, vol. 126, no. 4, pp. 510-517, 2004.

[51] M. J. S. Lowe, D. N. Alleyne, and P. Cawley, "Defect Detection in Pipes Using Guided Waves," *Ultrasonics*, vol. 36, no. 1-5, pp. 147-154, 1998.

[52] The MathWorks, Inc., "http://www.mathworks.com/access/helpdesk/help/techdoc/ref/unwrap.html (unwrap [MATLAB Functions])," 2004.

[53] W. H. Press, *Numerical Recipes in C++ the Art of Scientific Computing*, 2nd ed. Cambridge, UK: Cambridge University Press, 2002.

[54] W. D. Callister, *Materials Science and Engineering an Introduction*, 4th ed. New York: John Wiley & Sons, 1997.

[55] S. Banerjee, "Damage Detection in Homogeneous Plates and Layered Composites Using Ultrasonic Waves." Master of Technology Dissertation, Indian Institute of Technology, Bombay, 2001.

[56] Panametrics, Inc., "GE Panametrics Transducer Catalog," 2004.

Appendix A - Input Signal

A.1 Functional Form of Input Signal

The input signal used here is a Gaussian modulated sine function which is given in the time domain by:

$$f(t)=\begin{cases} 0, & t<0 \\ Ae^{(-a(st-\tau)^2)}\sin(s\omega_0 t), & t\geq 0\,. \end{cases} \tag{A.1}$$

The A, a, τ, and ω_0 are constants, t is time, in seconds, and s is a scaling factor which is related to the digital representation of equation (A.1) afforded by the arbitrary waveform generator. The scaling factor is used to set the "centre frequency" of the Gaussian modulated sine wave. The Fourier transform [see equation (2.62)] of equation (A.1) is determined using Maple® 8.00 by Maplesoft™ to be:

$$F(\omega)=\left\{\frac{-jA\sqrt{\pi}}{4s\sqrt{a}}\left[e^{\frac{(\omega+s\omega_0)(-\omega-s\omega_0+4j\tau as)}{4as^2}}-e^{\frac{(\omega-s\omega_0)(-\omega+s\omega_0+4j\tau as)}{4as^2}}\right.\right.$$
$$+erf\left(\frac{j\omega+2as\tau+js\omega_0}{2s\sqrt{a}}\right)e^{\frac{(\omega+s\omega_0)(-\omega-s\omega_0+4j\tau as)}{4as^2}} \tag{A.2}$$
$$\left.\left.-erf\left(\frac{2as\tau+j\omega-js\omega_0}{2s\sqrt{a}}\right)e^{\frac{(\omega-s\omega_0)(-\omega+s\omega_0+4j\tau as)}{4as^2}}\right]\right.$$

where *erf* is the complex error function defined by:

$$erf(x)=\frac{2}{\sqrt{\pi}}\int_0^x e^{-\sigma^2}d\sigma \tag{A.3}$$

and σ is a dummy parameter. For the experimental work, the constants A, a, τ, ω_0 are taken to be:

$$\begin{aligned} A &= 20\ V \\ a &\approx 2.29592\times10^{10}\ s^{-2} \\ \tau &= 1.4\times10^{-5}\ s \\ \omega_0 &= (5\times10^5)\pi\ rad/s, \end{aligned} \tag{A.4}$$

and

$$\begin{aligned} A &= 1\ \text{(Non-dimensional force)} \\ a &\approx 2.29592\times10^{10}\ s^{-2} \\ \tau &= 1.4\times10^{-5}\ s \\ \omega_0 &= (5\times10^5)\pi\ rad/s, \end{aligned} \tag{A.5}$$

for the computer predictions. The scaling factor, s, is selected to give the desired centre frequency. The relation between the centre frequency, f_c in Hz and s is:

$$f_c = (2.5\times10^5\ Hz)\,s. \tag{A.6}$$

Hence, for a centre frequency of 70 kHz, s equals 0.28. The constants a, τ, and ω_0 are selected to agree with those used in [55], while the selected s gives the centre frequency used in [16;17]. Time and frequency domain representations of the input signal for the constants given in equation (A.4) and s equals 0.28 are shown in Figure A.1. Note that this signal is smooth (differentiable) in both time and frequency. It has a relatively short duration, a relatively narrow frequency band and the signal is essentially band limited. The short duration is useful for "time of flight" applications, and the narrow band frequency behaviour allows the Fourier transform of the function to be approximated conveniently using a finite bandwidth.

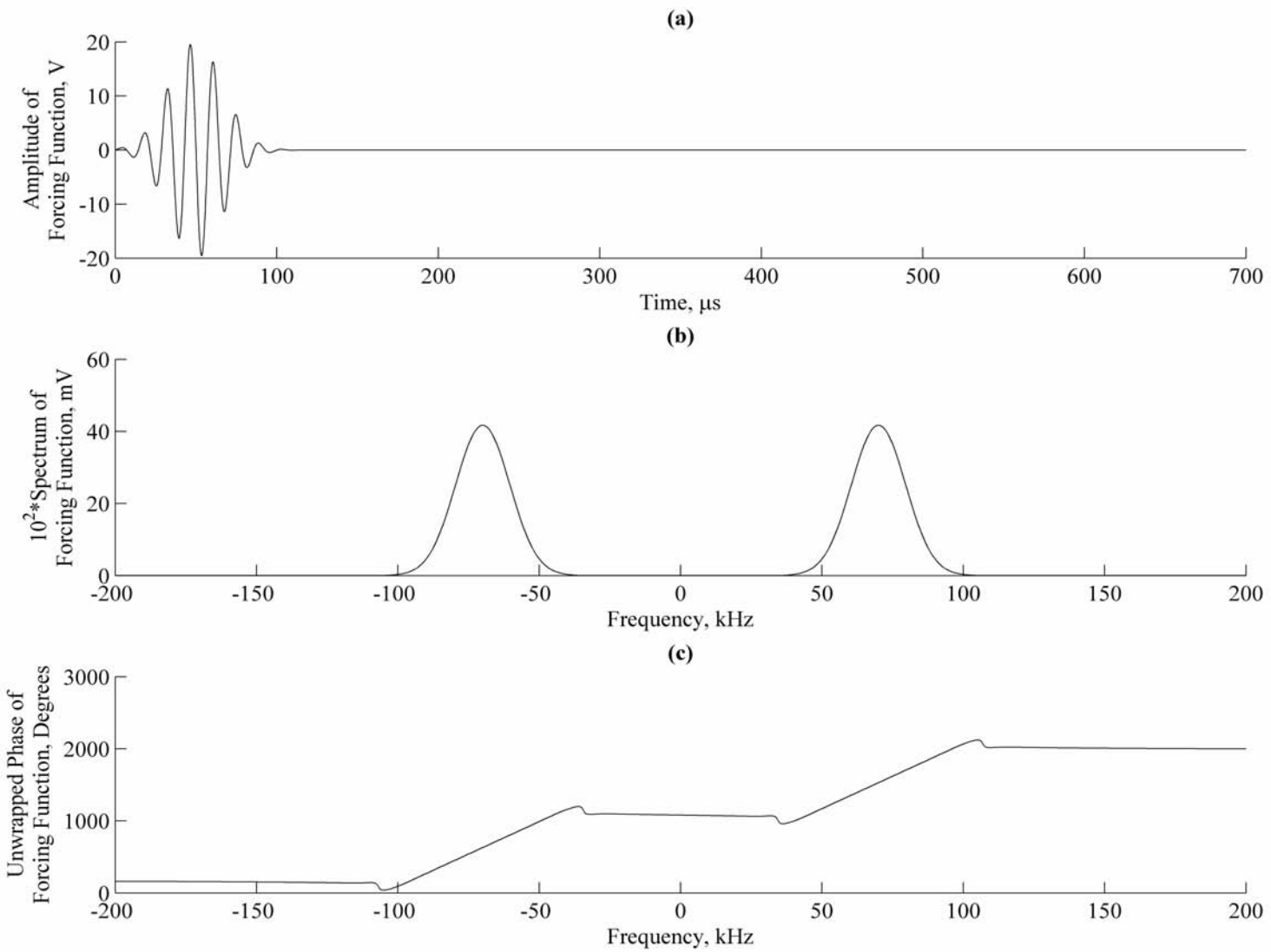

Figure A.1. Forcing Function With Centre Frequency of 70 kHz

Appendix B - Electronic Media

B.1 Contents of Electronic Media

Figure B.1 provides an annotated listing of the contents contained on the accompanying electronic media. The content is divided into four categories; Animations, Codecs, Normalized Transducer Transfer Functions, as well as Programs and Scripts. Each category is detailed next.

B.2 Animations and Codecs

The animation category contains the plan and perspective views of the radial component of the (steady state) Green's function for the cylinder's outer surface when the cylinder is subjected to a radially acting, point harmonic load having a non-dimensional frequency of 0.755. Furthermore, plan and perspective views are given of the (time) evolution of the radial displacement field when the forcing function described in Appendix A is used with a centre frequency of 70 kHz. Both sets of animations are in the same format as the analogous figures presented in Chapter 4. The animations are in Microsoft® Audio Video Interleave (AVI) format and they are compressed using the Indeo® video 5 codec (a Win32 implementation is contained in the Codec directory). These animations should be viewable on any Win32 platform for which appropriate viewing software is available. The animations of the Green's functions show the steady state, dynamic displacement of the cylinder's outer surface over ten periods of vibration. Consecutive frames are separated by 0.35 μs increments. The radial displacement animations show the evolution up to 700 μs after the load is applied. The time difference between consecutive frames is 0.35 μs again.

B.3 Normalized Transducer Transfer Functions

The normalized transducer transfer functions are provided in two formats for both the DWC B225 transmitter and receiver. The first format is the Matlab® mat format over the forcing bandwidth. The second format is ASCII Comma Separated Value (CSV) over the frequency bandwidth of each transducer. The files are as noted in Figure B.1.

B.4 Programs and Scripts

Contained in this category are the FORTRAN programs and Matlab® script files used in Chapter 2 for which copyright is available. The files are indicated again in Figure B.1. The FORTRAN programs are given in source code and Win32 binary executable form and sample input files are given. The Matlab® script files are provided as is. They will most likely need modifiying to suit future requirements. The documentation for the programs and script files is limited to the comments made in the source code.

```
CD-ROM Root
+---Animations
|  +---Radial_Component_of_Displacement_Green's_Function_Animation
|  |      Perspective_View_of_Radial_Component_of_Green's_Function-OMEGA=0.755.avi
|  |      Plan_View_of_Radial_Component_of_Green's_Function-OMEGA=0.755.avi
|  |
|  \---Radial_Displacement_Animation
|         Perspective_View-Radial_Displacement.avi
|         Plan_View-Radial_Displacement.avi
|
+---Codec
|      iv5setup.exe
|
+---Normalized_Transducer_Transfer_Functions
|      FRTR.mat (Receiver in Matlab format over forcing bandwidth)
|      FRTT.mat (Transmitter in Matlab format over forcing bandwidth)
|      NTTF-R.csv (Receiver in ASCII text format over transducer bandwidth)
|      NTTF-T.csv (Transmitter in ASCII text format over transducer bandwidth)
|
\---Programs_and_Scripts
   +---EVP1 (Recover wavenumber for a given frequency, written by H. Bai [34])
   |      evp1.exe (Win32 Executable)
   |      evp1.f (Source code)
   |      evp11.dat (Configuration file)
   |      evp11.nam (Name file)
   |
   +---EVP2 (Recover frequency for a given wavenumber, written by H. Bai [34])
   |      evp2.dat (Configuration file)
   |      EVP2.exe (Win32 Executable)
   |      evp2.f (Source code)
   |      evp2.nam (Name file)
   |
   +---Invert_to_Time
   |      maketime1.m (Extract required data from output of sumup)
   |      maketmw.m (Evaluate inverse Fourier Transform)
   |
   +---Ring (Compute displacements and stresses for a given circumferential harmonic,
   |               written by W. Zhuang [1], modified by D.K.S.)
   |      ring.dat (Configuration file)
   |      ring.exe (Win32 Executable)
   |      ring.f (Source code)
   |      ring.nam (Name file)
   |
   +---Split_Interlaced_Files
   |      split.m
   |
   \---Sum_Over_Circumferential_Wavenumbers
          makesum.m (Used to recurse directory structure to run sumup)
          sumup.m (Perform sum over circumferential wavenumbers to give FRF)
```

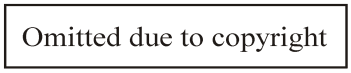

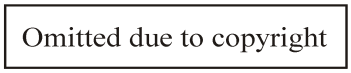

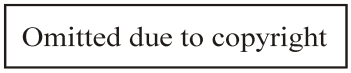

Figure B.1. Annotated Contents of Electronic Media

Appendix C - Signal Averaging

C.1 Signal Averaging

Noise is present in any experimental data acquisition. It is appropriate to use time averaging here in order to reduce the noise of the measured displacements because the signals are repeatable and the noise is incoherent. Hence a signal is measured many times and its true value is taken to be the arithmetic average over all the separate measurements. The *i*-th sample of the time averaged displacement, $\bar{X}_i$, is given by:

$$\bar{X}_i = \frac{1}{N}\sum_{j=1}^{N} x_{ij} \qquad \textbf{(C.1)}$$

where x_{ij} is the *i*-th sample of the radial displacement, say, obtained in the *j*-th measurement and *N* corresponds to the total number of measurements. Unless noted otherwise, 50 measurements are made for the measured displacements presented here.

Figure C.1 illustrates the effectiveness of time averaging. Figure C.1 (a) shows the output (radial displacement) measured when no input (radial force) is applied to the pipe. Only one measurement is made so there is effectively no averaging. Ideally the output should be identically zero but an examination of Figure C.1 shows this is definitely not the case. The Root Mean Square (RMS) average value is about 2.2 mV where the RMS average value, $\bar{X}_{RMS}$, is defined as:

$$\bar{X}_{RMS} = \sqrt{\frac{1}{N}\sum_{i=1}^{N} (x_i)^2} \qquad \textbf{(C.2)}$$

and x_i is the *i*-th sample, while *N* is the number of measurements same. Figure C.1 (b) again

shows the output measured when no input is applied to the pipe, but time averaging is now applied for 50 separate trials. This signal is clearly much closer to the ideal zero than the previous signal with no time averaging. The RMS value of this signal is about 0.4 mV or about 20 percent of the RMS value with no time averaging. (Note that this figure includes a constant offset that has not been filtered out.) Time averaging is clearly an effective method of reducing the incoherent measurement noise.

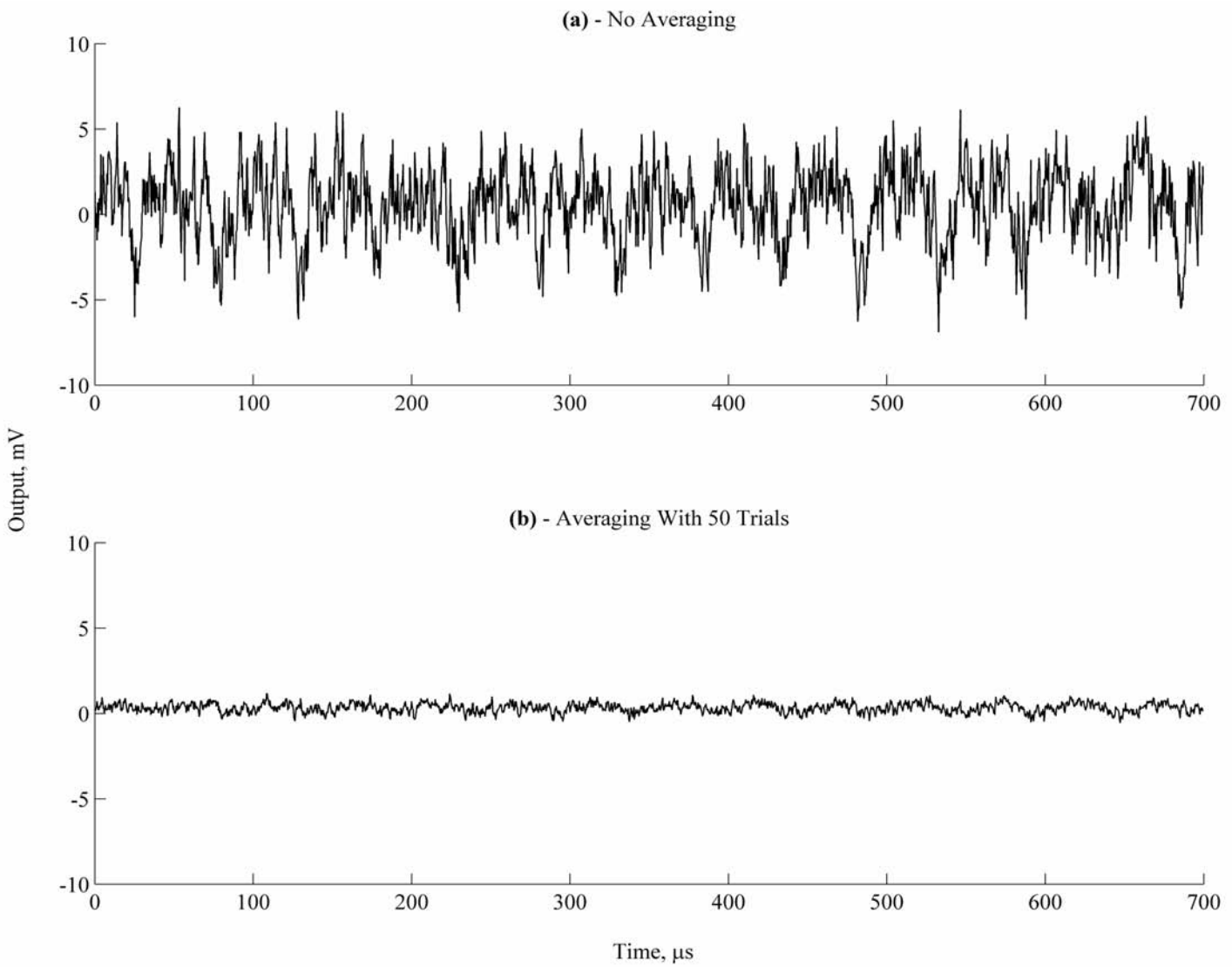

Figure C.2. Traces Illustrating Improvement of Noise With Averaging Over 50 Trials

Appendix D - Manufacturer's Data Sheets and Calibration Curves For the Ultrasonic Transducers and Pre-Amplifiers

D.1 Overview

A brief overview is given in this Appendix of the ultrasonic transducers and pre-amplifiers used. Manufacturer supplied, data sheets and calibration curves are reproduced where available. The discussion is given in two parts; the first part refers to the DWC transducers, the second part applies to the GE Panametrics transducer. A discussion of the pre-amplifier follows later.

D.2 Transducers

D.2.1 DWC Transducers

The DWC transducers are a piezoelectric contact type. The Original Equipment Manufacturer (OEM) specifications indicate that a voltage proportional to the normal component of the displacement vector is produced at a perfectly coupled surface when the transducer operates as a "receiver." It is assumed that the transducers produce a force proportional to the applied voltage when operated as a "transmitter." The nominal contact areas of the B1080LD, B1025, and B225 ultrasonic transducers are 0.0309±0.0002 in^2 (0.200±0.002 cm^2), 0.0995±0.0004 in^2 (0.642±0.003 cm^2), and 0.1099±0.0005 in^2 (0.709±0.003 cm^2), respectively. The manufacturer's data sheet for the B1080LD (B1025) [B225] transducer appears in Figure D.1 (D.4) [D.9], and the applicable, manufacturer supplied, calibration curves appear in Figures D.2 (D.5) [D.10] through D.3 (D.8) [D.15].

D.2.2 General Electric Panametrics Transducer

The GE Panametrics X1054, narrow band transducer is a piezoelectric contact type. It is only used here as a transmitter. From the GE Panametrics transducer catalogue [56], the leading "X" in the serial number indicates that this transducer is the "Miscellaneous" type and, therefore, limited technical data is available. The nominal area of the contact surface of the GE Panametrics X1054 ultrasonic transducer is 0.0491±0.0004 in^2 (0.317±0.003 cm^2). No manufacturer's data sheet is available for this transducer. The applicable, manufacturer supplied, calibration curves appear in Figure D.16.

D.3 Digital Wave Corporation PA2040G/A Pre-amplifiers

The DWC PA2040G/A pre-amplifiers have a selectable (voltage) gain of -20 dB, 0 dB, 20dB, or 40 dB when terminated into a 50 Ω impedance. They are low noise amplifiers. Their frequency responses are assumed reasonably to be essentially "flat" over their operating range as operational amplifiers are the active components. The manufacturer's data sheet for these amplifiers appears in Figure D.17.

B1080 Series Sensors

The B1080 AE Sensors are high fidelity, piezoelectric transducers. They are designed specifically for modal acoustic emission (MAE) measurements over a frequency range from 50 kHz to 2 MHz. The B1080 sensors employ a low Q piezoelectric ceramic in a rugged package that is 0.20" in diameter by 0.36" in height . The B1080 comes with an attached 2 foot, shielded, low noise cable and can be used with Digital Wave's external line driver and up to 125' of additional BNC cable.

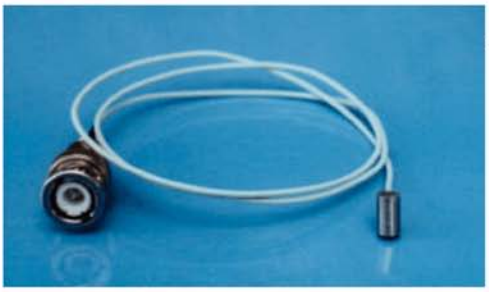

B1080 Specifications

Frequency Bandwidth: 50 kHz - 2 MHz
Temperature Range: -50°C - 100°C
Connector: Attached 2 foot cable
Dimensions: 0.20" OD x 0.36" H
Piezoelectric Crystal: 0.125" dia.

Also available:
B1080LD with an integral line driver

Common uses of the B1080

. metal fatigue
. aircraft inspection
. modal acoustic emission
. computer peripherals-hard disk monitoring

Key Attributes

. low mass-small
. broadband response

B1080 Calibration Curves

Absolute Surface Wave Calibration

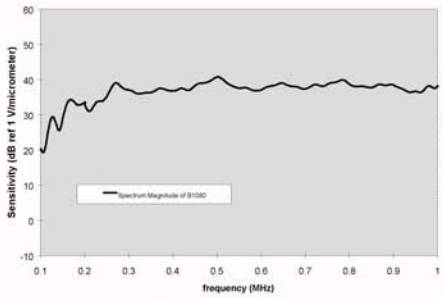

40dB = 100V/µm

Face-to-Face Calibration

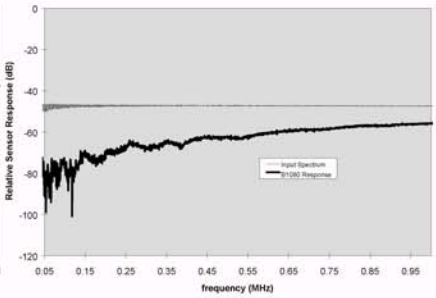

Generator: B1025
Receiver: B1080

11234A East Caley Avenue
Englewood, Colorado 80111
USA

DIGITAL WAVE™

Phone: (303) 790-7559
FAX: (303) 790-7567
info@digitalwavecorp.com

Figure D.1. DWC Supplied Data Sheet for B1080 Transducers

DIGITAL WAVE

DIGITAL WAVE CORPORATION 11234-A East Caley Avenue, Englewood, CO 80111 (303) 790-7559 FAX (303) 790-7567

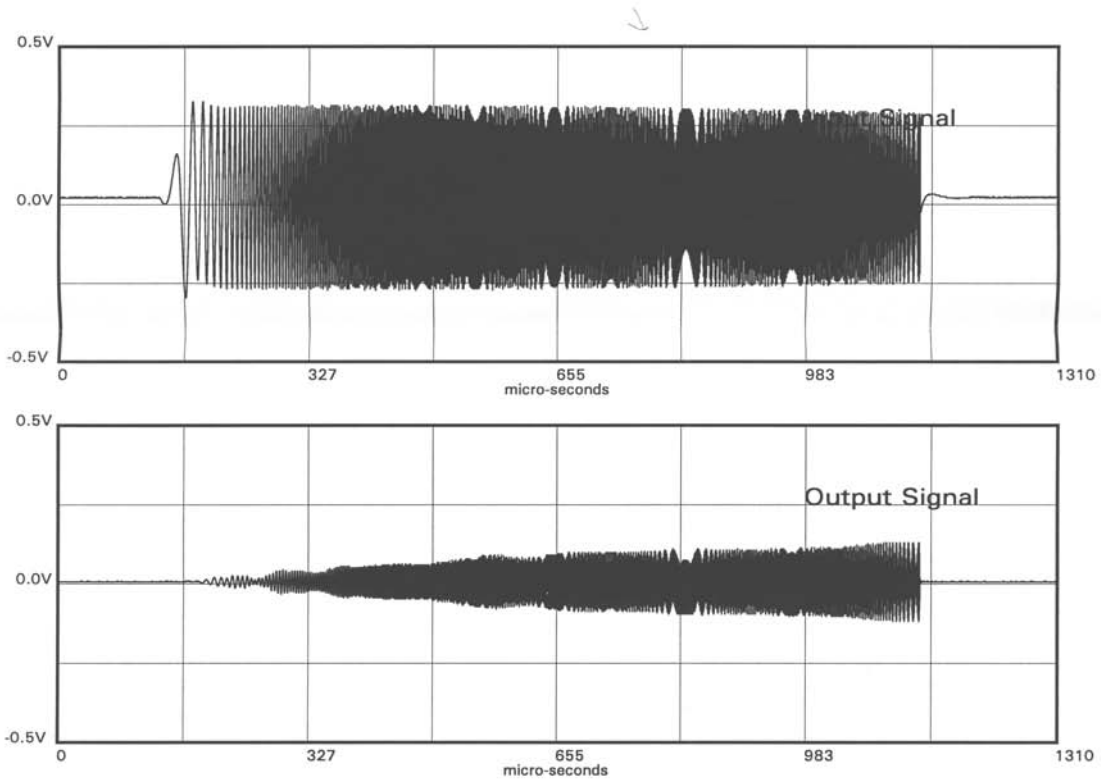

Swept Sine Wave Face-to-Face Sensor Calibration

Frequency Range:	1kHz - 1.5MHz
DUT:	B1080 LD
S/N:	0697098
Couplant:	Vacuum Grease
Contact Force:	3.0
Recorder:	DWC F4000
Gain:	6
Preamplifier:	DWC PA2040G/A
Gain:	20
Date:	04/24/01
Tested By:	RF

RW 4/25/01

Figure D.2. DWC Supplied Calibration Curve for B1080 LD Transducer (With Serial Number 0697098) in the Time Domain

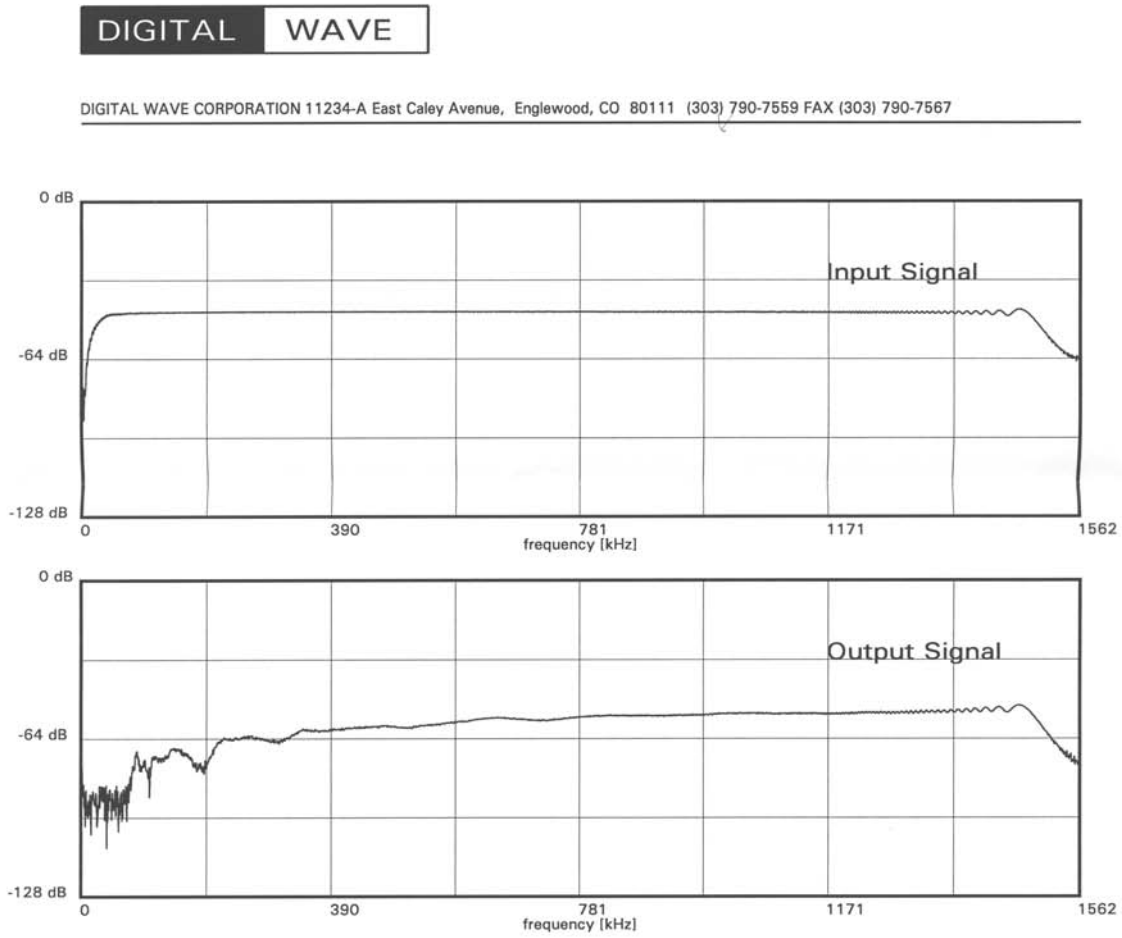

Figure D.3. DWC Supplied Calibration Curve for B1080 LD Transducer (With Serial Number 0697098) in the Frequency Domain

B1025 Series Sensors

The B1025 AE Sensors are high fidelity, piezoelectric transducers. They are designed specifically for modal acoustic emission (MAE) measurements over a frequency range from 50 kHz to 2 MHz. The B1025 sensors employ a low Q piezoelectric ceramic in a rugged package that is 0.365" in diameter by 0.50" in height with a microdot or BNC connector. Low noise, shielded signal cables are available in either three foot (3') or six foot (6') lengths.

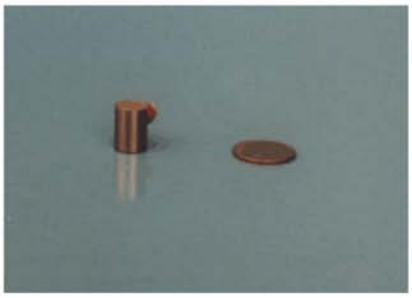

B1025 Specifications

Frequency Bandwidth:	50 kHz - 2 MHz
Temperature Range:	-50°C - 100°C
Connector:	Micro-dot or BNC
Dimensions:	0.365" OD x 0.5" H
Piezoelectric Crystal:	0.25" dia.

Also available:
B1025R in a ruggedized case
B1025HT for high temperature applications
B1025LD with a built in line driver

Common uses for the B1025

. metal fatigue
. aircraft inspection
. modal acoustic emission
. composite materials
. inspection of concrete
. pressure vessel inspection

Key Attributes

. broadband flat response
. general purpose testing

B1025 Calibration Curves

Absolute Surface Wave Calibration

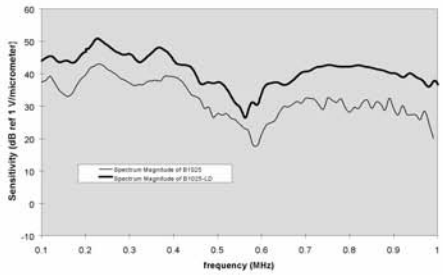

40dB = 100V/µm

Face-to-Face Calibration

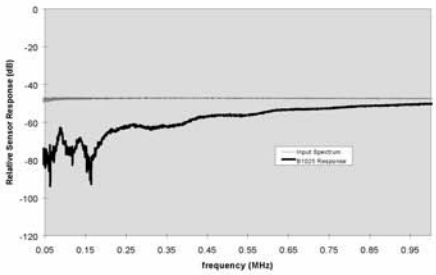

Generator: B1025
Receiver: B1025

www.digitalwavecorp.com

DIGITAL WAVE™

Figure D.4. DWC Supplied Data Sheet for B1025 Transducers

DIGITAL WAVE

DIGITAL WAVE CORPORATION 11234-A East Caley Avenue, Englewood, CO 80111 (303) 790-7559 FAX (303) 790-7567

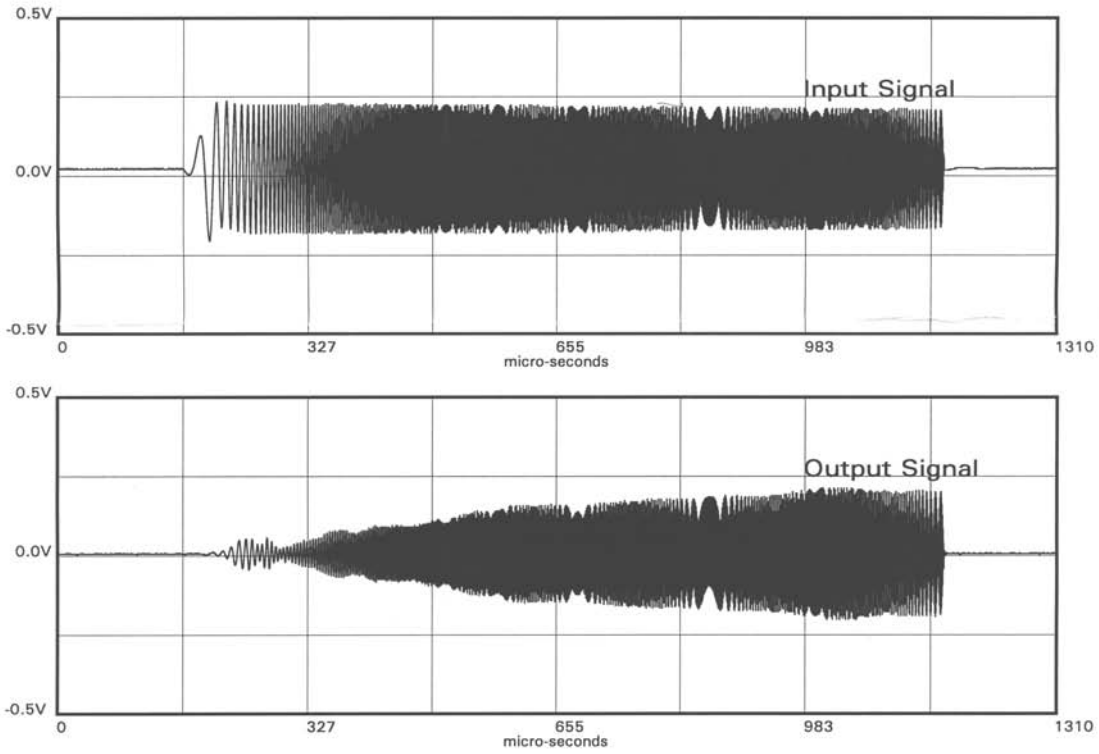

Swept Sine Wave Face-to-Face Sensor Calibration

Frequency Range:	1kHz - 1.5MHz
DUT:	B1025
S/N:	022020
Couplant:	Vacuum Grease
Contact Force:	3.0
Recorder:	DWC F4000
Gain:	18
Preamplifier:	DWC PA2040G/A
Gain:	20
Date:	12/12/02
Tested By:	MG

12/12/02

Figure D.5. DWC Supplied Calibration Curve for B1025 Transducer (With Serial Number 022020) in the Time Domain

DIGITAL WAVE

DIGITAL WAVE CORPORATION 11234-A East Caley Avenue, Englewood, CO 80111 (303) 790-7559 FAX (303) 790-7567

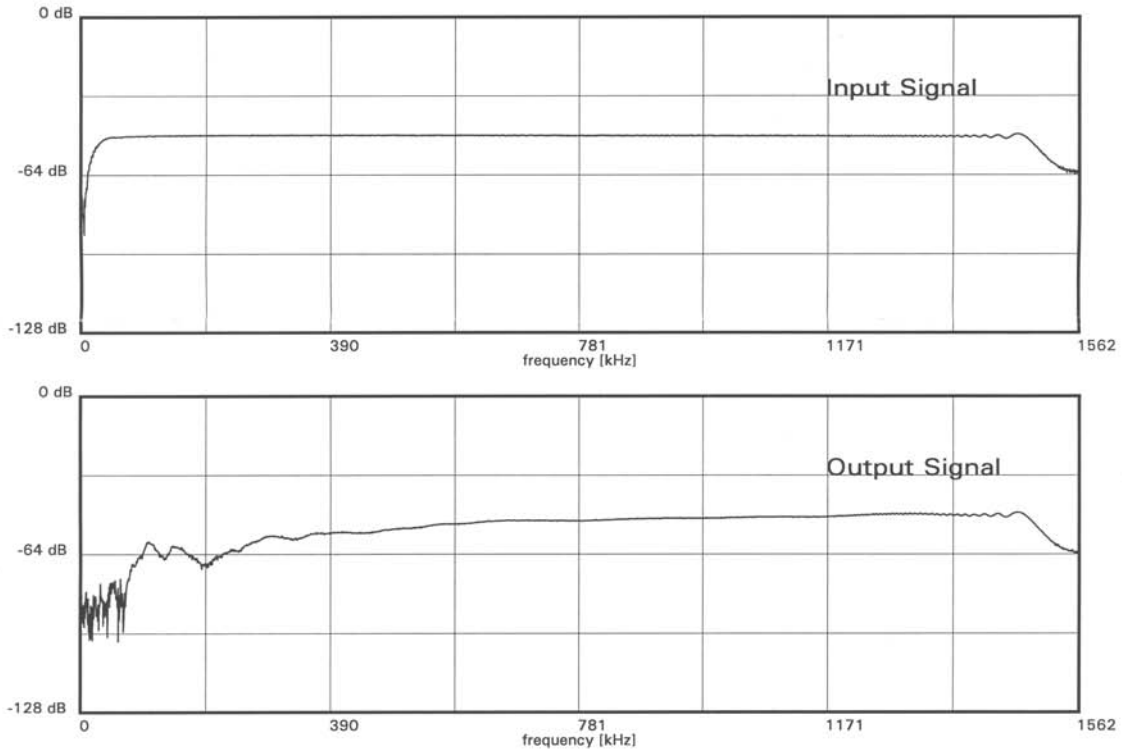

Swept Sine Wave Face-to-Face Sensor Calibration

Frequency Range:	1kHz - 1.5MHz
DUT:	B1025
S/N:	022020
Couplant:	Vacuum Grease
Contact Force:	3.0
Recorder:	DWC F4000
Gain:	1218
Preamplifier:	DWC PA2040G/A
Gain:	20
Date:	12/12/02
Tested By:	MG

Figure D.6. DWC Supplied Calibration Curve for B1025 Transducer (With Serial Number 022020) in the Frequency Domain

DIGITAL WAVE

DIGITAL WAVE CORPORATION 11234-A East Caley Avenue, Englewood, CO 80111 (303) 790-7559 FAX (303) 790-7567

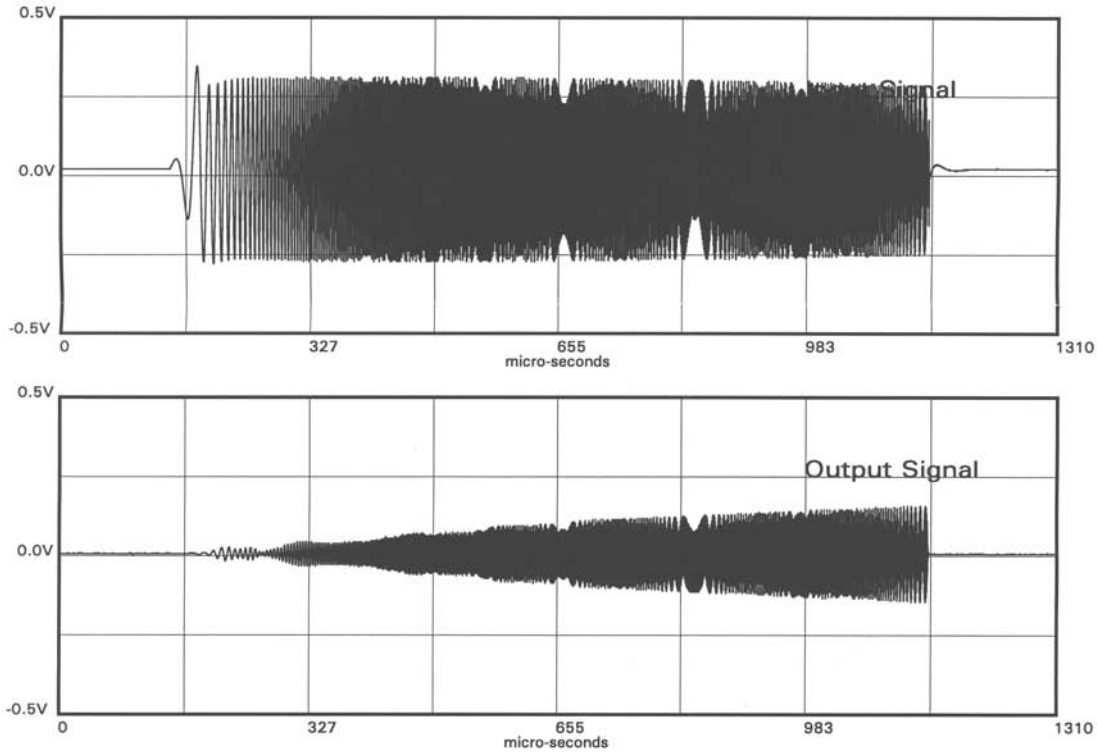

Swept Sine Wave Face-to-Face Sensor Calibration

Frequency Range:	1kHz - 1.5MHz
DUT:	B1025
S/N:	071087
Couplant:	Vacuum Grease
Contact Force:	3.0
Recorder:	DWC F4000
Gain:	18
Preamplifier:	DWC PA2040G/A
Gain:	20
Date:	08/22/01
Tested By:	RF

KW 8/22/01

Figure D.7. DWC Supplied Calibration Curve for B1025 Transducer (With Serial Number 071087) in the Time Domain

DIGITAL WAVE

DIGITAL WAVE CORPORATION 11234-A East Caley Avenue, Englewood, CO 80111 (303) 790-7559 FAX (303) 790-7567

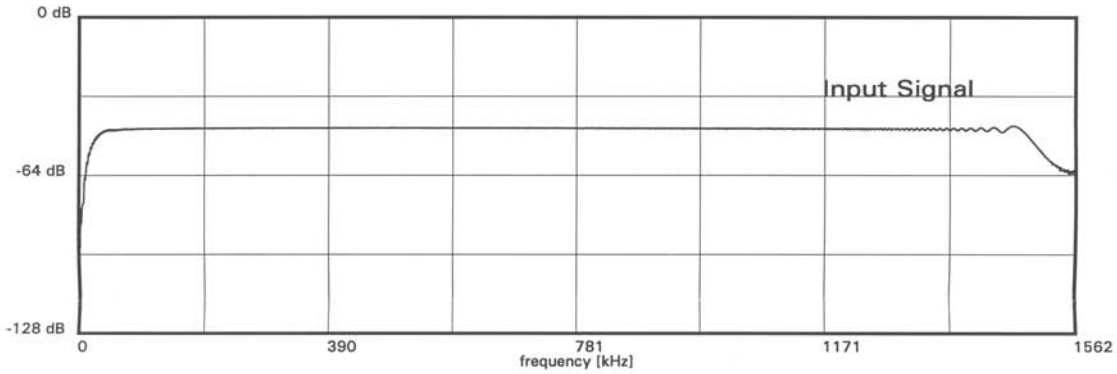

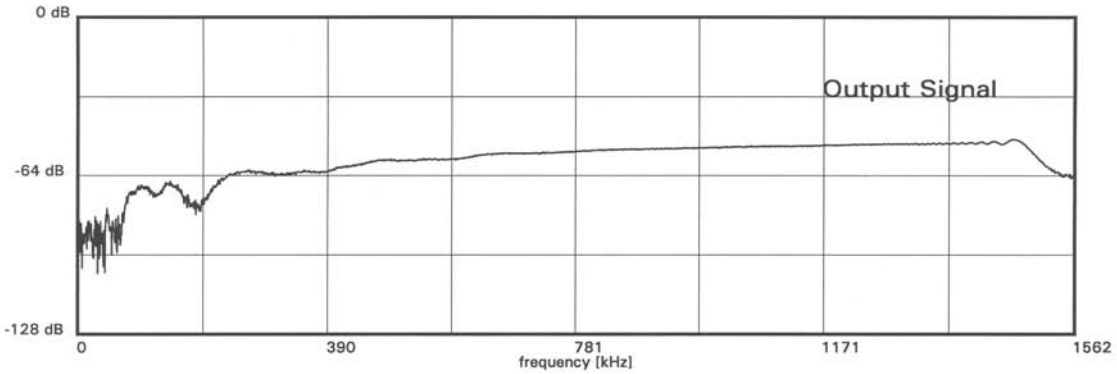

Swept Sine Wave Face-to-Face Sensor Calibration

Frequency Range:	1kHz - 1.5MHz
DUT:	B1025
S/N:	071087
Couplant:	Vacuum Grease
Contact Force:	3.0
Recorder:	DWC F4000
Gain:	18
Preamplifier:	DWC PA2040G/A
Gain:	20
Date:	08/22/01
Tested By:	RF

Figure D.8. DWC Supplied Calibration Curve for B1025 Transducer (With Serial Number 071087) in the Frequency Domain

B225 Series Sensors

The B225 provides additional sensitivity at low frequencies. The B225 is useful when inspecting thick plates or highly attenuative specimens. Low noise, shielded cables are available in either three foot (3') or six foot (6') lengths.

Frequency Bandwidth:	30 kHz - 300 kHz
Temperature Range:	-50ºC to 100ºC
Connector:	Micro-dot or BNC
Dimensions:	0.375" OD x 1.0" H

Also available:
B225LD with a built in line driver
B225-5 a 0.50" diameter B225

Common uses of the B225

. inspection of concrete
. inspection of metals with a large grain structure
. plate wave generation
. generates and receives in the LWI and VLF-UT systems
. metallic and composite applications
. metal pressure vessel inspection

Key Attributes

. low frequency pulser & receiver
. high sensitivity

Calibration Curve - B225

Absolute Calibration

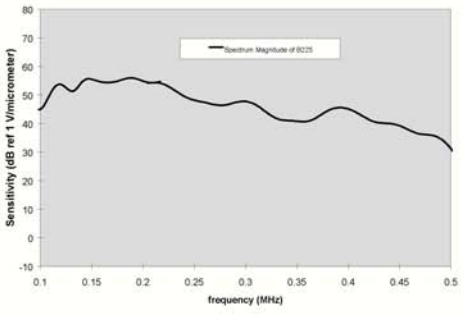

40dB = 100V/µm

Face-to-Face Calibration

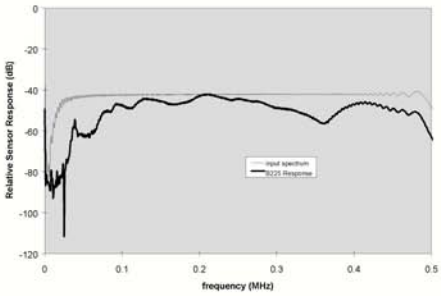

Generator: B1025
Receiver: B225

The Wave of the Future

DIGITAL WAVE™

Figure D.9. DWC Supplied Data Sheet for B225 Transducers

DIGITAL WAVE

DIGITAL WAVE CORPORATION 11234-A East Caley Avenue, Englewood, CO 80111 (303) 790-7559 FAX (303) 790-7567

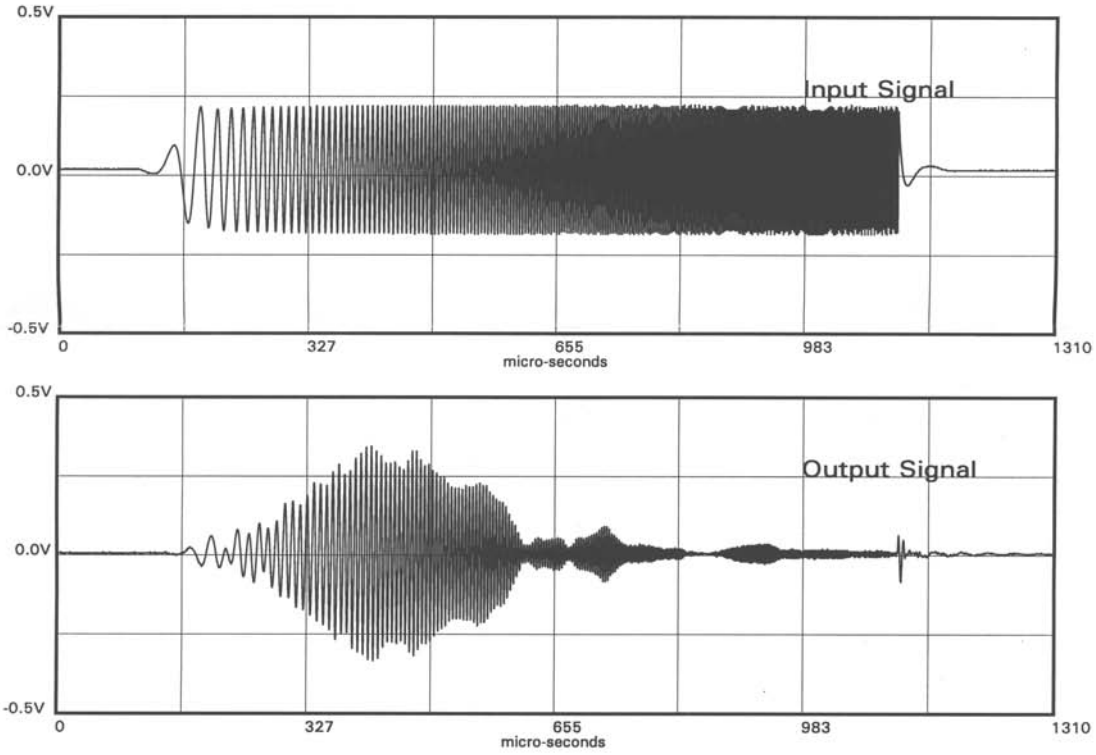

Swept Sine Wave Face-to-Face Sensor Calibration

Frequency Range:	1kHz - 500kHz
DUT:	B225
S/N:	022041
Couplant:	Vacuum Grease
Contact Force:	3.0
Recorder:	DWC F4000
Gain:	15
Preamplifier:	DWC PA2040G/A
Gain:	0
Date:	06/25/02
Tested By:	GW

GW 6/25/02

Figure D.10. DWC Supplied Calibration Curve for B225 Transducer (With Serial Number 022041) in the Time Domain

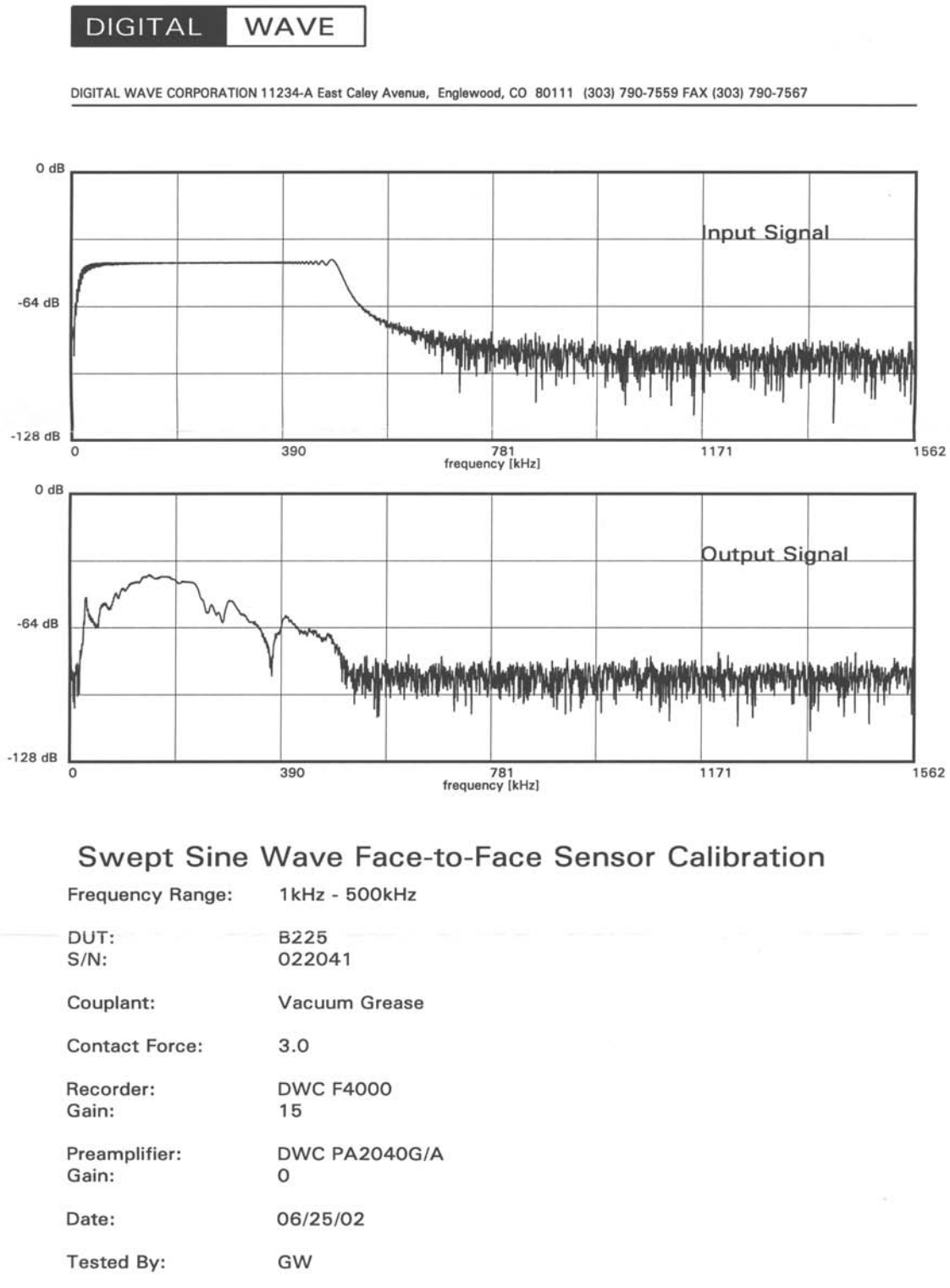

Figure D.11. DWC Supplied Calibration Curve for B225 Transducer (With Serial Number 022041) in the Frequency Domain

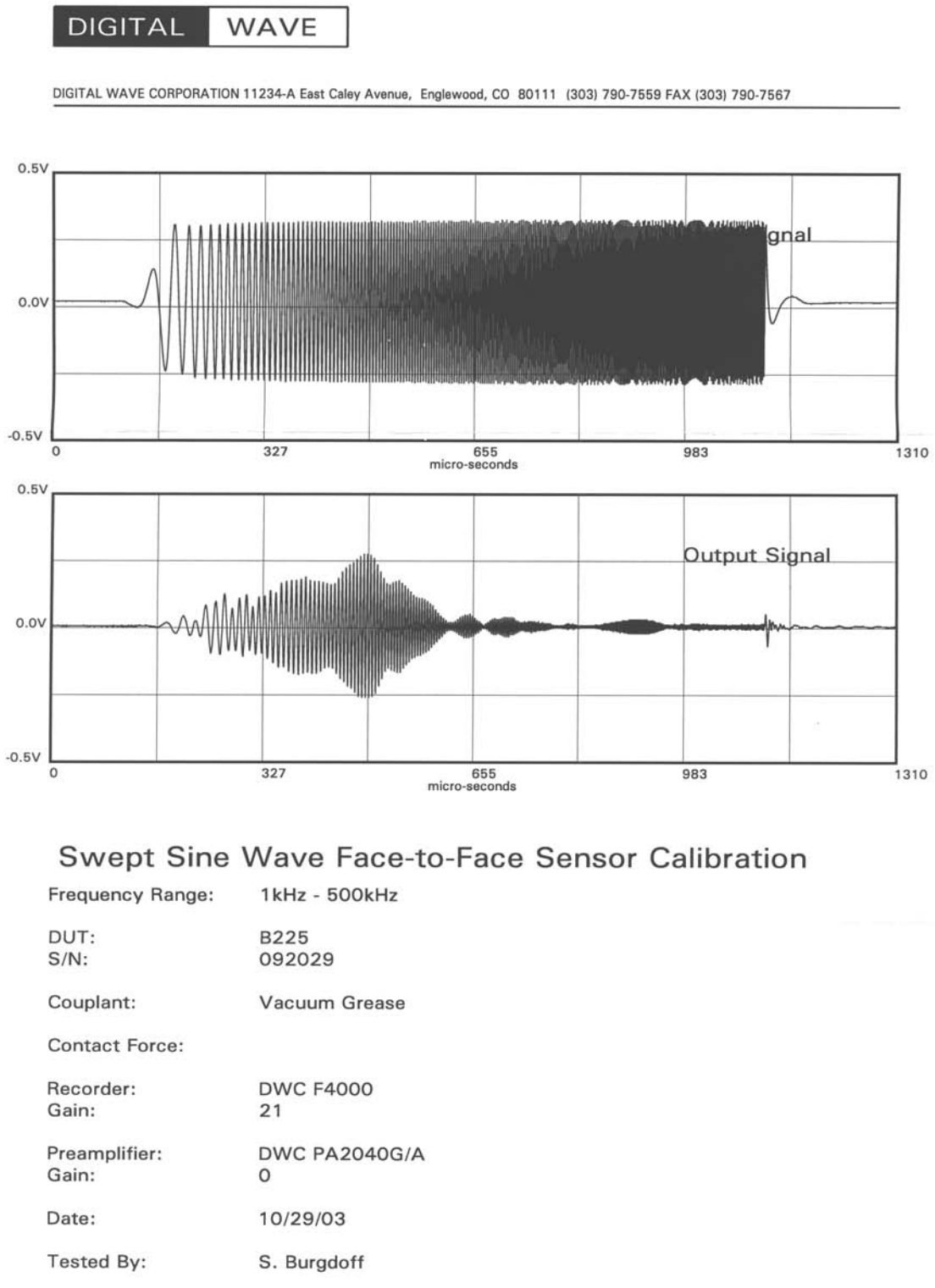

Figure D.12. DWC Supplied Calibration Curve for B225 Transducer (With Serial Number 092029) in the Time Domain

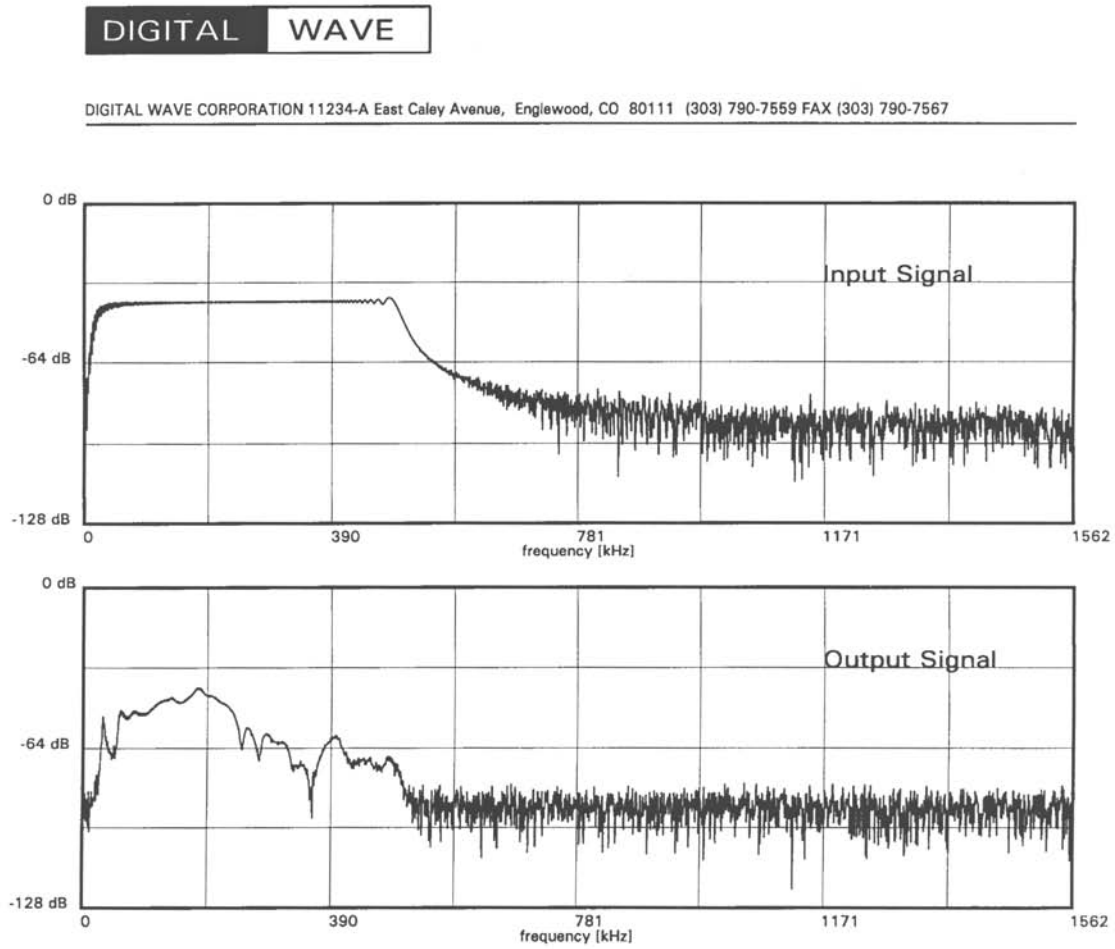

Figure D.13. DWC Supplied Calibration Curve for B225 Transducer (With Serial Number 092029) in the Frequency Domain

DIGITAL WAVE

DIGITAL WAVE CORPORATION 11234-A East Caley Avenue, Englewood, CO 80111 (303) 790-7559 FAX (303) 790-7567

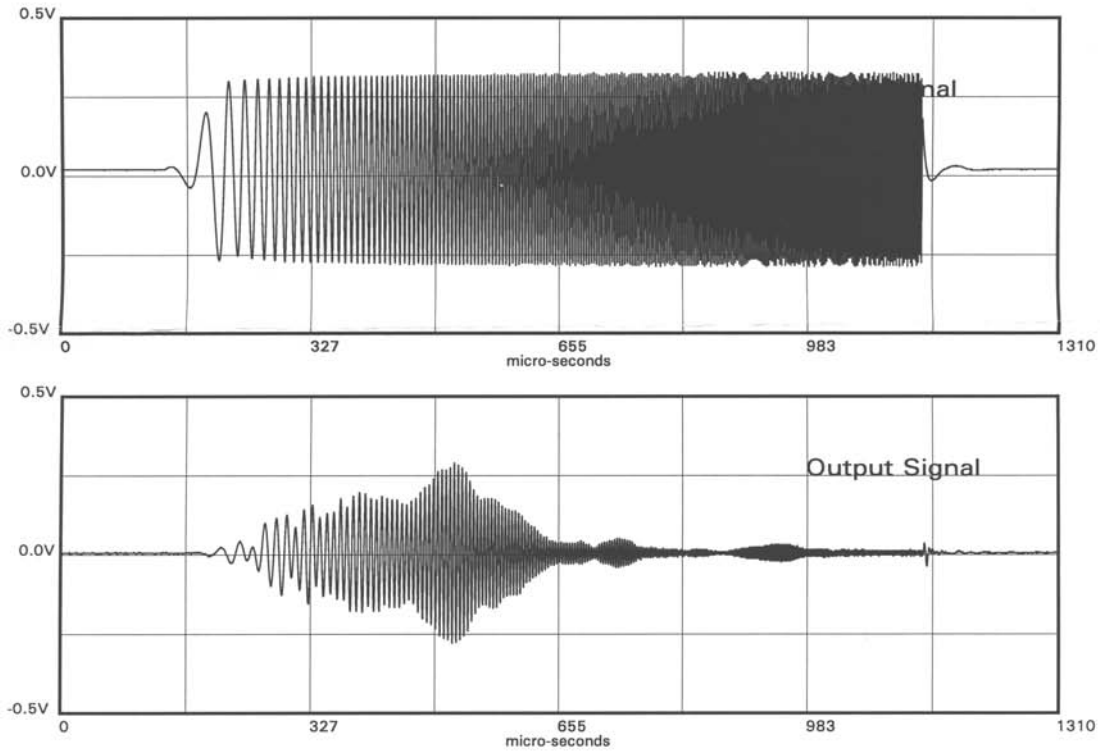

Swept Sine Wave Face-to-Face Sensor Calibration

Frequency Range:	1kHz - 500kHz
DUT:	B225
S/N:	092035
Couplant:	Vacuum Grease
Contact Force:	
Recorder:	DWC F4000
Gain:	21
Preamplifier:	DWC PA2040G/A
Gain:	0
Date:	10/29/03
Tested By:	S. Burgdoff

Figure D.14. DWC Supplied Calibration Curve for B225 Transducer (With Serial Number 092035) in the Time Domain

DIGITAL WAVE

DIGITAL WAVE CORPORATION 11234-A East Caley Avenue, Englewood, CO 80111 (303) 790-7559 FAX (303) 790-7567

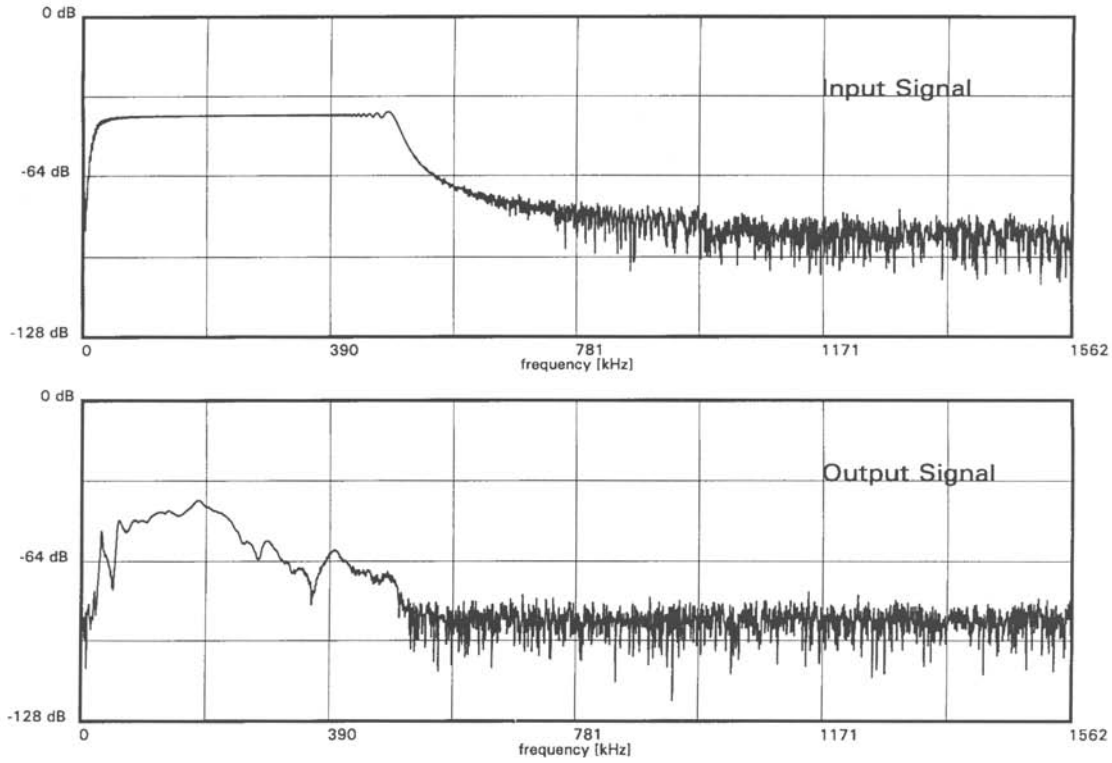

Swept Sine Wave Face-to-Face Sensor Calibration

Frequency Range:	1kHz - 500kHz
DUT:	B225
S/N:	092035
Couplant:	Vacuum Grease
Contact Force:	
Recorder:	DWC F4000
Gain:	21
Preamplifier:	DWC PA2040G/A
Gain:	0
Date:	10/29/03
Tested By:	S. Burgdoff

Figure D.15. DWC Supplied Calibration Curve for B225 Transducer (With Serial Number 092035) in the Frequency Domain

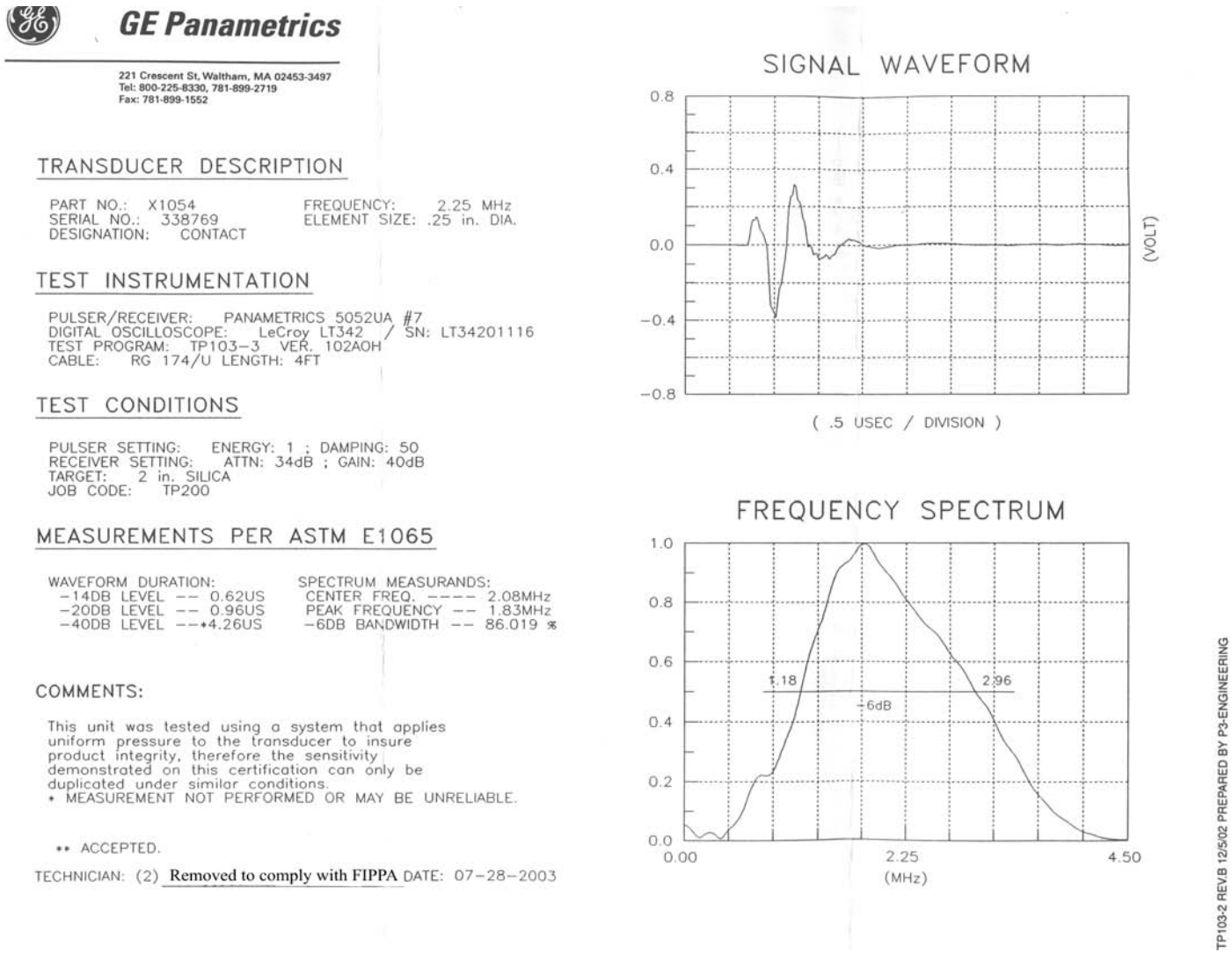

GE Panametrics

221 Crescent St, Waltham, MA 02453-3497
Tel: 800-225-8330, 781-899-2719
Fax: 781-899-1552

TRANSDUCER DESCRIPTION

PART NO.: X1054 FREQUENCY: 2.25 MHz
SERIAL NO.: 338769 ELEMENT SIZE: .25 in. DIA.
DESIGNATION: CONTACT

TEST INSTRUMENTATION

PULSER/RECEIVER: PANAMETRICS 5052UA #7
DIGITAL OSCILLOSCOPE: LeCroy LT342 / SN: LT34201116
TEST PROGRAM: TP103-3 VER. 102AOH
CABLE: RG 174/U LENGTH: 4FT

TEST CONDITIONS

PULSER SETTING: ENERGY: 1 ; DAMPING: 50
RECEIVER SETTING: ATTN: 34dB ; GAIN: 40dB
TARGET: 2 in. SILICA
JOB CODE: TP200

MEASUREMENTS PER ASTM E1065

WAVEFORM DURATION:
-14DB LEVEL -- 0.62US
-20DB LEVEL -- 0.96US
-40DB LEVEL --*4.26US

SPECTRUM MEASURANDS:
CENTER FREQ. ---- 2.08MHz
PEAK FREQUENCY -- 1.83MHz
-6DB BANDWIDTH -- 86.019 %

COMMENTS:

This unit was tested using a system that applies uniform pressure to the transducer to insure product integrity, therefore the sensitivity demonstrated on this certification can only be duplicated under similar conditions.
* MEASUREMENT NOT PERFORMED OR MAY BE UNRELIABLE.

** ACCEPTED.

TECHNICIAN: (2) Removed to comply with FIPPA DATE: 07-28-2003

SIGNAL WAVEFORM

0.8
0.4
0.0
-0.4
-0.8
(VOLT)
(.5 USEC / DIVISION)

FREQUENCY SPECTRUM

1.0
0.8
0.6
0.4
0.2
0.0
1.18
2.96
-6dB
0.00
2.25
4.50
(MHz)

TP103-2 REV.B 12/5/02 PREPARED BY P3-ENGINEERING

Figure D.16. GE Supplied Calibration Curves for X1054 Transducer (With Serial Number338769) in Both Time and Frequency Domains

PA2040G/A Preamplifier

- ***Broadband***
- ***Low Noise***
- ***Adjustable Gain***

The DWC preamplifier provides a wide range of gain settings with a low noise floor. The preamplifier is powered with a +/- 5V and +12V source. It is fully compatible with the 2002 FTM signal conditioning hardware. Internal jumper pins allow the user to configure +12 V on the signal line to power integral preamp LD sensors via a phantom power arrangement.

Frequency Bandwidth:
5 kHz - 4 MHz

Gain:
-20 / 0 / 20 / 40 dB

Noise Floor:
<10.0 mVpp @ 40 dB Gain

Impedance:
standard version
10 kΩ Input / 50 Ω Output

configured for LD sensors
75 Ω Input / 50 Ω Output

Output Voltage Swing:
+/- 0.5V into 50 Ω

I/O Connectors:
BNC

Dimensions:
H 2.0" x W 5.0" x D 2.5"

For more information visit out web site at
www.digitalwavecorp.com

11234A East Caley Avenue
Englewood, Colorado 80111

DIGITAL WAVE

Phone: (303) 790-7559
Fax: (303) 790-7567

Figure D.17. DWC Supplied Data Sheet for PA2040G/A Pre-amplifier

Appendix E - Manufacturer's Data Sheets for 3 Inch Nominal Pipe Size (80 mm Diameter Nominal) Schedule 40 Seamless Carbon Steel Pipe

E.1 Manufacturer's Data Sheets for 3 Inch NPS (80 mm DN) Schedule 40, Seamless Carbon Steel Pipe

Figures E.1 through E.3 reproduce the manufacturer's data for the 3 inch NPS (80 mm DN), schedule 40 seamless carbon steel pipe. These data sheets confirm the pipe's conformity to ASTM A106, with its material properties being specified by ASTM A530/A530M and its dimensional tolerance by ANSI® B 36.10.

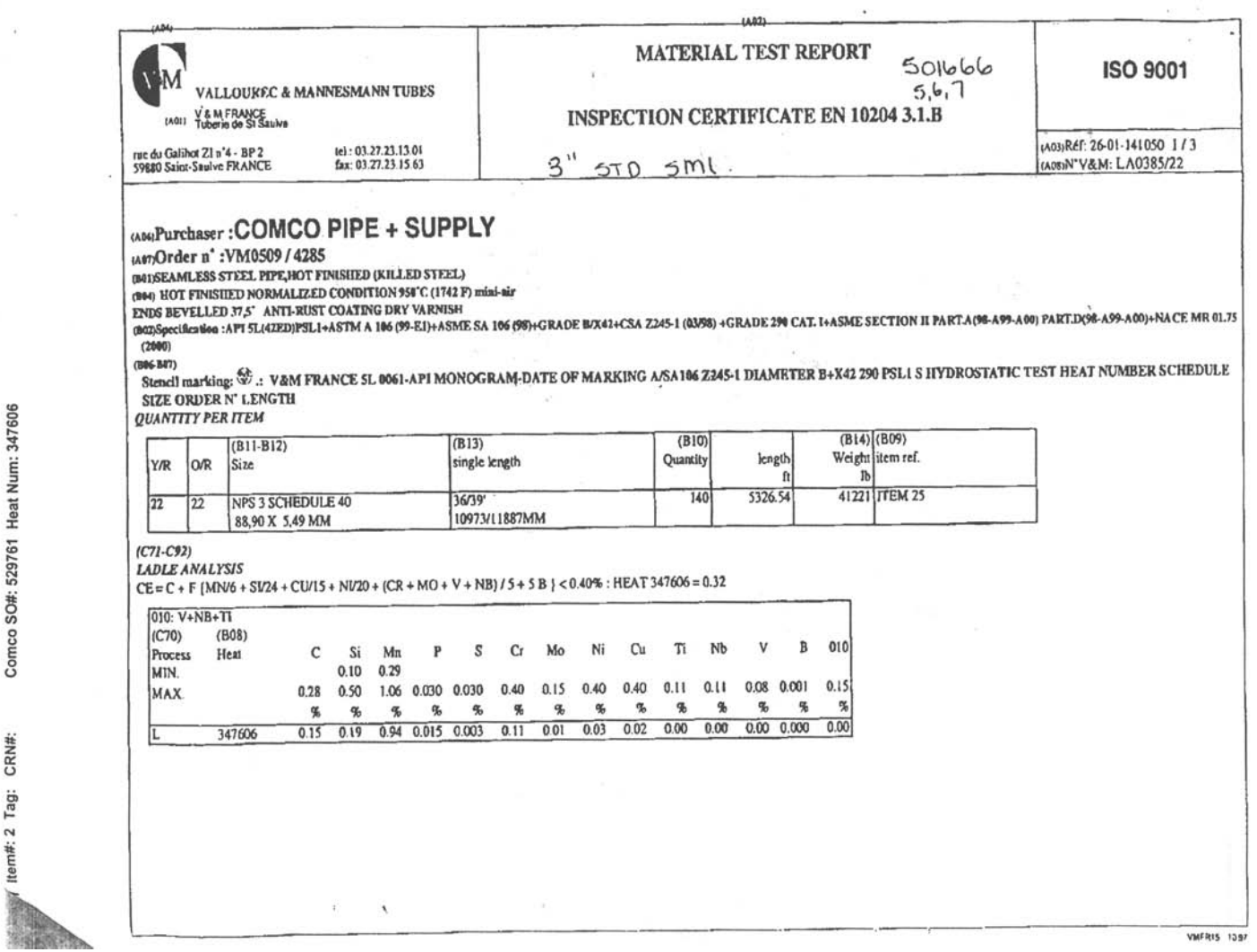

VALLOUREC & MANNESMANN TUBES

(A01) V & M FRANCE
Tuberie de St Saulve

rue du Galihot ZI n°4 - BP 2
59880 Saint-Saulve FRANCE

tel : 03.27.23.13.01
fax: 03.27.23.15.63

MATERIAL TEST REPORT

501666
5,6,7

INSPECTION CERTIFICATE EN 10204 3.1.B

3" STD SML.

ISO 9001

(A03)Réf: 26-01-141050 1 / 3
(A08)N°V&M: LA0385/22

(A04)Purchaser :COMCO PIPE + SUPPLY
(A07)Order n° :VM0509 / 4285
(B01)SEAMLESS STEEL PIPE,HOT FINISHED (KILLED STEEL)
(B04) HOT FINISHED NORMALIZED CONDITION 958°C (1742 F) mini-air
ENDS BEVELLED 37,5° ANTI-RUST COATING DRY VARNISH
(B02)Specification :API 5L(42ED)PSL1+ASTM A 106 (99-E1)+ASME SA 106 (98)+GRADE B/X42+CSA Z245-1 (03/98) +GRADE 290 CAT. I+ASME SECTION II PART.A(98-A99-A00) PART.D(98-A99-A00)+NACE MR 01.75 (2000)
(B06-B07)
Stencil marking: ⊛ .: V&M FRANCE 5L 0061-API MONOGRAM-DATE OF MARKING A/SA106 Z245-1 DIAMETER B+X42 290 PSL1 S HYDROSTATIC TEST HEAT NUMBER SCHEDULE SIZE ORDER N° LENGTH
QUANTITY PER ITEM

Y/R	O/R	(B11-B12) Size	(B13) single length	(B10) Quantity	length ft	(B14) Weight lb	(B09) item ref.
22	22	NPS 3 SCHEDULE 40 88,90 X 5,49 MM	36/39' 10973/11887MM	140	5326.54	41221	ITEM 25

(C71-C92)
LADLE ANALYSIS
CE = C + F [MN/6 + SI/24 + CU/15 + NI/20 + (CR + MO + V + NB) / 5 + 5 B] < 0.40% : HEAT 347606 = 0.32

010: V+NB+TI														
(C70)	(B08)													
Process	Heat	C	Si	Mn	P	S	Cr	Mo	Ni	Cu	Ti	Nb	V	B	010
MIN.			0.10	0.29											
MAX.		0.28	0.50	1.06	0.030	0.030	0.40	0.15	0.40	0.40	0.11	0.11	0.08	0.001	0.15
		%	%	%	%	%	%	%	%	%	%	%	%	%	%
L	347606	0.15	0.19	0.94	0.015	0.003	0.11	0.01	0.03	0.02	0.00	0.00	0.00	0.000	0.00

VMFR15 10/97

Item#: 2 Tag: CRN#: Comco SO#: 529761 Heat Num: 347606

PO#: 501666 Item#: 2 Tag: CRN#: Comco SO#: 210693 Qty:

Figure E.1. 3 inch NPS Manufacturer's Data Sheet - Page 1 of 3

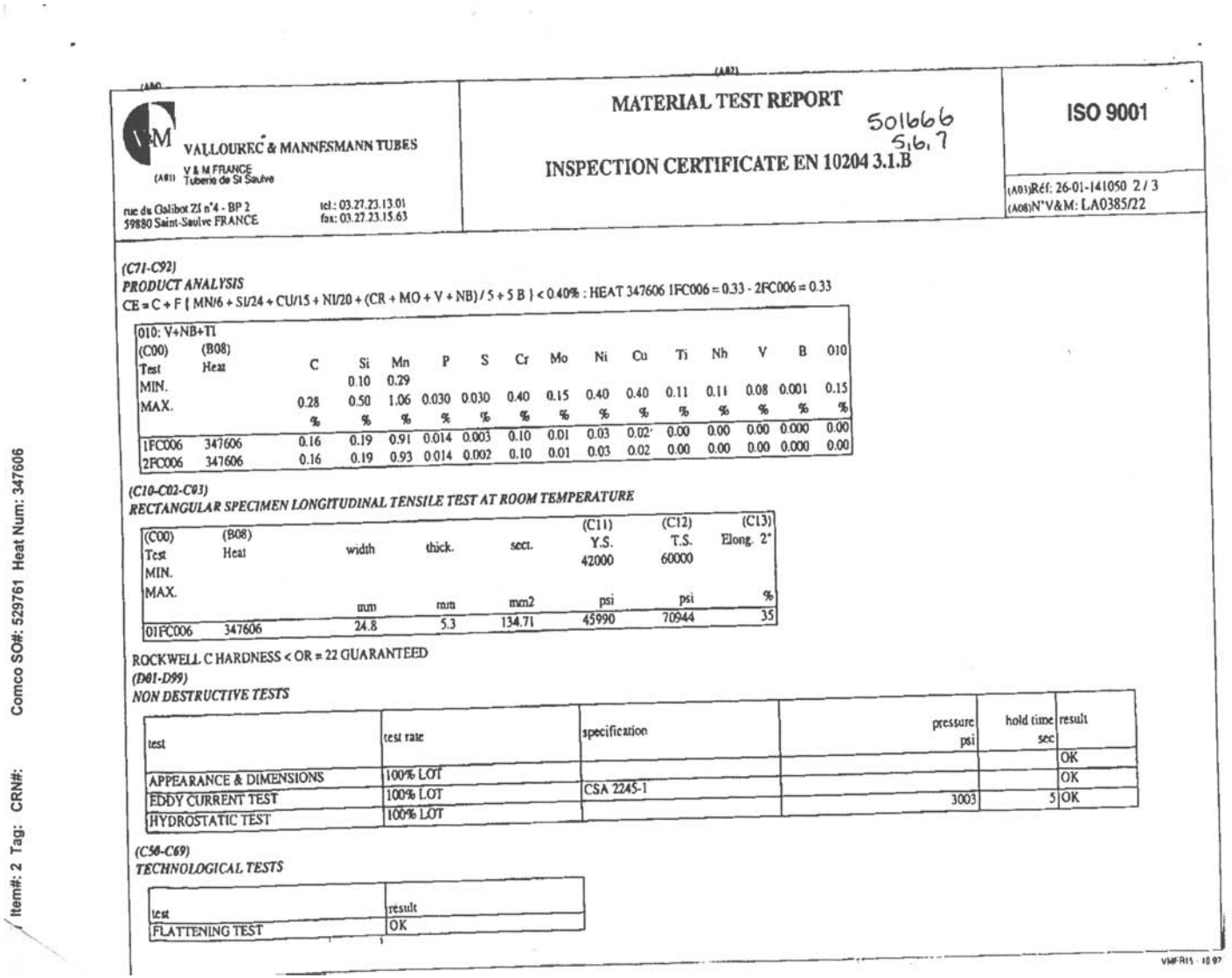

VALLOUREC & MANNESMANN TUBES
V & M FRANCE
Tuberie de St Saulve
rue du Calibot ZI n°4 - BP 2
59880 Saint-Saulve FRANCE
tel : 03.27.23.13.01
fax: 03.27.23.15.63

MATERIAL TEST REPORT

501666
516.7

INSPECTION CERTIFICATE EN 10204 3.1.B

ISO 9001

(A03)Réf: 26-01-141050 2 / 3
(A08)N°V&M: LA0385/22

(C71-C92)
PRODUCT ANALYSIS
CE = C + F [MN/6 + SI/24 + CU/15 + NI/20 + (CR + MO + V + NB) / 5 + 5 B] < 0.40% : HEAT 347606 1FC006 = 0.33 - 2FC006 = 0.33

010: V+NB+TI (C00) Test	(B08) Heat	C	Si	Mn	P	S	Cr	Mo	Ni	Cu	Ti	Nb	V	B	010
MIN.			0.10	0.29											
MAX.		0.28	0.50	1.06	0.030	0.030	0.40	0.15	0.40	0.40	0.11	0.11	0.08	0.001	0.15
		%	%	%	%	%	%	%	%	%	%	%	%	%	%
1FC006	347606	0.16	0.19	0.91	0.014	0.003	0.10	0.01	0.03	0.02	0.00	0.00	0.00	0.000	0.00
2FC006	347606	0.16	0.19	0.93	0.014	0.002	0.10	0.01	0.03	0.02	0.00	0.00	0.00	0.000	0.00

(C10-C02-C03)
RECTANGULAR SPECIMEN LONGITUDINAL TENSILE TEST AT ROOM TEMPERATURE

(C00) Test	(B08) Heat	width	thick.	sect.	(C11) Y.S. 42000	(C12) T.S. 60000	(C13) Elong. 2"
MIN.							
MAX.							
		mm	mm	mm2	psi	psi	%
01FC006	347606	24.8	5.3	134.71	45990	70944	35

ROCKWELL C HARDNESS < OR = 22 GUARANTEED
(D01-D99)
NON DESTRUCTIVE TESTS

test	test rate	specification	pressure psi	hold time sec	result
					OK
APPEARANCE & DIMENSIONS	100% LOT				OK
EDDY CURRENT TEST	100% LOT	CSA 2245-1			OK
HYDROSTATIC TEST	100% LOT		3003	5	OK

(C56-C69)
TECHNOLOGICAL TESTS

test	result
FLATTENING TEST	OK

VMFR15 - 10.97

Item#: 2 Tag: CRN#: Comco SO#: 529761 Heat Num: 347606

PO#: 501666 Item#: 2 Tag: CRN#: Comco SO#: 210683 Qty:

Figure E.2. 3 inch NPS Manufacturer's Data Sheet - Page 2 of 3

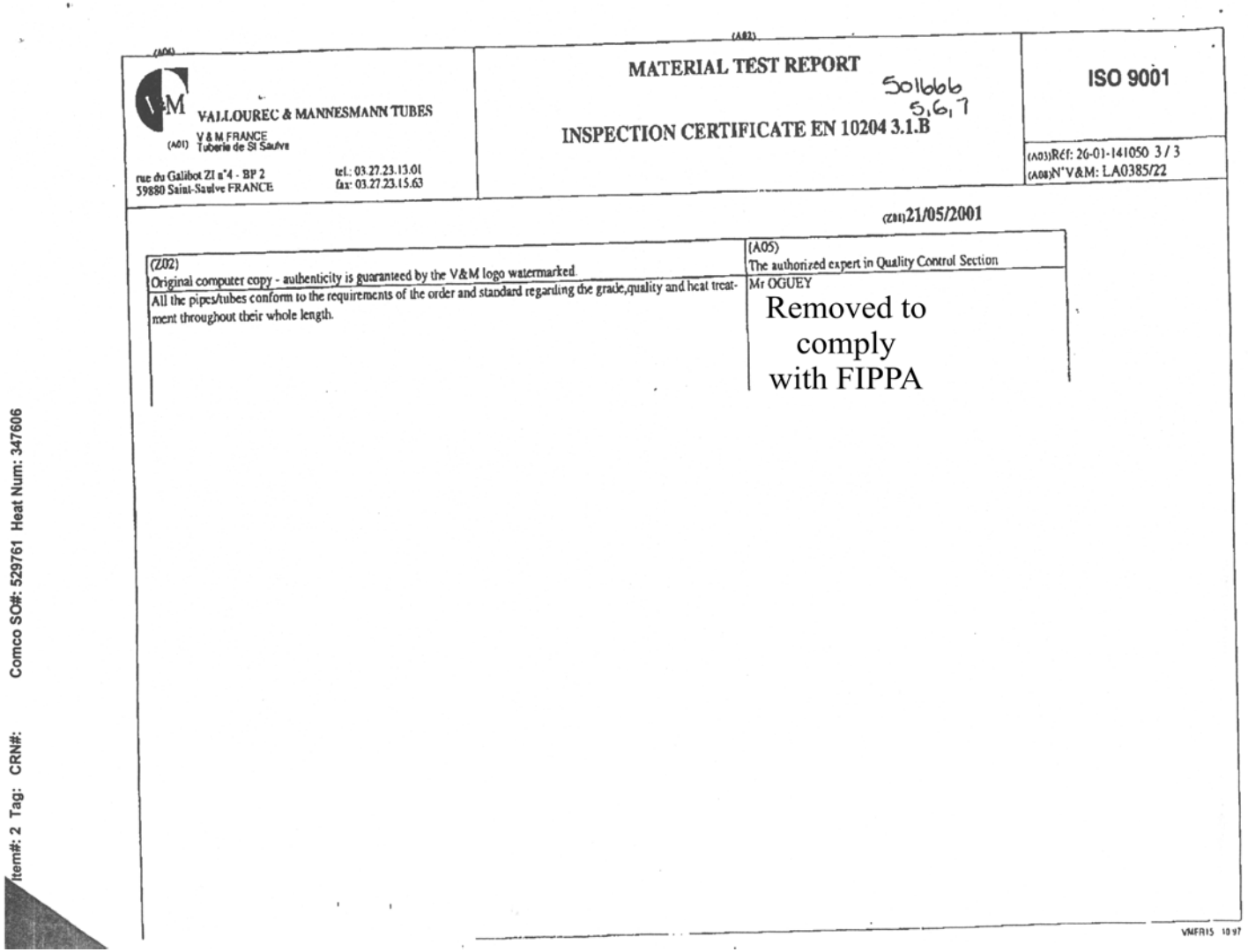

VALLOUREC & MANNESMANN TUBES
V & M FRANCE
Tuberie de St Saulve
rue du Galibot ZI n°4 - BP 2
59880 Saint-Saulve FRANCE
tel.: 03.27.23.13.01
fax: 03.27.23.15.63

MATERIAL TEST REPORT

501666
5,6,7

INSPECTION CERTIFICATE EN 10204 3.1.B

ISO 9001

(A03)Réf: 26-01-141050 3 / 3
(A08)N°V&M: LA0385/22

(Z01)21/05/2001

(Z02)
Original computer copy - authenticity is guaranteed by the V&M logo watermarked.
All the pipes/tubes conform to the requirements of the order and standard regarding the grade,quality and heat treatment throughout their whole length.

(A05)
The authorized expert in Quality Control Section
Mr OGUEY

Removed to comply with FIPPA

VMFR15 10 97

Item#: 2 Tag: CRN#: Comco SO#: 529761 Heat Num: 347606

PO#: 501666 Item#: 2 Tag: CRN#: Comco SO#: 210683 Qty:

Figure E.3. 3 inch NPS Manufacturer's Data Sheet - Page 3 of 3

Appendix F - Sensitivities of Transducers

F.1 Transducer Sensitivities

Figures F.1 through F. 15 give the traces for the transducer combinations listed in Table 3.3 that are not given in Chapter 3. Refer to Table 3.3 for details of the transducers, the orientations, centre frequencies, and the weights used in each figure.

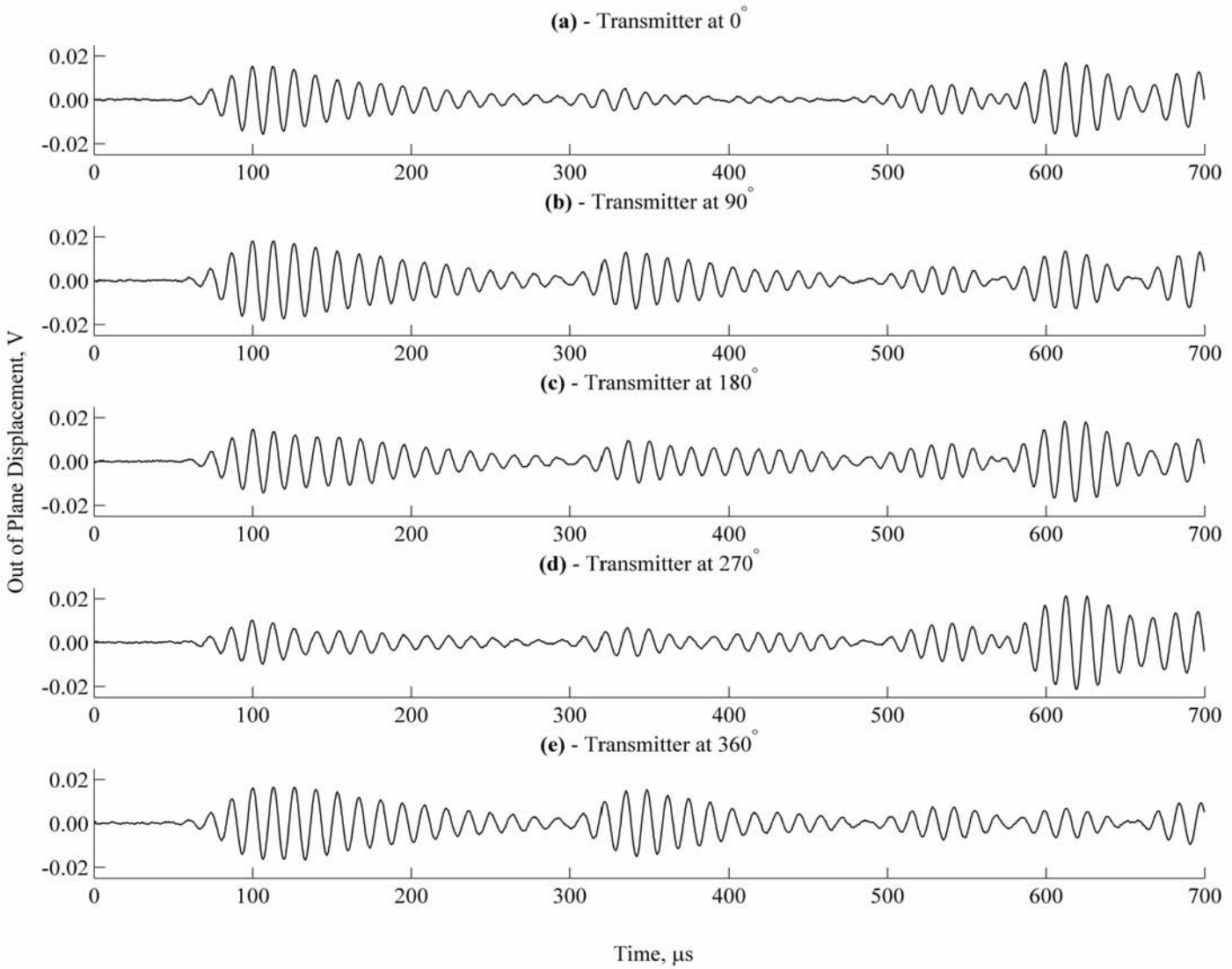

Figure F.1. Transducer Orientation Dependance, Series 1 - 70

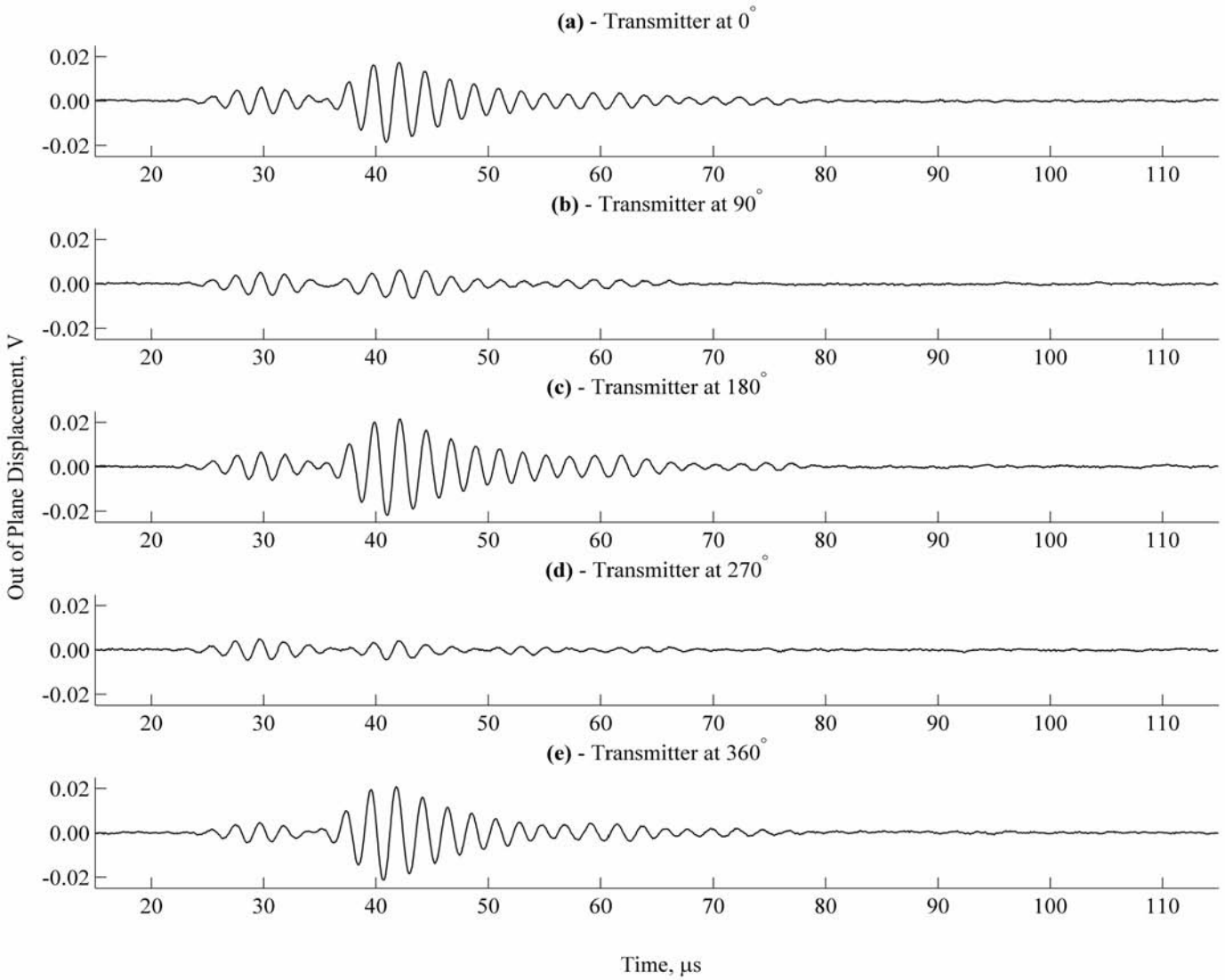

Figure F.2. Transducer Orientation Dependance, Series 1 - 450

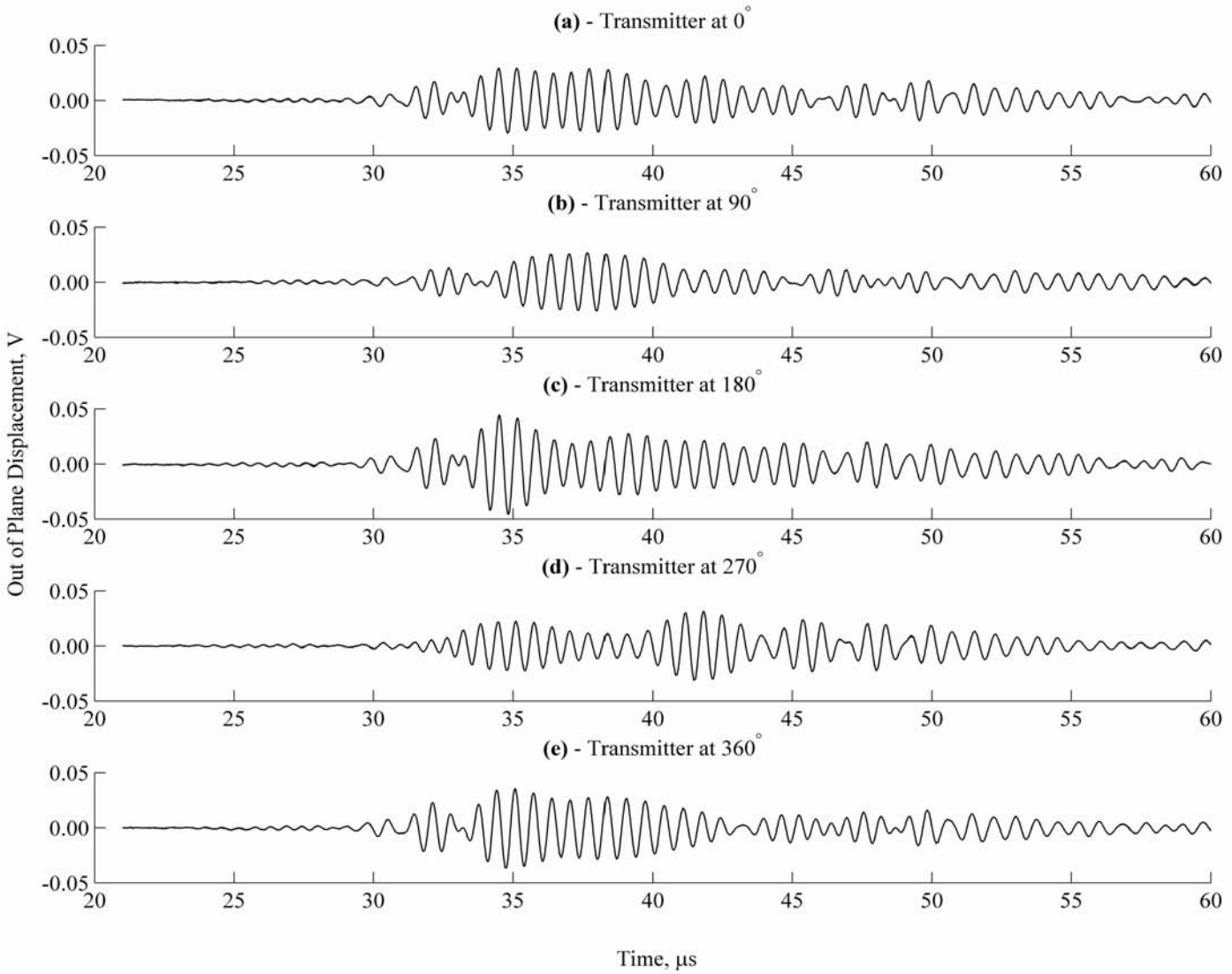

Figure F.3. Transducer Orientation Dependance, Series 1 - 1500

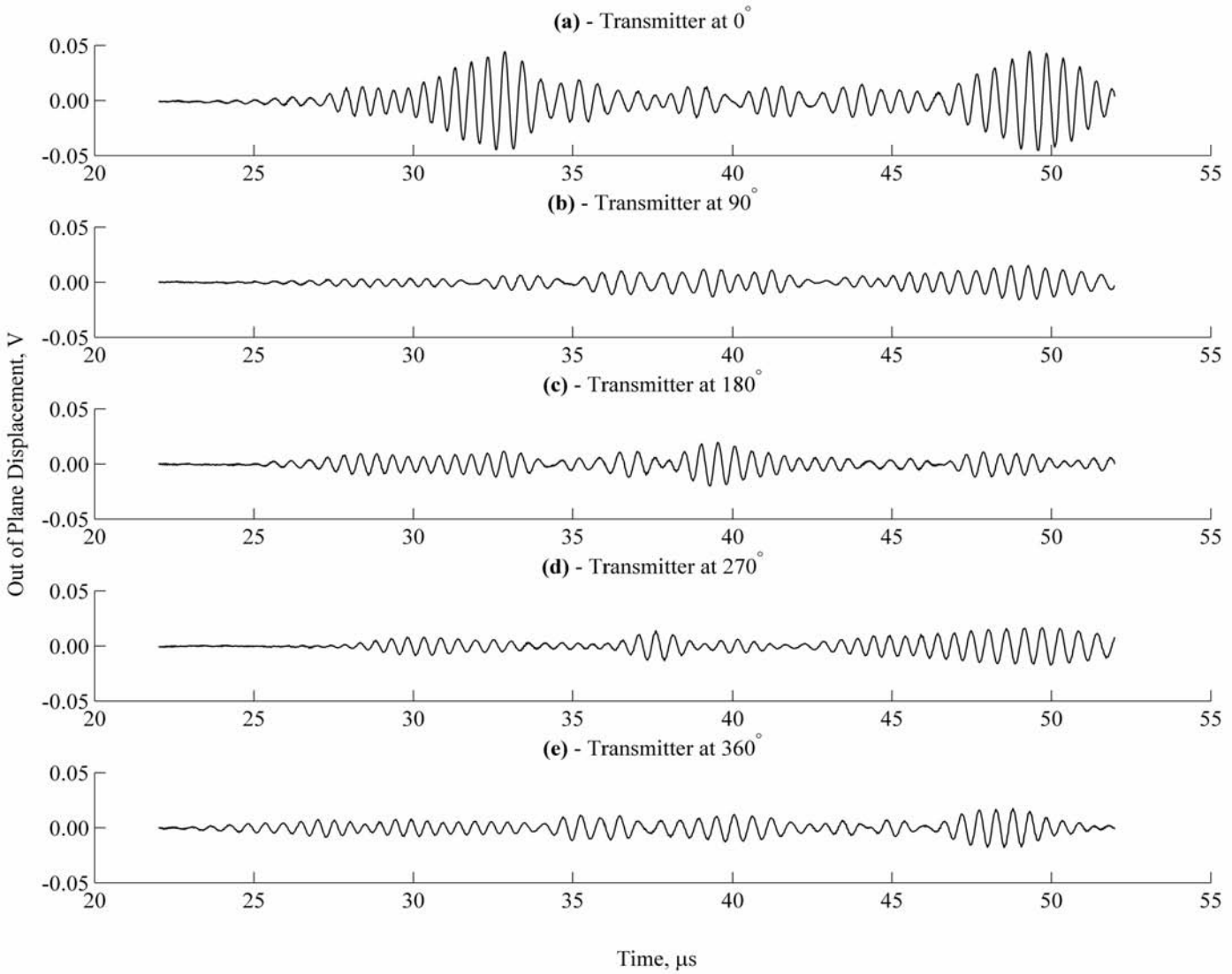

Figure F.4. Transducer Orientation Dependance, Series 3 - 2000

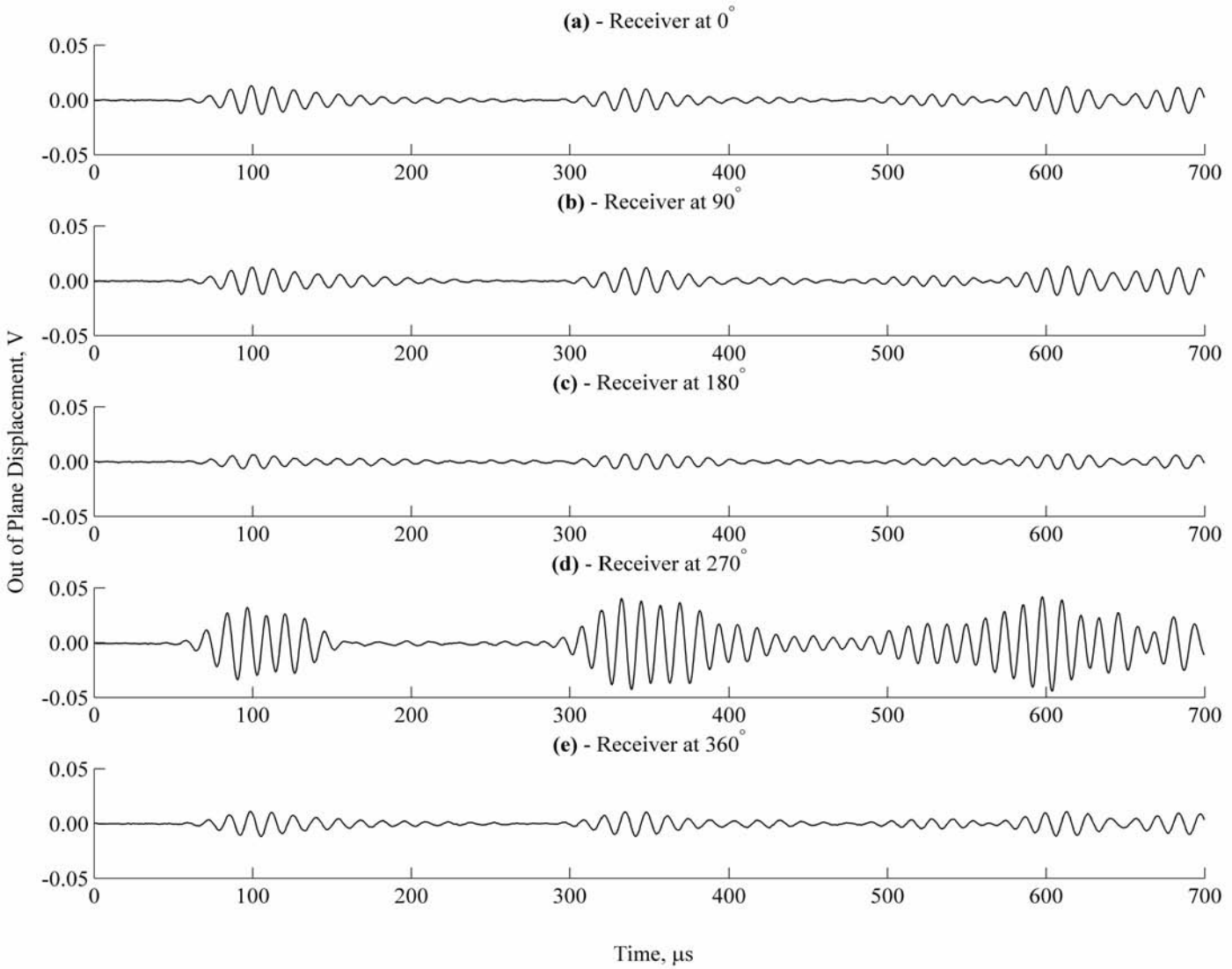

Figure F.5. Transducer Orientation Dependance, Series 4 - 70

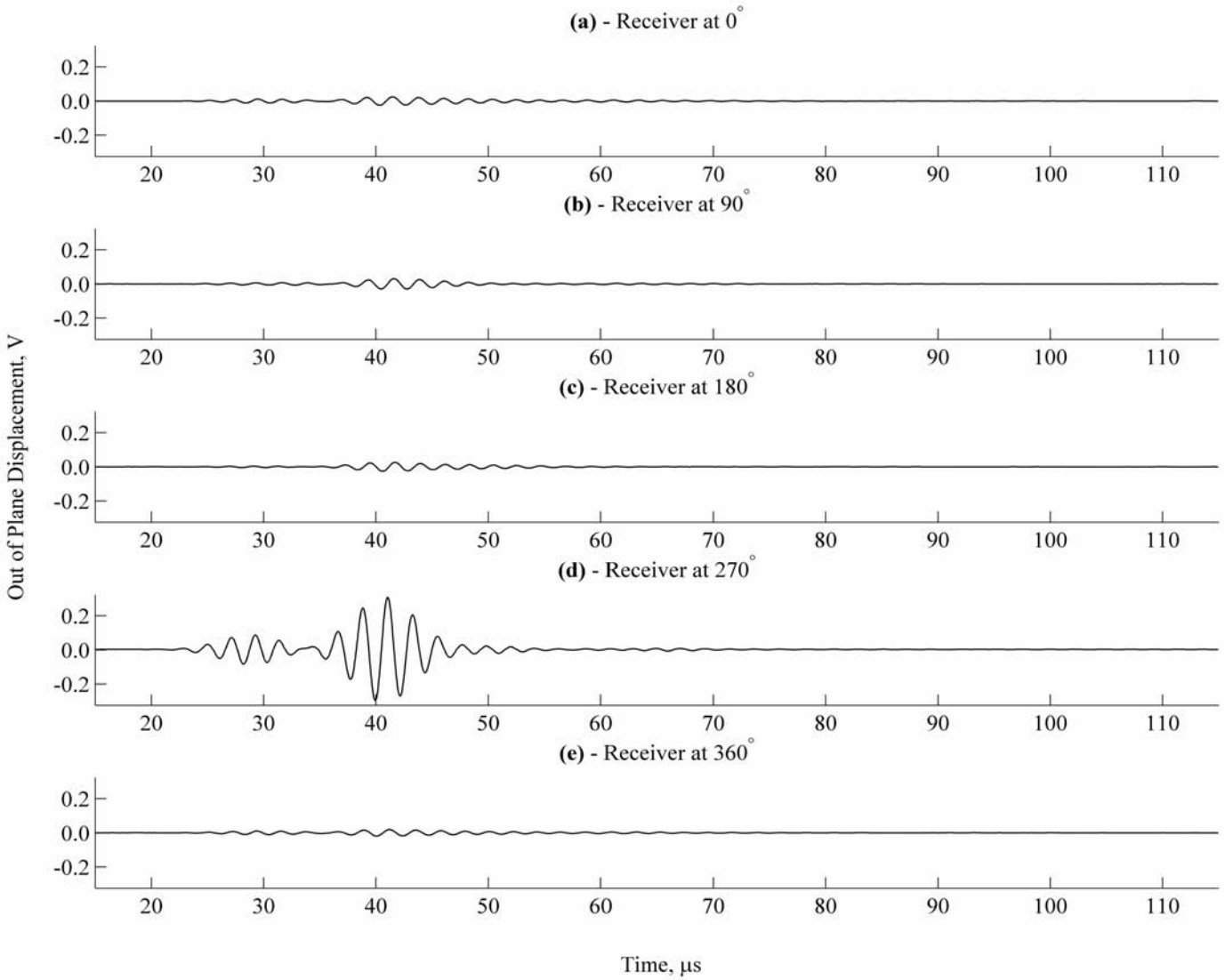

Figure F.6. Transducer Orientation Dependance, Series 4 - 450

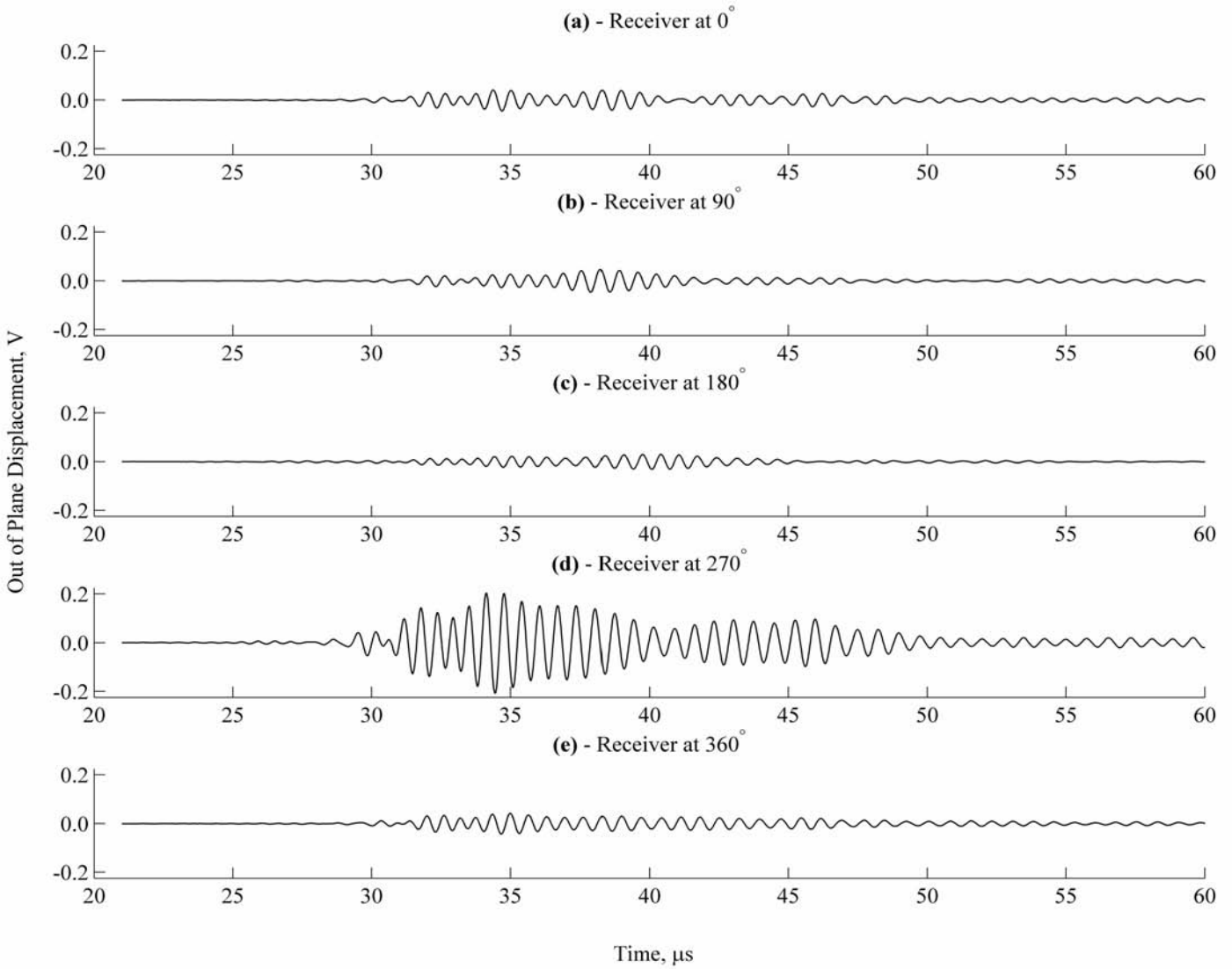

Figure F.7. Transducer Orientation Dependance, Series 4 - 1500

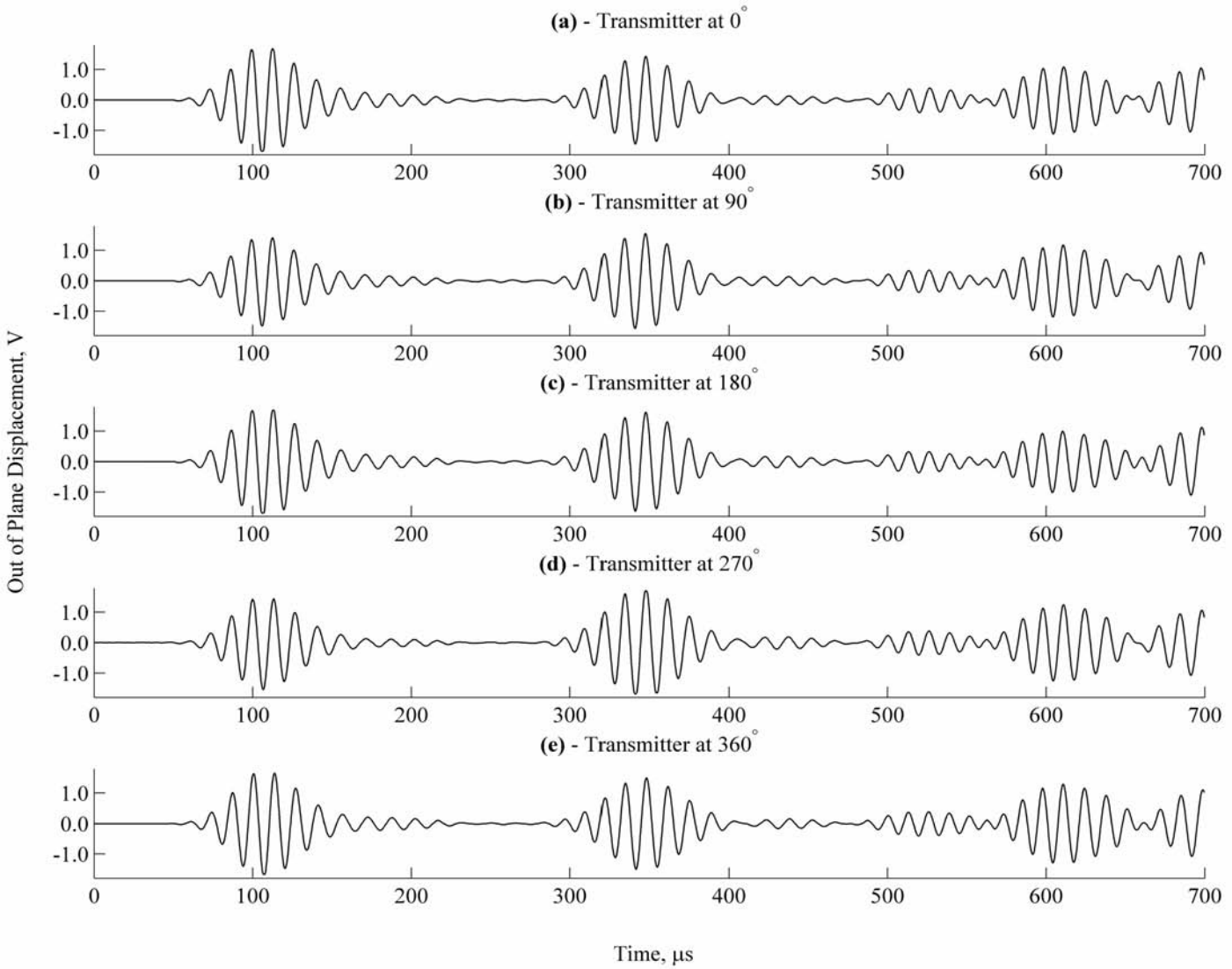

Figure F.8. Transducer Orientation Dependance, Series 6 - 70

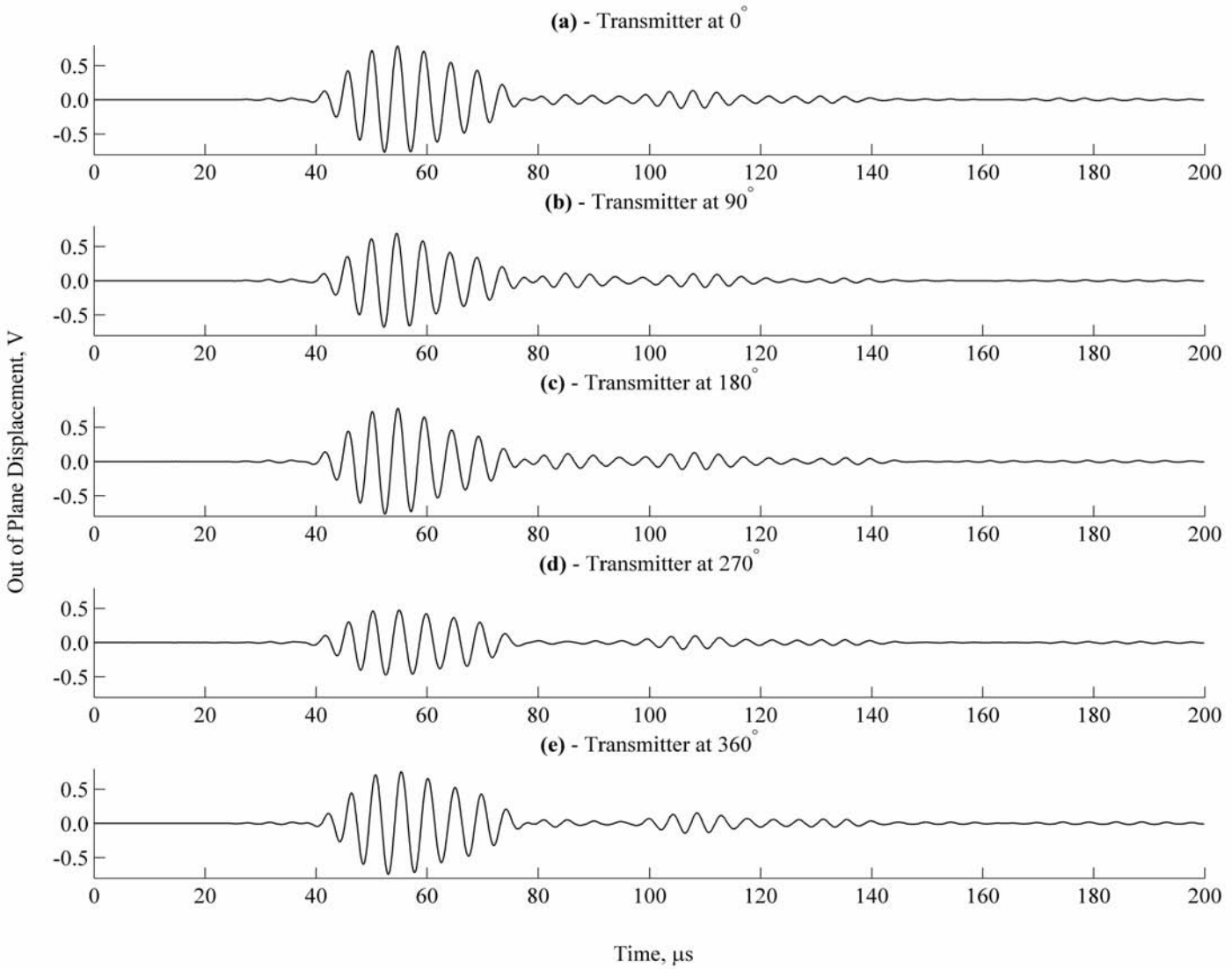

Figure F.9. Transducer Orientation Dependance, Series 6 - 250

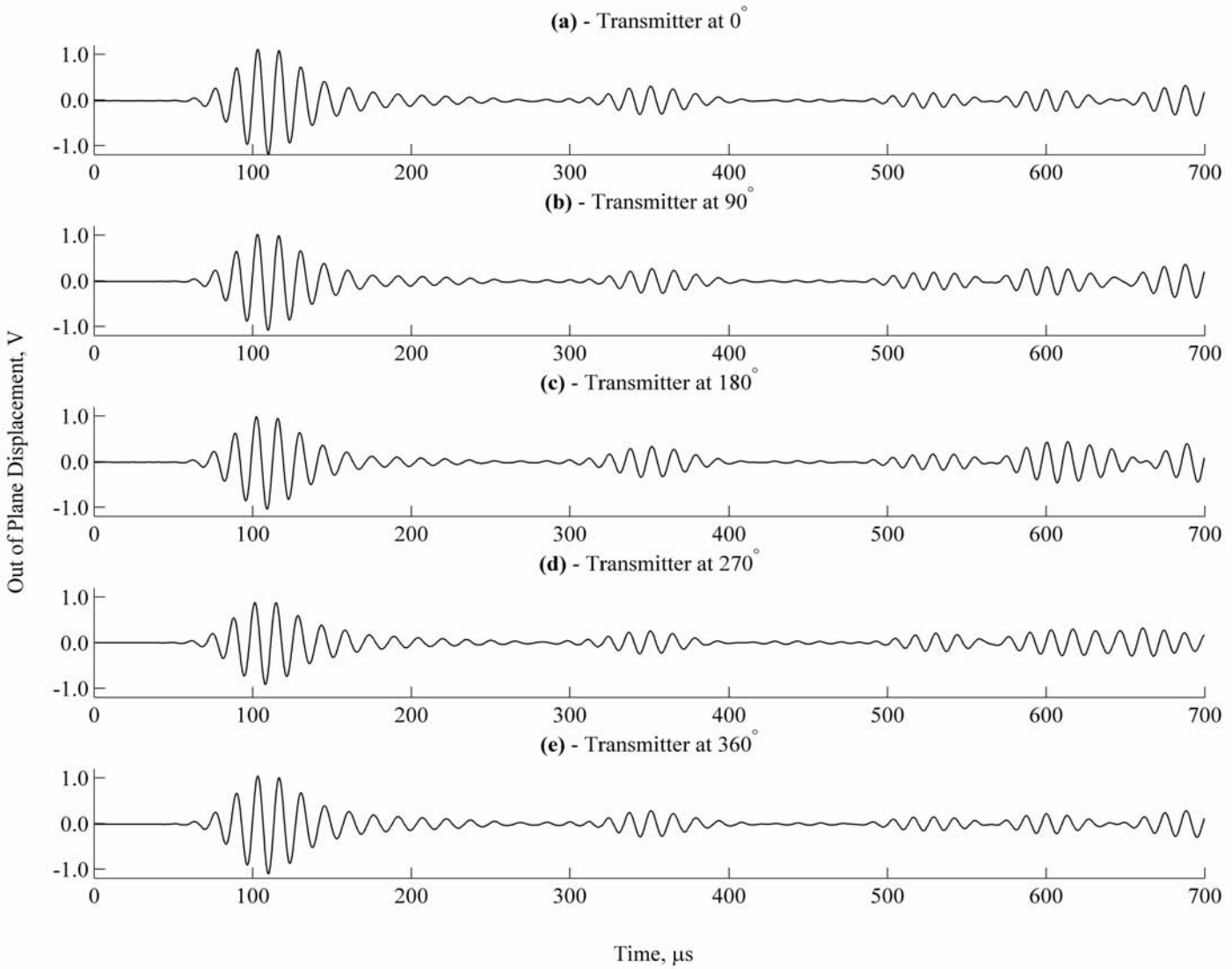

Figure F.10. Transducer Orientation Dependance, Series 7 - 70

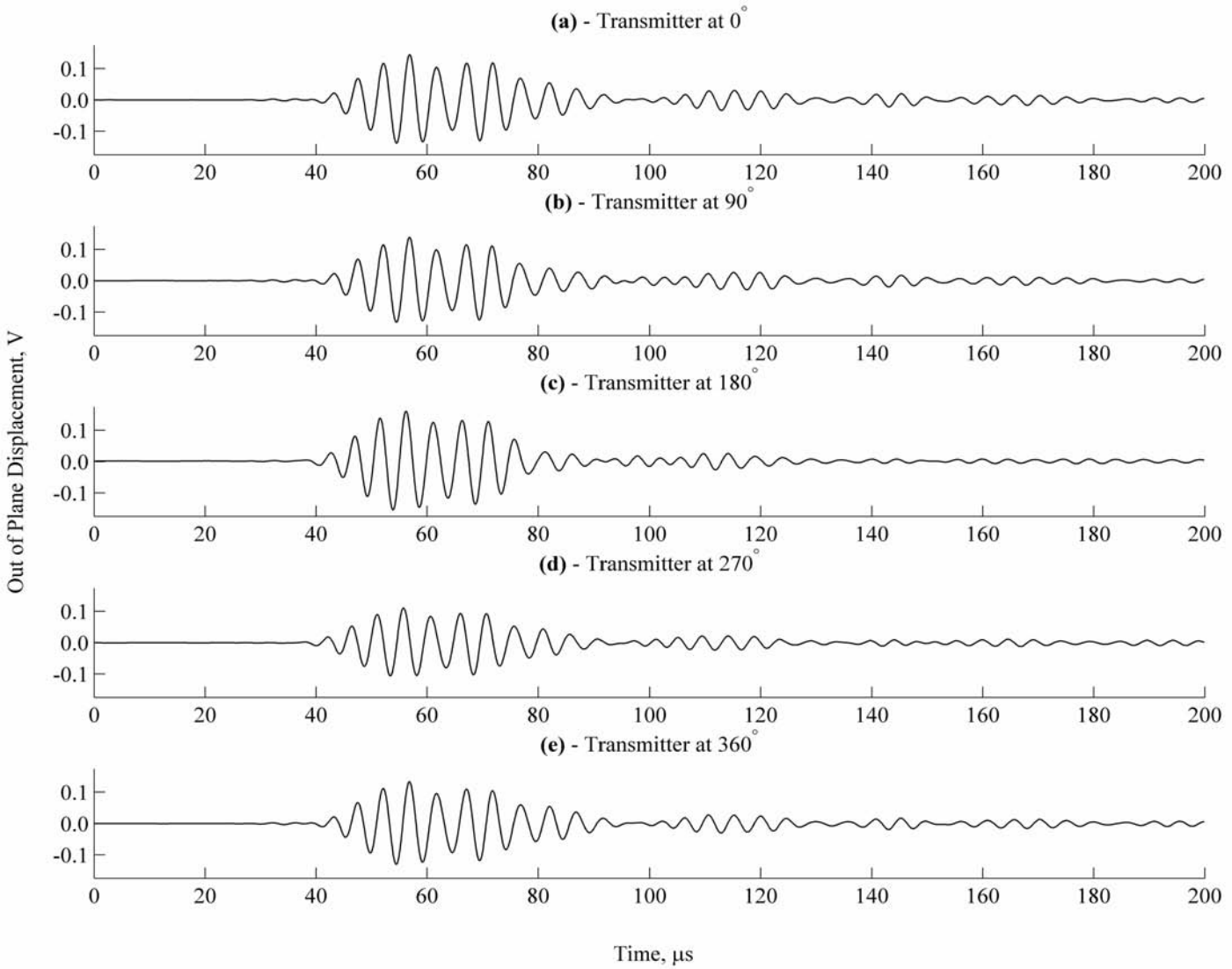

Figure F.11. Transducer Orientation Dependance, Series 7 - 250

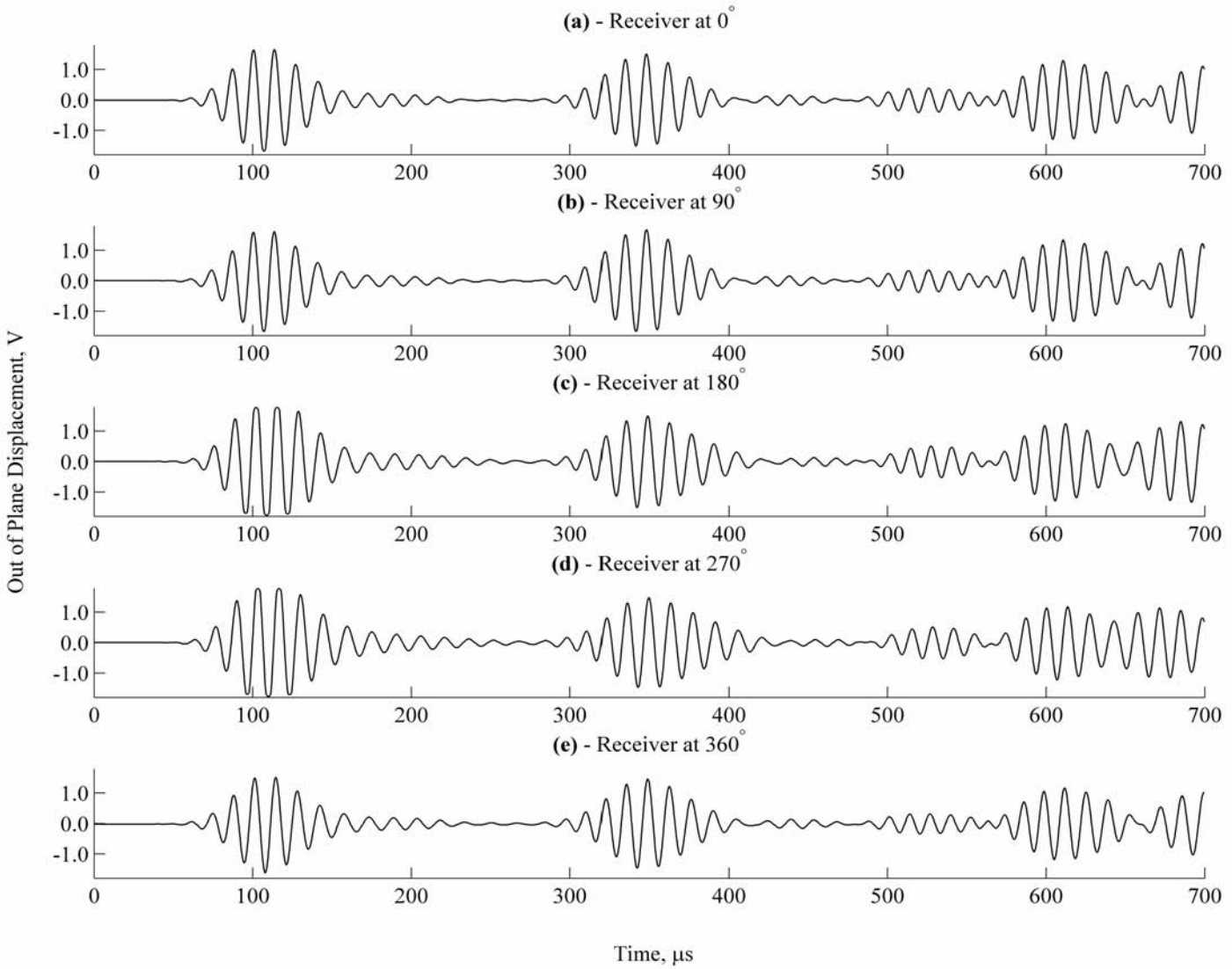

Figure F.12. Transducer Orientation Dependance, Series 8 - 70

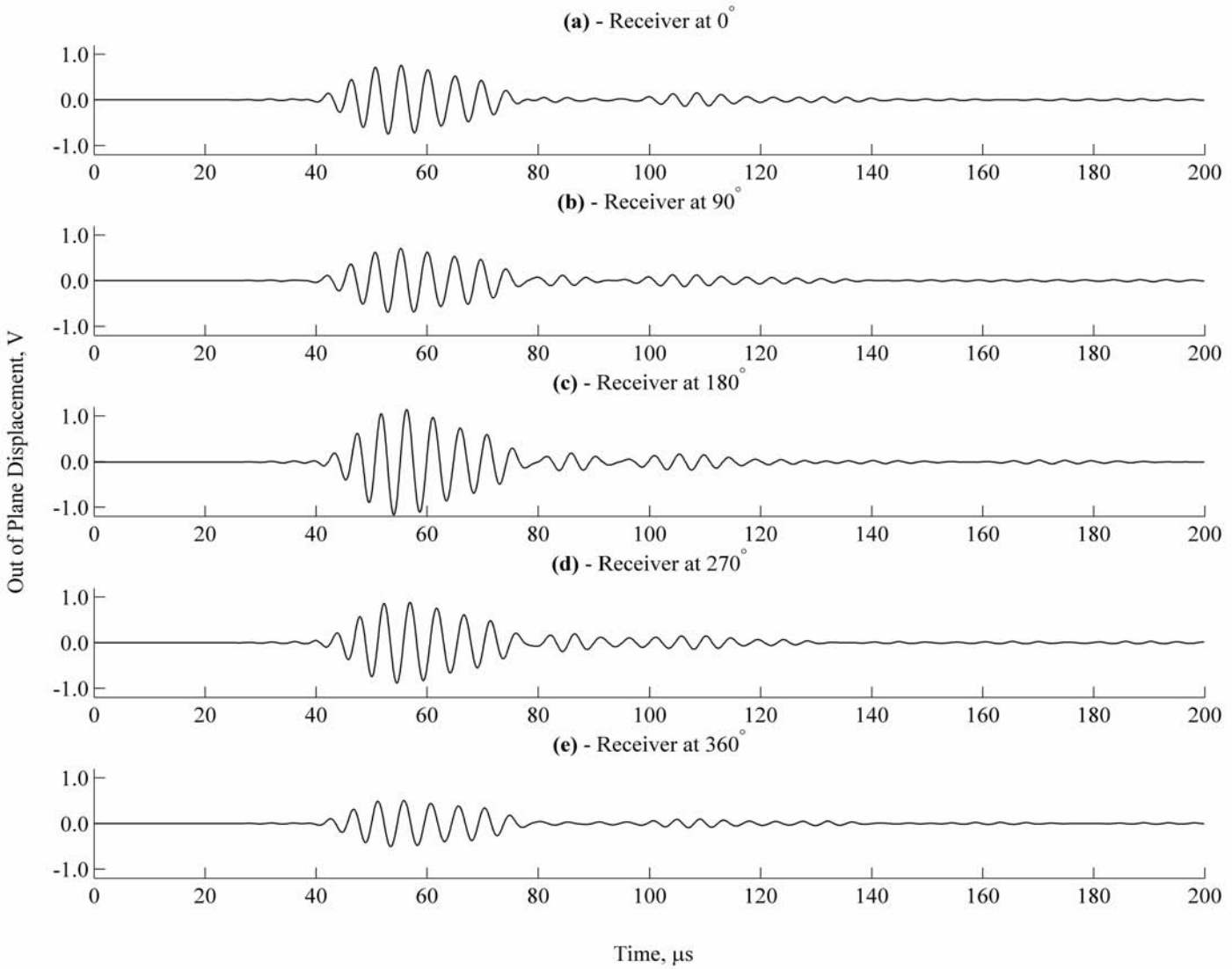

Figure F.13. Transducer Orientation Dependance, Series 8 - 250

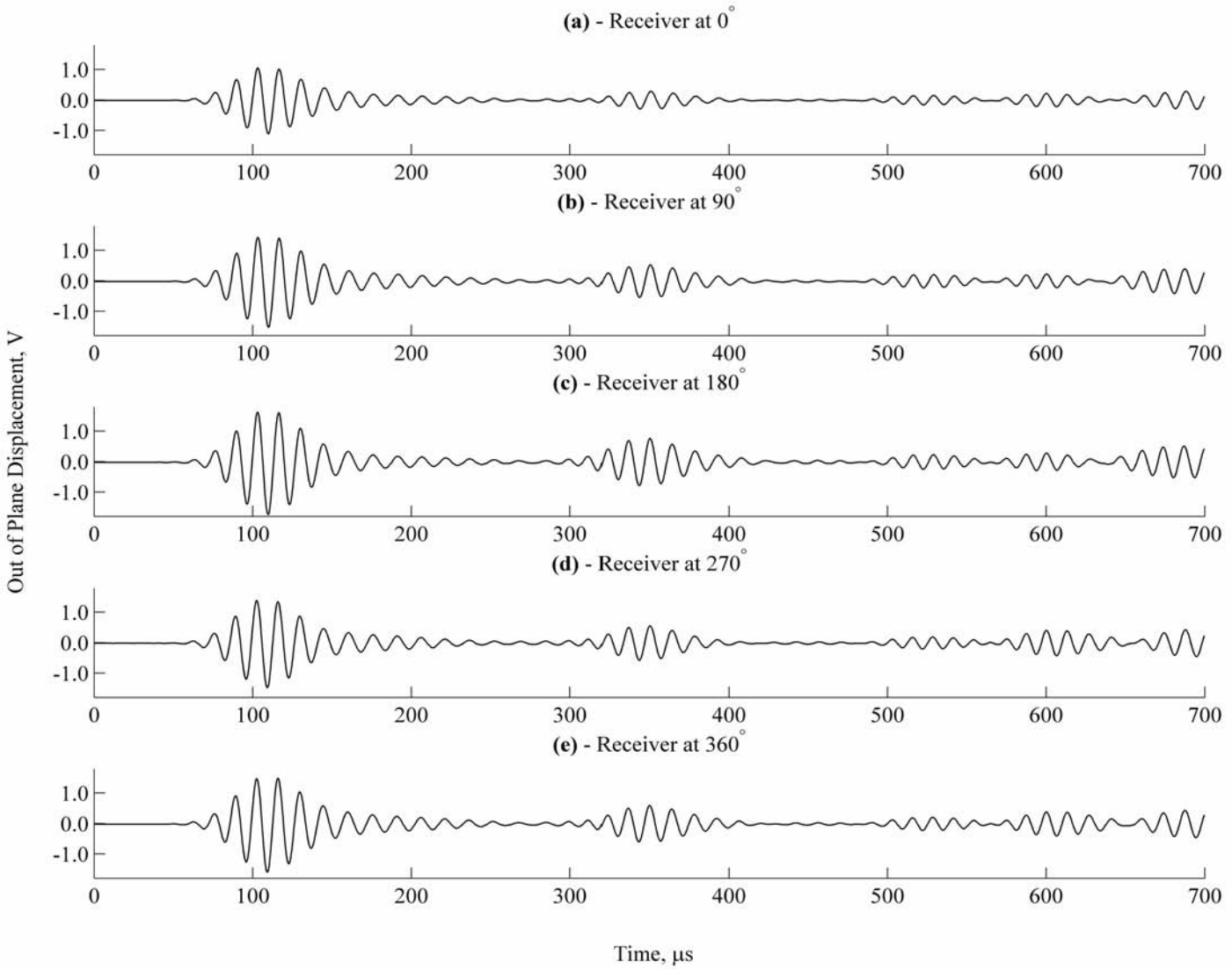

Figure F.14. Transducer Orientation Dependance, Series 9 - 70

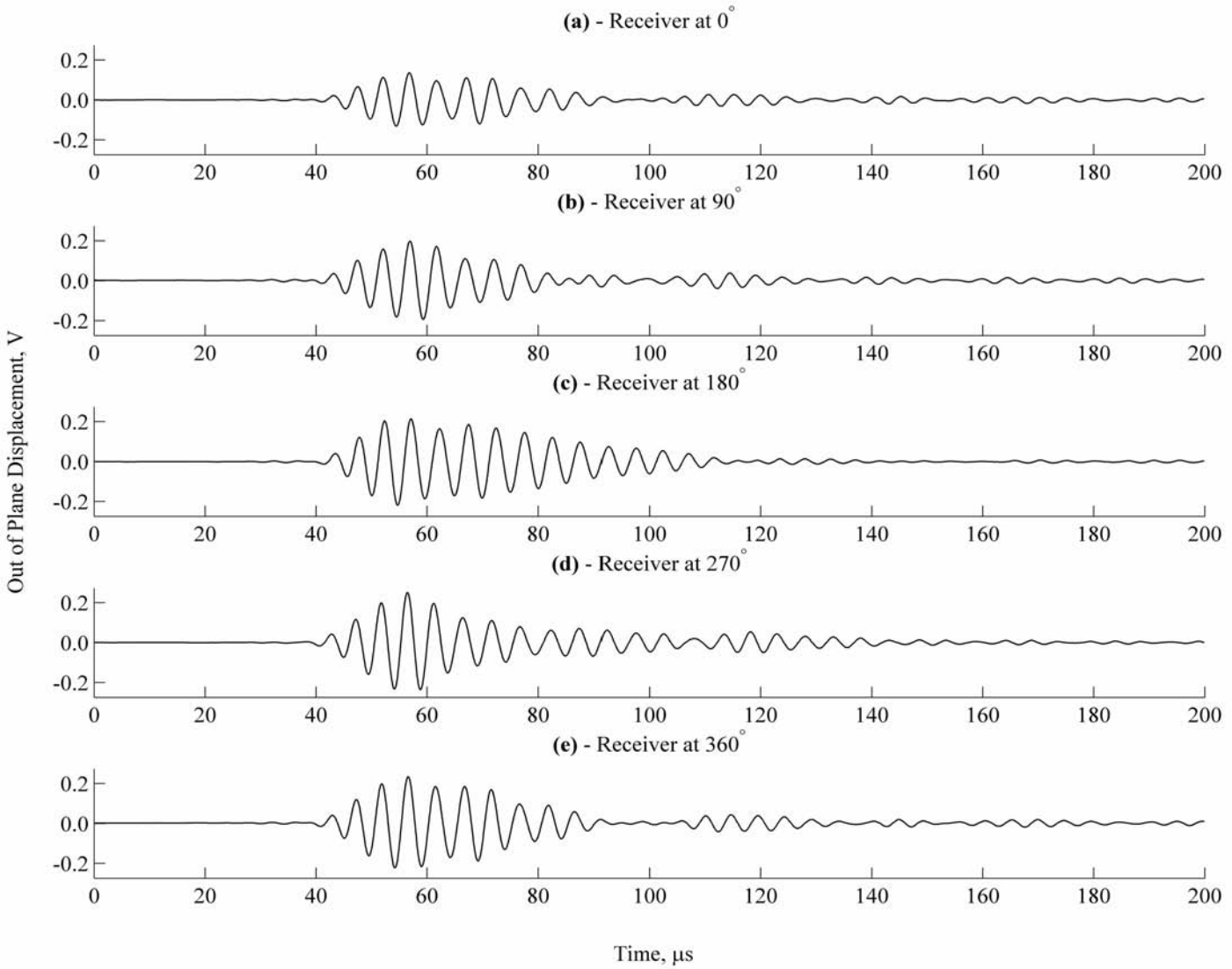

Figure F.15. Transducer Orientation Dependance, Series 9 - 250

Appendix G - Tabulated Values of the Normalized Transfer Functions

G.1 Tabulated Values of the Normalized Transfer Functions

Tables G.1 and G.2 give the normalized transfer functions (defined in Chapter 3) of the transmitter and receiver, respectively. See also Figures 3.20 and 3.22. In contrast to most of the other phase angles given here, the unwrapped phase angles supplied in Tables G.1 and G.2 (Figures 3.20 and 3.22) are given relative to $\Re(e^{+j\omega t})$. Note that this information is also contained, in electronic form, on the accompanying media.

Table G.1. Normalized Transfer Function for Transmitter

Frequency, kHz	Real Part	Imaginary Part	Magnitude	Unwrapped Phase Angle, Degrees
14.5	-0.01148	0.00851	0.01429	143.5
15.3	-0.02485	-0.00115	0.02488	182.7
16.0	-0.01149	-0.00087	0.01153	184.3
16.8	-0.00153	0.01113	0.01124	97.8
17.5	0.00622	-0.01289	0.01431	-64.2
18.3	0.01863	0.00731	0.02001	21.4
19.1	-0.01674	-0.01714	0.02396	-134.3
19.8	-0.01167	-0.01673	0.02039	-124.9
20.6	-0.01054	-0.00313	0.01099	-163.5
21.4	-0.04498	-0.01050	0.04619	-166.9
22.1	-0.02213	0.00477	0.02264	-192.2
22.9	-0.01437	0.00374	0.01485	-194.6
23.7	-0.01765	-0.00324	0.01795	-169.6
24.4	-0.01239	0.00351	0.01288	-195.8
25.2	-0.02331	-0.01368	0.02703	-149.6
25.9	-0.02094	-0.01128	0.02378	-151.7
26.7	-0.04154	-0.02593	0.04897	-148.0
27.5	-0.03934	-0.04337	0.05856	-132.2
28.2	-0.06442	-0.04783	0.08023	-143.4
29.0	-0.09333	-0.06818	0.11558	-143.8
29.8	-0.13655	-0.05958	0.14898	-156.4
30.5	-0.24239	-0.00718	0.24249	-178.3
31.3	-0.28927	0.14708	0.32452	-207.0
32	-0.14299	0.29479	0.32764	-244.1

Table G.1. Normalized Transfer Function for Transmitter (Continued)

Frequency, kHz	Real Part	Imaginary Part	Magnitude	Unwrapped Phase Angle, Degrees
32.8	-0.0383	0.25643	0.25928	-261.5
33.6	0.01040	0.19930	0.19957	-273.0
34.3	0.01931	0.16788	0.16899	-276.6
35.1	0.03677	0.12879	0.13394	-285.9
35.9	0.03087	0.11145	0.11564	-285.5
36.6	0.03630	0.10118	0.10750	-289.7
37.4	0.03836	0.09636	0.10372	-291.7
38.1	0.02837	0.08537	0.08996	-288.4
38.9	0.02921	0.08313	0.08811	-289.4
39.7	0.02669	0.07319	0.07791	-290.0
40.4	0.01889	0.06612	0.06877	-285.9
41.2	0.01806	0.05987	0.06254	-286.8
42.0	0.01325	0.06150	0.06291	-282.2
42.7	0.01458	0.06489	0.06651	-282.7
43.5	0.01613	0.05550	0.05780	-286.2
44.3	0.00731	0.05397	0.05446	-277.7
45.0	0.00491	0.05093	0.05116	-275.5
45.8	-0.00397	0.04570	0.04587	-265.0
46.5	-0.02013	0.04298	0.04746	-244.9
47.3	-0.01991	0.04651	0.05060	-246.8
48.1	-0.02406	0.06440	0.06874	-249.5
48.8	-0.03498	0.06365	0.07263	-241.2
49.6	-0.03114	0.05436	0.06264	-240.2
50.4	-0.02181	0.04518	0.05017	-244.2

Table G.1. Normalized Transfer Function for Transmitter (Continued)

Frequency, kHz	Real Part	Imaginary Part	Magnitude	Unwrapped Phase Angle, Degrees
51.1	-0.03156	0.05080	0.05981	-238.1
51.9	-0.04857	0.03985	0.06283	-219.4
52.6	-0.07555	0.03589	0.08365	-205.4
53.4	-0.08671	0.02498	0.09024	-196.1
54.2	-0.12713	0.02594	0.12975	-191.5
54.9	-0.17188	0.04359	0.17732	-194.2
55.7	-0.22256	0.10011	0.24403	-204.2
56.5	-0.23850	0.17442	0.29548	-216.2
57.2	-0.21954	0.24401	0.32824	-228.0
58.0	-0.18173	0.29841	0.34939	-238.7
58.7	-0.13401	0.33274	0.35871	-248.1
59.5	-0.08764	0.35454	0.36522	-256.1
60.3	-0.04196	0.35567	0.35813	-263.3
61.0	-0.00239	0.34557	0.34558	-269.6
61.8	0.02645	0.33156	0.33262	-274.6
62.6	0.04606	0.31959	0.32289	-278.2
63.3	0.06512	0.31692	0.32354	-281.6
64.1	0.07070	0.29082	0.29930	-283.7
64.8	0.08595	0.28412	0.29683	-286.8
65.6	0.09284	0.27536	0.29059	-288.6
66.4	0.09450	0.26369	0.28011	-289.7
67.1	0.09620	0.26394	0.28093	-290.0
67.9	0.09141	0.25556	0.27142	-289.7
68.7	0.09872	0.25266	0.27126	-291.3

Table G.1. Normalized Transfer Function for Transmitter (Continued)

Frequency, kHz	Real Part	Imaginary Part	Magnitude	Unwrapped Phase Angle, Degrees
69.4	0.09573	0.25858	0.27573	-290.3
70.2	0.09464	0.25600	0.27293	-290.3
71.0	0.10536	0.26019	0.28071	-292.0
71.7	0.10081	0.25643	0.27553	-291.5
72.5	0.10337	0.25668	0.27672	-291.9
73.2	0.11412	0.27155	0.29455	-292.8
74.0	0.11552	0.28110	0.30392	-292.3
74.8	0.12751	0.28150	0.30903	-294.4
75.5	0.14605	0.29112	0.32571	-296.6
76.3	0.15402	0.29033	0.32866	-297.9
77.1	0.16304	0.29328	0.33555	-299.1
77.8	0.17893	0.29303	0.34334	-301.4
78.6	0.20063	0.28815	0.35112	-304.8
79.3	0.20994	0.28035	0.35024	-306.8
80.1	0.22467	0.26688	0.34886	-310.1
80.9	0.23077	0.25923	0.34706	-311.7
81.6	0.24260	0.24987	0.34827	-314.2
82.4	0.24816	0.24763	0.35057	-315.1
83.2	0.25247	0.23586	0.34550	-316.9
83.9	0.25878	0.23215	0.34765	-318.1
84.7	0.25851	0.21624	0.33703	-320.1
85.4	0.25540	0.21327	0.33274	-320.1
86.2	0.25302	0.20511	0.32571	-321.0
87	0.26756	0.19669	0.33208	-323.7

Table G.1. Normalized Transfer Function for Transmitter (Continued)

Frequency, kHz	Real Part	Imaginary Part	Magnitude	Unwrapped Phase Angle, Degrees
87.7	0.25449	0.18874	0.31685	-323.4
88.5	0.25819	0.17829	0.31377	-325.4
89.3	0.25458	0.18058	0.31212	-324.7
90.0	0.26301	0.17584	0.31638	-326.2
90.8	0.25404	0.18094	0.31189	-324.5
91.6	0.26349	0.17747	0.31768	-326.0
92.3	0.25990	0.18023	0.31628	-325.3
93.1	0.25966	0.17870	0.31521	-325.5
93.8	0.25605	0.17738	0.31149	-325.3
94.6	0.25571	0.18580	0.31609	-324.0
95.4	0.26282	0.17253	0.31438	-326.7
96.1	0.27418	0.17274	0.32406	-327.8
96.9	0.26445	0.17312	0.31608	-326.8
97.7	0.26738	0.16488	0.31413	-328.3
98.4	0.26687	0.17086	0.31688	-327.4
99.2	0.26771	0.17172	0.31805	-327.3
99.9	0.27205	0.17234	0.32205	-327.6
100.7	0.26824	0.17665	0.32118	-326.6
101.5	0.27077	0.18400	0.32737	-325.8
102.2	0.27649	0.18888	0.33485	-325.7
103.0	0.28137	0.19187	0.34057	-325.7
103.8	0.29278	0.20006	0.35461	-325.7
104.5	0.29293	0.20482	0.35744	-325.0
105.3	0.30290	0.20560	0.36609	-325.8

Table G.1. Normalized Transfer Function for Transmitter (Continued)

Frequency, kHz	Real Part	Imaginary Part	Magnitude	Unwrapped Phase Angle, Degrees
106	0.31995	0.20729	0.38123	-327.1
106.8	0.32989	0.20524	0.38852	-328.1
107.6	0.33564	0.19236	0.38686	-330.2
108.3	0.33751	0.20305	0.39388	-329.0
109.1	0.34706	0.20735	0.40429	-329.1
109.9	0.36055	0.20750	0.41599	-330.1
110.6	0.36631	0.21004	0.42226	-330.2
111.4	0.37718	0.20028	0.42705	-332.0
112.2	0.39488	0.20366	0.44430	-332.7
112.9	0.40571	0.20397	0.45409	-333.3
113.7	0.41754	0.19524	0.46093	-334.9
114.4	0.43872	0.19026	0.47819	-336.6
115.2	0.43829	0.17864	0.47329	-337.8
116.0	0.45854	0.17165	0.48961	-339.5
116.7	0.46540	0.17497	0.49720	-339.4
117.5	0.47940	0.15802	0.50477	-341.8
118.3	0.49157	0.15880	0.51658	-342.1
119.0	0.50450	0.14480	0.52487	-344.0
119.8	0.50787	0.12934	0.52408	-345.7
120.5	0.51675	0.12355	0.53132	-346.6
121.3	0.53006	0.11601	0.54261	-347.7
122.1	0.53503	0.09534	0.54345	-349.9
122.8	0.54519	0.08295	0.55146	-351.3
123.6	0.55546	0.07424	0.56040	-352.4

Table G.1. Normalized Transfer Function for Transmitter (Continued)

Frequency, kHz	Real Part	Imaginary Part	Magnitude	Unwrapped Phase Angle, Degrees
124.4	0.56207	0.05629	0.56488	-354.3
125.1	0.57283	0.04356	0.57449	-355.7
125.9	0.55932	0.02468	0.55987	-357.5
126.6	0.57347	0.01354	0.57363	-358.6
127.4	0.57119	0.00458	0.57120	-359.5
128.2	0.58080	-0.01709	0.58105	-361.7
128.9	0.58191	-0.02248	0.58234	-362.2
129.7	0.58410	-0.04238	0.58564	-364.1
130.5	0.58186	-0.05892	0.58484	-365.8
131.2	0.58547	-0.07191	0.58987	-367.0
132.0	0.59487	-0.08802	0.60135	-368.4
132.8	0.58735	-0.09894	0.59563	-369.6
133.5	0.58317	-0.10592	0.59271	-370.3
134.3	0.58912	-0.10280	0.59802	-369.9
135.0	0.59724	-0.11671	0.60853	-371.1
135.8	0.60499	-0.13994	0.62097	-373.0
136.6	0.61090	-0.15938	0.63135	-374.6
137.3	0.61774	-0.19468	0.64769	-377.5
138.1	0.60966	-0.21839	0.64759	-379.7
138.9	0.59014	-0.24936	0.64066	-382.9
139.6	0.58438	-0.26024	0.63971	-384.0
140.4	0.56693	-0.27869	0.63172	-386.2
141.1	0.54834	-0.29789	0.62403	-388.5
141.9	0.53085	-0.29559	0.60760	-389.1

Table G.1. Normalized Transfer Function for Transmitter (Continued)

Frequency, kHz	Real Part	Imaginary Part	Magnitude	Unwrapped Phase Angle, Degrees
142.7	0.51193	-0.30825	0.59757	-391.1
143.4	0.50029	-0.31284	0.59005	-392.0
144.2	0.47682	-0.31697	0.57256	-393.6
145.0	0.47275	-0.31267	0.56679	-393.5
145.7	0.46257	-0.32009	0.56252	-394.7
146.5	0.44730	-0.32141	0.55080	-395.7
147.2	0.44113	-0.31535	0.54225	-395.6
148.0	0.43549	-0.31203	0.53573	-395.6
148.8	0.43173	-0.30732	0.52994	-395.4
149.5	0.42816	-0.30875	0.52787	-395.8
150.3	0.42121	-0.30846	0.52208	-396.2
151.1	0.42480	-0.30711	0.52419	-395.9
151.8	0.41965	-0.30673	0.51979	-396.2
152.6	0.41844	-0.29811	0.51377	-395.5
153.4	0.42324	-0.29859	0.51797	-395.2
154.1	0.42594	-0.30301	0.52273	-395.4
154.9	0.43143	-0.30662	0.52929	-395.4
155.6	0.42795	-0.30535	0.52572	-395.5
156.4	0.43711	-0.30920	0.53542	-395.3
157.2	0.44106	-0.31653	0.54289	-395.7
157.9	0.45028	-0.31209	0.54787	-394.7
158.7	0.45357	-0.32442	0.55765	-395.6
159.5	0.46354	-0.33416	0.57144	-395.8
160.2	0.46135	-0.34155	0.57402	-396.5

Table G.1. Normalized Transfer Function for Transmitter (Continued)

Frequency, kHz	Real Part	Imaginary Part	Magnitude	Unwrapped Phase Angle, Degrees
161	0.46937	-0.35563	0.58888	-397.1
161.7	0.47797	-0.35708	0.59663	-396.8
162.5	0.47564	-0.37157	0.60356	-398.0
163.3	0.48515	-0.38032	0.61645	-398.1
164.0	0.48148	-0.40560	0.62955	-400.1
164.8	0.48919	-0.41234	0.63979	-400.1
165.6	0.49630	-0.42211	0.65152	-400.4
166.3	0.50514	-0.44091	0.67050	-401.1
167.1	0.49585	-0.46138	0.67730	-402.9
167.8	0.49354	-0.47502	0.68500	-403.9
168.6	0.50611	-0.49002	0.70446	-404.1
169.4	0.49857	-0.50871	0.71229	-405.6
170.1	0.50413	-0.52964	0.73121	-406.4
170.9	0.50472	-0.55175	0.74777	-407.5
171.7	0.50651	-0.58037	0.77031	-408.9
172.4	0.50264	-0.60534	0.78681	-410.3
173.2	0.50779	-0.63610	0.81393	-411.4
174.0	0.49596	-0.67123	0.83458	-413.5
174.7	0.49459	-0.71058	0.86576	-415.2
175.5	0.47672	-0.74324	0.88299	-417.3
176.2	0.45277	-0.79003	0.91058	-420.2
177.0	0.43510	-0.82791	0.93528	-422.3
177.8	0.40535	-0.86624	0.95639	-424.9
178.5	0.36465	-0.90580	0.97644	-428.1

Table G.1. Normalized Transfer Function for Transmitter (Continued)

Frequency, kHz	Real Part	Imaginary Part	Magnitude	Unwrapped Phase Angle, Degrees
179.3	0.31321	-0.92497	0.97657	-431.3
180.1	0.25409	-0.94619	0.97971	-435.0
180.8	0.21621	-0.97635	1.00000	-437.5
181.6	0.15248	-0.97173	0.98362	-441.1
182.3	0.09578	-0.98358	0.98823	-444.4
183.1	0.04035	-0.98122	0.98205	-447.6
183.9	-0.01040	-0.96454	0.96460	-450.6
184.6	-0.05899	-0.94452	0.94636	-453.6
185.4	-0.10192	-0.91707	0.92271	-456.3
186.2	-0.14177	-0.89889	0.91000	-459.0
186.9	-0.17665	-0.87622	0.89385	-461.4
187.7	-0.20116	-0.82937	0.85342	-463.6
188.4	-0.21978	-0.81269	0.84189	-465.1
189.2	-0.24181	-0.78115	0.81772	-467.2
190.0	-0.24918	-0.75578	0.79580	-468.2
190.7	-0.25235	-0.72579	0.76841	-469.2
191.5	-0.26181	-0.70195	0.74919	-470.5
192.3	-0.27056	-0.67812	0.73010	-471.8
193.0	-0.27272	-0.67666	0.72955	-472.0
193.8	-0.28369	-0.66542	0.72336	-473.1
194.5	-0.28570	-0.64710	0.70737	-473.8
195.3	-0.29691	-0.63942	0.70499	-474.9
196.1	-0.29773	-0.62773	0.69476	-475.4
196.8	-0.30285	-0.62448	0.69404	-475.9

Table G.1. Normalized Transfer Function for Transmitter (Continued)

Frequency, kHz	Real Part	Imaginary Part	Magnitude	Unwrapped Phase Angle, Degrees
197.6	-0.31164	-0.62126	0.69504	-476.6
198.4	-0.32973	-0.60902	0.69256	-478.4
199.1	-0.34410	-0.60339	0.69461	-479.7
199.9	-0.36292	-0.60429	0.70490	-481.0
200.7	-0.38171	-0.58838	0.70135	-483.0
201.4	-0.39938	-0.56749	0.69394	-485.1
202.2	-0.42129	-0.54798	0.69121	-487.6
202.9	-0.43253	-0.53232	0.68589	-489.1
203.7	-0.44462	-0.51665	0.68162	-490.7
204.5	-0.45102	-0.48831	0.66474	-492.7
205.2	-0.45847	-0.47122	0.65745	-494.2
206.0	-0.47102	-0.45379	0.65405	-496.1
206.8	-0.48205	-0.43353	0.64833	-498.0
207.5	-0.47679	-0.40893	0.62813	-499.4
208.3	-0.48398	-0.39520	0.62484	-500.8
209.0	-0.48999	-0.36545	0.61127	-503.3
209.8	-0.48890	-0.35196	0.60241	-504.2
210.6	-0.48705	-0.32320	0.58453	-506.4
211.3	-0.48602	-0.31330	0.57825	-507.2
212.1	-0.48393	-0.30023	0.56949	-508.2
212.9	-0.47640	-0.29035	0.55791	-508.6
213.6	-0.48052	-0.27511	0.55370	-510.2
214.4	-0.47504	-0.25471	0.53902	-511.8
215.1	-0.47370	-0.23417	0.52842	-513.7

Table G.1. Normalized Transfer Function for Transmitter (Continued)

Frequency, kHz	Real Part	Imaginary Part	Magnitude	Unwrapped Phase Angle, Degrees
215.9	-0.46497	-0.22799	0.51786	-513.9
216.7	-0.47129	-0.21147	0.51656	-515.8
217.4	-0.46523	-0.20252	0.50740	-516.5
218.2	-0.47007	-0.18779	0.50620	-518.2
219.0	-0.46666	-0.17959	0.50003	-519.0
219.7	-0.47079	-0.16011	0.49728	-521.2
220.5	-0.47373	-0.14828	0.49639	-522.6
221.3	-0.47189	-0.13528	0.49090	-524.0
222.0	-0.46073	-0.12494	0.47737	-524.8
222.8	-0.46313	-0.10483	0.47485	-527.2
223.5	-0.45765	-0.09177	0.46676	-528.7
224.3	-0.45430	-0.07515	0.46047	-530.6
225.1	-0.45728	-0.05879	0.46104	-532.7
225.8	-0.44822	-0.03844	0.44987	-535.1
226.6	-0.43900	-0.02248	0.43957	-537.1
227.4	-0.42903	-0.00310	0.42904	-539.6
228.1	-0.42199	0.01427	0.42224	-541.9
228.9	-0.41346	0.02529	0.41423	-543.5
229.6	-0.39622	0.04276	0.39852	-546.2
230.4	-0.38282	0.05544	0.38681	-548.2
231.2	-0.35964	0.06701	0.36583	-550.6
231.9	-0.35695	0.06991	0.36373	-551.1
232.7	-0.34583	0.07207	0.35326	-551.8
233.5	-0.33861	0.08228	0.34846	-553.7

Table G.1. Normalized Transfer Function for Transmitter (Continued)

Frequency, kHz	Real Part	Imaginary Part	Magnitude	Unwrapped Phase Angle, Degrees
234.2	-0.32682	0.09037	0.33908	-555.5
235.0	-0.31129	0.10813	0.32954	-559.2
235.7	-0.29289	0.11814	0.31582	-562.0
236.5	-0.27533	0.12614	0.30285	-564.6
237.3	-0.25474	0.13445	0.28804	-567.8
238.0	-0.23791	0.13268	0.27241	-569.1
238.8	-0.21980	0.13200	0.25640	-571.0
239.6	-0.19709	0.13068	0.23648	-573.5
240.3	-0.17935	0.13439	0.22411	-576.8
241.1	-0.16053	0.12829	0.20550	-578.6
241.9	-0.15231	0.11735	0.19227	-577.6
242.6	-0.13560	0.11741	0.17937	-580.9
243.4	-0.12753	0.10447	0.16486	-579.3
244.1	-0.11454	0.10358	0.15443	-582.1
244.9	-0.10760	0.08986	0.14018	-579.9
245.7	-0.08612	0.07965	0.11731	-582.8
246.4	-0.07341	0.05993	0.09476	-579.2
247.2	-0.06511	0.04720	0.08042	-575.9
248.0	-0.07356	0.03249	0.08041	-563.8
248.7	-0.05725	0.02230	0.06144	-561.3
249.5	-0.06285	0.01198	0.06398	-550.8
250.2	-0.05941	-0.00293	0.05949	-537.2
251.0	-0.07435	-0.02331	0.07792	-522.6
251.8	-0.08004	-0.03347	0.08676	-517.3

Table G.1. Normalized Transfer Function for Transmitter (Continued)

Frequency, kHz	Real Part	Imaginary Part	Magnitude	Unwrapped Phase Angle, Degrees
252.5	-0.09481	-0.04036	0.10305	-516.9
253.3	-0.10032	-0.04621	0.11045	-515.3
254.1	-0.11588	-0.05322	0.12751	-515.3
254.8	-0.12777	-0.04635	0.13592	-520.1
255.6	-0.14289	-0.04165	0.14884	-523.8
256.3	-0.15689	-0.03561	0.16088	-527.2
257.1	-0.15689	-0.02544	0.15894	-530.8
257.9	-0.16177	-0.01095	0.16214	-536.1
258.6	-0.16198	-0.00182	0.16199	-539.4
259.4	-0.15574	0.00963	0.15604	-543.5
260.2	-0.15330	0.01297	0.15385	-544.8
260.9	-0.15270	0.02468	0.15468	-549.2
261.7	-0.14504	0.02960	0.14803	-551.5
262.5	-0.14065	0.03412	0.14473	-553.6
263.2	-0.13470	0.04402	0.14171	-558.1
264.0	-0.11010	0.03860	0.11667	-559.3
264.7	-0.11451	0.04259	0.12218	-560.4
265.5	-0.11077	0.04715	0.12038	-563.1
266.3	-0.10956	0.04204	0.11735	-561.0
267.0	-0.09712	0.04147	0.10560	-563.1
267.8	-0.09111	0.04127	0.10002	-564.4
268.6	-0.08932	0.04168	0.09857	-565.0
269.3	-0.07923	0.03840	0.08805	-565.9
270.1	-0.07474	0.03981	0.08468	-568.0

Table G.1. Normalized Transfer Function for Transmitter (Continued)

Frequency, kHz	Real Part	Imaginary Part	Magnitude	Unwrapped Phase Angle, Degrees
270.8	-0.06530	0.03505	0.07412	-568.2
271.6	-0.06818	0.02521	0.07270	-560.3
272.4	-0.05326	0.02429	0.05854	-564.5
273.1	-0.04706	0.02828	0.05490	-571.0
273.9	-0.05771	0.02068	0.06130	-559.7
274.7	-0.04746	0.01005	0.04852	-552.0
275.4	-0.03909	0.00420	0.03931	-546.1
276.2	-0.04042	0.00397	0.04062	-545.6
276.9	-0.03442	-0.00977	0.03578	-524.1
277.7	-0.03947	-0.02533	0.04690	-507.3
278.5	-0.03879	-0.02100	0.04411	-511.6
279.2	-0.04246	-0.03520	0.05516	-500.3
280.0	-0.04395	-0.03962	0.05917	-498.0
280.8	-0.04970	-0.05063	0.07095	-494.5
281.5	-0.07162	-0.06022	0.09357	-499.9
282.3	-0.07700	-0.05791	0.09634	-503.1
283.1	-0.08581	-0.05274	0.10072	-508.4
283.8	-0.09627	-0.05501	0.11088	-510.3
284.6	-0.10246	-0.04896	0.11356	-514.5
285.3	-0.10467	-0.04021	0.11213	-519.0
286.1	-0.10713	-0.04187	0.11502	-518.7
286.9	-0.11717	-0.03098	0.12120	-525.2
287.6	-0.11523	-0.02169	0.11726	-529.3
288.4	-0.12842	-0.01538	0.12934	-533.2

Table G.1. Normalized Transfer Function for Transmitter (Continued)

Frequency, kHz	Real Part	Imaginary Part	Magnitude	Unwrapped Phase Angle, Degrees
289.2	-0.12189	-0.00541	0.12201	-537.5
289.9	-0.11384	-0.00939	0.11422	-535.3
290.7	-0.11275	0.00122	0.11276	-540.6
291.4	-0.12114	0.00691	0.12134	-543.3
292.2	-0.11250	0.00794	0.11278	-544.0
293.0	-0.11377	0.01424	0.11466	-547.1
293.7	-0.10979	0.01046	0.11028	-545.4
294.5	-0.09985	0.01918	0.10167	-550.9
295.3	-0.09434	0.01877	0.09619	-551.3
296.0	-0.08267	0.01735	0.08447	-551.9
296.8	-0.09255	0.02168	0.09505	-553.2
297.5	-0.08998	0.01616	0.09142	-550.2
298.3	-0.08417	0.01893	0.08628	-552.7
299.1	-0.08591	0.02180	0.08863	-554.2
299.8	-0.08268	0.01406	0.08387	-549.7
300.6	-0.08474	0.01448	0.08597	-549.7
301.4	-0.08183	0.01804	0.08380	-552.4
302.1	-0.07977	0.01221	0.08070	-548.7
302.9	-0.08287	0.01786	0.08477	-552.2
303.6	-0.08358	0.01636	0.08516	-551.1
304.4	-0.07757	0.01920	0.07991	-553.9
305.2	-0.08059	0.02291	0.08379	-555.9
305.9	-0.07078	0.02510	0.07510	-559.5
306.7	-0.07411	0.01964	0.07667	-554.8

Table G.1. Normalized Transfer Function for Transmitter (Continued)

Frequency, kHz	Real Part	Imaginary Part	Magnitude	Unwrapped Phase Angle, Degrees
307.5	-0.07993	0.02648	0.08420	-558.3
308.2	-0.07533	0.02806	0.08039	-560.4
309.0	-0.07432	0.02321	0.07786	-557.3
309.8	-0.07553	0.02414	0.07929	-557.7
310.5	-0.07595	0.02062	0.07870	-555.2
311.3	-0.07898	0.02331	0.08235	-556.4
312.0	-0.07083	0.02450	0.07495	-559.1
312.8	-0.08020	0.03186	0.08630	-561.7
313.6	-0.07651	0.02996	0.08217	-561.4
314.3	-0.07614	0.03666	0.08450	-565.7
315.1	-0.07493	0.03345	0.08205	-564.1
315.9	-0.06628	0.03974	0.07728	-570.9
316.6	-0.07004	0.03849	0.07992	-568.8
317.4	-0.06614	0.03967	0.07712	-571.0
318.1	-0.05753	0.05086	0.07679	-581.5
318.9	-0.05361	0.04403	0.06937	-579.4
319.7	-0.04878	0.05003	0.06987	-585.7
320.4	-0.04892	0.05116	0.07078	-586.3
321.2	-0.04974	0.04527	0.06725	-582.3
322.0	-0.03849	0.04283	0.05758	-588.1
322.7	-0.04026	0.04136	0.05772	-585.8
323.5	-0.03138	0.04355	0.05368	-594.2
324.2	-0.02948	0.04261	0.05182	-595.3
325	-0.03010	0.03441	0.04571	-588.8

Table G.1. Normalized Transfer Function for Transmitter (Continued)

Frequency, kHz	Real Part	Imaginary Part	Magnitude	Unwrapped Phase Angle, Degrees
325.8	-0.01884	0.03465	0.03944	-601.5
326.5	-0.02319	0.02811	0.03644	-590.5
327.3	-0.01846	0.02747	0.03310	-596.1
328.1	-0.01374	0.02318	0.02695	-599.3
328.8	-0.01489	0.01875	0.02394	-591.6
329.6	-0.01937	0.01199	0.02278	-571.8
330.4	-0.02430	0.01860	0.03060	-577.4
331.1	-0.01421	0.01616	0.02152	-588.7
331.9	-0.01772	0.01091	0.02081	-571.6
332.6	-0.02648	0.01022	0.02839	-561.1
333.4	-0.02845	0.00358	0.02867	-547.2
334.2	-0.02821	0.00731	0.02914	-554.5
334.9	-0.02415	0.01511	0.02849	-572.0
335.7	-0.02648	0.00508	0.02696	-550.9
336.5	-0.02763	0.01343	0.03072	-565.9
337.2	-0.02411	0.00518	0.02466	-552.1
338.0	-0.02542	0.01046	0.02749	-562.4
338.7	-0.02345	0.00730	0.02456	-557.3
339.5	-0.02691	0.00677	0.02775	-554.1
340.3	-0.02596	0.01165	0.02846	-564.2
341.0	-0.02455	0.01283	0.02770	-567.6
341.8	-0.02997	0.00714	0.03081	-553.4
342.6	-0.03298	0.01537	0.03638	-565.0
343.3	-0.02276	0.01594	0.02779	-575.0

Table G.1. Normalized Transfer Function for Transmitter (Continued)

Frequency, kHz	Real Part	Imaginary Part	Magnitude	Unwrapped Phase Angle, Degrees
344.1	-0.02395	0.01364	0.02756	-569.7
344.8	-0.02468	0.01206	0.02747	-566.1
345.6	-0.02428	0.01336	0.02772	-568.8
346.4	-0.02487	0.01449	0.02878	-570.2
347.1	-0.02712	0.01179	0.02957	-563.5
347.9	-0.02469	0.01139	0.02719	-564.8
348.7	-0.02611	0.00759	0.02719	-556.2
349.4	-0.02199	0.00757	0.02326	-559.0
350.2	-0.02039	0.01006	0.02274	-566.3
351.0	-0.01998	0.01397	0.02438	-575.0
351.7	-0.01478	0.01090	0.01836	-576.4
352.5	-0.02112	0.01041	0.02355	-566.2
353.2	-0.02414	0.00328	0.02436	-547.7
354.0	-0.01239	0.00864	0.01510	-574.9
354.8	-0.01280	0.00684	0.01452	-568.1
355.5	-0.01003	0.01058	0.01458	-586.5
356.3	-0.00546	0.00916	0.01066	-599.2
357.1	-0.00543	-0.00073	0.00548	-532.4
357.8	-0.00874	-0.00035	0.00875	-537.7
358.6	-0.00306	0.00658	0.00726	-605.1
359.3	-0.00624	-0.00234	0.00666	-519.5
360.1	-0.01062	0.00041	0.01063	-542.2
360.9	-0.00212	-0.00101	0.00235	-514.5
361.6	-0.00461	-0.01165	0.01253	-471.6

Table G.1. Normalized Transfer Function for Transmitter (Continued)

Frequency, kHz	Real Part	Imaginary Part	Magnitude	Unwrapped Phase Angle, Degrees
362.4	-0.01898	-0.01002	0.02146	-512.2
363.2	-0.00923	-0.00696	0.01156	-503.0
363.9	-0.00768	-0.01249	0.01466	-481.6
364.7	-0.01214	-0.01655	0.02052	-486.3
365.4	-0.00613	-0.01469	0.01592	-472.7
366.2	-0.01087	-0.02108	0.02372	-477.3
367.0	-0.00895	-0.01581	0.01817	-479.5
367.7	-0.01150	-0.01821	0.02154	-482.3
368.5	-0.00656	-0.02403	0.02491	-465.3
369.3	-0.00698	-0.02980	0.03061	-463.2
370.0	-0.01279	-0.02653	0.02946	-475.7
370.8	-0.01561	-0.03230	0.03588	-475.8
371.6	-0.01999	-0.02788	0.03431	-485.6
372.3	-0.02412	-0.03221	0.04024	-486.8
373.1	-0.01830	-0.03056	0.03562	-480.9
373.8	-0.02147	-0.03799	0.04363	-479.5
374.6	-0.02660	-0.04096	0.04884	-483.0
375.4	-0.02416	-0.03703	0.04421	-483.1
376.1	-0.02675	-0.03806	0.04652	-485.1
376.9	-0.03745	-0.04272	0.05682	-491.2
377.7	-0.03986	-0.03657	0.05409	-497.5
378.4	-0.04351	-0.03904	0.05846	-498.1
379.2	-0.04682	-0.03985	0.06148	-499.6
379.9	-0.04395	-0.03829	0.05830	-498.9

Table G.1. Normalized Transfer Function for Transmitter (Continued)

Frequency, kHz	Real Part	Imaginary Part	Magnitude	Unwrapped Phase Angle, Degrees
380.7	-0.05776	-0.04036	0.07047	-505.1
381.5	-0.06119	-0.03705	0.07153	-508.8
382.2	-0.06195	-0.04063	0.07408	-506.7
383.0	-0.06616	-0.03775	0.07617	-510.3
383.8	-0.06494	-0.03536	0.07394	-511.4
384.5	-0.06633	-0.02977	0.07271	-515.8
385.3	-0.07167	-0.03742	0.08085	-512.4
386.0	-0.07366	-0.03237	0.08046	-516.3
386.8	-0.07934	-0.02786	0.08409	-520.7
387.6	-0.07991	-0.02910	0.08504	-520.0
388.3	-0.08420	-0.02337	0.08738	-524.5
389.1	-0.08659	-0.01959	0.08877	-527.3
389.9	-0.09866	-0.00182	0.09868	-538.9
390.6	-0.10055	-0.01021	0.10106	-534.2
391.4	-0.09500	-0.00200	0.09502	-538.8
392.2	-0.09831	0.00485	0.09843	-542.8
392.9	-0.10300	0.01629	0.10428	-549.0
393.7	-0.09694	0.01080	0.09754	-546.4
394.4	-0.09673	0.02974	0.10120	-557.1
395.2	-0.10484	0.02446	0.10766	-553.1
396.0	-0.09605	0.03401	0.10189	-559.5
396.7	-0.09958	0.03454	0.10540	-559.1
397.5	-0.09779	0.04936	0.10954	-566.8
398.3	-0.09409	0.05683	0.10992	-571.1

Table G.1. Normalized Transfer Function for Transmitter (Continued)

Frequency, kHz	Real Part	Imaginary Part	Magnitude	Unwrapped Phase Angle, Degrees
399	-0.08363	0.05763	0.10156	-574.6
399.8	-0.07918	0.06802	0.10439	-580.7
400.5	-0.06846	0.06948	0.09754	-585.4
401.3	-0.06624	0.07426	0.09951	-588.3
402.1	-0.06013	0.08314	0.10261	-594.1
402.8	-0.05217	0.07876	0.09447	-596.5
403.6	-0.03700	0.08482	0.09254	-606.4
404.4	-0.02968	0.07815	0.08360	-609.2
405.1	-0.03090	0.06894	0.07555	-605.9
405.9	-0.02181	0.07052	0.07382	-612.8
406.6	-0.02426	0.06569	0.07003	-609.7
407.4	-0.02143	0.06000	0.06371	-610.3
408.2	-0.01318	0.05792	0.05940	-617.2
408.9	-0.01749	0.05469	0.05742	-612.3
409.7	-0.00878	0.05468	0.05538	-620.9
410.5	-0.01647	0.04950	0.05217	-611.6
411.2	-0.01379	0.04900	0.05091	-614.3
412.0	-0.01328	0.04600	0.04788	-613.9
412.8	-0.01213	0.04358	0.04523	-614.4
413.5	-0.00801	0.04359	0.04432	-619.6
414.3	-0.00207	0.05060	0.05065	-627.7
415.0	-0.00672	0.04047	0.04102	-620.6
415.8	-0.00769	0.04228	0.04298	-619.7
416.6	-0.00255	0.03140	0.03150	-625.4

Table G.1. Normalized Transfer Function for Transmitter (Continued)

Frequency, kHz	Real Part	Imaginary Part	Magnitude	Unwrapped Phase Angle, Degrees
417.3	-0.00057	0.04298	0.04298	-629.2
418.1	-0.00649	0.03633	0.03690	-619.9
418.9	-0.00698	0.03322	0.03395	-618.1
419.6	-0.00091	0.03681	0.03682	-628.6
420.4	-0.00741	0.02635	0.02737	-614.3
421.1	-0.00602	0.02936	0.02997	-618.4
421.9	-0.00685	0.02994	0.03072	-617.1
422.7	-0.00861	0.02493	0.02638	-611.0
423.4	-0.00297	0.02626	0.02643	-623.6
424.2	-0.00181	0.02996	0.03002	-626.5
425.0	-0.01516	0.03241	0.03578	-604.9
425.7	-0.00819	0.02569	0.02697	-612.3
426.5	-0.00495	0.02218	0.02273	-617.4
427.2	-0.01566	0.03171	0.03536	-603.7
428.0	-0.01354	0.02808	0.03118	-604.3
428.8	-0.01324	0.02869	0.03159	-605.2
429.5	-0.01432	0.03095	0.03410	-605.2
430.3	-0.00847	0.02924	0.03044	-613.8
431.1	-0.01489	0.02678	0.03064	-600.9
431.8	-0.01479	0.03385	0.03694	-606.4
432.6	-0.01017	0.03217	0.03374	-612.5
433.3	-0.01306	0.03222	0.03477	-607.9
434.1	-0.01162	0.03520	0.03707	-611.7
434.9	-0.00451	0.02555	0.02595	-620.0

Table G.1. Normalized Transfer Function for Transmitter (Continued)

Frequency, kHz	Real Part	Imaginary Part	Magnitude	Unwrapped Phase Angle, Degrees
435.6	-0.01197	0.03385	0.03591	-610.5
436.4	-0.00705	0.03259	0.03335	-617.8
437.2	-0.01237	0.03759	0.03957	-611.8
437.9	-0.00968	0.03634	0.03761	-615.1
438.7	-0.00797	0.03751	0.03834	-618.0
439.5	-0.00783	0.03411	0.03499	-617.1
440.2	-0.00374	0.03574	0.03593	-624.0
441.0	-0.00209	0.03499	0.03505	-626.6
441.7	0.00445	0.03743	0.03769	-636.8
442.5	0.00304	0.03463	0.03476	-635.0
443.3	0.00325	0.03618	0.03633	-635.1
444.0	0.00004	0.02880	0.02880	-630.1
444.8	0.00648	0.03314	0.03377	-641.1
445.6	0.00512	0.03134	0.03175	-639.3
446.3	-0.00196	0.03289	0.03295	-626.6
447.1	0.00275	0.03846	0.03856	-634.1
447.8	-0.00081	0.03555	0.03556	-628.7
448.6	0.01303	0.03314	0.03561	-651.5
449.4	0.00478	0.03449	0.03482	-637.9
450.1	0.01056	0.03503	0.03658	-646.8
450.9	0.00845	0.03012	0.03128	-645.7
451.7	0.01260	0.03580	0.03795	-649.4
452.4	0.01791	0.03208	0.03675	-659.2
453.2	0.01506	0.03507	0.03817	-653.2

Table G.1. Normalized Transfer Function for Transmitter (Continued)

Frequency, kHz	Real Part	Imaginary Part	Magnitude	Unwrapped Phase Angle, Degrees
453.9	0.00393	0.02997	0.03023	-637.5
454.7	0.01003	0.02918	0.03086	-649.0
455.5	0.00619	0.03001	0.03064	-641.6
456.2	0.01264	0.02741	0.03018	-654.8
457.0	0.01284	0.02885	0.03158	-654.0
457.8	0.01337	0.02160	0.02540	-661.8
458.5	0.01163	0.02394	0.02661	-655.9
459.3	0.00921	0.02544	0.02706	-649.9
460.1	0.01336	0.02223	0.02594	-661.0
460.8	0.00756	0.02308	0.02428	-648.1
461.6	0.01920	0.02374	0.03054	-669.0
462.3	0.00763	0.02375	0.02495	-647.8
463.1	0.00747	0.01764	0.01916	-652.9
463.9	0.00938	0.02378	0.02556	-651.5
464.6	0.00965	0.02427	0.02612	-651.7
465.4	0.01060	0.01887	0.02164	-659.3
466.2	0.01281	0.02325	0.02655	-658.8
466.9	0.00885	0.02822	0.02957	-647.4
467.7	0.00917	0.02293	0.02469	-651.8
468.4	0.00287	0.02414	0.02431	-636.8
469.2	0.01954	0.02350	0.03056	-669.7
470.0	0.00902	0.02398	0.02562	-650.6
470.7	0.00927	0.02161	0.02352	-653.2
471.5	0.01533	0.02523	0.02952	-661.3

Table G.1. Normalized Transfer Function for Transmitter (Continued)

Frequency, kHz	Real Part	Imaginary Part	Magnitude	Unwrapped Phase Angle, Degrees
472.3	0.01550	0.02289	0.02764	-664.1
473.0	0.01441	0.02478	0.02867	-660.2
473.8	0.01156	0.02908	0.03129	-651.7
474.5	0.01668	0.02355	0.02885	-665.3
475.3	0.01370	0.02370	0.02737	-660.0
476.1	0.01681	0.02367	0.02903	-665.4
476.8	0.01726	0.02068	0.02693	-669.9
477.6	0.02399	0.02624	0.03555	-672.4
478.4	0.01865	0.02655	0.03245	-665.1
479.1	0.01670	0.02681	0.03158	-661.9
479.9	0.02256	0.02909	0.03681	-667.8
480.7	0.01573	0.02480	0.02937	-662.4
481.4	0.01757	0.02338	0.02924	-666.9
482.2	0.02643	0.02547	0.03670	-676.1
482.9	0.02378	0.02052	0.03141	-679.2
483.7	0.02383	0.02883	0.03740	-669.6
484.5	0.02418	0.02177	0.03253	-678.0
485.2	0.01809	0.02272	0.02905	-668.5
486.0	0.02484	0.02611	0.03604	-673.6
486.8	0.02855	0.02283	0.03655	-681.3
487.5	0.01956	0.02315	0.03031	-670.2
488.3	0.03173	0.01676	0.03589	-692.2
489.0	0.02441	0.01496	0.02863	-688.5
489.8	0.02850	0.02145	0.03567	-683.0

Table G.1. Normalized Transfer Function for Transmitter (Continued)

Frequency, kHz	Real Part	Imaginary Part	Magnitude	Unwrapped Phase Angle, Degrees
490.6	0.02581	0.01771	0.03130	-685.5
491.3	0.01829	0.00908	0.02042	-693.6
492.1	0.03632	0.01146	0.03808	-702.5
492.9	0.03739	0.01380	0.03985	-699.7
493.6	0.02483	0.01175	0.02747	-694.7
494.4	0.03114	0.01472	0.03445	-694.7
495.1	0.04048	0.01870	0.04459	-695.2
495.9	0.04071	0.01302	0.04274	-702.3
496.7	0.03424	0.01110	0.03600	-702.0
497.4	0.03932	0.00586	0.03976	-711.5
498.2	0.03004	0.00832	0.03117	-704.5
499.0	0.03516	0.01651	0.03885	-694.8
499.7	0.03038	0.00710	0.03119	-706.8
500.5	0.04465	0.00121	0.04466	-718.4
501.3	0.02675	0.01892	0.03276	-684.7
502.0	0.02400	0.00782	0.02524	-702.0
502.8	0.03253	-0.00278	0.03264	-724.9
503.5	0.03312	-0.01252	0.03541	-740.7
504.3	0.03411	0.01350	0.03669	-698.4
505.1	0.03523	-0.00344	0.03540	-725.6
505.8	0.00787	-0.01404	0.01609	-780.7
506.6	0.02541	0.01038	0.02745	-697.8
507.4	0.02378	-0.00360	0.02405	-728.6
508.1	0.03222	-0.00092	0.03224	-721.6

Table G.1. Normalized Transfer Function for Transmitter (Continued)

Frequency, kHz	Real Part	Imaginary Part	Magnitude	Unwrapped Phase Angle, Degrees
508.9	0.03198	0.00082	0.03199	-718.5
509.6	0.02155	-0.01770	0.02789	-759.4
510.4	0.02768	-0.00080	0.02769	-721.7
511.2	0.00104	-0.01662	0.01665	-806.4
511.9	0.02212	-0.01051	0.02449	-745.4
512.7	0.01645	-0.01421	0.02174	-760.8
513.5	0.01989	0.02143	0.02924	-672.9
514.2	0.04125	-0.03478	0.05395	-760.1
515.0	0.01170	-0.02169	0.02464	-781.7
515.7	0.03131	-0.00891	0.03256	-735.9
516.5	0.00713	-0.03785	0.03851	-799.3
517.3	0.04414	0.01301	0.04601	-703.6
518.0	0.00386	-0.02709	0.02736	-801.9
518.8	0.02562	-0.00541	0.02619	-731.9
519.6	0.02717	-0.02504	0.03695	-762.7
520.3	0.00246	0.01139	0.01166	-642.2
521.1	0.06477	-0.02284	0.06868	-739.4
521.9	0.03746	-0.00684	0.03808	-730.3
522.6	0.03393	-0.00282	0.03404	-724.8
523.4	0.04369	0.00454	0.04392	-714.1
524.1	0.01706	-0.00332	0.01738	-731.0
524.9	0.03864	-0.02134	0.04414	-748.9
525.7	0.02512	0.04313	0.04991	-660.2
526.4	0.04853	0.01488	0.05076	-703.0

Table G.1. Normalized Transfer Function for Transmitter (Continued)

Frequency, kHz	Real Part	Imaginary Part	Magnitude	Unwrapped Phase Angle, Degrees
527.2	0.00773	-0.02428	0.02548	-792.3
528.0	0.02557	-0.03073	0.03998	-770.2
528.7	-0.01809	-0.01926	0.02643	-853.2
529.5	0.00936	-0.00984	0.01358	-766.4

Table G.2. Normalized Transfer Function for Receiver

Frequency, kHz	Real Part	Imaginary Part	Magnitude	Unwrapped Phase Angle, Degrees
14.5	-0.00607	0.01507	0.01625	111.9
15.3	-0.00185	0.00898	0.00917	101.7
16.0	0.00990	-0.00582	0.01148	-30.5
16.8	-0.00979	-0.00449	0.01077	-155.4
17.5	-0.01353	-0.00605	0.01482	-155.9
18.3	-0.00771	0.00557	0.00951	-215.8
19.1	-0.00221	-0.01771	0.01785	-97.1
19.8	-0.01532	-0.01603	0.02218	-133.7
20.6	-0.02964	0.02209	0.03697	-216.7
21.4	-0.01420	-0.00061	0.01422	-177.5
22.1	-0.01392	0.00025	0.01392	-181.0
22.9	-0.00843	-0.00010	0.00843	-179.3
23.7	-0.01215	-0.00774	0.01441	-147.5
24.4	-0.00959	-0.00721	0.01200	-143.1
25.2	-0.01309	-0.01936	0.02337	-124.1
25.9	-0.02062	-0.03102	0.03725	-123.6
26.7	-0.03826	-0.02012	0.04323	-152.3
27.5	-0.03809	-0.04419	0.05834	-130.8
28.2	-0.06698	-0.05089	0.08412	-142.8
29.0	-0.08828	-0.06973	0.11250	-141.7
29.8	-0.16130	-0.06765	0.17492	-157.2
30.5	-0.26647	0.00289	0.26648	-180.6
31.3	-0.26984	0.20669	0.33991	-217.5
32	-0.10272	0.28439	0.30237	-250.1

Table G.2. Normalized Transfer Function for Receiver (Continued)

Frequency, kHz	Real Part	Imaginary Part	Magnitude	Unwrapped Phase Angle, Degrees
32.8	-0.02030	0.20582	0.20682	-264.4
33.6	0.01973	0.16178	0.16298	-277.0
34.3	0.03054	0.13015	0.13369	-283.2
35.1	0.02573	0.12136	0.12406	-282.0
35.9	0.02807	0.09934	0.10323	-285.8
36.6	0.01398	0.09798	0.09897	-278.1
37.4	0.02207	0.10084	0.10322	-282.3
38.1	0.02438	0.09194	0.09512	-284.9
38.9	0.02812	0.08524	0.08975	-288.3
39.7	0.03593	0.08677	0.09391	-292.5
40.4	0.03239	0.06974	0.07690	-294.9
41.2	0.02821	0.06785	0.07348	-292.6
42.0	0.02738	0.05749	0.06368	-295.5
42.7	0.02407	0.05928	0.06398	-292.1
43.5	0.01516	0.04580	0.04825	-288.3
44.3	0.02636	0.04648	0.05344	-299.6
45.0	0.01212	0.03699	0.03893	-288.1
45.8	0.00963	0.04284	0.04390	-282.7
46.5	0.00203	0.03437	0.03443	-273.4
47.3	0.00292	0.03299	0.03312	-275.1
48.1	-0.00329	0.01959	0.01986	-260.5
48.8	-0.00968	0.02323	0.02517	-247.4
49.6	-0.01447	0.01301	0.01946	-222.0
50.4	-0.02310	0.00332	0.02333	-188.2

Table G.2. Normalized Transfer Function for Receiver (Continued)

Frequency, kHz	Real Part	Imaginary Part	Magnitude	Unwrapped Phase Angle, Degrees
51.1	-0.04256	0.00943	0.04359	-192.5
51.9	-0.05075	0.00344	0.05087	-183.9
52.6	-0.07005	-0.00506	0.07023	-175.9
53.4	-0.08511	-0.03005	0.09025	-160.6
54.2	-0.13356	-0.04883	0.14220	-159.9
54.9	-0.19913	-0.04325	0.20377	-167.7
55.7	-0.28498	0.00633	0.28505	-181.3
56.5	-0.33862	0.10000	0.35308	-196.5
57.2	-0.34169	0.21074	0.40145	-211.7
58.0	-0.29544	0.30159	0.42219	-225.6
58.7	-0.23595	0.36209	0.43218	-236.9
59.5	-0.15600	0.39143	0.42137	-248.3
60.3	-0.09811	0.39967	0.41154	-256.2
61.0	-0.04243	0.38679	0.38911	-263.7
61.8	-0.00760	0.37399	0.37407	-268.8
62.6	0.02104	0.33847	0.33912	-273.6
63.3	0.04356	0.33165	0.33450	-277.5
64.1	0.05003	0.30872	0.31275	-279.2
64.8	0.06908	0.28904	0.29718	-283.4
65.6	0.06928	0.28219	0.29057	-283.8
66.4	0.06870	0.26695	0.27565	-284.4
67.1	0.07201	0.26117	0.27092	-285.4
67.9	0.06600	0.25822	0.26652	-284.3
68.7	0.06838	0.24622	0.25554	-285.5

Table G.2. Normalized Transfer Function for Receiver (Continued)

Frequency, kHz	Real Part	Imaginary Part	Magnitude	Unwrapped Phase Angle, Degrees
69.4	0.06020	0.24907	0.25624	-283.6
70.2	0.06558	0.24537	0.25398	-285.0
71.0	0.05986	0.24565	0.25284	-283.7
71.7	0.05283	0.24850	0.25406	-282.0
72.5	0.04914	0.26460	0.26912	-280.5
73.2	0.04731	0.26553	0.26972	-280.1
74.0	0.05126	0.27665	0.28136	-280.5
74.8	0.03875	0.28970	0.29228	-277.6
75.5	0.05535	0.31314	0.31799	-280.0
76.3	0.06304	0.32135	0.32748	-281.1
77.1	0.07459	0.33892	0.34703	-282.4
77.8	0.09138	0.34446	0.35638	-284.9
78.6	0.10691	0.36109	0.37659	-286.5
79.3	0.13151	0.36876	0.39151	-289.6
80.1	0.15627	0.37506	0.40631	-292.6
80.9	0.17307	0.36998	0.40846	-295.1
81.6	0.19310	0.37002	0.41737	-297.6
82.4	0.22008	0.36353	0.42496	-301.2
83.2	0.24440	0.34332	0.42143	-305.4
83.9	0.24876	0.33925	0.42068	-306.3
84.7	0.26032	0.32389	0.41554	-308.8
85.4	0.27401	0.30728	0.41170	-311.7
86.2	0.27790	0.29280	0.40368	-313.5
87	0.28659	0.28090	0.40130	-315.6

Table G.2. Normalized Transfer Function for Receiver (Continued)

Frequency, kHz	Real Part	Imaginary Part	Magnitude	Unwrapped Phase Angle, Degrees
87.7	0.27757	0.26694	0.38510	-316.1
88.5	0.27585	0.27284	0.38798	-315.3
89.3	0.27620	0.26627	0.38365	-316.0
90.0	0.28124	0.27863	0.39589	-315.3
90.8	0.28512	0.27304	0.39477	-316.2
91.6	0.29886	0.27349	0.40511	-317.5
92.3	0.30758	0.26941	0.40889	-318.8
93.1	0.31643	0.25878	0.40878	-320.7
93.8	0.32401	0.25386	0.41161	-321.9
94.6	0.31681	0.25087	0.40411	-321.6
95.4	0.33634	0.23626	0.41103	-324.9
96.1	0.33756	0.22488	0.40561	-326.3
96.9	0.34408	0.22120	0.40905	-327.3
97.7	0.34410	0.20968	0.40296	-328.6
98.4	0.34165	0.20339	0.39761	-329.2
99.2	0.33246	0.19762	0.38676	-329.3
99.9	0.33880	0.19048	0.38867	-330.7
100.7	0.33031	0.19704	0.38461	-329.2
101.5	0.32592	0.19009	0.37731	-329.7
102.2	0.31824	0.20501	0.37856	-327.2
103.0	0.32480	0.21430	0.38913	-326.6
103.8	0.33040	0.22030	0.39711	-326.3
104.5	0.34122	0.22710	0.40988	-326.4
105.3	0.34965	0.23967	0.42390	-325.6

Table G.2. Normalized Transfer Function for Receiver (Continued)

Frequency, kHz	Real Part	Imaginary Part	Magnitude	Unwrapped Phase Angle, Degrees
106	0.36879	0.23881	0.43936	-327.1
106.8	0.39067	0.24468	0.46097	-327.9
107.6	0.40660	0.23887	0.47158	-329.6
108.3	0.41952	0.23636	0.48153	-330.6
109.1	0.43968	0.23463	0.49837	-331.9
109.9	0.44205	0.22439	0.49575	-333.1
110.6	0.46143	0.21608	0.50952	-334.9
111.4	0.46619	0.21036	0.51145	-335.7
112.2	0.47847	0.19930	0.51832	-337.4
112.9	0.48820	0.18805	0.52316	-338.9
113.7	0.50134	0.18710	0.53511	-339.5
114.4	0.51263	0.17729	0.54242	-340.9
115.2	0.52368	0.16591	0.54933	-342.4
116.0	0.53138	0.14905	0.55189	-344.3
116.7	0.54189	0.13142	0.55760	-346.4
117.5	0.55690	0.12657	0.57111	-347.2
118.3	0.57090	0.10877	0.58117	-349.2
119.0	0.57301	0.09340	0.58058	-350.7
119.8	0.57521	0.08327	0.58120	-351.8
120.5	0.58206	0.05890	0.58503	-354.2
121.3	0.59264	0.04786	0.59457	-355.4
122.1	0.59193	0.02586	0.59250	-357.5
122.8	0.58767	0.00632	0.58771	-359.4
123.6	0.58985	-0.00051	0.58985	-360.0

Table G.2. Normalized Transfer Function for Receiver (Continued)

Frequency, kHz	Real Part	Imaginary Part	Magnitude	Unwrapped Phase Angle, Degrees
124.4	0.59789	-0.00828	0.59795	-360.8
125.1	0.59980	-0.03096	0.60060	-363.0
125.9	0.59229	-0.03702	0.59344	-363.6
126.6	0.59032	-0.06512	0.59390	-366.3
127.4	0.57638	-0.08526	0.58266	-368.4
128.2	0.57271	-0.09499	0.58053	-369.4
128.9	0.55980	-0.10777	0.57008	-370.9
129.7	0.54967	-0.10414	0.55945	-370.7
130.5	0.54036	-0.10623	0.55070	-371.1
131.2	0.55118	-0.10258	0.56064	-370.5
132.0	0.55314	-0.09957	0.56203	-370.2
132.8	0.57805	-0.10110	0.58682	-369.9
133.5	0.58949	-0.11898	0.60137	-371.4
134.3	0.59959	-0.14043	0.61581	-373.2
135.0	0.60438	-0.16572	0.62669	-375.3
135.8	0.59999	-0.19746	0.63165	-378.2
136.6	0.58750	-0.21510	0.62563	-380.1
137.3	0.57636	-0.24088	0.62467	-382.7
138.1	0.56652	-0.24971	0.61911	-383.8
138.9	0.54778	-0.27759	0.61410	-386.9
139.6	0.52777	-0.27723	0.59616	-387.7
140.4	0.51135	-0.28054	0.58325	-388.8
141.1	0.50658	-0.28535	0.58142	-389.4
141.9	0.48917	-0.28507	0.56617	-390.2

Table G.2. Normalized Transfer Function for Receiver (Continued)

Frequency, kHz	Real Part	Imaginary Part	Magnitude	Unwrapped Phase Angle, Degrees
142.7	0.48195	-0.29148	0.56324	-391.2
143.4	0.47696	-0.29203	0.55926	-391.5
144.2	0.46180	-0.30081	0.55113	-393.1
145.0	0.45533	-0.29643	0.54332	-393.1
145.7	0.45107	-0.29349	0.53814	-393.0
146.5	0.44409	-0.30682	0.53977	-394.6
147.2	0.43124	-0.30052	0.52562	-394.9
148.0	0.42415	-0.30174	0.52053	-395.4
148.8	0.42594	-0.30387	0.52322	-395.5
149.5	0.40994	-0.30330	0.50994	-396.5
150.3	0.39757	-0.29008	0.49215	-396.1
151.1	0.41545	-0.28980	0.50655	-394.9
151.8	0.41096	-0.28997	0.50297	-395.2
152.6	0.41274	-0.28326	0.50058	-394.5
153.4	0.41763	-0.27934	0.50244	-393.8
154.1	0.41672	-0.28427	0.50444	-394.3
154.9	0.42524	-0.28196	0.51023	-393.5
155.6	0.42499	-0.28848	0.51365	-394.2
156.4	0.43926	-0.28821	0.52538	-393.3
157.2	0.43623	-0.29446	0.52631	-394.0
157.9	0.43925	-0.28965	0.52616	-393.4
158.7	0.44927	-0.29738	0.53878	-393.5
159.5	0.45215	-0.31107	0.54882	-394.5
160.2	0.46293	-0.31090	0.55764	-393.9

Table G.2. Normalized Transfer Function for Receiver (Continued)

Frequency, kHz	Real Part	Imaginary Part	Magnitude	Unwrapped Phase Angle, Degrees
161	0.47447	-0.32465	0.57491	-394.4
161.7	0.47773	-0.33715	0.58472	-395.2
162.5	0.49351	-0.34996	0.60500	-395.3
163.3	0.49767	-0.35633	0.61208	-395.6
164.0	0.50166	-0.37037	0.62357	-396.4
164.8	0.50024	-0.38664	0.63224	-397.7
165.6	0.50938	-0.40268	0.64933	-398.3
166.3	0.50453	-0.42259	0.65813	-399.9
167.1	0.49689	-0.43307	0.65913	-401.1
167.8	0.51612	-0.45098	0.68539	-401.1
168.6	0.51695	-0.46040	0.69225	-401.7
169.4	0.51346	-0.48301	0.70494	-403.3
170.1	0.51062	-0.49948	0.71430	-404.4
170.9	0.51289	-0.52294	0.73248	-405.6
171.7	0.51780	-0.54064	0.74861	-406.2
172.4	0.51680	-0.56168	0.76326	-407.4
173.2	0.52104	-0.59619	0.79179	-408.8
174.0	0.51945	-0.62442	0.81224	-410.2
174.7	0.50946	-0.65704	0.83142	-412.2
175.5	0.50482	-0.67956	0.84655	-413.4
176.2	0.48792	-0.72164	0.87111	-415.9
177.0	0.48092	-0.76338	0.90224	-417.8
177.8	0.45239	-0.79850	0.91775	-420.5
178.5	0.43098	-0.82902	0.93435	-422.5

Table G.2. Normalized Transfer Function for Receiver (Continued)

Frequency, kHz	Real Part	Imaginary Part	Magnitude	Unwrapped Phase Angle, Degrees
179.3	0.39057	-0.87281	0.95621	-425.9
180.1	0.35397	-0.90987	0.97629	-428.7
180.8	0.31398	-0.93015	0.98171	-431.3
181.6	0.26936	-0.93846	0.97635	-434.0
182.3	0.22965	-0.95755	0.98470	-436.5
183.1	0.18081	-0.98352	1.00000	-439.6
183.9	0.12380	-0.97905	0.98685	-442.8
184.6	0.07799	-0.98870	0.99177	-445.5
185.4	0.01228	-0.97139	0.97146	-449.3
186.2	-0.02896	-0.95792	0.95836	-451.7
186.9	-0.08100	-0.93994	0.94342	-454.9
187.7	-0.12458	-0.91811	0.92652	-457.7
188.4	-0.15199	-0.88709	0.90002	-459.7
189.2	-0.18541	-0.85825	0.87805	-462.2
190.0	-0.20509	-0.82008	0.84533	-464.0
190.7	-0.22795	-0.79295	0.82506	-466.0
191.5	-0.23544	-0.76705	0.80237	-467.1
192.3	-0.24351	-0.73954	0.77860	-468.2
193.0	-0.24741	-0.72217	0.76337	-468.9
193.8	-0.25413	-0.71424	0.75811	-469.6
194.5	-0.25976	-0.70469	0.75104	-470.2
195.3	-0.26928	-0.69686	0.74707	-471.1
196.1	-0.27580	-0.68034	0.73412	-472.1
196.8	-0.28676	-0.67078	0.72950	-473.1

Table G.2. Normalized Transfer Function for Receiver (Continued)

Frequency, kHz	Real Part	Imaginary Part	Magnitude	Unwrapped Phase Angle, Degrees
197.6	-0.30691	-0.66645	0.73372	-474.7
198.4	-0.31892	-0.65732	0.73060	-475.9
199.1	-0.33652	-0.64575	0.72817	-477.5
199.9	-0.35880	-0.63278	0.72743	-479.6
200.7	-0.36901	-0.59917	0.70369	-481.6
201.4	-0.37557	-0.58625	0.69623	-482.6
202.2	-0.37847	-0.56216	0.67769	-484.0
202.9	-0.39530	-0.54899	0.67651	-485.8
203.7	-0.40522	-0.52244	0.66117	-487.8
204.5	-0.40050	-0.50447	0.64412	-488.4
205.2	-0.40554	-0.48951	0.63568	-489.6
206.0	-0.40572	-0.47619	0.62559	-490.4
206.8	-0.39946	-0.47030	0.61705	-490.3
207.5	-0.40713	-0.46071	0.61482	-491.5
208.3	-0.40869	-0.45141	0.60893	-492.2
209.0	-0.41737	-0.45241	0.61552	-492.7
209.8	-0.43294	-0.43582	0.61431	-494.8
210.6	-0.43994	-0.42257	0.61001	-496.2
211.3	-0.43916	-0.40764	0.59920	-497.1
212.1	-0.44594	-0.38728	0.59064	-499.0
212.9	-0.45118	-0.37432	0.58624	-500.3
213.6	-0.45529	-0.35954	0.58014	-501.7
214.4	-0.44827	-0.34968	0.56853	-502.0
215.1	-0.45544	-0.33917	0.56785	-503.3

Table G.2. Normalized Transfer Function for Receiver (Continued)

Frequency, kHz	Real Part	Imaginary Part	Magnitude	Unwrapped Phase Angle, Degrees
215.9	-0.46407	-0.33208	0.57064	-504.4
216.7	-0.47072	-0.31884	0.56854	-505.9
217.4	-0.47506	-0.30027	0.56200	-507.7
218.2	-0.49066	-0.27873	0.56430	-510.4
219.0	-0.48881	-0.26654	0.55676	-511.4
219.7	-0.48447	-0.24540	0.54308	-513.1
220.5	-0.48821	-0.22808	0.53886	-515.0
221.3	-0.49100	-0.20967	0.53389	-516.9
222.0	-0.47826	-0.19503	0.51649	-517.8
222.8	-0.47643	-0.17957	0.50915	-519.3
223.5	-0.47843	-0.16198	0.50510	-521.3
224.3	-0.47048	-0.14968	0.49372	-522.4
225.1	-0.46644	-0.13402	0.48531	-524.0
225.8	-0.46484	-0.11925	0.47990	-525.6
226.6	-0.46209	-0.10034	0.47286	-527.7
227.4	-0.45418	-0.08806	0.46264	-529.0
228.1	-0.44539	-0.06854	0.45063	-531.3
228.9	-0.44010	-0.06239	0.44450	-531.9
229.6	-0.43162	-0.04356	0.43381	-534.2
230.4	-0.42128	-0.02918	0.42229	-536.0
231.2	-0.41373	-0.01842	0.41414	-537.5
231.9	-0.40644	-0.00166	0.40644	-539.8
232.7	-0.39912	-0.00166	0.39912	-539.8
233.5	-0.38691	0.01590	0.38724	-542.4

Table G.2. Normalized Transfer Function for Receiver (Continued)

Frequency, kHz	Real Part	Imaginary Part	Magnitude	Unwrapped Phase Angle, Degrees
234.2	-0.37262	0.03737	0.37449	-545.7
235.0	-0.36546	0.04230	0.36790	-546.6
235.7	-0.34625	0.04374	0.34901	-547.2
236.5	-0.33474	0.04906	0.33831	-548.3
237.3	-0.31746	0.06471	0.32399	-551.5
238.0	-0.30616	0.05887	0.31177	-550.9
238.8	-0.28590	0.06947	0.29422	-553.7
239.6	-0.27437	0.06782	0.28263	-553.9
240.3	-0.26643	0.05771	0.27261	-552.2
241.1	-0.25386	0.05811	0.26042	-552.9
241.9	-0.24950	0.05512	0.25552	-552.5
242.6	-0.25024	0.05371	0.25594	-552.1
243.4	-0.23674	0.06488	0.24547	-555.3
244.1	-0.23094	0.06838	0.24085	-556.5
244.9	-0.22746	0.06876	0.23763	-556.8
245.7	-0.21684	0.07209	0.22851	-558.4
246.4	-0.19628	0.07629	0.21058	-561.2
247.2	-0.19455	0.07722	0.20931	-561.6
248.0	-0.18081	0.07439	0.19551	-562.4
248.7	-0.16132	0.07278	0.17698	-564.3
249.5	-0.15427	0.06293	0.16661	-562.2
250.2	-0.14566	0.05854	0.15699	-561.9
251.0	-0.14170	0.04359	0.14825	-557.1
251.8	-0.13645	0.03727	0.14145	-555.3

Table G.2. Normalized Transfer Function for Receiver (Continued)

Frequency, kHz	Real Part	Imaginary Part	Magnitude	Unwrapped Phase Angle, Degrees
252.5	-0.14137	0.03042	0.14461	-552.1
253.3	-0.14036	0.02825	0.14317	-551.4
254.1	-0.13541	0.01992	0.13687	-548.4
254.8	-0.13709	0.01928	0.13844	-548.0
255.6	-0.13531	0.01164	0.13581	-544.9
256.3	-0.13677	0.01248	0.13733	-545.2
257.1	-0.14163	0.01018	0.14200	-544.1
257.9	-0.15080	0.00609	0.15092	-542.3
258.6	-0.15134	0.01105	0.15174	-544.2
259.4	-0.15361	0.00728	0.15378	-542.7
260.2	-0.15285	0.01525	0.15361	-545.7
260.9	-0.14071	0.01773	0.14183	-547.2
261.7	-0.14726	0.02028	0.14865	-547.8
262.5	-0.14028	0.02343	0.14223	-549.5
263.2	-0.14300	0.02097	0.14453	-548.3
264.0	-0.14011	0.03206	0.14373	-552.9
264.7	-0.13227	0.03619	0.13713	-555.3
265.5	-0.12903	0.03502	0.13369	-555.2
266.3	-0.13054	0.03436	0.13499	-554.7
267.0	-0.12613	0.03397	0.13063	-555.1
267.8	-0.12128	0.03775	0.12702	-557.3
268.6	-0.10974	0.03930	0.11657	-559.7
269.3	-0.10414	0.03732	0.11062	-559.7
270.1	-0.09893	0.03539	0.10507	-559.7

Table G.2. Normalized Transfer Function for Receiver (Continued)

Frequency, kHz	Real Part	Imaginary Part	Magnitude	Unwrapped Phase Angle, Degrees
270.8	-0.09516	0.03506	0.10142	-560.2
271.6	-0.09045	0.02879	0.09492	-557.7
272.4	-0.09116	0.02153	0.09367	-553.3
273.1	-0.08815	0.02280	0.09105	-554.5
273.9	-0.07883	0.02543	0.08283	-557.9
274.7	-0.06845	0.01651	0.07042	-553.6
275.4	-0.07313	0.00903	0.07368	-547.0
276.2	-0.06593	-0.00190	0.06596	-538.3
276.9	-0.06619	-0.00151	0.06621	-538.7
277.7	-0.06915	-0.01014	0.06989	-531.7
278.5	-0.06385	-0.02130	0.06731	-521.6
279.2	-0.06465	-0.02239	0.06842	-520.9
280.0	-0.06832	-0.02691	0.07342	-518.5
280.8	-0.07076	-0.03225	0.07776	-515.5
281.5	-0.07728	-0.04457	0.08921	-510.0
282.3	-0.08805	-0.04819	0.10038	-511.3
283.1	-0.09845	-0.04861	0.10980	-513.7
283.8	-0.10548	-0.05541	0.11915	-512.3
284.6	-0.11200	-0.04754	0.12167	-517.0
285.3	-0.11795	-0.05276	0.12921	-515.9
286.1	-0.12862	-0.04796	0.13727	-519.6
286.9	-0.14223	-0.03783	0.14718	-525.1
287.6	-0.14100	-0.03029	0.14422	-527.9
288.4	-0.14347	-0.01848	0.14465	-532.7

Table G.2. Normalized Transfer Function for Receiver (Continued)

Frequency, kHz	Real Part	Imaginary Part	Magnitude	Unwrapped Phase Angle, Degrees
289.2	-0.15643	-0.01931	0.15761	-533.0
289.9	-0.14871	-0.00618	0.14884	-537.6
290.7	-0.15725	-0.00281	0.15727	-539.0
291.4	-0.15867	0.00698	0.15882	-542.5
292.2	-0.14954	0.00682	0.14970	-542.6
293.0	-0.14696	0.01807	0.14807	-547.0
293.7	-0.15255	0.03089	0.15565	-551.4
294.5	-0.14458	0.03806	0.14951	-554.7
295.3	-0.14072	0.03659	0.14540	-554.6
296.0	-0.13478	0.04533	0.14220	-558.6
296.8	-0.13159	0.05273	0.14176	-561.8
297.5	-0.11729	0.04654	0.12619	-561.6
298.3	-0.11709	0.05037	0.12747	-563.3
299.1	-0.11823	0.05554	0.13062	-565.2
299.8	-0.11104	0.05593	0.12433	-566.7
300.6	-0.10211	0.05382	0.11543	-567.8
301.4	-0.10350	0.05337	0.11645	-567.3
302.1	-0.09491	0.05519	0.10979	-570.2
302.9	-0.08971	0.05398	0.10470	-571.0
303.6	-0.09786	0.05105	0.11038	-567.6
304.4	-0.08795	0.05246	0.10241	-570.8
305.2	-0.08105	0.05647	0.09879	-574.9
305.9	-0.08312	0.05562	0.10002	-573.8
306.7	-0.07935	0.05803	0.09830	-576.2

Table G.2. Normalized Transfer Function for Receiver (Continued)

Frequency, kHz	Real Part	Imaginary Part	Magnitude	Unwrapped Phase Angle, Degrees
307.5	-0.07646	0.05469	0.09401	-575.6
308.2	-0.06528	0.05856	0.08769	-581.9
309.0	-0.06428	0.05350	0.08363	-579.8
309.8	-0.05625	0.04992	0.07520	-581.6
310.5	-0.05485	0.05165	0.07534	-583.3
311.3	-0.05115	0.04675	0.06929	-582.4
312.0	-0.05829	0.04349	0.07273	-576.7
312.8	-0.04927	0.04467	0.06650	-582.2
313.6	-0.05146	0.03801	0.06397	-576.5
314.3	-0.05154	0.03737	0.06366	-575.9
315.1	-0.05205	0.03938	0.06527	-577.1
315.9	-0.05235	0.03231	0.06152	-571.7
316.6	-0.04810	0.03881	0.06180	-578.9
317.4	-0.04768	0.03245	0.05768	-574.2
318.1	-0.05093	0.02874	0.05848	-569.4
318.9	-0.04512	0.02892	0.05359	-572.7
319.7	-0.04645	0.03124	0.05598	-573.9
320.4	-0.04879	0.03376	0.05933	-574.7
321.2	-0.04639	0.03737	0.05957	-578.8
322.0	-0.05166	0.03721	0.06367	-575.8
322.7	-0.04810	0.03254	0.05807	-574.1
323.5	-0.04256	0.03017	0.05217	-575.3
324.2	-0.04358	0.03511	0.05596	-578.9
325	-0.04335	0.04277	0.06090	-584.6

Table G.2. Normalized Transfer Function for Receiver (Continued)

Frequency, kHz	Real Part	Imaginary Part	Magnitude	Unwrapped Phase Angle, Degrees
325.8	-0.04210	0.03134	0.05249	-576.7
326.5	-0.03651	0.03579	0.05112	-584.4
327.3	-0.03247	0.03636	0.04875	-588.2
328.1	-0.03316	0.02326	0.04050	-575.0
328.8	-0.02737	0.02828	0.03935	-585.9
329.6	-0.02714	0.02213	0.03502	-579.2
330.4	-0.02688	0.02647	0.03773	-584.6
331.1	-0.02724	0.02102	0.03441	-577.7
331.9	-0.03078	0.01717	0.03524	-569.1
332.6	-0.03460	0.00817	0.03556	-553.3
333.4	-0.03618	0.01176	0.03804	-558.0
334.2	-0.03963	0.01545	0.04254	-561.3
334.9	-0.03480	0.00784	0.03568	-552.7
335.7	-0.03211	0.00694	0.03285	-552.2
336.5	-0.03683	0.01391	0.03937	-560.7
337.2	-0.03727	0.01139	0.03897	-557.0
338.0	-0.03631	0.00917	0.03745	-554.2
338.7	-0.03980	0.01148	0.04142	-556.1
339.5	-0.03838	0.01281	0.04046	-558.5
340.3	-0.04266	0.01666	0.04580	-561.3
341.0	-0.03895	0.01116	0.04052	-556.0
341.8	-0.04263	0.01630	0.04564	-560.9
342.6	-0.03915	0.01529	0.04203	-561.3
343.3	-0.04182	0.01437	0.04422	-559.0

Table G.2. Normalized Transfer Function for Receiver (Continued)

Frequency, kHz	Real Part	Imaginary Part	Magnitude	Unwrapped Phase Angle, Degrees
344.1	-0.03820	0.01527	0.04114	-561.8
344.8	-0.03687	0.01336	0.03922	-559.9
345.6	-0.03824	0.02029	0.04329	-568.0
346.4	-0.03565	0.02127	0.04151	-570.8
347.1	-0.03828	0.02222	0.04426	-570.1
347.9	-0.03864	0.01768	0.04250	-564.6
348.7	-0.03446	0.01413	0.03724	-562.3
349.4	-0.03887	0.01777	0.04274	-564.6
350.2	-0.02785	0.01653	0.03238	-570.7
351.0	-0.03198	0.01919	0.03729	-571.0
351.7	-0.02255	0.02501	0.03367	-588.0
352.5	-0.02589	0.01885	0.03203	-576.1
353.2	-0.02274	0.02004	0.03031	-581.4
354.0	-0.02555	0.02206	0.03375	-580.8
354.8	-0.02380	0.01987	0.03100	-579.9
355.5	-0.02607	0.01675	0.03099	-572.7
356.3	-0.01600	0.01897	0.02481	-589.9
357.1	-0.02081	0.01760	0.02725	-580.2
357.8	-0.01458	0.01376	0.02005	-583.3
358.6	-0.01862	0.01232	0.02232	-573.5
359.3	-0.01725	0.01120	0.02056	-573.0
360.1	-0.01655	0.01756	0.02412	-586.7
360.9	-0.01059	0.01197	0.01598	-588.5
361.6	-0.00739	0.00244	0.00779	-558.3

Table G.2. Normalized Transfer Function for Receiver (Continued)

Frequency, kHz	Real Part	Imaginary Part	Magnitude	Unwrapped Phase Angle, Degrees
362.4	-0.01279	0.00711	0.01463	-569.1
363.2	-0.01583	0.00116	0.01587	-544.2
363.9	-0.01159	0.00156	0.01169	-547.7
364.7	-0.01556	-0.00187	0.01568	-533.2
365.4	-0.01332	-0.00247	0.01355	-529.5
366.2	-0.01406	-0.00133	0.01412	-534.6
367.0	-0.01190	-0.00883	0.01482	-503.4
367.7	-0.01298	-0.01539	0.02013	-490.2
368.5	-0.01552	-0.01198	0.01961	-502.3
369.3	-0.01628	-0.01901	0.02502	-490.6
370.0	-0.01917	-0.02223	0.02935	-490.8
370.8	-0.02378	-0.01352	0.02735	-510.4
371.6	-0.02706	-0.01099	0.02920	-517.9
372.3	-0.02618	-0.01742	0.03145	-506.4
373.1	-0.02724	-0.02084	0.03430	-502.6
373.8	-0.02431	-0.02438	0.03443	-494.9
374.6	-0.02822	-0.02120	0.03530	-503.1
375.4	-0.04063	-0.02321	0.04680	-510.3
376.1	-0.02842	-0.02270	0.03638	-501.4
376.9	-0.03407	-0.01924	0.03913	-510.6
377.7	-0.04224	-0.02348	0.04833	-510.9
378.4	-0.04254	-0.02093	0.04741	-513.8
379.2	-0.04283	-0.02626	0.05023	-508.5
379.9	-0.04880	-0.02148	0.05332	-516.2

Table G.2. Normalized Transfer Function for Receiver (Continued)

Frequency, kHz	Real Part	Imaginary Part	Magnitude	Unwrapped Phase Angle, Degrees
380.7	-0.05060	-0.01863	0.05392	-519.8
381.5	-0.04612	-0.01998	0.05027	-516.6
382.2	-0.05150	-0.02251	0.05620	-516.4
383.0	-0.05183	-0.02433	0.05726	-514.9
383.8	-0.05872	-0.01497	0.06060	-525.7
384.5	-0.05694	-0.01992	0.06033	-520.7
385.3	-0.06471	-0.02215	0.06839	-521.1
386.0	-0.07230	-0.02289	0.07584	-522.4
386.8	-0.06723	-0.01708	0.06936	-525.7
387.6	-0.06850	-0.01705	0.07059	-526.0
388.3	-0.07720	-0.01450	0.07855	-529.4
389.1	-0.08237	-0.01388	0.08353	-530.4
389.9	-0.07526	-0.00688	0.07558	-534.8
390.6	-0.09348	-0.00131	0.09349	-539.2
391.4	-0.08787	0.00364	0.08794	-542.4
392.2	-0.09379	0.00772	0.09410	-544.7
392.9	-0.08520	0.01572	0.08663	-550.5
393.7	-0.08607	0.02494	0.08961	-556.2
394.4	-0.09121	0.01871	0.09311	-551.6
395.2	-0.09147	0.02881	0.09590	-557.5
396.0	-0.09918	0.03220	0.10428	-558.0
396.7	-0.09521	0.04432	0.10502	-565.0
397.5	-0.08950	0.05048	0.10276	-569.4
398.3	-0.08310	0.05487	0.09958	-573.4

Table G.2. Normalized Transfer Function for Receiver (Continued)

Frequency, kHz	Real Part	Imaginary Part	Magnitude	Unwrapped Phase Angle, Degrees
399	-0.07872	0.05145	0.09405	-573.2
399.8	-0.07839	0.06275	0.10041	-578.7
400.5	-0.07291	0.06301	0.09637	-580.8
401.3	-0.06786	0.07483	0.10101	-587.8
402.1	-0.05825	0.07544	0.09532	-592.3
402.8	-0.05027	0.07413	0.08957	-595.9
403.6	-0.04092	0.07272	0.08344	-600.6
404.4	-0.03645	0.07498	0.08337	-604.1
405.1	-0.03207	0.07505	0.08161	-606.9
405.9	-0.03089	0.06778	0.07449	-605.5
406.6	-0.02865	0.06545	0.07145	-606.4
407.4	-0.02815	0.06969	0.07516	-608.0
408.2	-0.02247	0.06493	0.06871	-610.9
408.9	-0.01909	0.06293	0.06576	-613.1
409.7	-0.01929	0.05894	0.06202	-611.9
410.5	-0.02461	0.06274	0.06739	-608.6
411.2	-0.02300	0.05440	0.05906	-607.1
412.0	-0.02137	0.06129	0.06491	-610.8
412.8	-0.01782	0.05739	0.06009	-612.7
413.5	-0.01562	0.05660	0.05871	-614.6
414.3	-0.01545	0.05956	0.06153	-615.5
415.0	-0.00912	0.06033	0.06101	-621.4
415.8	-0.00555	0.05664	0.05691	-624.4
416.6	-0.01522	0.05715	0.05914	-615.1

Table G.2. Normalized Transfer Function for Receiver (Continued)

Frequency, kHz	Real Part	Imaginary Part	Magnitude	Unwrapped Phase Angle, Degrees
417.3	-0.00974	0.05737	0.05819	-620.4
418.1	-0.00758	0.05583	0.05635	-622.3
418.9	-0.01160	0.05438	0.05560	-618.0
419.6	-0.00598	0.04765	0.04803	-622.8
420.4	0.00546	0.04928	0.04958	-636.3
421.1	-0.00222	0.05086	0.05091	-627.5
421.9	-0.00437	0.04980	0.04999	-625.0
422.7	-0.00061	0.04388	0.04389	-629.2
423.4	0.00176	0.04556	0.04559	-632.2
424.2	0.00669	0.04672	0.04719	-638.1
425.0	0.00342	0.03908	0.03923	-635.0
425.7	0.00668	0.03330	0.03396	-641.3
426.5	0.00460	0.04619	0.04642	-635.7
427.2	0.00343	0.04361	0.04374	-634.5
428.0	0.00744	0.04148	0.04215	-640.2
428.8	0.00739	0.04079	0.04146	-640.3
429.5	-0.00215	0.03811	0.03817	-626.8
430.3	0.00235	0.03359	0.03367	-634.0
431.1	-0.00100	0.03618	0.03619	-628.4
431.8	0.00520	0.03100	0.03143	-639.5
432.6	0.00535	0.03915	0.03951	-637.8
433.3	0.00928	0.03836	0.03947	-643.6
434.1	0.00425	0.03690	0.03714	-636.6
434.9	0.00205	0.03742	0.03748	-633.1

Table G.2. Normalized Transfer Function for Receiver (Continued)

Frequency, kHz	Real Part	Imaginary Part	Magnitude	Unwrapped Phase Angle, Degrees
435.6	0.00250	0.03523	0.03532	-634.1
436.4	0.00425	0.03155	0.03184	-637.7
437.2	0.00366	0.04339	0.04355	-634.8
437.9	0.00225	0.03525	0.03532	-633.7
438.7	0.00900	0.03502	0.03616	-644.4
439.5	0.00793	0.03693	0.03777	-642.1
440.2	0.00454	0.03485	0.03515	-637.4
441.0	0.00972	0.03286	0.03427	-646.5
441.7	0.00670	0.03308	0.03375	-641.5
442.5	0.00644	0.03418	0.03478	-640.7
443.3	0.00967	0.03823	0.03943	-644.2
444.0	0.00792	0.03198	0.03295	-643.9
444.8	0.00782	0.03216	0.03310	-643.7
445.6	0.00962	0.03596	0.03723	-645.0
446.3	0.01048	0.03849	0.03989	-645.2
447.1	0.00790	0.03070	0.03171	-644.4
447.8	0.01280	0.03430	0.03661	-650.5
448.6	0.01188	0.03698	0.03884	-647.8
449.4	0.01381	0.03432	0.03699	-651.9
450.1	0.01135	0.03827	0.03992	-646.5
450.9	0.00913	0.03484	0.03602	-644.7
451.7	0.01026	0.03551	0.03696	-646.1
452.4	0.01663	0.03013	0.03441	-658.9
453.2	0.00878	0.03670	0.03774	-643.5

Table G.2. Normalized Transfer Function for Receiver (Continued)

Frequency, kHz	Real Part	Imaginary Part	Magnitude	Unwrapped Phase Angle, Degrees
453.9	0.01085	0.03191	0.03370	-648.8
454.7	0.01627	0.03119	0.03518	-657.5
455.5	0.01528	0.03114	0.03468	-656.1
456.2	0.01196	0.02442	0.02719	-656.1
457.0	0.01646	0.02629	0.03102	-662.1
457.8	0.02131	0.02631	0.03386	-669.0
458.5	0.01325	0.02275	0.02632	-660.2
459.3	0.01273	0.01716	0.02136	-666.6
460.1	0.01755	0.02126	0.02756	-669.5
460.8	0.01558	0.01424	0.02111	-677.6
461.6	0.01388	0.02131	0.02543	-663.1
462.3	0.01884	0.02121	0.02837	-671.6
463.1	0.01182	0.01647	0.02027	-665.7
463.9	0.02076	0.01840	0.02774	-678.4
464.6	0.01461	0.02620	0.03000	-659.1
465.4	0.01546	0.02529	0.02964	-661.4
466.2	0.01047	0.02171	0.02410	-655.8
466.9	0.01169	0.02048	0.02358	-659.7
467.7	0.01640	0.02322	0.02843	-665.2
468.4	0.01354	0.01669	0.02149	-669.0
469.2	0.01845	0.02280	0.02932	-669.0
470.0	0.01119	0.02152	0.02426	-657.5
470.7	0.01216	0.02390	0.02681	-657.0
471.5	0.01527	0.02275	0.02740	-663.9

Table G.2. Normalized Transfer Function for Receiver (Continued)

Frequency, kHz	Real Part	Imaginary Part	Magnitude	Unwrapped Phase Angle, Degrees
472.3	0.01778	0.01864	0.02575	-673.6
473.0	0.02021	0.02493	0.03209	-669.0
473.8	0.01983	0.02971	0.03571	-663.7
474.5	0.01375	0.01987	0.02417	-664.7
475.3	0.01367	0.02466	0.02819	-659.0
476.1	0.01825	0.01969	0.02685	-672.8
476.8	0.02425	0.01994	0.03140	-680.6
477.6	0.01908	0.01943	0.02723	-674.5
478.4	0.01952	0.02231	0.02964	-671.2
479.1	0.01971	0.01508	0.02482	-682.6
479.9	0.01849	0.01566	0.02423	-679.7
480.7	0.02112	0.01809	0.02781	-679.4
481.4	0.02660	0.01806	0.03215	-685.8
482.2	0.02254	0.01475	0.02694	-686.8
482.9	0.01882	0.01494	0.02403	-681.6
483.7	0.02432	0.01589	0.02905	-686.8
484.5	0.02102	0.01665	0.02681	-681.6
485.2	0.01838	0.01279	0.02239	-685.2
486.0	0.02453	0.01723	0.02998	-684.9
486.8	0.02205	0.01898	0.02910	-679.3
487.5	0.01916	0.01046	0.02183	-691.4
488.3	0.02583	0.01026	0.02779	-698.3
489.0	0.02748	0.01703	0.03233	-688.2
489.8	0.02600	0.01586	0.03046	-688.6

Table G.2. Normalized Transfer Function for Receiver (Continued)

Frequency, kHz	Real Part	Imaginary Part	Magnitude	Unwrapped Phase Angle, Degrees
490.6	0.02968	0.01077	0.03157	-700.1
491.3	0.02369	0.01464	0.02785	-688.3
492.1	0.02480	0.01094	0.02711	-696.2
492.9	0.02677	0.01108	0.02897	-697.5
493.6	0.03040	0.01606	0.03438	-692.2
494.4	0.02714	0.01321	0.03019	-694.0
495.1	0.02595	0.00948	0.02763	-699.9
495.9	0.03108	0.00365	0.03129	-713.3
496.7	0.02807	0.01074	0.03006	-699.1
497.4	0.02922	0.00536	0.02971	-709.6
498.2	0.02465	0.01652	0.02968	-686.2
499.0	0.01741	0.00571	0.01832	-701.8
499.7	0.02617	0.00467	0.02658	-709.9
500.5	0.00876	0.00165	0.00891	-709.3
501.3	0.02652	0.00515	0.02702	-709.0
502.0	0.01832	0.00237	0.01848	-712.6
502.8	0.02580	-0.00263	0.02594	-725.8
503.5	0.03651	-0.00339	0.03667	-725.3
504.3	0.02674	0.00950	0.02838	-700.4
505.1	0.02486	-0.00065	0.02487	-721.5
505.8	0.01321	-0.01156	0.01755	-761.2
506.6	0.03088	-0.00167	0.03092	-723.1
507.4	0.02678	0.00367	0.02703	-712.2
508.1	0.02274	0.00625	0.02358	-704.6

Table G.2. Normalized Transfer Function for Receiver (Continued)

Frequency, kHz	Real Part	Imaginary Part	Magnitude	Unwrapped Phase Angle, Degrees
508.9	0.02054	-0.00719	0.02176	-739.3
509.6	0.01593	-0.00098	0.01596	-723.5
510.4	0.02491	0.00041	0.02492	-719.1
511.2	0.02928	0.00203	0.02935	-716.0
511.9	0.02157	0.01006	0.02380	-695.0
512.7	0.01976	-0.01535	0.02502	-757.8
513.5	0.02127	0.02651	0.03399	-668.7
514.2	0.02518	-0.02336	0.03434	-762.9
515.0	0.03766	-0.03483	0.05130	-762.8
515.7	0.03264	-0.02176	0.03923	-753.7
516.5	0.01481	-0.01209	0.01912	-759.2
517.3	0.00735	0.00761	0.01058	-674.0
518.0	0.03296	0.03599	0.04880	-672.5
518.8	-0.00047	-0.00901	0.00902	-813.0
519.6	0.00551	-0.00183	0.00580	-738.4
520.3	0.02670	-0.00979	0.02844	-740.1
521.1	0.04410	0.00565	0.04446	-712.7
521.9	0.02222	0.02216	0.03138	-675.1
522.6	-0.00310	0.01906	0.01931	-620.8
523.4	0.00875	-0.06021	0.06085	-441.7
524.1	0.01361	-0.00471	0.01440	-379.1
524.9	0.00360	0.00490	0.00607	-306.3
525.7	0.00763	-0.01440	0.01630	-422.1
526.4	0.02910	-0.00188	0.02916	-363.7

Table G.2. Normalized Transfer Function for Receiver (Continued)

Frequency, kHz	Real Part	Imaginary Part	Magnitude	Unwrapped Phase Angle, Degrees
527.2	0.05735	0.01901	0.06042	-341.7
528.0	-0.00838	0.04440	0.04519	-259.3
528.7	0.00995	0.00864	0.01317	-319.0
529.5	-0.02168	-0.05416	0.05834	-471.8

Appendix H - Comparisons Between Measurements and Predictions

H.1 Comparisons Between Measurements and Predictions

Figures H.1 through H.93 give the measured and predicted normalized radial displacements for the locations listed in Table 4.1. These figures are presented by increasing circumferential offset for each axial offset. The smallest axial offsets are presented first.

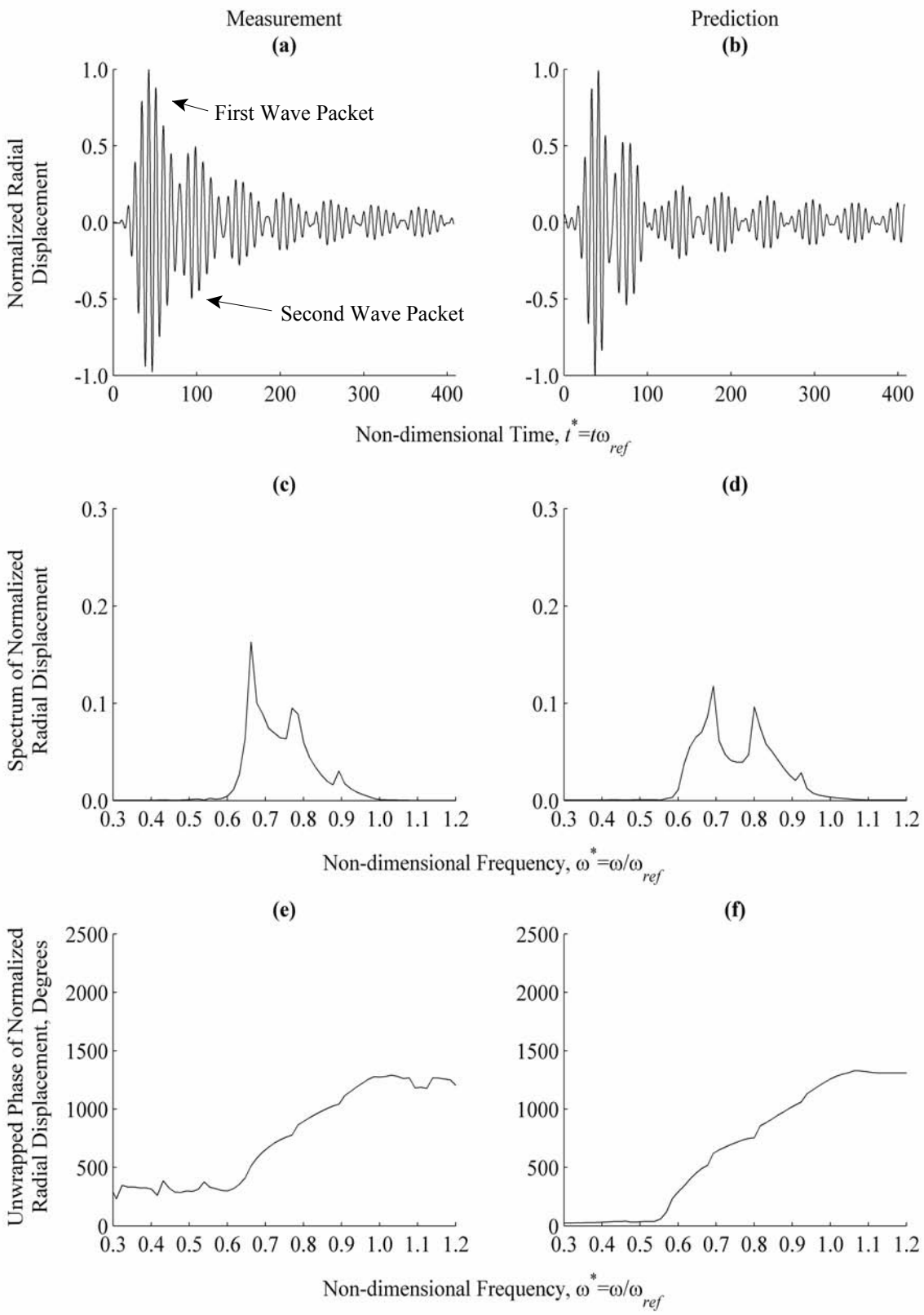

Figure H.1. Measurement and Prediction at $\theta=20^{\circ}$, $z^*=0.00$

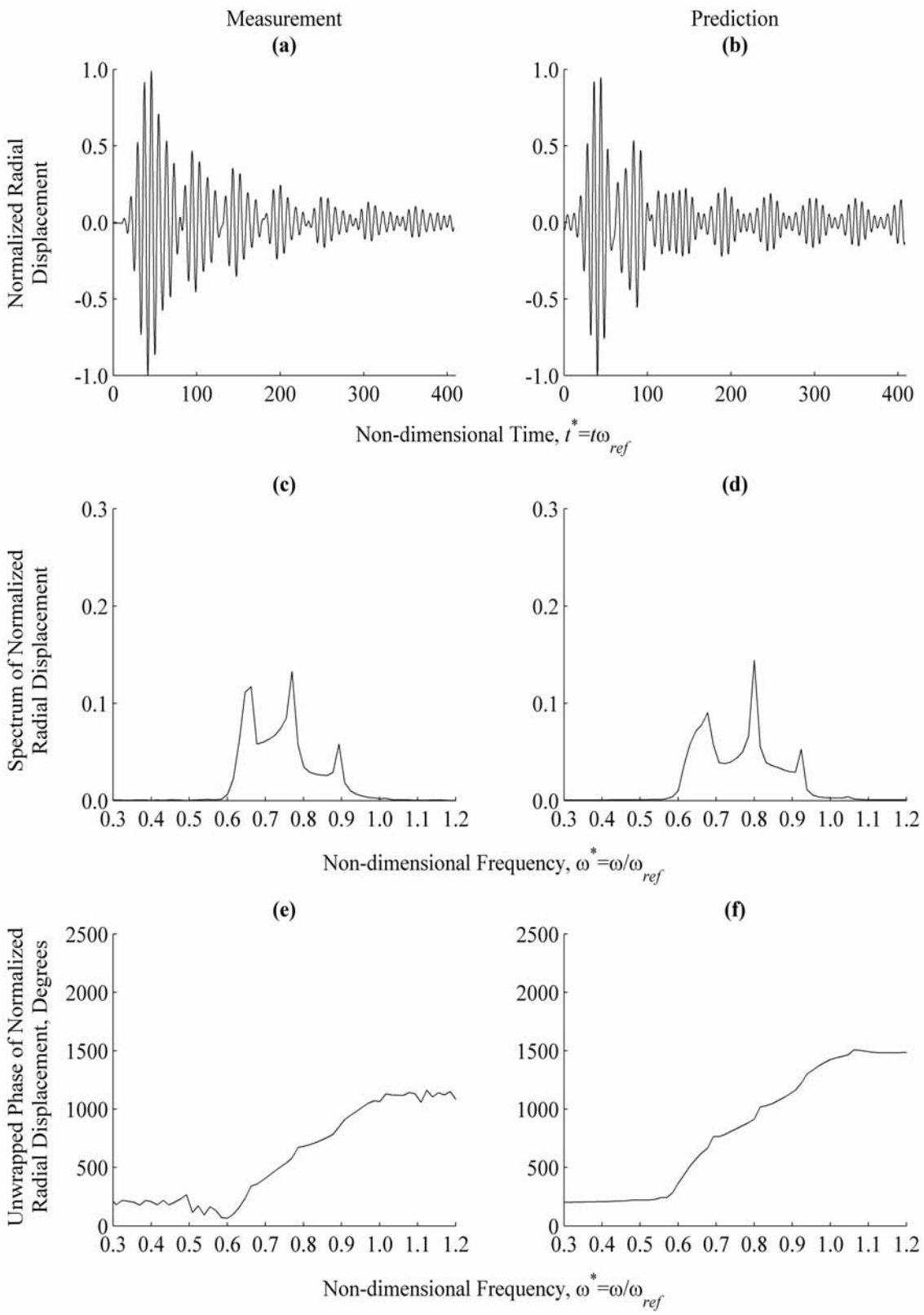

Figure H.2. Measurement and Prediction at $\theta=30^{\circ}$, $z^*=0.00$

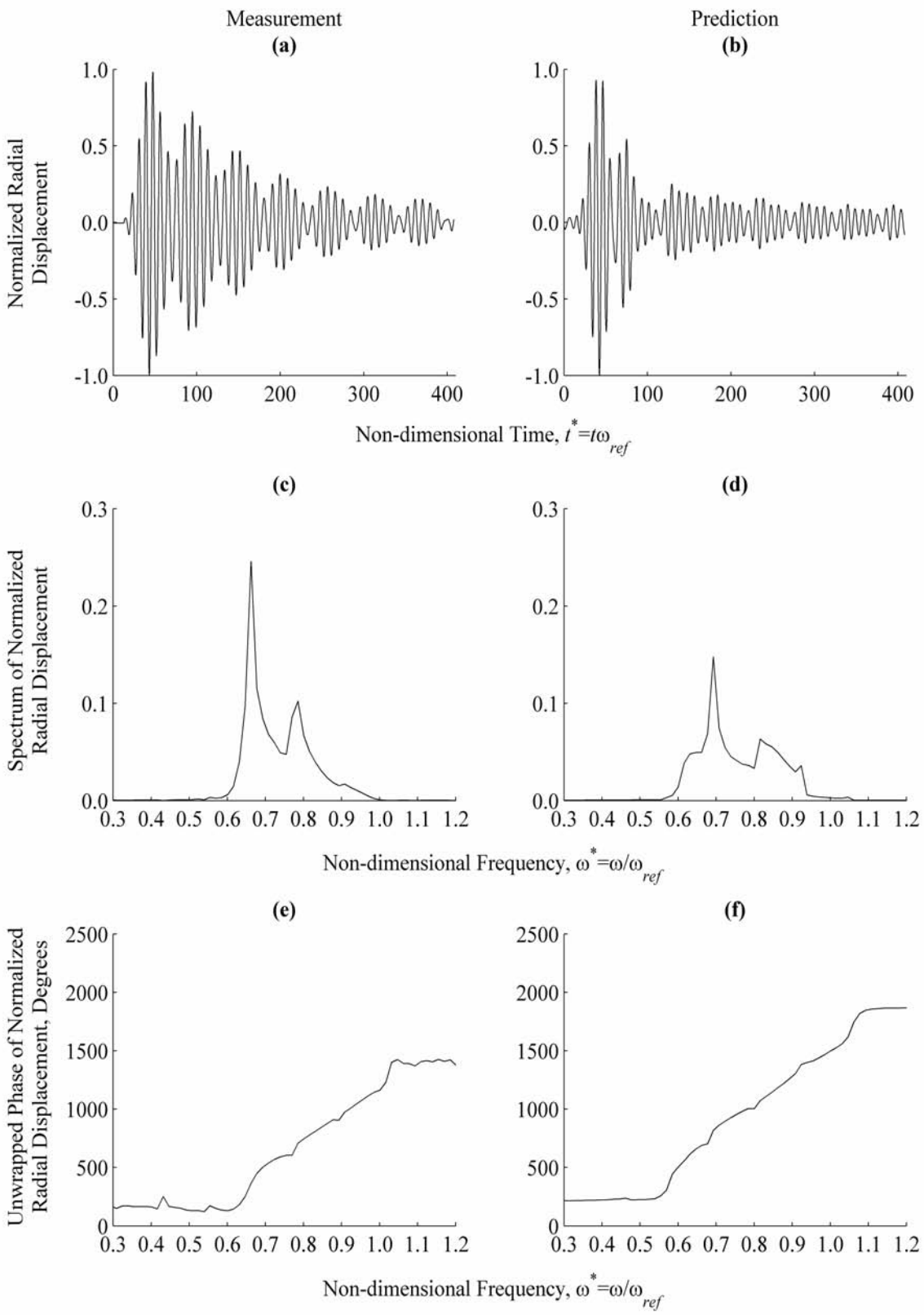

Figure H.3. Measurement and Prediction at $\theta=40^{\circ}$, $z^*=0.00$

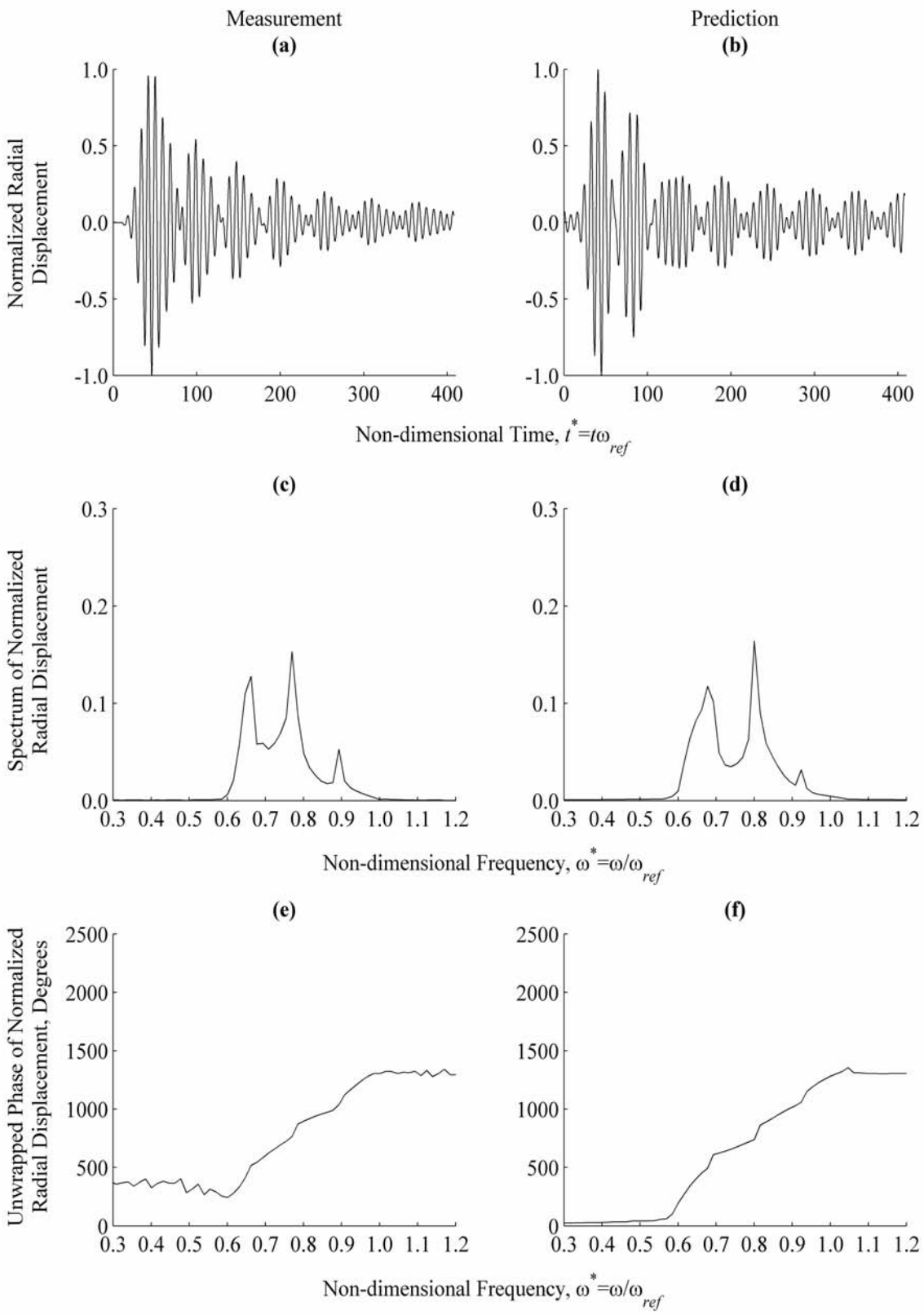

Figure H.4. Measurement and Prediction at $\theta=50^{\circ}$, $z^*=0.00$

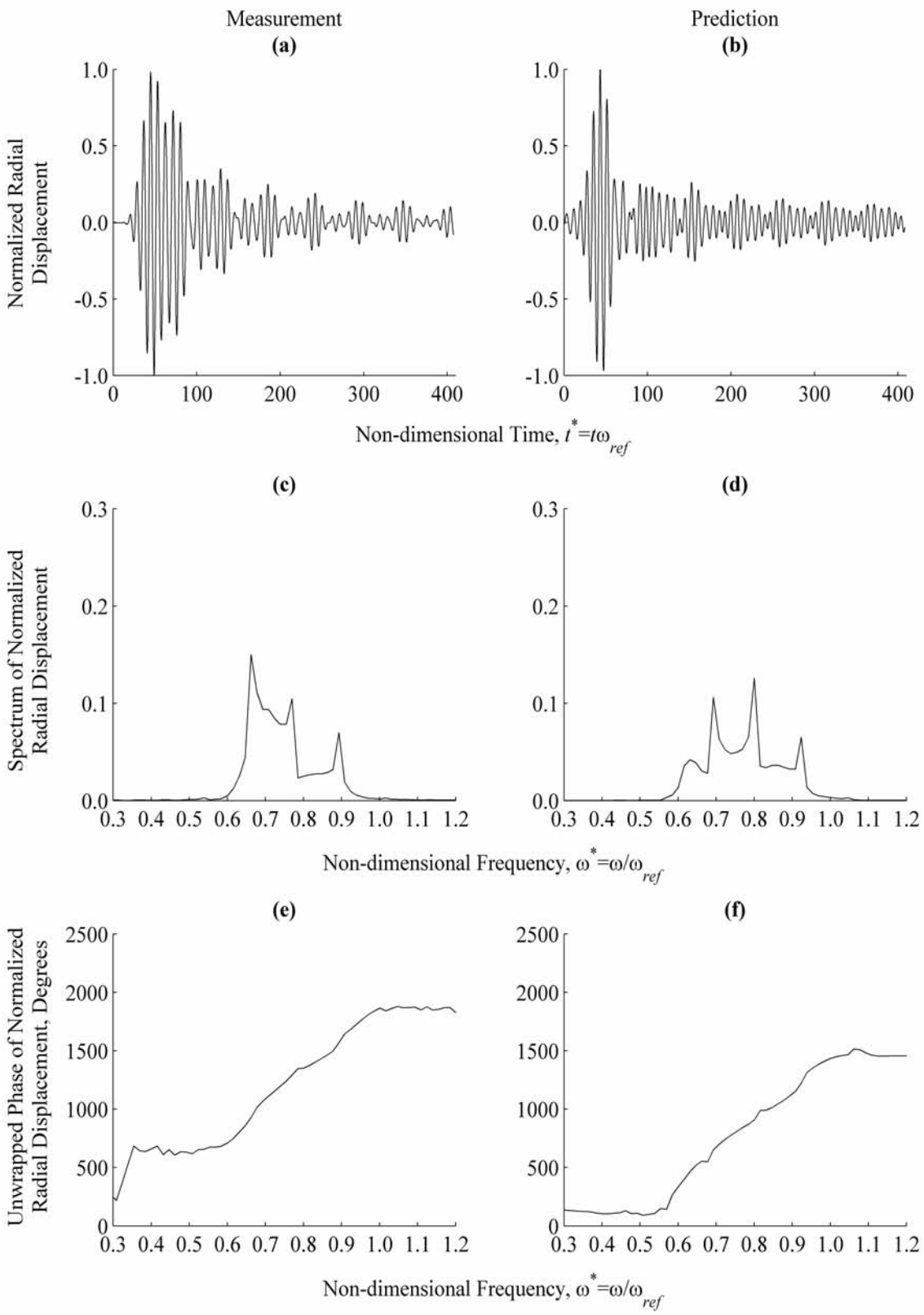

Figure H.5. Measurement and Prediction at $\theta=60^{\circ}$, $z^*=0.00$

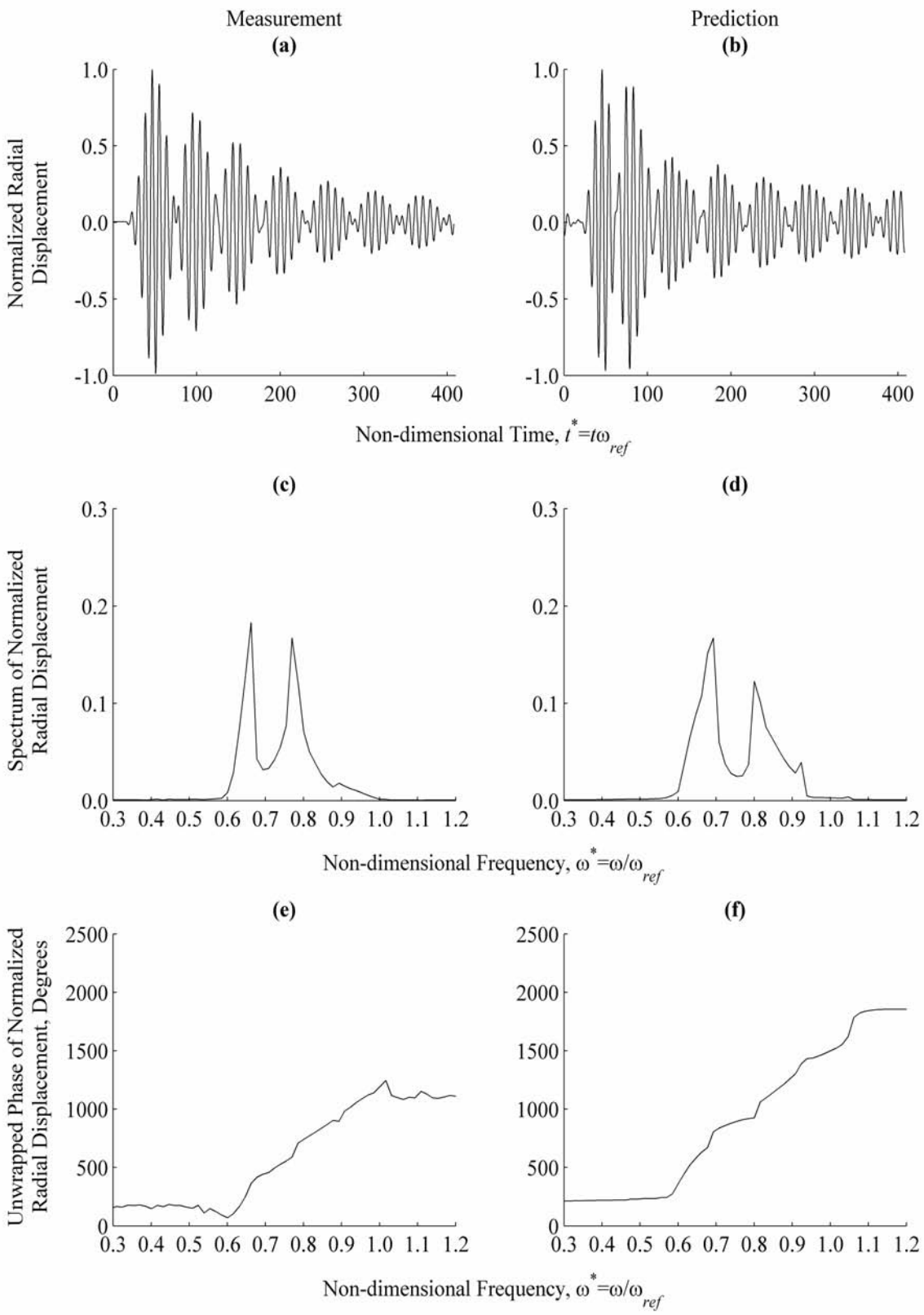

Figure H.6. Measurement and Prediction at $\theta=70^{\circ}$, $z^*=0.00$

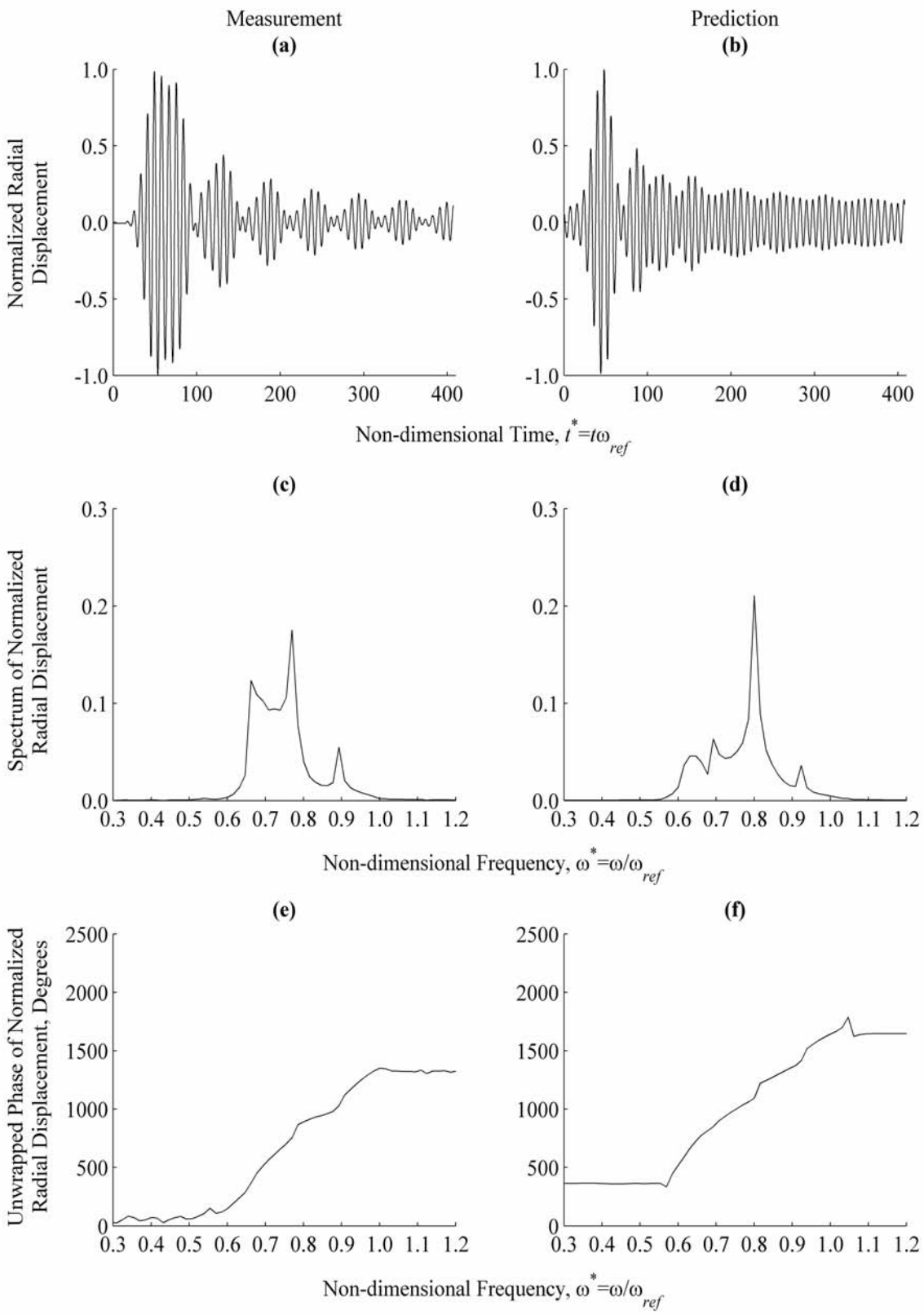

Figure H.7. Measurement and Prediction at $\theta=80^{\circ}$, $z^*=0.00$

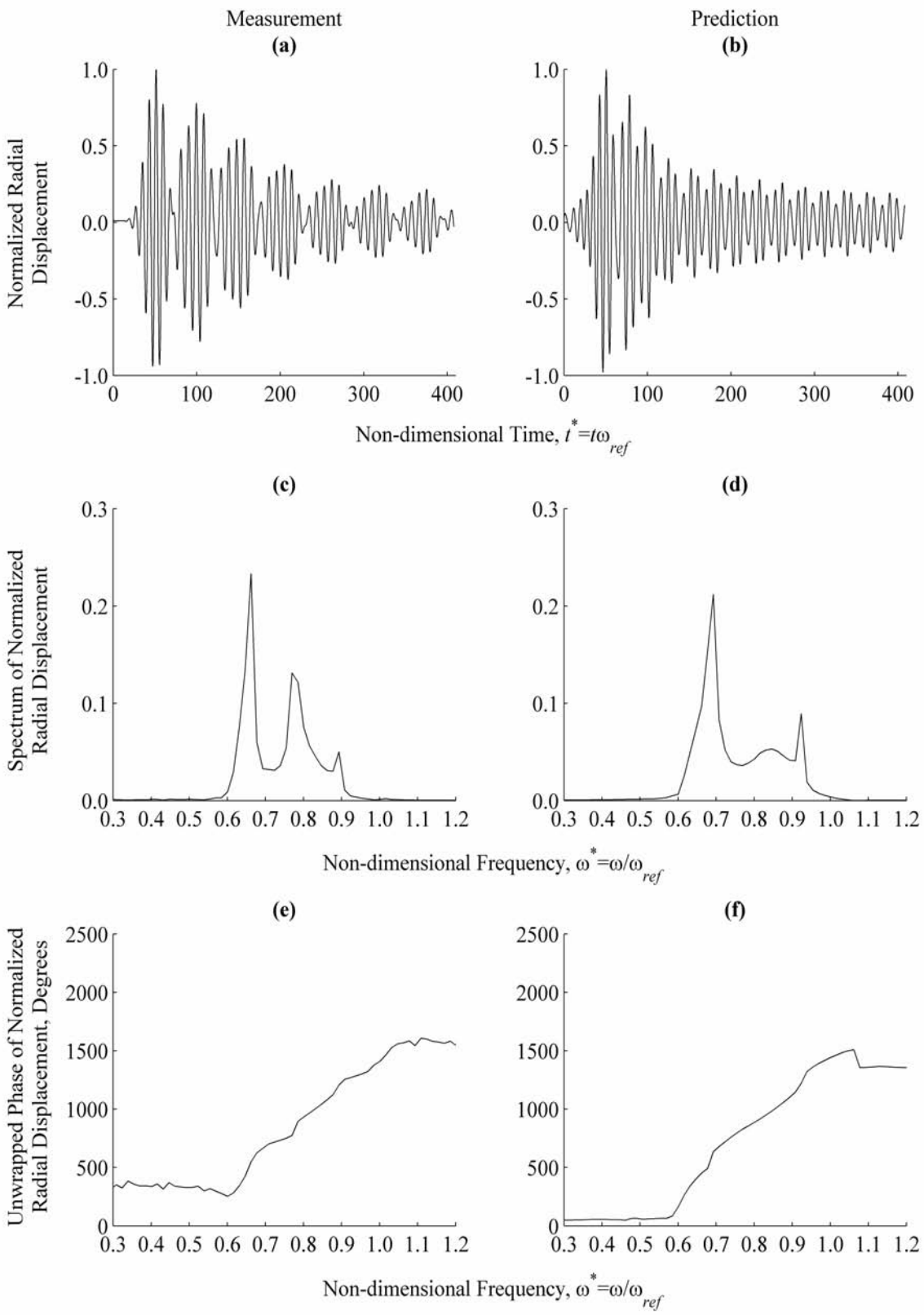

Figure H.8. Measurement and Prediction at $\theta=90^{\circ}$, $z^*=0.00$

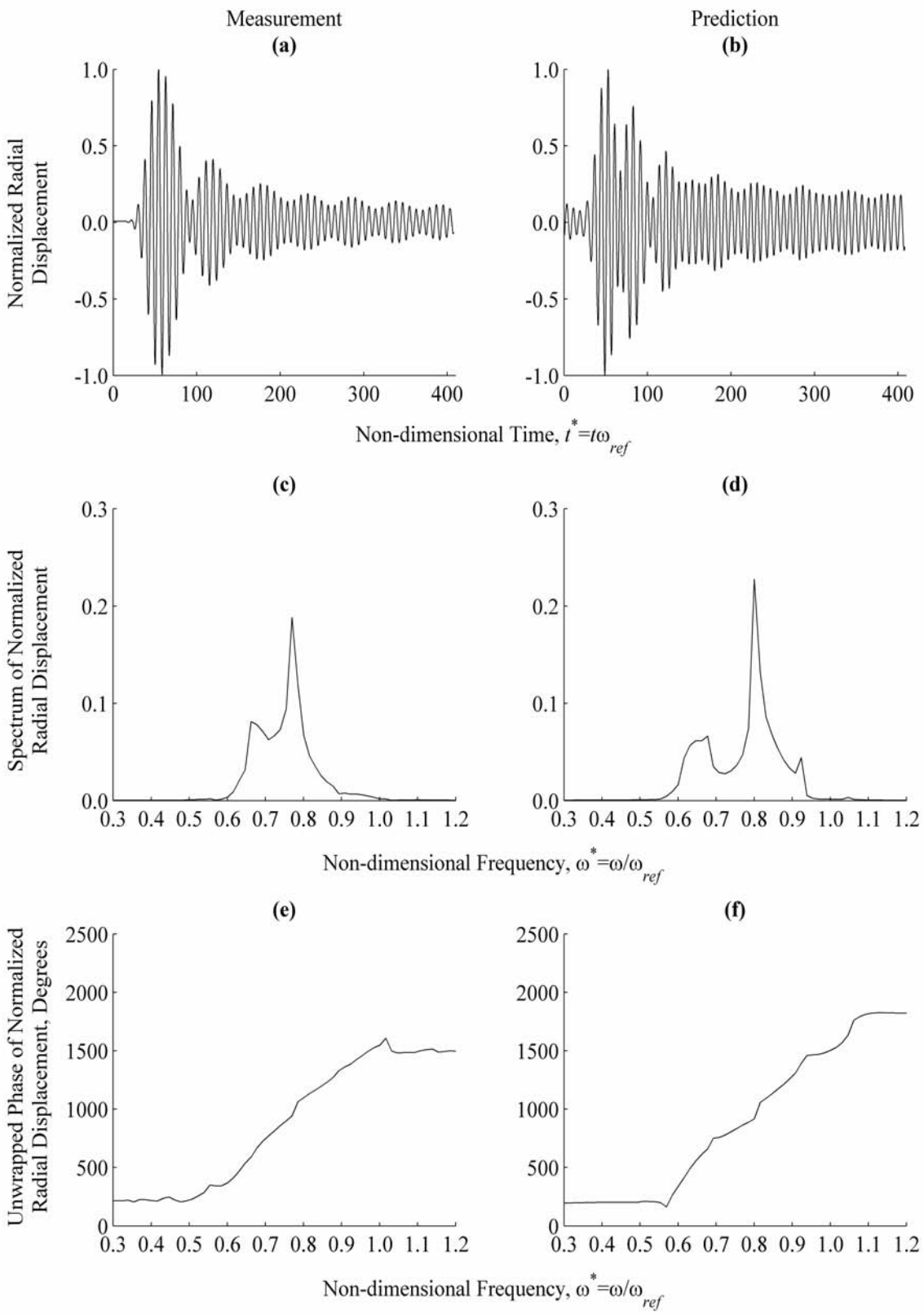

Figure H.9. Measurement and Prediction at $\theta=100^{\circ}$, $z^*=0.00$

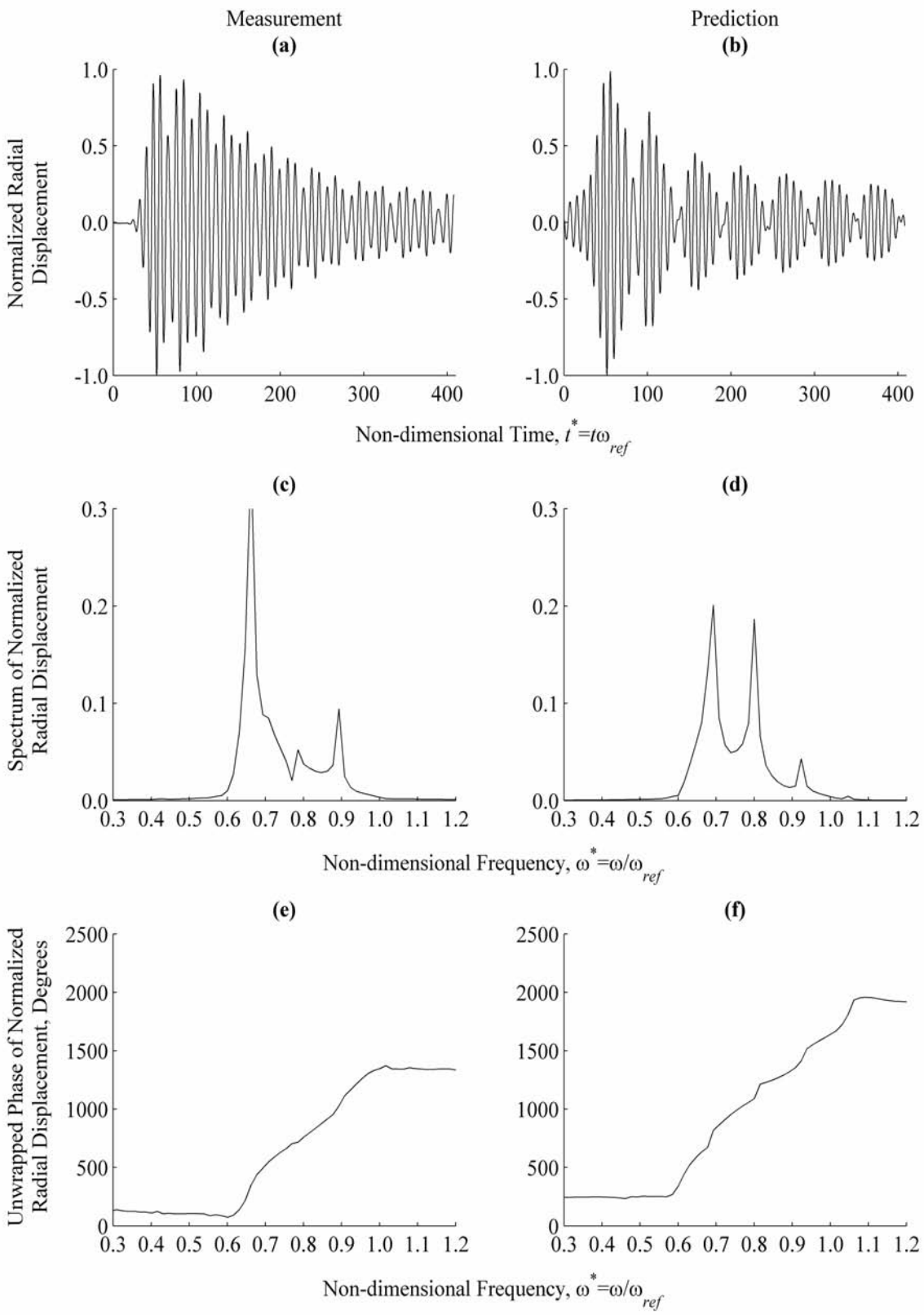

Figure H.10. Measurement and Prediction at $\theta=110^{\circ}$, $z^*=0.00$

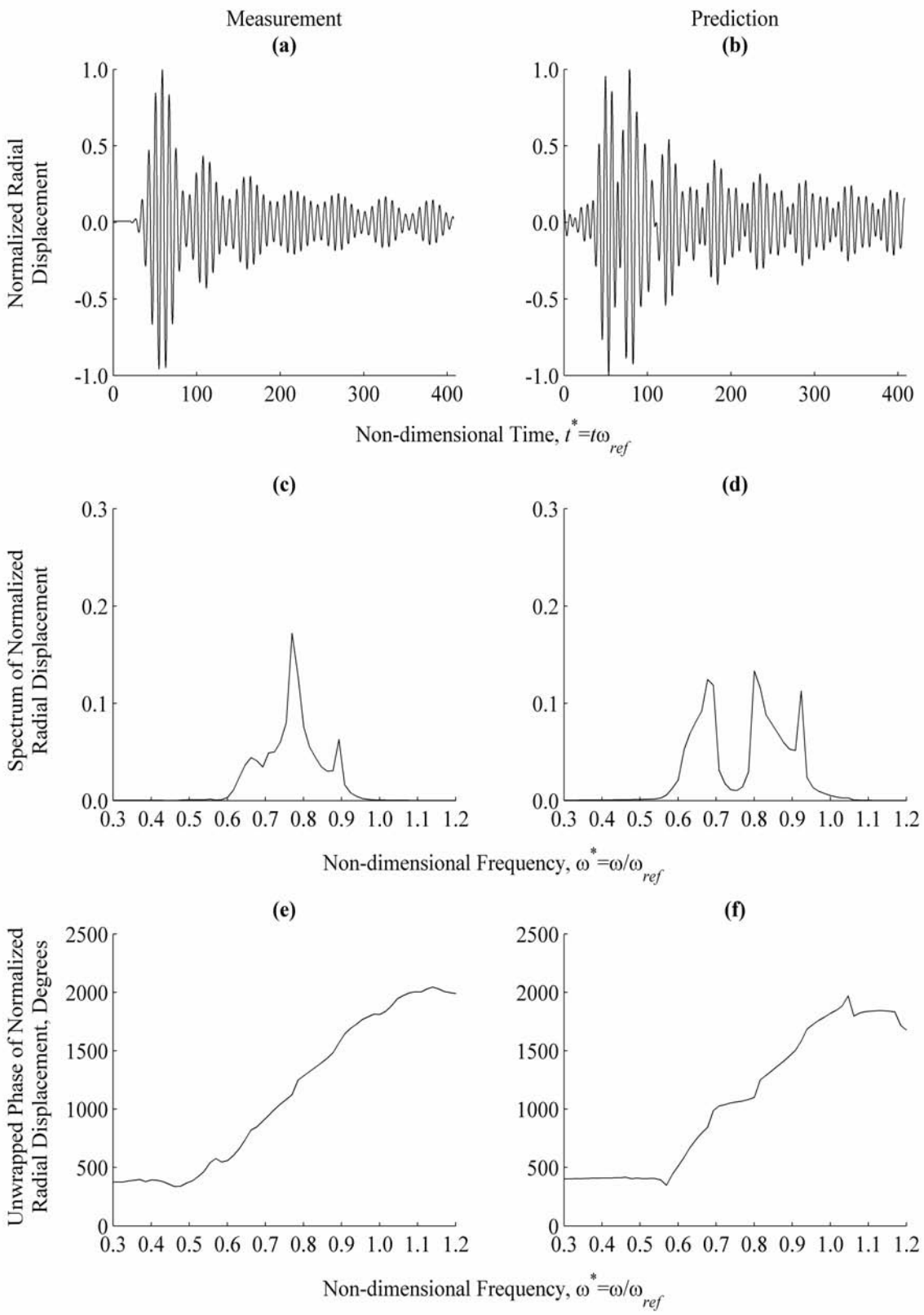

Figure H.11. Measurement and Prediction at $\theta=120^{\circ}$, $z^*=0.00$

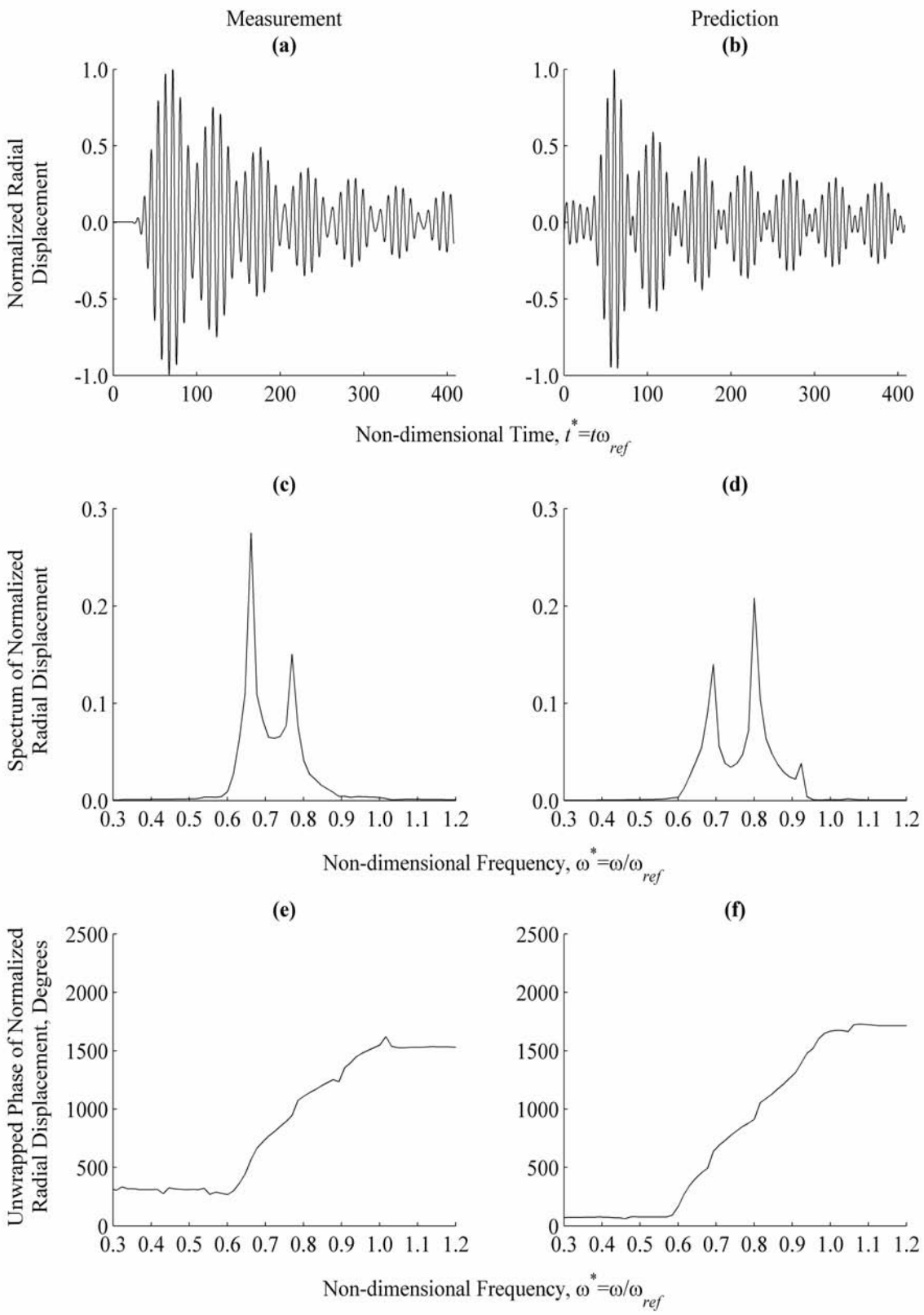

Figure H.12. Measurement and Prediction at $\theta=130^{\circ}$, $z^*=0.00$

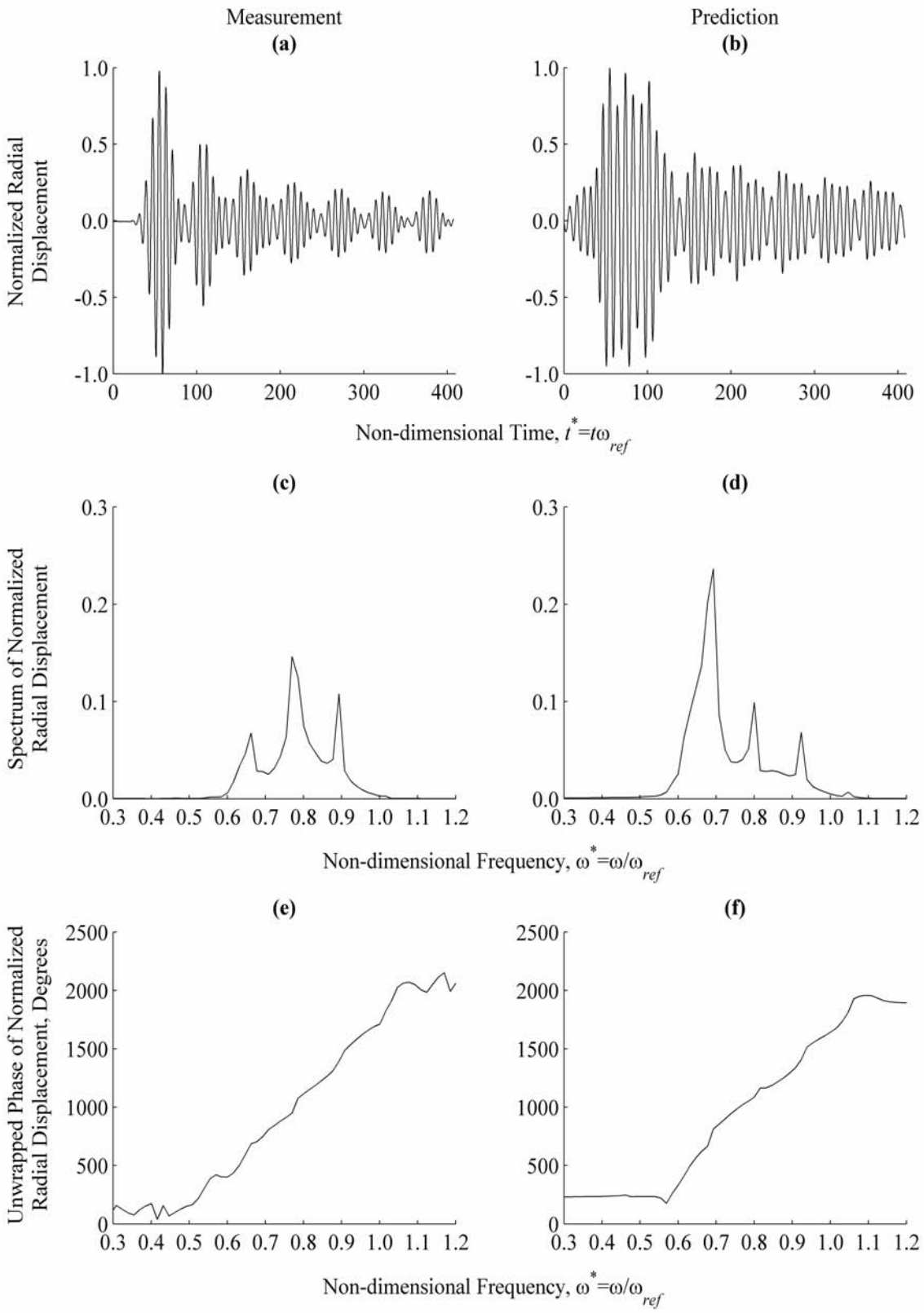

Figure H.13. Measurement and Prediction at $\theta=140^{\circ}$, $z^*=0.00$

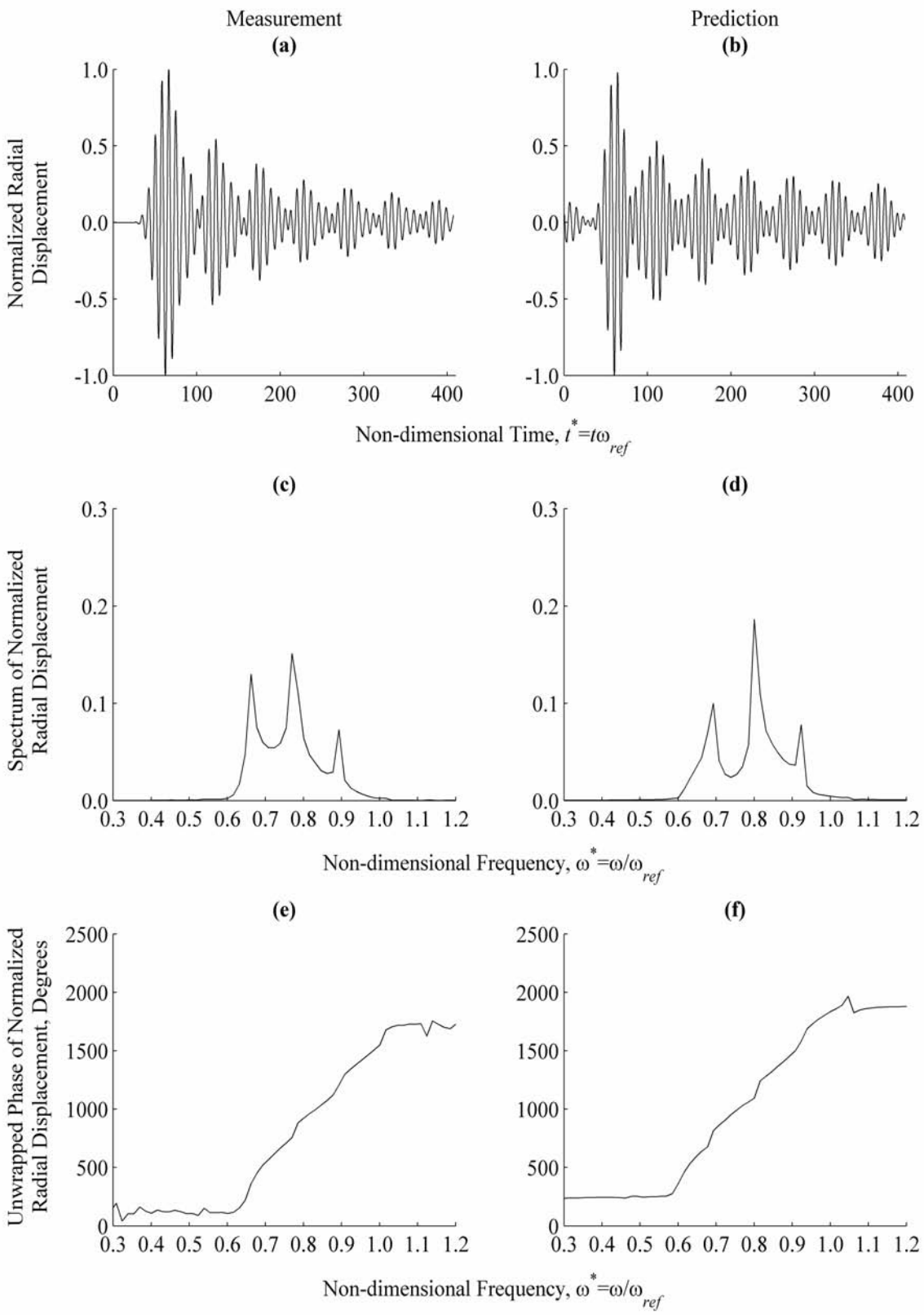

Figure H.14. Measurement and Prediction at $\theta=150^{\circ}$, $z^*=0.00$

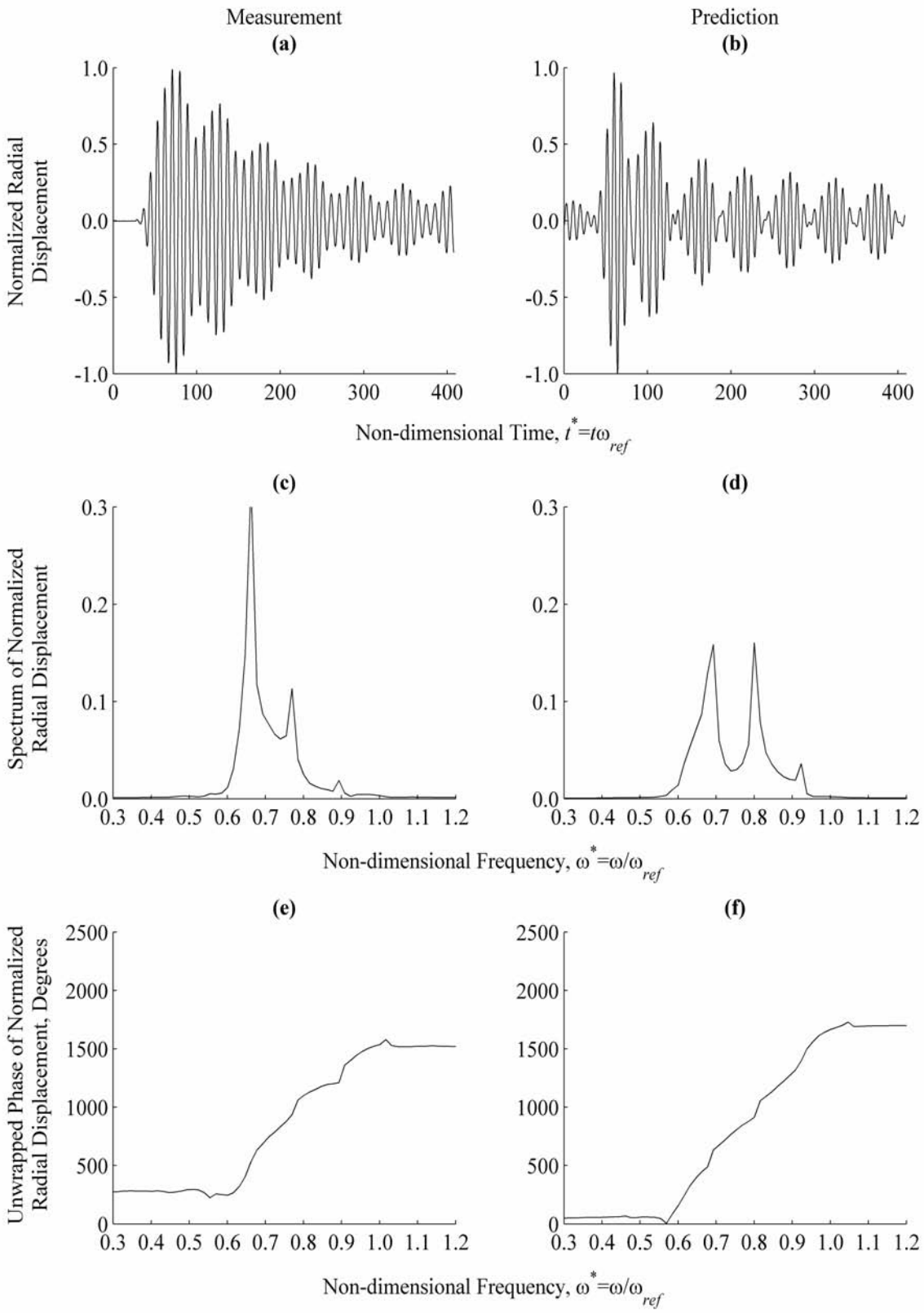

Figure H.15. Measurement and Prediction at $\theta=160^{\circ}$, $z^*=0.00$

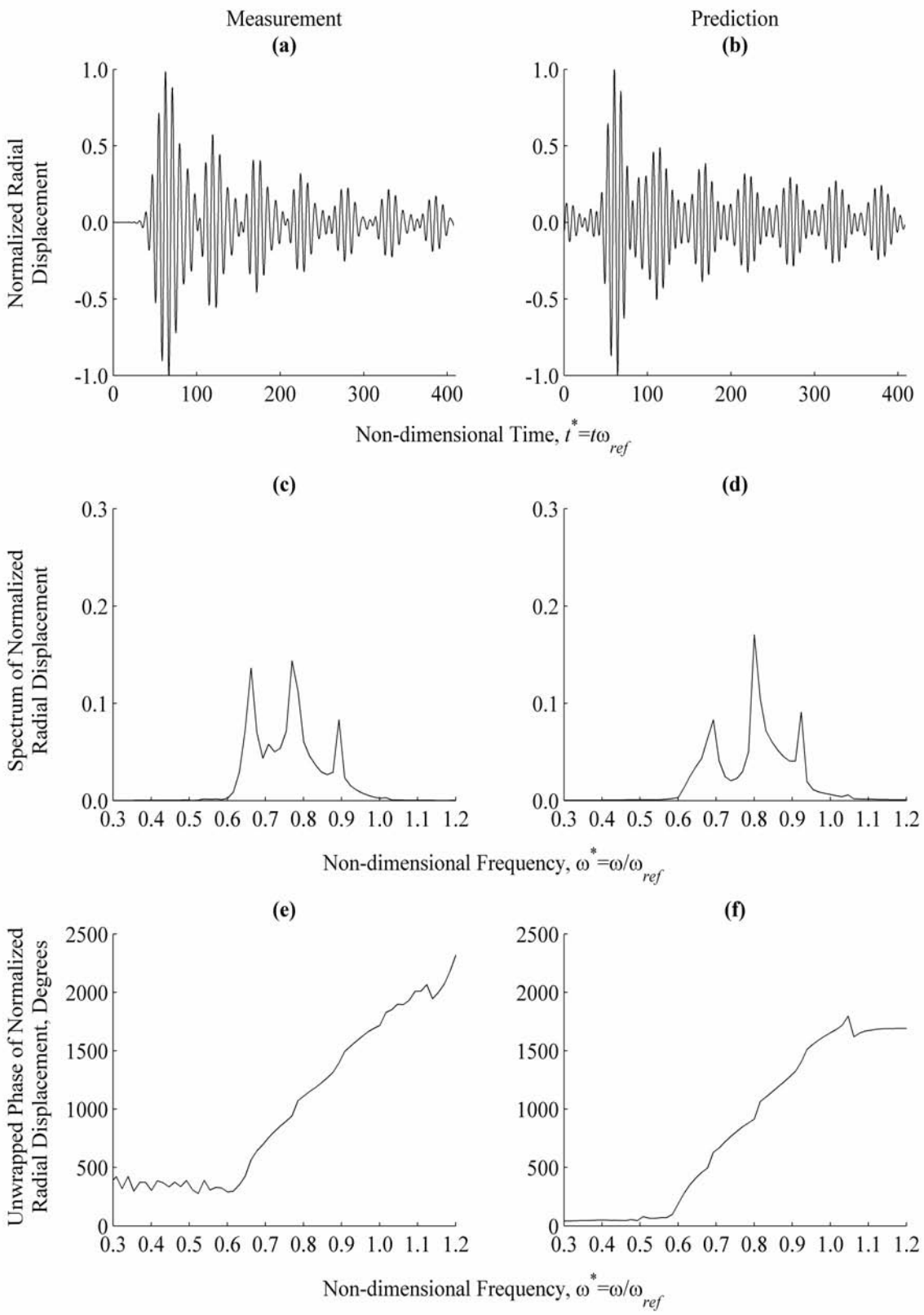

Figure H.16. Measurement and Prediction at $\theta=170^{\circ}$, $z^*=0.00$

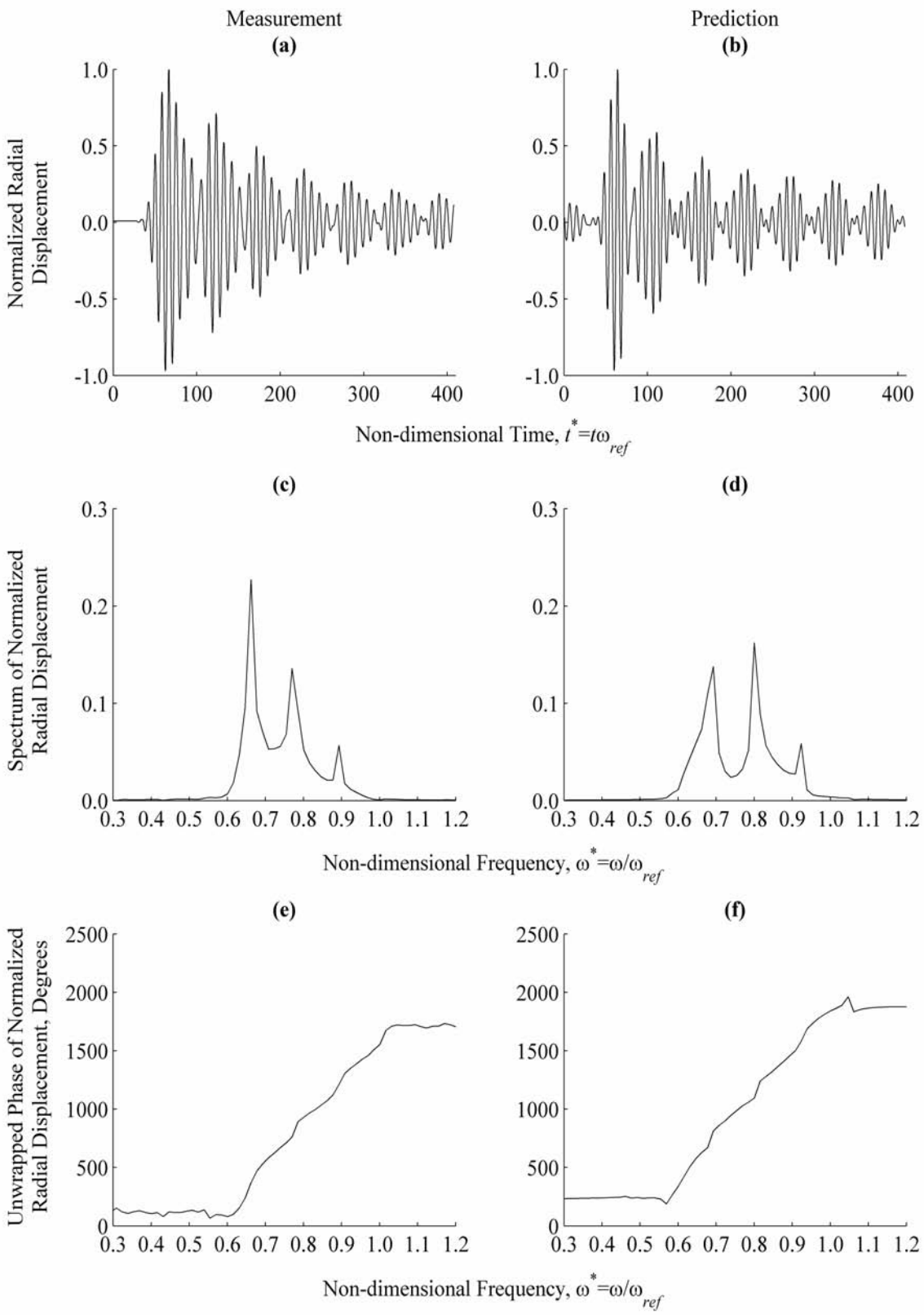

Figure H.17. Measurement and Prediction at $\theta=180^{\circ}$, $z^*=0.00$

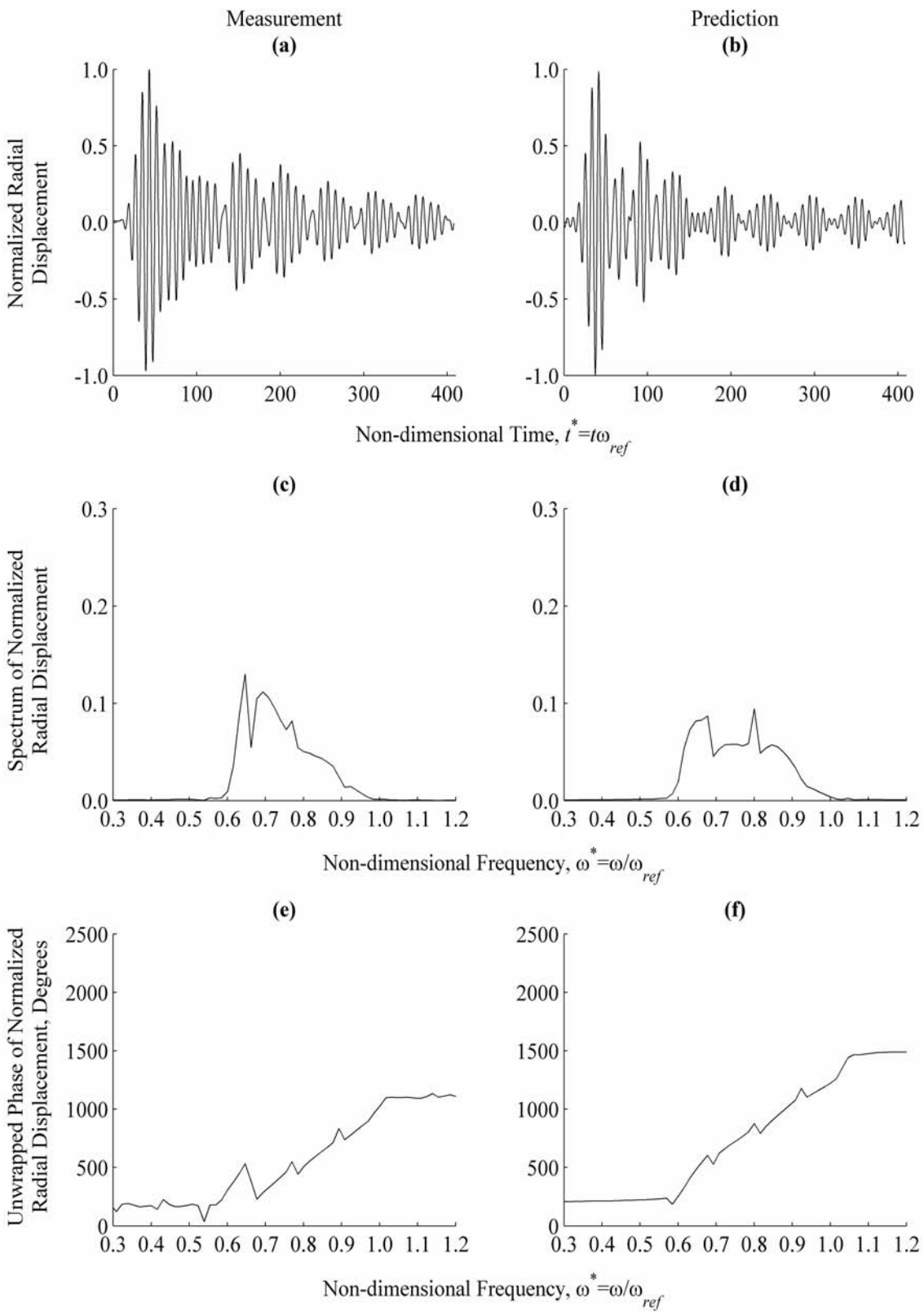

Figure H.18. Measurement and Prediction at $\theta=0^{\circ}$, $z^*=2.55$

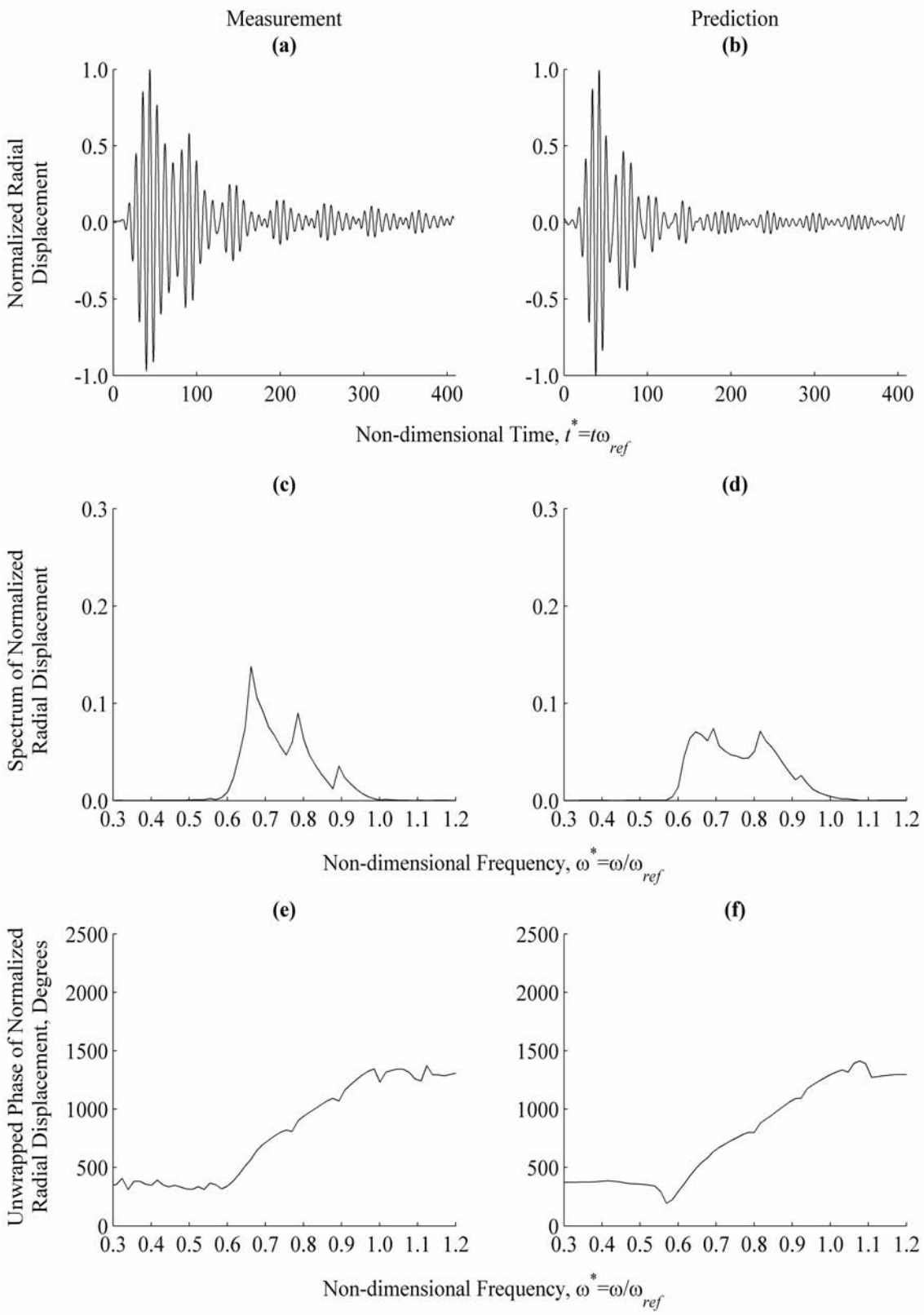

Figure H.19. Measurement and Prediction at $\theta=10^{\circ}$, $z^*=2.55$

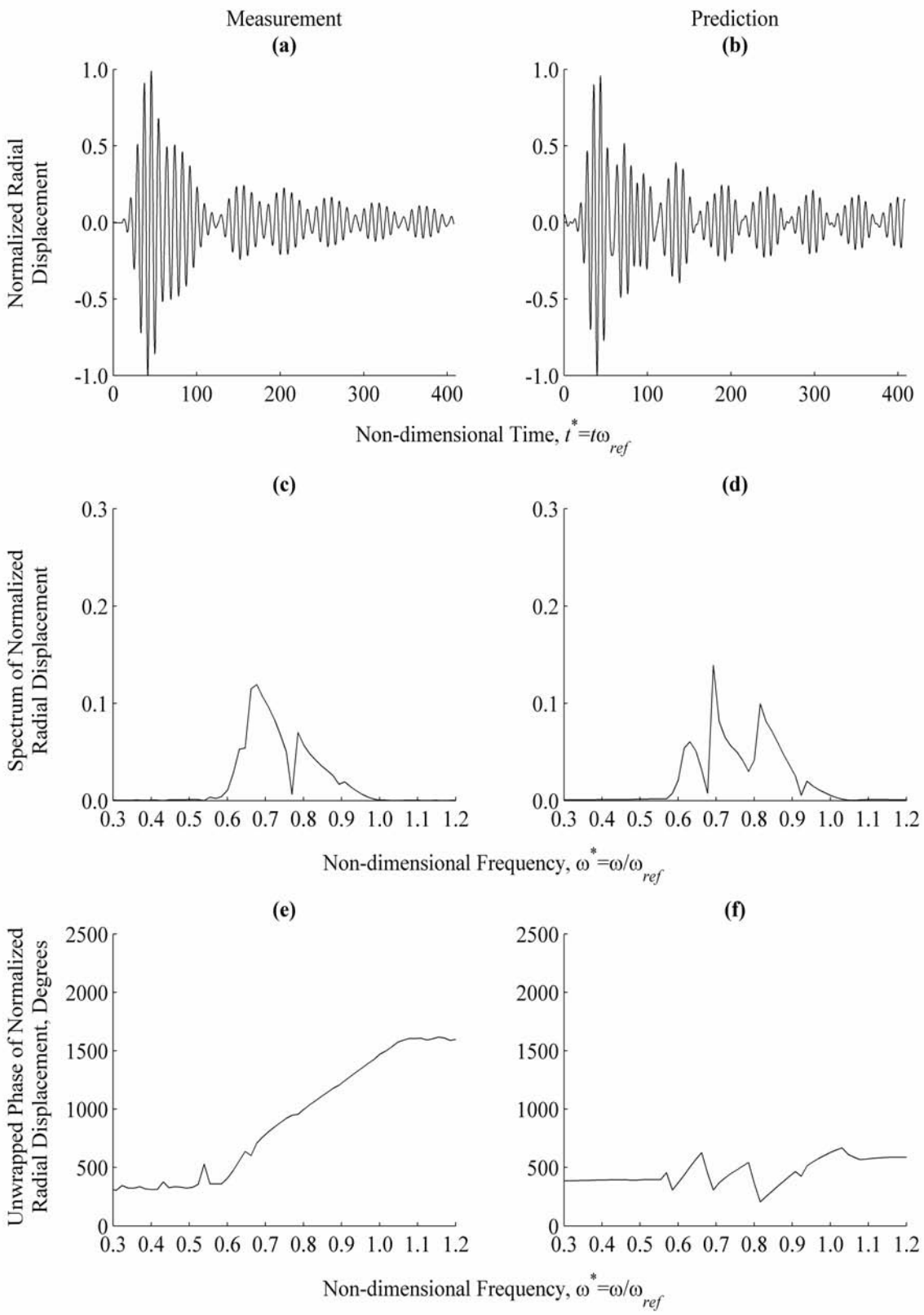

Figure H.20. Measurement and Prediction at $\theta=20^{\circ}$, $z^*=2.55$

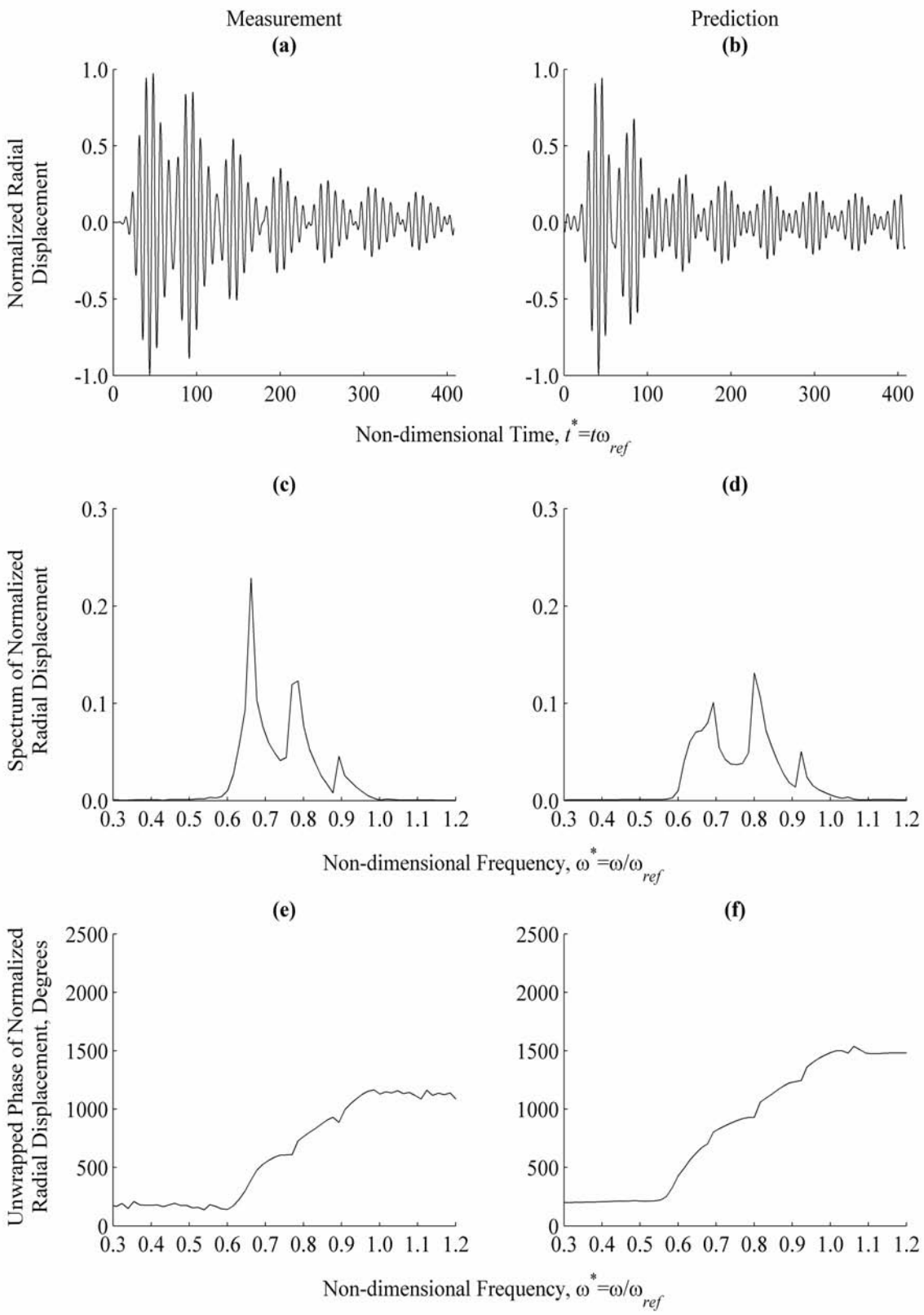

Figure H.21. Measurement and Prediction at $\theta=30^{\circ}$, $z^*=2.55$

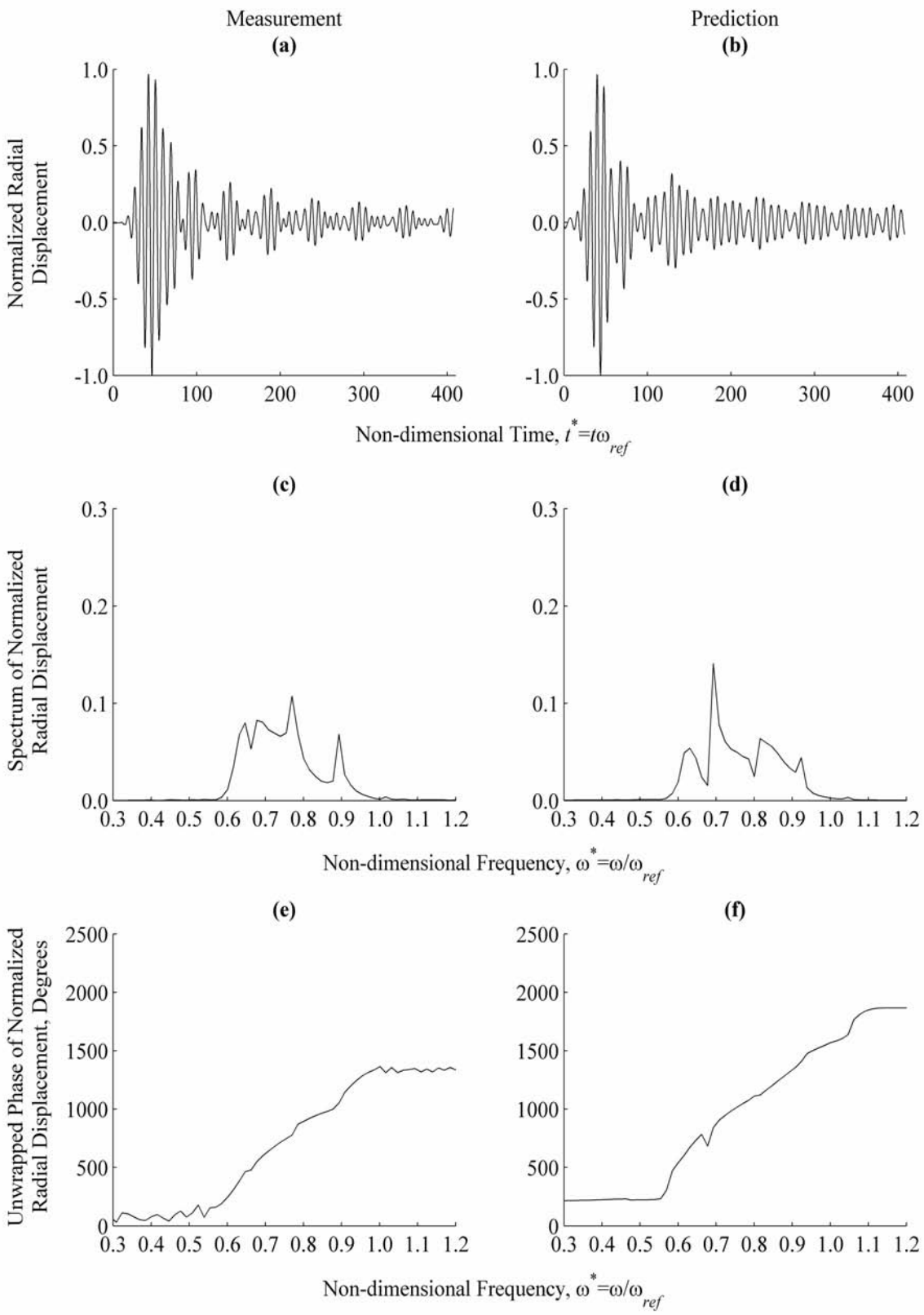

Figure H.22. Measurement and Prediction at $\theta=40^{\circ}$, $z^*=2.55$

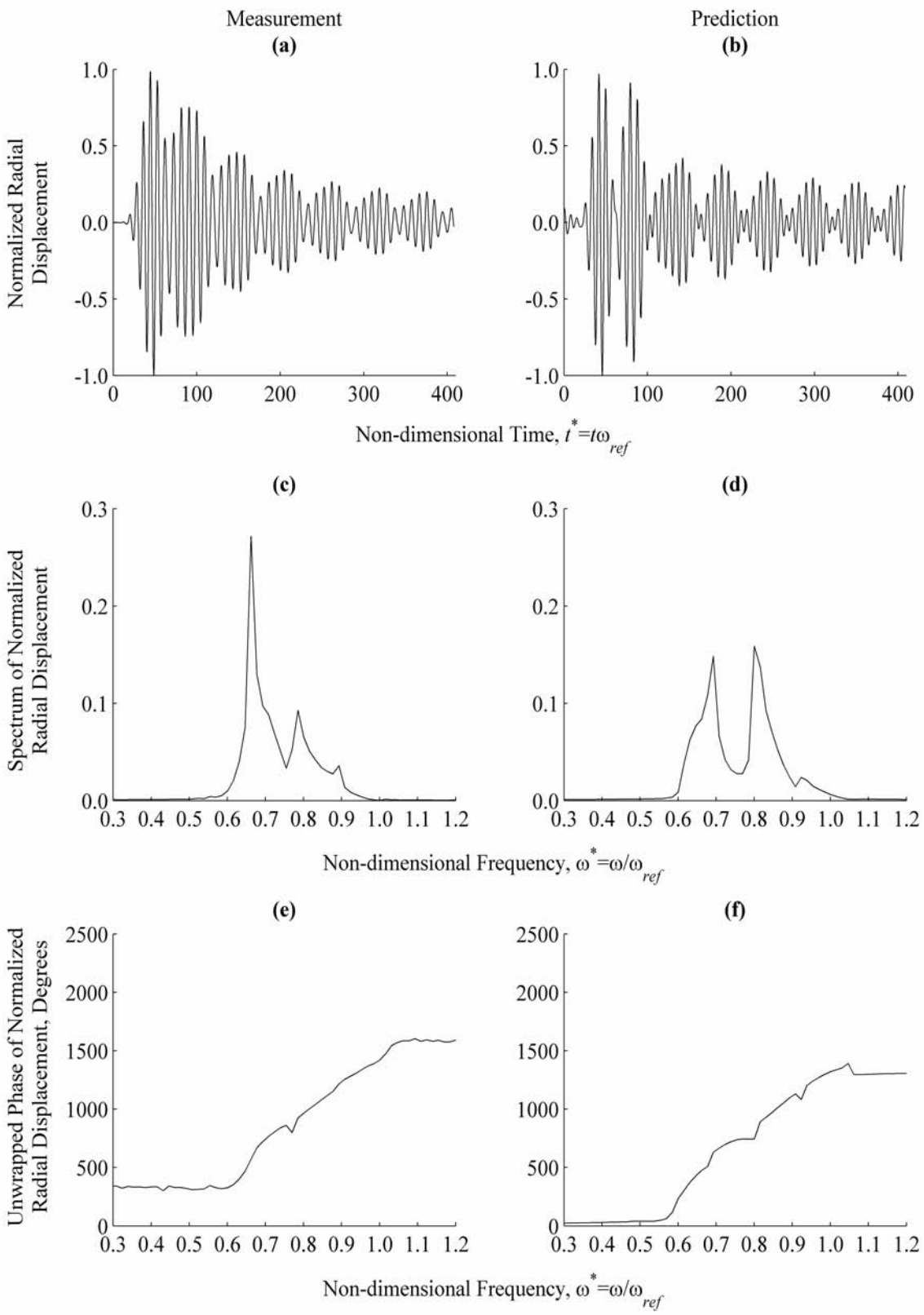

Figure H.23. Measurement and Prediction at $\theta=50^{\circ}$, $z^*=2.55$

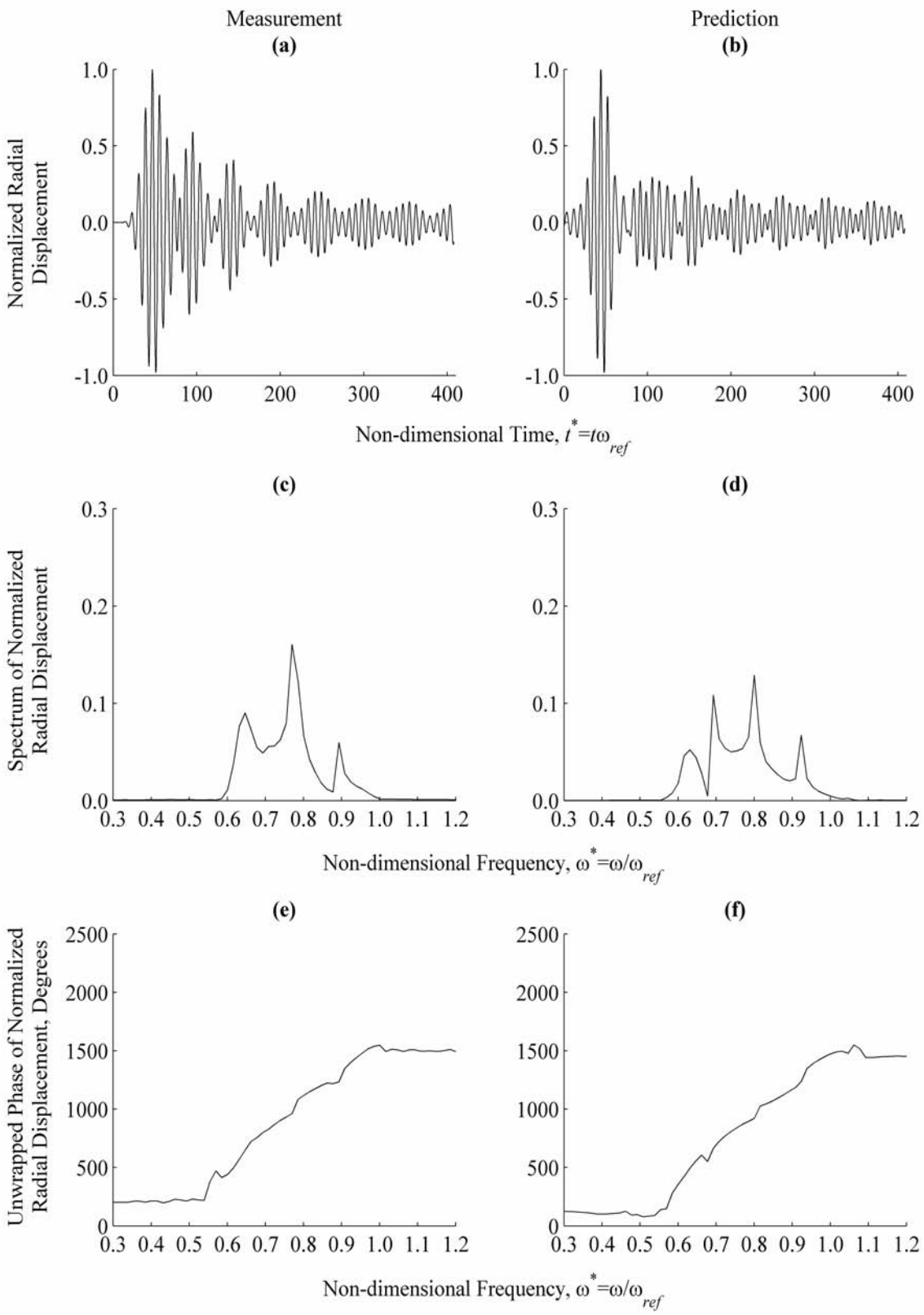

Figure H.24. Measurement and Prediction at $\theta=60^{\circ}$, $z^*=2.55$

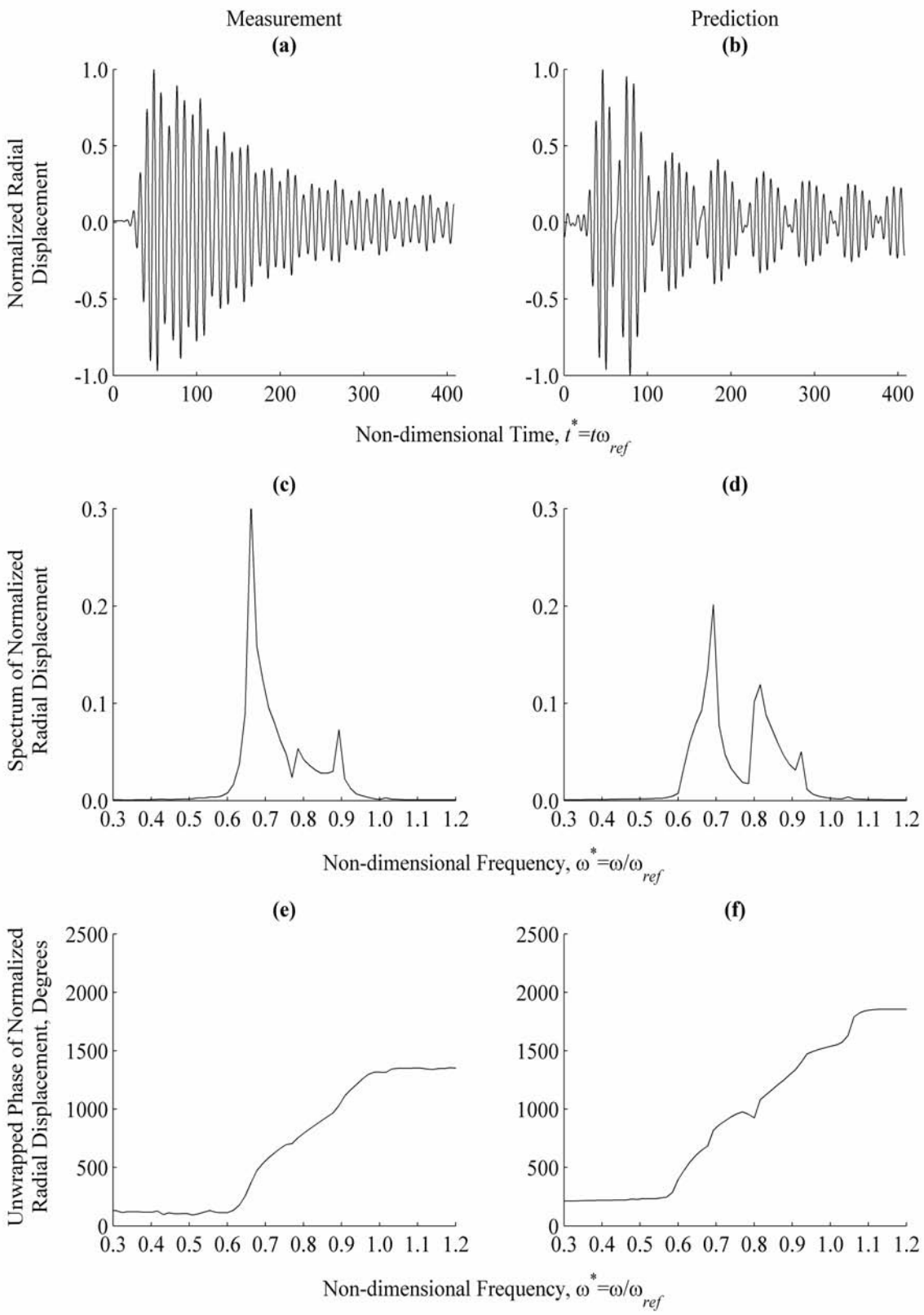

Figure H.25. Measurement and Prediction at $\theta=70^{\circ}$, $z^*=2.55$

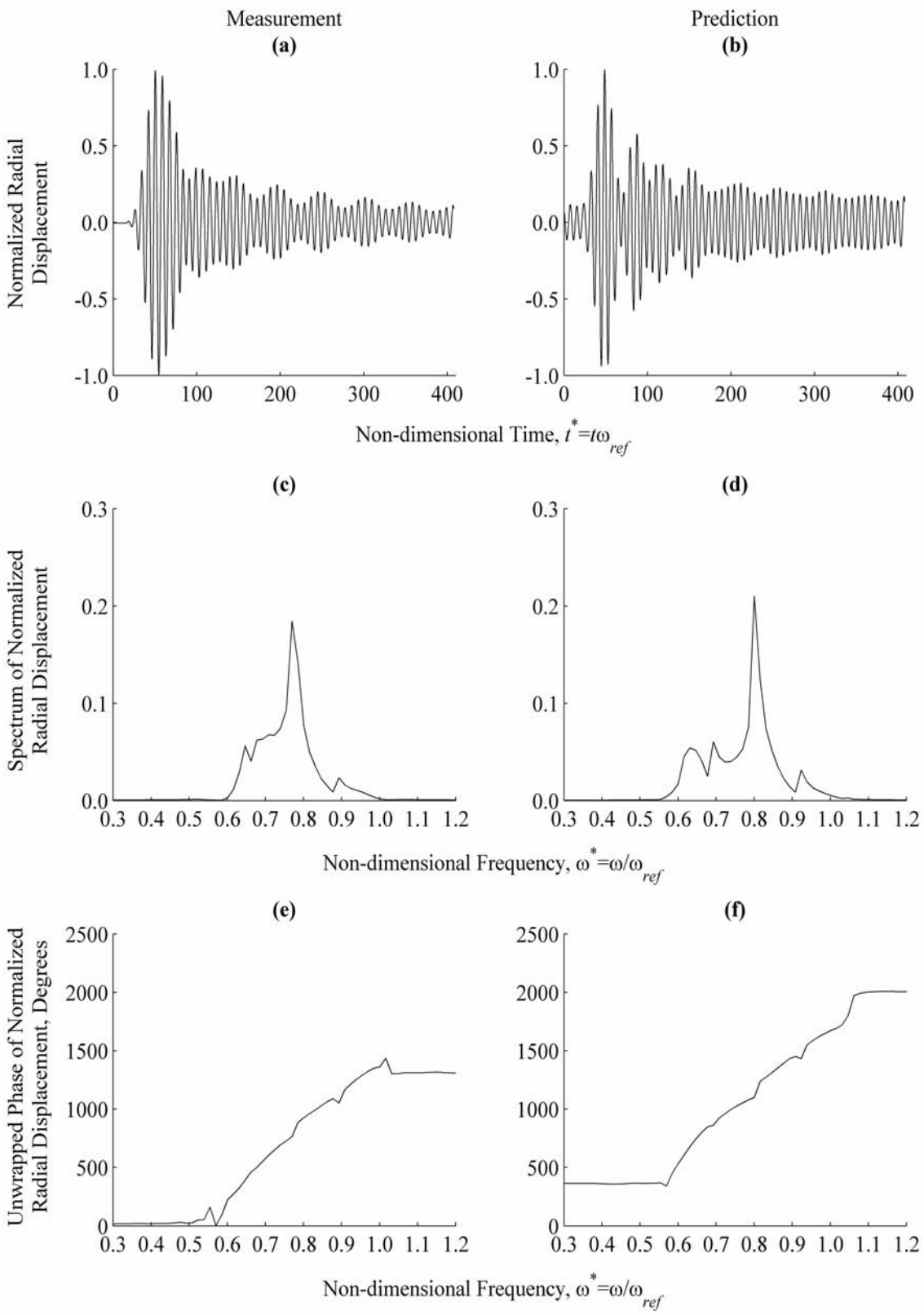

Figure H.26. Measurement and Prediction at $\theta=80^{\circ}$, $z^*=2.55$

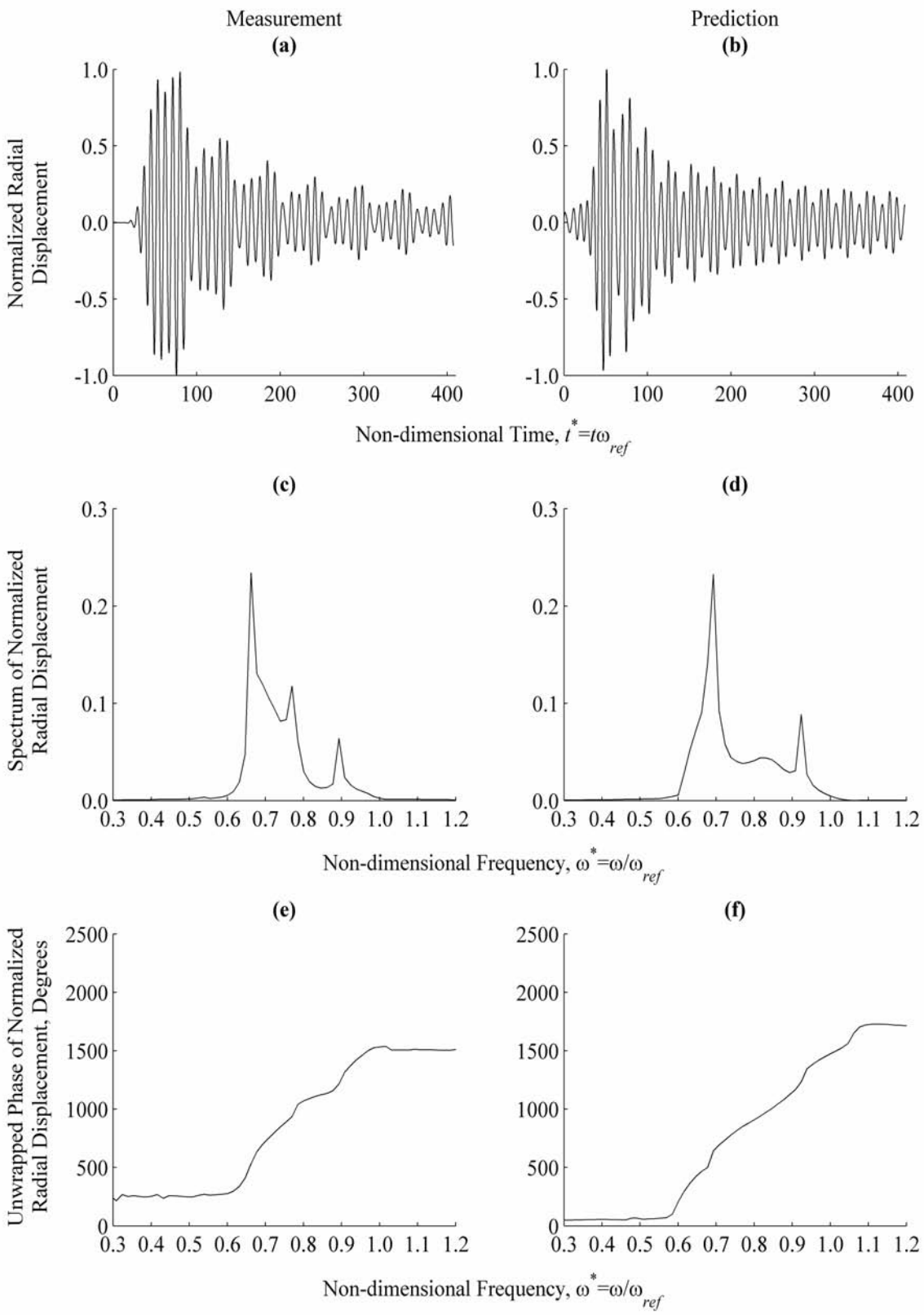

Figure H.27. Measurement and Prediction at $\theta=90^{\circ}$, $z^*=2.55$

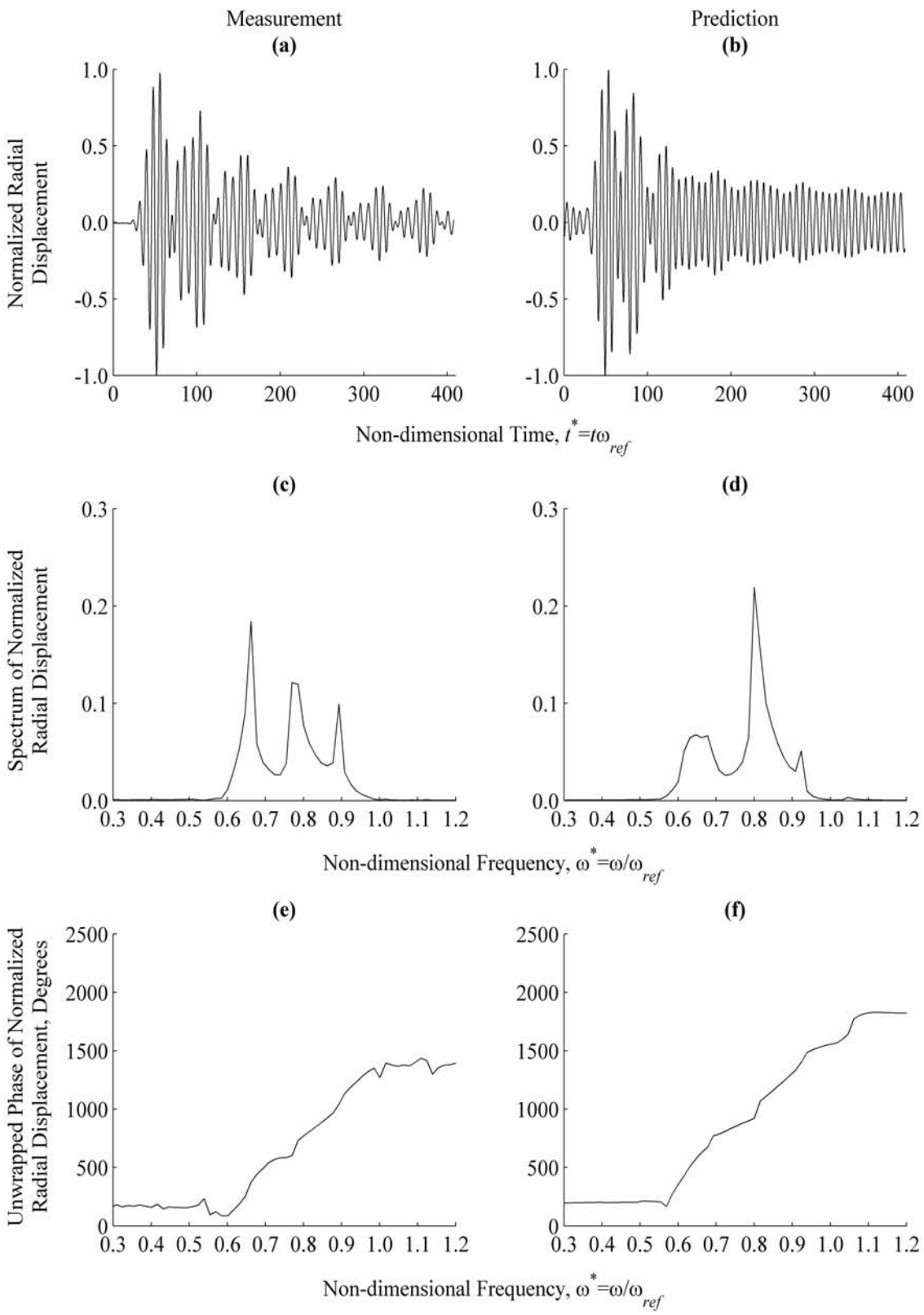

Figure H.28. Measurement and Prediction at $\theta=100^{\circ}$, $z^*=2.55$

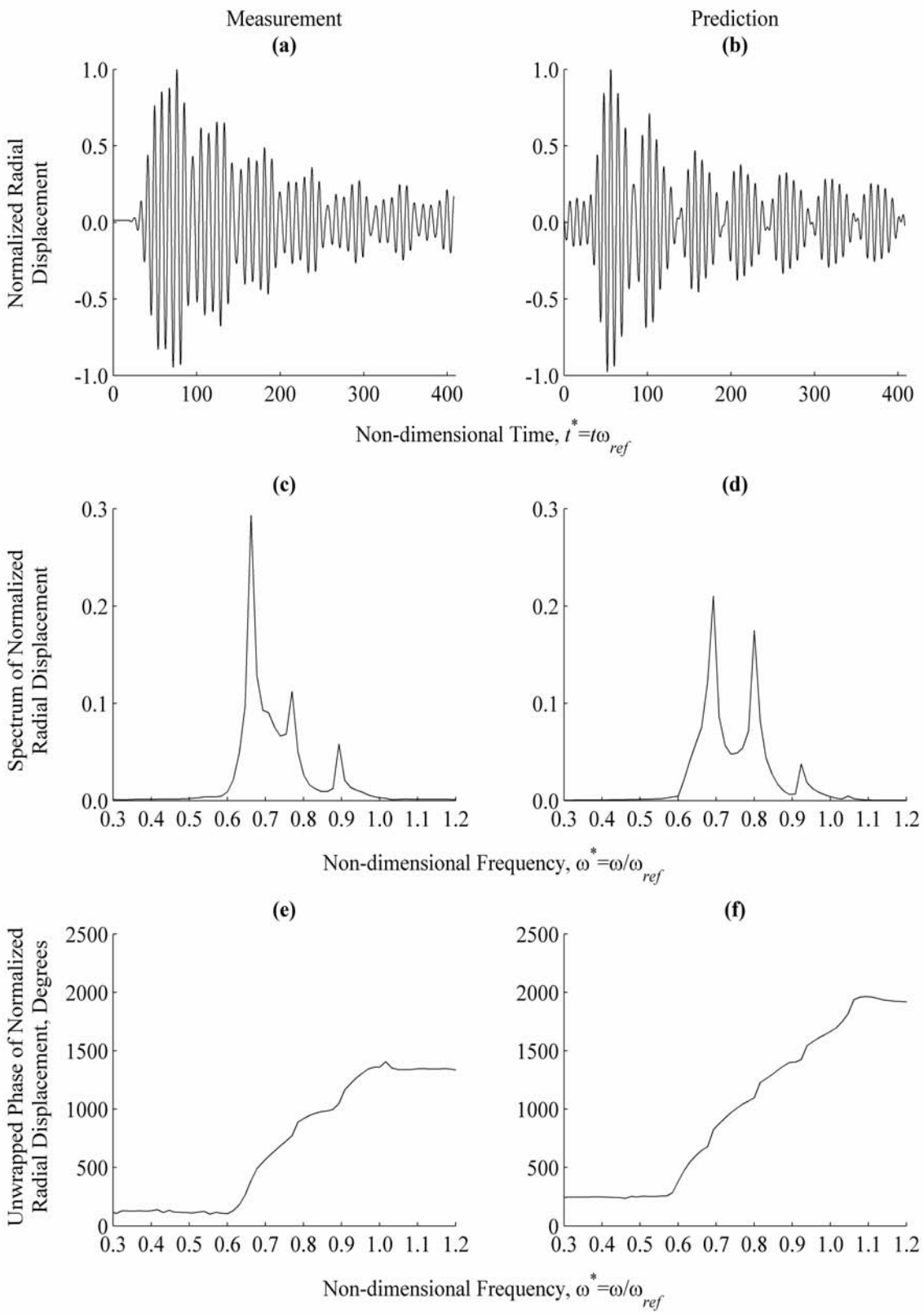

Figure H.29. Measurement and Prediction at $\theta=110^{\circ}$, $z^*=2.55$

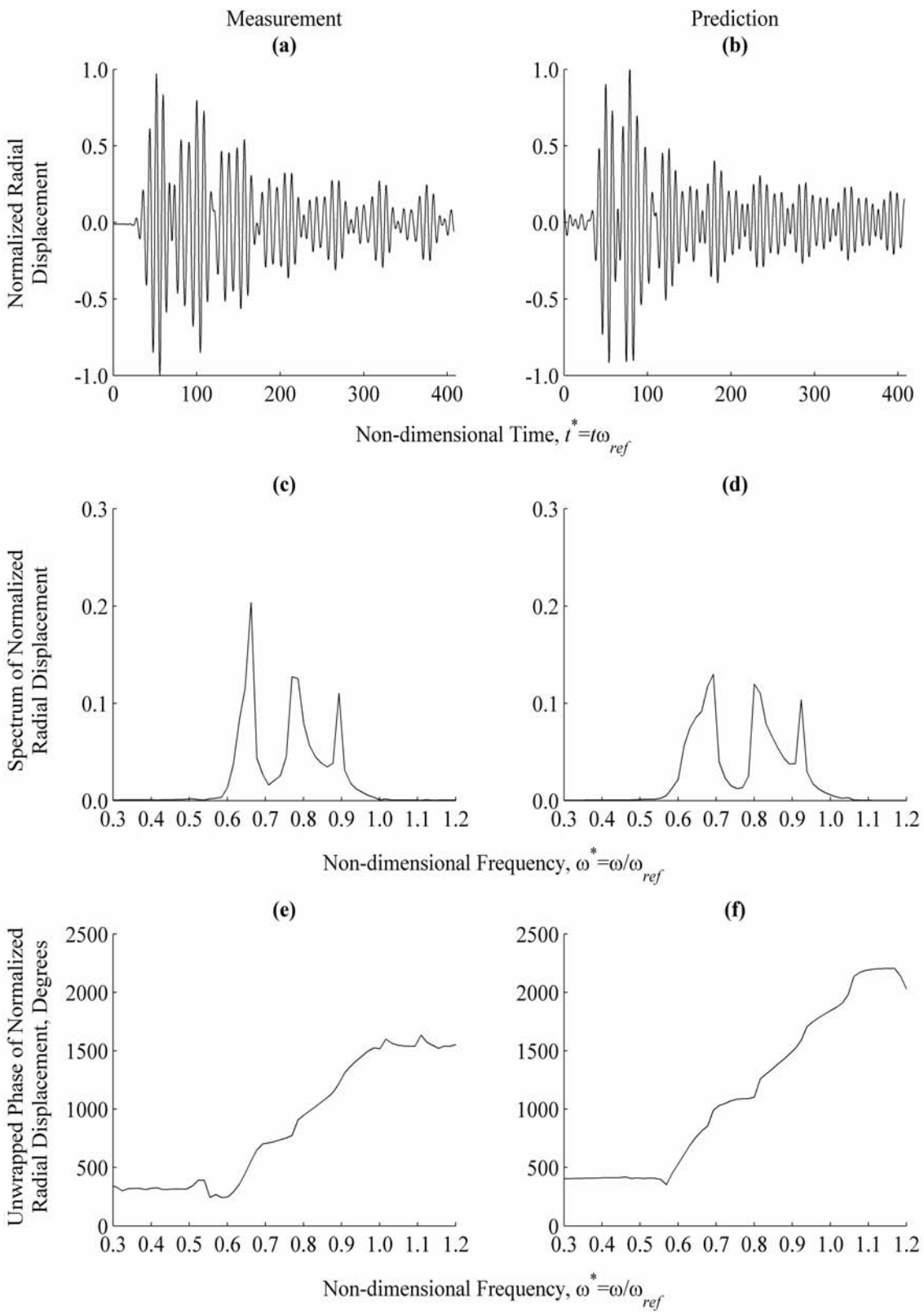

Figure H.30. Measurement and Prediction at $\theta=120^{\circ}$, $z^*=2.55$

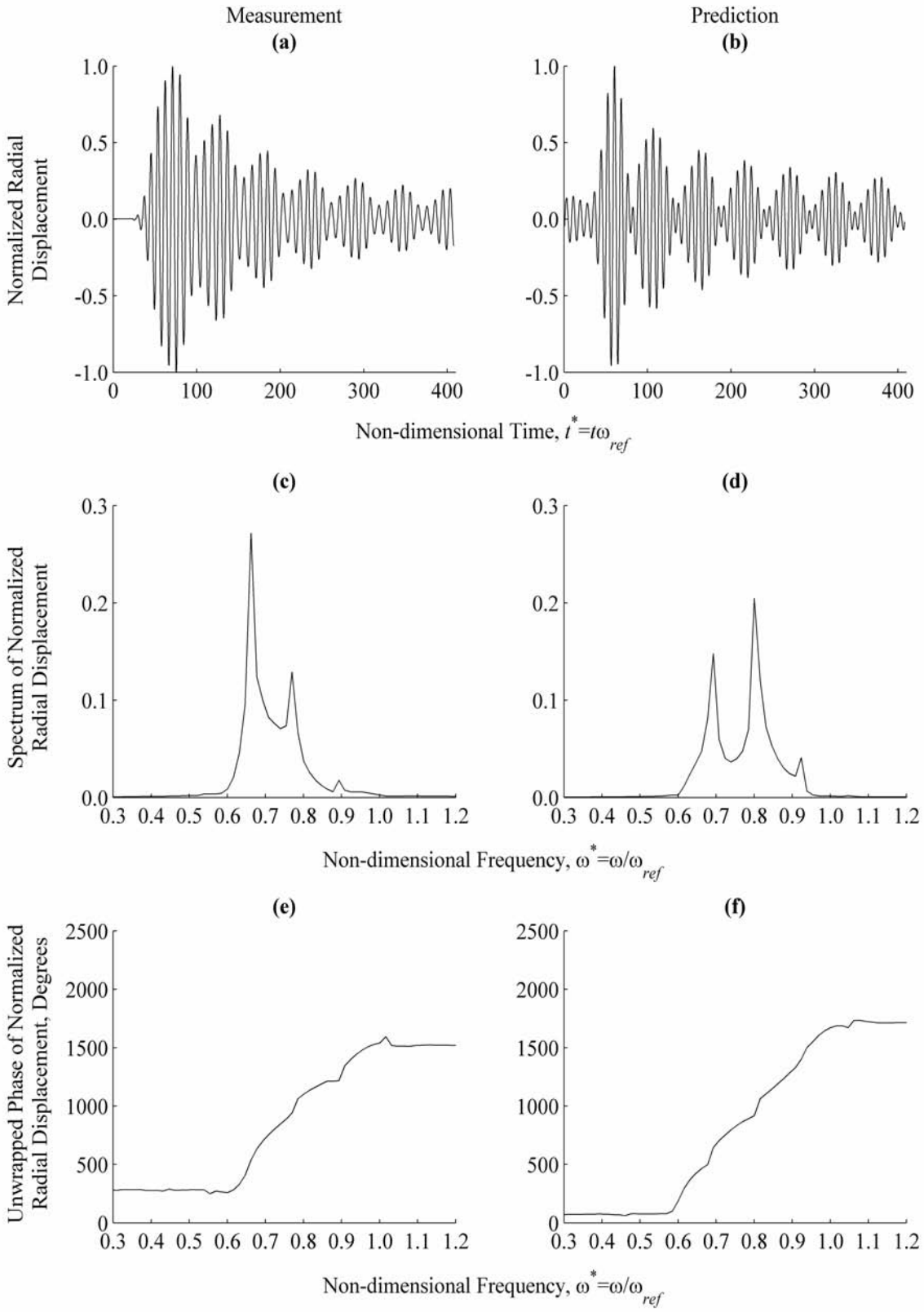

Figure H.31. Measurement and Prediction at $\theta=130^{\circ}$, $z^*=2.55$

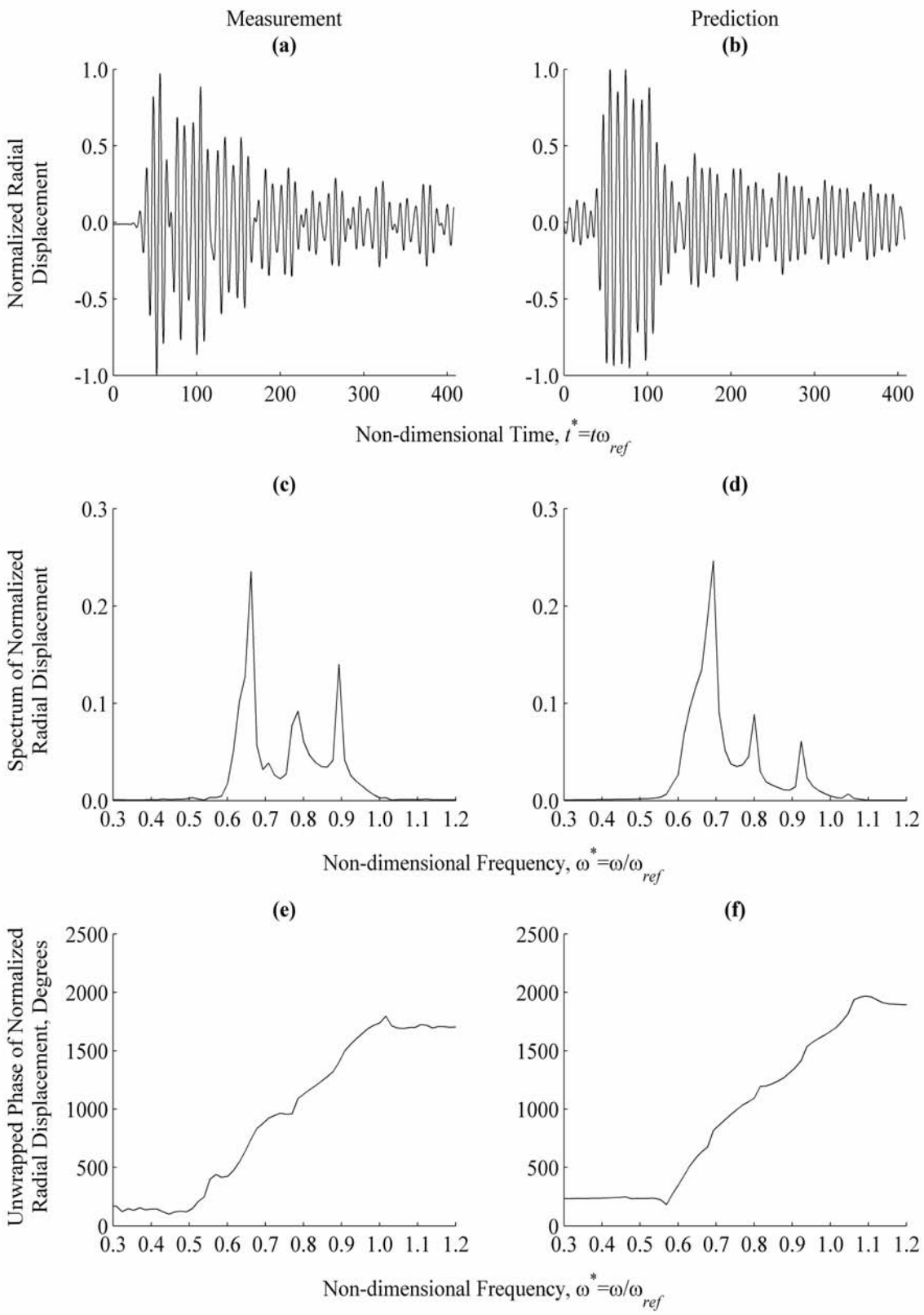

Figure H.32. Measurement and Prediction at $\theta=140^{\circ}$, $z^*=2.55$

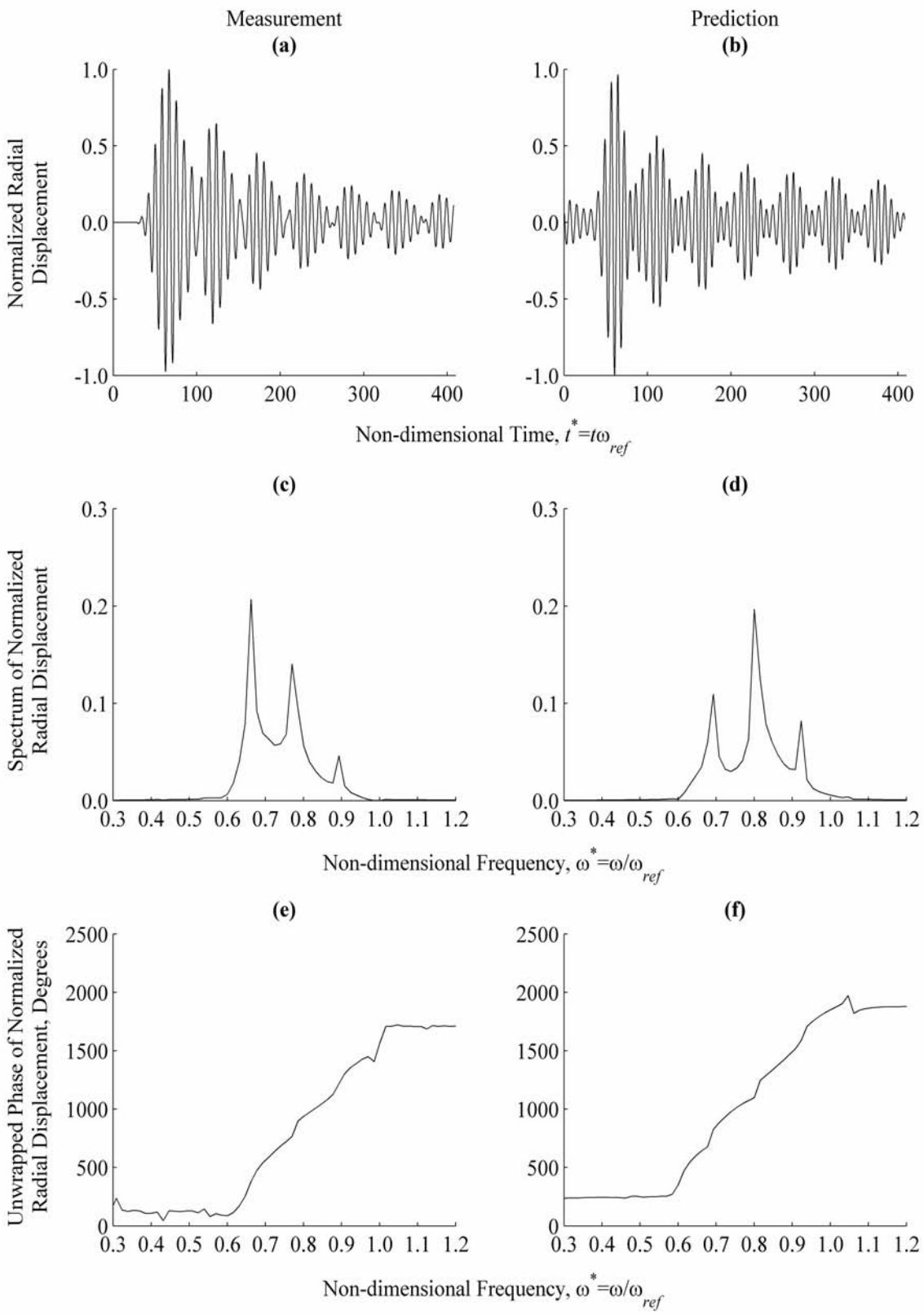

Figure H.33. Measurement and Prediction at $\theta=150^{\circ}$, $z^*=2.55$

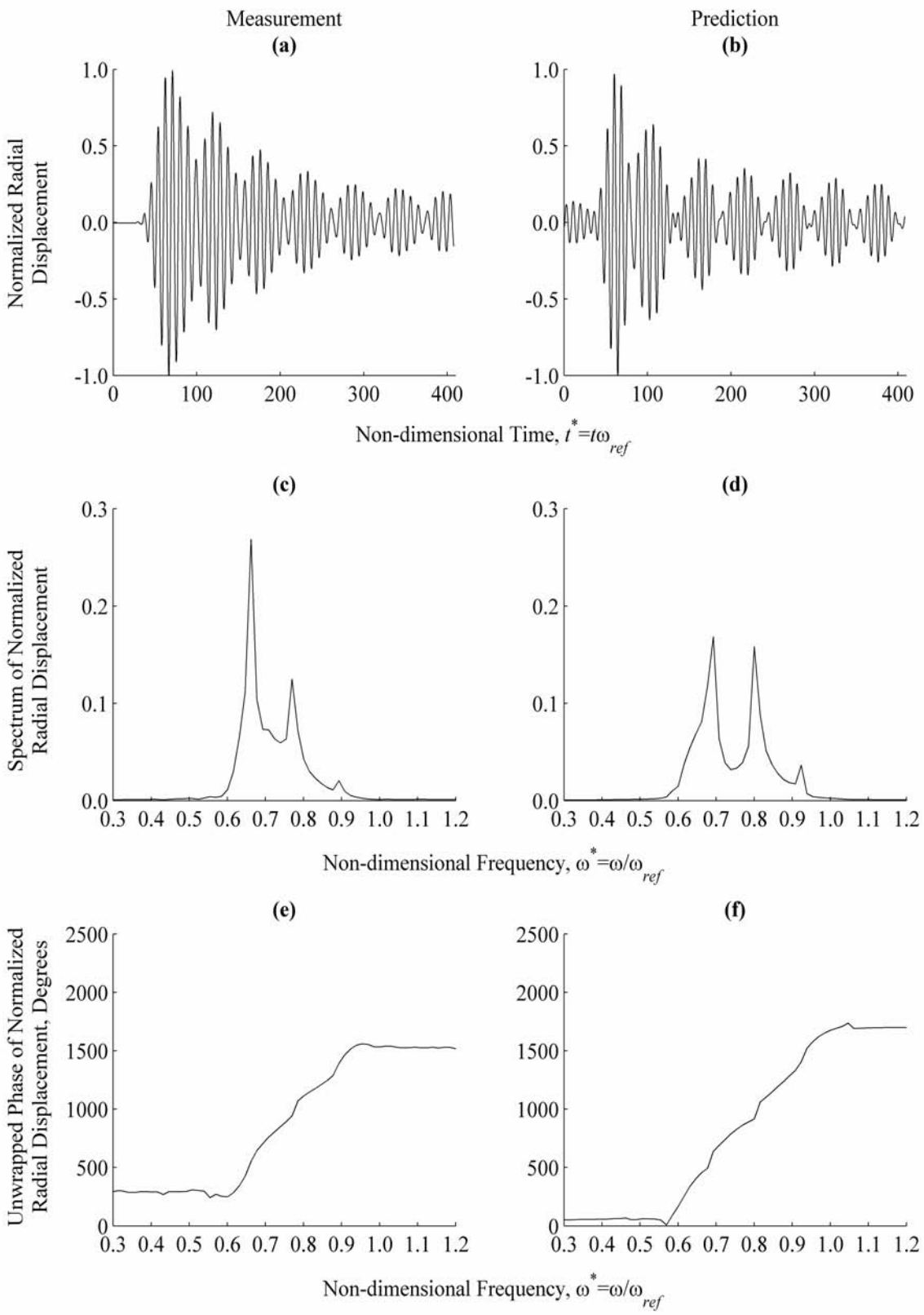

Figure H.34. Measurement and Prediction at $\theta=160^{\circ}$, $z^*=2.55$

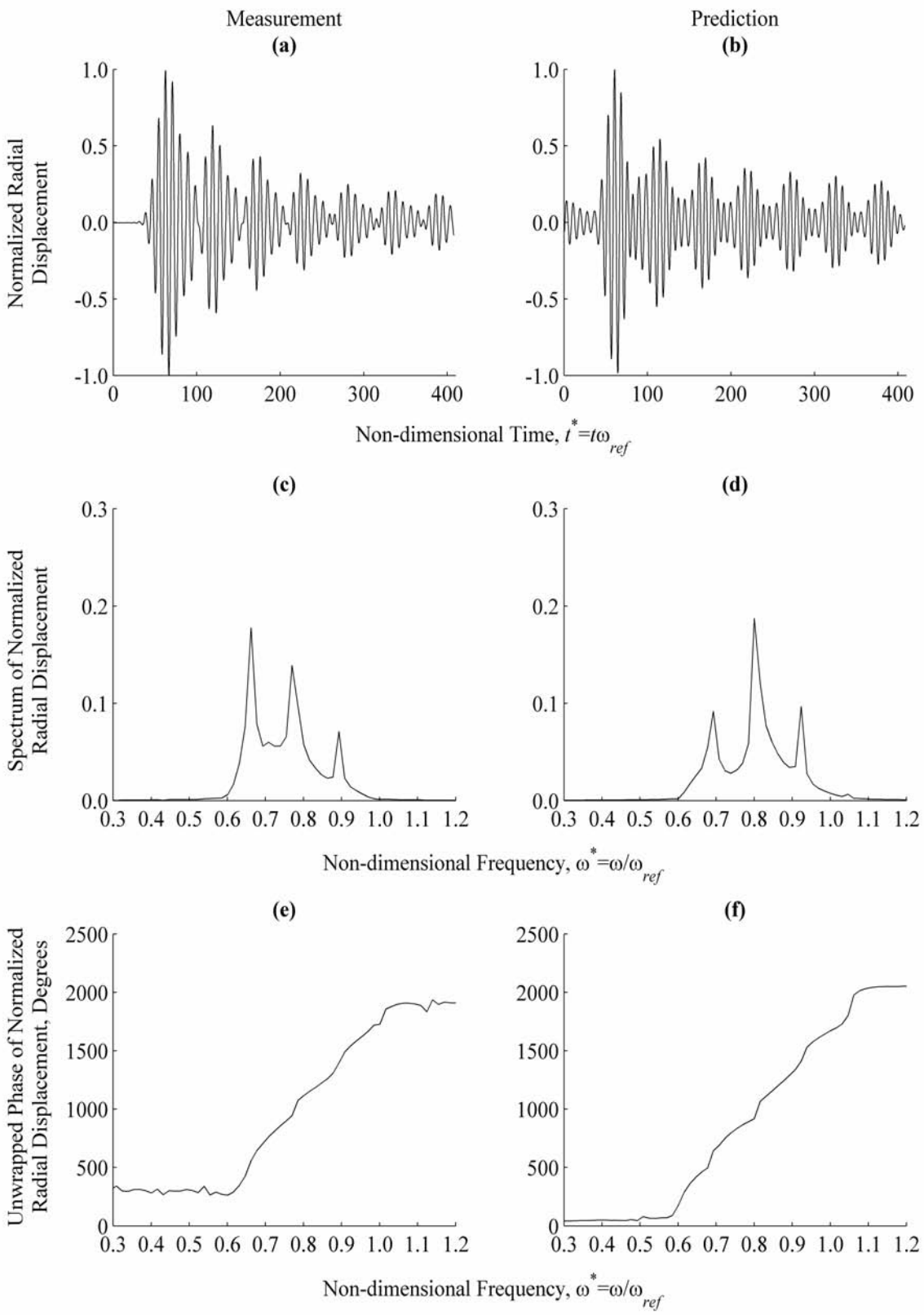

Figure H.35. Measurement and Prediction at $\theta=170^{\circ}$, $z^*=2.55$

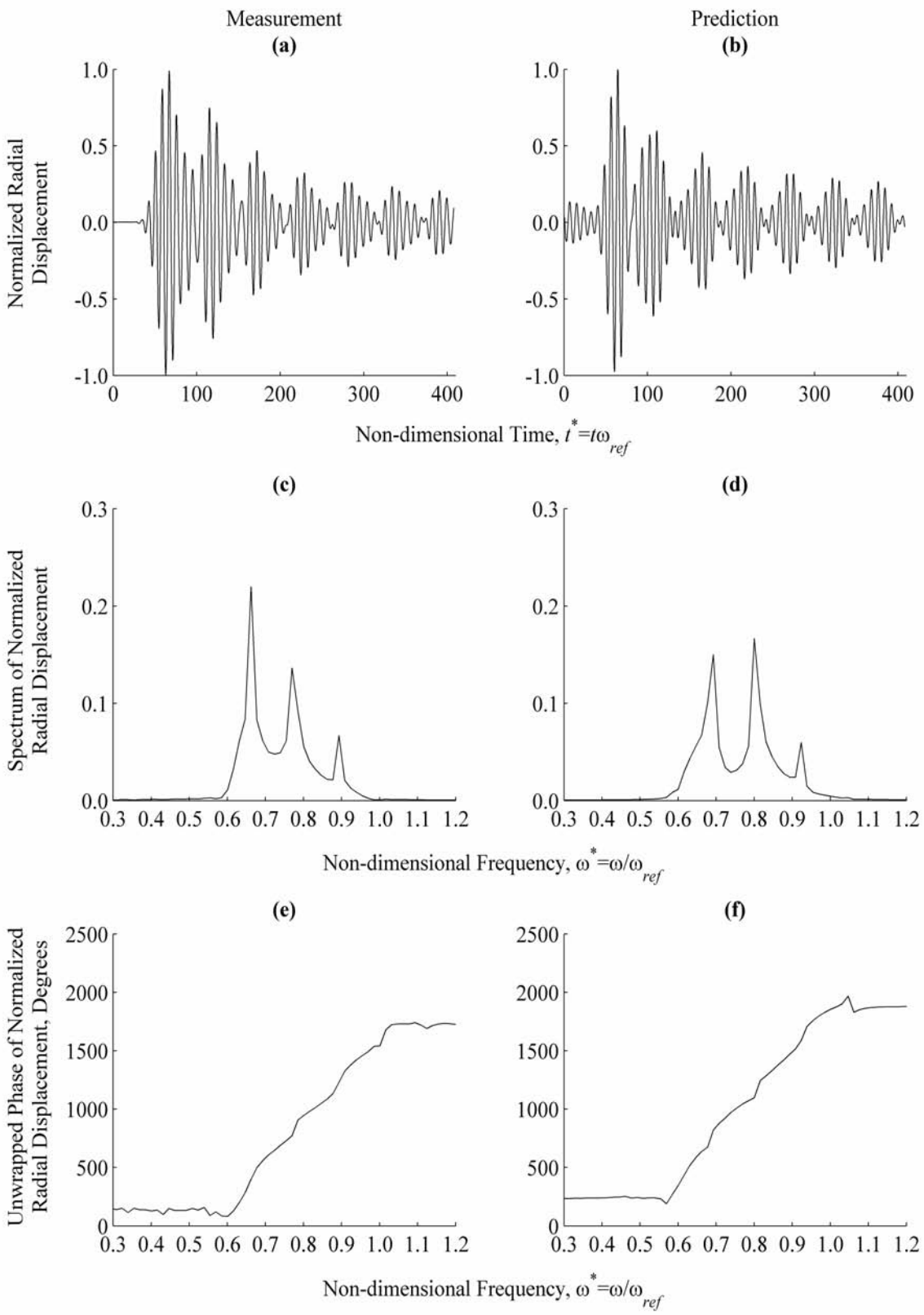

Figure H.36. Measurement and Prediction at $\theta=180^{\circ}$, $z^*=2.55$

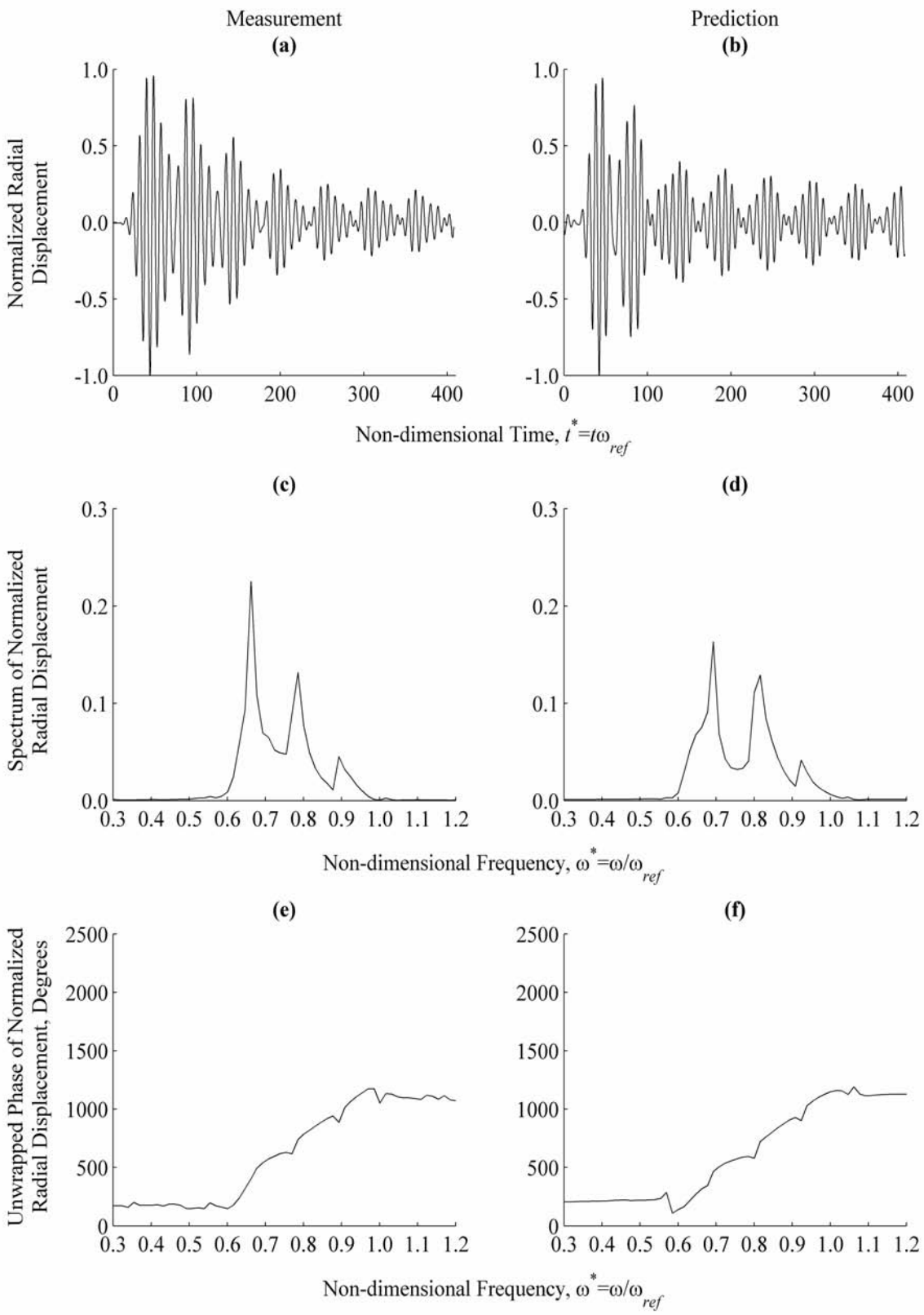

Figure H.37. Measurement and Prediction at $\theta=0^{\circ}$, $z^*=5.10$

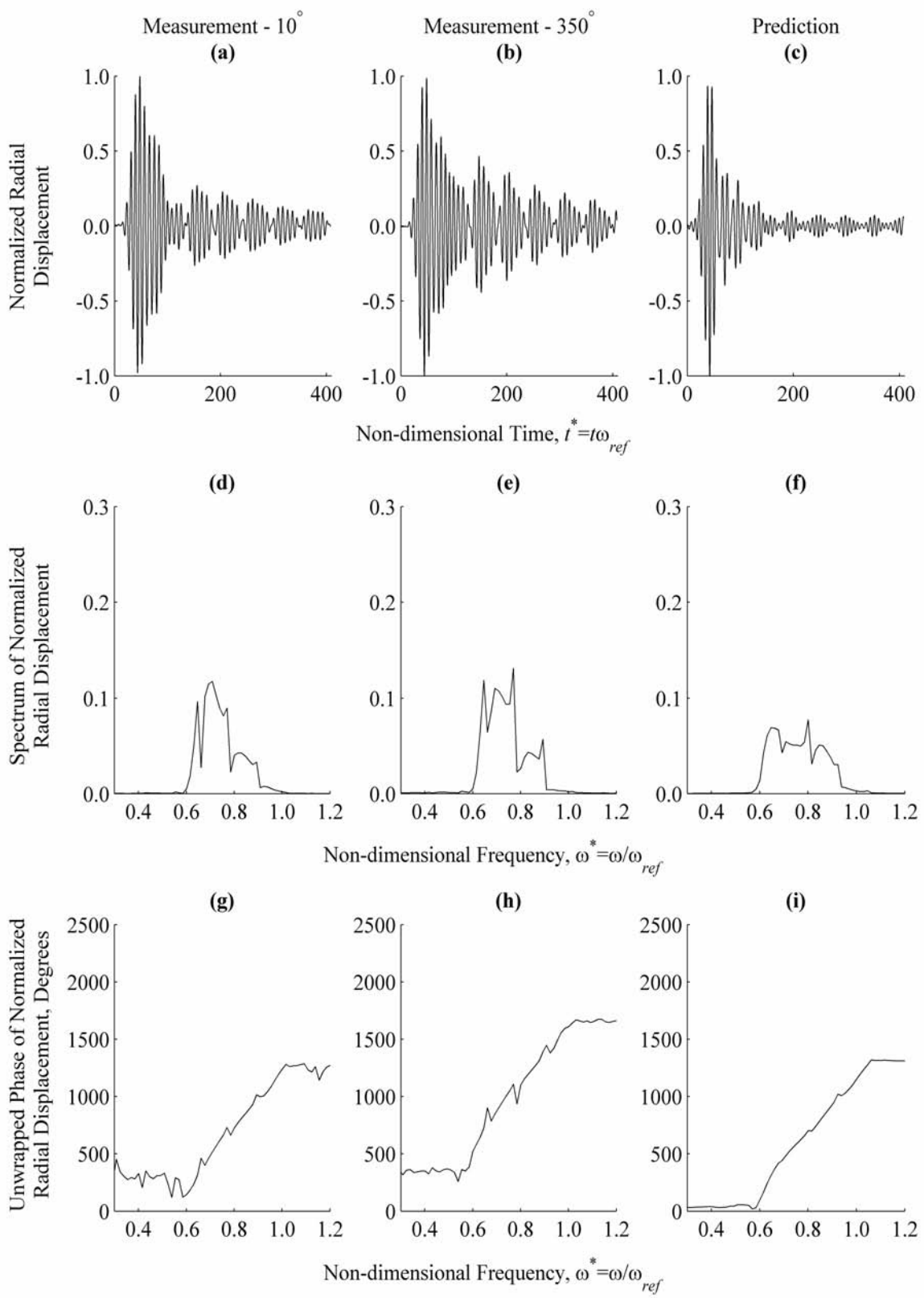

Figure H.38. Measurement and Prediction at θ=10° and θ=350°, z^*=5.10

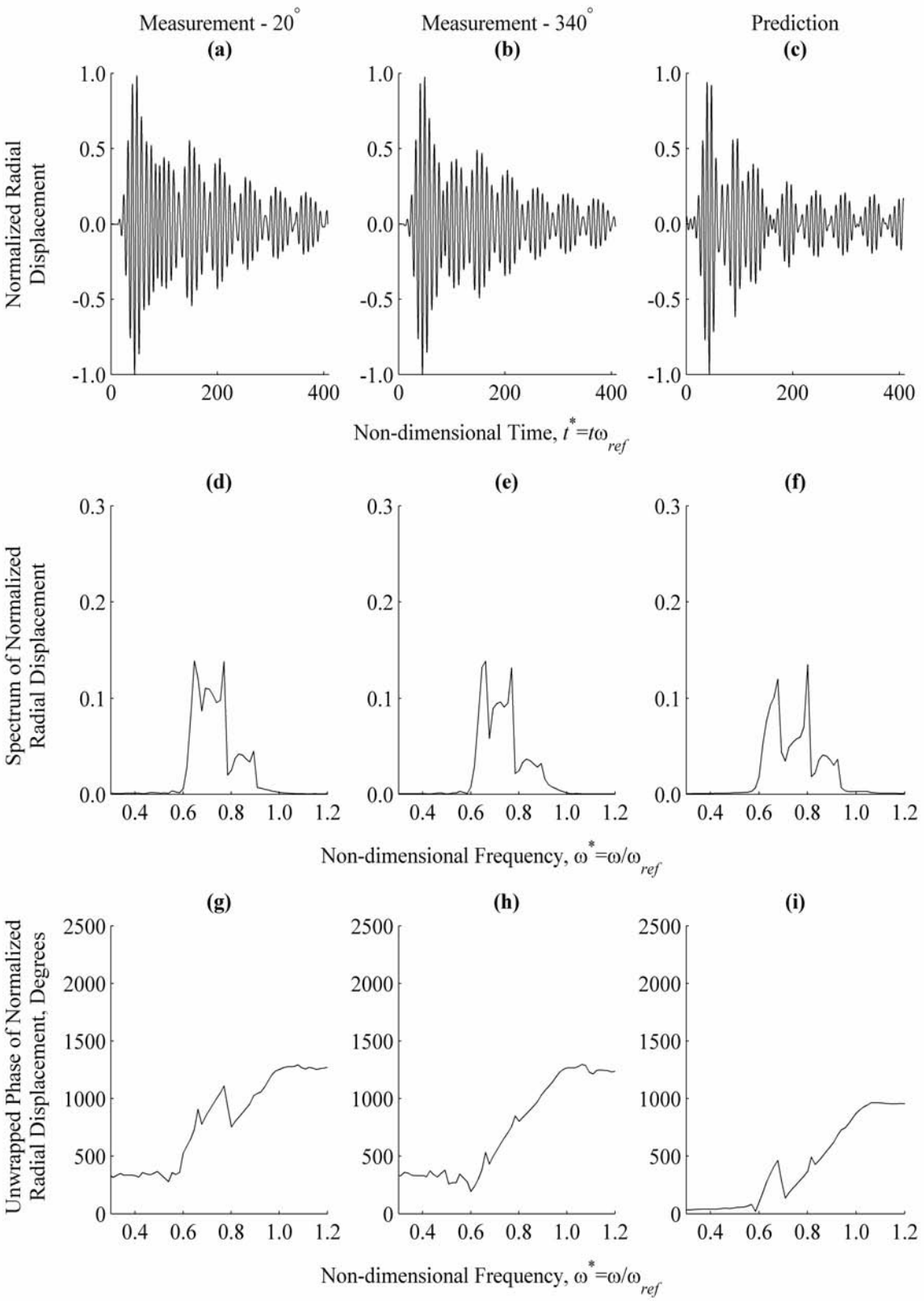

Figure H.39. Measurement and Prediction at θ=20° and θ=340°, z^*=5.10

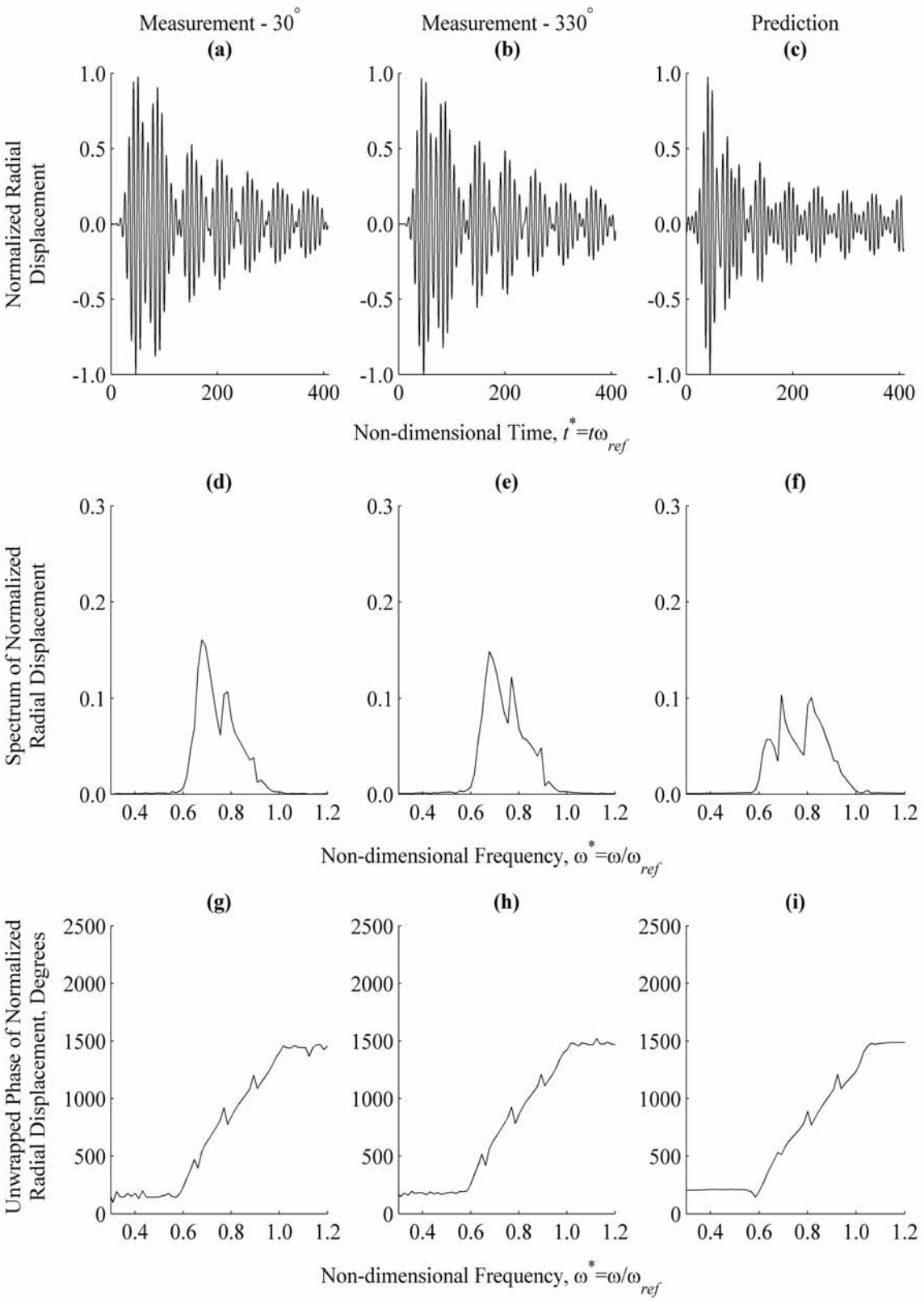

Figure H.40. Measurement and Prediction at θ=30° and θ=330°, z^*=5.10

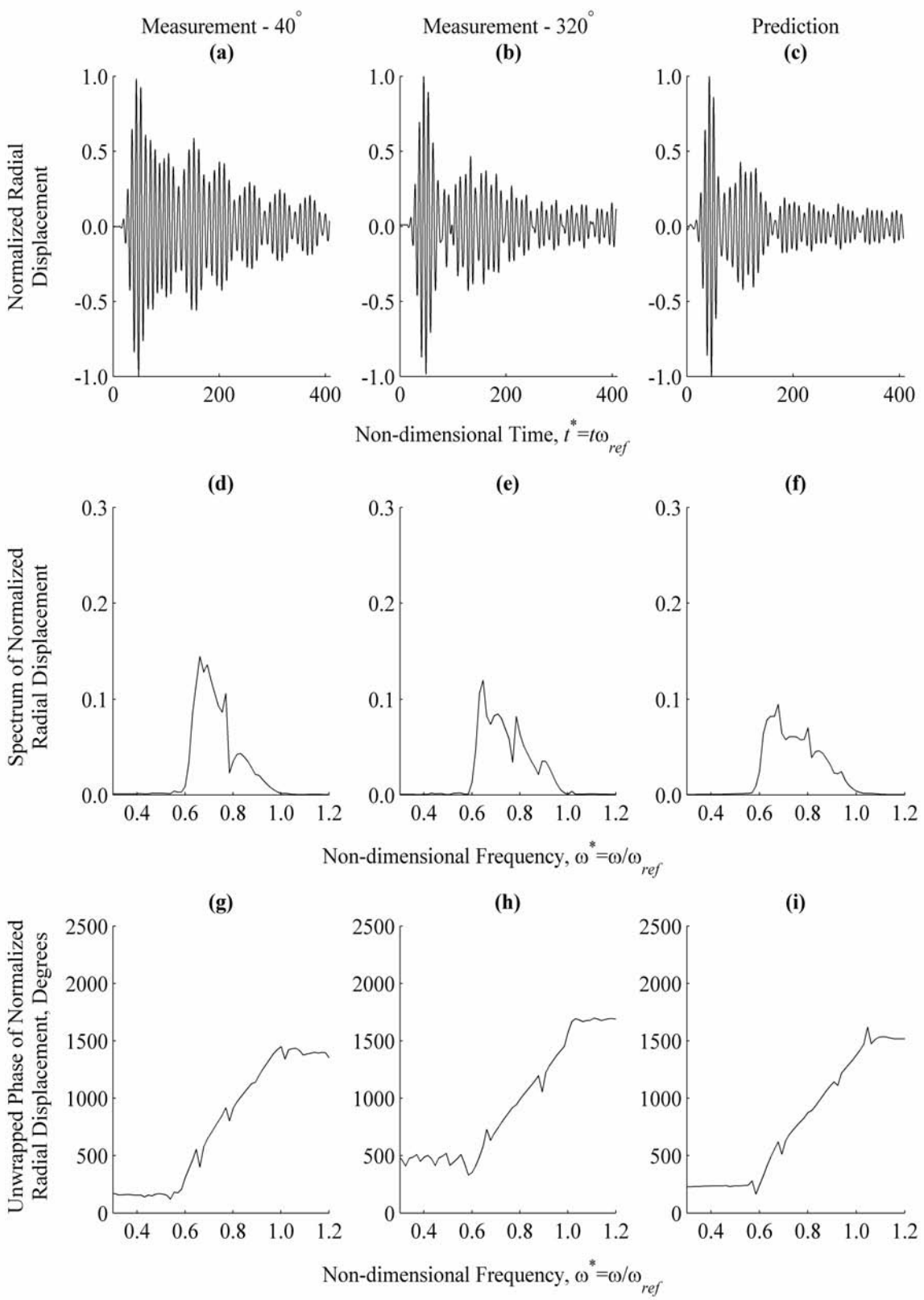

Figure H.41. Measurement and Prediction at θ=40° and θ=320°, z^*=5.10

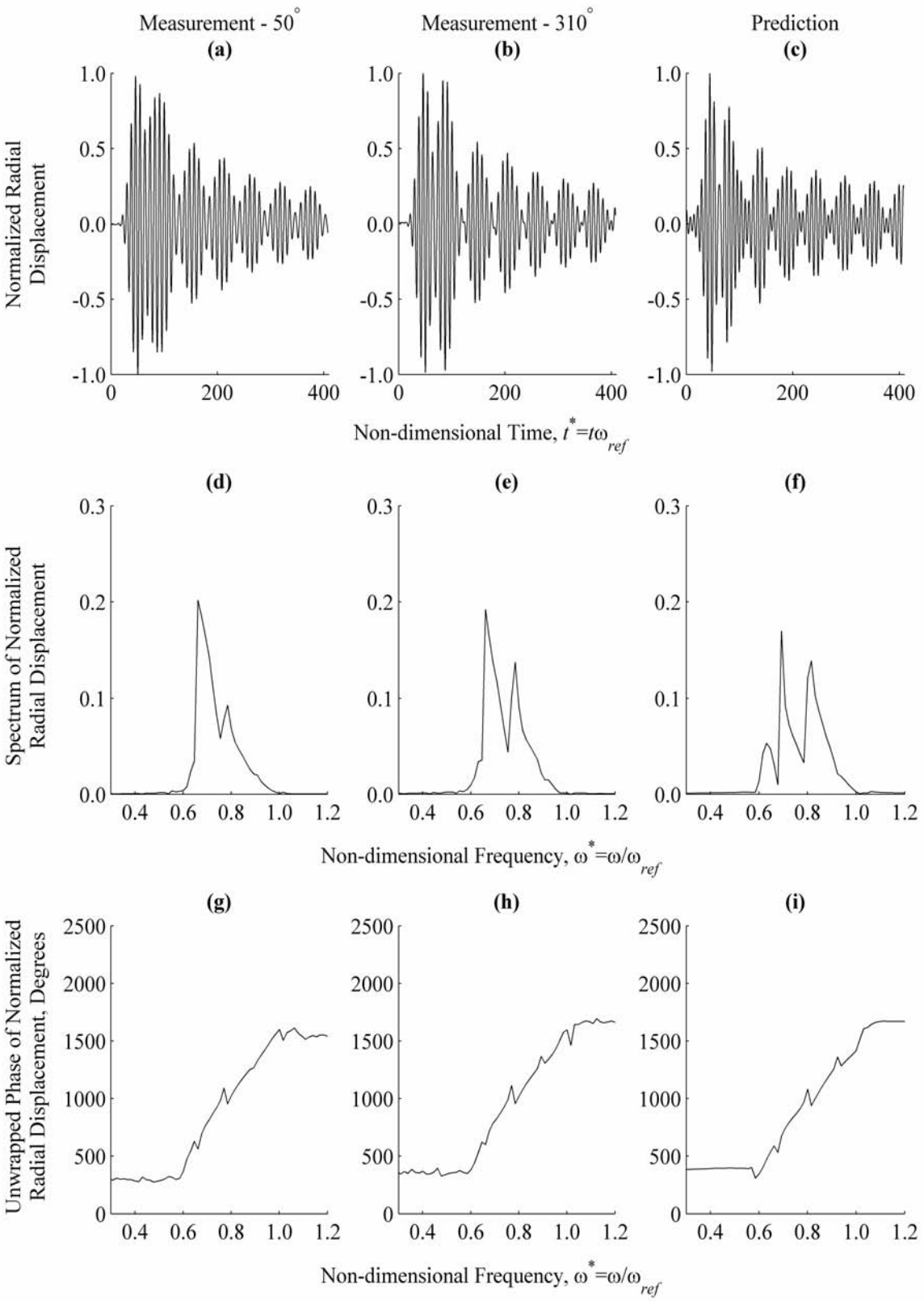

Figure H.42. Measurement and Prediction at θ=50° and θ=310°, z^*=5.10

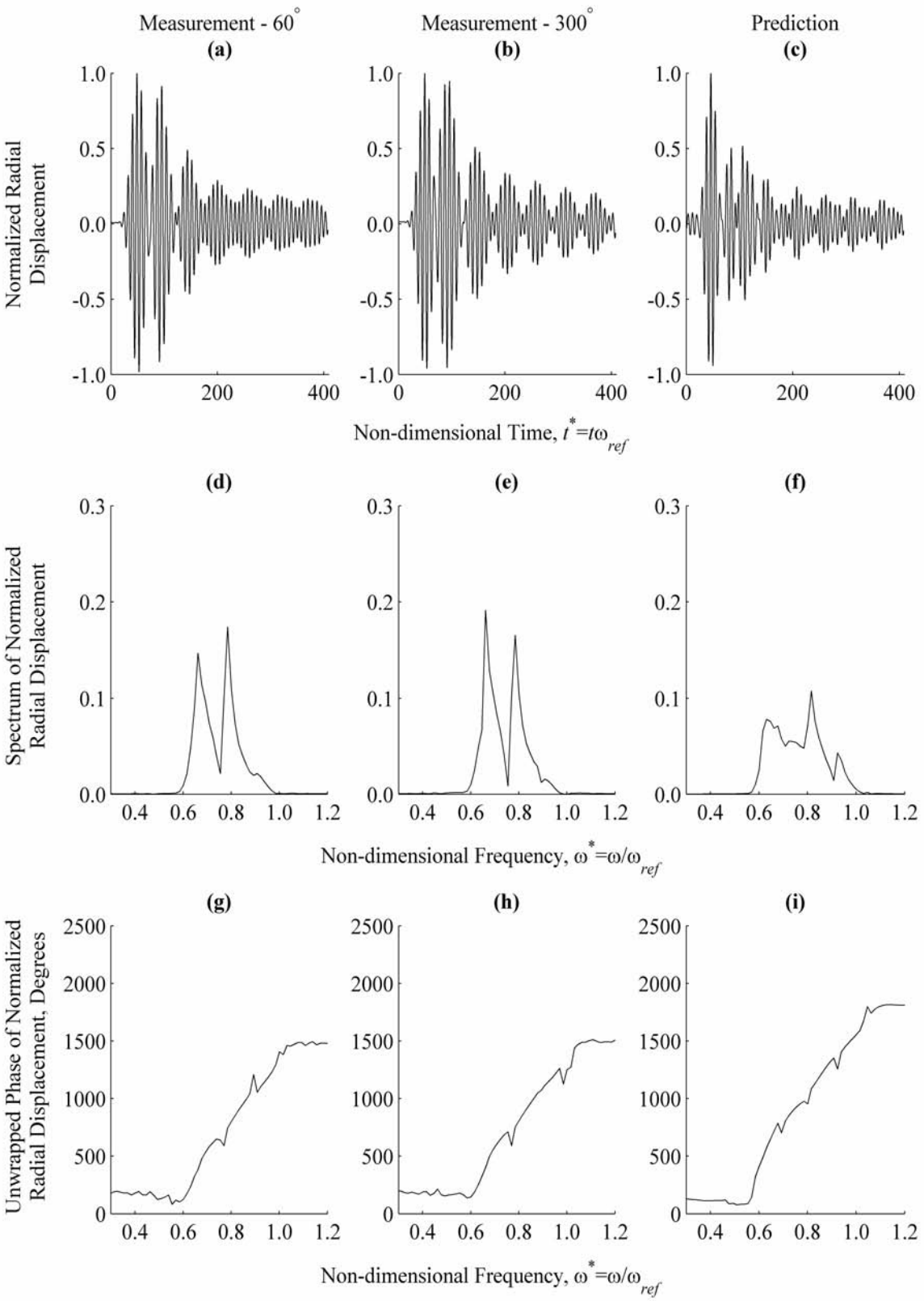

Figure H.43. Measurement and Prediction at $\theta=60^{\circ}$ and $\theta=300^{\circ}$, $z^*=5.10$

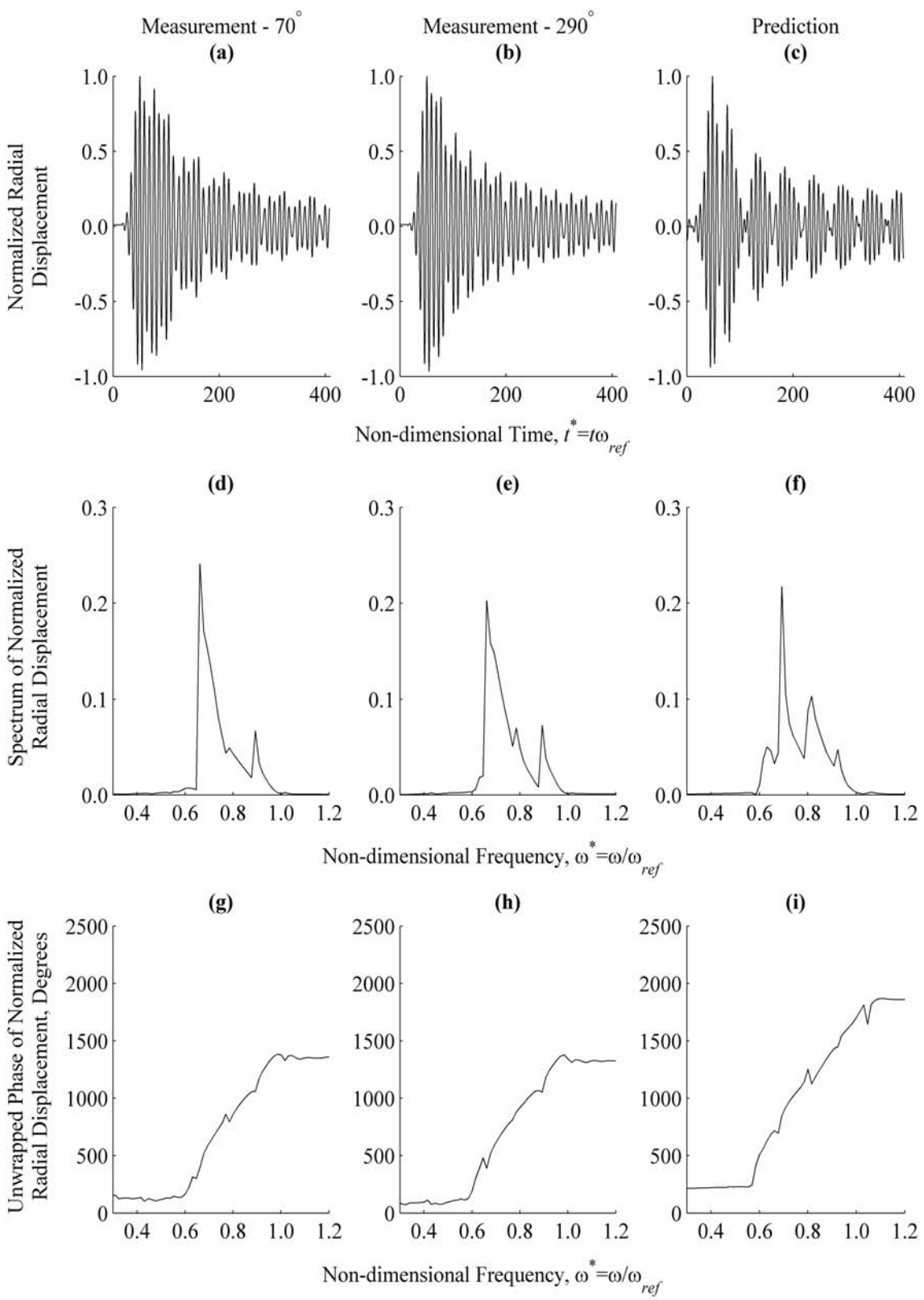

Figure H.44. Measurement and Prediction at θ=70° and θ=290°, z^*=5.10

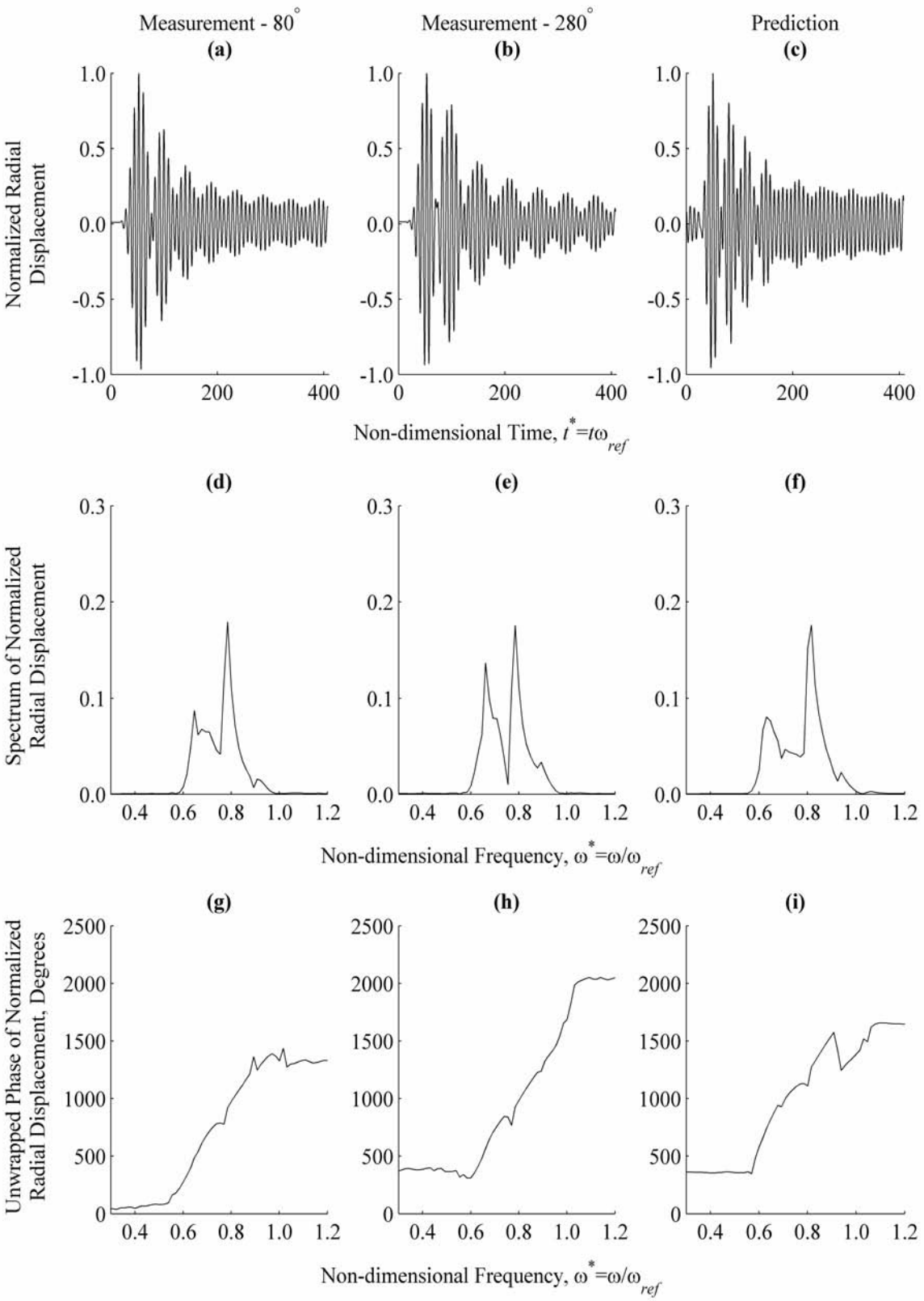

Figure H.45. Measurement and Prediction at θ=80° and θ=280°, z^*=5.10

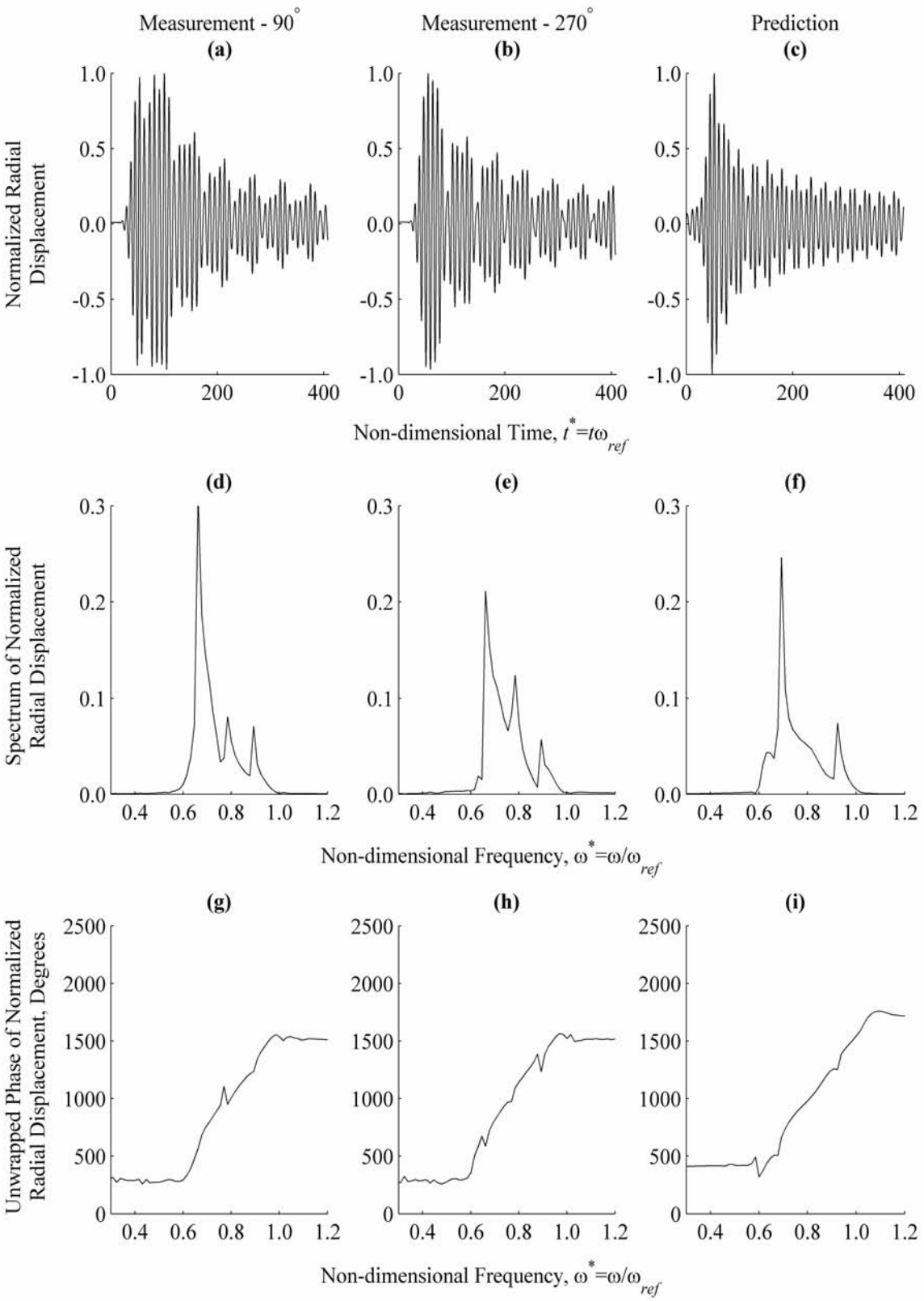

Figure H.46. Measurement and Prediction at θ=90° and θ=270°, z^*=5.10

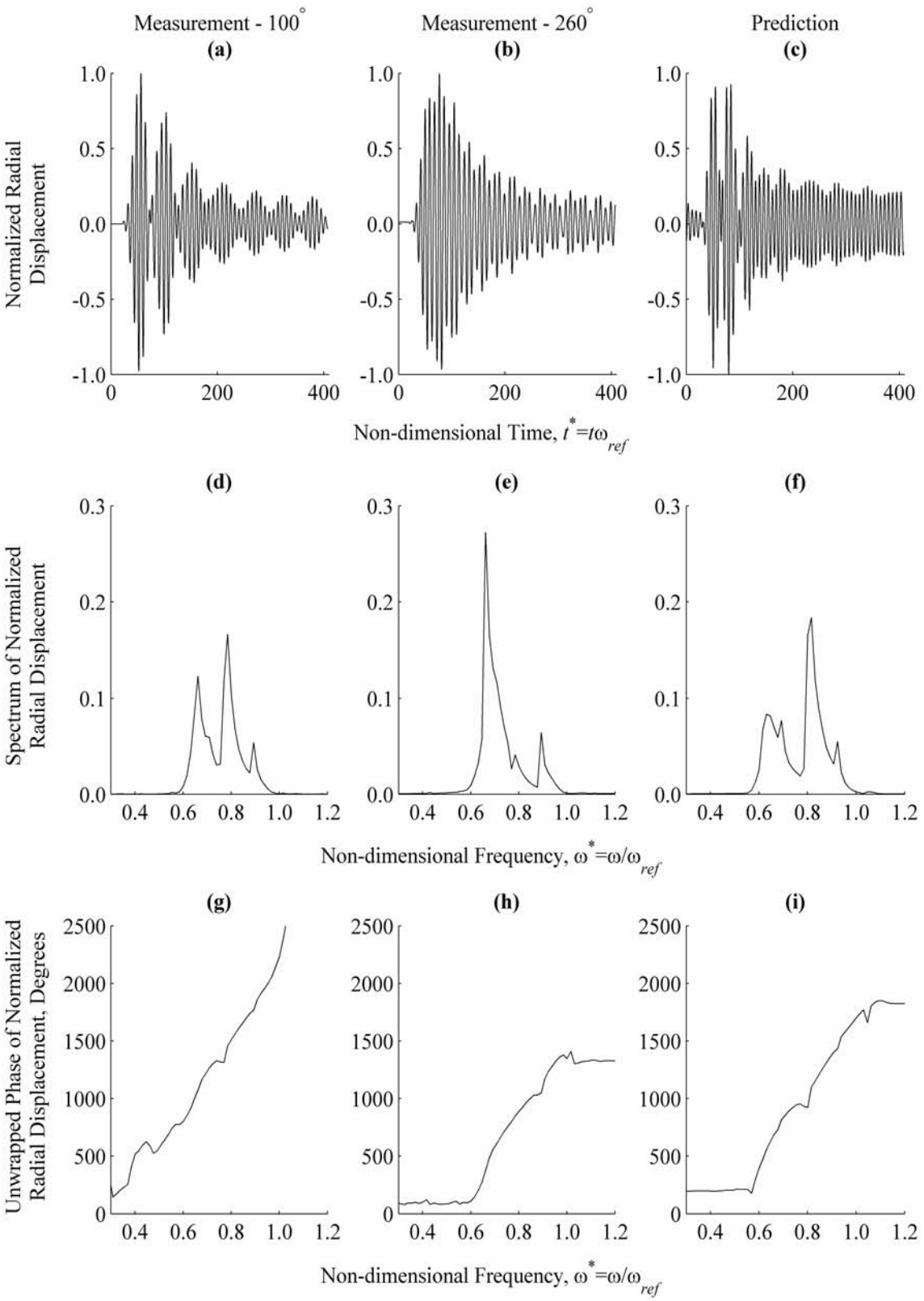

Figure H.47. Measurement and Prediction at θ=100° and θ=260°, z^*=5.10

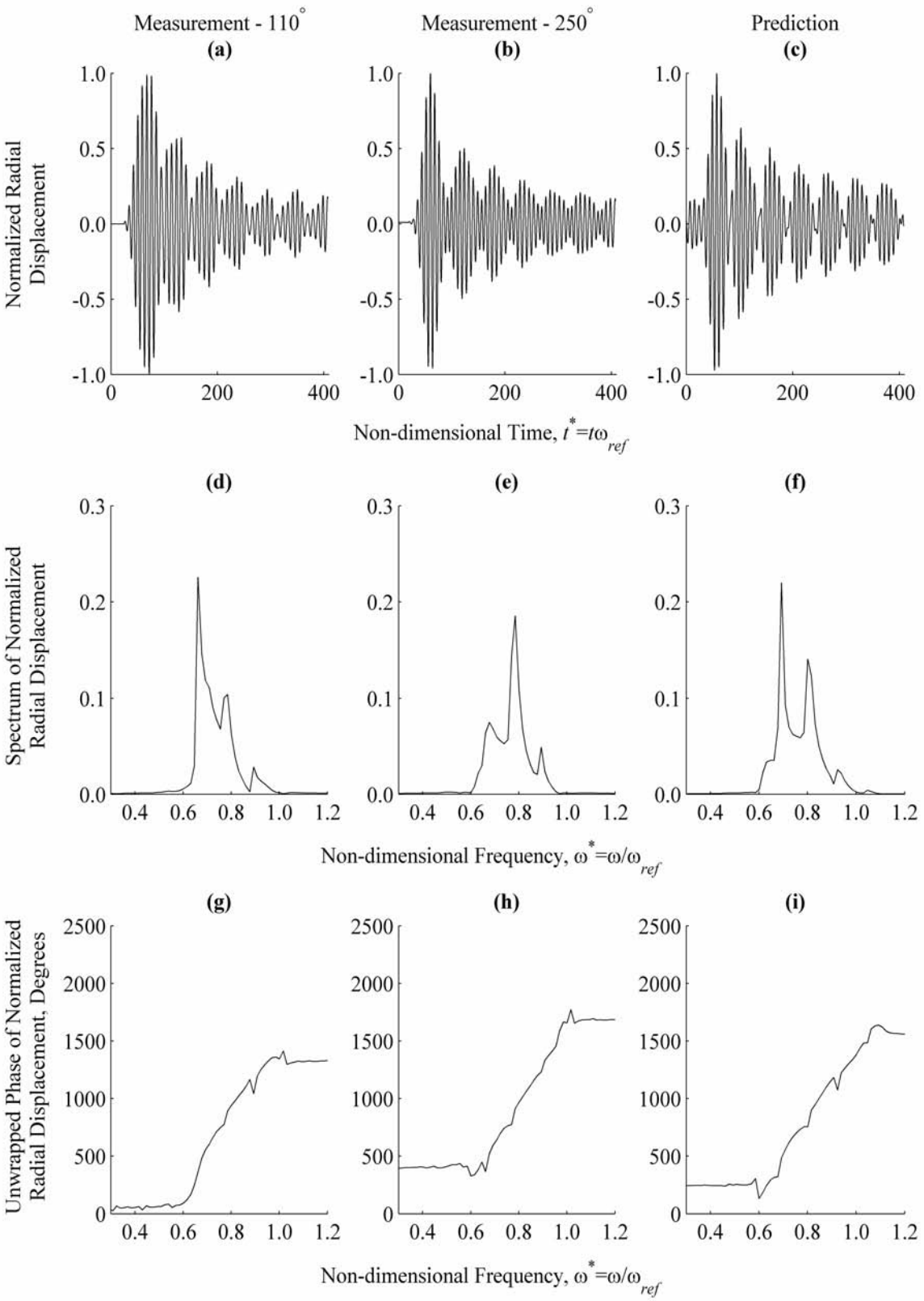

Figure H.48. Measurement and Prediction at θ=110° and θ=250°, z^*=5.10

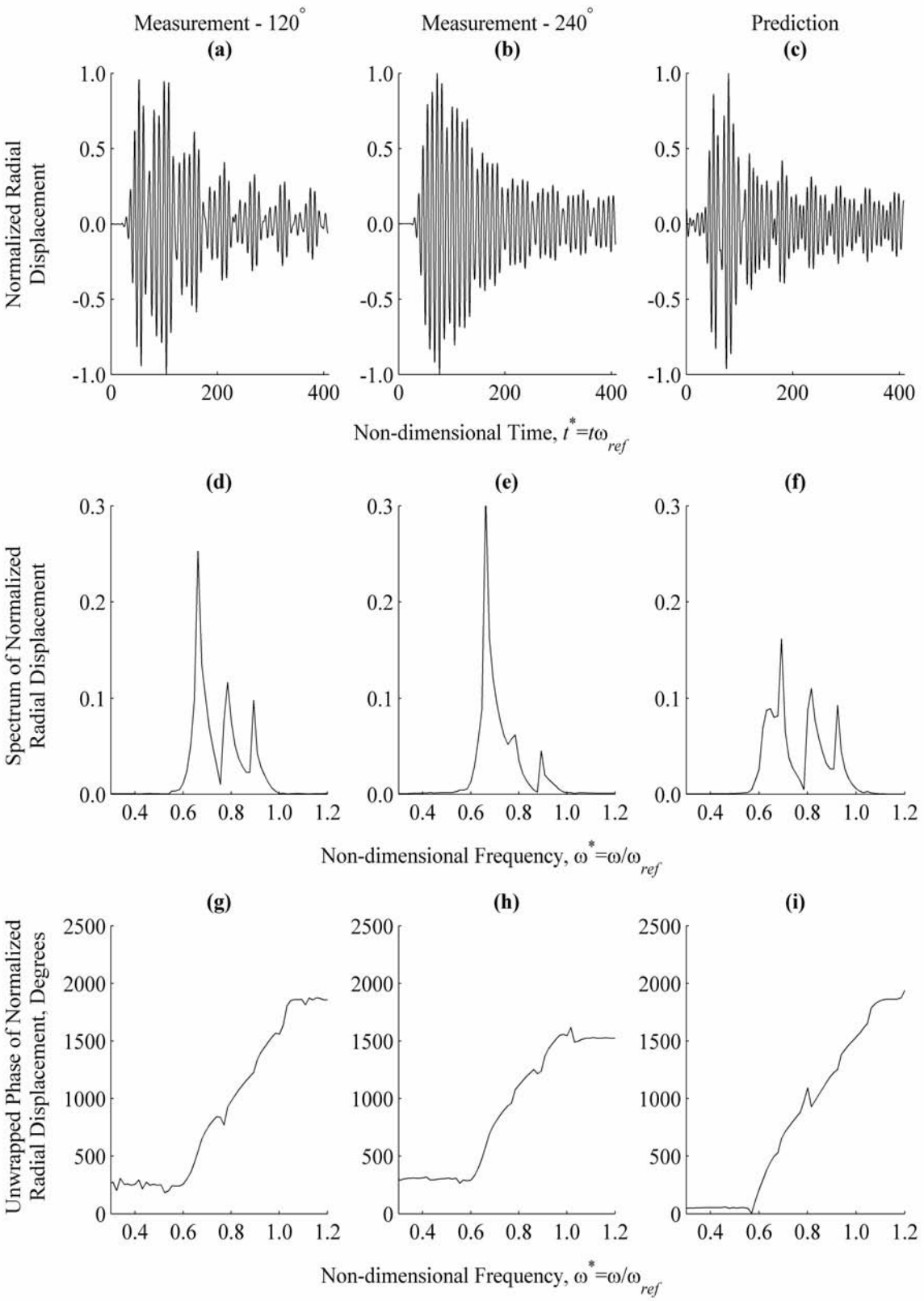

Figure H.49. Measurement and Prediction at θ=120° and θ=240°, z^*=5.10

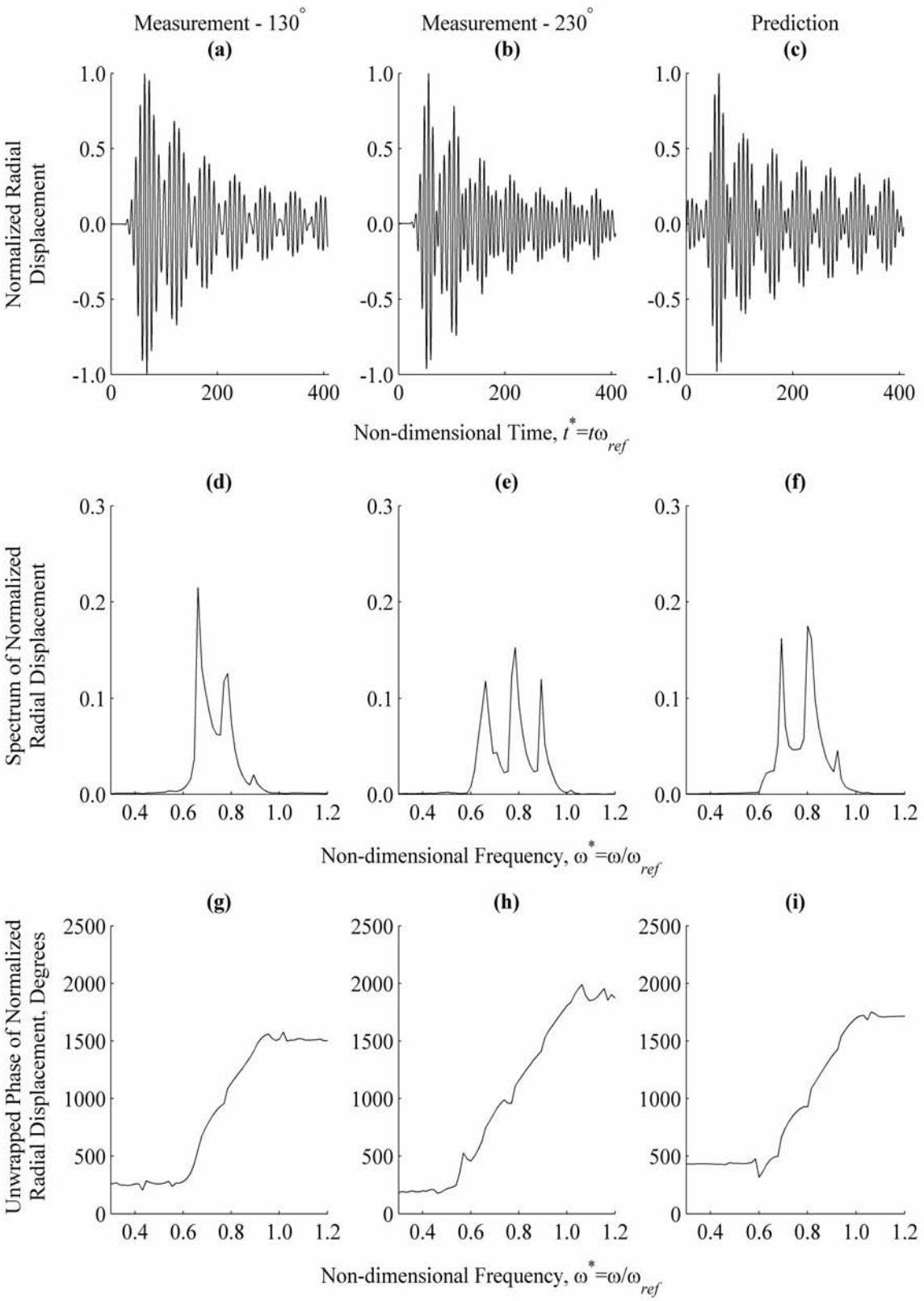

Figure H.50. Measurement and Prediction at θ=130° and θ=230°, z^*=5.10

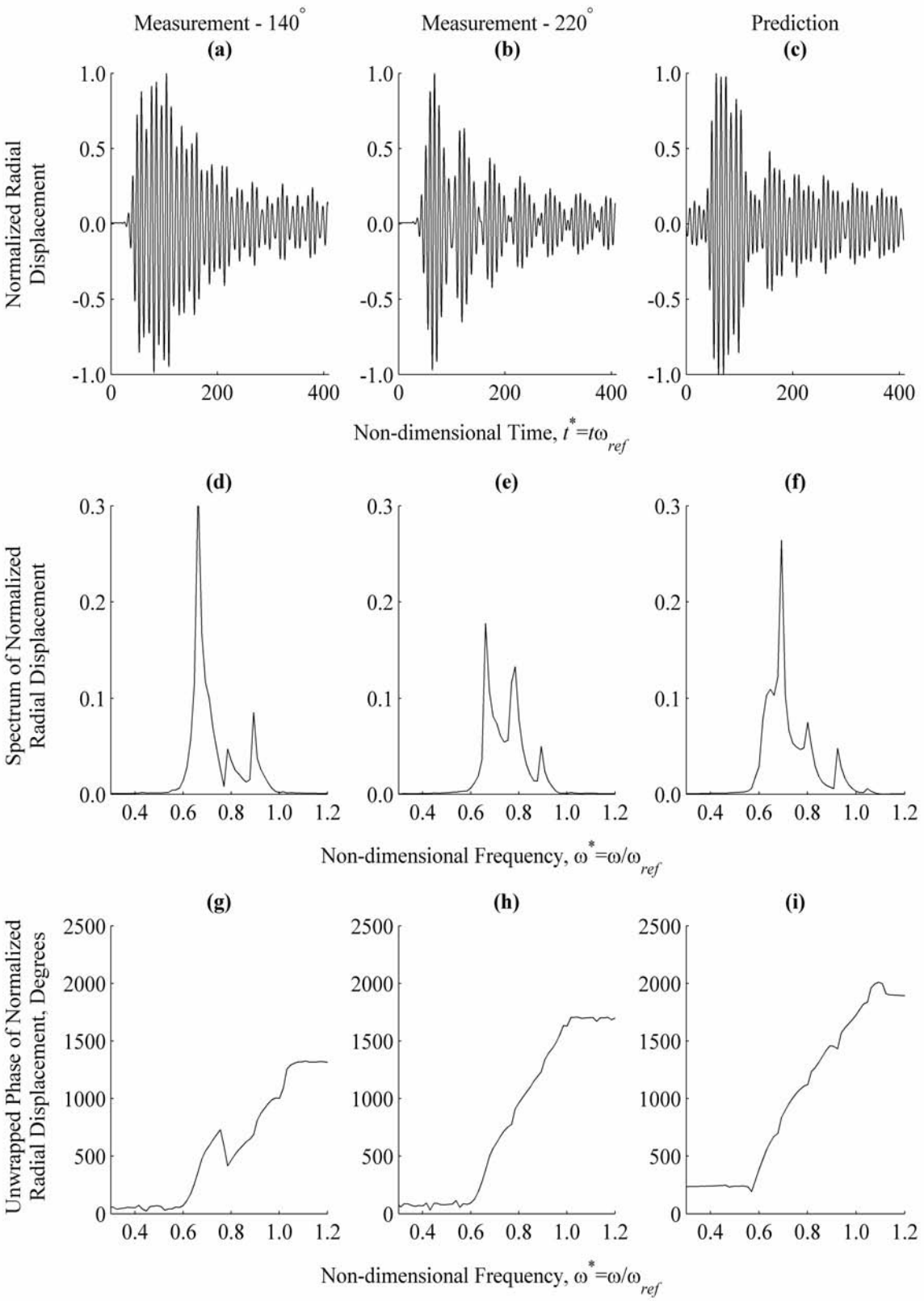

Figure H.51. Measurement and Prediction at θ=140° and θ=220°, z^*=5.10

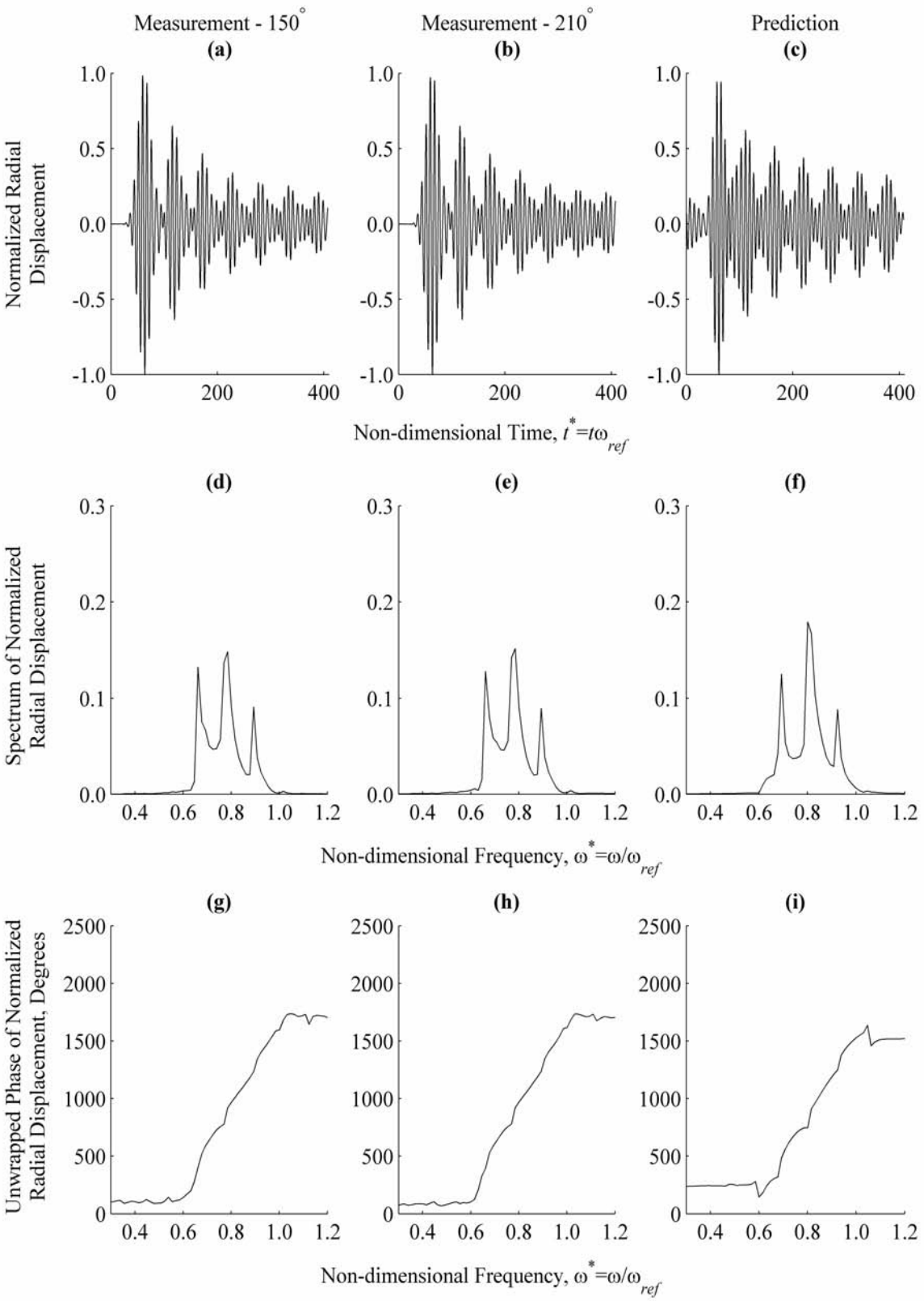

Figure H.52. Measurement and Prediction at θ=150° and θ=210°, z^*=5.10

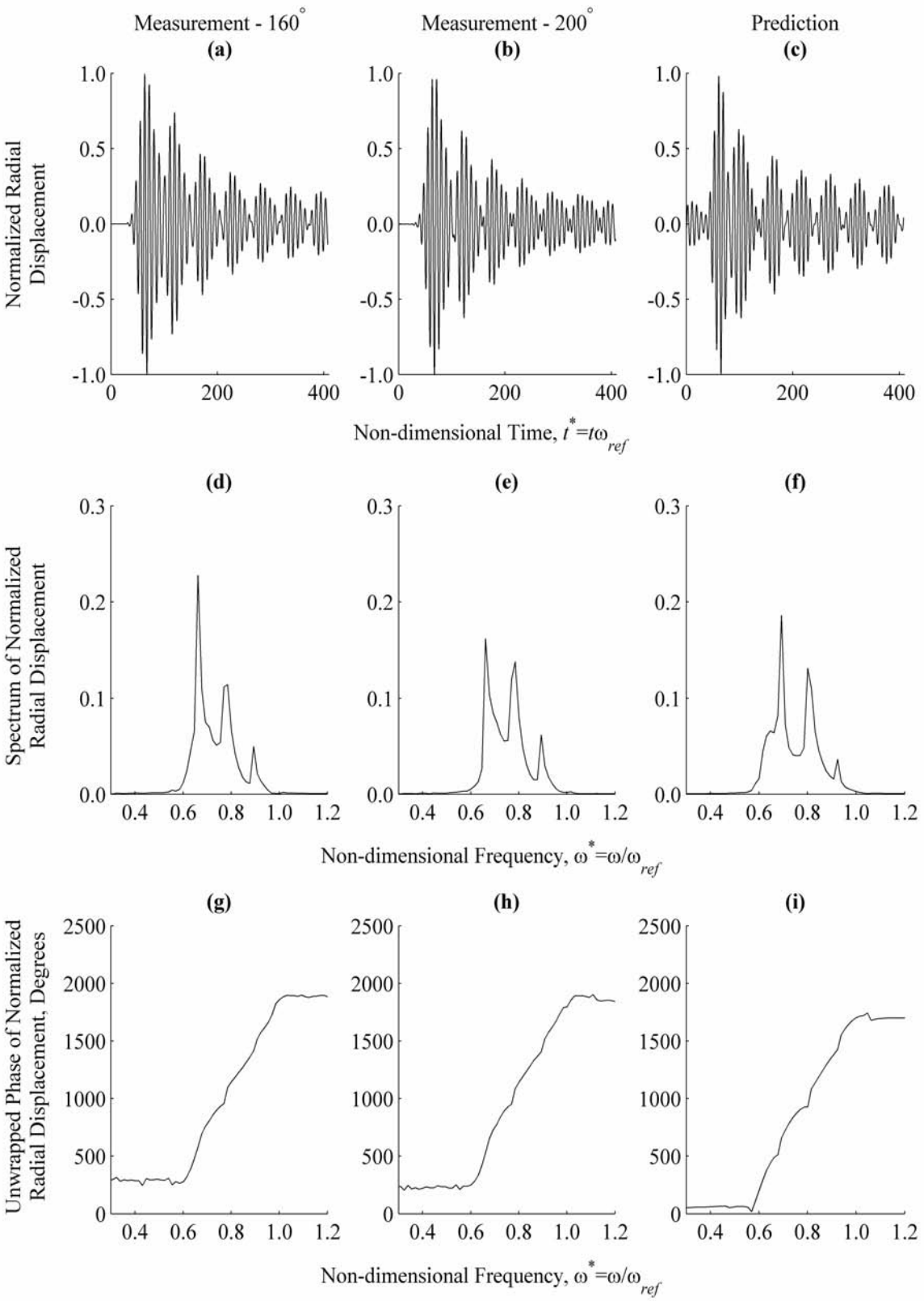

Figure H.53. Measurement and Prediction at θ=160° and θ=200°, z^*=5.10

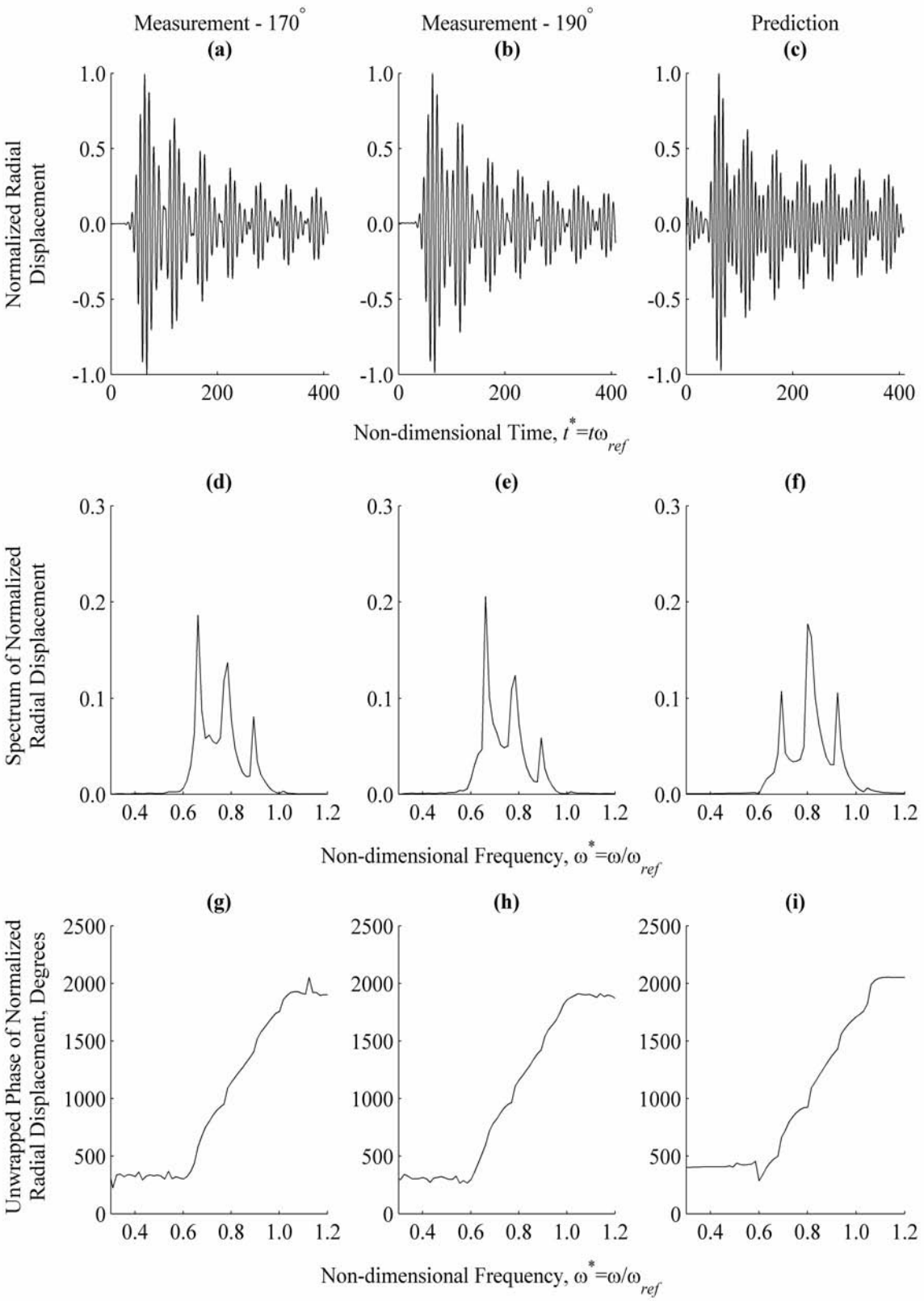

Figure H.54. Measurement and Prediction at θ=170° and θ=190°, z^*=5.10

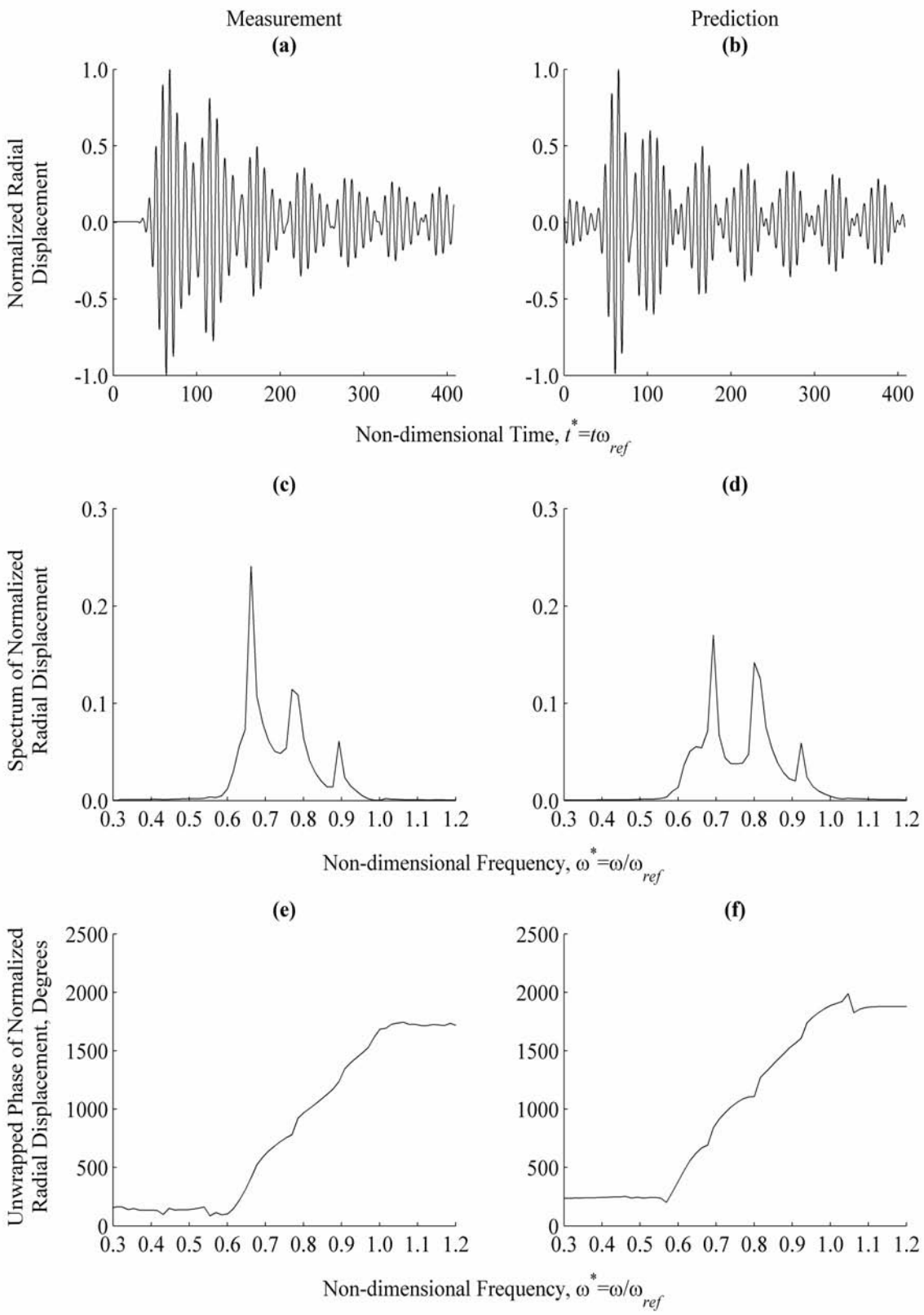

Figure H.55. Measurement and Prediction at $\theta=180^{\circ}$, $z^*=5.10$

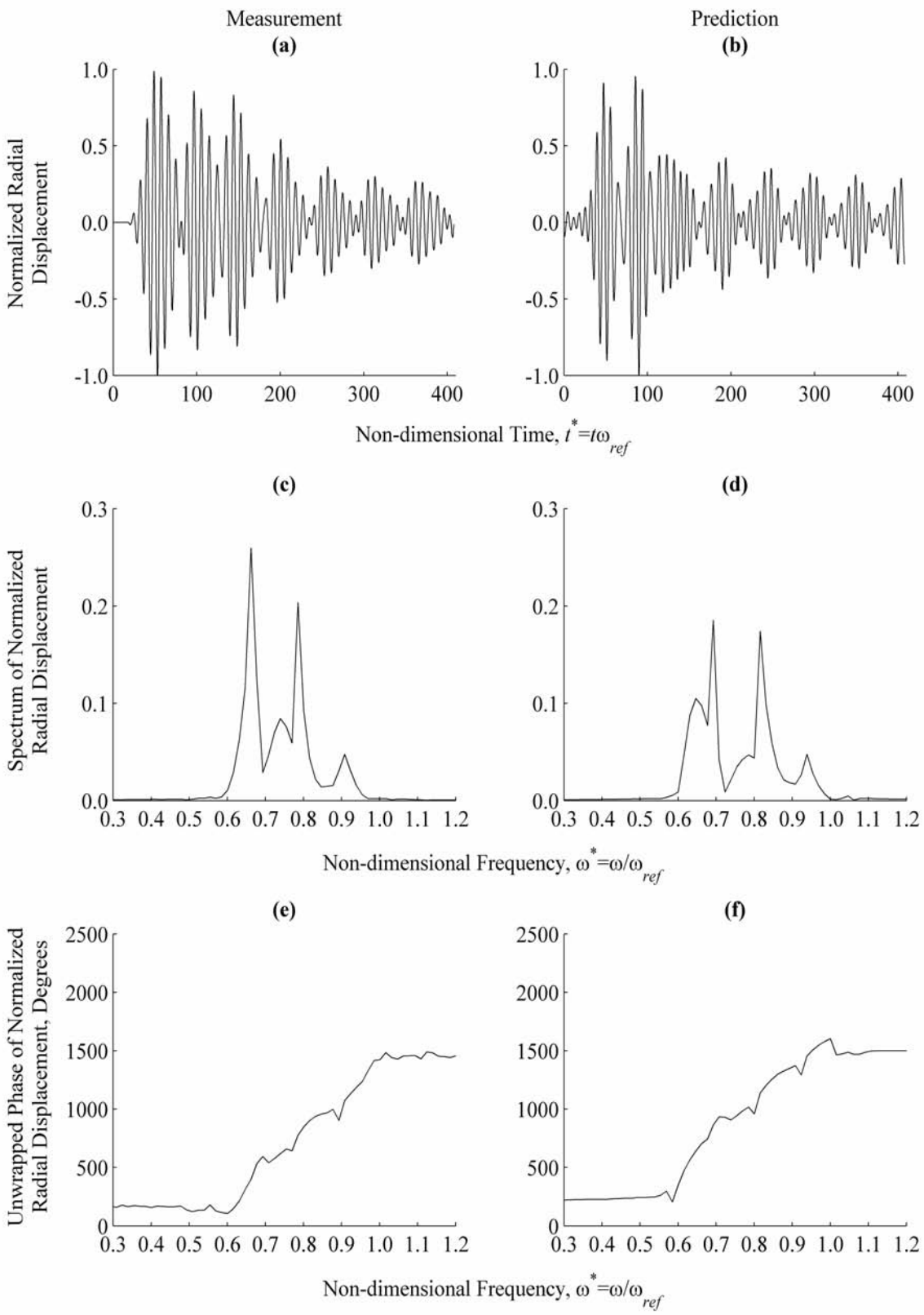

Figure H.56. Measurement and Prediction at $\theta=0^{\circ}$, $z^*=10.20$

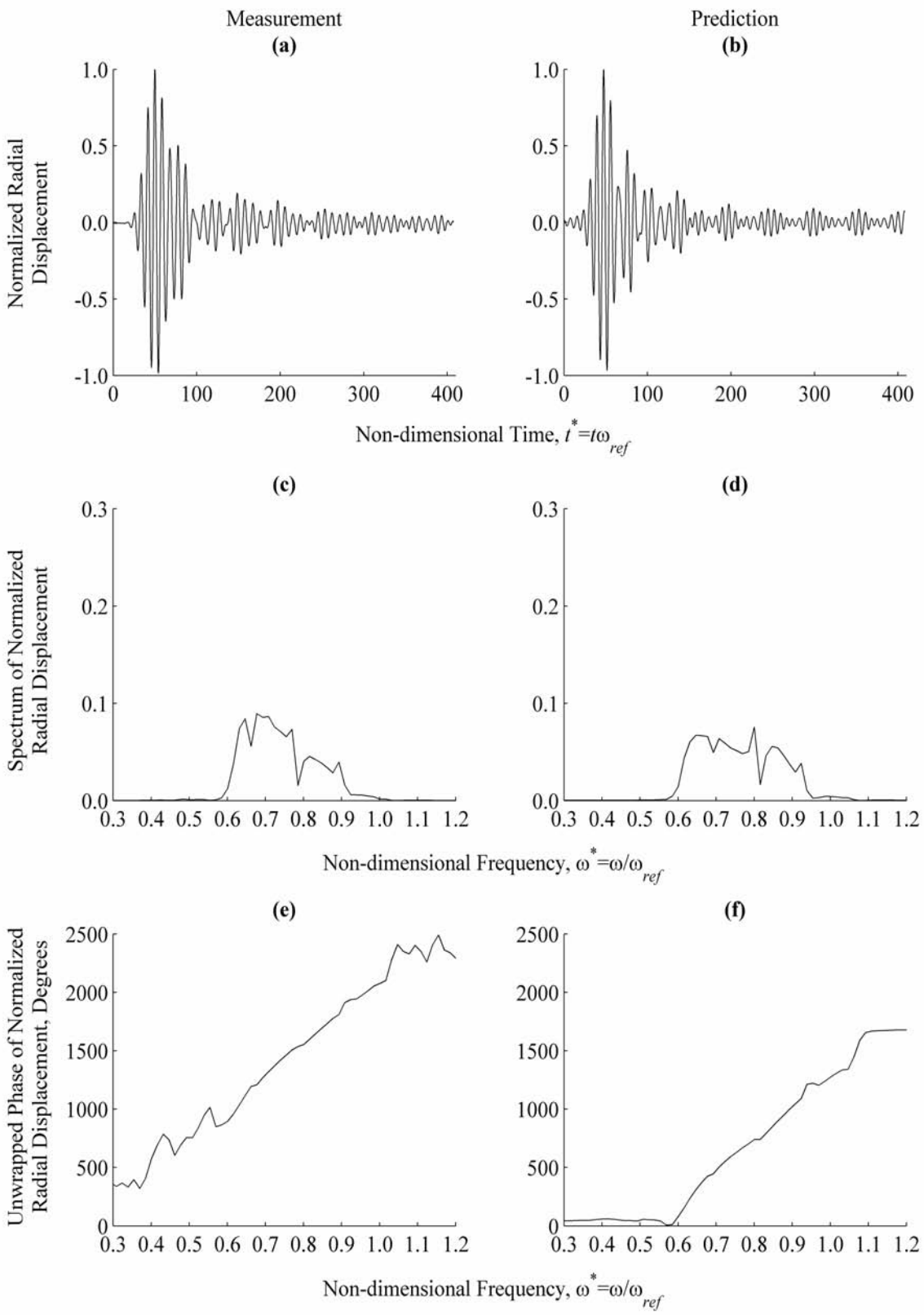

Figure H.57. Measurement and Prediction at $\theta=10^{\circ}$, $z^*=10.20$

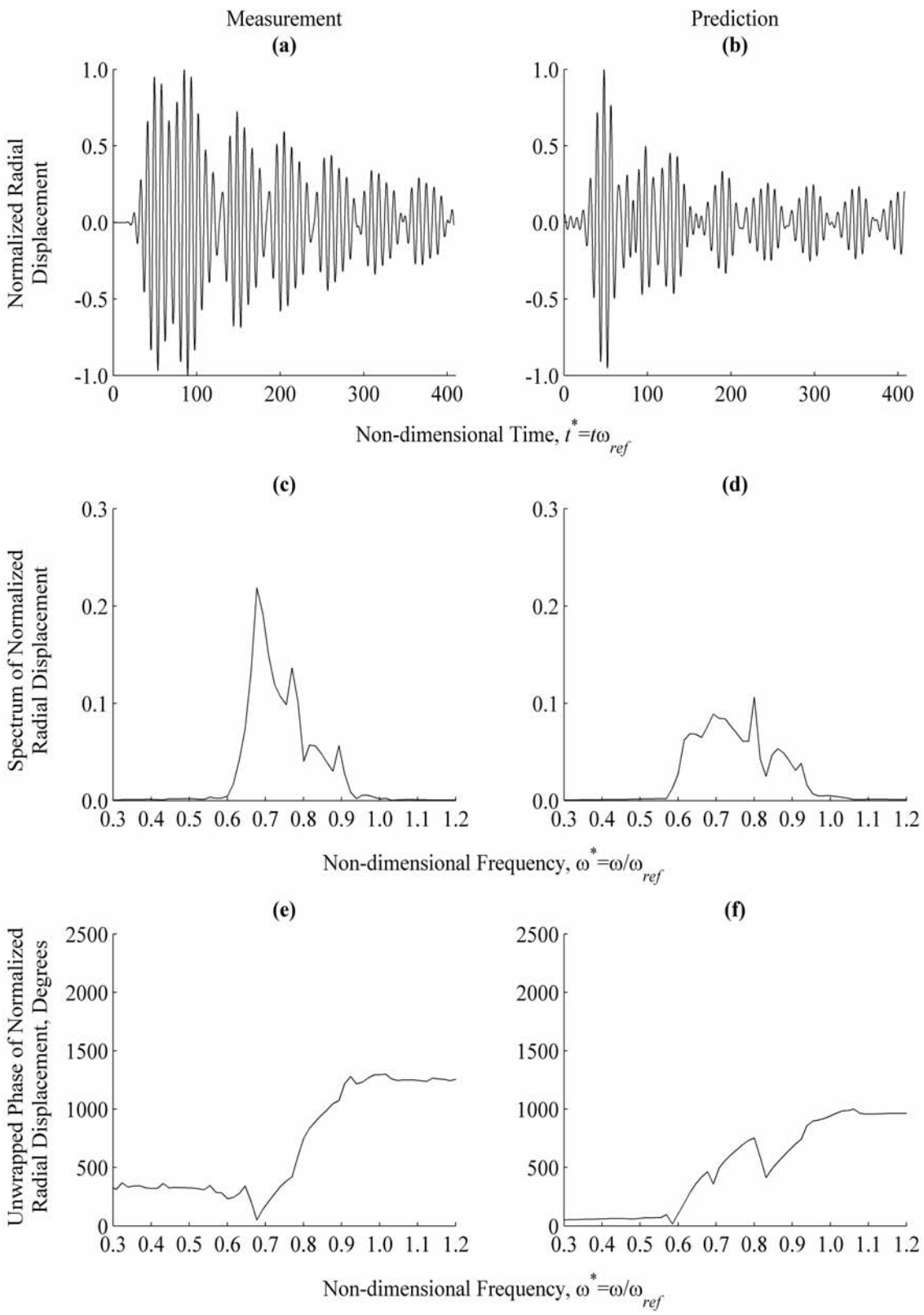

Figure H.58. Measurement and Prediction at $\theta=20^{\circ}$, $z^*=10.20$

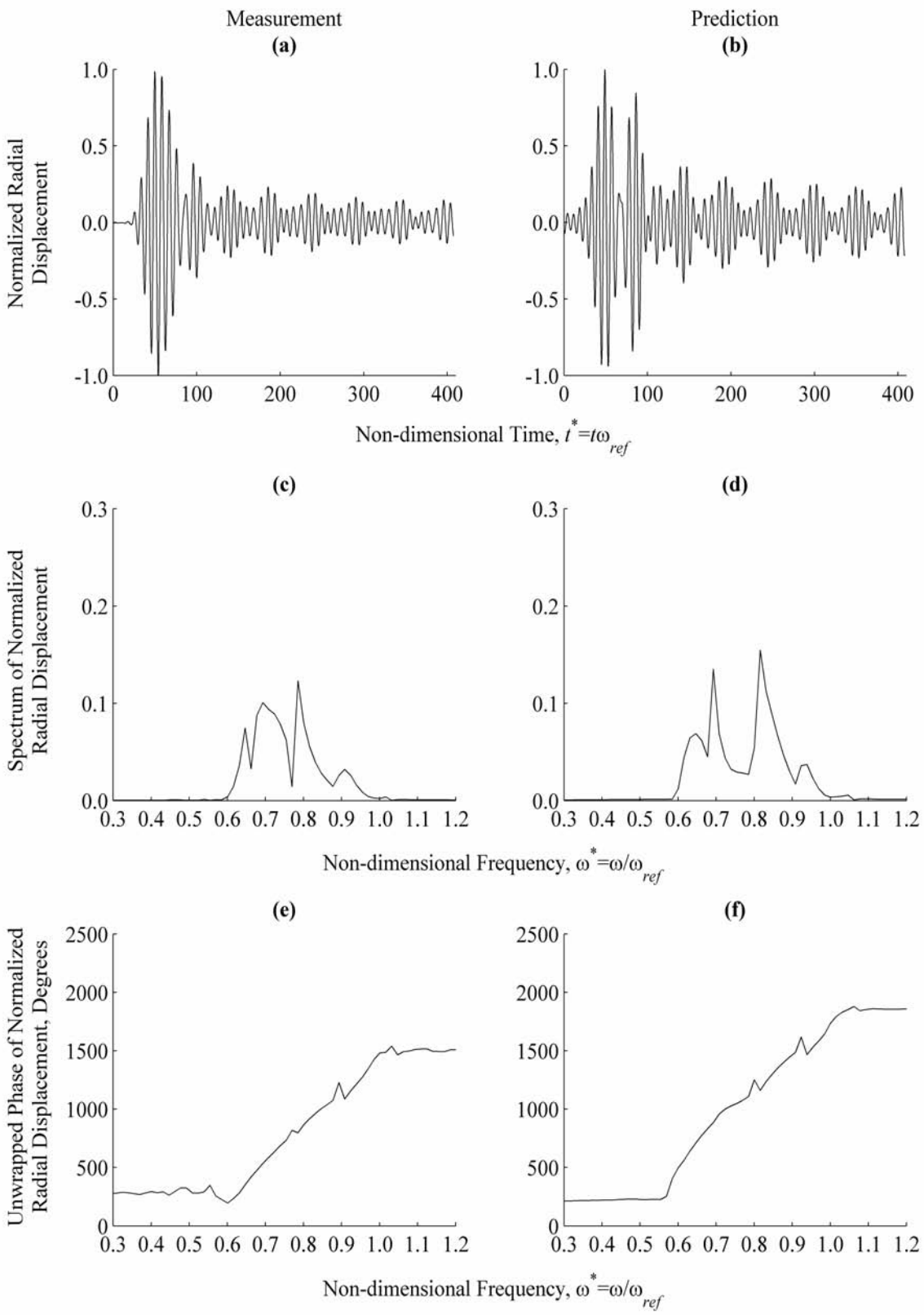

Figure H.59. Measurement and Prediction at $\theta=30^{\circ}$, $z^*=10.20$

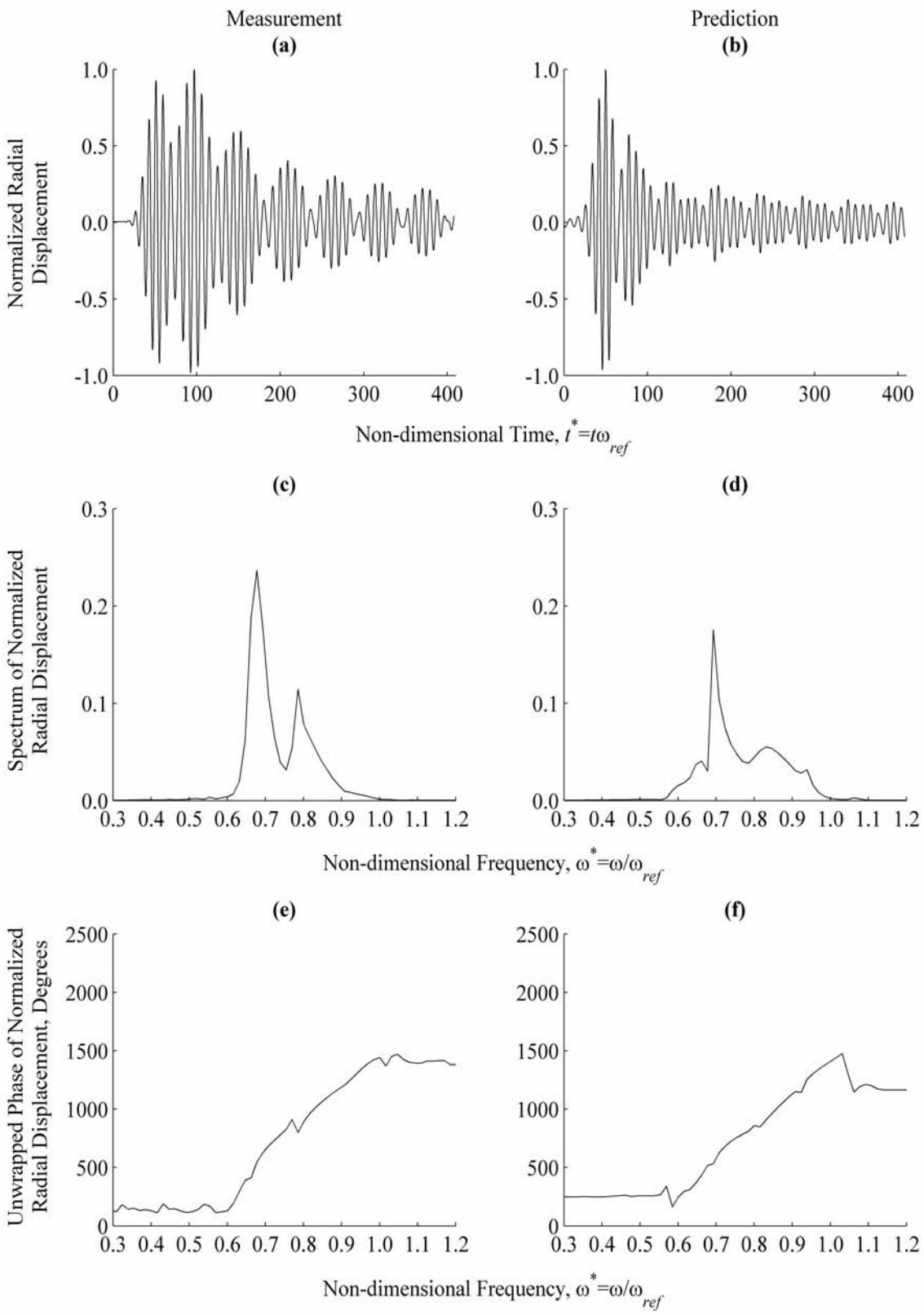

Figure H.60. Measurement and Prediction at $\theta=40^{\circ}$, $z^*=10.20$

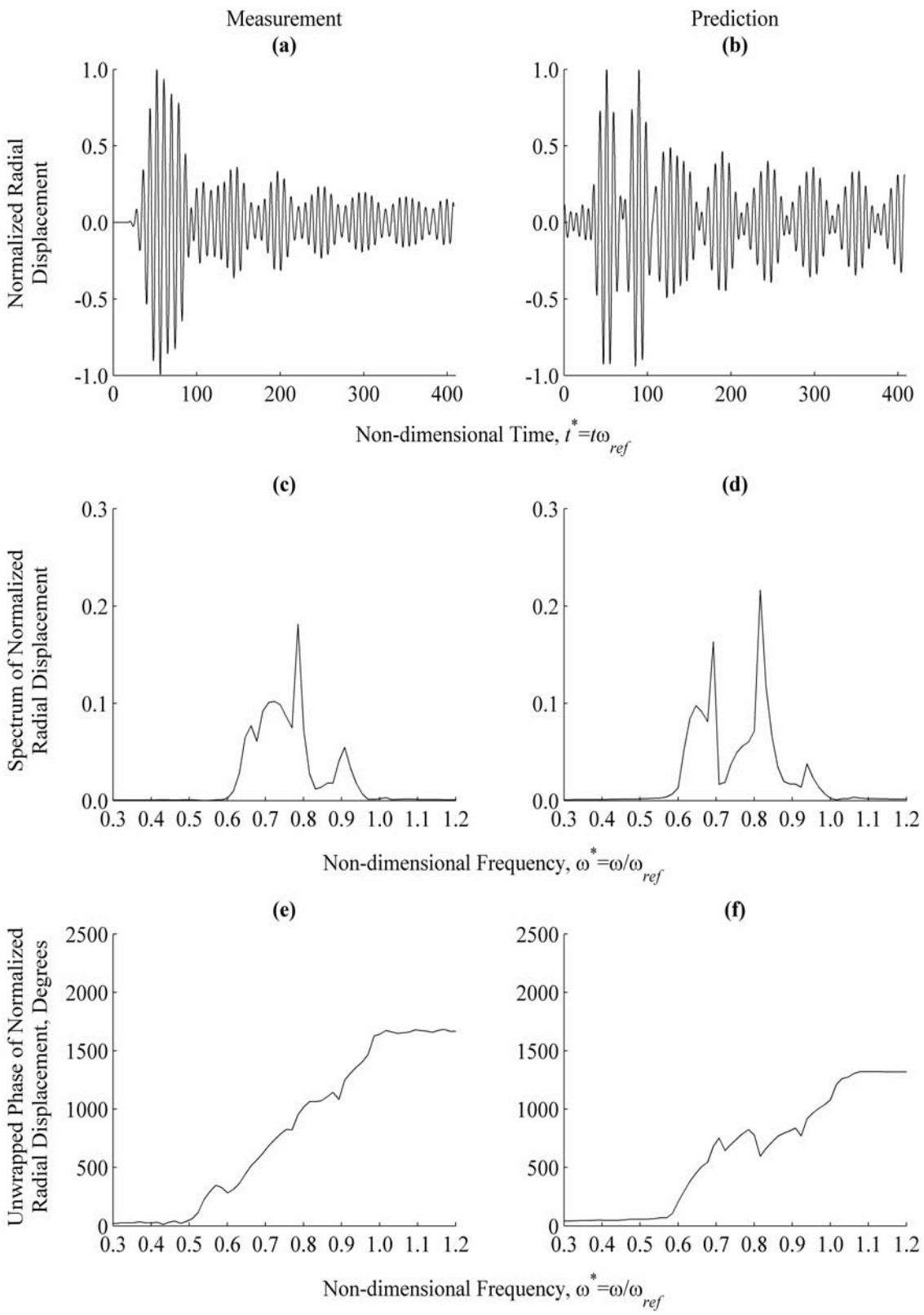

Figure H.61. Measurement and Prediction at $\theta=50^{\circ}$, $z^*=10.20$

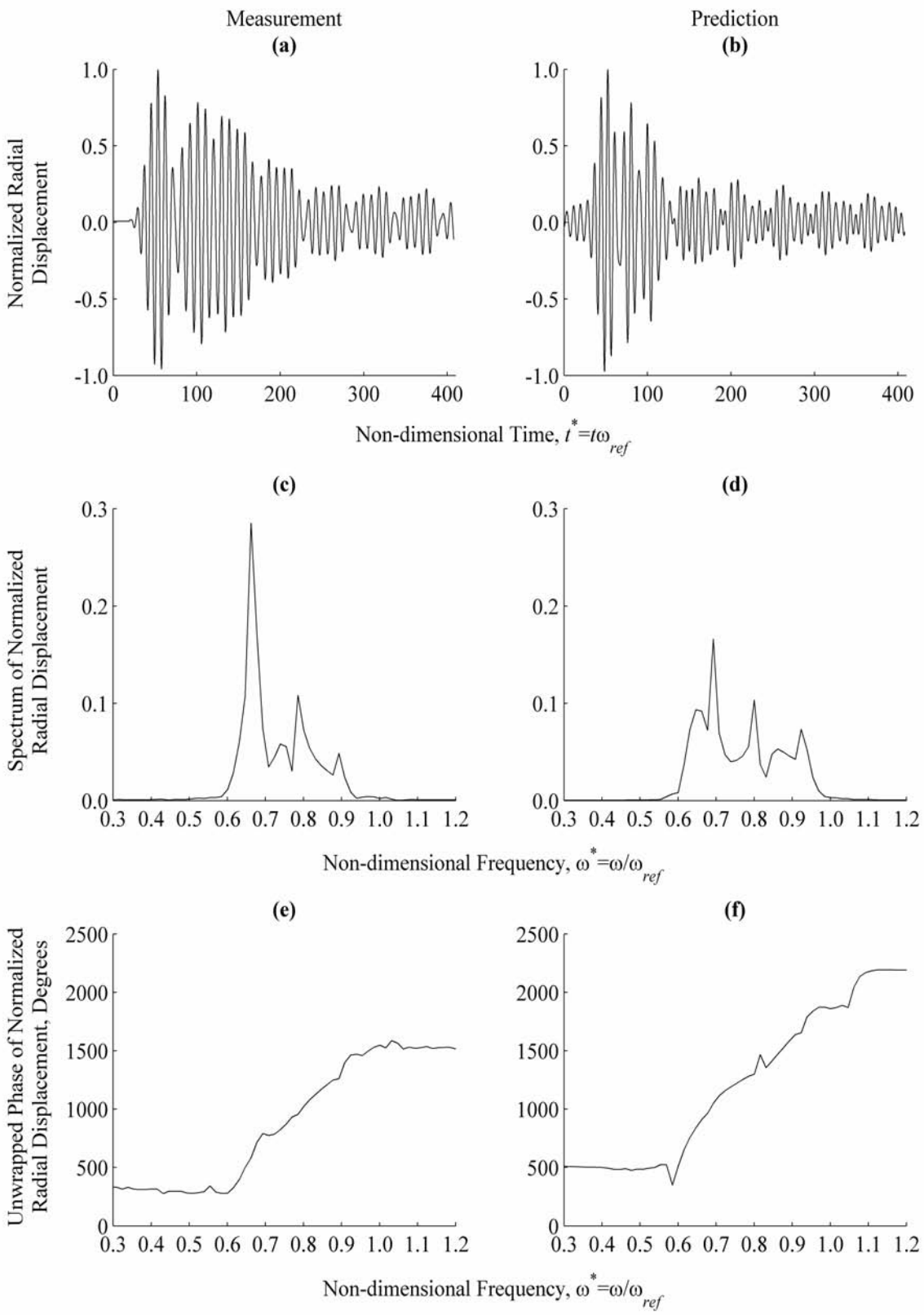

Figure H.62. Measurement and Prediction at $\theta=60^{\circ}$, $z^*=10.20$

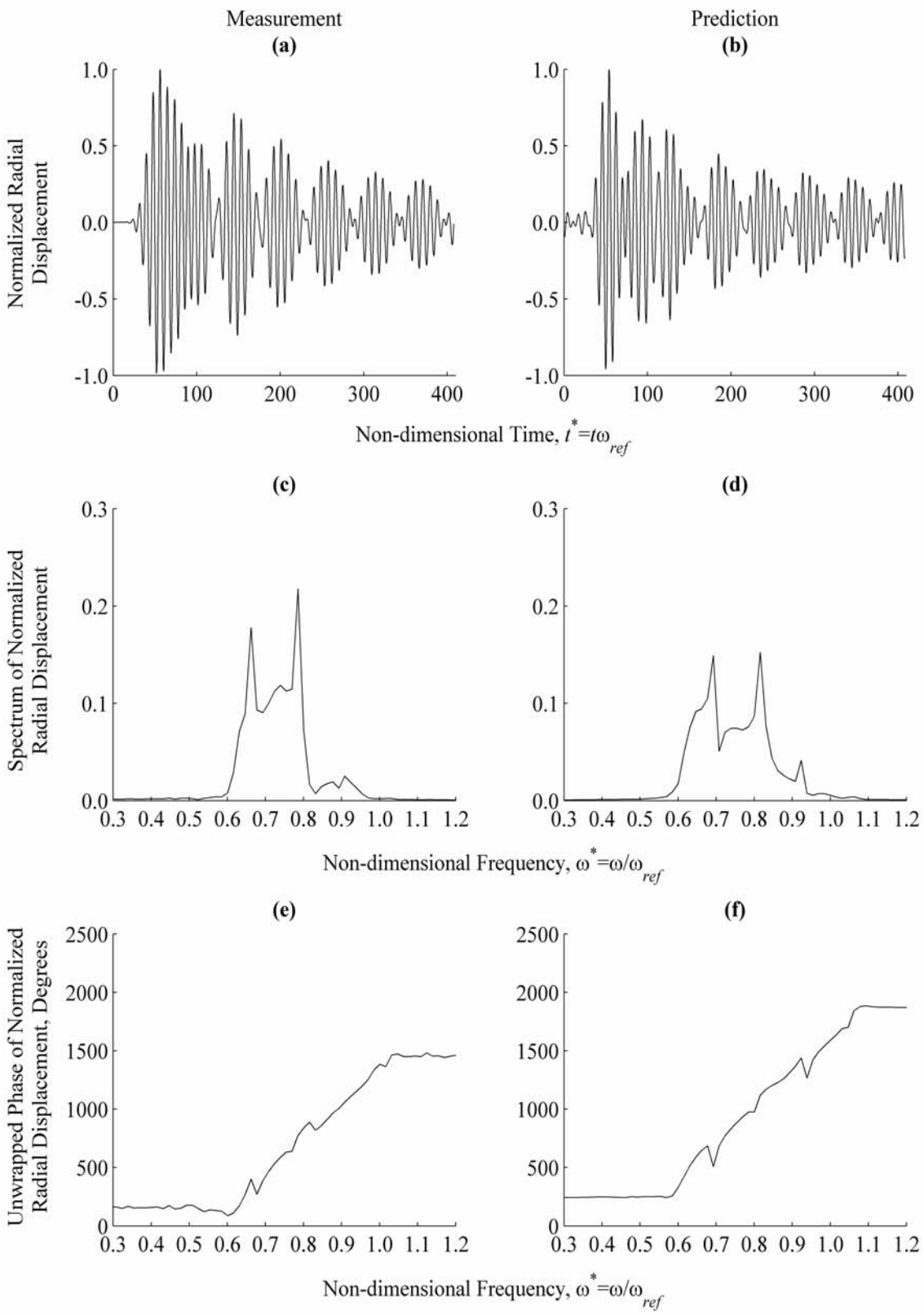

Figure H.63. Measurement and Prediction at $\theta=70^{\circ}$, $z^*=10.20$

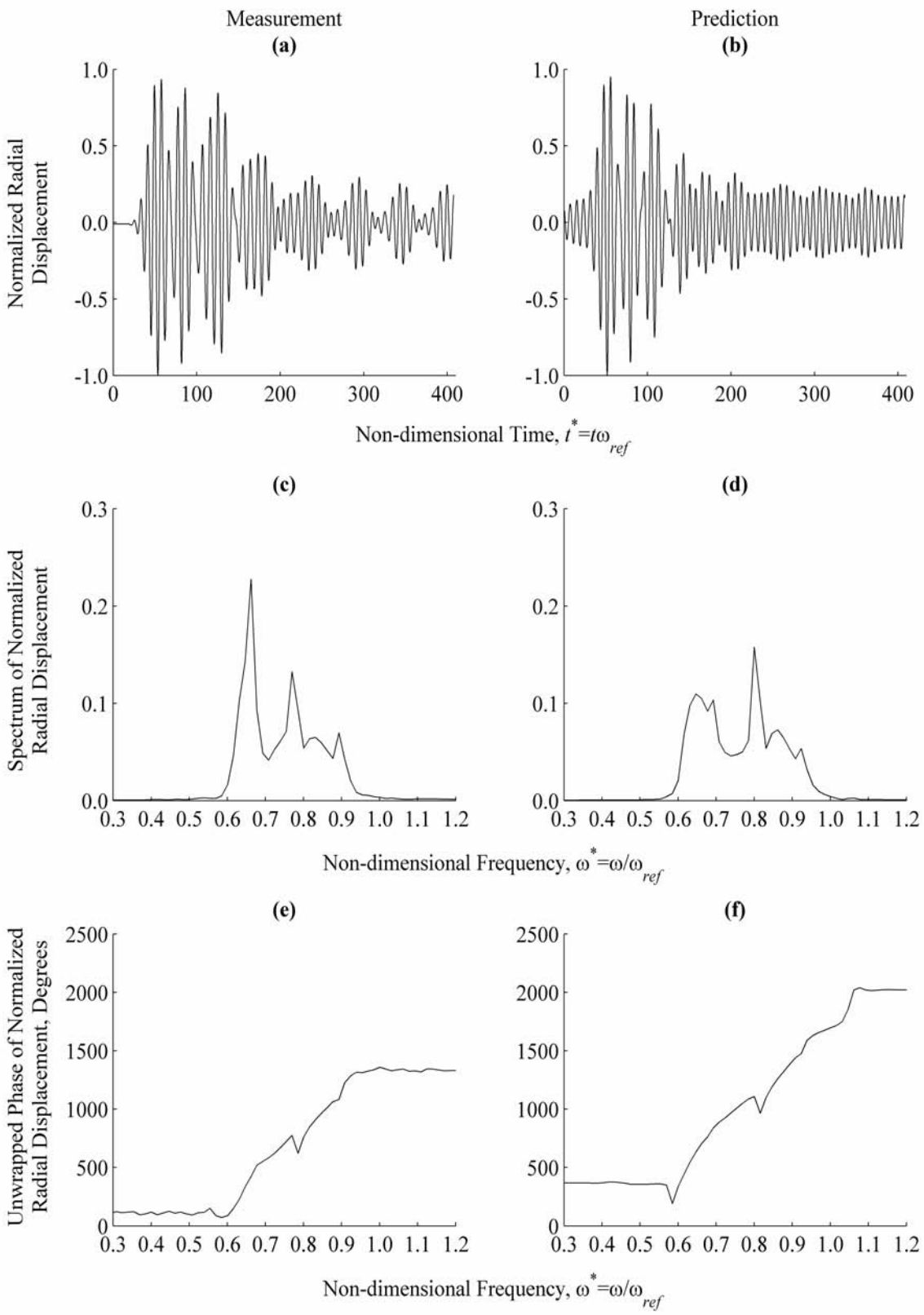

Figure H.64. Measurement and Prediction at $\theta=80^{\circ}$, $z^*=10.20$

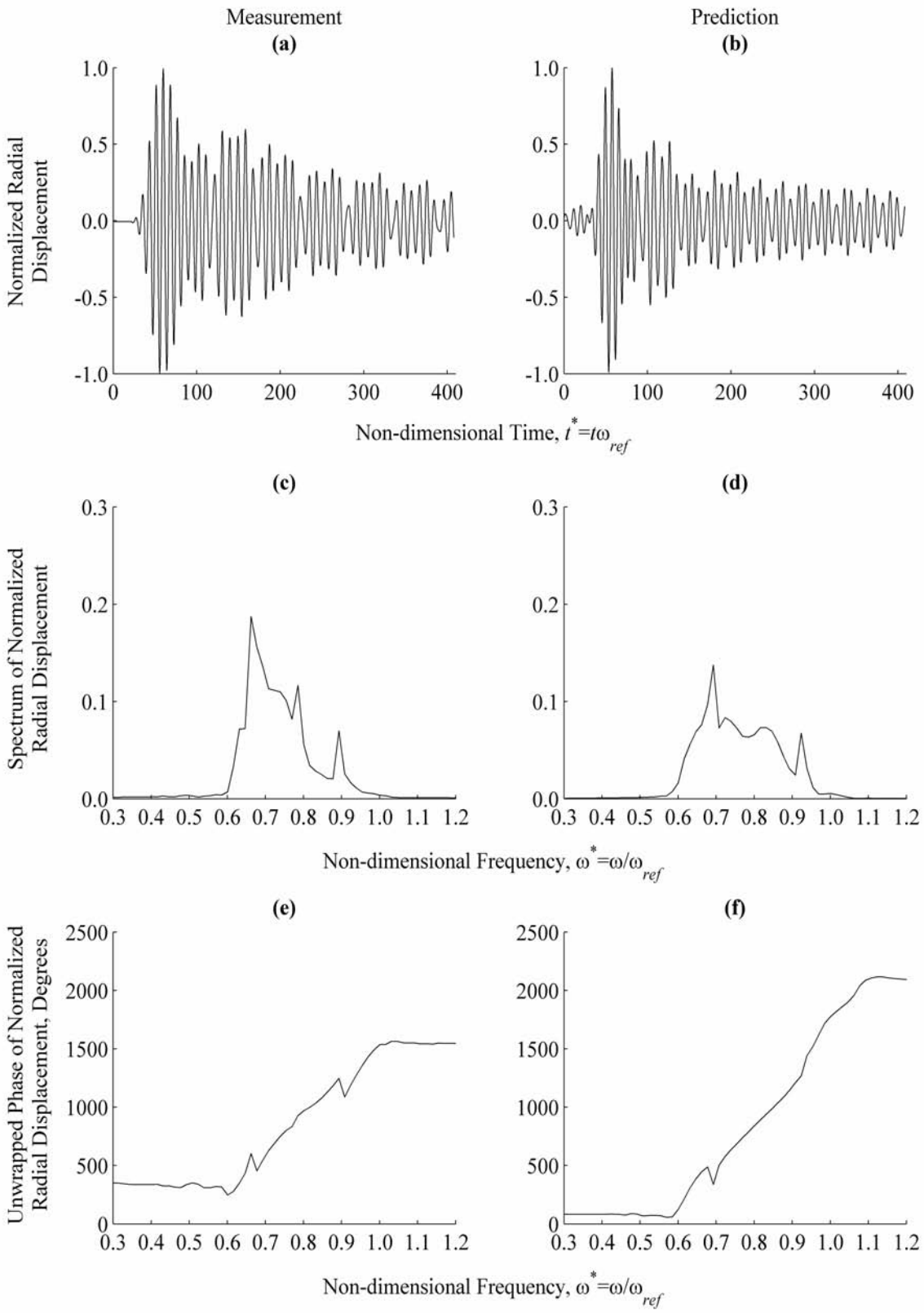

Figure H.65. Measurement and Prediction at $\theta=90^{\circ}$, $z^*=10.20$

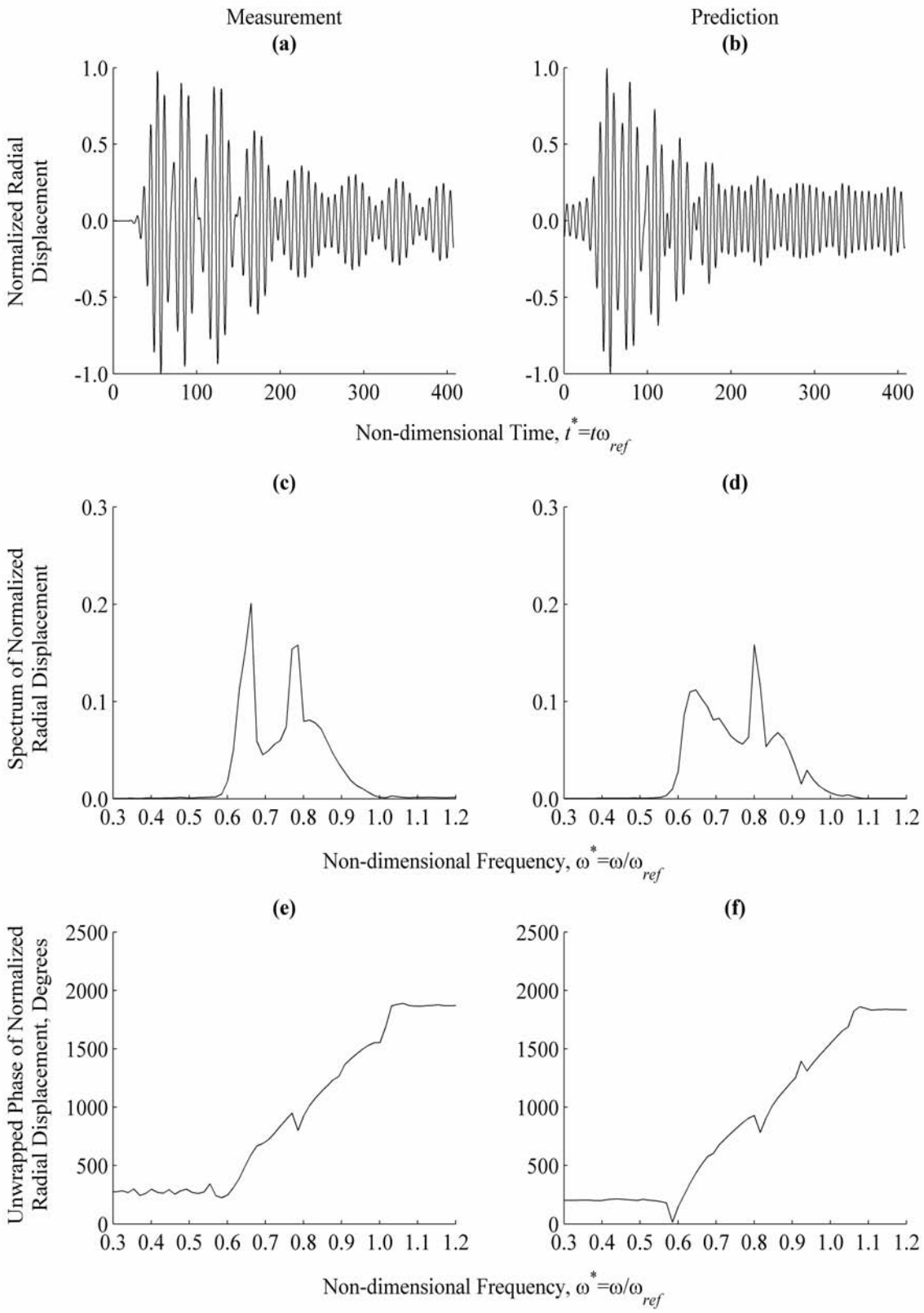

Figure H.66. Measurement and Prediction at $\theta=100^{\circ}$, $z^*=10.20$

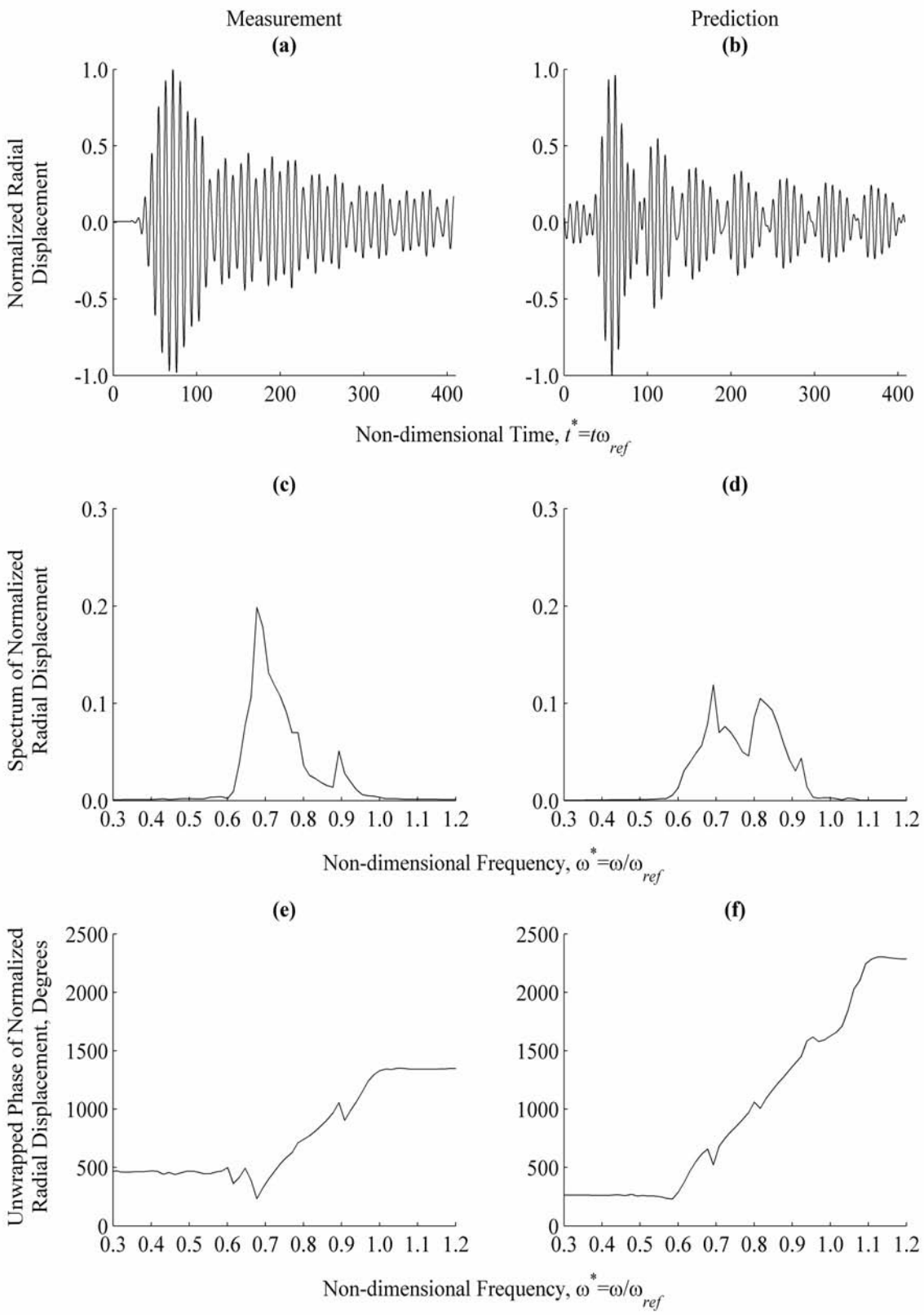

Figure H.67. Measurement and Prediction at $\theta=110^{\circ}$, $z^*=10.20$

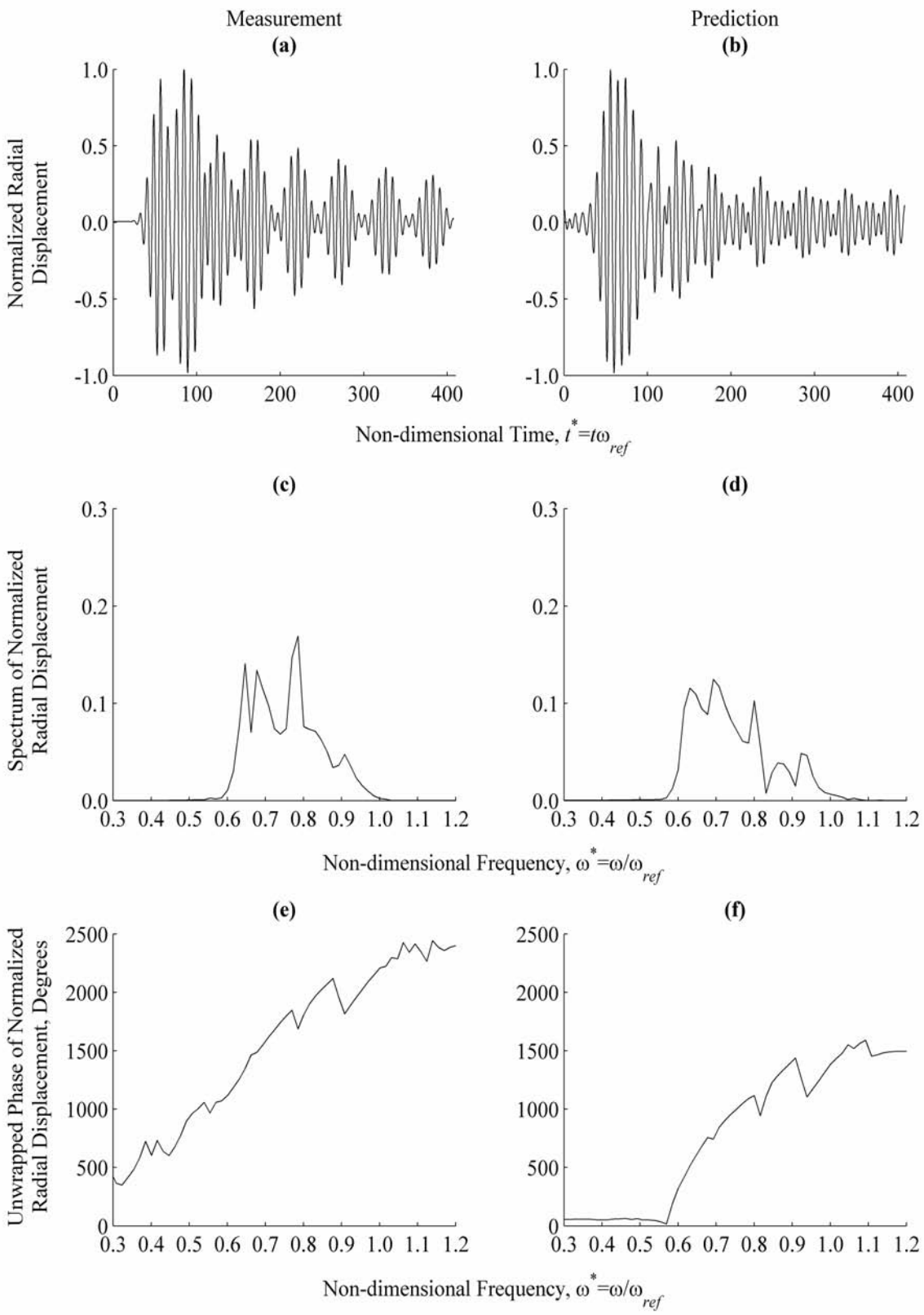

Figure H.68. Measurement and Prediction at $\theta=120^{\circ}$, $z^*=10.20$

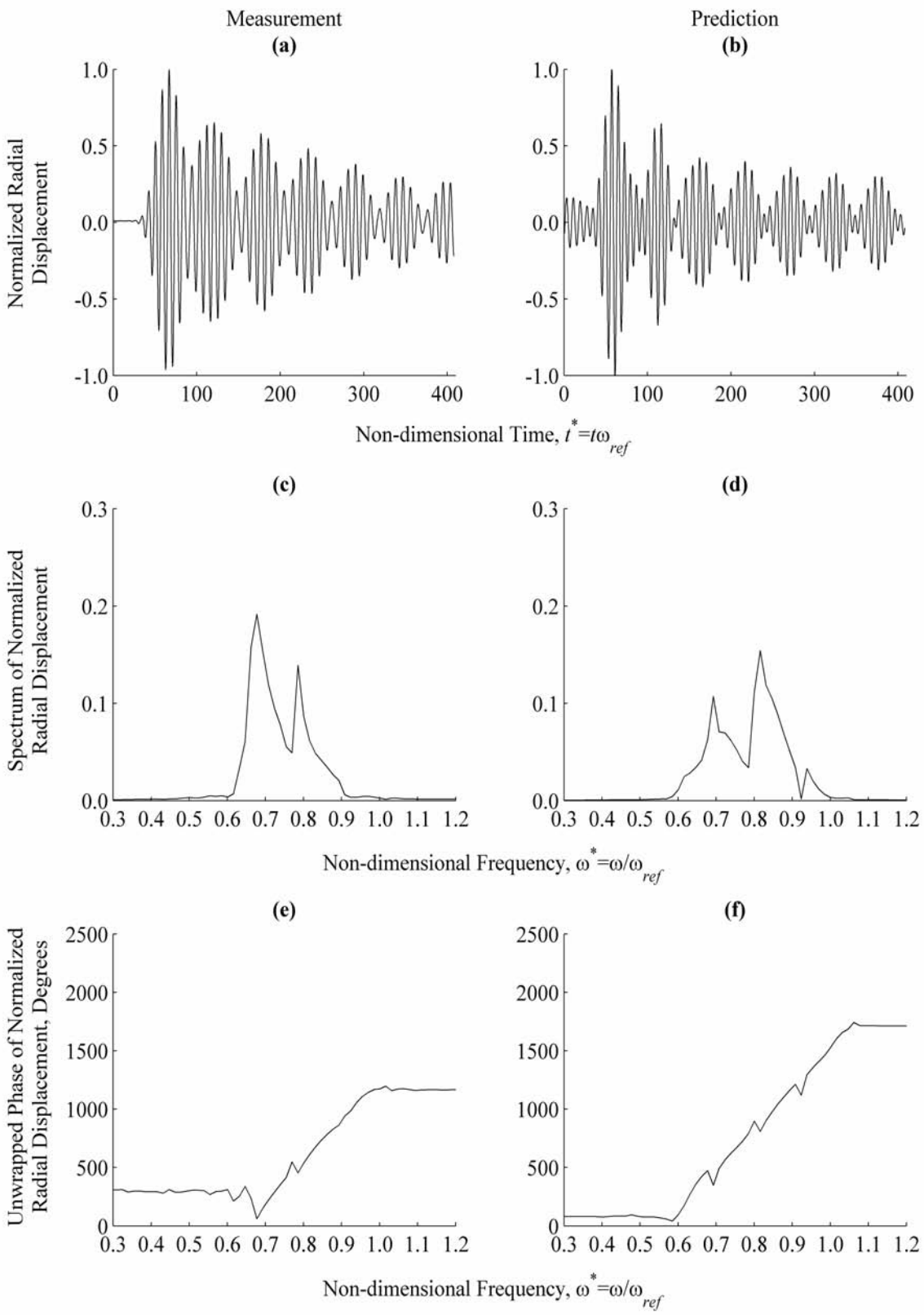

Figure H.69. Measurement and Prediction at $\theta=130^{\circ}$, $z^*=10.20$

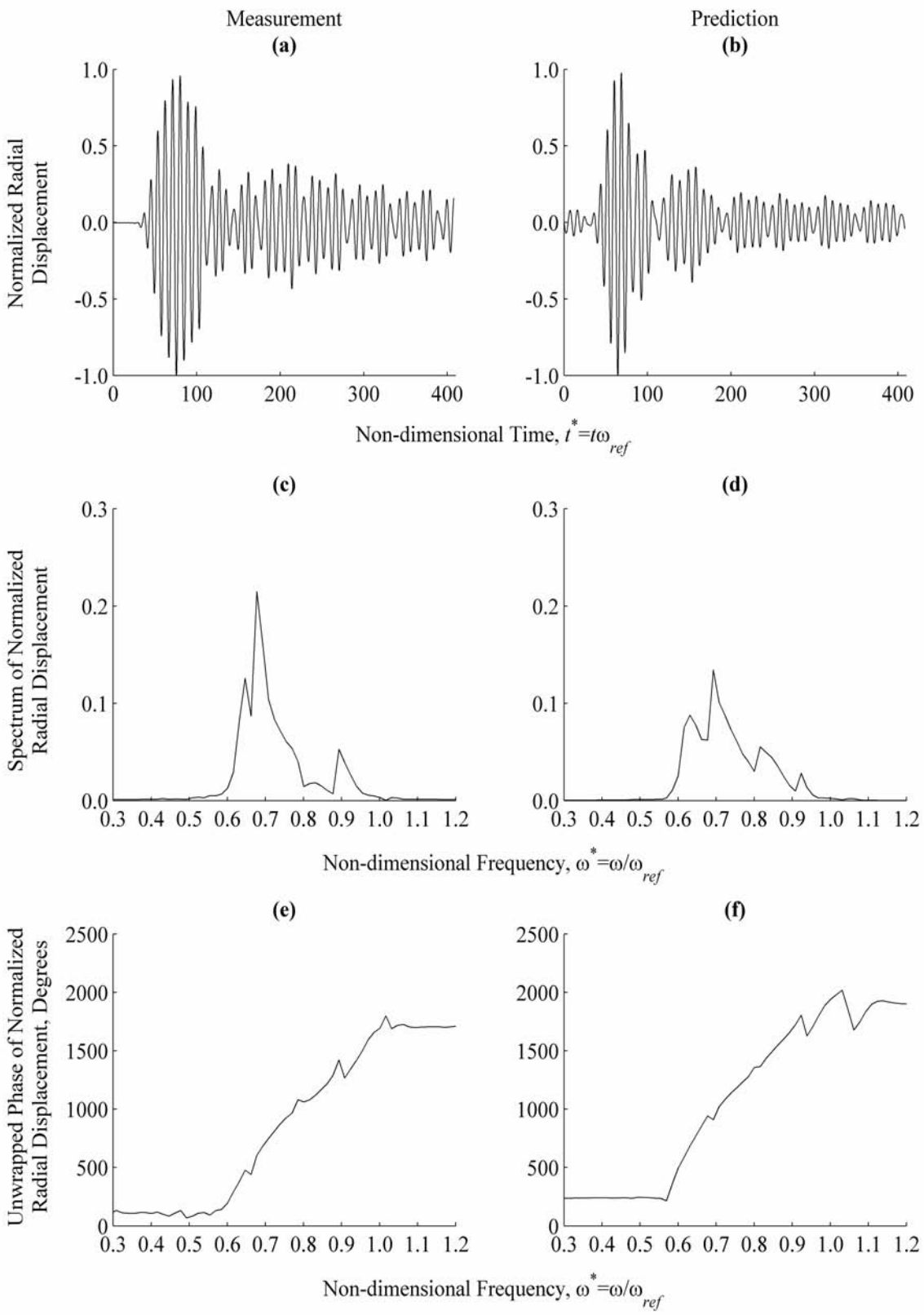

Figure H.70. Measurement and Prediction at $\theta=140^{\circ}$, $z^*=10.20$

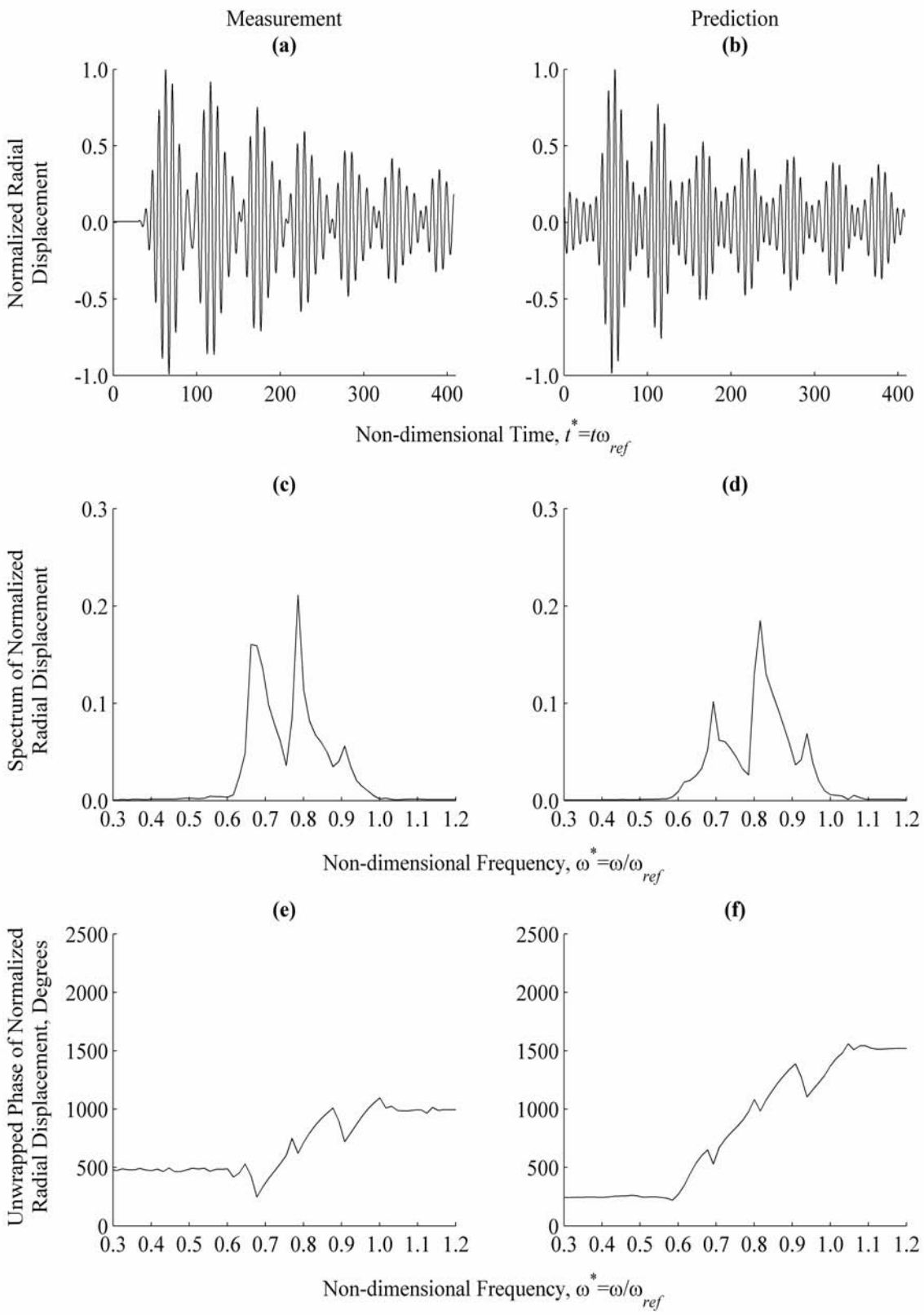

Figure H.71. Measurement and Prediction at $\theta=150^{\circ}$, $z^*=10.20$

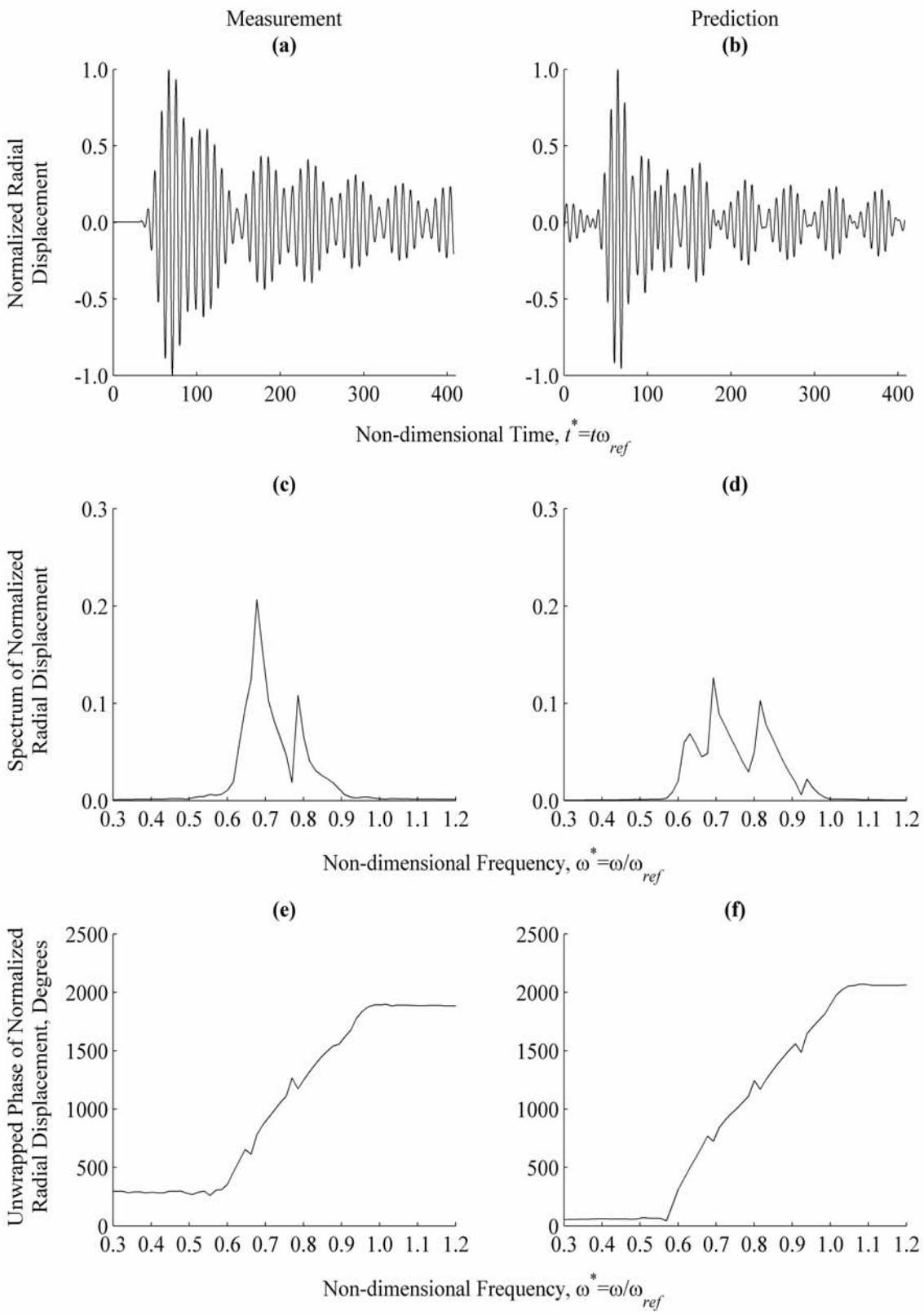

Figure H.72. Measurement and Prediction at $\theta=160^{\circ}$, $z^*=10.20$

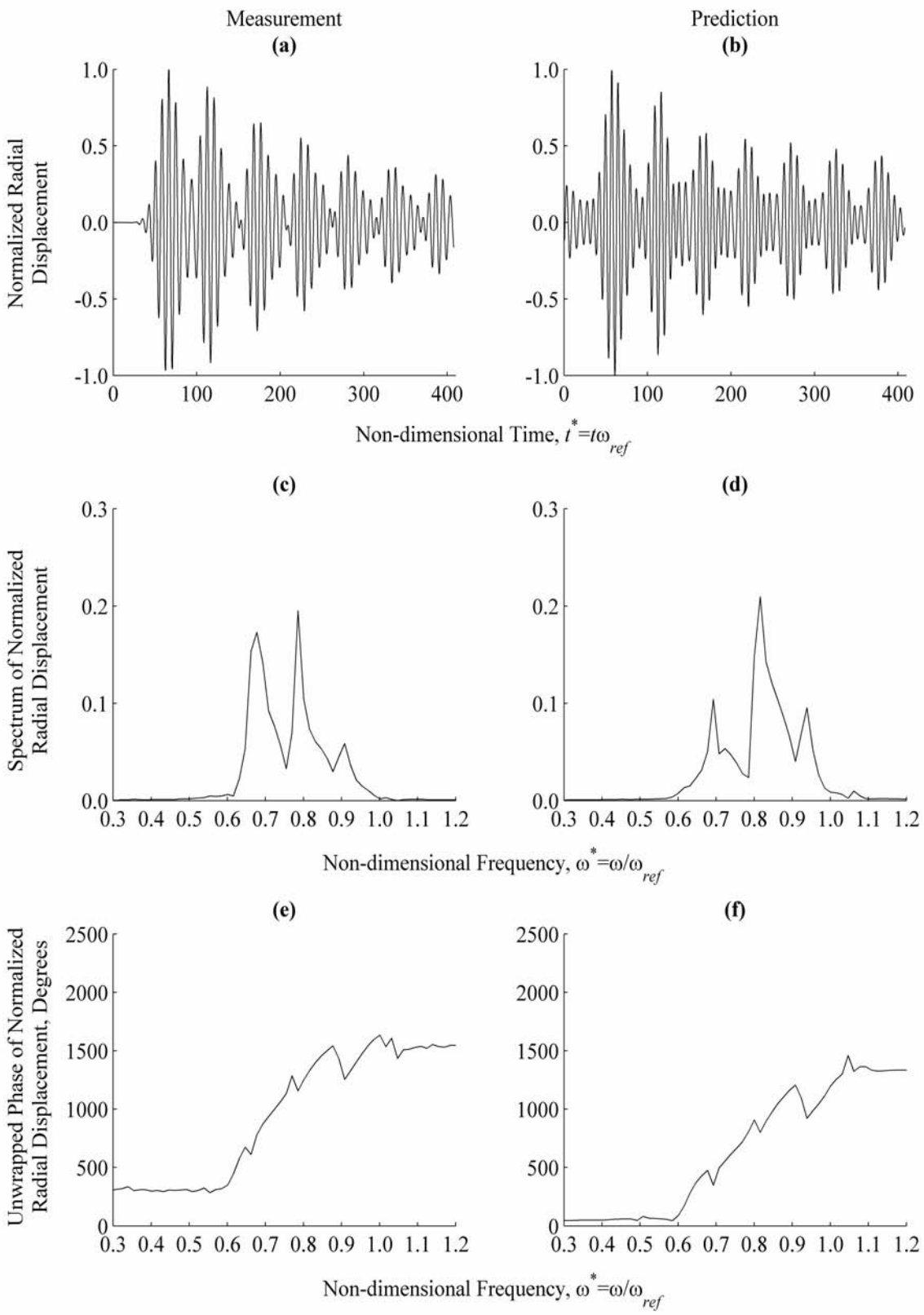

Figure H.73. Measurement and Prediction at $\theta=170^{\circ}$, $z^*=10.20$

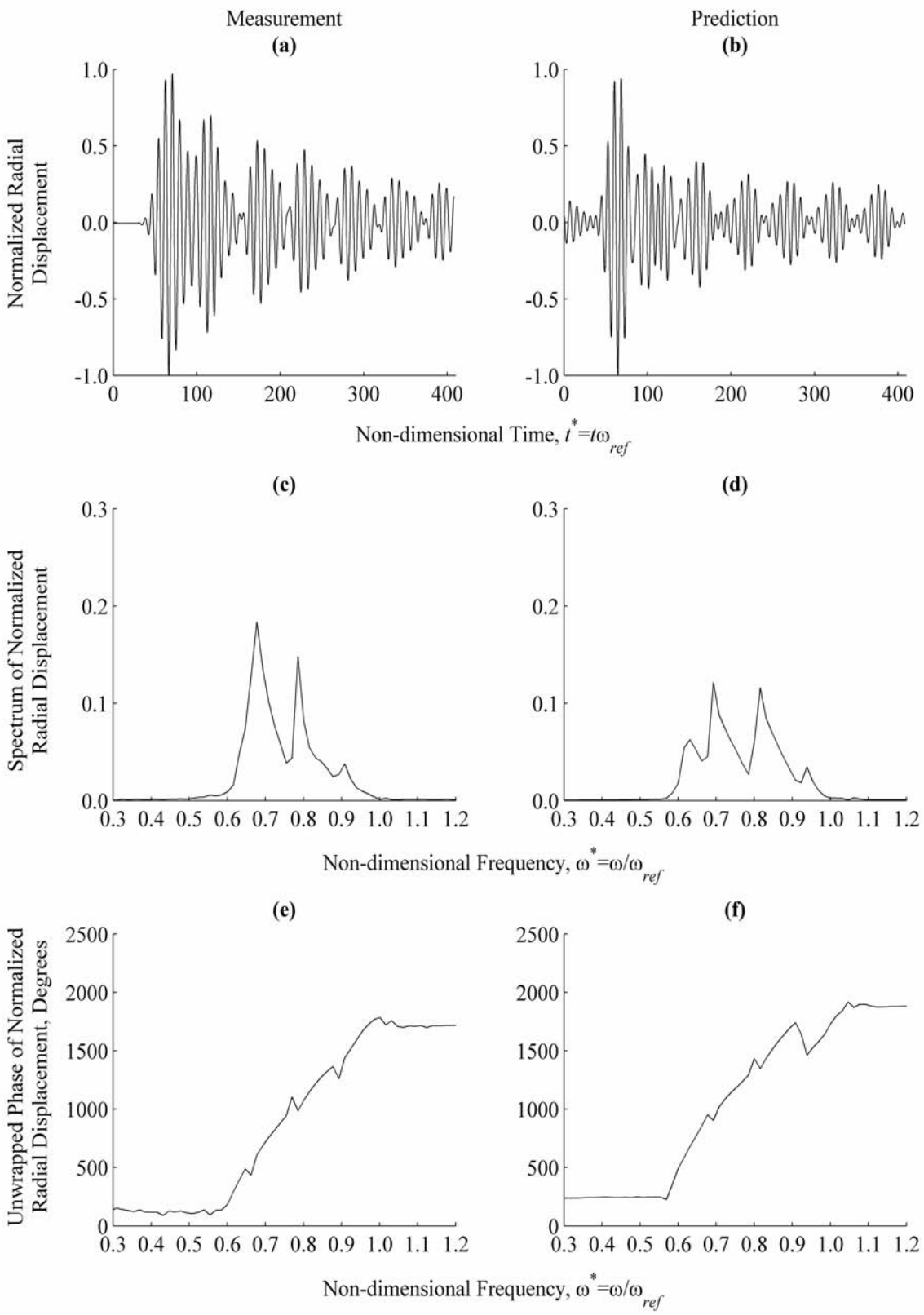

Figure H.74. Measurement and Prediction at $\theta=180^{\circ}$, $z^*=10.20$

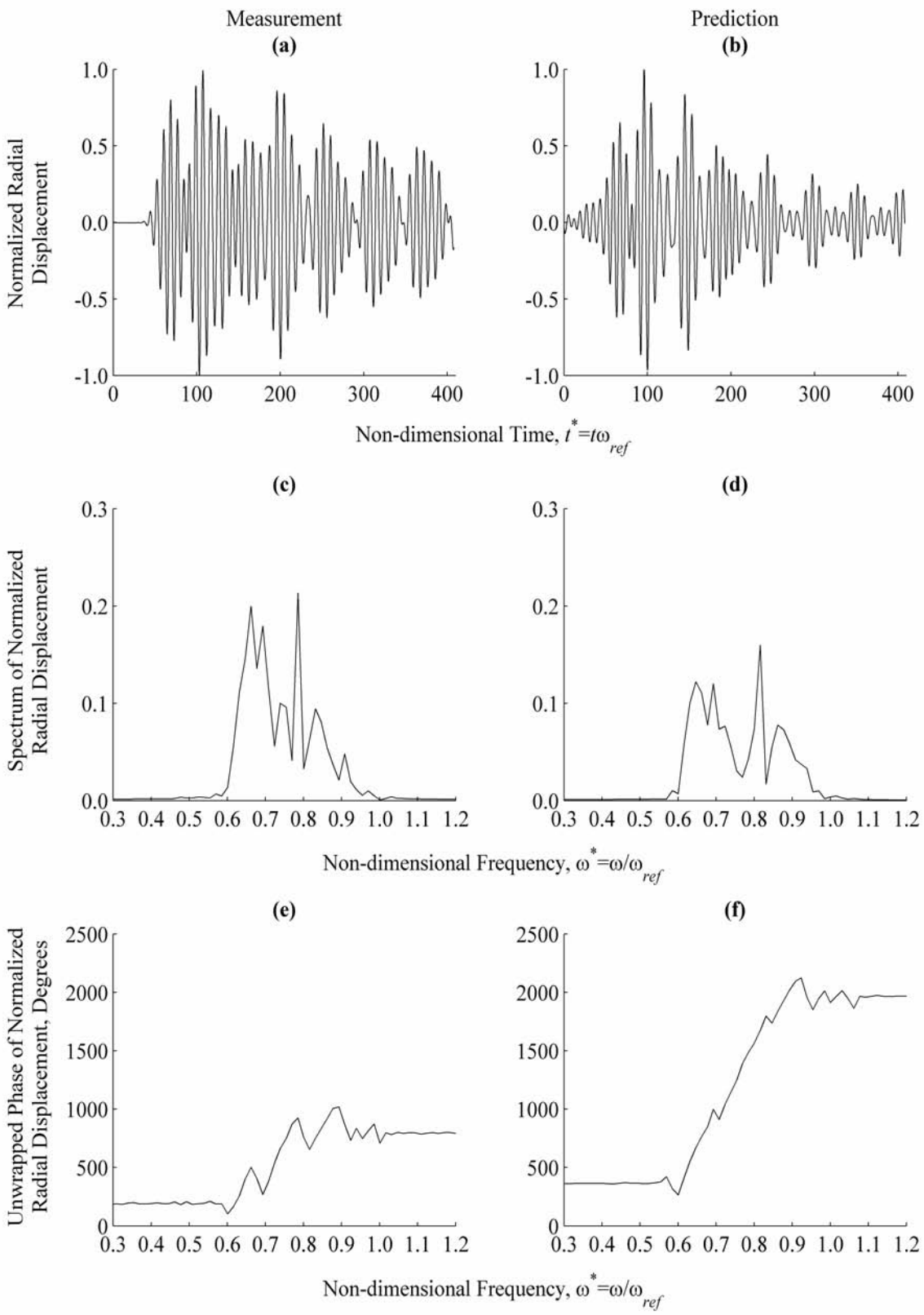

Figure H.75. Measurement and Prediction at $\theta=0^{\circ}$, $z^*=25.50$

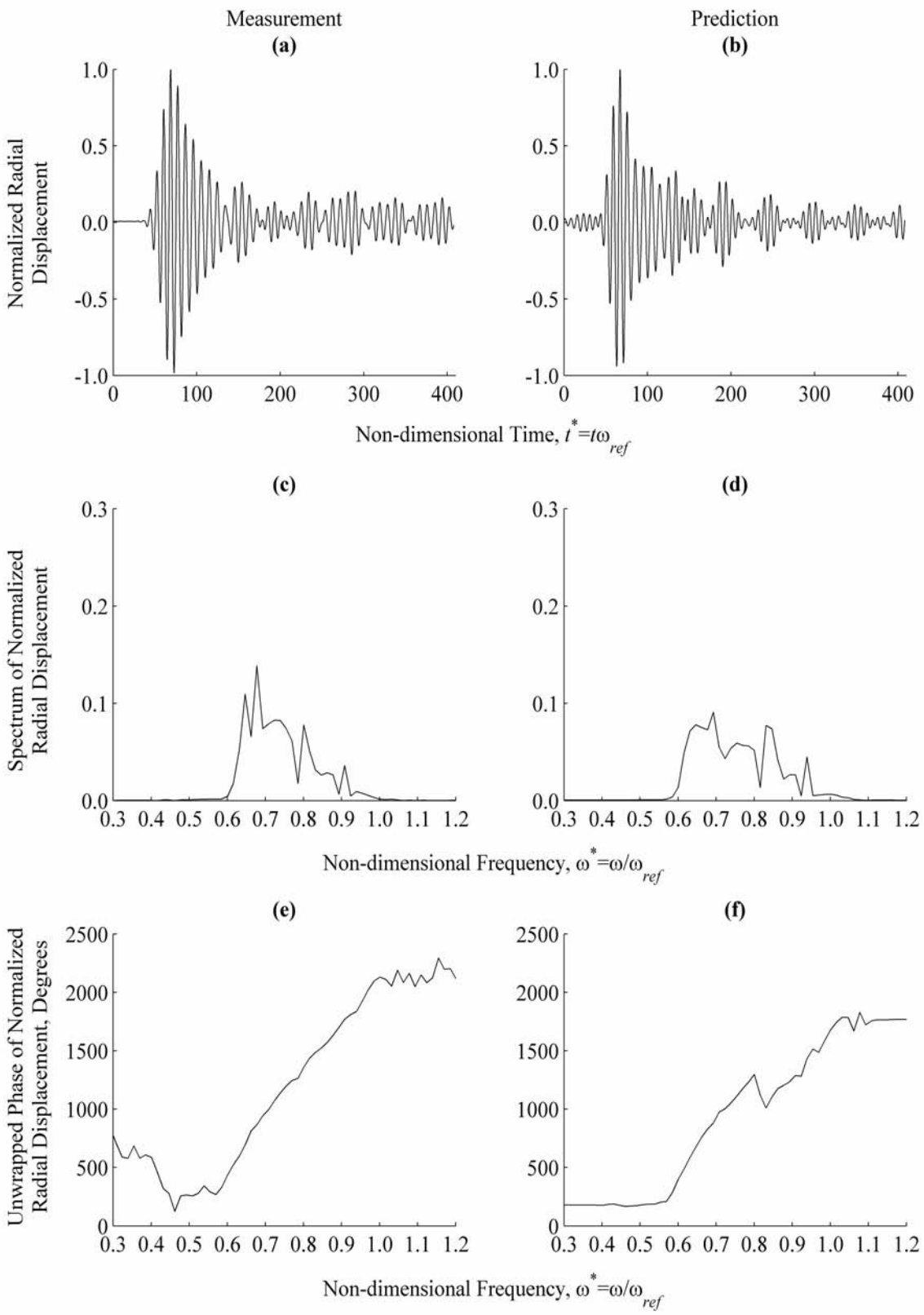

Figure H.76. Measurement and Prediction at $\theta=10^{\circ}$, $z^*=25.50$

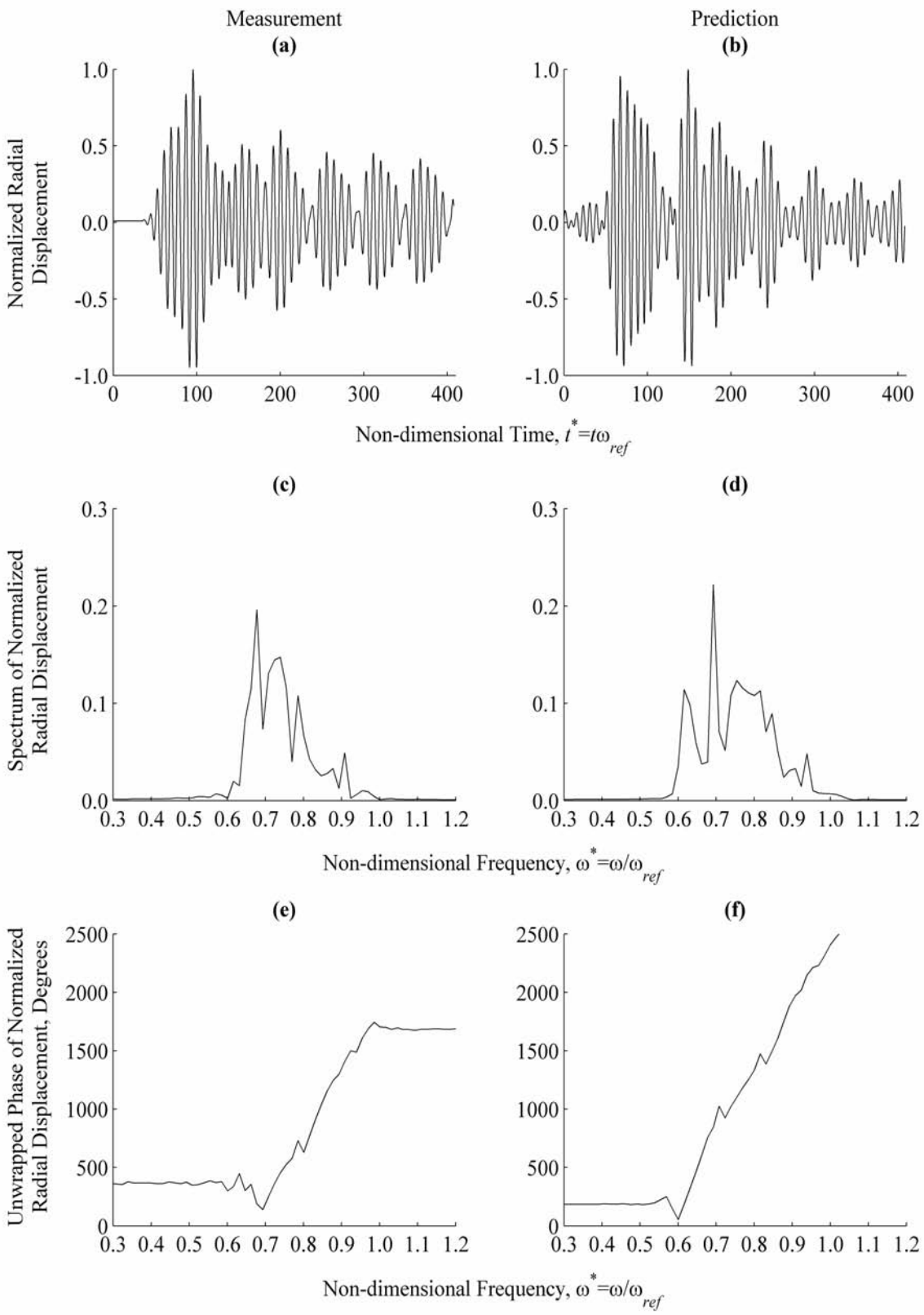

Figure H.77. Measurement and Prediction at $\theta=20^{\circ}$, $z^*=25.50$

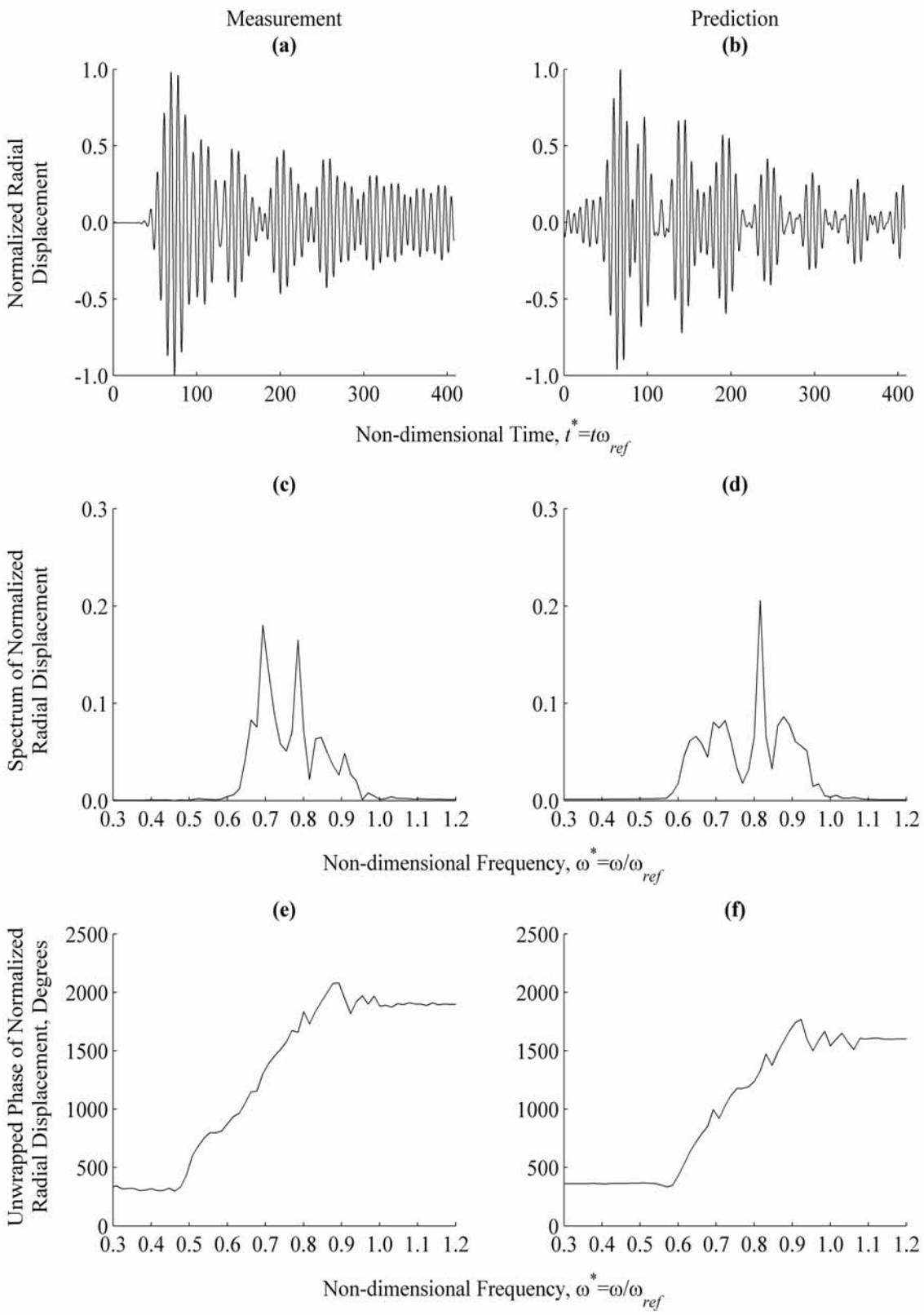

Figure H.78. Measurement and Prediction at $\theta=30^{\circ}$, $z^*=25.50$

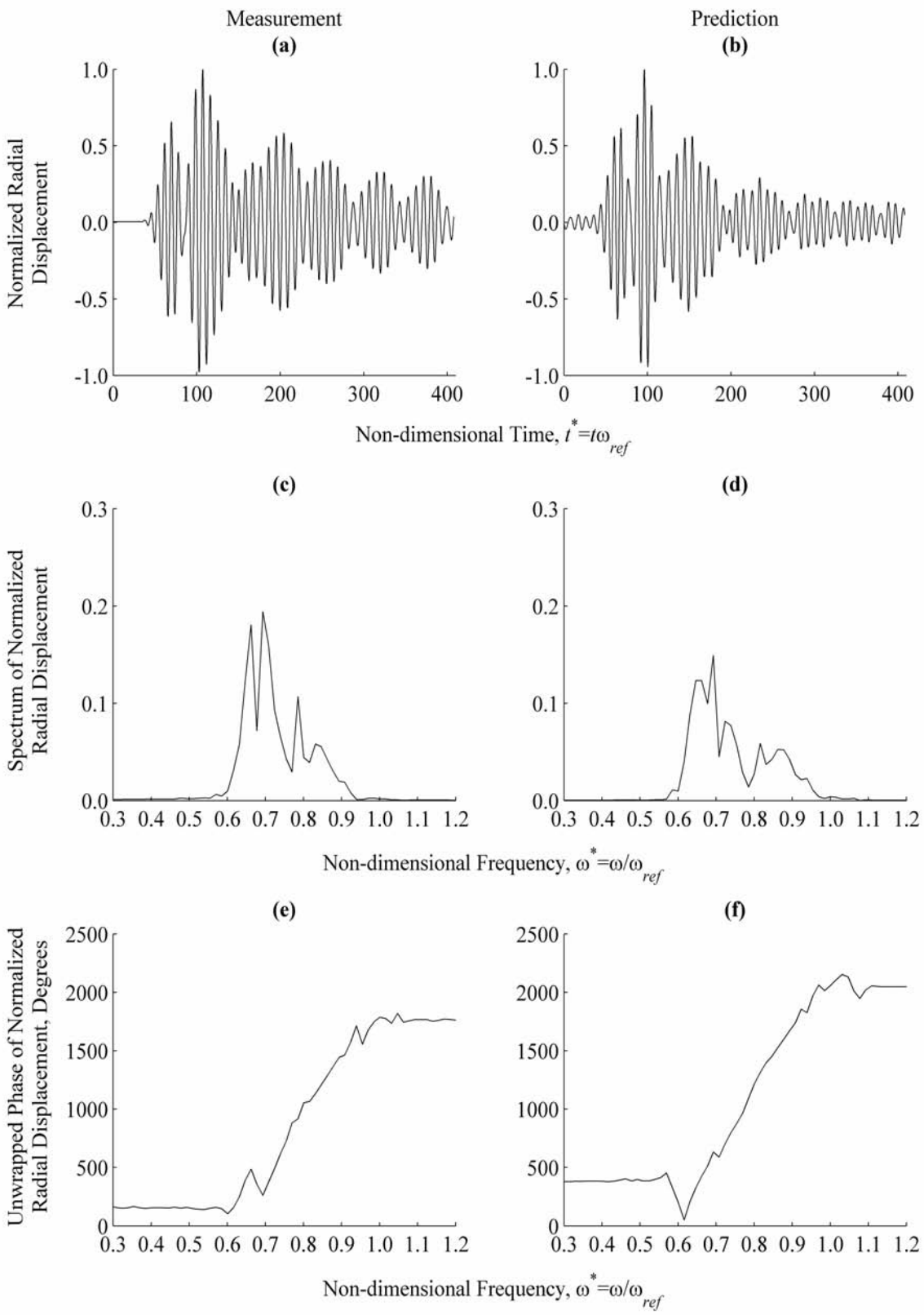

Figure H.79. Measurement and Prediction at $\theta=40^{\circ}$, $z^*=25.50$

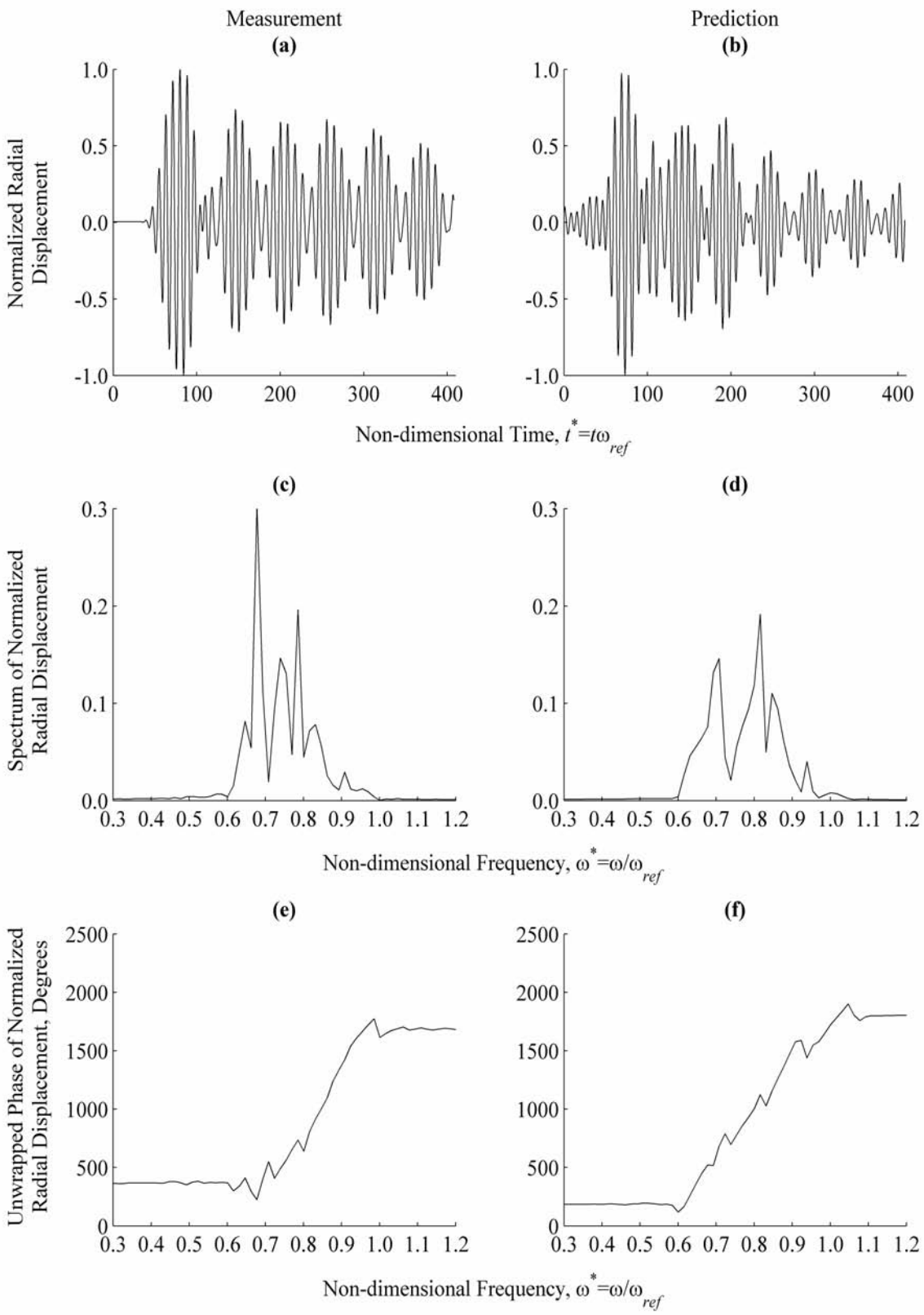

Figure H.80. Measurement and Prediction at $\theta=50^{\circ}$, $z^*=25.50$

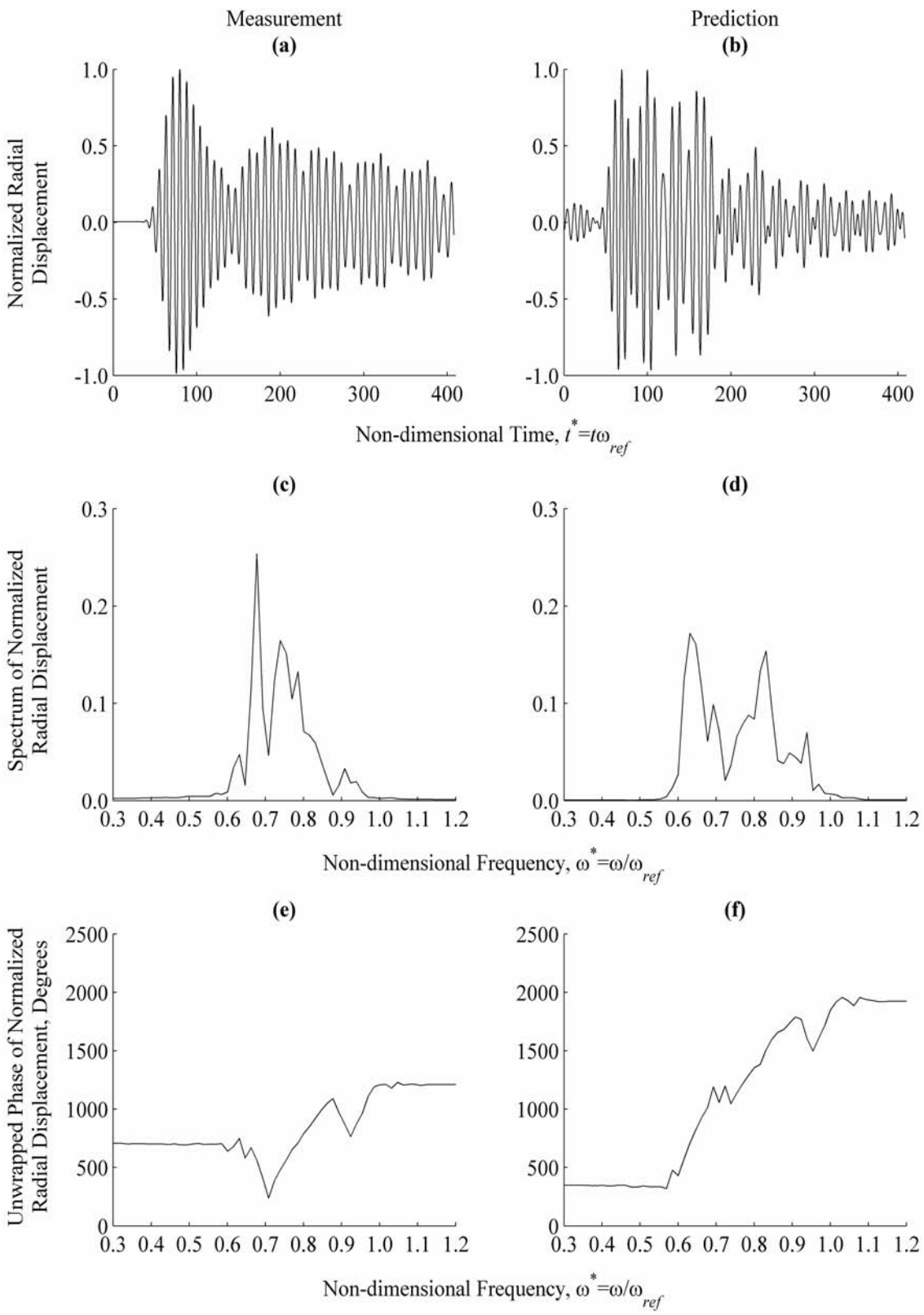

Figure H.81. Measurement and Prediction at $\theta=60^{\circ}$, $z^*=25.50$

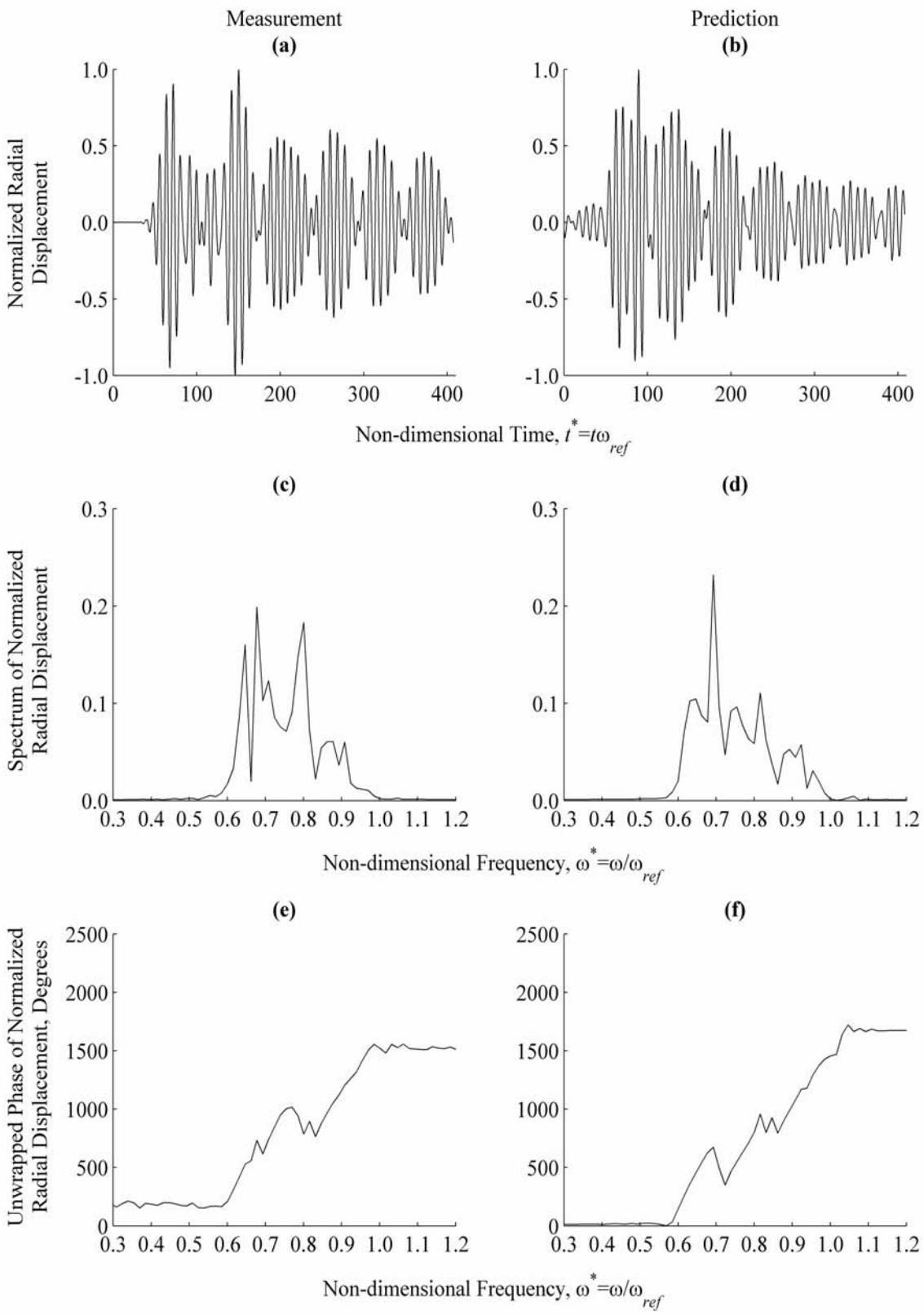

Figure H.82. Measurement and Prediction at $\theta=70^{\circ}$, $z^*=25.50$

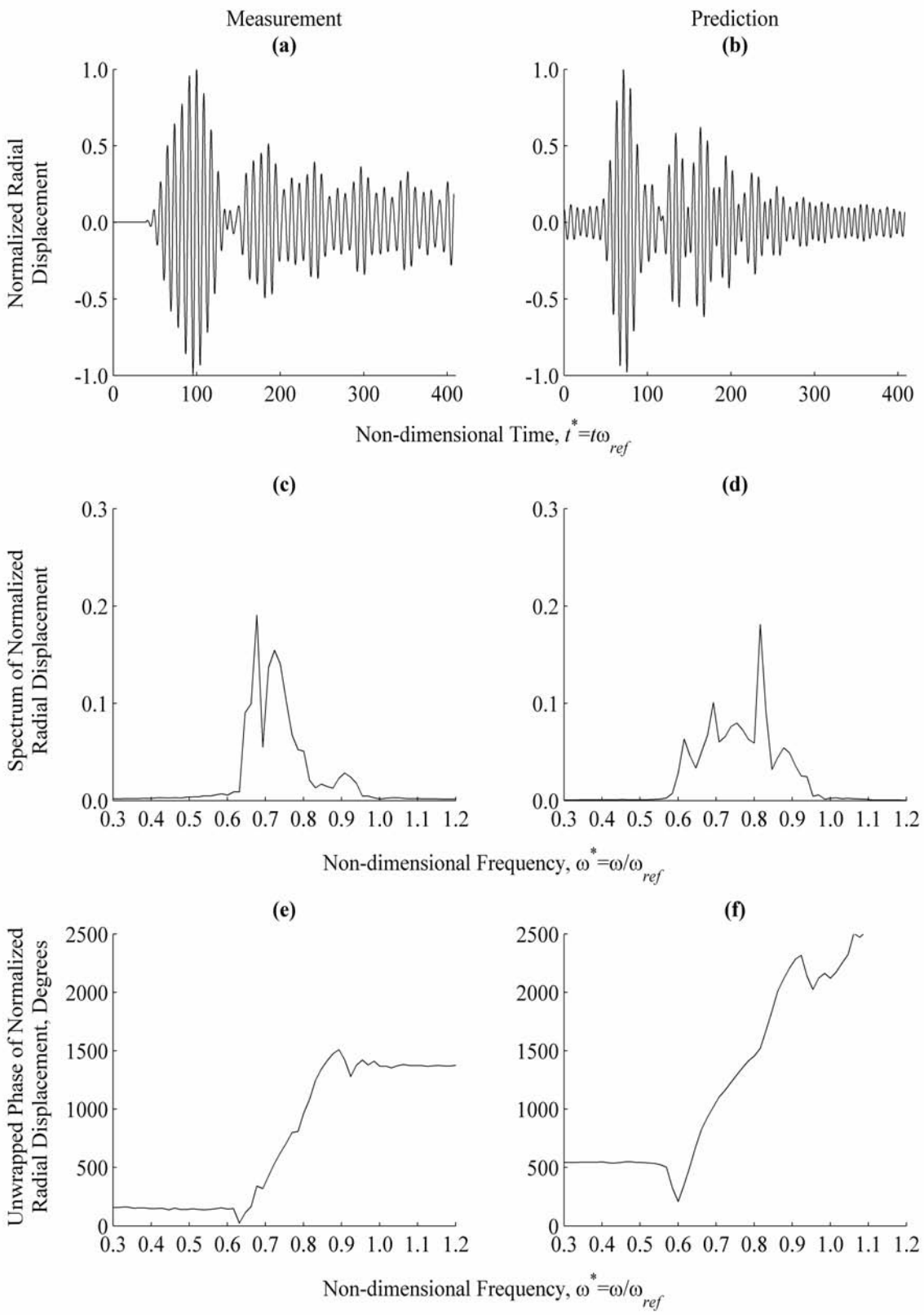

Figure H.83. Measurement and Prediction at $\theta=80^{\circ}$, $z^*=25.50$

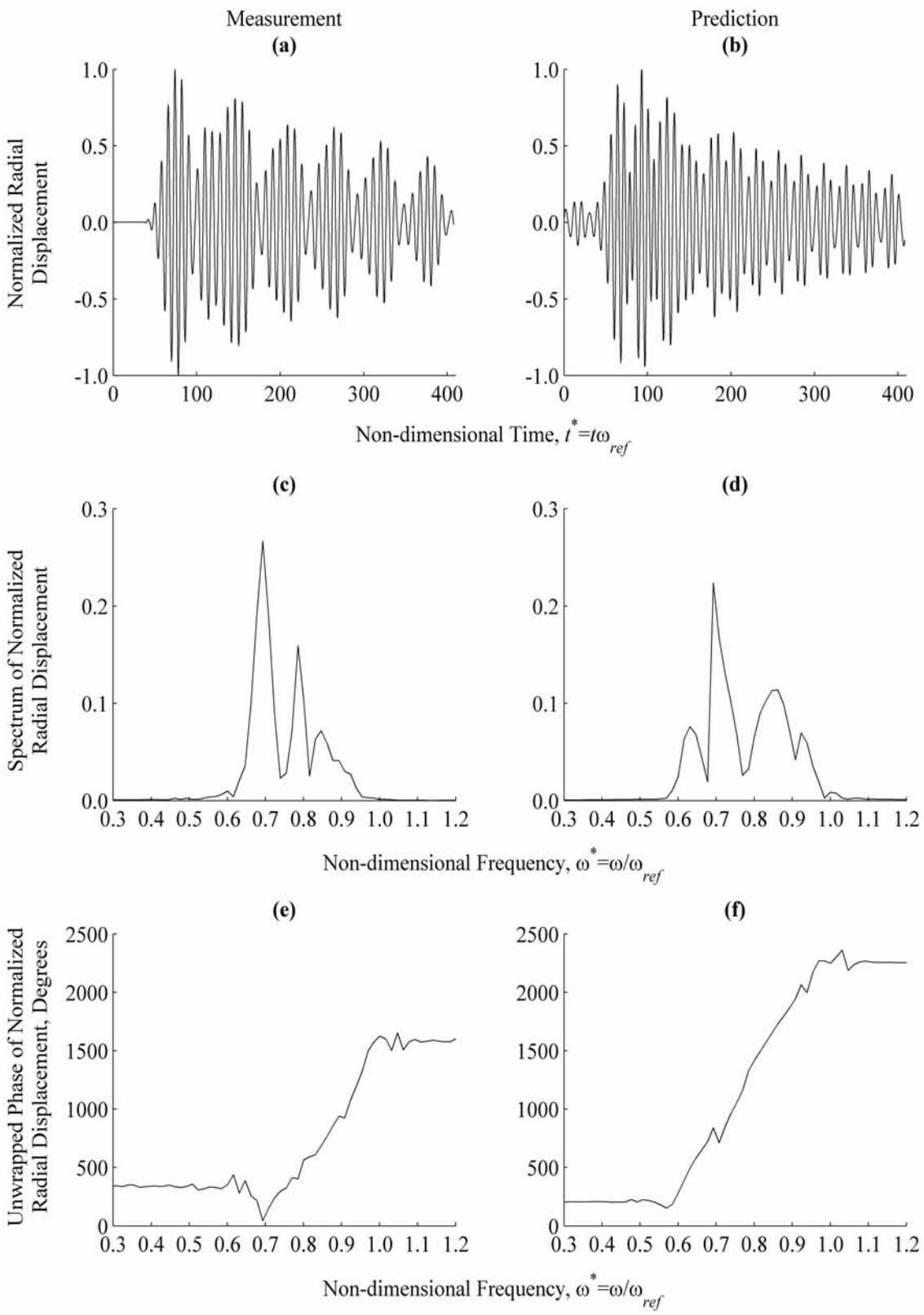

Figure H.84. Measurement and Prediction at $\theta=90^{\circ}$, $z^*=25.50$

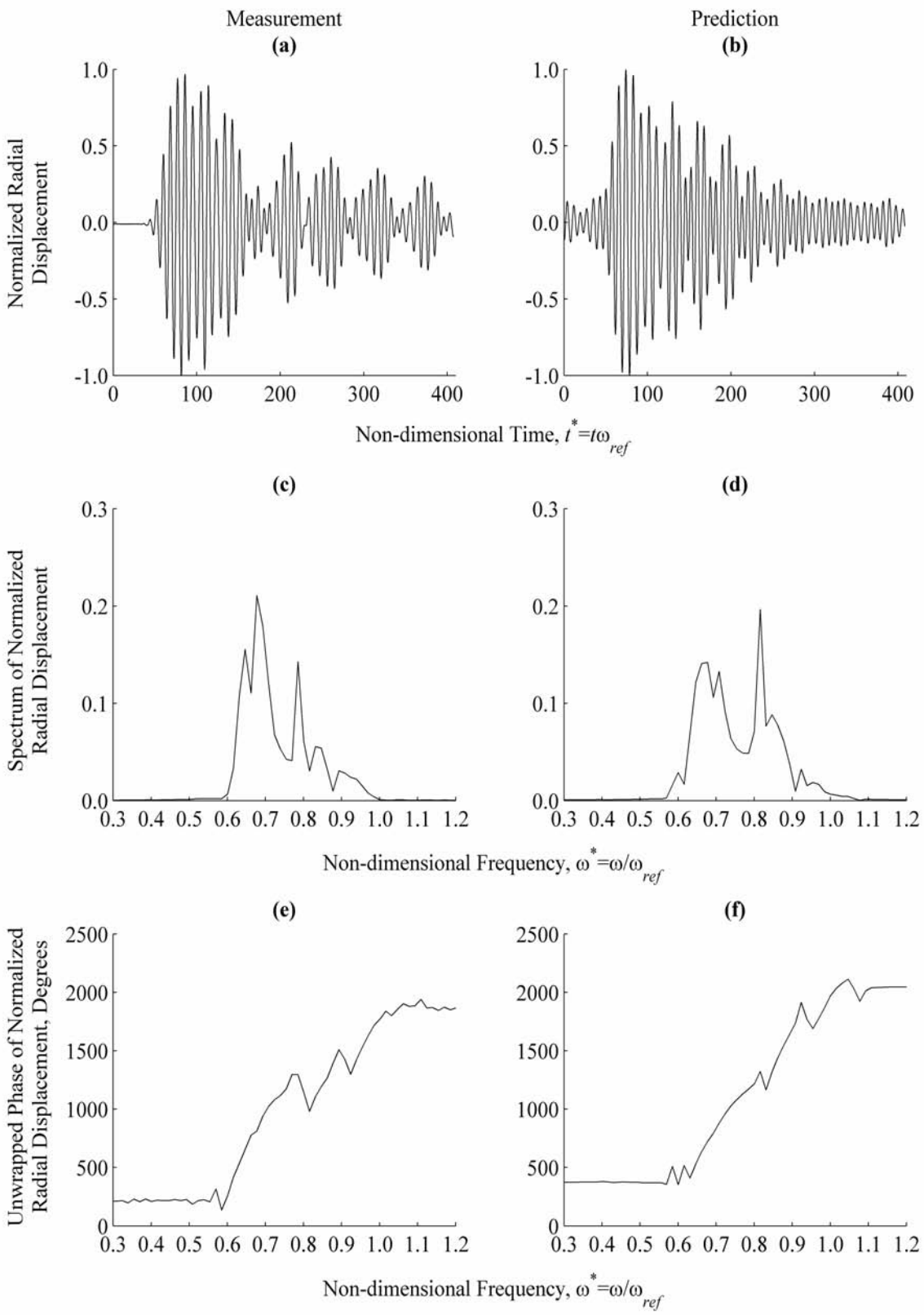

Figure H.85. Measurement and Prediction at $\theta=100^{\circ}$, $z^*=25.50$

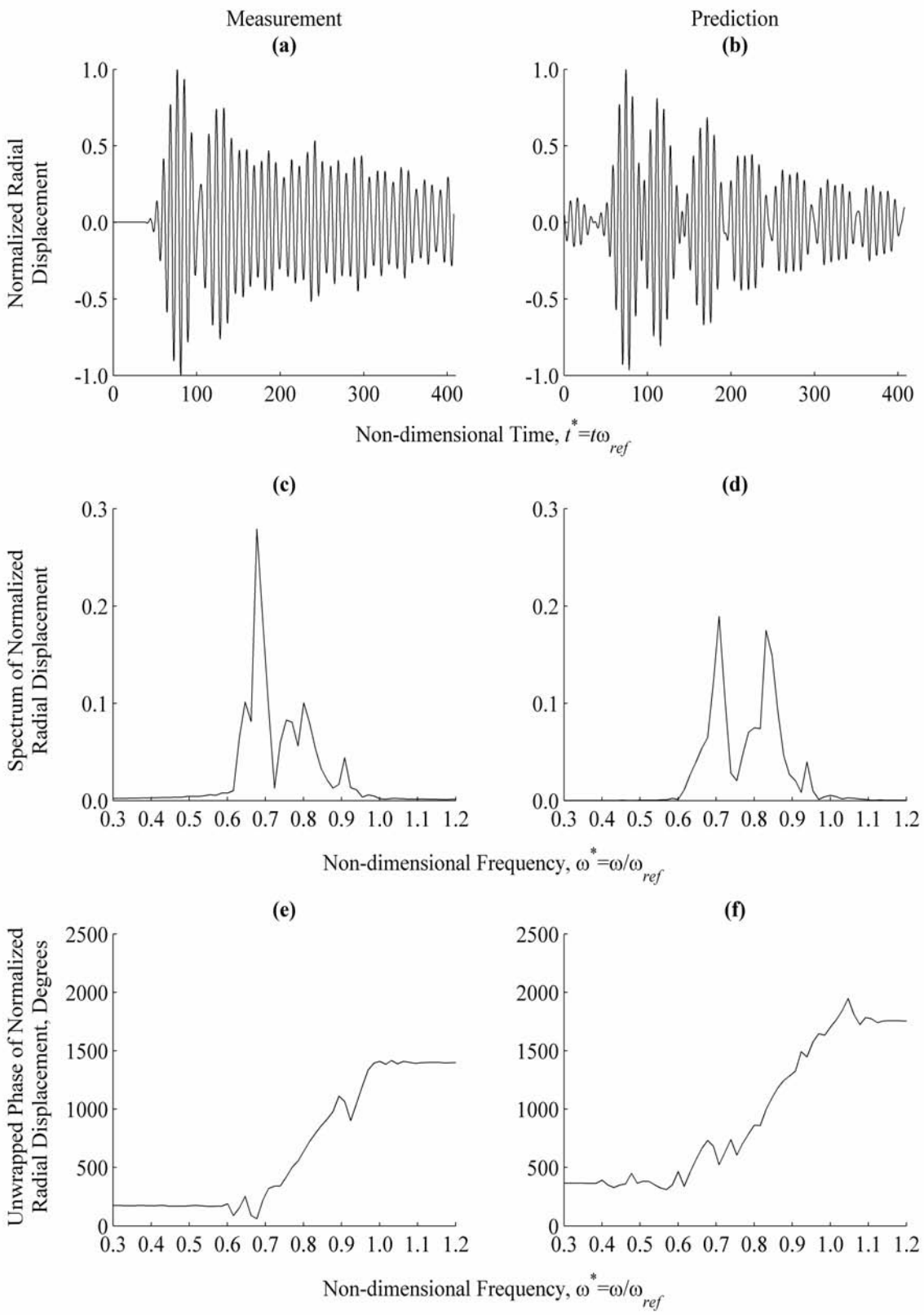

Figure H.86. Measurement and Prediction at $\theta=110^{\circ}$, $z^*=25.50$

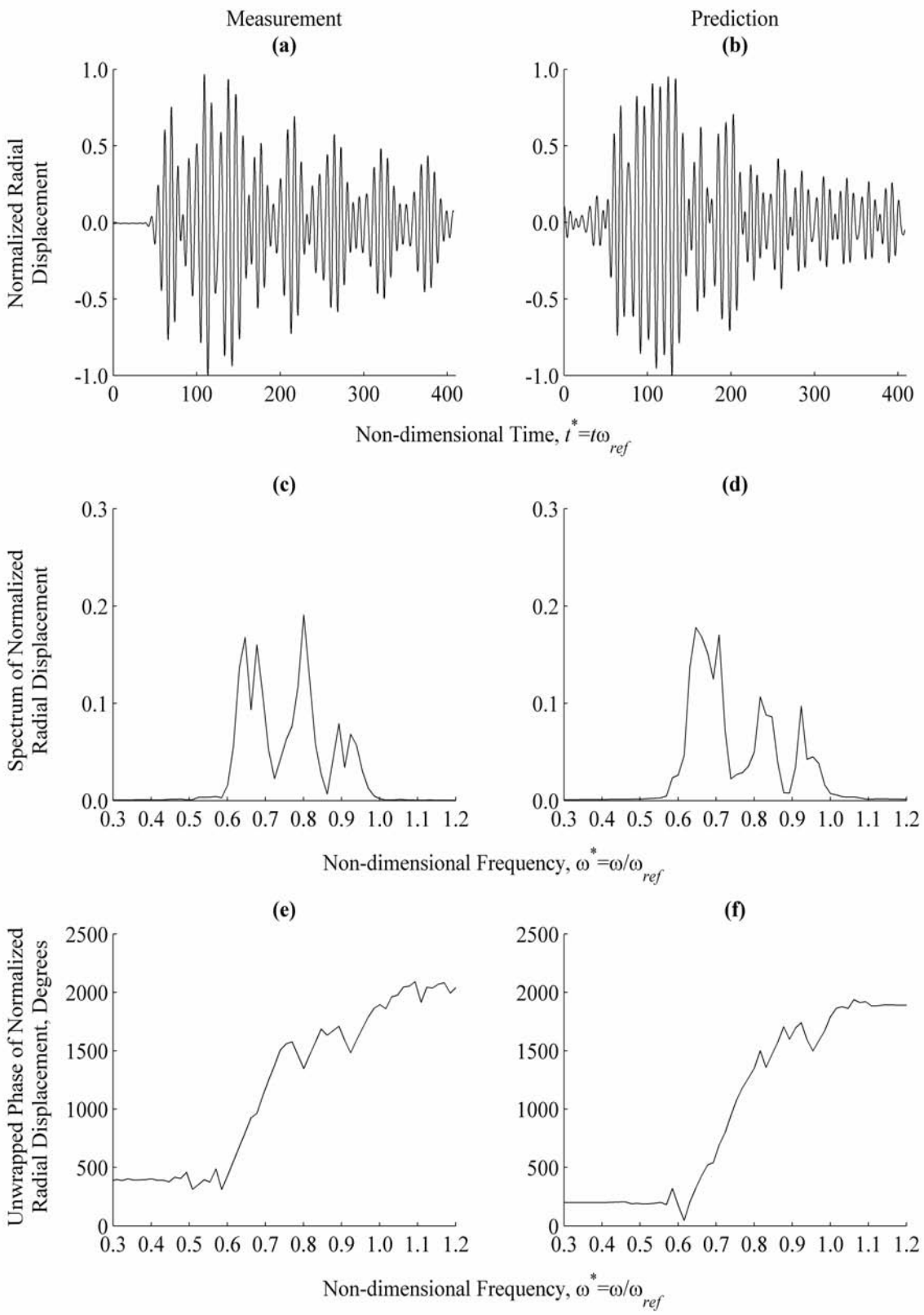

Figure H.87. Measurement and Prediction at $\theta=120^{\circ}$, $z^*=25.50$

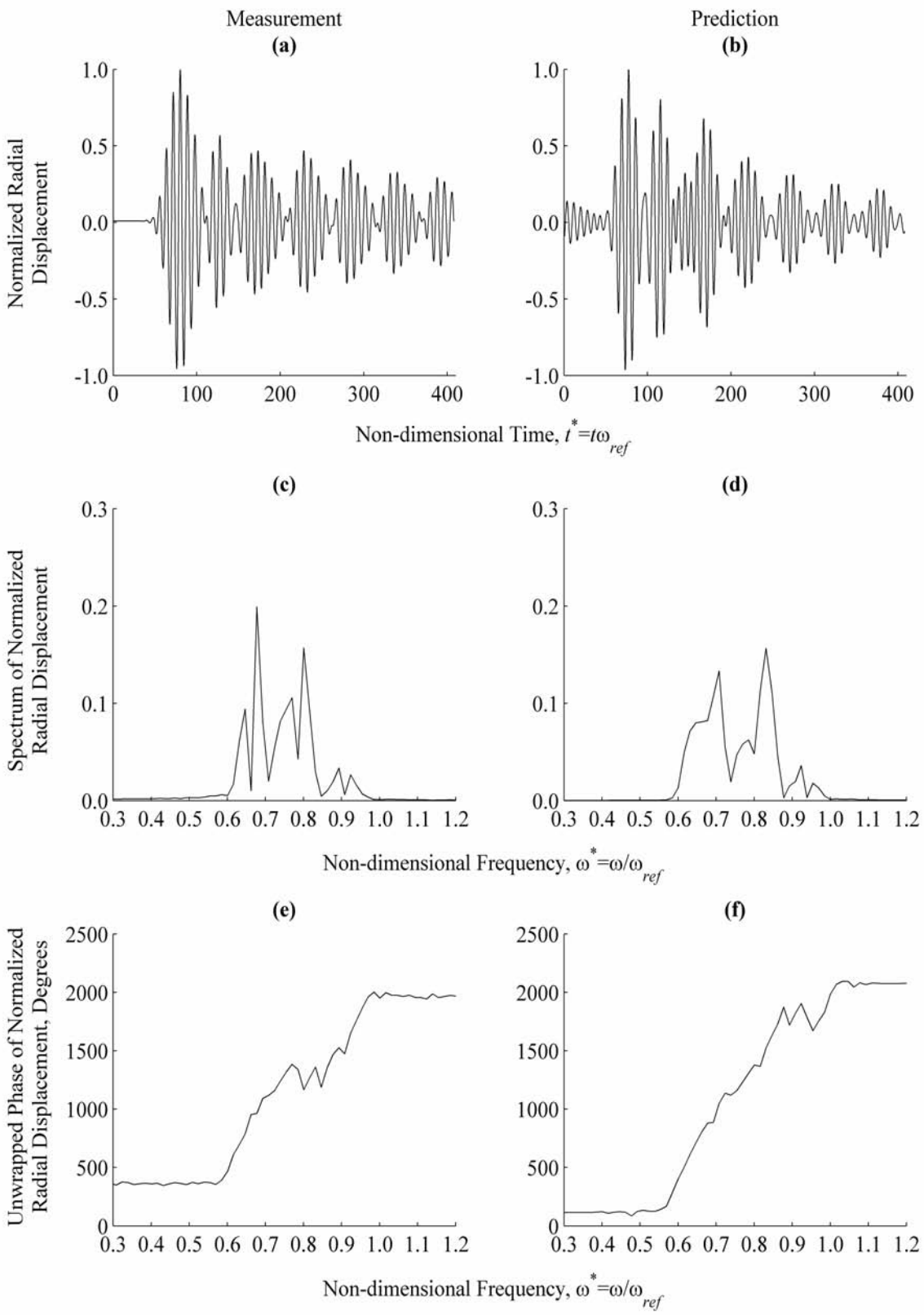

Figure H.88. Measurement and Prediction at $\theta=130^{\circ}$, $z^*=25.50$

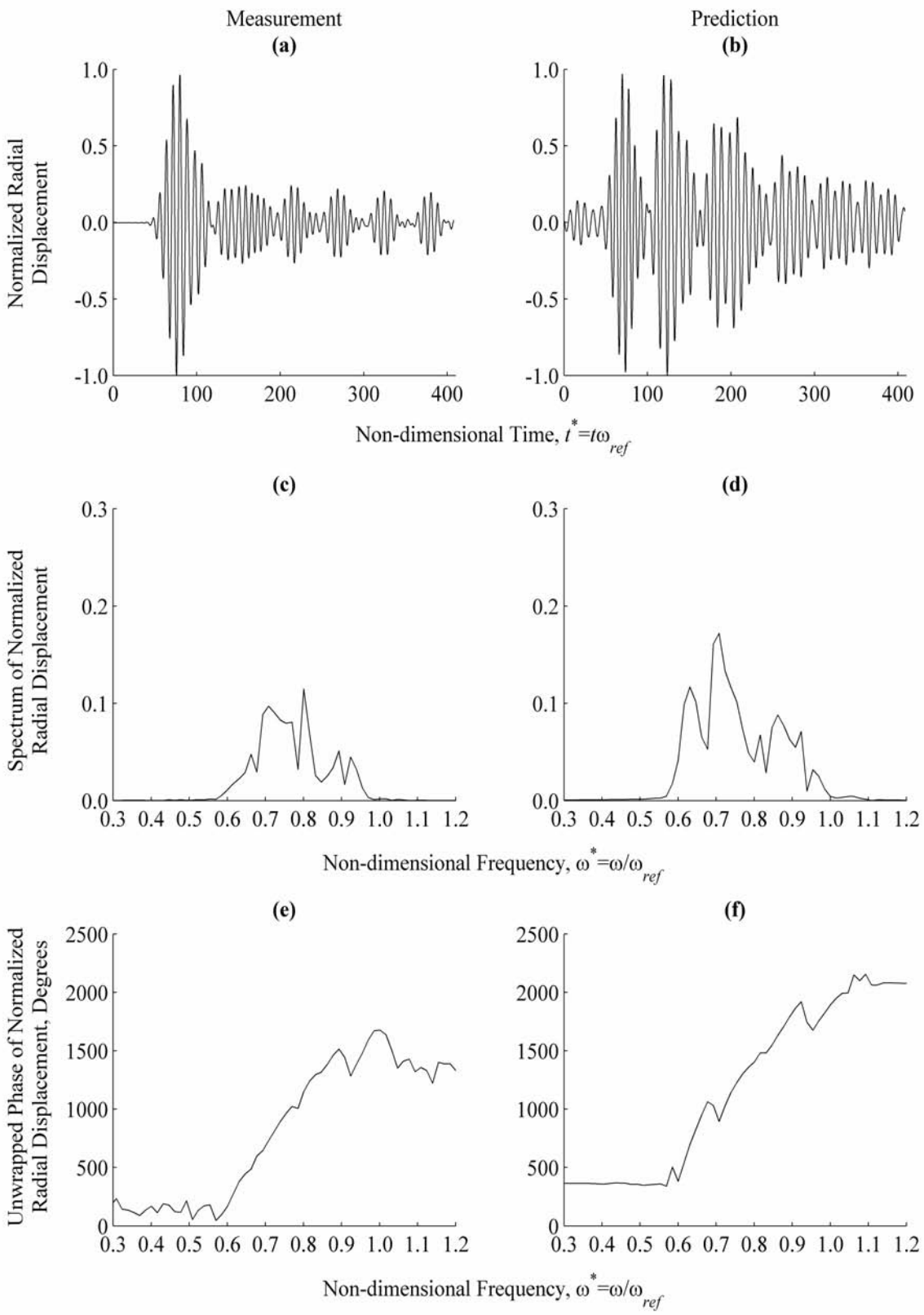

Figure H.89. Measurement and Prediction at $\theta=140^{\circ}$, $z^*=25.50$

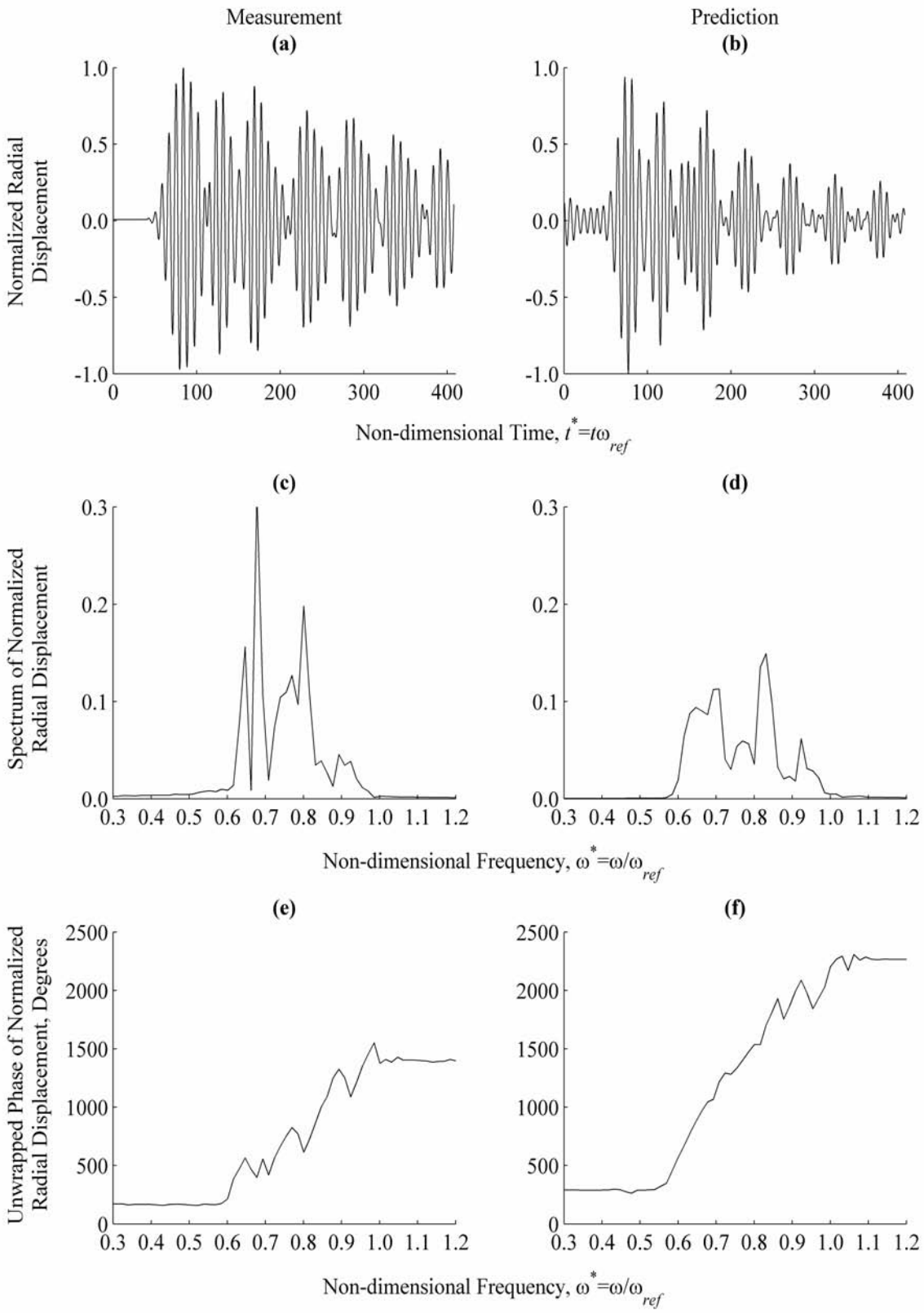

Figure H.90. Measurement and Prediction at $\theta=150^{\circ}$, $z^*=25.50$

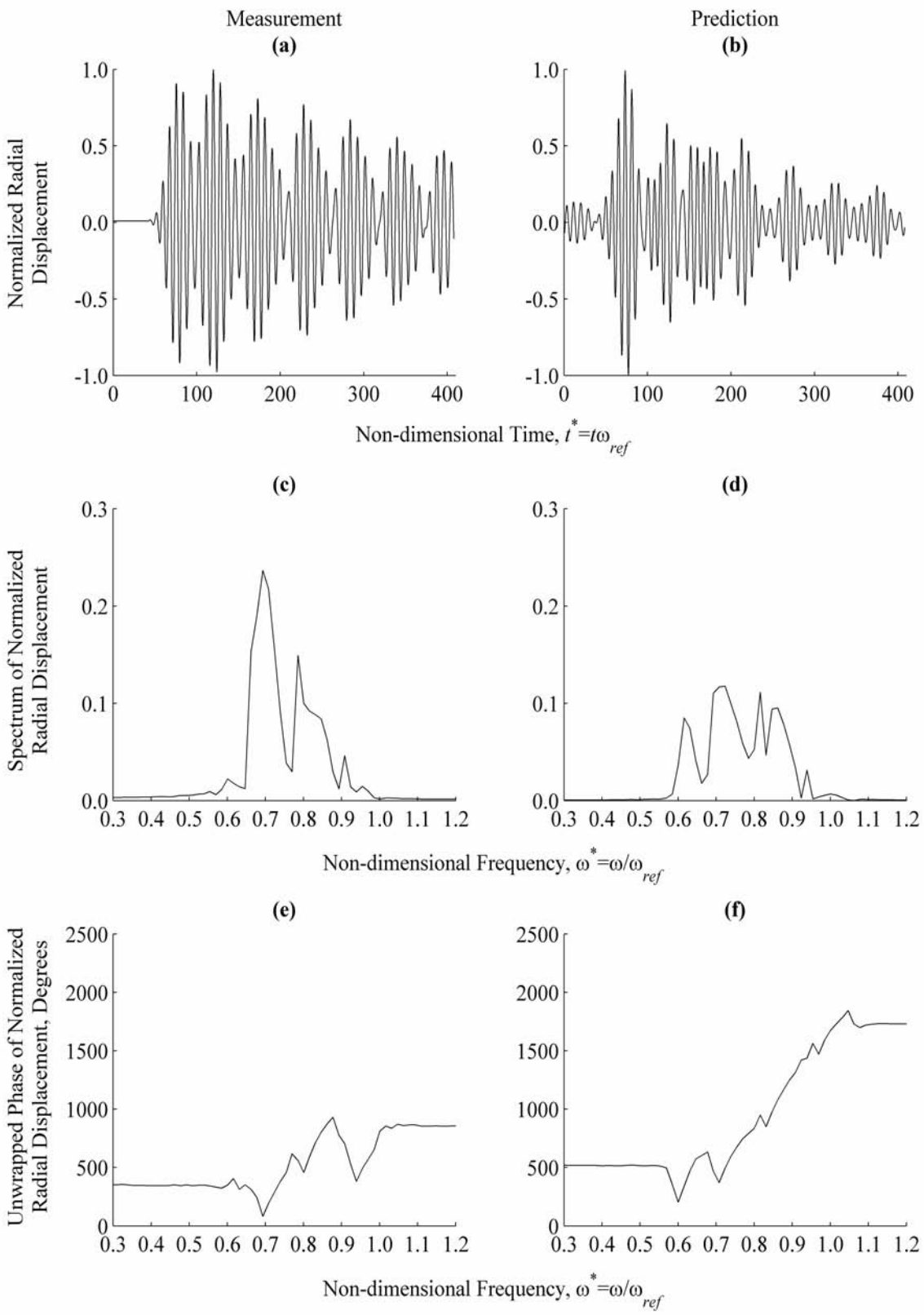

Figure H.91. Measurement and Prediction at $\theta=160^{\circ}$, $z^*=25.50$

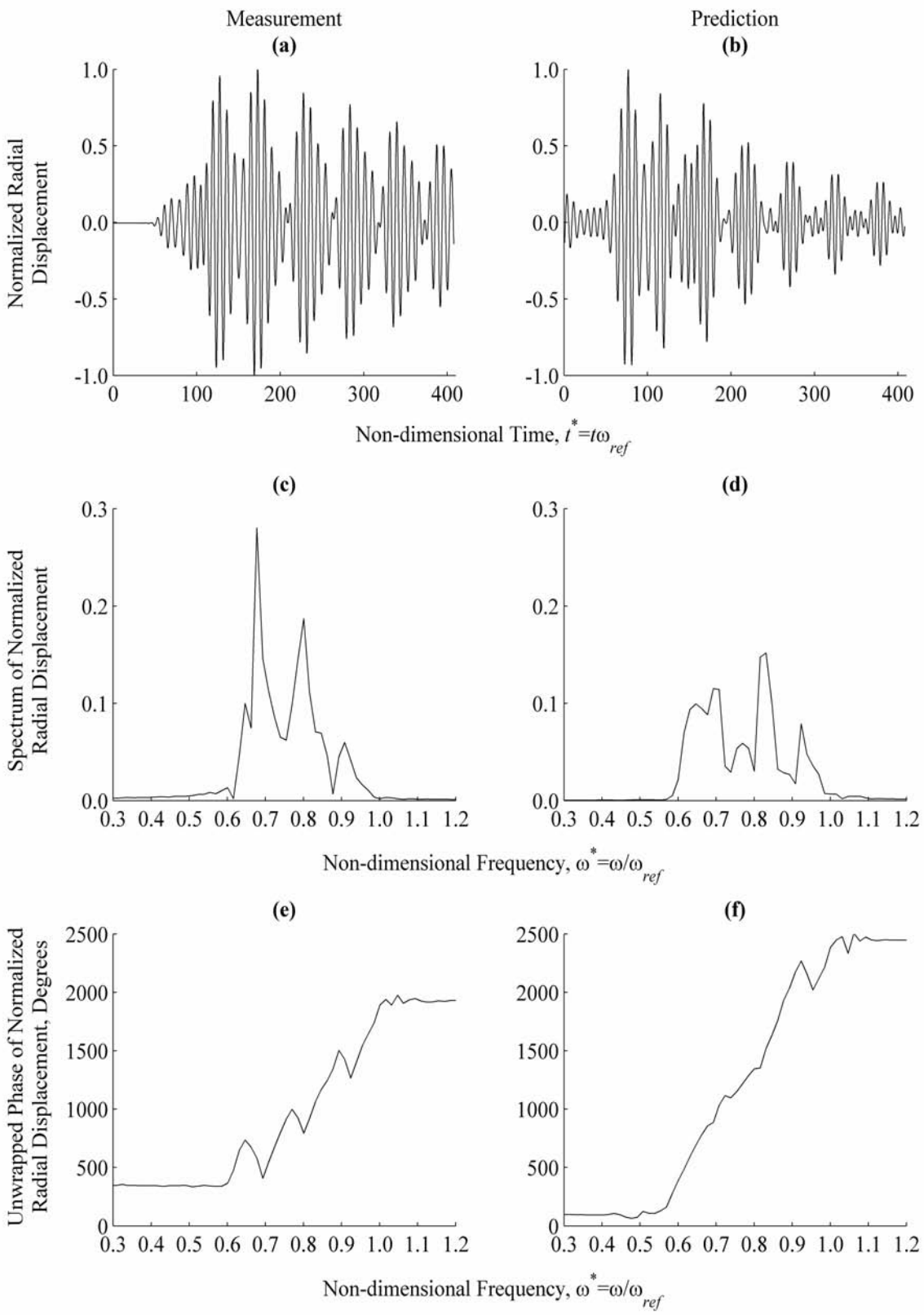

Figure H.92. Measurement and Prediction at $\theta=170^{\circ}$, $z^*=25.50$

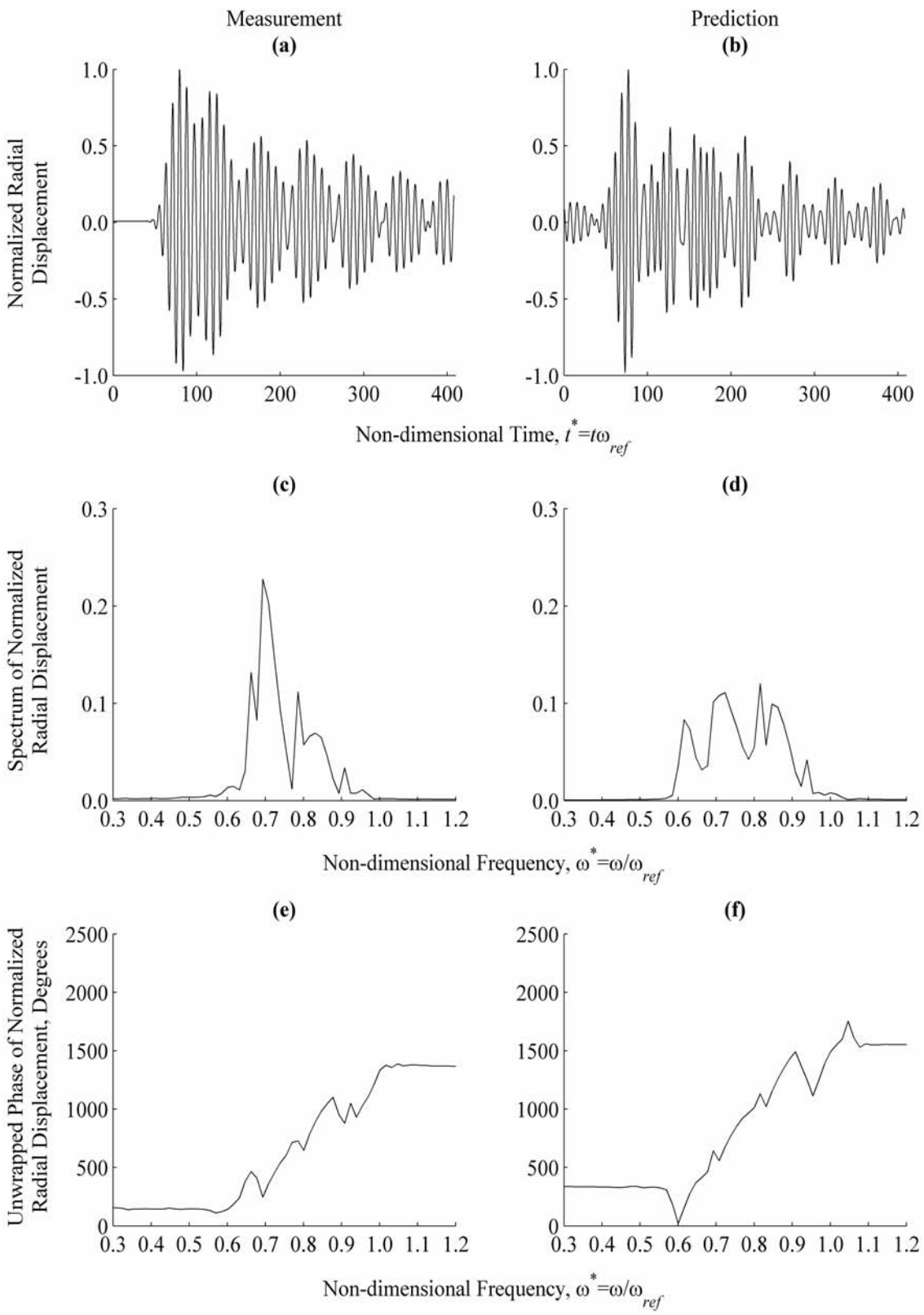

Figure H.93. Measurement and Prediction at $\theta=180^{\circ}$, $z^*=25.50$